Sandwich-HP

Vertical Hydraulic Sandwich Sealing System

A joint project of:

In cooperation with associated partners:

GRS - 745

Gesellschaft für Anlagen-
und Reaktorsicherheit
(GRS) gGmbH

Sandwich-HP

Vertical Hydraulic Sandwich Sealing System

Final Report

Klaus Wieczorek (GRS)
Katja Emmerich (KIT-CMM)
Thomas Nagel (TUBAF)
Eleanor Bakker (KIT-CMM)
Ralf Diedel (SSKG)
Markus Furche (BGR)
José Luis García-Siñeriz (Amberg)
Uwe Glaubach (IBeWa)
Jürgen Hesser (BGR)
Matthias Hinze (GRS)
Martin Hofmann (TUBAF)
David Jaeggi (swisstopo)
Franz Königer (ISU)
Juan Carlos Mayor Zurdo (Enresa)
Lysann Räbiger (IBeWa)
María Rey Mazón (Amberg)
Christopher Rölke (IfG)
Philipp Schädle (ENSI)
Rainer Schuhmann (ISU)
Hua Shao (BGR)
Susana Tuñón (Amberg)
Maria Victoria Villar Galicia (Ciemat)
Thomas Wilsnack (IBeWa)
Robert Yeatman (BDS)

February 2024

Remark:

This report refers to the joint research project under 02E11799A, 02E11799B and 02E11799C which has been funded by the German Federal Ministry for the Environment, Nature Conservation, Nuclear Safety and Consumer Protection (BMUV).

The work was conducted by GRS, KIT-CMM and TUBAF, the associated partner organizations BGR, swisstopo, Enresa, ENSI, NWMO, NWS and other contractors.

The authors are responsible for the content of the report.

GRS - 745
ISBN 978-3-910548-36-7

Keywords

Bentonite, Geological Repository, Mont Terri Rock Laboratory, Opalinus clay, Sandwich Sealing System, Shaft Sealing

Acknowledgement

The authors gratefully acknowledge the funding received by the German Federal Ministry of Economics and Energy (BMWi) and later by the German Federal Ministry for the Environment, Nature Conservation, Nuclear Safety and Consumer Protection (BMUV), represented by the Project Management Agency Karlsruhe (PTKA), contracts 02E11799A, 02E11799B, 02E11799C.

The authors are also thankful for the fruitful collaboration with all project partners. Regarding the in-situ experiment, particular thanks go to Senecio Schefer and Thierry Theurillat (swisstopo) for the on-site management of the experiment, to the technical staff of GRS represented by Julia Gose, Michael Komischke, Abram Rogalski and Bernd Zehle for the work associated to rock instrumentation, to Schützeichel for shaft sinking, to the Amberg, BGR and Solexperts crews for the installation and instrumentation work as well as for data acquisition.

Regarding the laboratory work, special thanks go to Silke Schönauer (KIT) for sample preparation for HTV-8 and help with the preparation of figures, Kristian Nikoloski (KIT-AGW) for his introduction to the sample preparation equipment, Nadja Werling (KIT) for the mineralogical analysis for HTV-8, Marita Heinle (KIT-IFG) for the ICP-OES measurements, Silke Berberich (KIT) for IC and ICP-OES measurements, Wiebke Baille (RUB) for the swelling pressure measurements and determination of Proctor curves of ES material, Michael Skubisch (RUB) for determination of the Proctor density of N45, Sarah Häußer (SSKG) for material selection, Carlos Gutiérrez-Álvarez, Rubén Javier Iglesias, G. García-Herrera and Iglesias Martinez (CIEMAT) for determination of water retention curves and swelling pressure tests, Nora Groschopf (University Mainz) for the XRF analysis, Jan Aurich, Holger Kempe, Tilo Tobies, Rico Steffen and Volker Beyer (TUBAF) for installation and sampling of HTV-7 to HTV-9 and FGK for measurements of the mass gain of bentonites.

Abstract

An important component for the closure of deep geological repositories (being accessed by a shaft) is a shaft sealing system which limits the fluid inflow from the adjacent rock to the repository in the early post-closure phase and delays the release of possibly contaminated fluids from the repository at a later stage. The KIT-developed Sandwich sealing system is a multi-component barrier which can contribute to this sealing function and is considered as part of the shaft sealing concepts for a final repository of radioactive waste in Germany.

The Sandwich sealing system consists of alternating sealing segments of bentonite and equipotential segments that are characterized by a high hydraulic conductivity. Within the equipotential segments fluid is evenly distributed over the cross section of the seal. Water bypassing the seal via the excavation damaged zone, or penetrating the seal inhomogeneously, is contained and a more homogeneous hydration and swelling of the sealing segment is obtained.

The functionality of the system has already been proven in semi-technical scale experiments. It was the aim of this project to install a large-scale in-situ experiment that addresses the interaction between the sealing system and the host rock. The experiment at the Mont Terri rock laboratory consists of two experimental shafts in which Sandwich sealing systems have been installed. The sealing systems can be saturated from pressure chambers located at the shaft bottoms via inclined lateral feeding boreholes. The seals and the surrounding rock will be intensely monitored.

The experiment objectives were to demonstrate the feasibility of installation, to investigate the saturation process, to qualify measurement and monitoring techniques, and to assess the sealing effectiveness. Particularly, the investigation of the long-lasting saturation process and the latter two objectives will be pursued in follow-up projects. The in-situ work was complemented by a laboratory testing campaign for material characterization, by further semi-technical scale experiments and model simulation.

Kurzfassung

Eine wichtige Komponente für den Verschluss von geologischen Tiefenlagern (die über einen Schacht erschlossen werden) ist ein Schachtverschlusssystem, das in der frühen Nachverschlussphase den Lösungszutritt aus dem angrenzenden Gestein in das Endlager begrenzt und die spätere Freisetzung von möglicherweise kontaminierten Flüssigkeiten aus dem Endlager verzögert. Das am KIT entwickelte Sandwich-Dichtsystem ist eine Mehrkomponenten-Barriere, die zu dieser Abdichtungsfunktion beitragen kann und als Komponente in Schachtverschlusskonzepten für ein Endlager für radioaktive Abfälle in Deutschland in Betracht gezogen wird.

Das Sandwich-System besteht aus alternierenden Dichtsegmenten aus Bentonit und Äquipotentialsegmenten, die sich durch eine hohe hydraulische Leitfähigkeit auszeichnen. Innerhalb der Äquipotentialsegmente wird Lösung gleichmäßig über den Querschnitt der Dichtung verteilt. Wasser, das die Dichtung über die Auflockerungszone umgeht oder die Dichtung inhomogen durchströmt, wird aufgefangen, und es kommt zu einer gleichmäßigeren Aufsättigung und Quellung des Dichtsegments.

Die Funktionalität des Systems wurde bereits in halbtechnischen Versuchen nachgewiesen. Ziel dieses Projekts war es, ein groß angelegtes In-situ-Experiment zu installieren, das die Wechselwirkung zwischen dem Dichtsystem und dem Wirtsgestein untersucht. Das Experiment im Felslabor Mont Terri besteht aus zwei Versuchsschächten, in denen Sandwich-Systeme installiert wurden. Die Dichtsysteme können von Druckkammern, die sich an den Schachtsohlen befinden, über geneigte seitliche Zuführungsbohrungen aufgesättigt werden. Das Dichtsystem und das umgebende Gebirge werden intensiv durch Sensoren überwacht.

Ziel des Experiments ist es, die Machbarkeit des Einbaus zu demonstrieren, den Sättigungsprozess zu untersuchen, die Mess- und Überwachungstechniken zu qualifizieren und die Wirksamkeit der Abdichtung zu bewerten. Insbesondere die langandauernde Aufsättigung sowie die beiden letzten Ziele können erst zu einem späteren Zeitpunkt in Folgevorhaben erreicht werden. Die In-situ-Arbeiten wurden durch umfangreiche Laboruntersuchungen zur Materialcharakterisierung, durch weitere halbtechnische Versuche sowie Modellsimulationen ergänzt.

Table of contents

1 Introduction

1.1 Multi-barrier concept and shaft sealing

Repositories for disposal of radioactive waste generally rely on a muti-barrier system to isolate the waste from the biosphere. This multi-barrier system typically comprises the natural geological barrier provided by the repository host rock and its surroundings and an engineered barrier system (EBS) /NEA 03/. In addition, treatment and encapsulation of the radioactive waste is considered as technical barrier and thus part of the multi-barrier system.

Shaft seals are part of the EBS and are designed to block potential pathways for radio-nuclide migration between a nuclear waste repository and the biosphere. Their role is to limit the fluid inflow from the adjacent rock in the early stage after closure of the repository and to delay the release of possibly contaminated fluids from the repository at later stage.

The German regulator demands that with respect to the reliability of containment, the interplay of barriers has to be optimized in diverse redundancy and shaft seals should be constructed of diverse redundant components /BMU 20/. Current German concepts of shaft seals contain the hydraulic Sandwich sealing system as a component of the lower seal in the host rock /KUD 21/.

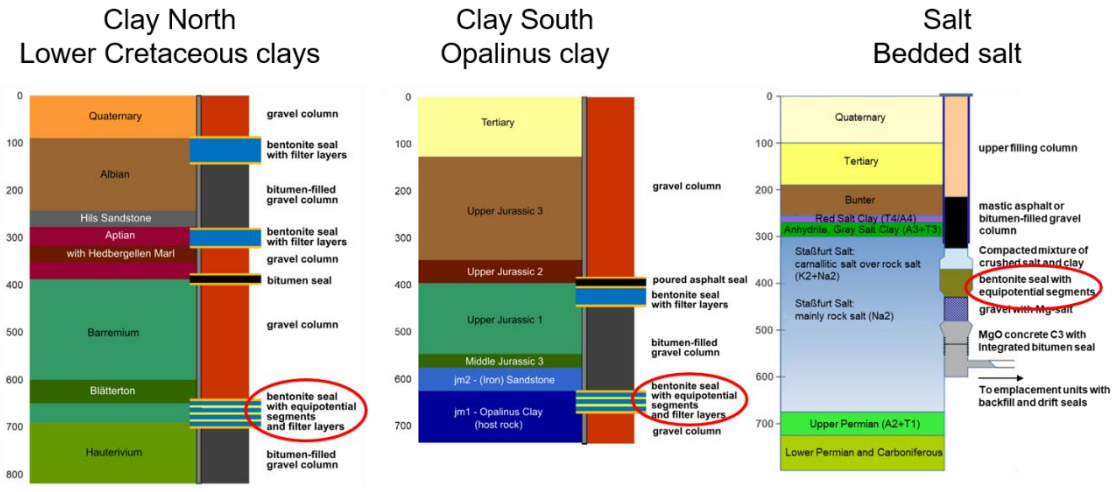

Fig. 1.1 Shaft seals in generic site models of Germany

1.2 The Sandwich sealing system

In contrast to conventional shaft seals of monolithic bentonite /NOL 02/ the Sandwich sealing system (Fig. 1.2), developed by KIT /NÜE 02/, consists of sealing segments (DS) of bentonite and equipotential segments (ES) that are characterized by a higher hydraulic conductivity. Within the ES fluid is evenly distributed over the cross section of the seal. Water bypassing the seal via the excavation damaged zone (EDZ) or penetrating the seal inhomogeneously by fingering or along sensors, is contained and a more homogeneous hydration and swelling of the DS is obtained. Proof of functionality of the system has been produced in semi-technical scale experiments /SCH 09/ and /EMM 19/.

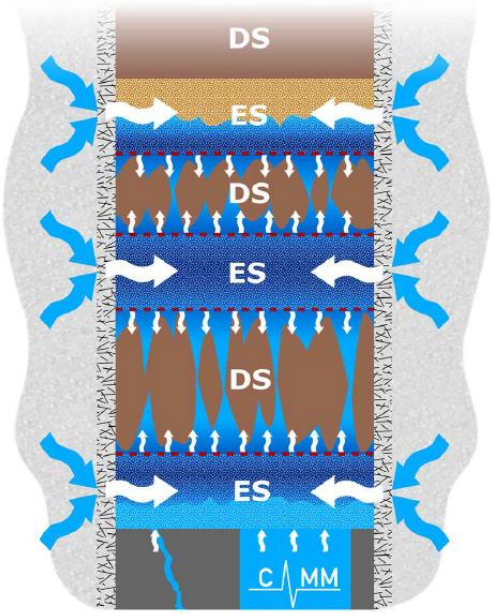

Fig. 1.2 Scheme of the Sandwich sealing system

1.3 The Sandwich-VP project

After mock-up experiments showing the functionality of the Sandwich system have been successfully completed, a large-scale experiment considering the interaction with a clay host rock was envisaged at the international Mont Terri rock laboratory (MTRL, Switzerland) situated in Opalinus clay. The comprehensive planning was performed in the frame of the Sandwich pre-project (VP) from 7/2017 to 6/2019 funded by BMWi (02E11587) in cooperation with international partners. During the Sandwich-VP already, a niche was excavated at MTRL in the lower sandy facies of the Opalinus clay to provide the test site

for the large-scale experiment. Furthermore, material parameters for different raw materials mined in Germany for DS and ES in interaction with Pearson water, which is the pore fluid of Opalinus clay at MTRL, were studied in single material tests as well as in MiniSandwich and in semi-technical scale experiments. Scoping calculations showed that the experiment could be performed without an inadmissible mutual interaction between the two planned shafts or the seal systems in the shafts and the gallery. Furthermore, the bentonite suction pressure and not the injection pressure will govern the resaturation process. The draft test plan for Shaft 1 was generated /EMM 19/.

2 Sandwich-HP objectives and project organization

2.1 Objectives

The aim of the project “Sandwich-HP: Vertical hydraulic Sandwich sealing system” with the original German title “Vertikales hydraulisches Dichtsystem nach dem Sandwich-Prinzip – Hauptprojekt” was to install a large-scale in-situ experiment using a Sandwich sealing system. The following objectives of the experiment were defined /EMM 19/:

1. Feasibility of installation
   - Scale transition (semi-technical scale to large scale, but not full scale)
   - Meeting requirements of real scale (e.g., workplace safety)
   - Hydration system
   - Compaction of DS und ES around the sensors
2. Investigation of the saturation process
   - Hydration of the seal by injection
   - Resaturation of the host rock
   - Interaction of the excavation damaged zone (EDZ) with equipotential and sealing segments
3. Qualification of measurement and monitoring techniques (instrumentation)
   - Durability of instrumentation
   - Multi-parameter monitoring (fiber-optics)
   - Optional: wireless data transmission
4. Assessment of sealing effectiveness
5. Evaluation and validation, risk management – second experimental shaft
   - Back-up for failures due to experiment design and execution
   - Allowing for the evolution of a pronounced EDZ before seal emplacement
   - Variation of emplacement technology – partly saturated ES

The Sandwich-HP project can be understood as the physical implementation of the results from the Sandwich-VP project (Chap. 1.3). However, not all the above objectives can be pursued within one project phase. Particularly, the investigation of the saturation process and the durability of instrumentation are long-term tasks to be continued in the follow-up project Sandwich-HP2 (contracts 02E12163A, 02E12163B, 02E12163C) and the assessment of the sealing effectiveness can only be conducted by a further monitoring phase and a complete dismantling of the experiment in a subsequent project phase.

The work program of the Sandwich-HP project comprises besides the installation of the in-situ experiment (Chap 3) and associated measurements (Chap. 4) also laboratory work for material characterization (Chap. 5) and model simulation for parameter calibration and prediction of the system behavior (Chap. 6). The laboratory part is associated to the support project Sandwich-SP1 (contracts 02E12001A, 02E12001B) dealing with the heterogeneous hydration of bentonite.

2.2 Organization and roles

The project was conducted by the following partner organizations:

- Gesellschaft für Anlagen- und Reaktorsicherheit (GRS) gGmbH, Germany
- Competence Center for Material Moisture at Karlsruhe Institute of Technology (KIT-CMM), Germany
- TU Bergakademie Freiberg (TUBAF), Germany
- Federal Institute for Geosciences and Natural Resources (BGR), Germany
- Swiss Federal Office of Topography (swisstopo), Switzerland
- Empresa Nacional de Residuos Radiactivos, S.A., S.M.E. (Enresa), Spain
- Swiss Nuclear Safety Inspectorate (ENSI), Switzerland
- Nuclear Waste Management Organization (NWMO), Canada
- Nuclear Waste Services (NWS), Great Britain

Funding was provided by the German Federal Ministry of Economics and Energy (BMWi) and later by the German Federal Ministry for the Environment, Nature Conservation, Nuclear Safety and Consumer Protection (BMUV) to KIT-CMM, GRS and TUBAF

(contracts 0211799A, 0211799B, 0211799C) and the associated partners BGR, swisstopo, Enresa, ENSI, NWMO and NWS contributed with own resources. Moreover, the following contractors worked on the project:

- Amberg Infraestructuras, S.A. (Amberg), Spain
- Centro de Investigaciones Energéticas, Medioambientales y Tecnológicas (CIEMAT), Spain
- Ingenieur-Gesellschaft für Sensorik in der Umwelttechnik (ISU), Germany
- Ingenieurpartnerschaft für Bergbau, Wasser und Deponietechnik Wilsnack und Partner (IBeWa), Germany
- Institut für Gebirgsmechanik GmbH Leipzig (IfG), Germany
- Stephan Schmidt KG (SSKG), Germany
- Gerätebau Wiedtal Schützeichel GmbH & Co. KG (Schützeichel), Germany
- Solexperts AG (Solexperts), Switzerland
- Sigeom SA (Sigeom), Switzerland
- Glötzl Gesellschaft für Baumesstechnik mbH (Glötzl), Germany
- VersuchsStollen Hagerbach AG (VSH), Switzerland
- Better Data Systems (BDS), Switzerland

The work program of the project was split in eight work packages (WP):

- WP 1 Test plan: The test plan for the two experimental shafts was developed by Amberg with the support of the remaining partners.
- WP 2 Rock instrumentation: The rock instrumentation in the vicinity of the experimental shafts including sampling was accomplished by BGR and GRS.
- WP 3 Shaft sinking and EDZ characterization: The associated work was performed by GRS, swisstopo, BGR and Schützeichel.
- WP 4 Installation and instrumentation of seal and EDZ: The associated work was performed by KIT-CMM, GRS, BGR, swisstopo, Enresa, SSKG, ISU, IBeWa and Amberg.

- WP 5 Operation, monitoring and data handling: The associated work was performed by GRS, KIT-CMM, BGR, ISU, swisstopo, Amberg and BDS.
- WP 6 Laboratory works: The laboratory works were conducted by KIT-CMM, GRS, BGR, IfG, ISU, TUBAF, SSKG, IBeWa and CIEMAT.
- WP 7 Modelling: The modelling was performed by GRS, BGR and ENSI.
- WP 8 Documentation and reporting: The associated work including project organization and supervision was accomplished by GRS and KIT-CMM.

An overview of the project organization is given in Fig. 2.1.

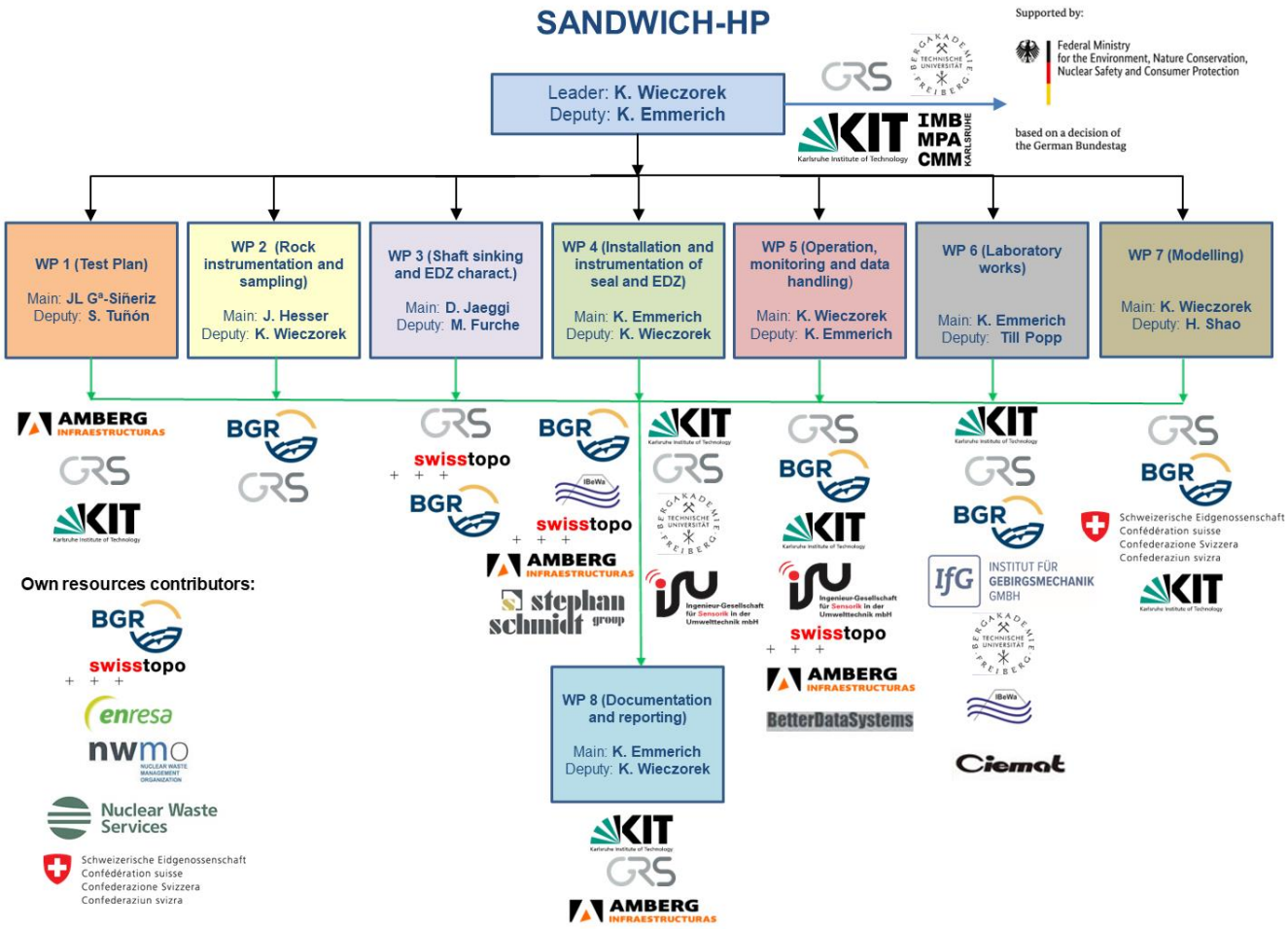

Fig. 2.1 Organization of the Sandwich-HP project

3 The in-situ experiment – design and construction

A major part of the Sandwich-HP project is a large-scale in-situ experiment assessing the functionality of the Sandwich sealing system interacting with the surrounding host rock. This experiment, called SW-A, is performed at the Mont Terri rock laboratory (MTRL) in St-Ursanne (Switzerland).

The SW-A experiment was launched in July 2019. It consists of two experimental shafts of 1.18 m diameter and 10 m – 12.6 m depth, constructed using a core drilling technique in a new niche in the sandy facies of the Opalinus clay. Vertical hydraulic Sandwich sealing systems have been installed in both shafts which can be saturated from pressure chambers located at the shaft bottoms via lateral feeding boreholes (Fig. 3.1). The sealing systems and the surrounding rock are intensely monitored.

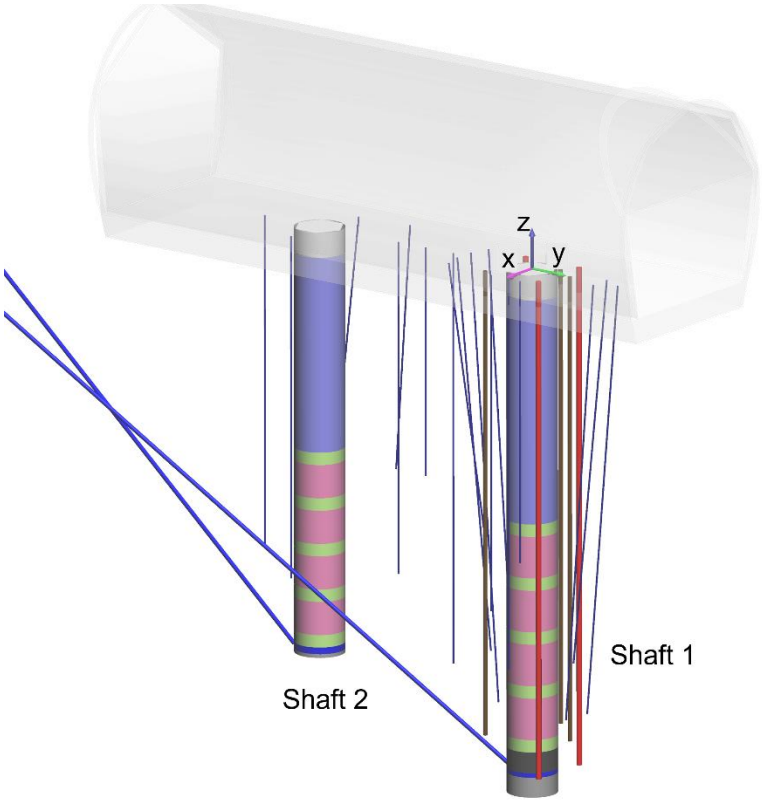

Fig. 3.1 Overview of the SW-A experiment

The sealing system in Shaft 1 consists of four DS (made of the calcium bentonite Calcigel) of 1 m thickness and five ES (made of fine-grained quartz sand), each 30 cm thick and has been in operation since May 2021. Shaft 2 hosts a slightly modified system which was emplaced in the second half of 2022 and is in operation since the end of May

2023. The four DS are 80 cm thick and only the upper two DS are made of Calcigel whereas the lower two are made of the calcium bentonite Securso l® MHP1 (70/30). The configuration of both shafts is given in Fig. 3.2.

All information regarding construction, instrumentation and measurement results for the SW-A experiment are described in Chap. 3 and Chap. 4. More details regarding Shaft 1 can be found in the as-built document /GAR 22/ and the two data reports /WIE 23a/ and /WIE 23b/. For Shaft 2, the details are given in the test plan /WIE 22a/ and the as-built documents /GAR 23a/, /GAR 23b/ and /GAR 23c/.

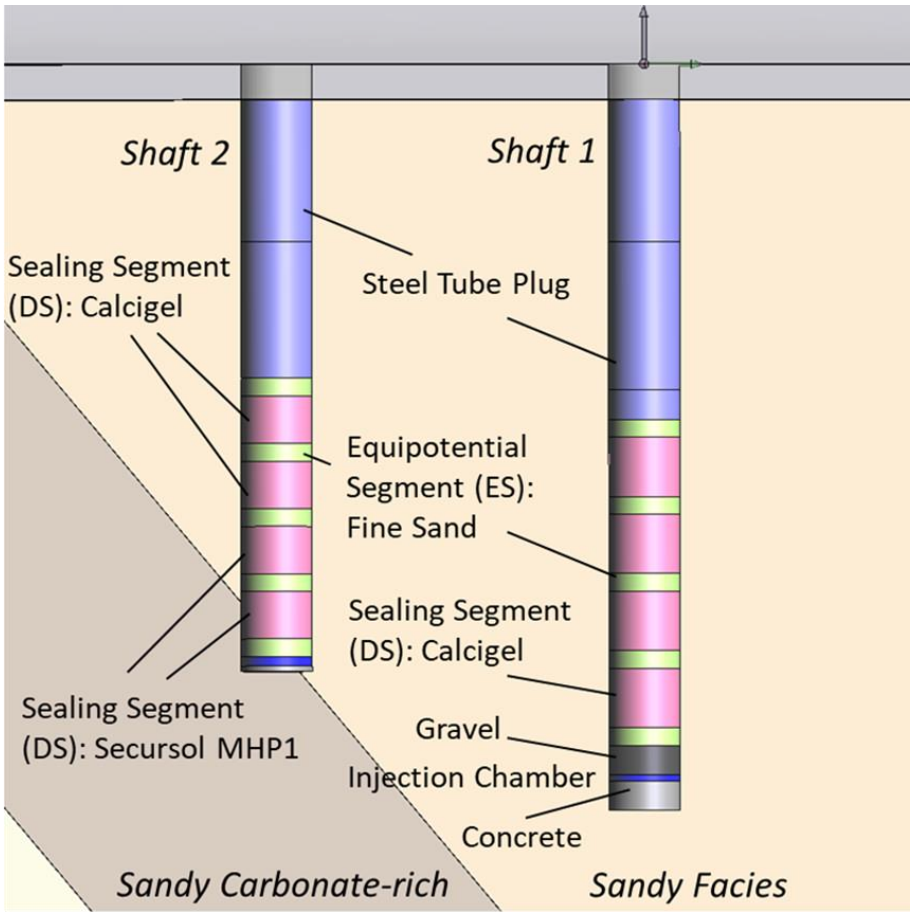

Fig. 3.2 Configuration of the experimental shafts

3.1 Location in the MTRL

The two experimental shafts are located in Niche 7 at MTRL, the so-called Sandwich niche which was excavated in 2018. The niche is located entirely in the sandy facies of

the Opalinus clay in the southern part of the laboratory in the extension (Gallery 18) excavated in 2018 (Fig. 3.3).

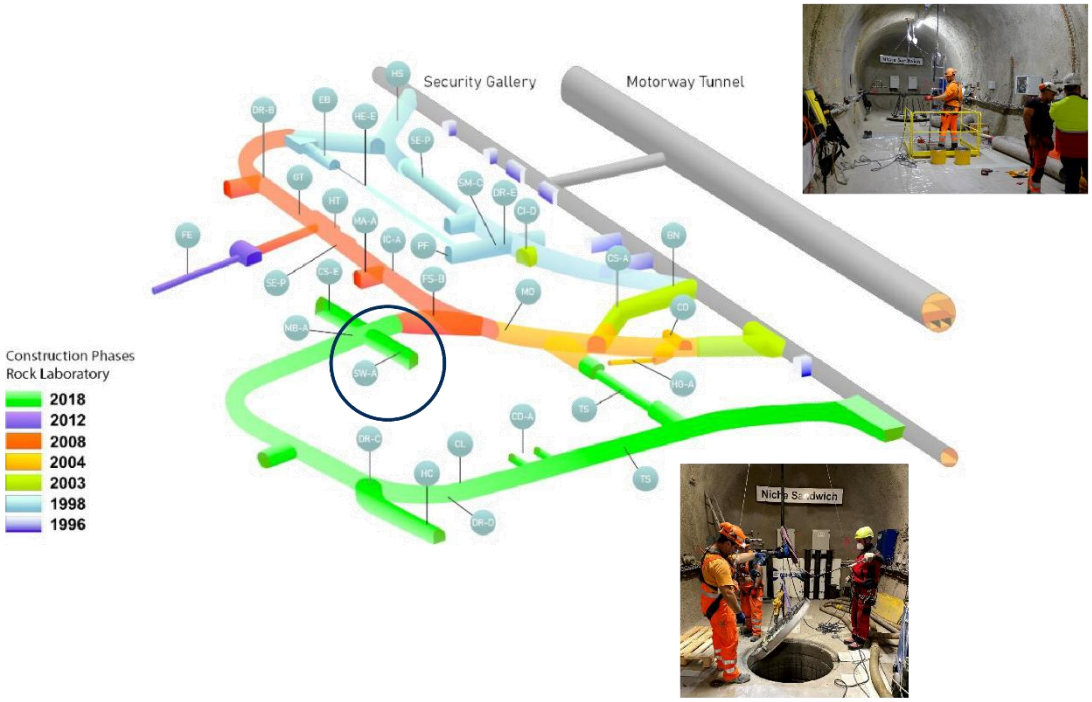

Fig. 3.3 Location of the SW-A experiment in the Mont Terri rock laboratory

3.2 Rock instrumentation and feeding boreholes

The rock around the experimental shafts has been instrumented (mostly) prior to shaft sinking with the aim to characterize the initial state of the rock and to observe the interaction of the rock with the sealing system during the experiment. Pore pressure, radial stress, temperature, seismic and ERT measurements have been performed. The details regarding the used sensors and their exact positions are given in Tab. A. 6.

The feeding boreholes were drilled to supply the hydration chambers at the bottoms of the experimental shafts with Pearson water A3 by a hydration tube coming from the surface of the adjacent Gallery 18.

3.2.1 Pore pressure sensors

Pore pressure sensors in the surrounding rock of the two experimental shafts have been installed to monitor the reaction of the fluid pressure in the rock to shaft sinking and hydration of the sealing system. A total number of 18 boreholes with a length between

5.5 m and 10.7 m and a diameter of 42 mm (and 20 mm near the bottom) were drilled and instrumented by GRS with mini-piezometer sensors. The location of the sensors relative to the experimental shafts is shown in Fig. 3.4. The boreholes BSW01 – BSW16 were drilled and installed prior to shaft sinking between October 2019 and January 2020. Two more boreholes (BSW32 and BSW33) were drilled and installed next to Shaft 2 in February 2023. It was found that, due to the angle between the boreholes and the bedding, the boreholes had a significant deviation in the direction of the niche entrance. BSW05_PP_1, which was originally located at the same side of Shaft 1 as BSW03_PP_1, BSW04_PP_1 and BSW06_PP_1 was hit by the later drilled stress measurement borehole BSW_A22. It was replaced by a new borehole on the other side of Shaft 1 (Fig. 3.4).

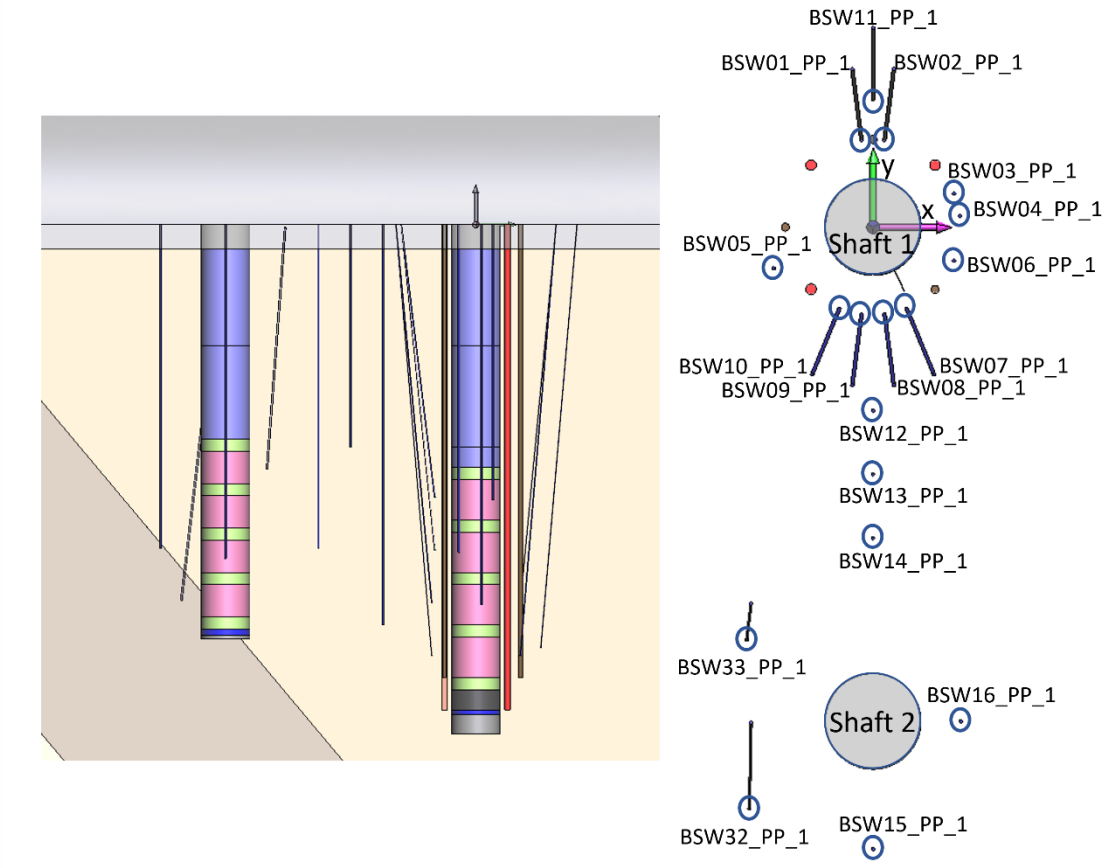

Fig. 3.4 Borehole locations and nomenclature of pore pressure sensors

The installed mini-piezometer sensors (Fig. 3.5) are mechanical mini-packers at the bottom of each borehole with a small test interval sealed to the top with synthetic resin. The test interval is connected to an absolute pressure sensor and the measured data are

recorded by the Geomonitor system which is the front-end data acquisition system for all conventional sensors in the experiment (see Chap. 3.6).

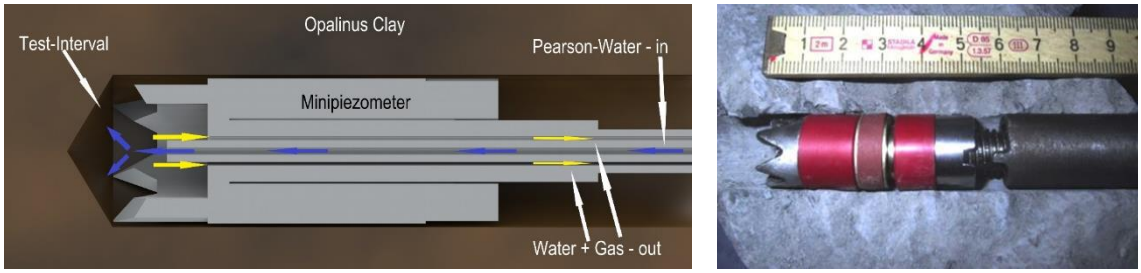

Fig. 3.5 GRS mini-piezometer sensor

3.2.2 Radial stress and temperature sensors

Stress monitoring stations are installed in three vertical boreholes in the surrounding rock mass to observe the reaction of the rock mass to the resaturation of the sealing system in Shaft 1, especially to the bentonite's swelling pressure. These boreholes are located in the strike direction of clay bedding (BSW-A20, BS01), in dipping direction of the clay bedding (BSW-A21, BS02) and with an angle of 45° to striking and dipping (BSW-A22, BS03). Locations of the three boreholes are depicted in Fig. 3.6. The boreholes were drilled by BGR with a diameter of 131 mm and a distance of 50 cm to the shaft contour. The stress monitoring stations were manufactured and installed by Glötzl Baumesstechnik in Rheinstetten, Germany.

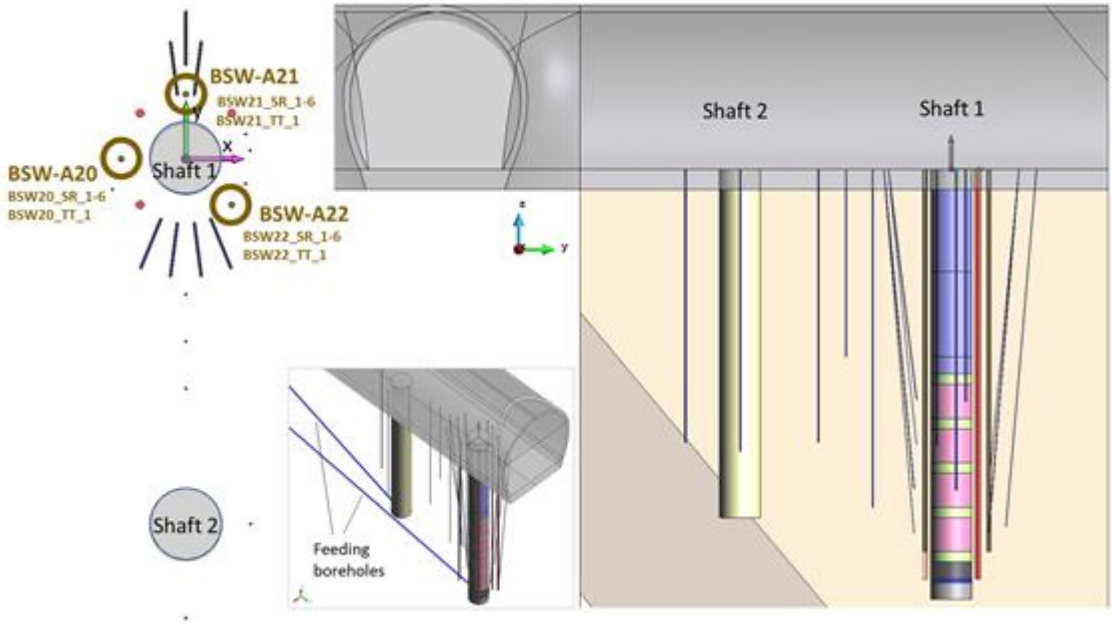

Fig. 3.6 Borehole locations for stress monitoring stations

The boreholes have a length of about 11.2 m. Each stress monitoring station consists of six stress cells with a rectangular surface of 20 cm x 30 cm. These cells are implemented in a steel frame and are oriented in a way to measure the radial stresses (perpendicular to the shaft contour). Each station has a length of 3.15 m. A temperature sensor is installed between the stress cells No. 3 and No. 4, in the center of the frame. The depths of the stress cells have been fixed based on the sealing segments' dimensions. Fig. 3.7 shows a picture of a stress monitoring station, a sketch with the depths of the stress cells in the boreholes and photos of the installation and reinjection works.

The sensors are connected to a data switch multiplexer. The analogue sensor signal is switched into a digital signal and sent to the central data acquisition unit MCC 5S. The MCC 5S is secured with a small uninterruptible power supply against short-term power losses. The internet access of the MCC 5S enables a remote maintenance and the change of parameters and the measuring intervals. More about the data acquisition is described in Chapter 3.6.

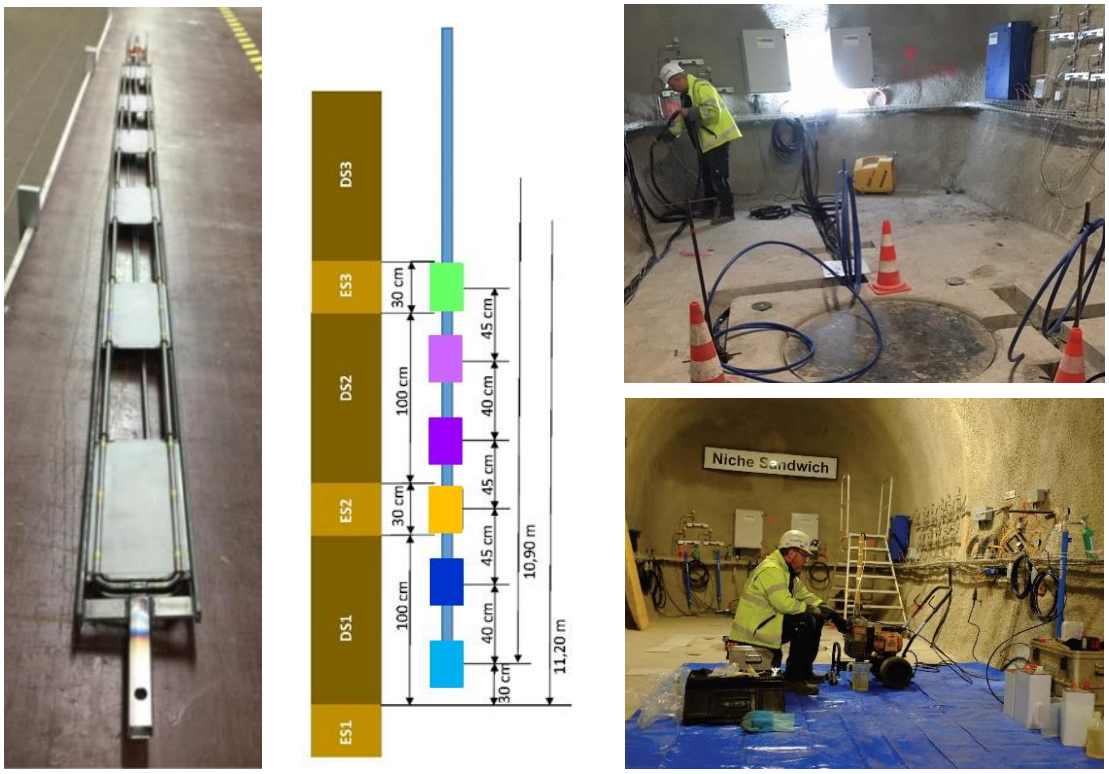

Fig. 3.7 Stress monitoring station with depth of the stress cells and documentation of installation and reinjection works

Each frame of the stress monitoring stations is equipped with a temperature sensor AD592 to observe the temperature during hydration of grout and the reinjection. Of

course, temperature development can be observed during duration of the experiment as well. The AD592 is a two-terminal monolithic temperature transducer that provides an output proportional to the absolute temperature. It is placed in the frame between the stress cells No. 3 and No. 4 (depth approximately 9.82 m). Sensor connection and data transfer is the same as described in Chapter 3.6 for the stress monitoring station.

3.2.3 Seismics and ERT

Seismic and ERT measurements were performed in three geophysical exploration boreholes (BSW-B17 – BSW-B19) to characterize the rock in the vicinity of Shaft 1. Boreholes BSW-B17 and BSW-B18 are located in the strike of the bedding, borehole BSW-B19 is perpendicular to it (Fig. 3.8). The boreholes were drilled by BGR with a diameter of 131 mm and in a distance of 51 cm to the shaft contour. The boreholes have a length of about 11.2 m. Casing and grouting of the boreholes were done by Solexperts.

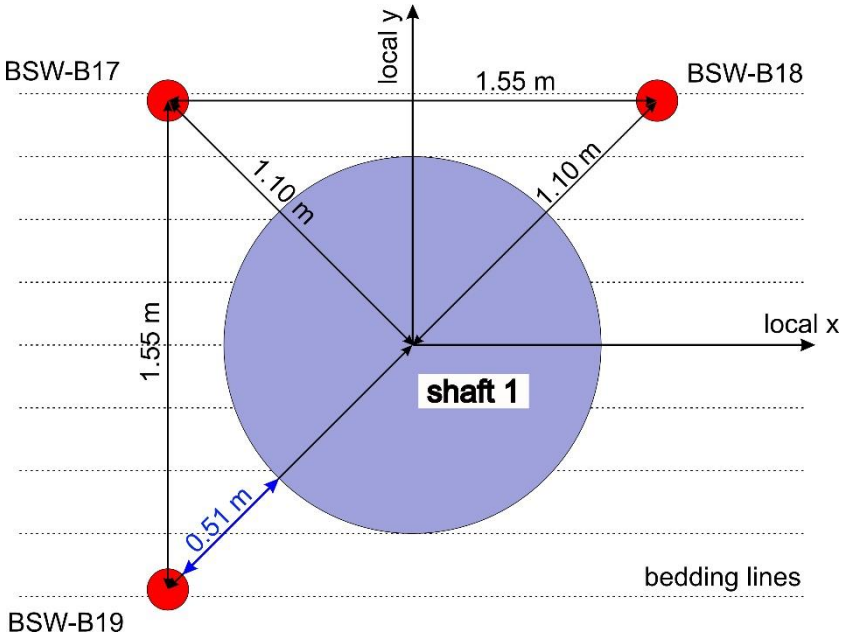

Fig. 3.8 Layout of the geophysical exploration boreholes BSW-B17 - B19

Seismic measurements were performed in each borehole (interval velocity measurements, IVM) and between separate boreholes as well as between a borehole and Shaft 1 (cross-hole velocity measurements, XHM), see Fig. 3.9. For the acquisition of interval velocity data, a seismic borehole probe with one seismic source and seven receivers was moved stepwise along the surveyed boreholes with 5 cm intervals. At each step, the probe actuator and sensors were pneumatically attached to the borehole wall to establish sufficient mechanical coupling for the generation and detection of the emitted impulsive

(“shot”) elastic waves (Fig. 3.10). For cross-hole measurements, a separate source probe (Fig. 3.11 left) was moved stepwise in one borehole, while the receiving probe was moved in the other. For the cross-hole measurements between BSW-B17 and Shaft 1, 1-channel and 3-channel piezo sensors were used along the shaft wall for signal acquisition (Fig. 3.11 right).

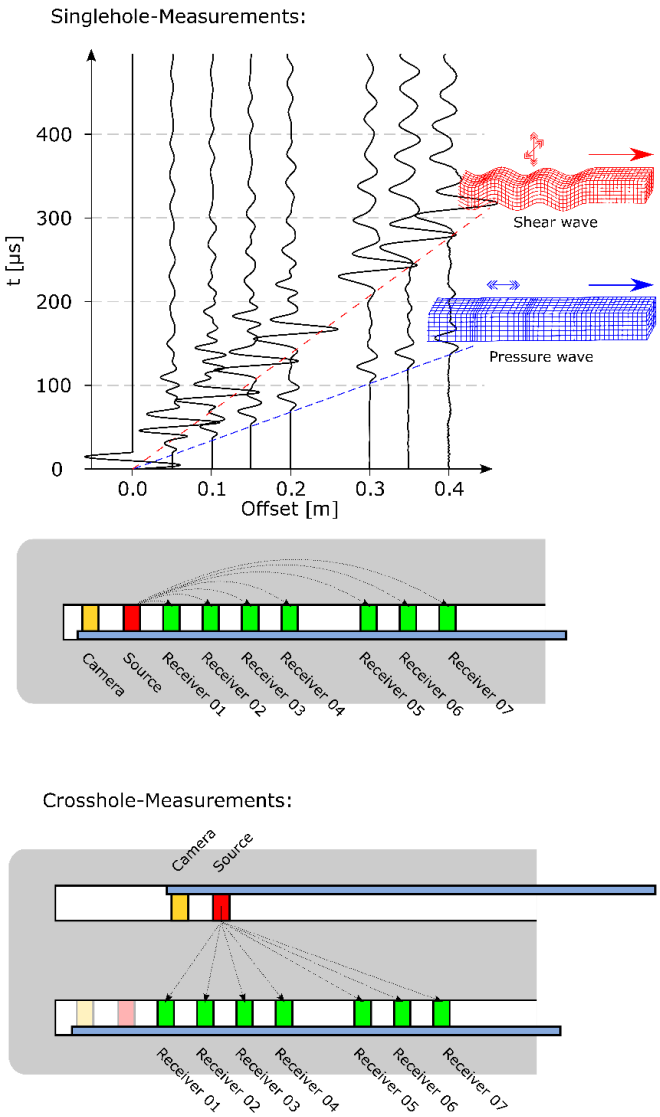

Fig. 3.9 Principle of seismic velocity measurements

Top: Emitted and recorded wave field at 0 to 40 cm distance. Blue: sketch of pressure wave propagation. Red: sketch of shear wave propagation. Bottom: geometry of interval velocity measurements (single hole) and cross hole velocity measurements

Fig. 3.10 Equipment for the BGR seismic velocity measurements

Top left to right: DAQ unit Gen2i, Pre-Amplifier, Pneumatic control unit, in front: borehole probe 8KUBS. Bottom left to right: signal generator with signal conditioner on top, laptop case, cable drum

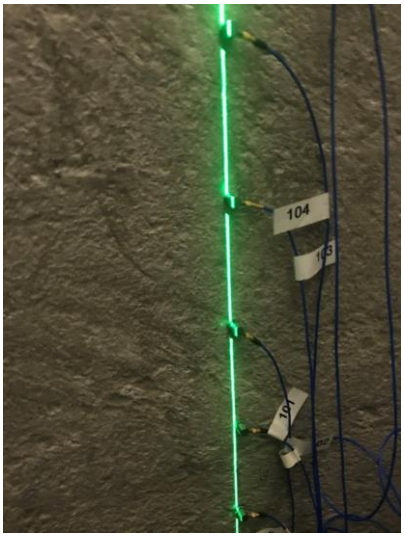

Fig. 3.11 Borehole source unit BIQ-2 (left) and 1-channel piezo sensors glued to the wall of Shaft 1 (right)

The ERT borehole measurements were performed using the high-resolution earth resistivity meter 4 point light 10W (Lippmann Geophysikalische Messgeräte), controlled by the GeoTest software (Geophysik – Dr. Rauen) installed on a laptop (Fig. 3.12).

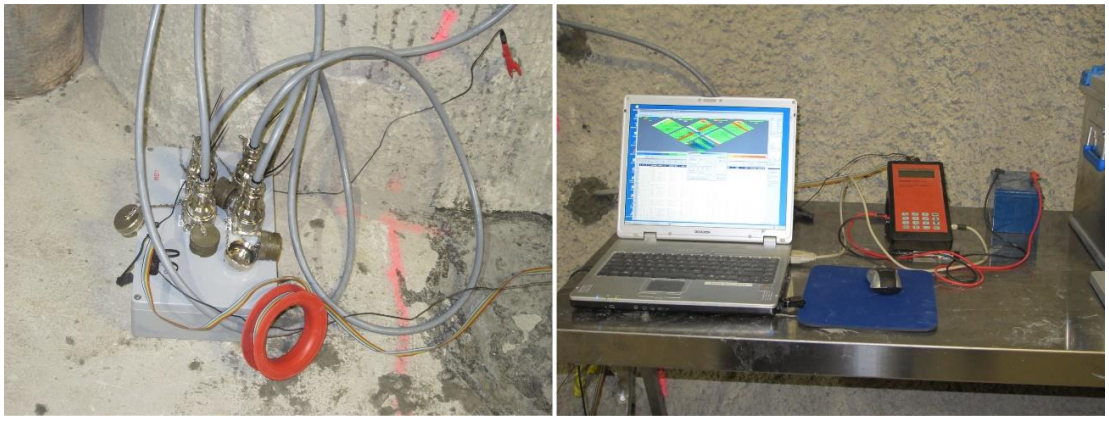

Fig. 3.12 ERT measuring system: multiplexer (left), resistivity meter and control laptop (right)

The BGR borehole probe GB100-15 (Fig. 3.13) consists of 100 electrodes with an electrode distance of 15 mm. The function of the electrodes is controlled by a multiplexer. The electrodes can be shifted pneumatically, retracted for probe movement, and extended for connection to the borehole wall. The tool diameter represents 80 mm for typical boreholes of 86 mm, the greater diameter of 132 mm was adapted.

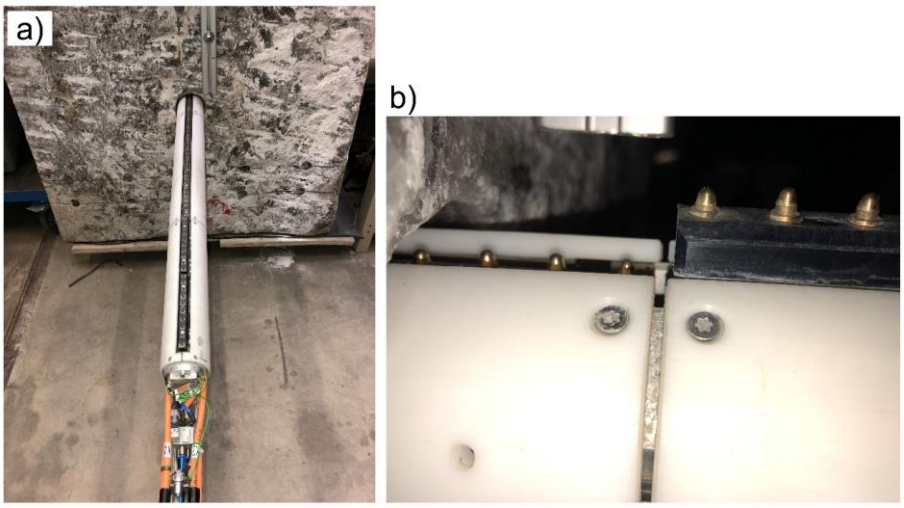

Fig. 3.13 BGR resistivity probe for high resolution single hole measurements (GB100-15)

a) overview
b) detailed view, left side electrodes retracted for probe movement, right side electrodes extended for connection to the borehole wall

3.2.4 Feeding boreholes

The drilling of the feeding boreholes BSW-B24 (Shaft 1) and BSW-B25 (Shaft 2) with a diameter of 76 mm was done by Schützeichel KG (see location of the boreholes in Fig. 3.1). Casings of 60 mm diameter (stainless steel, final segment PVC) were installed by Solexperts, see /RÖS 20/. The annulus between the borehole and the casing was filled with resin. At the wellhead of every feeding borehole a flange with an injection port and a ventilation port is mounted (Fig. 3.14).

Fig. 3.14 Feeding borehole BSW-B25 with steel casing

3.3 Experimental shafts

3.3.1 Shaft sinking

The excavation of the two 1180 mm diameter shafts was done by Schützeichel KG using a custom-made reinforced drill rig (two towers) electric/hydraulic, (Fig. 3.15). No casing is required provided that the shaft remains stable. Coring was done with air flushing using a strata cut crown on a single core barrel yielding cores of 1100 mm diameter. Core was broken off with hydraulic pads, which were inserted laterally into the annulus. Cores of 1100 mm diameter were retrieved with a core barrel over a 10 t winch, mounted on a forklift.

Fig. 3.15 Custom-made drill ring used by the company Schützeichel KG

The main facts about the excavation machine are as follows:

- Height: 4100 mm
- Width: 2460 x 2400 mm
- Lifting length 2.5 or 3.0 m depending on start rod
- Length of core barrel: 1500 mm
- Core barrel diameter 1180 mm (AD)
- Core diameter 1100 mm
- Total weight of core and core barrel: ca. 4 t
- Estimated RPM at operation (30)

The excavation of Shaft 1 took from August 17, 2020, to September 17, 2020 (including the last core extraction). Total excavated length was 12.59 m, and the feeding borehole has crossed at 12.12 m.

Afterwards, the excavation of the second shaft was performed as well. It started on October 12, 2020, and finished November 5, 2020. Total excavated length was 10.2 m (more details of shaft sinking, incl. geological documentation and daily reports are given in /JAE 22/). In Tab. 3.1 the drilling sequence for both shafts is given with the corresponding daily advance.

Tab. 3.1 Drilling sequence of both shafts with corresponding daily advance

Shaft	Date	Drilling interval	Advance	Actual depth
BSW – A1	17.08.2020 – 20.08.2020	0.60 – 2.10 m	1.50 m	2.10 m
	20.08.2020 – 24.08.2020	2.10 – 3.50 m	1.40 m	3.50 m
	26.08.2020	3.50 – 4.60 m	1.10 m	4.60 m
	27.08.2020 + 31.08.2020	4.60 – 6.00 m	1.40 m	6.00 m
	01.09.2020 – 02.09.2020	6.00 – 7.35 m	1.35 m	7.35 m
	07.09.2020	7.35 – 8.70 m	1.35 m	8.70 m
	08.09.2020 – 09.09.2020	8.70 – 10.06 m	1.36 m	10.06 m
	10.09.2020 + 14.09.2020	10.06 – 11.35 m	1.29 m	11.35 m
	16.09.2020	11.35 – 12.59 m	1.24 m	12.59 m
BSW – A2	13.10.2020	0.60 – 2.10 m	1.50 m	2.10 m
	15.10.2020	2.10 – 3.50 m	1.40 m	3.50 m
	26.10.2020	3.50 – 4.60 m	1.10 m	4.60 m
	27.10.2020 – 29.10.2020	4.60 – 6.50 m	1.90 m	6.50 m
	30.10.2020	6.50 – 7.60 m	1.10 m	7.60 m
	02.11.2020 – 03.11.2020	7.60 – 9.00 m	1.40 m	9.00 m
	04.11.2020	9.00 – 10.20 m	1.20 m	10.20 m

After drilling, the shafts were equipped with a foldable steel mesh K196, serving as a temporary lining. Then, as well ventilation, ladder and illumination were installed (Fig. 3.16).

Fig. 3.16 Safety installations including steel mesh lining, ventilation, illumination and access ladder (Photos by D. Jaeggi, swisstopo)

3.3.2 Geology

The Sandwich experiment is located in the Sandwich niche, which is entirely located in the lower sandy facies of the Opalinus Clay (Fig. 3.17). This facies type is characterized by calcareous and silty-sandy claystones, see /JAE 20/. In the Sandwich niche bedding dips to about 150/43°. At the entrance of the niche, in Ga18, the transition of lower sandy facies towards carbonate-rich sandy facies was observed. Thus, this transition is dipping towards the rear part of the niche which was taken into account for the planning of the two shafts. Already for the geological prognosis for the two shafts it was clear that Shaft 2 will hit the transition towards the carbonate-rich sandy facies at greater depth. Below, the encountered geology is described for each shaft separately. For more details of the geological description, including daily reports, see /JAE 22/.

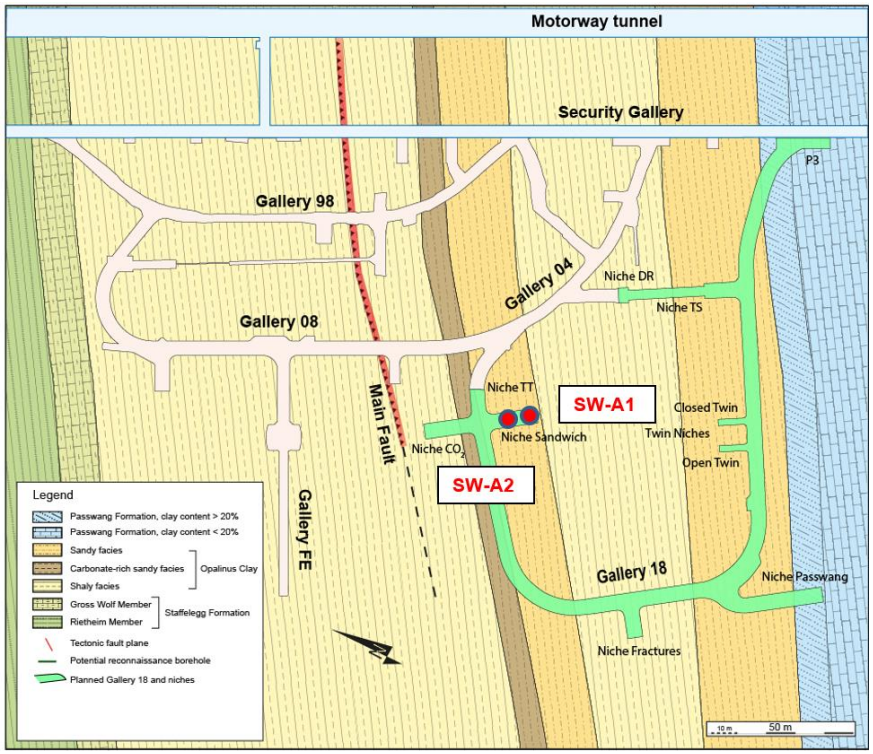

Fig. 3.17 Localization of shafts SW-A1 and SW-A2 in the Mont Terri rock laboratory

Shaft BSW-A1 was drilled entirely in the upper sandy facies represented by calcareous and silty-sandy claystones. The borehole reached a final depth of 12.59 m. EDZ structures are visible at the beginning of the shaft and some beddings are identifiable with an orientation of 150/43°. The EDZ mostly consists of bedding parallel fractures and is detectable until a depth of approximately 2.1 m (Fig. 3.18). At 0.7 m some sub-horizontal

EDZ fractures related to stress unloading close to the gallery floor are visible. The EDZ is not critical for the stability of the shaft.

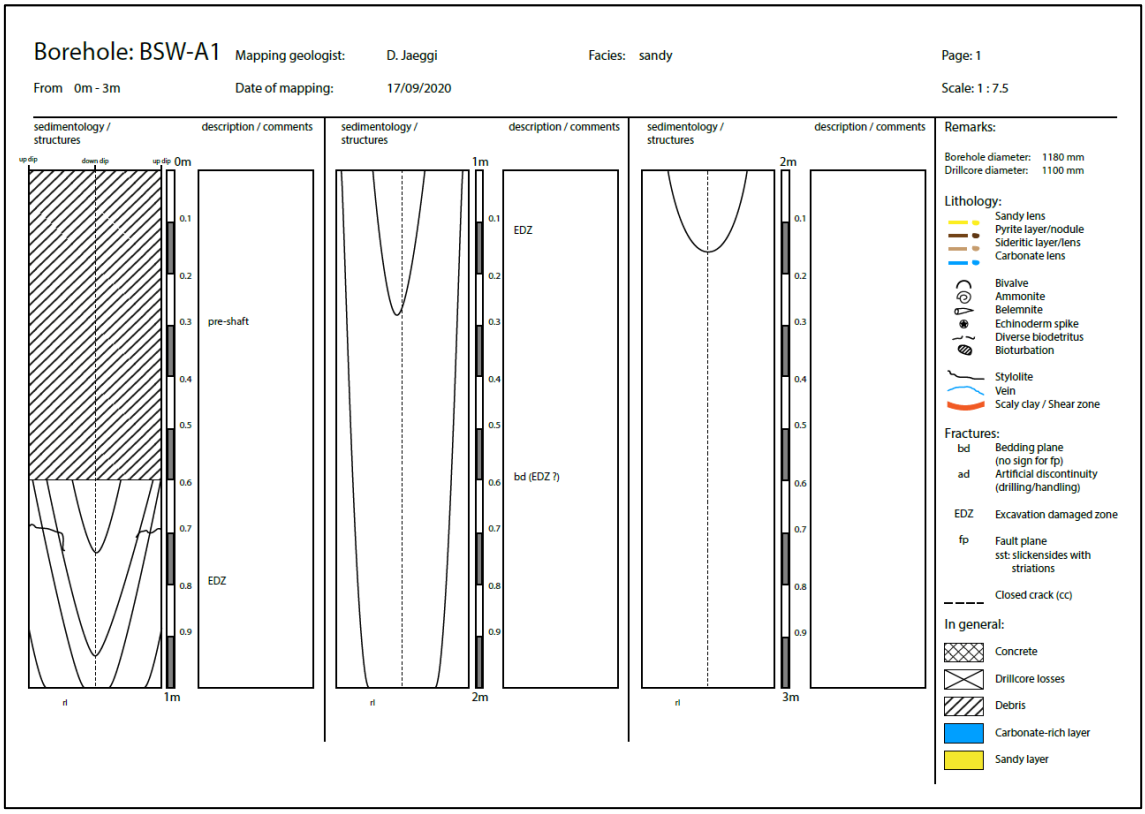

Fig. 3.18 Mapping 0-3 m with observed EDZ fractures just below the reservation

At 3 different levels, mini-piezometers were observed at the borehole wall. At 7.15 m BSW-B1, at 7.95 m BSW-B2 and at 9.40 m BSW-B11. The drillings for the piezometers obviously were deviating too much from the planned orientation. Boreholes in general tend to deviate towards perpendicular to bedding. The feeding borehole BSW-B24 that is used to inject fluids at the bottom of the shaft was crossed at a depth of 12.12 m.

Three sub-horizontal fault structures appear between 9 and 11.5 meters and have the same orientation which is 240/8°. In all these faults sinistral displacement in the order of 2 cm could be detected. At the uppermost fault at 9.2 m depth, two distinct associated veins could be detected (Fig. 3.19 and Fig. 3.20). From a sedimentary point of view the rock is a nodular, laminated silty claystone, largely heterogeneous, with some sporadic larger shells of bivalves, which is typical for lower sandy facies.

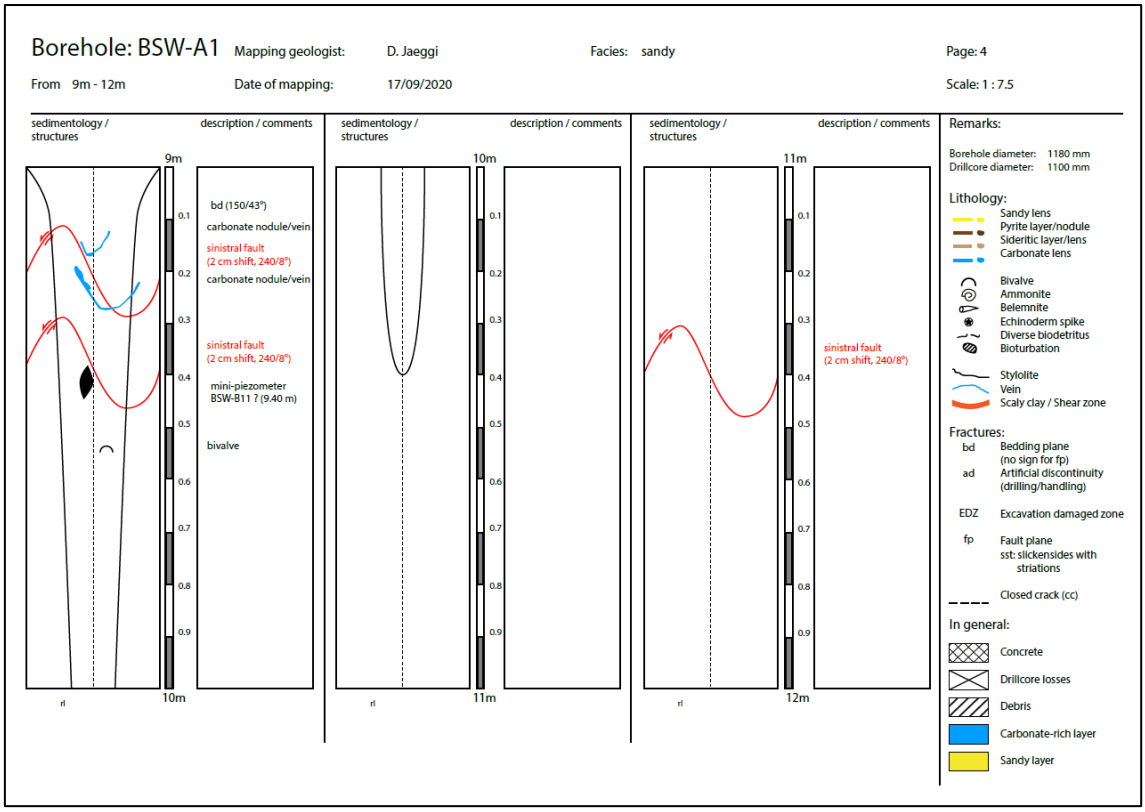

Fig. 3.19 Mapping 9-12 m with system of sinistral faults

There was no wet spot observed and the stability of the shaft was very good at any time until the backfill was completed.

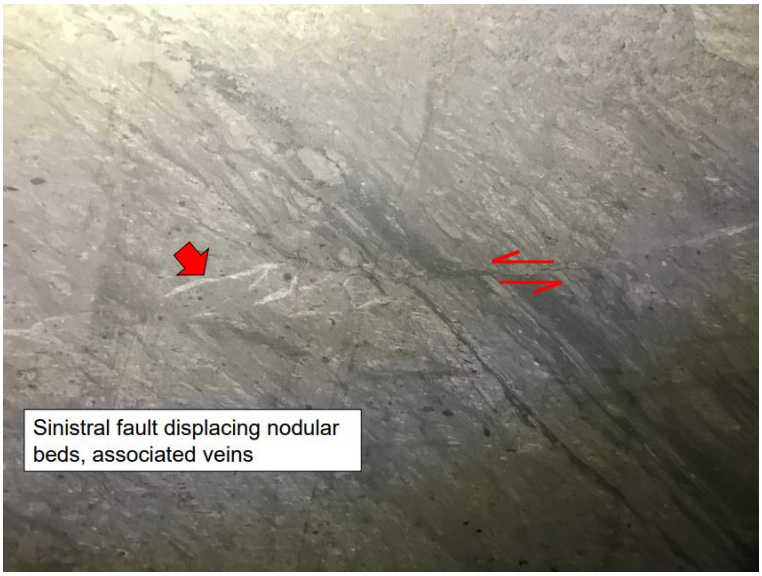

Fig. 3.20 Fault with sinistral shear displacing a nodular sedimentary layer by about 2 cm. On the left-hand side, there are conjugated Calcite veins occurring (Photo by D. Jaeggi, swisstopo)

The second shaft BSW-A2 was drilled in the upper sandy facies represented by calcareous and silty-sandy claystones until a depth of 9.40 m. Below the transition to the carbonate-rich sandy facies was encountered until the end of the borehole at 10.24 m depth. EDZ structures are clearly visible at the beginning of the shaft until a max depth of about 1.5 m. The EDZ fractures are oriented parallel to bedding. Here again the EDZ is not critical for the stability of the shaft and no breakouts are observed. In the uppermost 3 m the shaft wall is extremely rough and developed in a spiral manner. This is due to the core barrel, which was not the same, as in Shaft 1 and which at the teeth of the crown had some severe irregularities. The core barrel was changed back to the initial one at a depth of 3 m.

From 4.4 m to 6.1 m depth a black bedding layer was encountered, which yields a bedding orientation of 150/43°. On this bedding layer there was probably a small bedding-parallel shear zone, as there are always some indications of tectonic shear along these black clay rich layers in the sandy facies (see /JAE 20/). Clay layers and extremely hard silty-calcareous nodules are visible in the upper part of the shaft. At 8.8 m a distinct silty layer with some nodular accumulations of biodetritic material occurs and just below at 9.40 m the distinct transition towards the carbonate-rich facies is encountered (Fig. 3.21 and Fig. 3.22). There a nodular layer, 12 cm thick with coarse grained carbonate debris and crinoids surrounded by dark clayey matrix marks this change in facie type. The feeding borehole BSW-B25 that is used to inject fluids at the bottom of the shaft was crossed at a depth of 9.92 m and the borehole ends at 10.24 m depth. There was no wet spot observed and the stability of the shaft was very good at any time.

Fig. 3.21 Lowermost part of Shaft 2 in carbonate-rich sandy facies and with outlet of feeding borehole (Photo by D. Jaeggi, swisstopo)

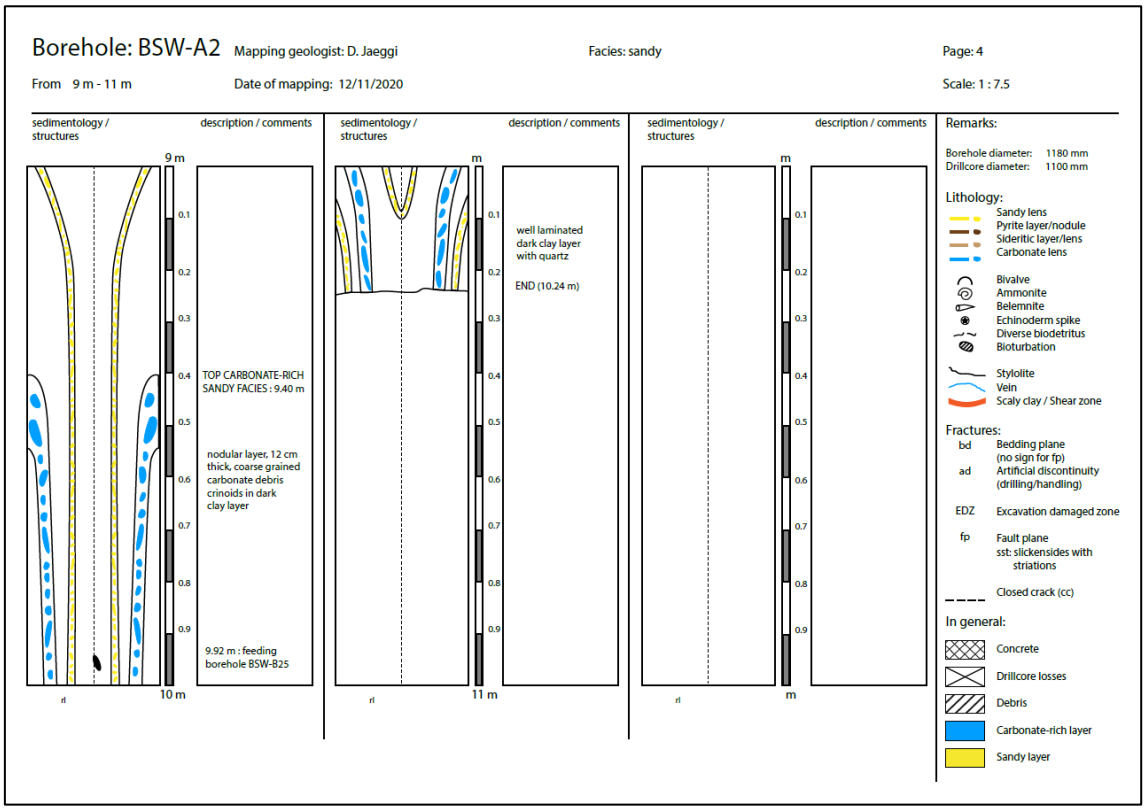

Fig. 3.22 Mapping 9-10.24 m with transition of lower sandy facies to carbonate-rich sandy facies

The encountered geology fits very well with the geological prognosis for both shafts (Fig. 3.23). Bedding is oriented towards 150/43° and very consistent over the entire length of the Sandwich niche and the two shafts. According to information from Ga18 excavation

and especially Niche CO2, which is the opposite niche of the Sandwich niche, the thickness of the carbonate-rich sandy facies is in the order of 4.5 m. Thus, below the bottom of Shaft 2 there is still about 3 m of carbonate-rich sandy facies left. The mapping of the Sandwich niche revealed the transition between lower sandy facies and upper shaly facies in the rear part and the uppermost corner of the niche. Consequently, the thickness of lower sandy facies is in the order of 20 m.

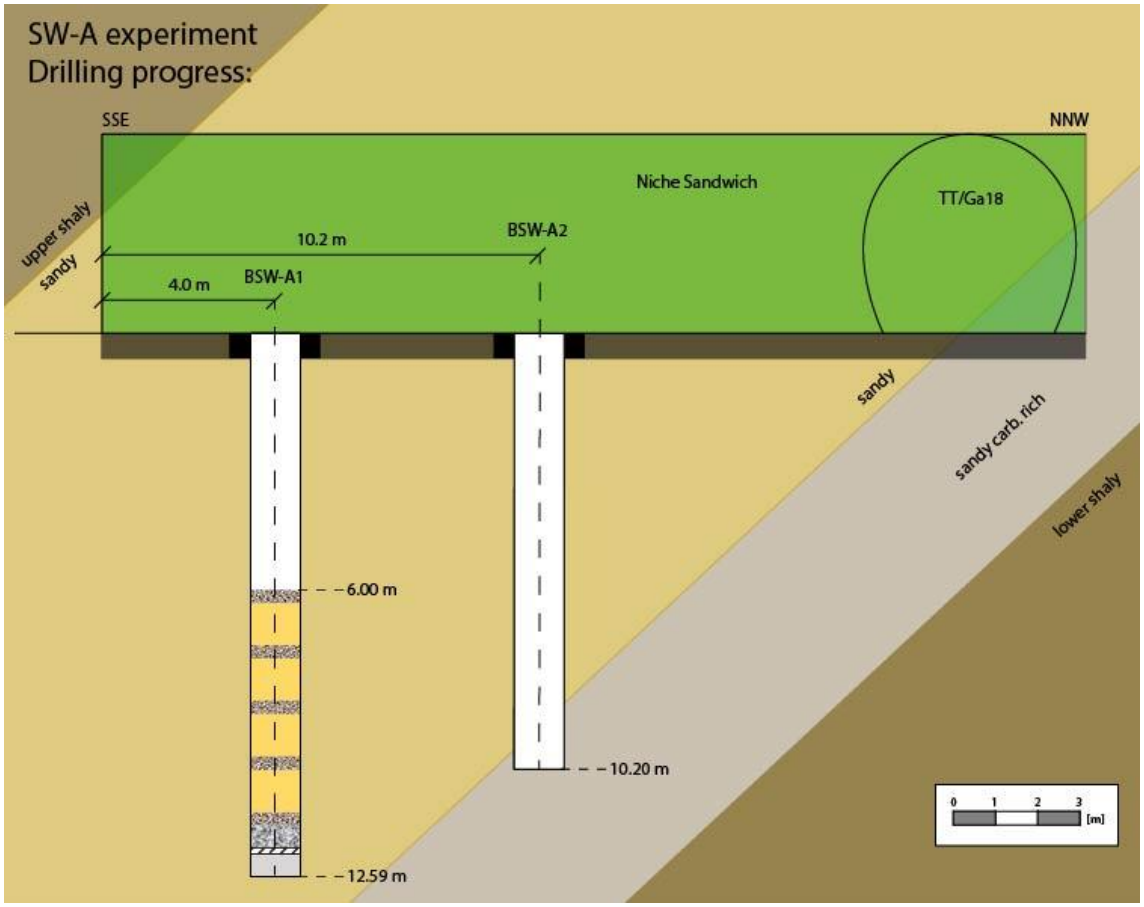

Fig. 3.23 Geological cross section along the axis of the Sandwich niche

3.3.3 Laser scans

Laser scanning in both shafts was carried out by the company Sigeom with a custom-made Laser scanner (see /SIG 21/). First fixpoints were installed in the shafts, three at 0.05 m, -4.5 m, -9.5 m measured from the invert (bottom of the niche). These points were measured with a special theodolite oriented upside down mounted on a tripod at the shaft entrance and then as well from the shaft bottom. The 9 points were then equipped with tracker targets and the laser scan was performed as well from the shaft head and its bottom.

The surface of Shaft 1 is very smooth and varying in the millimeter range for the uppermost 5 m and in the sub-millimeter range in the lower part. The surface of Shaft 2 is not a smooth as in Shaft 1 and varying in the millimeter range along the entire shaft (Fig. 3.24). The reason for that was mainly the temporary change of the crown to a new one, which was not as circular as the first one. The change was necessary since the performance of the first crown diminished due to abrasion in the quartz-rich sandy facies.

Shaft 1

Profondeur (m)	Rayon (m)	Diamètre Mesuré (mm)	Diamètre Théorique (mm)	Diamètre Ecart (mm)
-0.5	0.6233	1246.7	1180.0	66.7
-1.5	0.5902	1180.5	1180.0	0.5
-2.5	0.5914	1182.9	1180.0	2.9
-3.5	0.5917	1183.5	1180.0	3.5
-4.5	0.5916	1183.2	1180.0	3.2
-5.5	0.5895	1179.0	1180.0	-1.0
-6.5	0.5899	1179.7	1180.0	-0.3
-7.5	0.5899	1179.8	1180.0	-0.2
-8.5	0.5908	1181.7	1180.0	1.7
-9.5	0.5902	1180.3	1180.0	0.3
-10.5	0.5902	1180.5	1180.0	0.5
-11.5	0.5904	1180.9	1180.0	0.9
-12.0	0.5901	1180.3	1180.0	0.3
-12.1	0.5901	1180.2	1180.0	0.2
-12.2	0.5902	1180.3	1180.0	0.3

Verticalité de -5.5 m à - 1.5 m

DY (mm)	DX (mm)
-7.9	-7.9

Verticalité de -12 m à - 1.5 m

DY (mm)	DX (mm)
-10.1	-6.7

Shaft 2

Profondeur (m)	Rayon (m)	Diamètre Mesuré (mm)	Diamètre Théorique (mm)	Diamètre Ecart (mm)	Ecart-type à 95% (mm)
-0.5	0.6222	1244.4	1180.0	64.4	1.8
-1.0	0.5930	1186.1	1180.0	6.1	1.3
-2.0	0.5932	1186.4	1180.0	6.4	2.3
-3.0	0.5910	1182.0	1180.0	2.0	2.0
-4.0	0.5909	1181.8	1180.0	1.8	1.3
-5.0	0.5914	1182.7	1180.0	2.7	1.4
-6.0	0.5939	1187.8	1180.0	7.8	1.4
-7.0	0.5964	1192.8	1180.0	12.8	1.2
-8.0	0.5945	1189.0	1180.0	9.0	1.8
-9.0	0.5921	1184.1	1180.0	4.1	1.8
-9.9	0.5926	1185.2	1180.0	5.2	1.7
-10.0	0.5925	1185.0	1180.0	5.0	2.0
-10.1	0.5932	1186.3	1180.0	6.3	1.8

Verticalité de -5 m à - 1 m

DY (mm)	DX (mm)
2.6	-29.3

Verticalité de -10 m à - 1 m

DY (mm)	DX (mm)
1.8	-47.4

Model with profiles at 12.0, 12.1 and 12.2 m

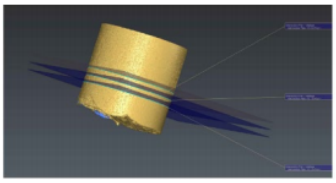

Fig. 3.24 Results from laser scanning at different depth levels. The deviation from the originally planned diameter of 1180 mm is very low in both shafts

In Shaft 2 after the measurement of 13 November 2020 another measurement just before backfilling on 3 June 2022 could be performed in order to check for convergences during that period of open shaft. The resolution of this survey was 1 mm and the accuracy in the order of 2-3 mm. the exact procedure is given in /SIG 22/. The results of the comparison of the two laser scan campaigns are given in Fig. 3.25 and Fig. 3.26. The uppermost section from 0.8 to 3.5 m depth just above a distinct bedding plane which is in the soft pure black clay shows some swelling phenomenon. This bedding plane could as well mark a bedding parallel fault which makes the stress decoupling towards the gallery and thus marks the lower boundary of developing borehole breakouts, which are nicely observed downdip at 150° and updip at 330°. Another distinct bedding plane with similar soft swelling clay material hits the shaft at 5 m updip and 6.4 m downdip. Finally, the

bottom is marked by some heaves due to stress redistribution and unloading oblique to the bedding planes. The convergences observed are in the order of 5 mm (yellow and orange) to max. 20 mm (reddish colour).

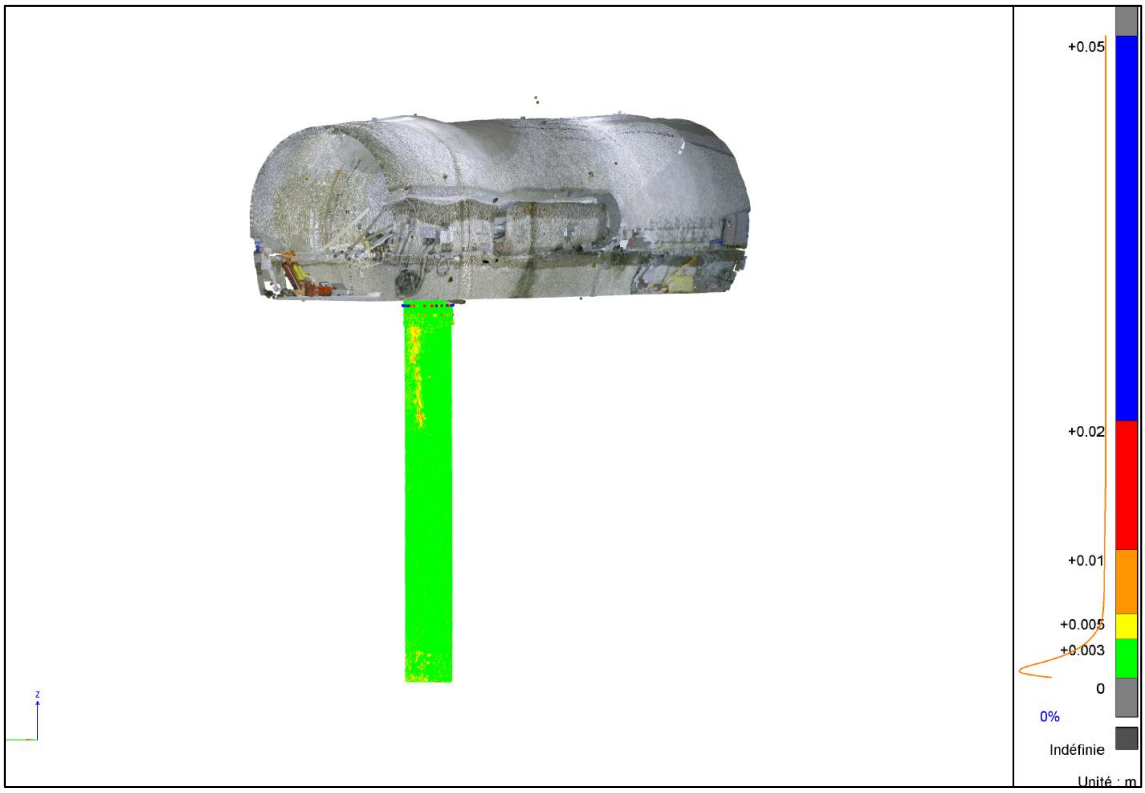

Fig. 3.25 Differences of laser scans in perspective 3D view for Shaft 2

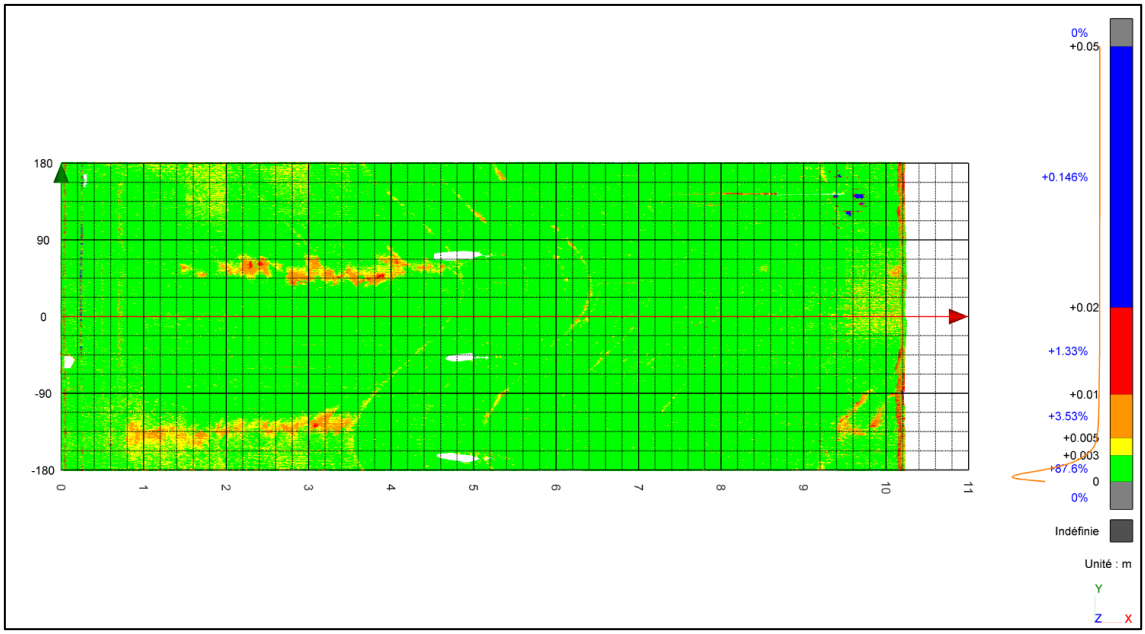

Fig. 3.26 Differences of laser scans in 2D view unrolled for Shaft 2

3.4 Shaft 1 installation and instrumentation

3.4.1 Description of components

Levelling layer

The shaft bottom had a rough surface resulting from the shaft sinking which was compensated by a levelling layer made of a three-components epoxy resin-based mortar (Sikadur 43 HE). The levelling was done by VersuchsStollen Hagerbach (VSH) in September 2020. The upper level of the levelling layer reached 12.18 m depth with a maximum thickness of 41 cm.

Pressure chamber and connection piece to feeding borehole

The pressure chamber at the shaft bottom was designed to provide a homogeneous hydration of the sealing system from the bottom and to support the sealing system and resist its developing swelling pressures. The chamber (material 1.4571) is composed of a base and a top. The base consists of a bottom plate (Ø 110 cm with thickness 15 mm), a supporting ring (height 80 mm) and 39 supporting pillars (height 80 mm) fixed to it (Fig. 3.27). The pillars are made from standard I-Beam (HEA 100 DIN 1025-3) cut into pieces. At the rim of the base plate, the supporting ring is fixed with a 5 cm gap for the access of the feeding line. The inner free volume of the pressure chamber is 69 dm³.

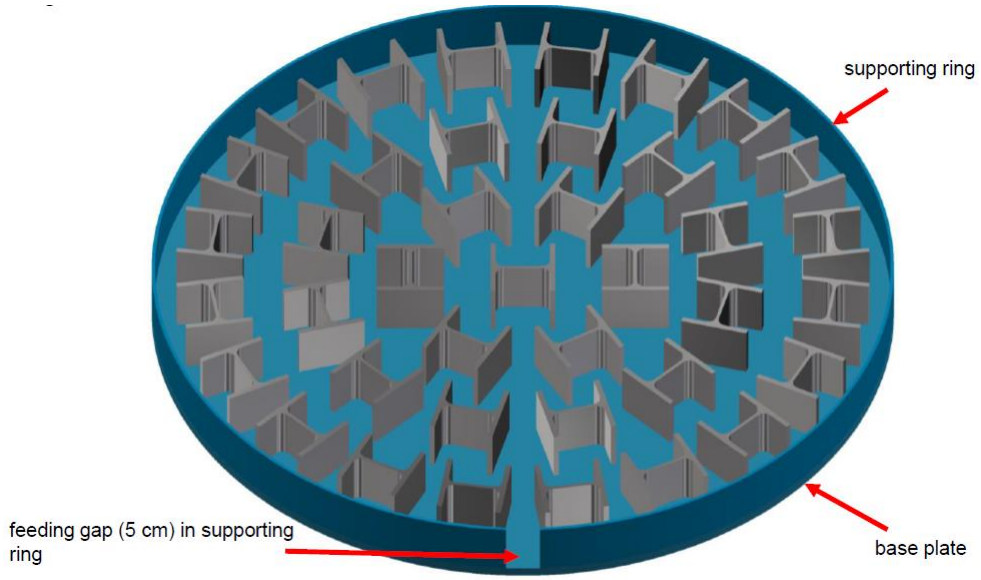

Fig. 3.27 Base of the pressure chamber for Shaft 1

The top lid of the chamber (Ø 116 cm, thickness 15 mm) is divided into quarters (4 plates), each perforated with 311 holes (Ø 8 mm) to ensure a homogeneous hydration (Fig. 3.28). The top framework contains four cable entries to pass the cables of the sensors foreseen in the chamber. The total height of the pressure chamber, including the top plates, is 11 cm.

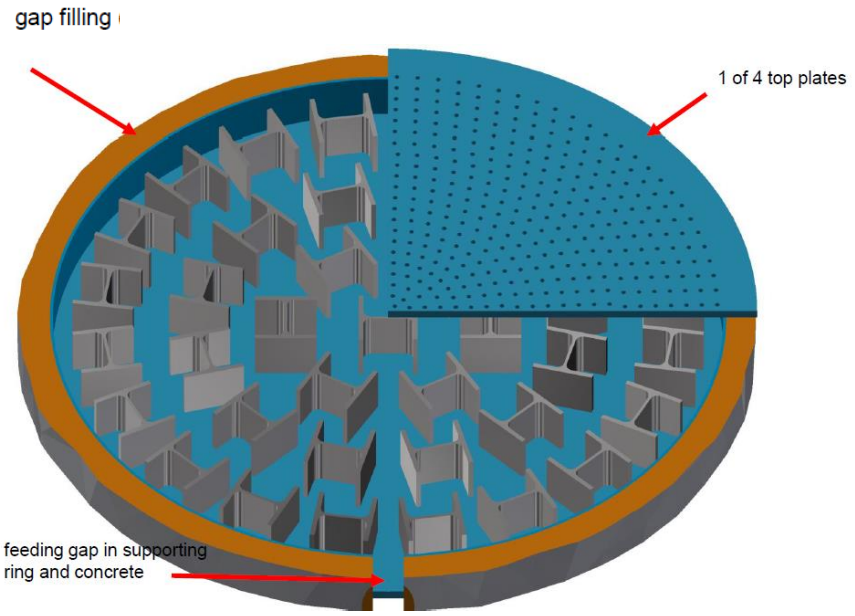

Fig. 3.28 Detail of the top of the pressure chamber for Shaft 1

The connection of the pressure chamber to the feeding borehole is provided by a bent (approx. 60°) PVC pipe of around 125 mm length and with an outer diameter of approximately 45 mm. The inner diameter of the connecting piece is in the order of 35 mm.

Sandwich sealing system

The installed sealing system consists of five ES (thickness 30 cm) and four DS (thickness 100 cm) in alternating arrangement.

The required materials for DS and ES were prepared and delivered by SSKG. For the DS, a binary mixture of bentonite pillows and bentonite granular material (BGM) made of Calcigel is used. The compacted bentonite pillows have a bulk density of about 2.2 g/cm³ (moisture 10 % (105 °C) and 11.25 % (200 °C) or water content 11.15 % / 12.7 %). About 30 % of the pillows were crushed to provide the BGM for filling the gap between the pillows. 5 big bags of pillows and 2 big bags of bentonite granular material were delivered by a lorry. For the ES, fine sand (N45) in air dry state with a water content of < 1 % is used.

Instrumentation

The following description of the instrumentation is rather condensed, and, particularly, the sensor positions are summarized in Fig. 3.32 and Fig. 3.33 at the end of this paragraph as well as Tab. A. 7 and Tab. A. 8. The details are given in /GAR 22/.

Sensors in the pressure chamber

The pressure chamber contains two temperature sensors (Termya Pt-100 class 1/10 DIN, sensor range: -50-250 °C) and two pore pressure sensors (Geosense strain gauge piezometer SGP-3400, signal: 4-20 mA, sensor range: 0-6.9 MPa relative pressure). The sensor cables pass the pressure chamber through cable glands in the perforated top plate.

ERT

Measurements of the electrical resistivity are realized by installing electrodes on the shaft wall. There is a limitation that a maximum of 255 electrodes can be controlled by the measuring instrument. In order to achieve a certain spatial resolution in the filling, the distances between the electrodes must not become too large. This results in the layout shown in Fig. 3.29:

- Arrangement of the electrodes in horizontal rings, each ring consists of 36 electrodes (10° angular distance, i.e., a length distance of approx. 10 cm).
- The maximum number of electrodes allows the installation of 7 rings, with respective distances of 10 cm and 15 cm respectively.
- The observation area was the upper part of the DS1 segment and the transition zone to the ES2 segment.
- Brass plugs are used as electrodes (short pre-drilling required) into which brass screws are turned. This ensures that the cable lugs of the individual cables leading to each electrode are securely attached.

The resistivity meter is a device from Lippmann Geoelektrische Messgeräte (LGM) of type *4 point light 10W*, which is controlled by the software *GeoTest*, installed on a laptop. The switching electronics are housed in specially manufactured multiplexer boxes. The measurement system is secured by a UPS and is connected to the Mont Terri network

via a LAN cable. The installed measuring system in the Sandwich niche is shown in Fig. 3.30. In the meantime, additional cable boxes have been installed to seal the cables.

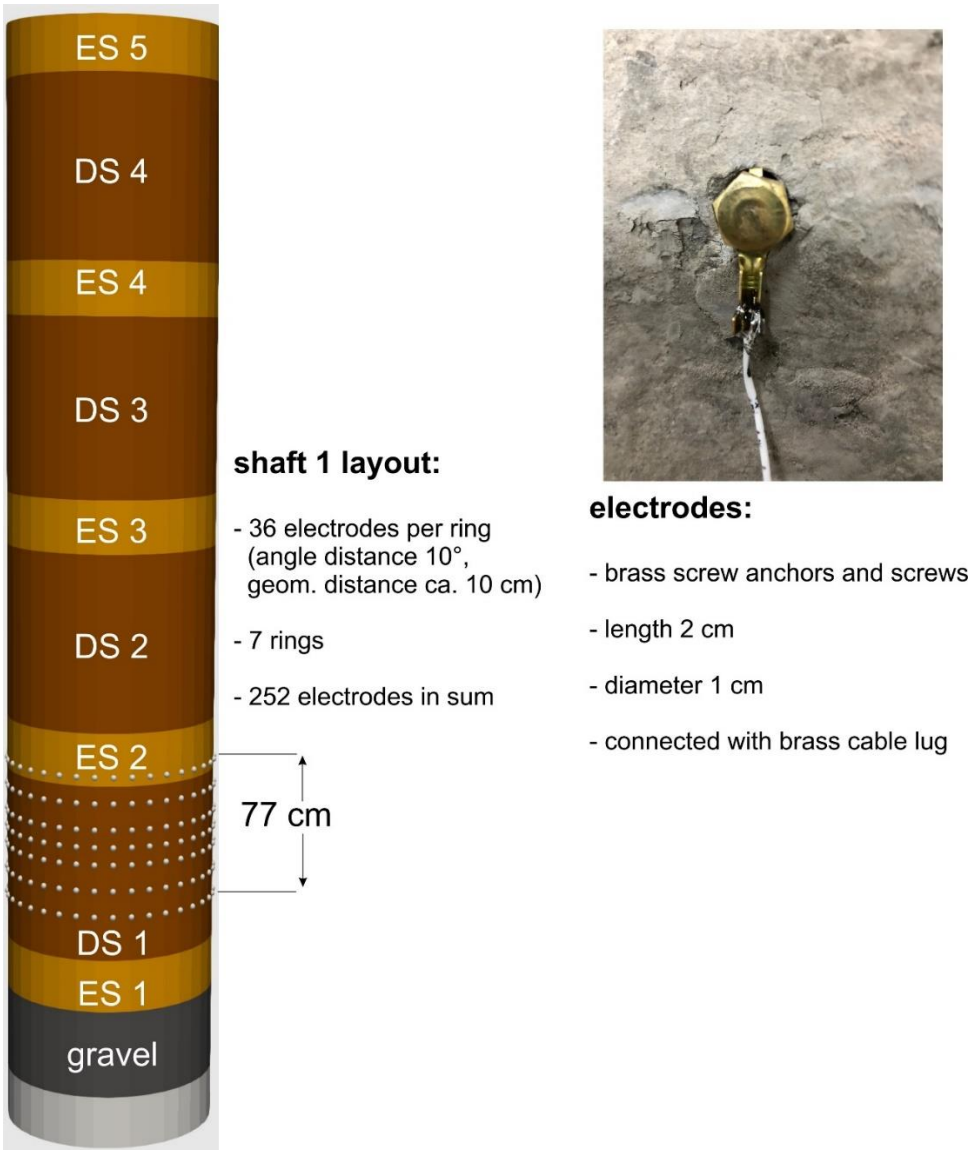

Fig. 3.29 Layout of the ERT measuring system and detailed illustration of an electrode

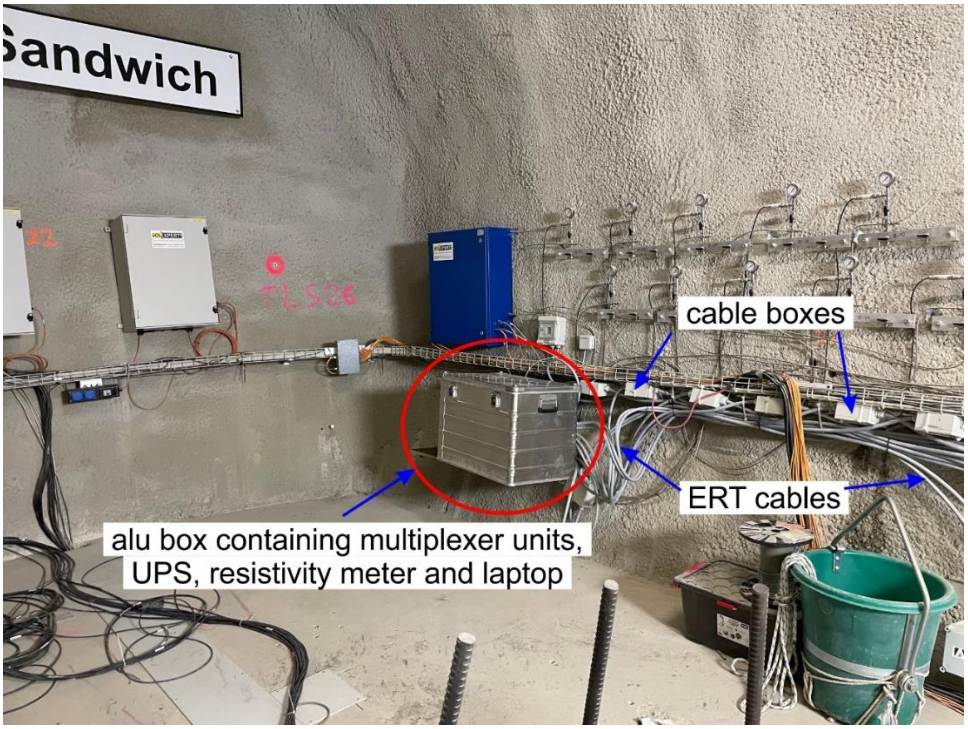

Fig. 3.30 Elements of the ERT measurement system in the Sandwich niche

Further details are shown in /GAR 22/ and /WIE 23/.

Twin rod TDR

Twin rod TDR sensors with rod length of 30 cm from IMKO GmbH have been installed at all ES into the rock wall to monitor events inside the rock wall, like inflow of liquid or building up of an EDZ.

Taupe TDR

Five Taupe TDR sensors are installed vertically through the entire shaft, one along the center and four placed close to the rock wall, each placed 90 degrees apart from each other and about 15 cm from the rock. Five Taupe TDR sensors are located across each ES.

Relative humidity and temperature

Eight relative humidity sensors with integrated temperature (RH&T) sensors (Vaisala HMP7, sensor range: 0-100 % RH / -70-180 °C) are installed in the DS. Each DS contains two sensors at different heights.

Pore pressure / fluid pressure

A total number of 18 pore pressure (PP) sensors (Geosense strain gauge piezometer SGP-3400, signal: 4-20 mA, sensor range: 0-6.9 MPa relative pressure) are installed in the DS (two each at different heights) and ES (two each) of the sealing system.

Axial and radial stress

Four circular total pressure (TP) sensors (GLÖTZL/ EAI 17 K200 A circular, signal: 4-20 mA, sensor range: 0-20 MPa) are horizontally installed close to the center of the shaft at the interface DS / ES, on top of each DS. They measure the axial stress changes in the column induced by the swelling pressure.

A total of 12 square flat cells for radial stress measurement (GLÖTZL/ EAI 10/20 K200 A Z4 rectangular, signal: 4-20 mA, sensor range: 0-20 MPa) are installed at the shaft contour for determination of the swelling pressure evolution. Some of the sensors are arranged opposite to the flat cells in the rock to enable a direct comparison.

Vertical displacement

The vertical displacement measuring system is composed of three extensometers in a circular arrangement (angular distance of 120º to each other). The rear ends of the extensometers' sliding rods are attached to a flexible circular surface which is close to the rock wall of the shaft and moves with the interface (Fig. 3.31). The sensor bodies are clamped to the rock wall to provide a fixed reference for displacements.

The flexible surface is a plastic frame of PE-HD covered with a geotextile mat, installed at the interface of ES3 and DS3. The extensometers (RDP D5/400AW) are based on the linear variable differential transformer (LVDT) principle.

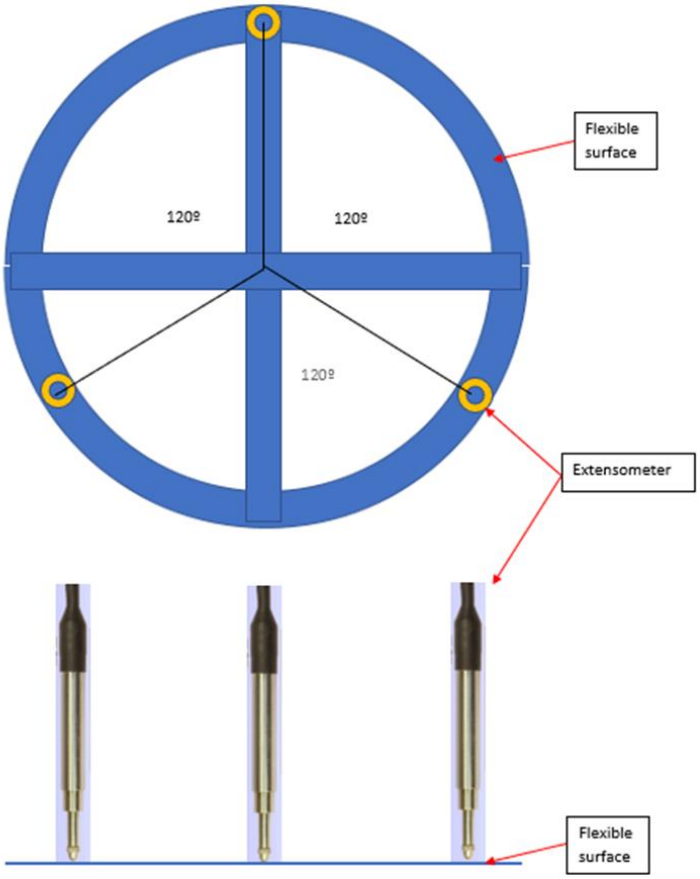

Fig. 3.31 General arrangement of the displacement measuring system, plan view on top and side view at the bottom

An overview of all sensor positions is given in Fig. 3.32 and Fig. 3.33.

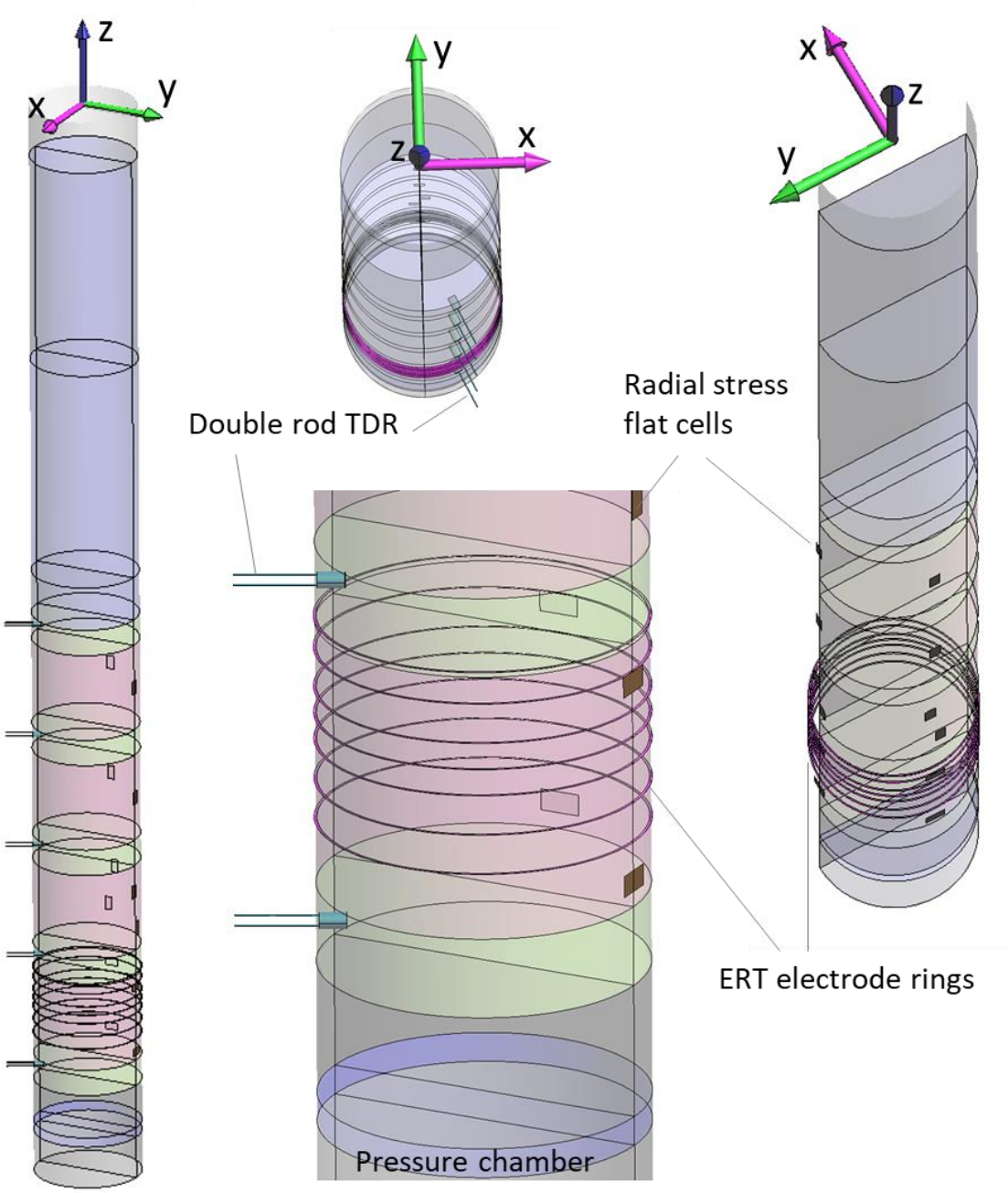

Fig. 3.32 Sensors at the interface of rock and sealing system of Shaft 1

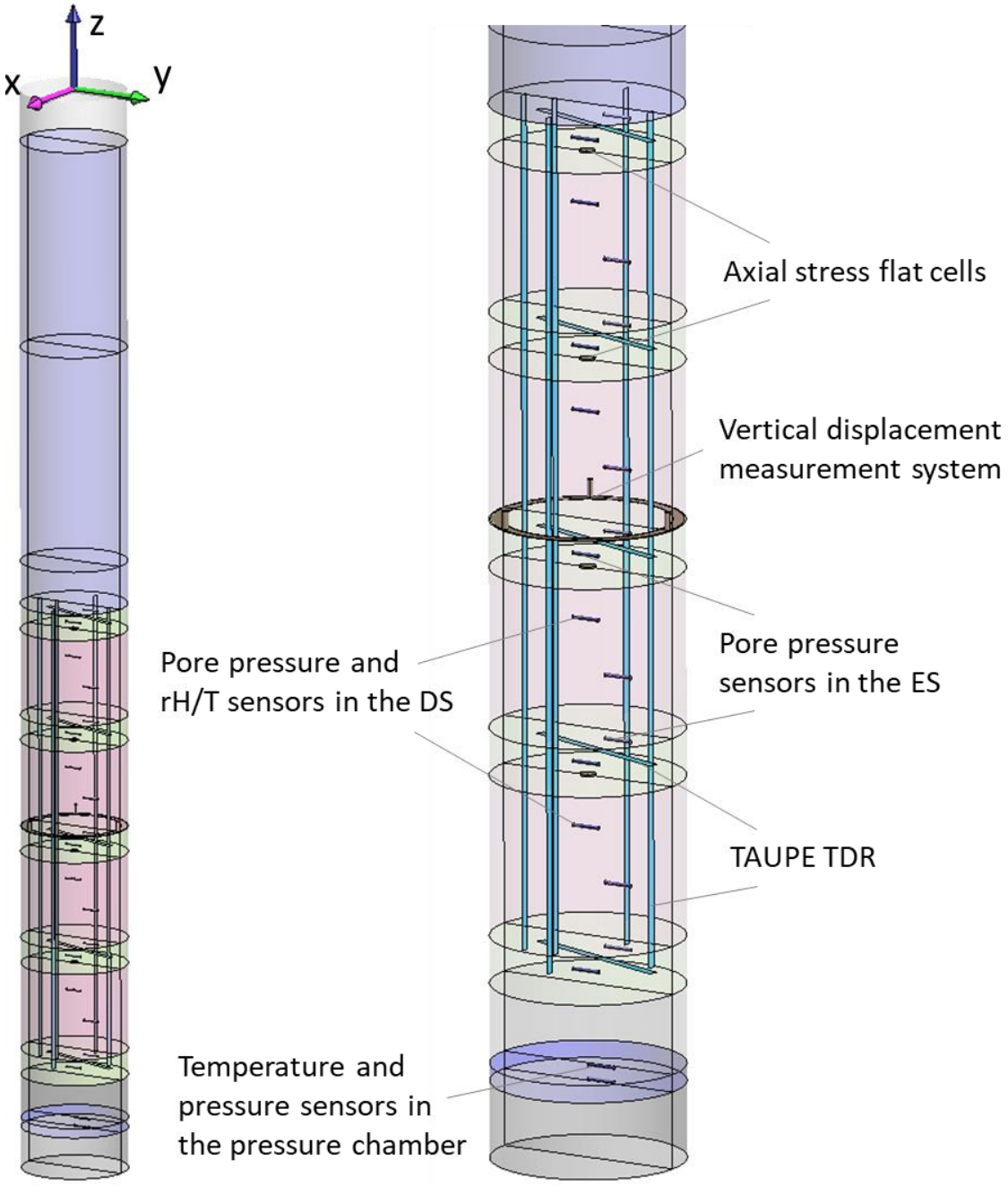

Fig. 3.33 Sensors in the pressure chamber and in the sealing system of Shaft 1

Back-up hydration

The back-up hydration system in Shaft 1 allows for an additional hydration of the sealing system starting from ES3. The system consists of a hydration line reaching ES3 from the top and a hydraulic short-circuit simulating an enhanced EDZ in DS2. The hydration line consists of a plastic tubing coming from the hydration system (Technotex 8x15 mm, 80 bar burst pressure) connected to a stainless steel line (outer diameter 6 mm, length

1.3 m, L-shaped). The hydraulic short-circuit is realized by a half-pipe sand tube running along DS2, connecting ES2 and ES3. This set-up enables fluid injection from the hydration system to be distributed within ES3 and ES2 (Fig. 3.34).

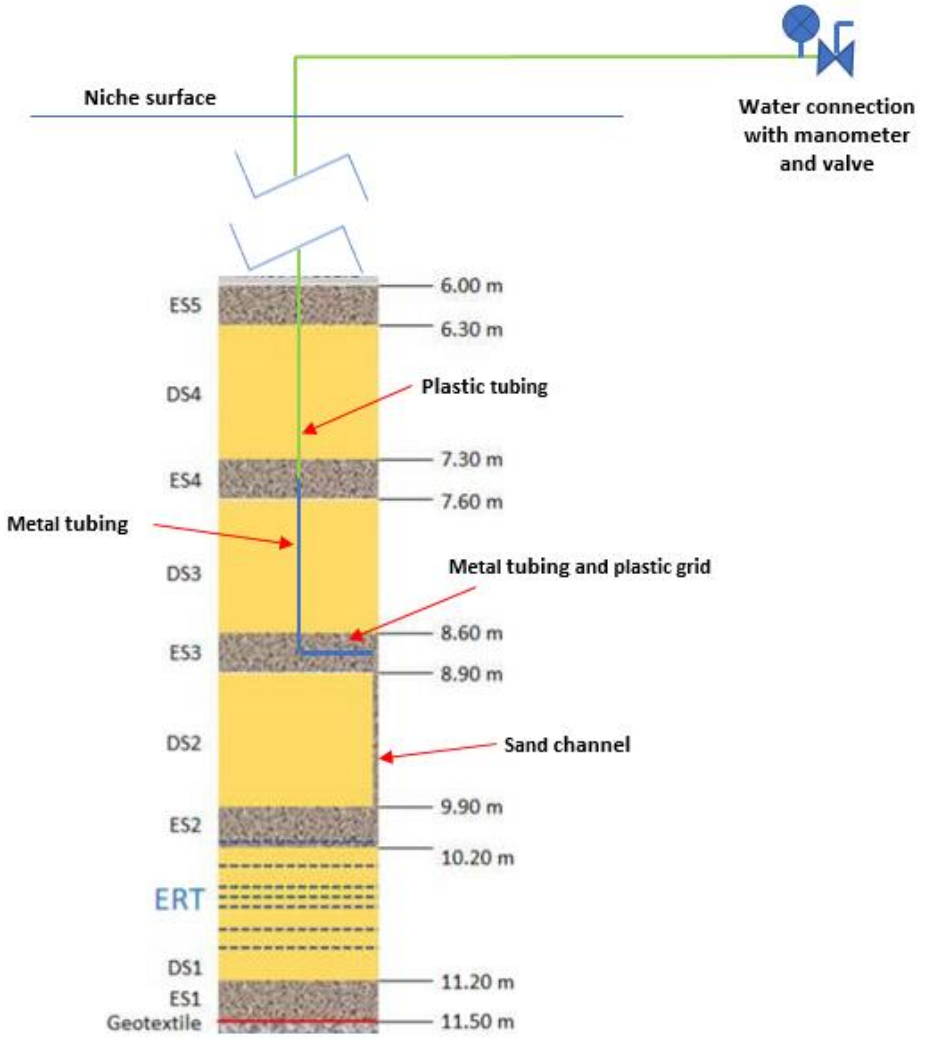

Fig. 3.34 Back-up hydration system in Shaft 1

Plug and shaft cover

The sealing system in Shaft 1 is covered by a metallic plug to confine it mechanically. The plug consists of a confining tube and a top lid bolted to the rock surrounding the shaft (Fig. 3.35). The vertical confining tube (total length 6 m) reaches from the top of the sealing system to the niche floor. It is composed of three cylindrical tubes joined by inner screwed flanges. Each section consists basically of a carbon steel tube (length 2 m each) with an external diameter of 1160 mm and a thickness of 20 mm. The bottom section features a circular steel plate closing its bottom that remains in contact with the

top of the seal to confine it. Twelve radial reinforcement plates transmit the pushing force the bottom plate to the tube. The plate features a central circular hole with a diameter of 280 mm to pass through the sensor cables (Fig. 3.36). The top section is covered by a circular steel top lid (diameter 2 m, thickness 50 mm) which provides the mechanical confinement by transmitting the pushing force from the tube to the surrounding rock. This is done by means of 8 steel bolts anchored through holes around the outer part of the lid. The bolts are chemically anchored to inclined boreholes (length 3 m) drilled around the shaft. The top lid has a central hole to allow for accessing the bottom lid inside the tube.

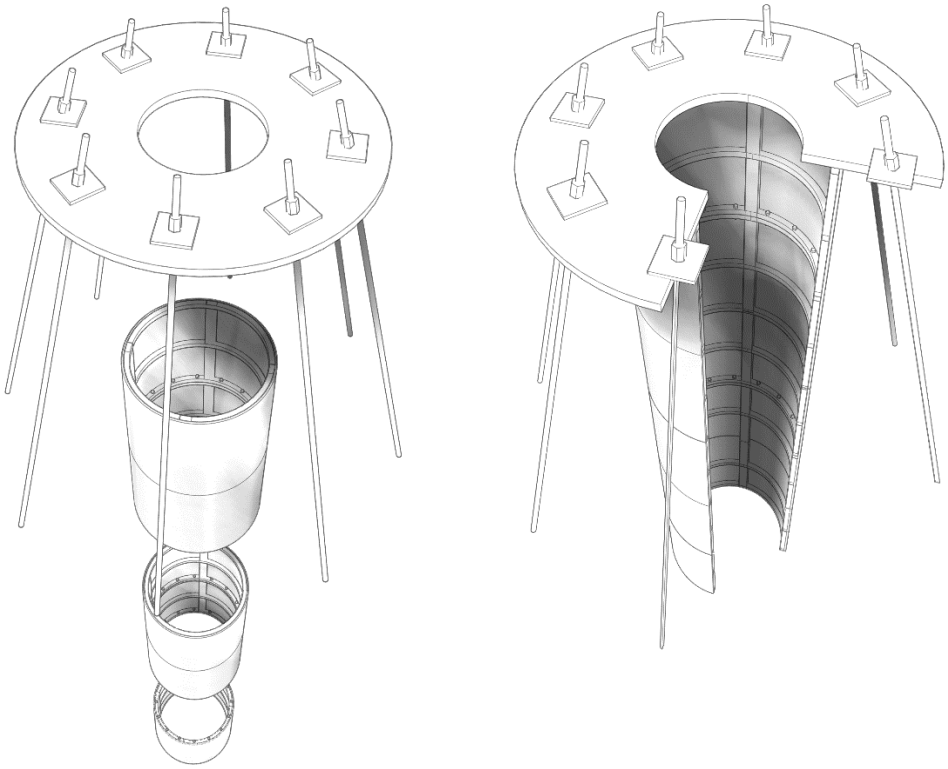

Fig. 3.35 Concept of the metal plug in Shaft 1

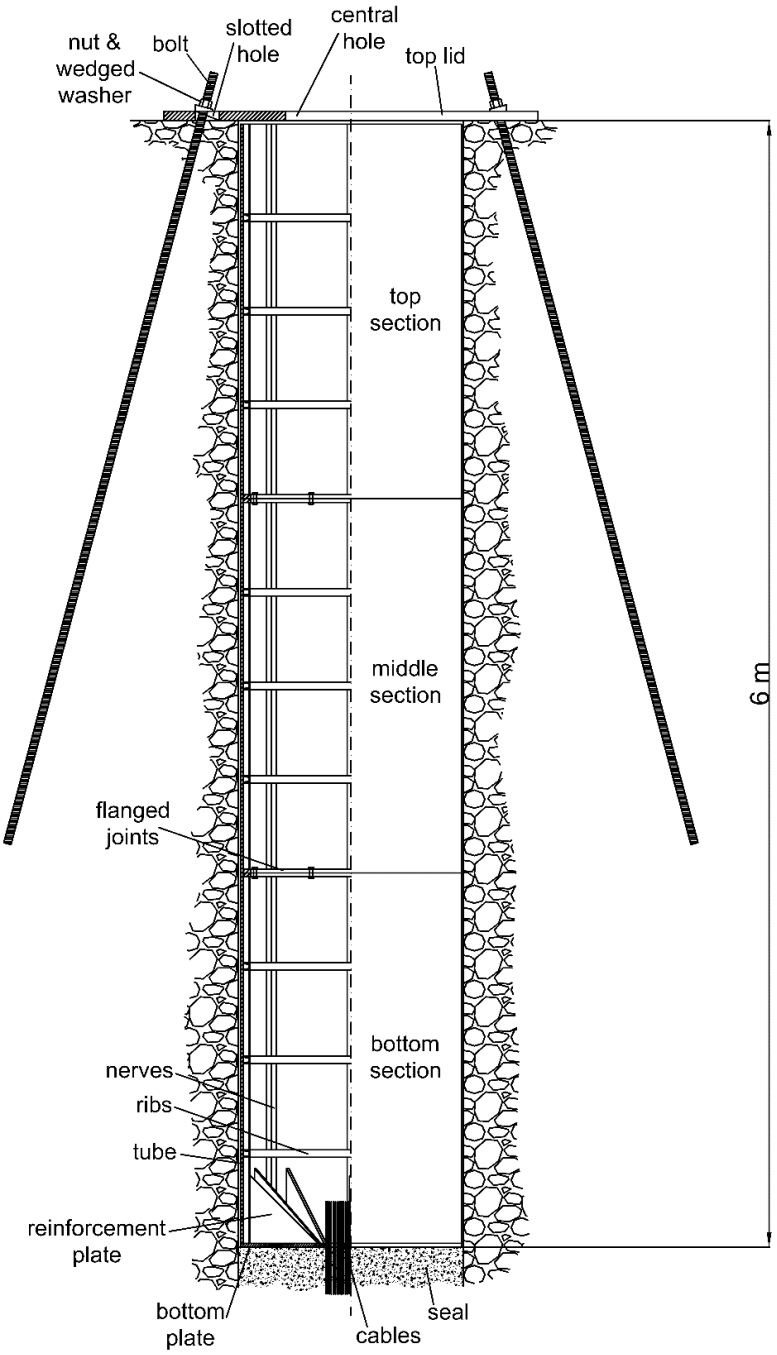

Fig. 3.36 Longitudinal section of the metal plug in Shaft 1

Hydration system

The sealing system in the shaft can be artificially hydrated by means of a hydration system to supply the pressure chamber via the feeding borehole (or the back-up hydration line) with Pearson water. The expected fluid injection pressure is at most 3 MPa and should be kept as constant as possible given that the fluid uptake of the seal is expected

to be as low as 0-25 ml/h when increasing DS saturation. The injection system is located in Gallery 18 next to the Sandwich niche and its expected running time is 4 to 10 years.

The hydration is performed by using pressurized reservoirs. This technique is widely used when the flow range and the pressure of injection vary significantly, and particularly, if the flow rate cannot be anticipated. The system consists of:

- main water tank (1000 l) filled with Pearson water A3
- low pressure tank (LPT, 112 l, at most 8.5 bar) with scale
- high pressure tank (HPT, 5 l, at most 50 bar) with scale
- nitrogen bottle with pressure regulator for fluid pressurization
- pump to transfer the Pearson water from the main water tank to LPT or HPT
- connection to the pressure chamber via the feeding borehole
- operation cabinet containing relays for actuating electrical valves
- hydration cabinet containing tanks, scales, valves, pressure sensors etc.

The injection is realized with the help of the LPT and the HPT that can be pressurized by using the nitrogen bottle and a regulator. During the initial hydration phase, the LPT is used for injection as the flow rates are typically high and pressures are low. In a later phase, when the saturation of the sealing system evolves, the HPT is used for hydration as flow rates become smaller and the injection pressure can be increased. In both cases, the flow rate is measured by using industrial scales. Both water tanks can be manually refilled from the main water tank with the help of the transfer pump. Fig. 3.37 shows the scheme of the hydration system.

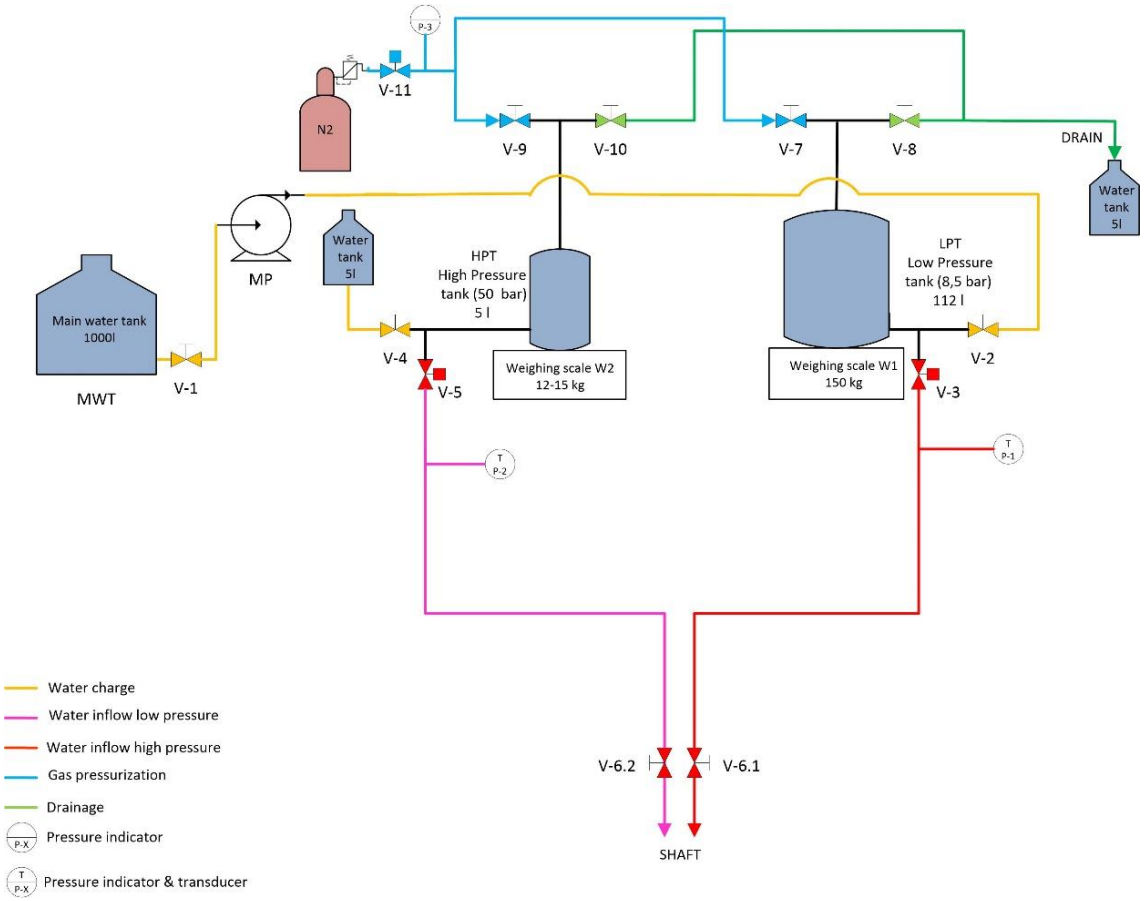

Fig. 3.37 Scheme of the hydration system for Shaft 1

3.4.2 Preparatory works

Measurements in the open Shaft

Surface packer tests

To measure the permeability of the immediate near field (EDZ) around the borehole, the surface packer system was used (CTN, 1999). The surface packer consists of a hollow metal cylinder with a diameter of 100 mm, a metal ring, which was glued on the shaft wall with a special adhesive in order not to damage the surface. The resulting cavity (packer interval) is connected to an injection pipe and a pressure and a temperature sensor. The packer was not fixed by the conventional method using two heavy anchors, but by a support beam propped against the opposite shaft wall (Fig. 3.38).

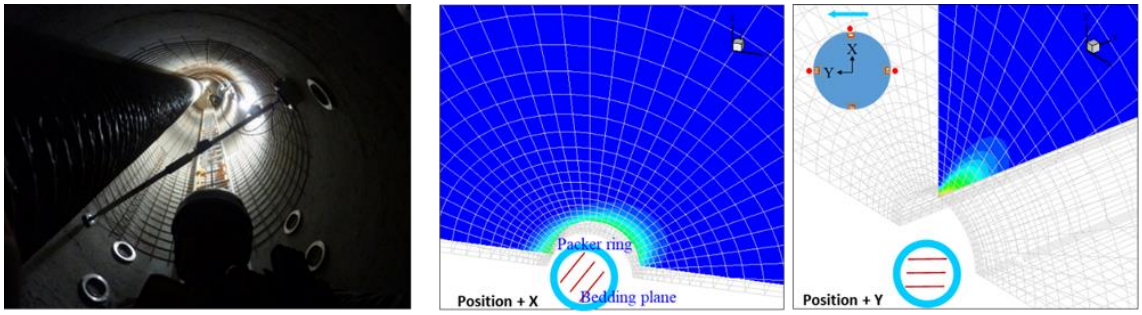

Fig. 3.38 Bottom view of the test locations and support beam during a test (left) and a numerical model to interpret the measured pressure development (right)

Due to the swelling capability of clay stones when water is in contact with them, gas (nitrogen) is injected as test medium for hydraulic pulse tests. Three levels (0.8, 1.45, and 1.8 m from the bottom) with four different orientations (+Y: parallel to the niche orientation in direction to the niche end, others clockwise, see Fig. 3.38) have been tested, in total 12. Results show variation of three orders of magnitude between the minimum of $7*10^{-17}$ m² (0.8 m, direction -Y) and the maximum of $7*10^{-14}$ m² (1.8 m, direction -Y) with no clear correlation with depth and orientation (Fig. 3.39).

Compared to the measured permeability in the boreholes (BSW-B17, -B18 & -B19), which was estimated to be lower than 10^{-20} m², the surface roughness may form a possible flow path for resaturation in the experiment. This flow path may be suggested to have a permeability of $1.5*10^{-15}$ m² with a thickness of about 1 cm for the EDZ simulation.

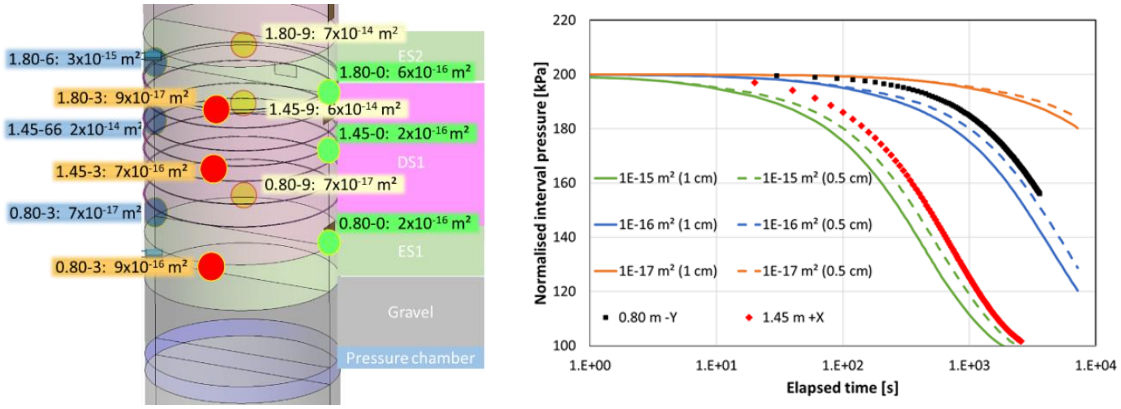

Fig. 3.39 Permeability distribution (left) and numerical interpretation with variation of permeability and thickness of the EDZ (right) of Shaft 1

Temporary lining, light and ventilation

The planned location of the shaft is given in Fig. 3.40, see as well /BUR 22/. Right after excavation, the shaft was equipped with K196 steel wire meshes (Fig. 3.41 and Fig. 3.42). The foldable meshes were installed from top to bottom and during the backfilling procedure in turn removed from bottom to top. A ladder with a self-locking rope safety device was installed and the illumination and ventilation hose placed. The ventilation mode was aspiring the air at the bottom, yielding a vertical air inflow into the shaft. The working zone was completely separated from the public zone, by a fence restricting the access to Sandwich niche and the shafts. Only workers equipped with harness, helmet, Dräger gas warning device (O2, CO, H2S, CH4) and the safety permit were allowed to approach or enter the shafts.

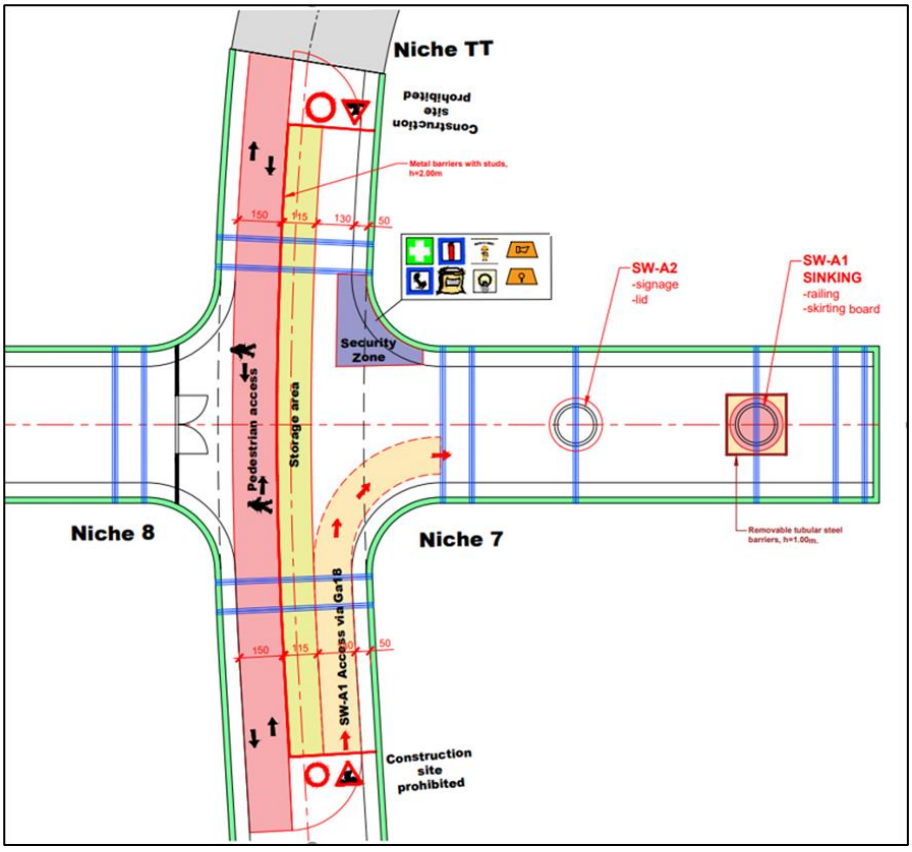

Fig. 3.40 General safety concept for Shaft 1

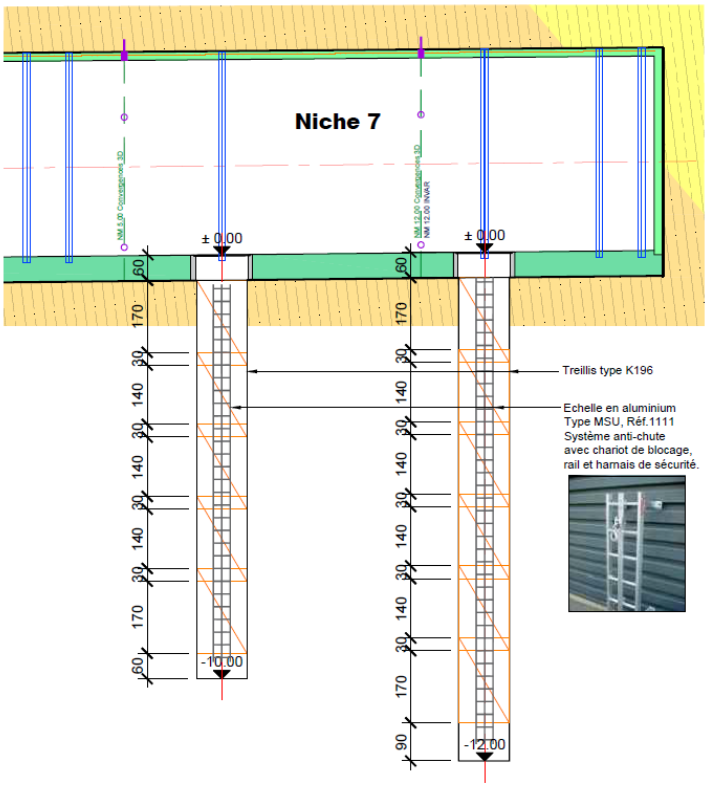

Fig. 3.41 Side view showing the metallic mesh to be used for protection in the shafts

Fig. 3.42 View of the Shaft 1 during installation phase

3.4.3 Installation procedure

Levelling layer, pressure chamber, gravel

The levelling layer was installed in September 2020, followed by the pressure chamber with the connection to the feeding borehole (Fig. 3.43). After installing the sensors inside the pressure chamber, a geotextile sheet (thickness 5 mm) was placed on top and a layer of 51.8 cm of angular Maggia Gneis gravel 16/32 from the company Bernasconi Natursteine AG in Bern was added to reach the desired depth for building the sealing system at 11.5 m depth (Fig. 3.44). On top of the gravel, another sheet of geotextile was installed to minimize the loss of sand inside the gravel layer.

Fig. 3.43 Installation of the pressure chamber, the connection to the feeding borehole (middle) and the pressure chamber sensors (right) for Shaft 1

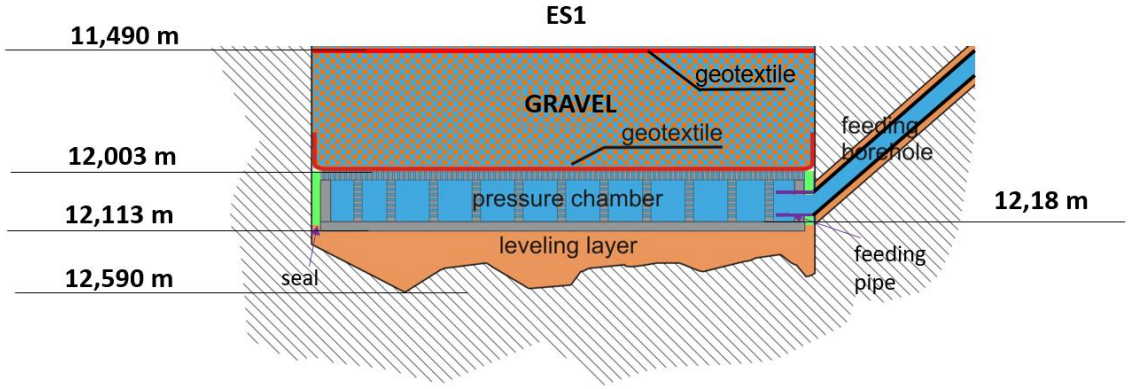

Fig. 3.44 General setup of the bottom of Shaft 1

Sensors at the shaft wall

The twin rod TDR sensors were installed horizontally into the rock at the planned location of the ES to determine the apparent relative dielectric permittivity (ARDP) and interpolate the water content evolution in the EDZ (Fig. 3.45). The position of the rods is vertically aligned.

Fig. 3.45 Installation of twin rod TDR sensors in Shaft 1

The ERT electrodes at the shaft wall were installed in seven rings with 36 electrodes each (Fig. 3.46). For one ring, two cables with 18 cores each were used, which terminate in one plug at the measuring device.

The radial stress sensors were installed at different locations along the shaft wall. Small areas of the shaft wall had to be excavated in order to emplace the sensors' surfaces in the tangent planes of the shaft wall. The sensors were fixed with cement to the excavated shaft surface (Fig. 3.47). Some of the sensors were located very close to ERT electrodes and needed to be carefully marked before doing the rock excavation. All the excavations at the rock were done first and then the sensors were installed and fixed.

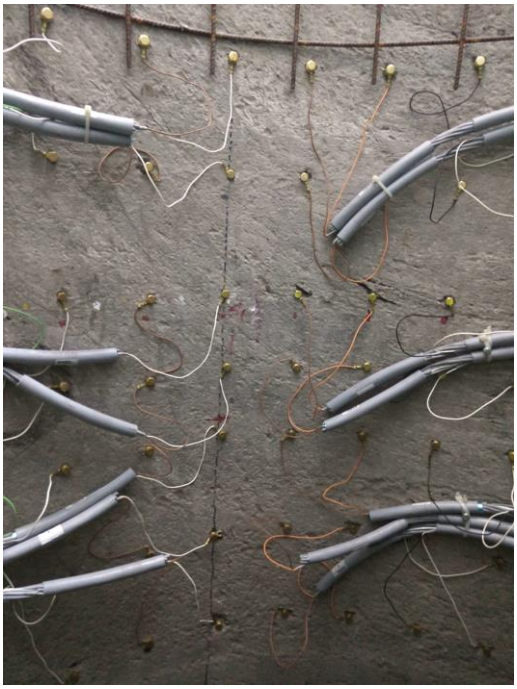

Fig. 3.46 Installed ERT electrodes in Shaft 1

Fig. 3.47 Installation of radial stress sensors at the wall of Shaft 1

ES/DS installation and embedded instrumentation

The segments of the sealing system were installed in layers and the sensors embedded in these layers. The DS (total thickness 100 cm) were emplaced in layers of 8-9 cm in order to compact them to get a final dry density of 1.57 g/cm^3, resulting in 12 layers for each DS (L1 to L12). The instrumentation of the DS was placed in the layers L3, L9 and L12. For each layer, first bentonite pillows were emplaced and then BGM was brushed in to fill the gaps in between with a small broom/brush. The ratio was 1.22 parts of pillows and one part of bentonite granular material (55:45). In the vicinity of the sensors, BGM was used to ensure good contact. The layers were compacted slightly with a beating wood, so to reach the required density. The emplacement dry density (105 °C) was about 1.52 to 1.60 g/cm³ and averaged 1.55 and 1.56 g/cm³ for all DS. The average water content at 105 °C was 11.5 % for the pillows and 10.2 % for the BGM close to the water content determined just prior to delivery.

The ES (total thickness 30 cm) were emplaced in two layers (L1, L2) of 15 cm. The instrumentation of each ES was emplaced in layer L1. After pouring the fine sand in the shaft, a slight compaction with the beating wood was performed to reach a target dry density of 1.6 g/cm³.

The first segment installed was ES1 (Fig. 3.48). It was installed in two layers with the instrumentation located in the middle of the segment, between the two layers: two PP sensors and one horizontal TAUPE TDR. Besides, four vertical TAUPE TDRs of 5 m length were emplaced. These vertical TAUPE TDRs were handled in all the layers installed on top.

While ascending along the shaft, the protective metal grid that was installed around the entire borehole was cut and removed.

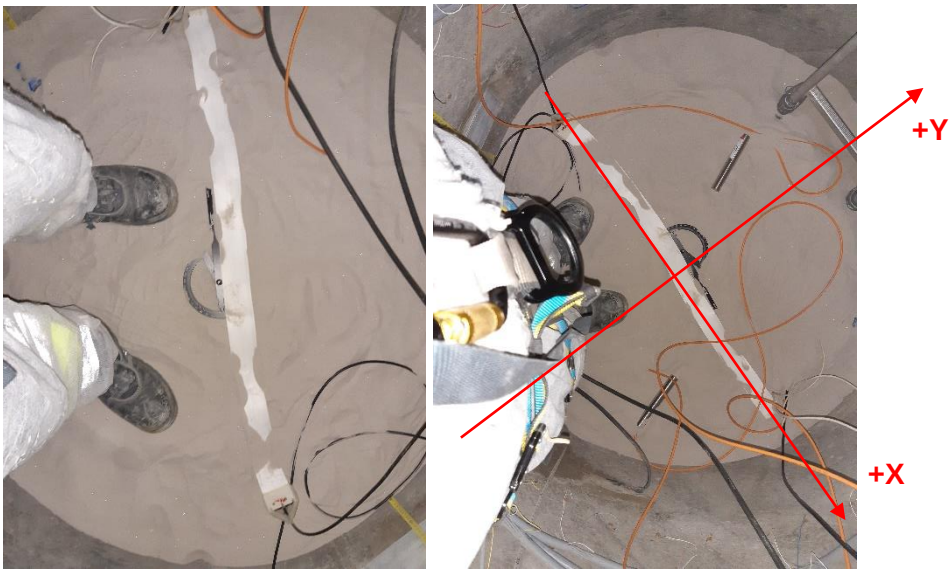

Fig. 3.48 Installation of ES1 in Shaft 1

DS1 was installed in 12 different layers, using the mixture of bentonite pillows and bentonite granular material, which was mixed inside the shaft (Fig. 3.49). The mixture of each layer was compacted (carefully to prevent the pillows from breaking) to reach the planned dry density. The sensors were emplaced in layers L3 and L9: two PP sensors and two RH&T sensors. At the top of the last bentonite layer, a TP sensor (axial stress cell) was installed, with the measurement face looking towards DS1.

Fig. 3.49 Installation of DS1 in Shaft 1

ES2 was installed with two PP sensors and one horizontal TAUPE TDR in the middle of the segment (Fig. 3.50).

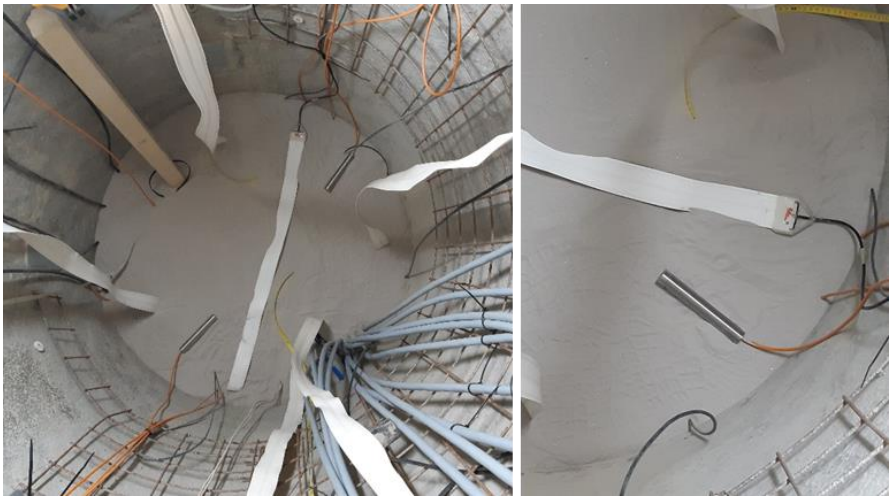

Fig. 3.50 Installation of ES2 in Shaft 1

DS2 was installed, including two PP sensors and two RH&T sensors on L3 and L9, one TP sensor (axial stress cell) on L12 and the sand pipe connection to ES2 for the backup hydration system. The sand connection was made leaving a PVC half pipe of 200 mm close to the shaft wall during the bentonite compaction, which was filled with sand and then removed (Fig. 3.51).

Fig. 3.51 Installation of DS2 in Shaft 1 including the sand connection two ES2

The following ES3 contains two PP sensors and one horizontal TAUPE TDR installed in the middle of the segment as well as the metal tube of the back-up hydration system (Fig. 3.52). Additionally, the displacement measurement system was installed in this segment on a rigid plastic surface located on the upper sand layer (Fig. 3.54).

Fig. 3.52 Installation of ES3 in Shaft 1 with metal tube of back-up hydration system

Fig. 3.53 Installation of displacement measurement system on top of ES3 in Shaft 1

DS3 was installed including two PP sensors and two RH&T sensors on L3 and L9 as well as one TP sensor (axial stress cell) on L12 (Fig. 3.54).

Fig. 3.54 Installation of DS3 in Shaft 1

ES4 contains two PP sensors and one horizontal TAUPE TDR in the middle of the segment (Fig. 3.55).

Fig. 3.55 Installation of ES4 in Shaft 1

The uppermost sealing segment (DS4) includes two PP sensors and two RH&T sensors on L3 and L9 as well as one TP sensor (axial stress cell) on L12 (Fig. 3.56).

Fig. 3.56 Installation of DS4 in Shaft 1

The last segment (ES5) contains two PP sensors and one horizontal TAUPE TDR sensor (Fig. 3.57).

Fig. 3.57 Installation of ES5 in Shaft 1

Sealing System Quality control

The water content of each DS was measured on site during installation, by drying samples at temperatures of 105 °C and 200 °C. For each of the 48 layers, a sample of bentonite pillows and another of BGM were taken during the emplacement, wrapped in a thick plastic bag and stored in plastic buckets covered with plastic until the end of the working shift. A sample of each layer (binary mixture) was also taken.

Each layer of the ES was sampled by 3 x 10 g. The water content was determined at 105 °C and 200 ºC.

The results can be found in /GAR 22/, Table 25.

Plug and shaft cover

The installation of the confining structure was done during the first week of February 2021. The shaft wall was lined with a steel mesh to protect the operators working at the bottom from falling loose pieces of rock. The components of the metallic plug were delivered and stored in the hall of access to the security gallery. The three tube sections were transported with a forklift along the security gallery to the Niche P3 at the laboratory entrance and stored there until their installation.

Prior to emplacement of the metal plug, depth measurements from the gallery to the top of the seal were taken to check if there had been swelling after installation of the sealing system. The same measuring protocol implemented during the backfilling of the shaft

was applied. It was stated that the sealing system had swelled 1.54 cm in average, resulting in an average total height of 6.021 m from the shaft bottom and an average depth of 5.988 m from the gallery.

The cable harness was packed as tight as possible with zip ties to minimize its volume and to ease the installation of the first section of the plug. Nevertheless, it was stated that it would not fit through the central hole of the bottom plate as the cables did not exit the sealing system perfectly centered. Therefore, it was necessary to center the cable harness as much as possible and to protect the exposed cables on top of the sealing system from potential damages prior to installation of the bottom section of the plug. This was done by adding an extra layer of sand of a few centimeters. A total of 116.77 kg of sand were poured and evenly distributed. The average increase in height was 7.7 cm, resulting in an average total height of 6.098 m from the shaft bottom and an average depth of 5.911 m from the gallery. Afterwards, it was stated that even after centering and re-packing, the cable harness would not fit through the hole in the bottom plate, and it was decided to widen the hole of the bottom plate with the help of a plasm cutter to adapt the hole to the harness (Fig. 3.58).

Fig. 3.58 Centering the cable harness within the additional sand layer (left) and widening of the hole in the lower confining tube (right) for Shaft 1

Once finished, the tube section was uplifted, transported to the niche, and positioned close to the shaft. The safety steel mesh lining at the shaft wall was removed. All the cables were passed from bottom to top through the tube section. The tube was suspended over the shaft with the forklift and gently descended until it was half inserted. At this point, the tube was attached with slings to the winch anchored to the ceiling over the shaft, and the descent continued with the winch all the way down to the bottom (Fig.

3.59). The middle and upper tube section were inserted in a similar way and the flanges of each two tube sections were bolted.

Fig. 3.59 Sequence of inserting the bottom section of the metal plug into Shaft 1

To minimize the interaction of the shaft wall with the atmosphere, the gap between the tube and the rock wall was filled with sand poured from the top. A total of 428 kg of sand was added. The top lid was brought in from the storage area with the forklift, hanged from the winch and placed on top of the tube in the right orientation (Fig. 3.60).

Fig. 3.60 Installation of the top lid for Shaft 1

The bolting of the top lid was carried out by VS Hagerbach during the first week of March 2021. Eight 3 m long boreholes were drilled at an outwards angle of 20º as foreseen, and eight 4 m long bolts with a diameter of 32 mm were anchored into them with four 0.5 m long, two-component resin cartridges each (Fig. 3.61).

Fig. 3.61 Bolting of the top lid for Shaft 1

Hydration system

The installation of the hydration system was done in the first week of May 2021. The hydration and operation cabinets arrived at the URL on the 3rd of May. The cabinets were installed next to the feeding borehole in Gallery 18. Scales and water tanks were put in place and all electrical and hydraulic connections were established. A first dry test was performed to check that all the valves and scales work as expected. After ensuring proper working conditions of the installed equipment, the cabinets were connected to the Geomonitor system.

Prior to filling the system with water, the tanks and valves were tested at working pressure. The tanks were filled with water using the transfer pump and a pressurized nitrogen bottle was connected to the main cabinet to provide the required overpressure, leaving the hydration system ready for injection (Fig. 3.62).

Fig. 3.62 Hydration system for Shaft 1

3.5 Shaft 2 installation and instrumentation

3.5.1 Description of components

Levelling layer

As in Shaft 1, the bottom of Shaft 2 had a rough surface resulting from the shaft sinking which was compensated by a levelling layer made of a three-components epoxy resin-based mortar (Sikadur 43 HE and Sikadur 42 HE). The levelling was done by VSH in September 2022. The levelling layer reached a maximum thickness of 21 cm.

Pressure chamber and connection piece to feeding borehole

The pressure chamber of Shaft 2 is similar to the one for Shaft 1. The height was increased by 5 cm to fit the dimensions of the feeding borehole entry. The chamber (material 1.4571) is composed of a base and a top. The base consists of a bottom plate (Ø 110 cm with thickness 15 mm), a supporting ring (height 130 mm) and 39 supporting pillars (height 130 mm) fixed to it (Fig. 3.27). The pillars are made from standard I-Beam (HEA 100 DIN 1025-3) cut into pieces. At the rim of the base plate, the supporting ring is fixed with a 10 cm gap for the access of the feeding line. The inner free volume of the pressure chamber is 111 dm³.

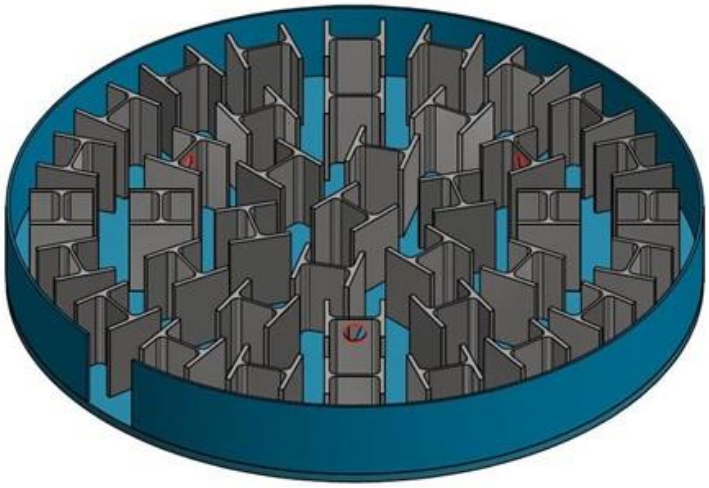

Fig. 3.63 Base of the pressure chamber for Shaft 2

The top of the chamber is divided into quarters (4 plates), each perforated with 311 holes (Ø 8 mm) to ensure a homogeneous hydration (Fig. 3.28). The total height of the pressure chamber, including the top plates, is 16 cm.

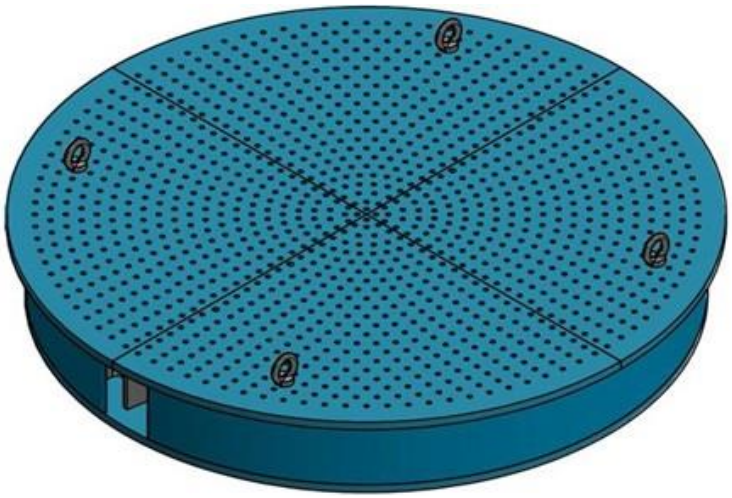

Fig. 3.64 Pressure chamber with top plates for Shaft 2

The connection of the pressure chamber to the feeding borehole is provided by a bent (approx. 60°) PVC pipe of around 125 mm length and with an outer diameter of approximately 45 mm. The inner diameter of the connecting piece is in the order of 35 mm.

Sandwich sealing system

The installed sealing system consists of five ES (thickness 30 cm) and four DS (thickness 80 cm) in alternating arrangement.

The required materials for DS and ES were prepared and delivered by SSKG. The materials used for the DS in Shaft 2 are Securisol® MHP1 (70/30) in the lower segments (DS1 and DS2) and Calcigel in the upper ones (DS3 and DS4). Both Securisol® and Calcigel are German Ca-bentonites. As the swelling pressure must not exceed the rock minor principal stress of 3 MPa, the natural Securisol® UHP is blended with the kaolinitic-illitic sulfide free clay F1623.00, to reduce the swelling pressure. The resulting material is Securisol® MHP1 (70/30). Furthermore, the maximum expected swelling pressure must be adjusted via the dry density and water content of the bentonite during installation. To produce the DS material, bentonite pillows with a bulk density of about 2.2 g/cm³ were compacted both of Calcigel and Securisol® MHP1 (70/30). The moisture of the bentonites after processing and prior to the delivery to MTRL corresponded to the air-dry state at ambient conditions (about 45-55 % RH and 20-25 °C), with a value of about 10 % (105 °C) and 11.25 % (200 °C) corresponding to a water content of 11.15 % / 12.7 %. About 45 % of the pillows were crushed to provide the bentonite granular material (BGM) for the gap filling during installation. About 30 % (ES material) and 50 % (DS

material) spare material were produced and delivered to MTRL to have them available to adjust dimensions of either ES and DS or the mixing ratio (pillows/BGM) in DS during installation. The water content of DS material at installation is the result of the water content after compaction of bentonite pillows and production of the BGM for the binary mixture and the equilibration water content during transportation and storage prior to installation.

A fine sand (N45) with a water content in air dry state of < 1 % is used for the ES. The proctor density of fine sand is about 1.7 g/cm³. In air dry state an installation density close to 1.6 g/cm³ could be obtained in several semi-scale lab experiments (HTV).

Instrumentation

The following description of the instrumentation is rather condensed, and, particularly, the sensor positions are summarized in Fig. 3.69 at the end of this paragraph as well as Tab. A. 10 and Tab. A. 11. The details are given in /WIE 22a/ and /GAR 23c/.

Sensors in the pressure chamber

Two temperature sensors (thermocouples, Termya Type T, range: -185-300 °C) are placed inside the pressure chamber. The thermocouples are led to the pressure chamber through the feeding borehole. The sensors are installed in the center and fixed to the pressure chamber.

The fluid pressure is not measured directly in the pressure chamber (as it is in Shaft 1). The pressure sensors are located at the flange of the feeding borehole.

ERT

The ERT installation in the second shaft aims to gain an extended insight into the overall system. The number of electrodes used has been increased to 480 for this purpose. This was made possible by further development by the equipment manufacturer. The concept of arranging the electrodes in horizontal rings from Shaft 1 was retained. However, in order to be able to observe almost the complete sealing system, the distances between the electrodes had to be enlarged, which leads to a slightly poorer spatial resolution. The configuration now consists of 20 rings with 24 electrodes each. The layout with the explicit installation coordinates is shown in Fig. 3.65.

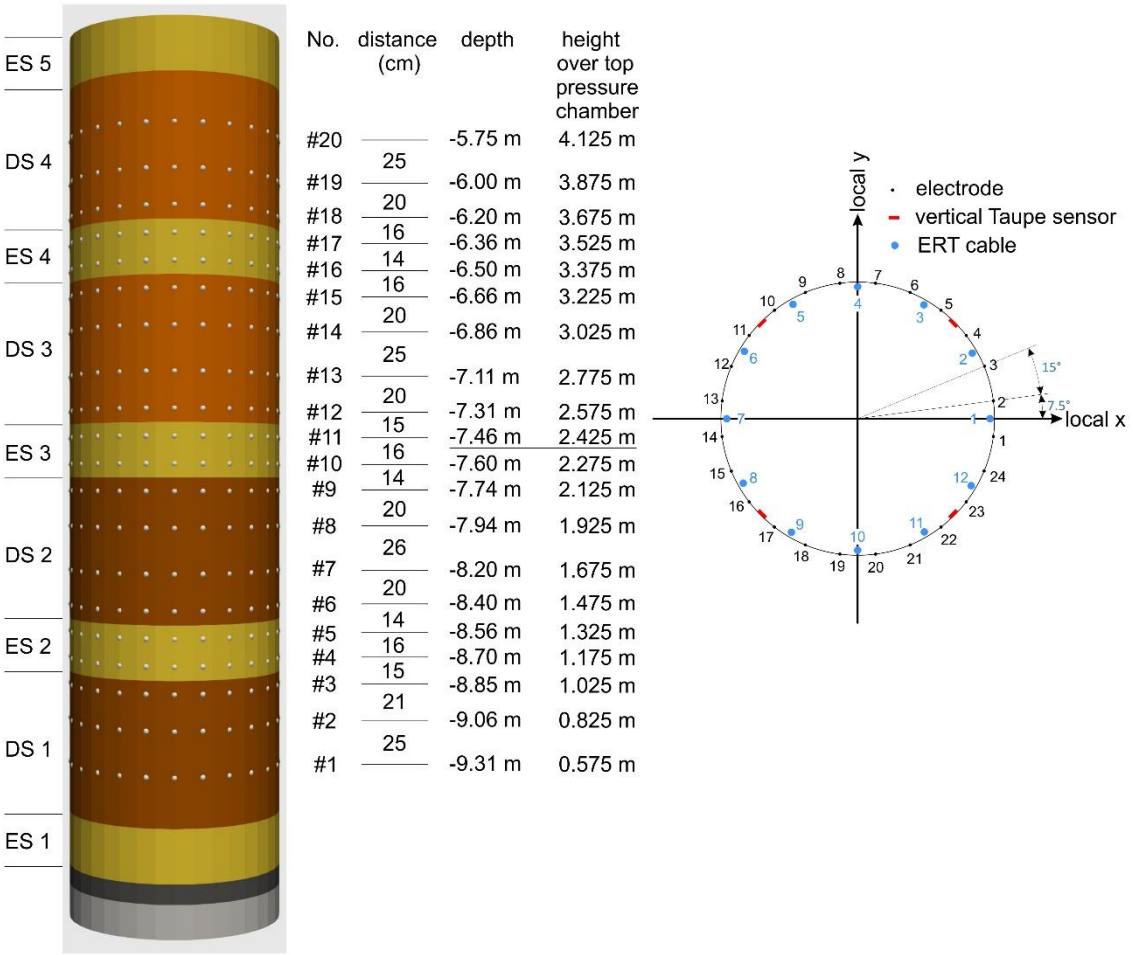

Fig. 3.65 Layout of the ERT measurement system in Shaft 2 in relation to the embedded segments of the Sandwich system

The individual components for the ERT system were procured separately and installed as compactly as possible in a cabinet, which was mounted on the niche wall. The picture shows the finished installation and a detailed excerpt from the cabinet. Here one can see the still open cable boxes for sealing the cables, which were subsequently filled with epoxy resin.

Further details can be found in the test plan /WIE 22a/.

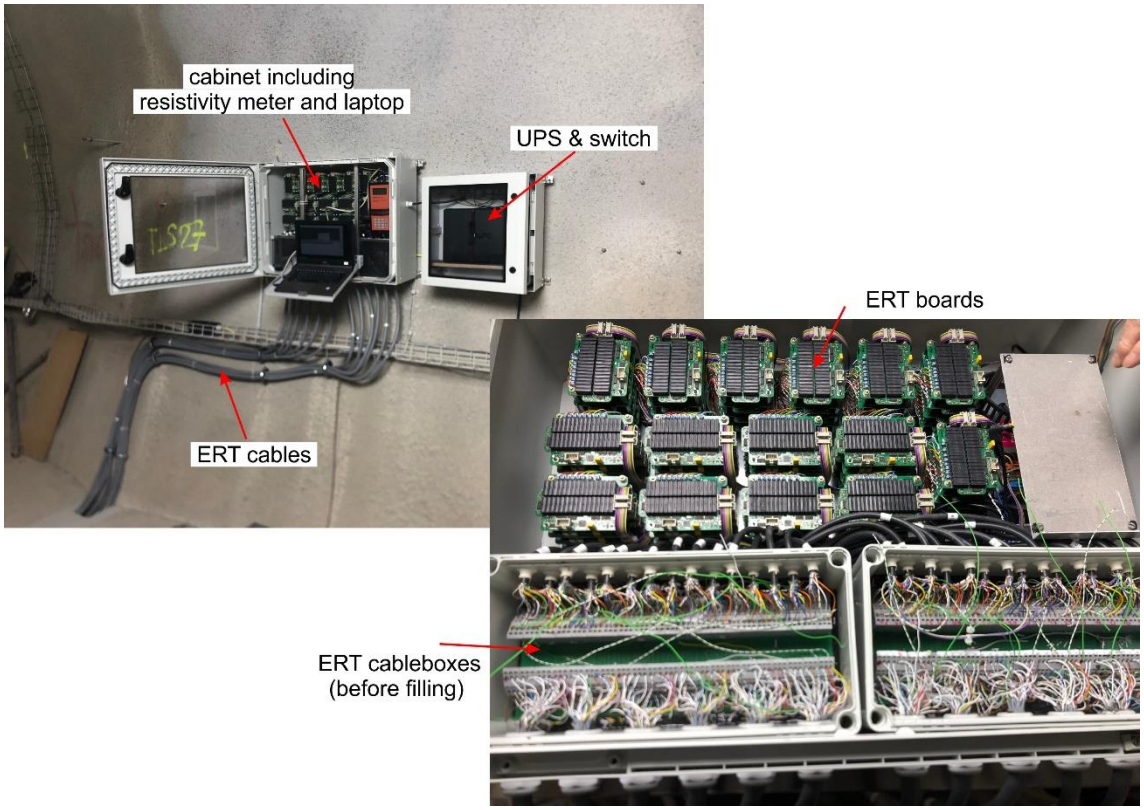

Fig. 3.66 Installed ERT measuring system for Shaft 2 in the Sandwich niche with a detailed picture of the cabinet

Taupe TDR

At the rock interface, 4 sensors, fixed at the rock wall, opposite to bulk sensors inside the shaft filling, will monitor the interface between shaft and rock wall. Because the ARDP of the rock wall is normally higher than the bulk materials after installation, TDR Taupe sensors should represent values in between. Right before installation, it has been decided not to lead the sensors completely through all shaft segments but leave out the lowest ES1 by forming a U-turn with the cables inside DS1. Because the contact to the rock wall could not be assured completely, this should prevent an immediate breakthrough along the cables. Liquid coming from the pressure chamber is collected in ES1 and slowly distributed to DS1. A distance of about 5 to 7 cm has to be overcome to reach the lowest point of the interface sensors. This does not avoid potential fingering along the sensors but reduces the probability of such events. After all, immediate swelling of the surrounding clay materials should help anyway.

Five embedded Taupe TDR sensors or bulk sensors, monitor the center of the shaft filling and at four positions about 15 cm apart from the adjacent interface sensors. This

gives the ability to see, what happens at the interface with possible intruding of liquid coming from rock wall and liquid propagating inside shaft materials. Additionally, the distance of 15 cm between outer sensors and interface sensors adds some information about the actions in this area.

Relative humidity and temperature

Two RH&T sensors (Vaisala HMP7, sensor range: 0-100 % RH / -70-180 °C) are installed in each DS, as in Shaft 1. The sensors are, however, slightly different, featuring a longer cable so that electronics and connector can be placed outside the sealing system, minimizing the risk of water leakage and reducing the number of obstacles inside the sealing system.

Pore pressure / fluid pressure

The performance of the Geosense pore pressure sensors used in Shaft 1 was not satisfactory. For Shaft 2, they are replaced by Keller pressure sensors (Keller PA23SY, signal: 4-20 mA, sensor range: 0-6 MPa absolute pressure). Two pressure sensors are emplaced in each of the ES and DS, both with a stainless-steel sintered filter.

Axial and radial stress

Four circular total pressure (TP) sensors (GLÖTZL/ EAI 10/20 K200 A Z4 circular, signal: 4-20 mA, sensor range: 0-20 MPa) are horizontally installed close to the center of the shaft at the interface DS / ES, on top of each DS. They measure the axial stress changes in the column induced by the swelling pressure.

A total of four flat cells for radial stress measurement (GLÖTZL/ EAI 10/20 K200 A Z4 rectangular, signal: 4-20 mA, sensor range: 0-20 MPa) are installed at the rock wall in Shaft 2 to determine the swelling pressure evolution. The radial stress is measured at the interface of the DS and the shaft contour.

Vertical displacement

A fiber optical (FO) displacement measurement device is installed in the sealing system which measures relative vertical displacements in one plane. The device is installed in the upper part of DS2. For absolute position measurement, the system is coupled to

three vertical displacement transducers fixed to the shaft wall. A detailed description of the system is given in /GAR 23a/.

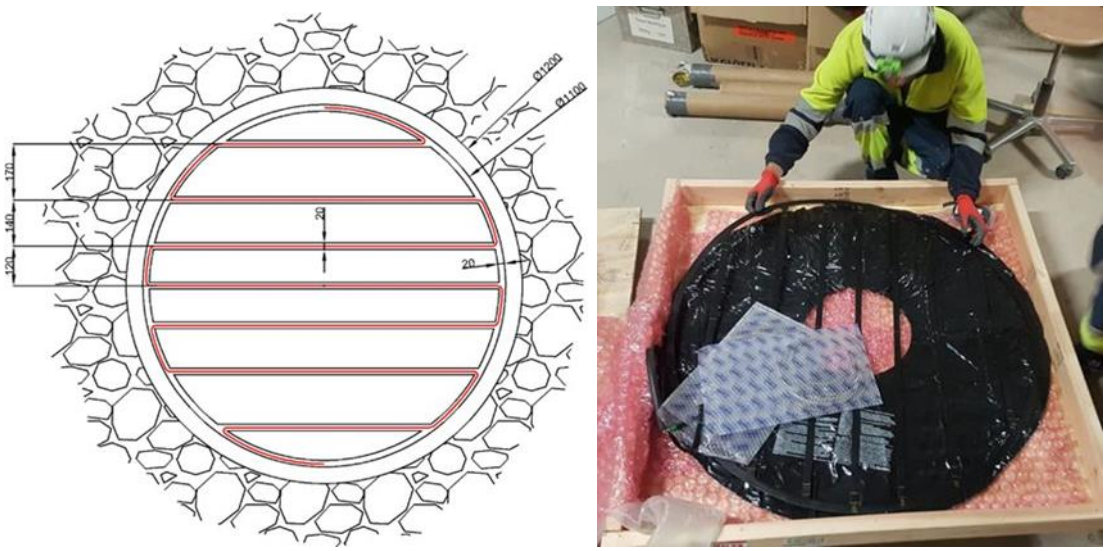

Fig. 3.67 Layout of the 2D FO sensor

The 2D FO sensor (Fig. 3.67) consists of a thin strip of fiberglass (or support) with multiple beams covering a circular area, with a sensing fiber bonded on the top and bottom surfaces along the strip's entire length. The dimensions and the design of the sensor were done according to the restrictions imposed by the inner diameter of the shaft, (1.18 m), and the need of having cables running through the sensor and along the rock walls. The sensor is provided with fiber extensions for both sensing optical fibers to reach the measuring device. Two fibers exit the support to reach broadband reflectors (BBR-010) which are located close to the shaft. The BBR-010 are connected to the optical frequency domain reflectometer (OFDR) with another fiber having around 3 m in length. It features 4 channels, out of which only two are used to connect the top and bottom sensing fibers of the 2D shape sensor.

The three vertical displacement sensors are arranged at 120º angular distance and fixed to the shaft wall (Fig. 3.68). The sensors are magnetostrictive linear position sensors (Firstrate FST400-1100, signal 4-20 mA, range 50 mm).

Fig. 3.68 Vertical displacement sensors in Shaft 2

Wireless data transfer system and related sensors

Additional redundant sensors are installed for testing a wireless data transmission (WDT) system which has been developed in the frame of WT experiment at Mont Terri. All details about the development and characteristics of this system can be found in /MAY 23/.

A new radio, specifically developed to support low data rate wireless communications under buried conditions is being used. The term transmit unit (TU) refers to the very low frequency (VLF) transmitter and receiver unit (RU) to the VLF receiver, each of which is connected to a separate antenna and power source. Data communication from the TU to the RU occurs through the earth using magnetic induction at frequencies in the VLF range. The combination of one or more TUs with one RU is called the TTE system.

The TU is provided with a sensor interface for up to 6 sensors to digitalize the field measured parameters (sensors) and transmit them to the RU. The RU is equipped with a 3D antenna and a serial port that allows the demodulated data to be viewed on an external PC via a serial-USB adapter cable. The RU output may be viewed on a simple serial port terminal application (i.e., PUTTY) running on a PC. The transmission range is given by the distance between the TU and RU antennas.

The sensors connected to the WDT are emplaced in DS2 and ES3. They are one PP sensor (Keller PAA-26 Y, signal 4-20 mA, range 0.8-11 bar absolute pressure), two

RH&T sensors (Amberg SHT85V1, range 0-100 % RH, -40-125 °C), one TP cell (EARTHSYSTEM CP-02-TO-10-C, signal 4-20 mA, range 0-10 MPa absolute pressure) and one temperature sensor (Termya Pt-100 class 1/10 DIN, -50-250 °C).

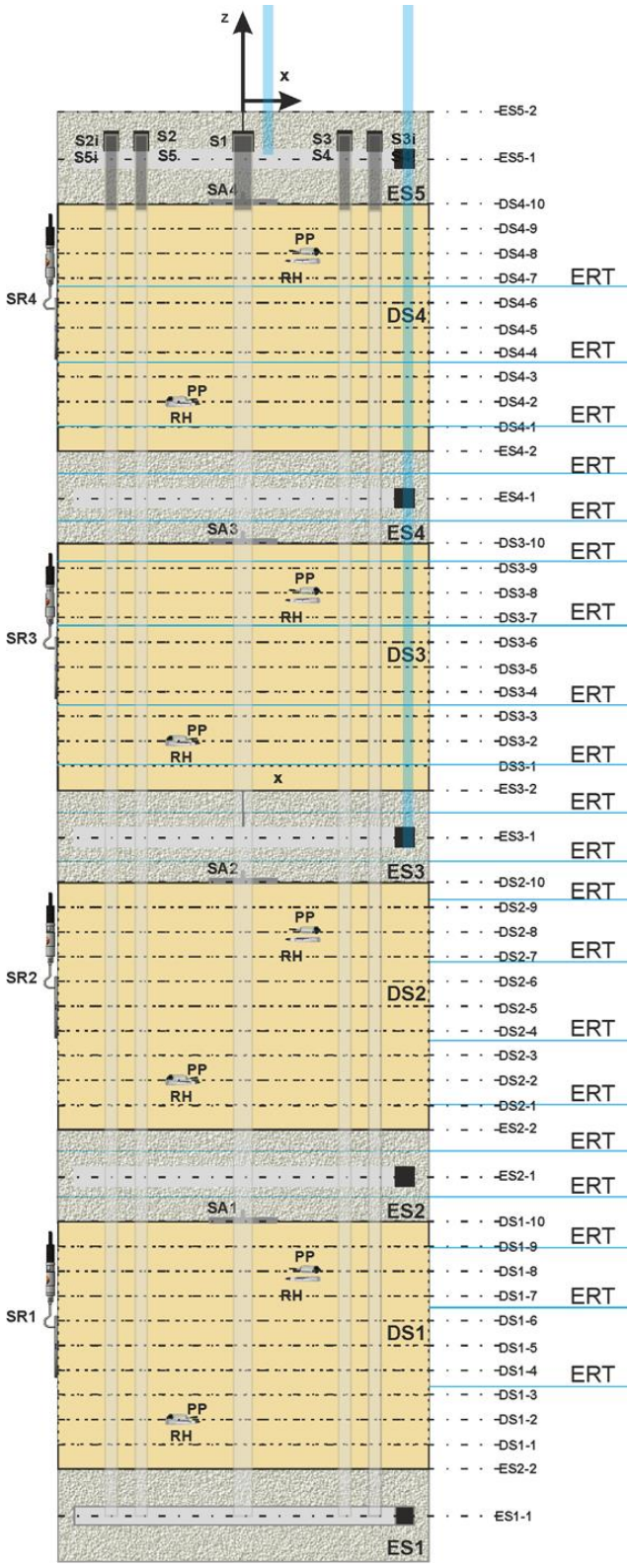

Fig. 3.69 Sensors in the sealing system and at the rock interface of Shaft 2

Back-up hydration

The back-up hydration system in Shaft 2 allows for an additional (gravitational) hydration of the sealing system starting in ES3 and ES5. The system consists of two hydration lines reaching ES3 and ES5 from the top. The hydration lines consist of a plastic tubing (Parker Polyamide (PA) semi-rigid tubing 6x4) coming from the hydration system connected to a stainless-steel line (outer diameter 6 mm). The set-up enables fluid injection from the hydration system to be distributed within ES3 and ES5. The line reaching ES5 is equipped with a manual valve and a manometer (Wika/233.50.63, range 0-0.6 bar relative pressure). The line reaching ES3 is equipped with a manual valve and a wider range manometer (Wika/233.50.63, range 0-25 bar relative pressure) and pressure transducer (up to 25 bar).

Plug and shaft cover

The sealing system in Shaft 2 is also covered by a metallic plug to confine it mechanically. As in Shaft 1, the plug consists of a confining tube and a top lid bolted to the rock surrounding the shaft (Fig. 3.35). As there will be (gravitational) hydration from the top in Shaft 2, the metal plug must be watertight. This implies to avoid the injected water to move upwards by the gap between the metal plug and the rock or along the cables and lines. Accordingly, a cables sealing lid is added to the confining system. It rests on top of ES5 and below the confining tube.

The cables sealing lid consists basically of an external stainless-steel cylindrical body comprising two circular plates on top and bottom, with a diameter of 1160 mm / 1110 mm and a thickness of 20 mm, and a frame with a diameter of 1160 mm, a thickness of 20 mm and a height of 180 mm. The bottom plate consists of four quarter plates, each with an opening to install IP68 cable seals to allow the passthrough of the injection lines and the cables from the sensors installed in the sealing system below (Fig. 3.70). The frame with the bottom plate bolted on it can be filled with support tubes and potted with resin. The top plate (made of four quarters) can be screwed to the frame of the lid (Fig. 3.71).

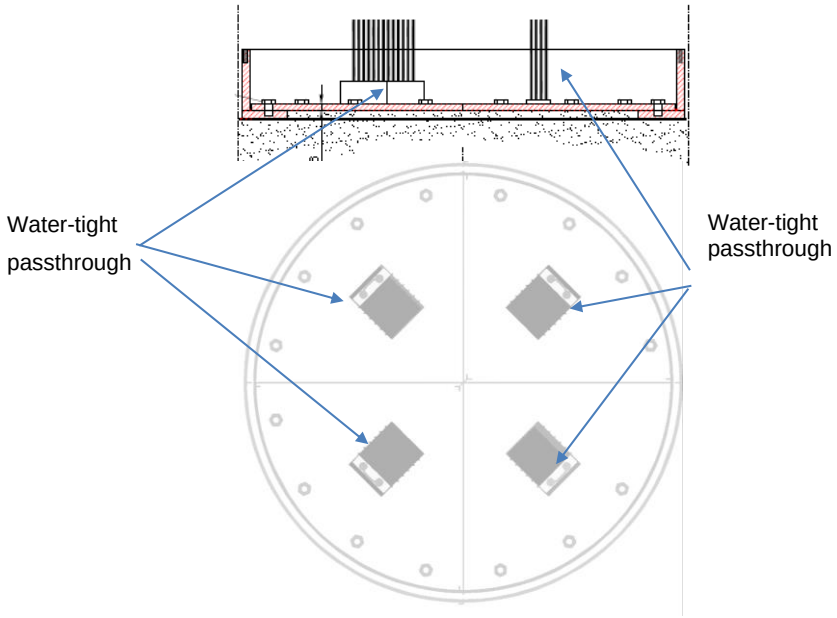

Fig. 3.70 Scheme of the bottom plate of the cables sealing lid below the confining tube in Shaft 2

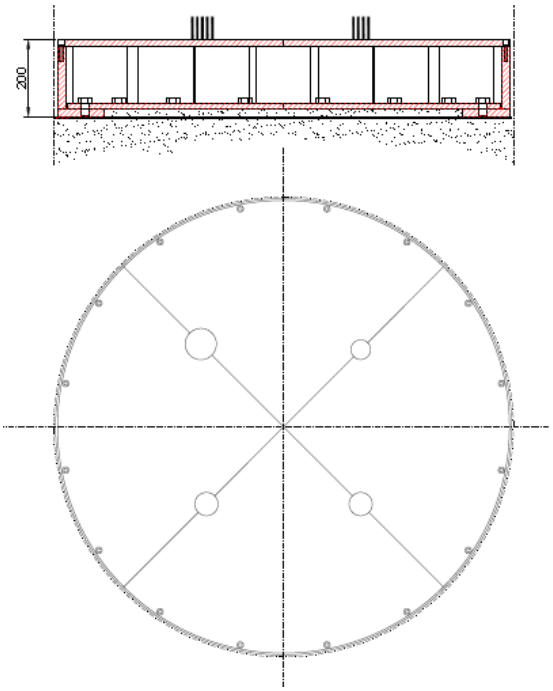

Fig. 3.71 Scheme of the top plate of the cables sealing lid below the confining tube in Shaft 2

The vertical confining tube (total length 4.74 m) reaches from the top of the sealing system to the niche floor. It is composed of four cylindrical tubes (lengths 0.5 m, 2 m, 1.12 m, 1.12 m) joined by inner screwed flanges. Each section consists basically of a carbon steel tube with an external diameter of 1170 mm and a thickness of 20 mm. The bottom section features a circular steel plate closing its bottom that remains in contact with the cables seal lid. Eight radial plates transmit the pushing force from the bottom plate to the tube. The plate features four circular holes with a diameter of 100 mm to pass through the sensor cables (Fig. 3.36). The top section is covered by a circular steel top lid (diameter 2 m, thickness 50 mm) which provides the mechanical confinement by transmitting the pushing force from the tube to the surrounding rock. This is done by means of 8 steel bolts anchored through holes around the outer part of the lid. The bolts are chemically anchored to inclined boreholes (length 3 m) drilled around the shaft. The top lid has a central hole to allow for accessing the bottom lid inside the tube.

Hydration system

As for Shaft 1, the seal will be artificially hydrated by means of a hydration system. ES1 will be hydrated from the pressure chamber below, so that the hydration of the (lower) Securisol® MHP1 (70/30) part of the sealing system will be comparable to Shaft 1, with the essential difference of using a different sealing material. ES5 will be hydrated from the top. Since there are the same materials and similar geometries at the top half of Shaft 2 and at Shaft 1, the essential difference is the hydration direction. Moreover, hydration will be performed by gravity only – there will be no additional pressurization. An additional hydration of the system via ES3 will be possible to implement a more symmetric swelling of DS. This option could be used if the EDZ is less effective than expected.

The expected fluid injection pressure is max. 30 bar (3 MPa) and should be kept as constant as possible given that the fluid uptake of the seal is expected to be as low as 0-25 ml/h when increasing DS saturation. The injection system is mounted next to the one for Shaft 1 and its expected running time is more than four years.

The hydration system is based on pressurized reservoirs. As for Shaft 1, the hydration via the bottom pressure chamber is done using a low-pressure tank (LPT) and a high-pressure tank (HPT), depending on the water injection pressure (below or above 8.5 bar injection pressure). The hydration system for Shaft 2 features some improvements:

– For hydration via the top ES, only a second low-pressure tank is needed, because hydration from the top will run only by gravitation. The low-pressure tank of the hydration system of Shaft 1 will be used for Shaft 2 given it is not necessary anymore.

– All valves are operated manually.

– Automatic safety valves are installed in the inflow lines to avoid air in the system in case the water tanks run low.

– The high-pressure tank has a bigger volume, around 25 l, to avoid frequent recharging.

As shown in Fig. 3.72, the exit valves of the tanks, V-3, V-5, and V-13, are electrically operated safety valves, normally open, which are triggered when the weight of the corresponding scale reaches a minimum. The output of LPT of Shaft 1 is connected to the back-up hydration lines (not shown in Fig. 3.72).

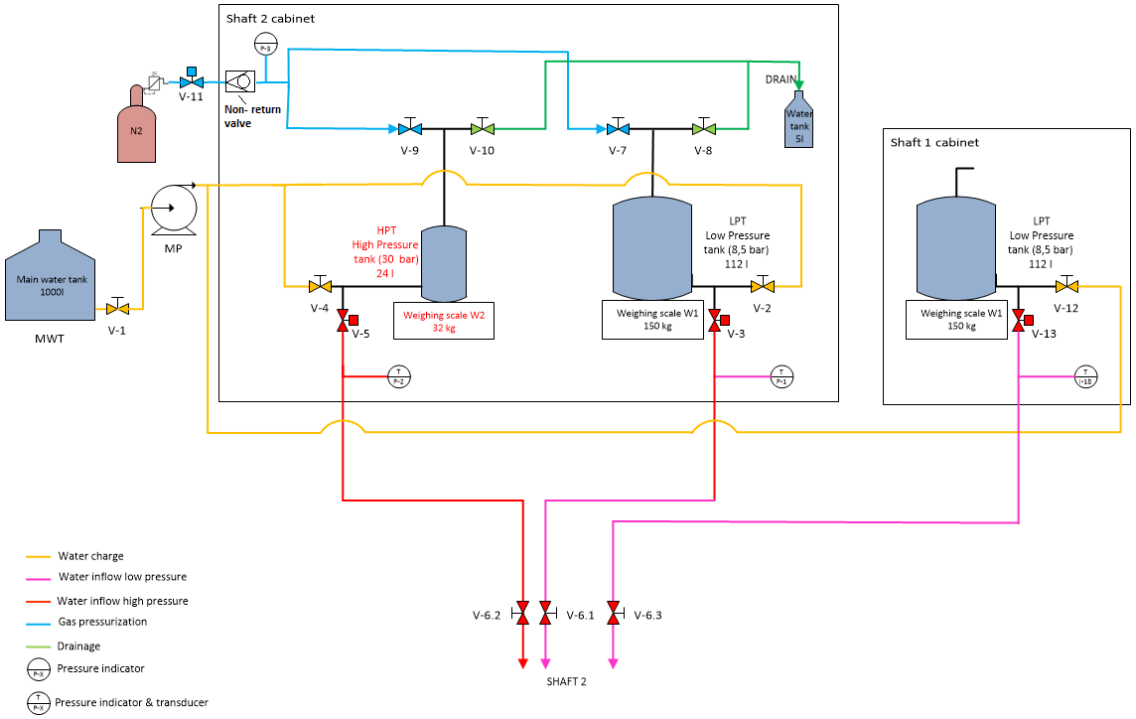

Fig. 3.72 Scheme of the hydration system for Shaft 2

The hydration system is equipped with two scales, for the LPT and HPT of the bottom part of the sealing system, plus the scale of the LPT of Shaft 1 to be used for hydrating the upper part. Two pressure transducers record the injection pressure at LPT and HPT for the bottom part and another provides the gas pressure used for the tanks.

3.5.2 Preparatory works

Measurements in the open Shaft

Surface packer tests

A similar test program was designed in the shaft BSW-A2 with a much more systematic test approach. Only two orientations (definition as in Shaft 1: (+Y: parallel to the niche orientation in direction to the niche end, others clockwise), but every half meter along the shaft vertically between -5.0 and -9.5 m including future sections ES3-ES5 and DS1-DS4. In addition, two tests at -9.8 m were selected in order to estimate the permeability of EDZ in the Carbonate-rich sandy facies. In case 0 the normal direction of the packer and bedding is at an angle and in case 3 the normal direction of the packer is parallel to the strikes.

As results, the permeability in the orientation to +X is twice that in the +Y orientation. The permeability of the EDZ in the Carbonate-rich facies shows the maximum permeability of $1*10^{-13}$ m². The interpretation of all measurement data suggested a relatively higher permeability of $3.5*10^{-14}$ m² with a thickness of 1.5 cm compared to the result from the measurement in the Shaft 1. This can be explained by the fact that the measurements in Shaft 2 were carried out two years after excavation, while the measurements in Shaft 1 were done immediately after the drilling. On the other hand, the surface of the shaft wall was in parts much rougher. Whether the increased permeability zone (rough EDZ) is closed by the installation of the sealing system, by swelling deformation of the DS, and by swelling deformation of the OPA itself is still being examined. Therefore, a constitutive model to describe the EDZ development under hydromechanical conditions is needed.

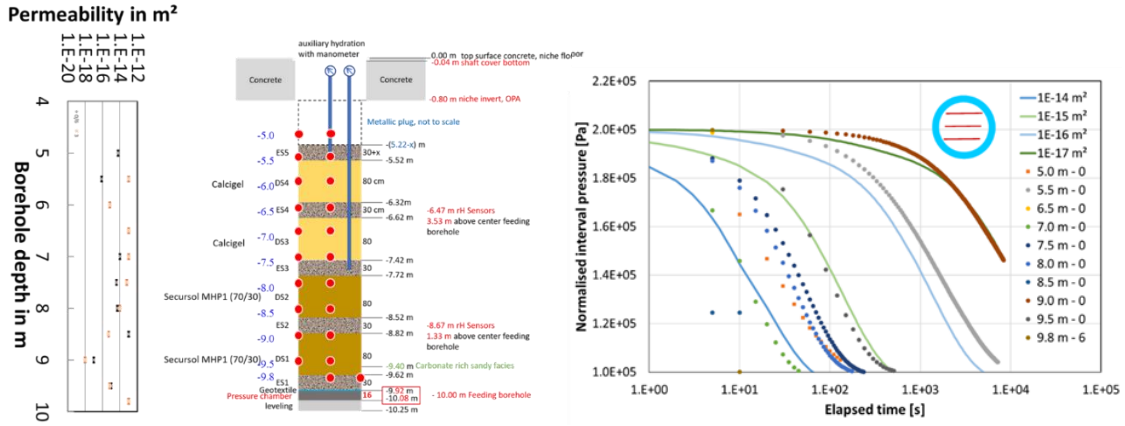

(a) (b) (c)

Fig. 3.73 Permeability distribution along the borehole BSW-A2 (a), measurement locations (b), and numerical interpretations with the orientation +Y

Relative humidity measurement in the EDZ of Shaft 2

Relative humidity measurements were carried out by swisstopo from 12 July 2022 until the end of September 2022 in the shaft wall of Shaft 2 at two different depth levels (measured from the center of the feeding borehole intersection with the shaft) (Fig. 3.74). The lower array of 4 RH-sensors was installed at 1.33 m and the upper one at 3.53 m above the feeding borehole. The sensors for every depth level were installed at 5, 10, 15 and 25 cm radial distance, drilled with a 10 mm percussion drill. The system installed temporarily was a HyDry/IRES acquisition system including 4 RH/T sensors and an additional sensor for air humidity.

The data of the measurements is given in Fig. 3.75 and Fig. 3.76. At the upper level RH in the niche could be measured with the sensor extension and an RH of 80 % was measured all the time, just slightly increasing over the period of 2.5 months. Temperature in the shaft and within the rock wall was equally at about 16 °C. RH in the rock did not allow for a distinction of the different monitoring depths and was constantly at the maximum of 99 %. The RH in the rock at the level of 1.33 m was as well similarly at 99 % for all sensors no matter which installation depth. Temperature in the shaft and within the rock wall was equally at 16 °C for all sensors and only the humidity in the shaft was rising from 90 % RH to 99 % RH over the 2.5 months period. Thus, with this monitoring concept and system no desaturation within the rock wall could be detected at all. Since the general monitoring range of these sensors is 20-80 % RH, a monitoring bias cannot be excluded. Reliable monitoring of humidity above 95 % RH is a difficult task.

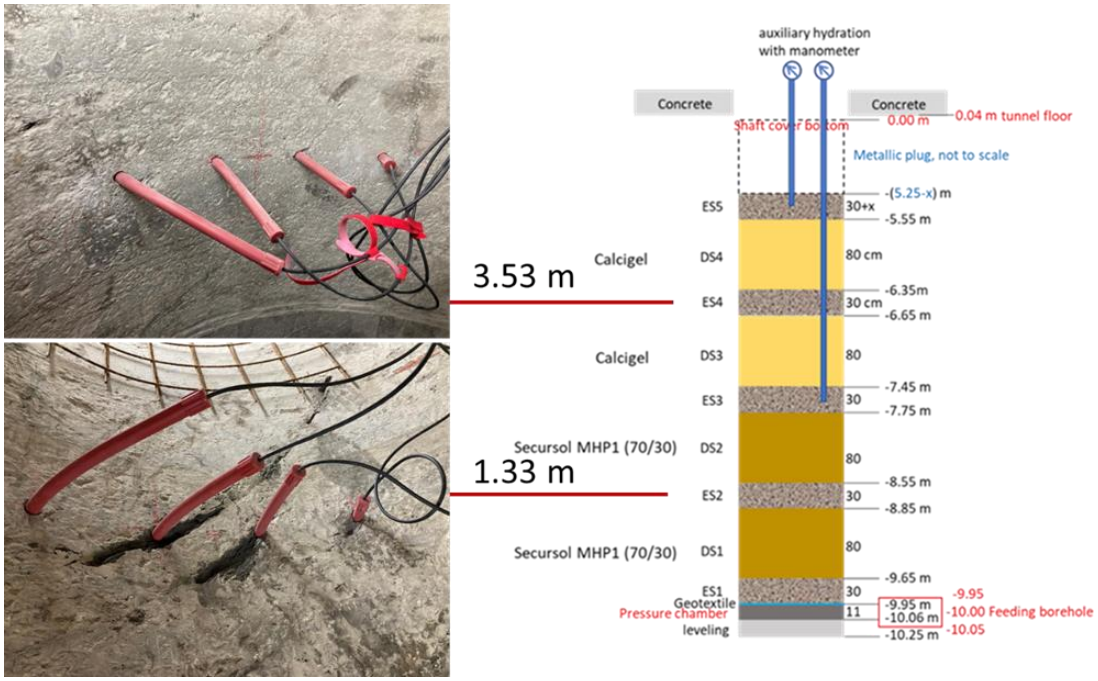

Fig. 3.74 Situation of the temporary RH monitoring locations in Shaft 2

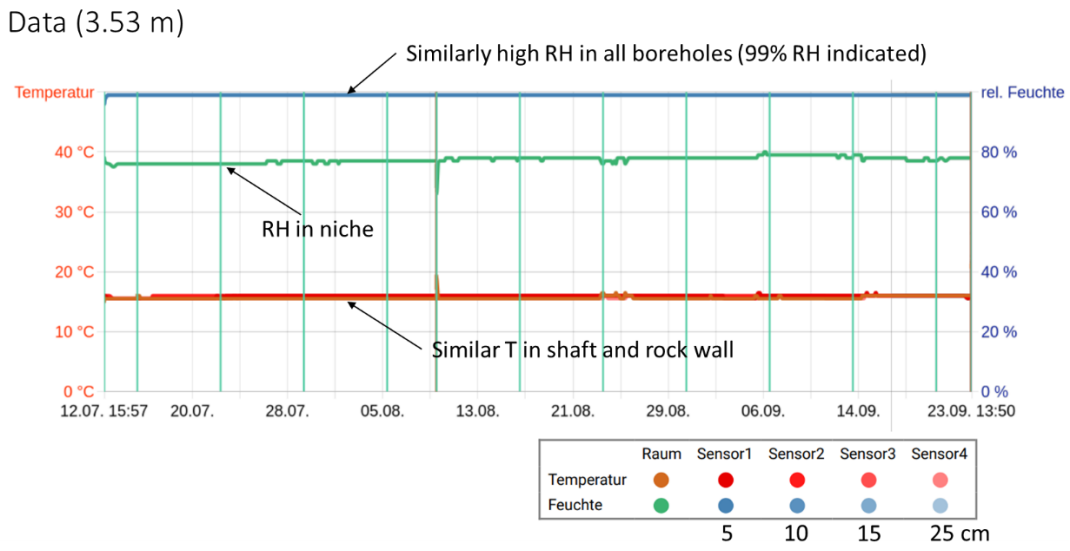

Fig. 3.75 RH data at depth level 3.53 m

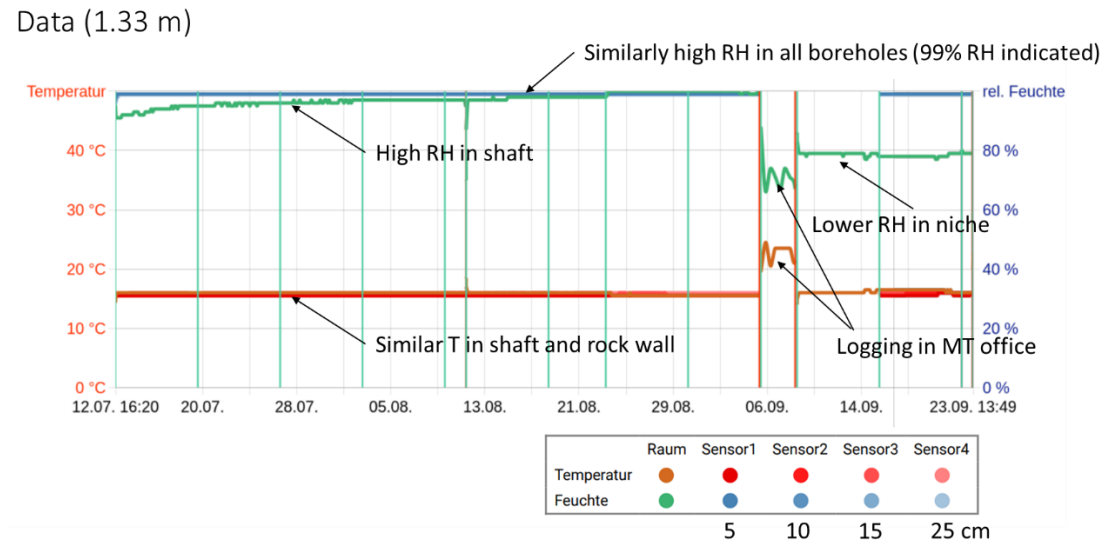

Fig. 3.76 RH data at depth level 1.33 m

Temporary lining, light and ventilation

The planned location of the shaft is given in Fig. 3.77, see as well /BUR 22/. Right after excavation, the shaft was equipped with K196 steel wire meshes (Fig. 3.41 and Fig. 3.42). The foldable meshes were installed from top to bottom and during the backfilling procedure in turn removed from bottom to top. A ladder with a self-locking rope safety device was installed and the illumination and ventilation hose placed. The ventilation mode was aspiring the air at the bottom, yielding a vertical air inflow into the shaft. The working zone was completely separated from the public zone, by a fence restricting the access to the Sandwich niche and the shafts. Only workers equipped with harness, helmet, Dräger gas warning device (O2, CO, H2S, CH4) and the safety permit were allowed to approach or enter the shafts.

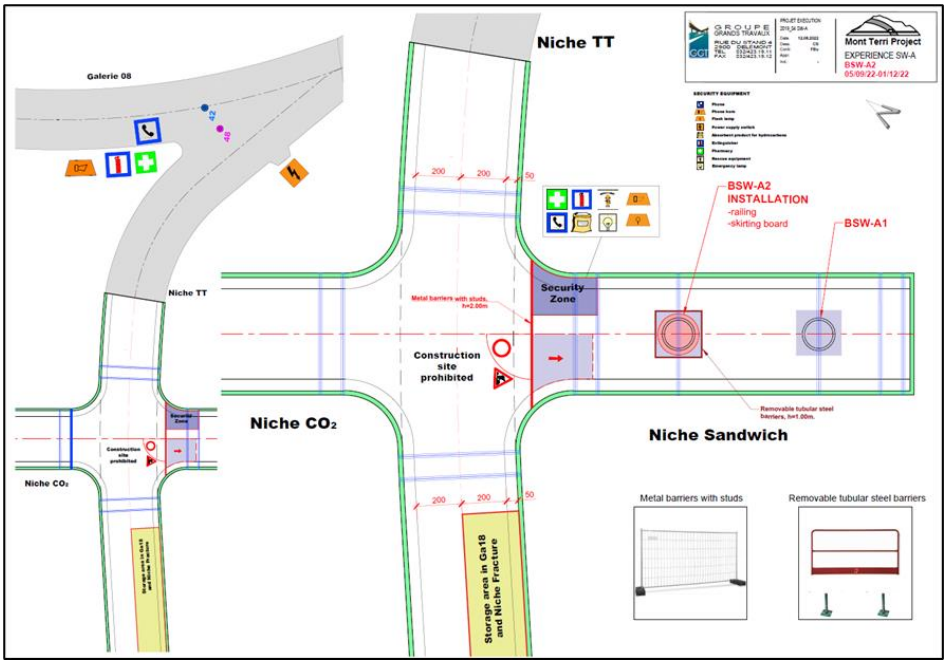

Fig. 3.77 General safety concept for Shaft 2

3.5.3 Installation procedure

Levelling layer and pressure chamber

The levelling layer was installed in September 2022, followed by the pressure chamber with the connection to the feeding borehole (Fig. 3.78). The thermocouples were led to the pressure chamber through the feeding borehole and the sensors were installed in the center and fixed to the pressure chamber before covering it with the top frame. On top of the pressure chamber, a sheet of geotextile was installed to minimize the loss of sand from ES1 to the pressure chamber (Fig. 3.79).

Fig. 3.78 Installation of the pressure chamber, the connection to the feeding bore-hole and inserting the thermocouples in pressure chamber for Shaft 2

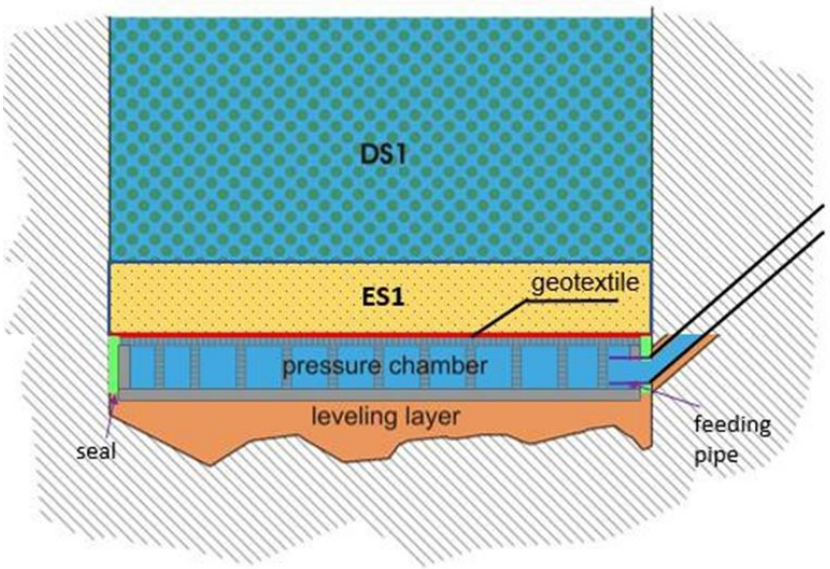

Fig. 3.79 General setup of the bottom of Shaft 2

Sensors at the shaft wall

The four radial stress sensors were installed vertically aligned along the shaft wall, each in the planned depth of one of the DS. Small areas of the shaft wall had to be excavated in order to emplace the sensors' surfaces in the tangent planes of the shaft wall. The sensors were fixed with cement to the excavated shaft surface (Fig. 3.80). Some of the sensors were located very close to ERT electrodes and needed to be carefully marked before doing the rock excavation. All the excavations at the rock were done first and then the sensors were installed and fixed.

Fig. 3.80 Installation of radial stress sensors at the wall of Shaft 2

The vertical TDR sensors were emplaced next to the shaft wall running all along the planned location of the sealing system (Fig. 3.81). They were fixed to the rock surface with plastic screws. Afterwards, their coordinates were measured in every layer.

Fig. 3.81 Vertical TDR sensors installed at the wall of Shaft 2

ES/DS installation and embedded instrumentation

The segments of the sealing system were installed in layers and the sensors embedded in these layers. The DS (total thickness 80 cm) were emplaced in layers of 8 cm in order to compact them to obtain the target dry density, resulting in 10 layers for each DS (L1 to L10). The layers were installed in two phases of 4 cm thickness. First, the bentonite pillows were emplaced and distributed as homogeneously as possible, then BGM was added and mixed manually. Compaction was performed with an electrical compactor and manually. The construction of DS1 and DS2 took longer as the material had to be sieved on site to obtain intact pillows before installation.

The ES (total thickness 30 cm) were emplaced in two layers (L1, L2) of 15 cm. The instrumentation of each ES was emplaced in layer L1. After pouring the fine sand in the shaft, a slight compaction with the beating wood was performed to reach the target dry density.

During installation of ES1, the dry density of the sand for installation was determined to be 1.61 g/cm³. The sensors in ES1 were emplaced on top of L1. Five vertical TDR sensors (in addition to the four TDR sensors at the shaft wall) were installed with the bottom end U-shaped to avoid water entering and moving along them during the hydration phase (Fig. 3.82). Moreover, two PP sensors and one antenna of the wireless system were installed before the second layer was added.

Fig. 3.82 Installation of ES1 in Shaft 2

At the beginning of the installation of DS1, the target dry density between 1.55 g/cm³ and 1.57 g/cm³ could not be reached with the envisaged composition of 55 % bentonite pillows and 45 % BGM. Several tests were performed with ratios pillows/BGM of 55/45,

60/40, 65/45, 70/30 and 100 % pillows. The best results were obtained for the ratio 70/30 which was used for this and the following DS. Two PP sensors and two RH&T sensors were installed in L2 and L8 (one each). One TP sensor (axial stress cell) was installed on top of DS1 (Fig. 3.83).

Fig. 3.83 Installation of DS1 in Shaft 2

ES2 contains one horizontal TDR sensor and two PP sensors (Fig. 3.84).

Fig. 3.84 Installation of ES2 in Shaft 2

In DS2, two PP sensors and two RH&T sensors were installed in L2 and L8 (one each). Moreover, the 2D FO sensor covered with geotextile and the three vertical displacement sensors were installed in L9 (Fig. 3.85). On top of DS2, one TP sensor (axial stress cell) and the antenna of the wireless transmitter were emplaced. Additionally, three of the sensors (PP, RH&T, Pt-100) to be connected to the wireless device were emplaced in this location.

Fig. 3.85 Installation of the 2D FO displacement system within DS2 in Shaft 2

ES3 contains one horizontal TDR sensor, two PP sensors as well as one TP sensor (axial stress cell) and one RH&T sensor to be connected to the wireless device. Moreover, one back-up hydration tube is emplaced in the center of the segment (Fig. 3.86).

Fig. 3.86 Installation of ES3 in Shaft 2 including one back-up hydration tube

During the initial phase of installation of DS3, the reached dry densities of the Calcigel were too high. The first three layers had to be removed and alternative mixtures of bentonite pillows and BGM were tested. Particularly, the ratios pillows/BGM of 55/45, 60/40, 65/45, 70/30 and 72/28 were checked and the best results occurred for the ratio 70/30, which was then used for compaction. DS3 contains two PP sensors and two RH&T sensors in L2 and L8 (one each) as well as one TP sensor (axial stress cell) on top (Fig. 3.87).

Fig. 3.87 Installation of DS3 in Shaft 2

ES4 was installed including one horizontal TDR and two PP sensors. As in all other segments, the position of the vertical TDRs was checked (Fig. 3.88).

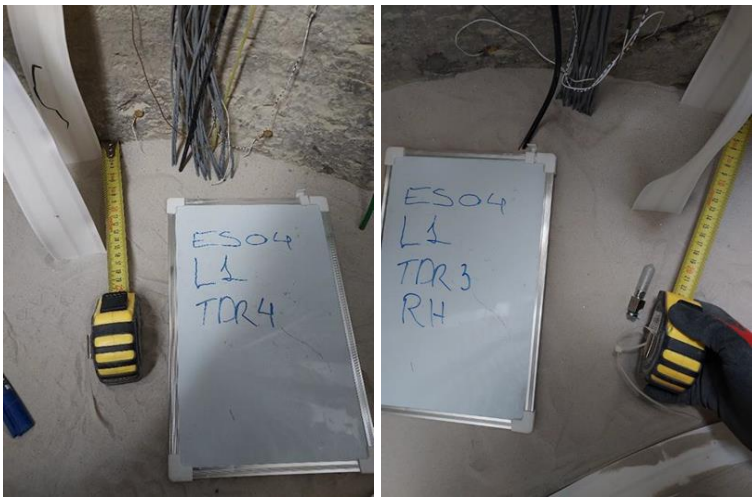

Fig. 3.88 Check of TDR positions during installation of ES4 in Shaft 2

DS4 contains two PP sensors and two RH&T sensors in L2 and L8 (one each) as well as one TP sensor (axial stress cell) on top (Fig. 3.89).

Fig. 3.89 Top view of DS4 in Shaft 2

ES5 was installed including one horizontal TDR and two PP sensors. The second back-up hydration line was planned to be installed in this segment. However, the crew forgot to install the tube before emplacing the cables sealing lid and the confining system. The hydration tube had to be installed in a remedial action by drilling a hole through the bottom plate of the confining tube and the sealing lid, inserting the tube, and sealing with resin. The details are given in /GAR 23c/, Chapter 6.

Sealing System Quality control

The water content of the compacted bentonite pillows and of the BGM obtained during transportation and storage prior to installation was measured daily at the Mont Terri chemical laboratory during installation.

Fig. 3.90 Water content analysis for the material used in Shaft 2

Plug and shaft cover

The installation of the plug was carried out by Amberg between January and March 2023. The bolting of the closure lid was again performed by VSH.

An extra amount of sand had to be added on top of ES5 to reach the target depth of 4.83 m below the niche floor. Afterwards, the remaining metal grid lining was removed to be able to start the installation of the plug. Some steps during installation of the cables sealing lid are shown in Fig. 3.91. The four components of the confining tube as well as the closure lid (Fig. 3.92) were installed in a similar way as for Shaft 1. The details are given in /GAR 23b/.

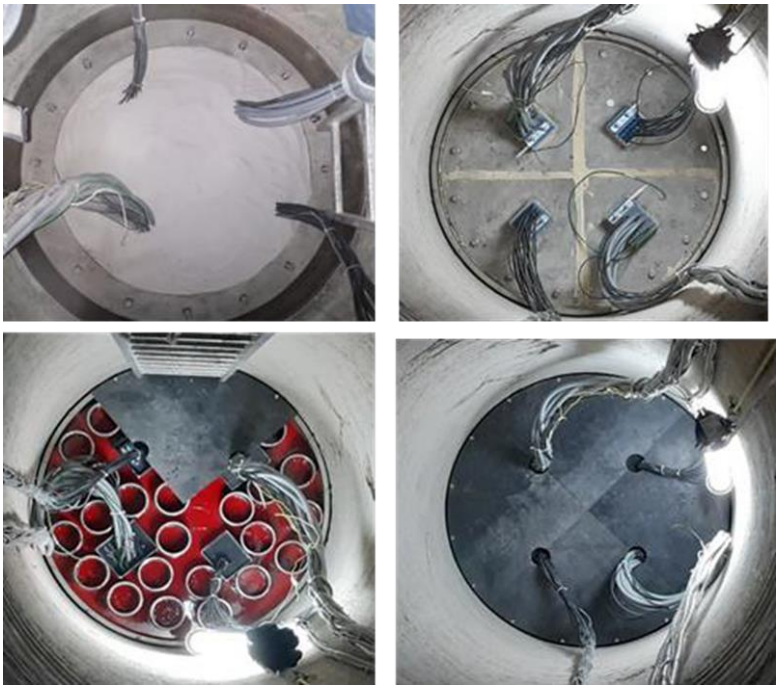

Fig. 3.91 Installation of the cables sealing lid in Shaft 2

Fig. 3.92 Installation of the confining tube and the closure lid for Shaft 2

Hydration system

Most of the components of the hydration cabinet had been installed before delivery to Mont Terri. Only the tanks and the electrical box were installed on site in addition to the water and gas inlet as well as the pressurized water outlet connections. An overview of the components within the hydration cabinet is shown in Fig. 3.93.

Once all elements of the system were installed, the system was tested with pressurized air and water for leaks. Some leaks were found, probably due to the vibration experienced by the different connections during transport. All leaks were repaired.

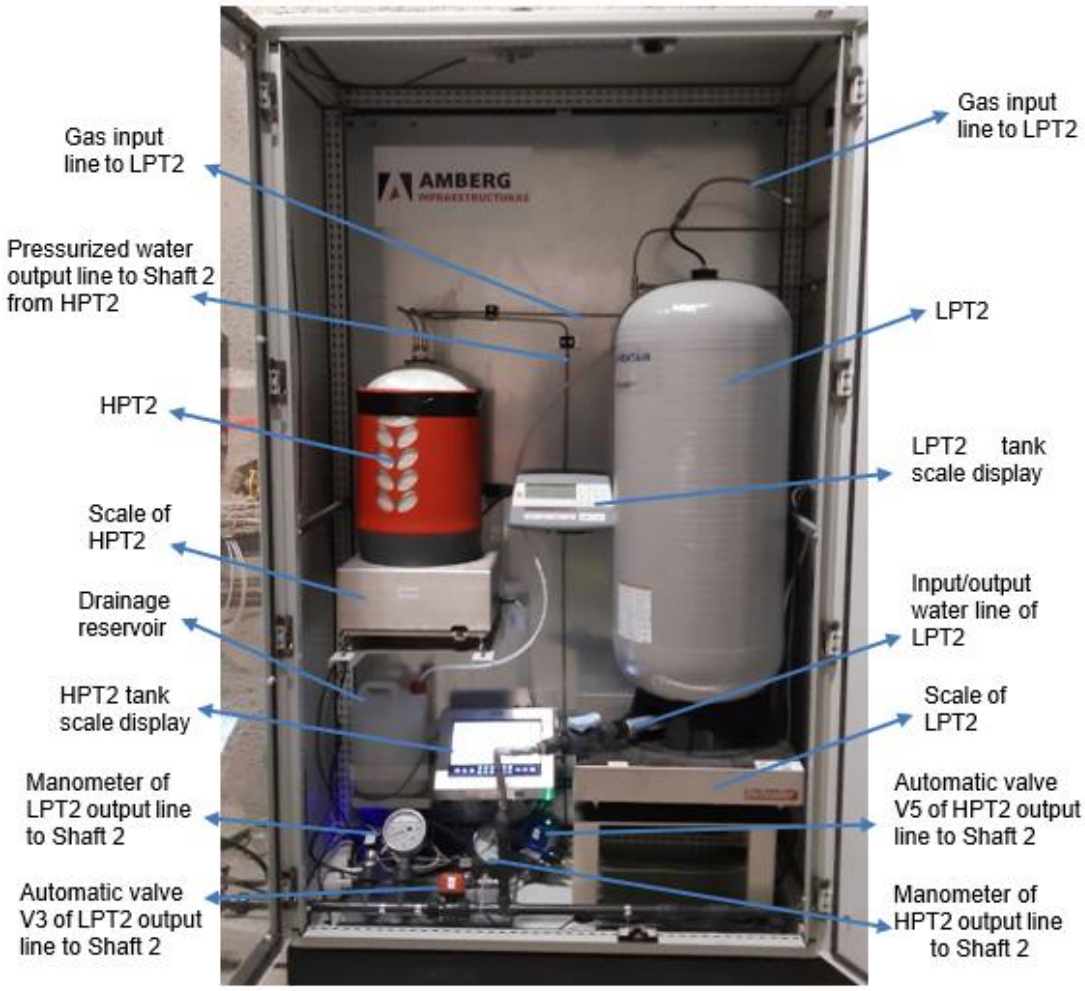

Fig. 3.93 Overview of the hydration system components of Shaft 2

3.6 Data acquisition and management

3.6.1 Data acquisition

Geomonitor

The Geomonitor system consists of an acquisition PC, which is connected over a BUS-cable to two interfaces dedicated to SW-A (Fig. 3.94). The Geomonitor III system acquires data of conventional sensors in Swiss standard wintertime. Data is transferred over ftp transfer to Geoscope and OASIS. The files are exported with a *.csv extension.

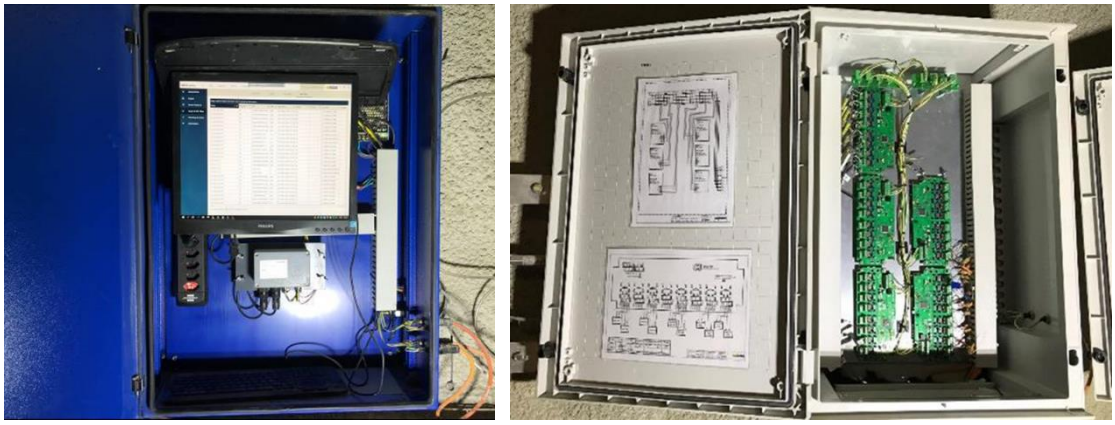

Fig. 3.94 Geomonitor III acquisition PC (left) and interface box (right)

Glötzl

Stress cells of Glötzl are installed in observation boreholes around the shafts and inside the shafts. All these sensors are connected over MUX to the Glötzl acquisition PC (Fig. 3.95). Data is transferred over FTP transfer to Geoscope and OASIS. Host for Geoscope is URL ftp://montterri.soldata.info and for OASIS it is IP 144.76.93.111. The system is described in detail in the installation report /GLÖ 20/.

Fig. 3.95 Glötzl acquisition PC and multiplexer MUM30

Taupe TDR

Data acquisition of TDR data received from Taupe TDR sensors is done continuously by ISU directly. TDR raw data are stored locally and processed, then sent to OASIS. Additionally, TDR raw data are sent to the data acquisition system of swisstopo and stored on the system server.

Amberg DAS

The RH&T sensors, scales measuring the weight of the water tanks and electronic valves of the hydration system are connected to a local acquisition PC of Amberg (Fig. 3.96). The associated data are transferred via ftp connection to Geoscope and OASIS and via VPN to the Amberg server in Madrid.

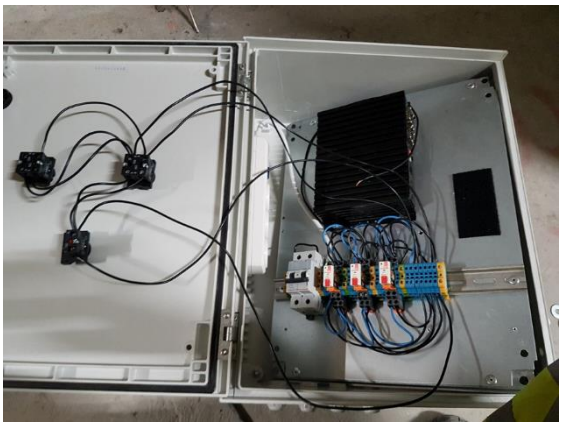

Fig. 3.96 Amberg acquisition PC

Wireless system

The data of the sensors connected to the wireless transfer system are collected by a receiver unit (RU) being connected to an acquisition PC via a serial port. The RU output can be viewed with the serial port terminal application PUTTY. The associated data are transferred via ftp connection to Geoscope and OASIS and via VPN to the Amberg server in Madrid.

Fiber-optic system

The fiber-optical data are collected by the SUMMIT reader being connected to the acquisition PC which is also used for wireless data transfer. The associated data are transferred via VPN to the Amberg server in Madrid and processed by Amberg.

ERT system

ERT data is stored on acquisition laptops by BGR. The laptops are protected in an aluminum box and a cabinet at the niche wall, respectively, and connected over a LAN cable to the Mont Terri network. Data retrieval and processing is done remotely by BGR.

Seismic DAS

Seismic measurements are performed in campaigns. All data (raw data, intermediate results, models, illustrations) are stored on the raid system of the BGR. The raw data, including the logging, are also stored in a BGR database (INIS).

3.6.2 MTRL central DAS (Geoscope) and OASIS

Most sensors are connected to the central data acquisition system (DAS) of Mont Terri URL. Swisstopo provides network access and data integration into Geoscope, incl. backup. A rack with the acquisition PC was installed in Niche 7. The acquisition PC and the connected data loggers are connected to individual UPS. The acquisition PC is accessible over team viewer for instance. Data is sent over ftp transfer to Mont Terri DAS, where it is accessible to all project partners of the SW-A experiment. The entire DAS of the SW-A experiment is connected to the secured power supply (Diesel generator). For data storage and visualization, the following two main systems are employed (see as well Fig. 3.97).

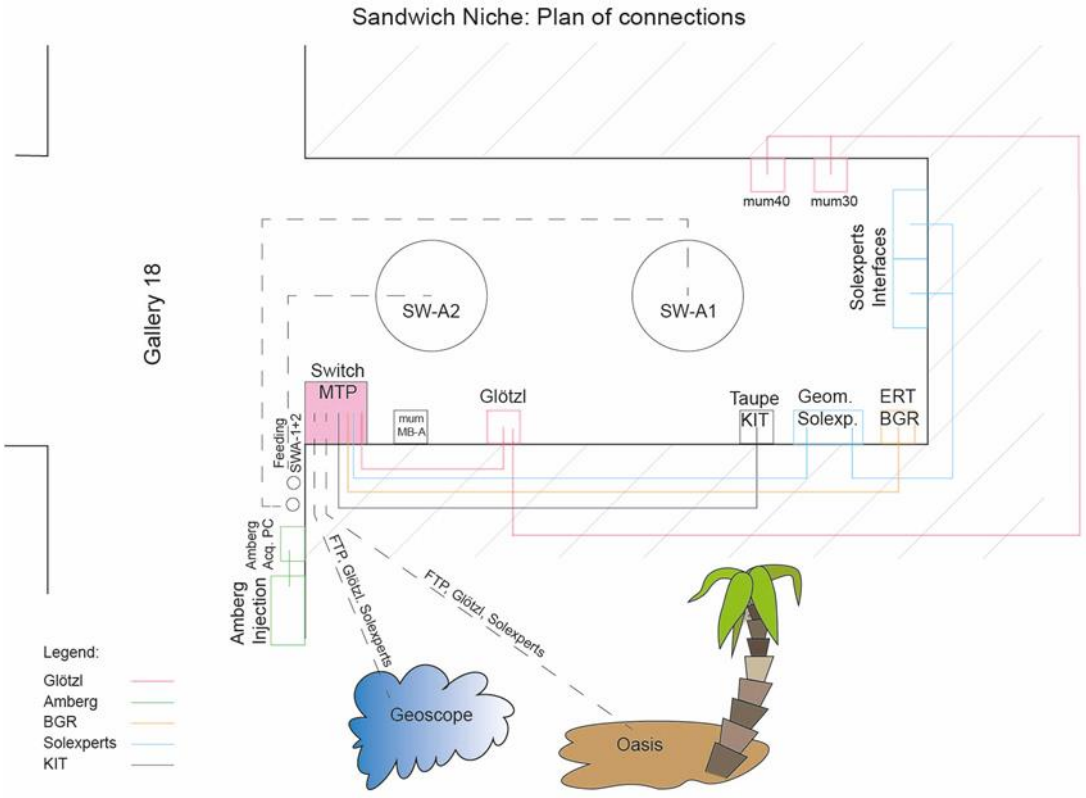

Fig. 3.97 Overview of data acquisition in the Sandwich niche

Geoscope system

The Geoscope system is hosted by Sixense Monitoring (former Soldata). This system is collecting/receiving all acquired data of the Mont Terri experiments except for large and raw FO data, seismic data and data from some standalone systems, such as Glötzl, ERT or Taupe measurements. The system consists of a FO connection from the main switch in the rock laboratory at St. Barbe, a FO data cable from the rock lab to Fabrique de Chaux, a data server, which is physically located at Fabrique de Chaux in a server room and a replication/backup server, which is physically located at swisstopo in Wabern/Bern. The database is accessible for Mont Terri partners over personalized access over a graphical user interface. Access to Geoscope is possible over the Geoscope client software.

OASIS

The OASIS system consists of a data-pipeline to collect and centralize sensor data from the project's multiple monitoring systems, a high-speed database backend and a fast web-based browser application. The system spatially links together (3D) sensor data and project information and provides project summaries, project activity logs, a report figure generator, calculated "virtual" sensors and email alarm notices. OASIS is data-driven meaning the database information determines the system's operation, layout, and design. The system is open source and license free.

The system receives data from the individual acquisition PCs via FTP transfer and thus acts as an additional data storage for monitoring data besides the Geoscope system. The data acquisition rate of each monitoring system is independent and each system stores data in a unique format. The OASIS data-pipeline automatically collects the project monitoring system data files, archives the data files and appends new data from the files to the database.

The Web app provides the system's user interface and runs in any modern Web browser. No plugins or additional software are required. Authorized users can access the Web app online via https://oasis-info.org/sandwich/. OASIS models the project in 3D space based on the local coordinate system (Fig. 3.98).

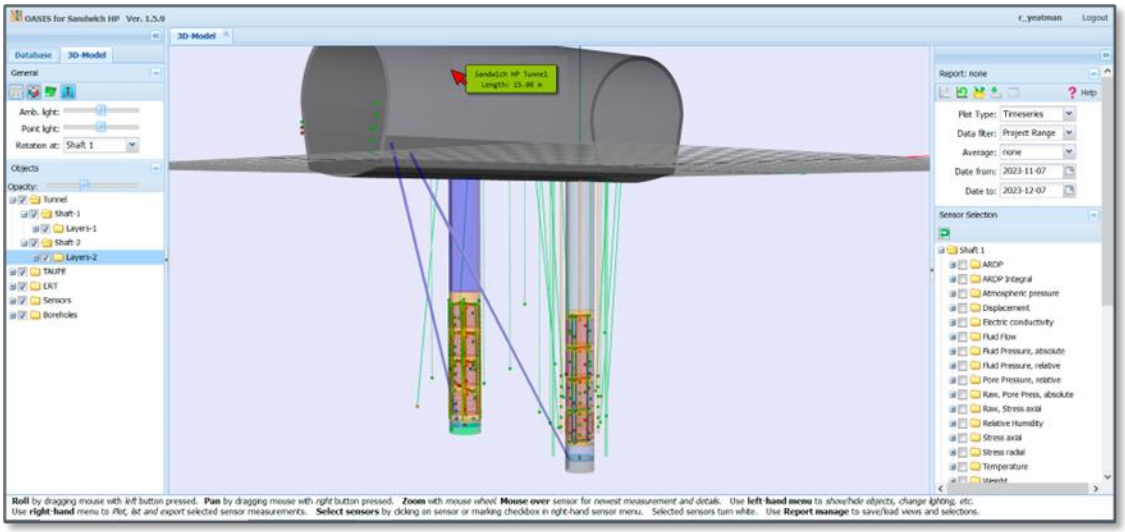

Fig. 3.98 OASIS: Database generated interactive 3D-view

OASIS facilitates fixed-point measurements from standard sensors with dynamic searchable tables and interactive time-series plots. Distributed sensors generate 3D measurements (time vs distance along a sensor vs measurement value). OASIS provides several viewing options for distributed measurements (Fig. 3.99).

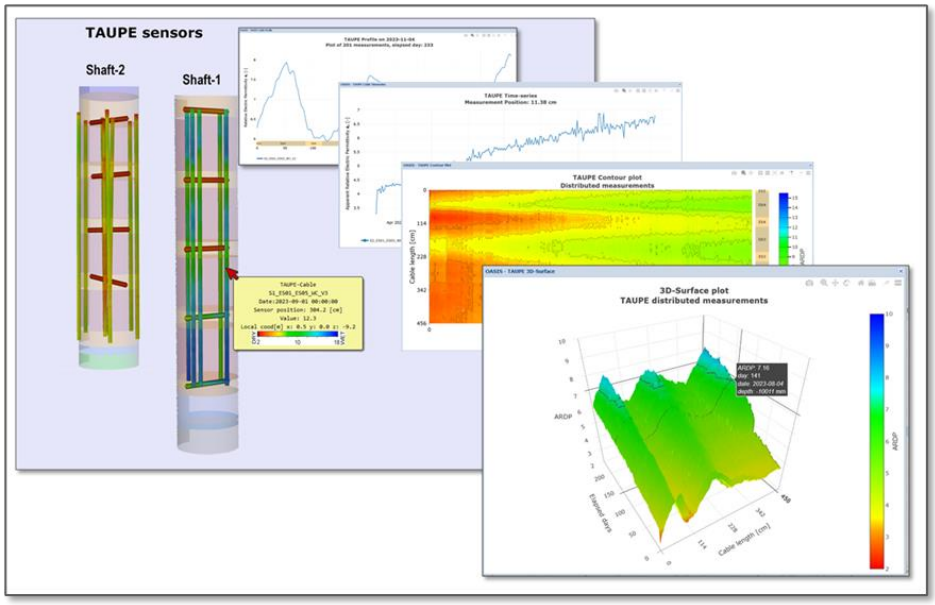

Fig. 3.99 OASIS: TAUPE distributed measurement plot options

The database relates measurements along the sensor to the actual position within the project in profile and contour plots and 3D-views. Plots can be saved and reloaded. Both plots and table data can be downloaded.

4 In-situ measurements

4.1 Measurements in the rock

4.1.1 Pore pressure

The evolution of the pore pressure sensors in the rock surrounding the experimental shafts is given in Fig. 4.1 – Fig. 4.4. An interpretation of the results for different periods of the experiment is given hereafter.

March – August 2020: Most of the mini-piezometers located near Shaft 1 reacted strongly to an overcoring test performed in the pilot of Shaft 1 in March 2020 (Fig. 4.1 – Fig. 4.4). Injection of the stress measurement boreholes for improvement of the coupling which was performed end of May 2020 (see Chapters 3.2.2 and 4.1.2) is also visible as a pore pressure response at many of the sensors close to Shaft 1 (Fig. 4.1 – Fig. 4.3).

April 2020 – May 2021: The sensors reacted to sinking of Shaft 1 with a pressure decrease, sometimes preceded by a short-term pressure increase when the drilling head came close. All three mini-piezometers located towards the end of the niche (Fig. 4.1) were lost in the course of shaft sinking. The deviation of the respective boreholes was more than 0.5 m, and so they were cut by the drill head. However, the pressure sensors remained connected to the water-filled pressure lines which now end in Shaft 1. They showed a pressure below ambient (i.e., suction) until the water bypass event of 11 August 2021 (see below). It can be expected that the deviation of the other mini-piezometer boreholes is similar, but since they are always deflected towards the niche entrance, they were not hit during shaft sinking.

The pressure at the other sensors close to Shaft 1 (Fig. 4.2 and Fig. 4.3) decays with time to ambient pressure, BSW03_PP_1 even goes into suction. The reaction of BSW06_PP_1 is rather muted, possibly there is air in the tube system.

The sensors between the shafts (BSW12_PP_1, BSW13_PP_1, BSW14_PP_1, Fig. 4.4) reacted to Shaft 1 sinking but started to stabilize at pressures between 0.3 and 0.4 MPa. Only when sinking of Shaft 2 started in November 2020, the pressure dropped further. At BSW13_PP_1 which is located at mid-distance between the two shafts a pressure (0.2 MPa) above ambient pressure is maintained until April 2021.

BSW15_PP_1 (Fig. 4.4) is possibly untight because it never showed pressure values significantly differing from ambient pressure. It is, however, located close to the transition between sandy facies and carbonate-rich sandy facies of the Opalinus clay, which may play a role.

BSW16_PP_1 close to Shaft 2 was found blocked during installation. During sinking of Shaft 2, however, the sensor reacted with a pressure loss, so that now it seems to measure.

June 2021 – July 2021: Start-up of Shaft 1 hydration resulted in a gradual pressure increase at the lowermost mini-piezometers at or close to the level of DS1 (BSW05_PP_1 (Fig. 4.2), BSW09_PP_1 (Fig. 4.3), and BSW12_PP_1 (Fig. 4.4)).

August 2021: With the water bypass event of DS1 of 11 August 2021 (see Chapter 4.2) all three cut pressure lines leading from the niche end into the shaft (BSW01_PP_1, BSW02_PP_1, BSW11_PP_1) showed a sudden pressure increase (Fig. 4.1). All pressure lines end at depth of DS1 or ES2 and record the pressure at the shaft wall during this event. Two of the sensors returned to ambient pressure within a few weeks. The third, possibly clogged during the event, took more than half a year. The reaction of these sensors suggests that the water breakthrough occurred at the shaft contour.

September 2021 – May 2023: Continuous hydration led to a further steady increase in pore pressure close to Shaft 1 at the level of the lowermost sealing element DS1 (BSW05_PP_1 (Fig. 4.2), BSW09_PP_1 (Fig. 4.3), and BSW12_PP_1 (Fig. 4.4)).

The readings of the three sensors are quite similar until beginning of October 2022, when BSW12_PP_1 gradually decreases again, while the other two continue to increase. The reason for the difference is the ventilation of Shaft 2 with the start of the installation works. BSW12_PP_1 is close enough to Shaft 2 to be affected, while the others do not react.

Of the mini-piezometers at lower depths, only the ones at 9.4 m which are at mid-height of DS2 (BSW04_PP_1 (Fig. 4.2), BSW08_PP_1 (Fig. 4.3)) show a slow pressure increase. The others are not affected by the swelling of DS1, their pressure readings are close to atmospheric pressure.

The sensors BSW32_PP_1 and BSW33_PP_1 installed in February 2023 did not show any reaction within the reporting period.

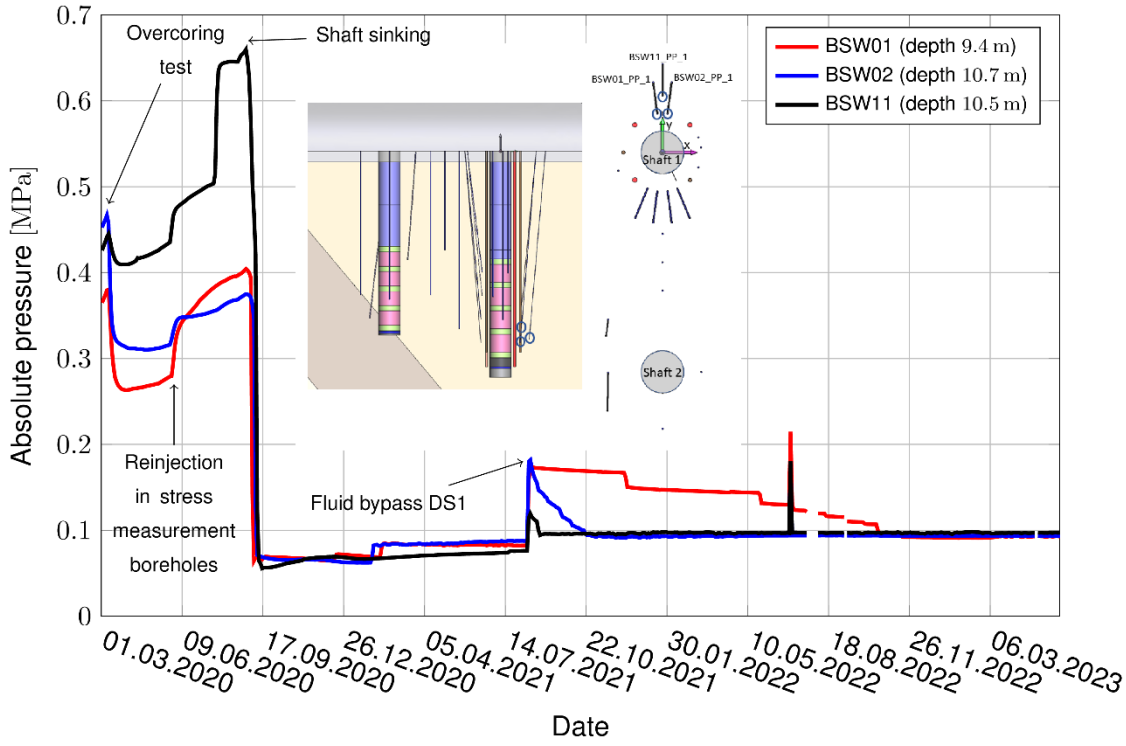

Fig. 4.1 Pore pressure data of the mini-piezometers south of Shaft 1 (towards the end of the niche)

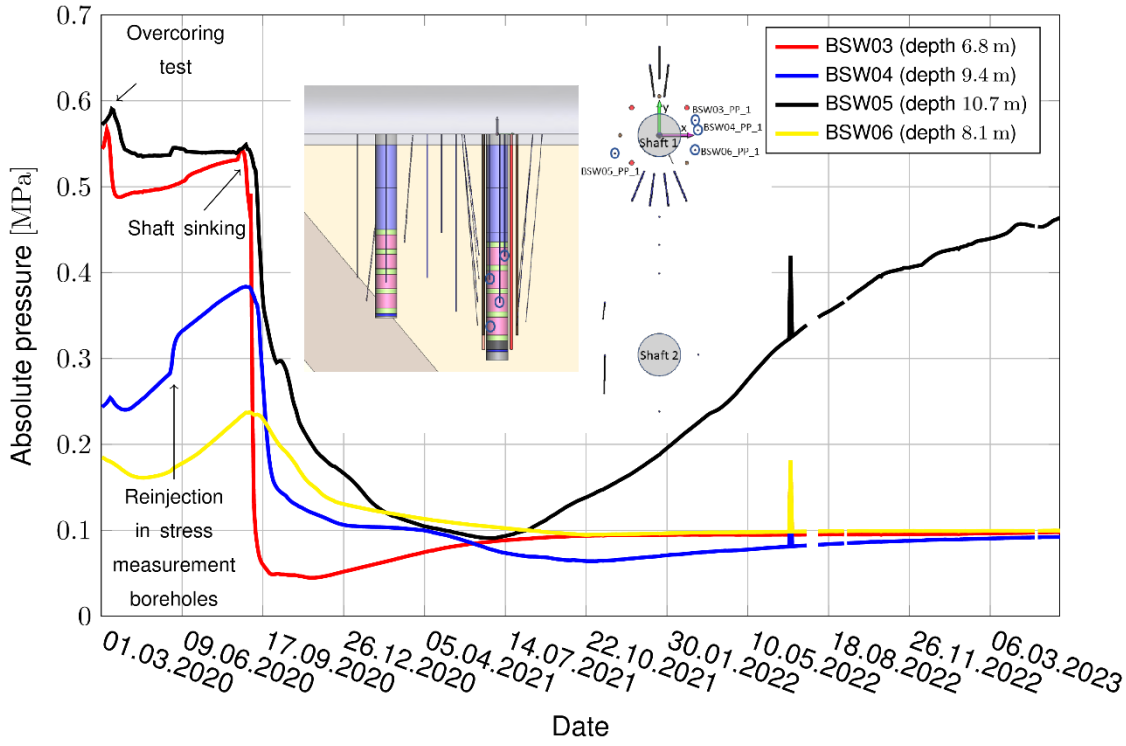

Fig. 4.2 Pore pressure data of the mini-piezometers east and west of Shaft 1 (towards the niche walls)

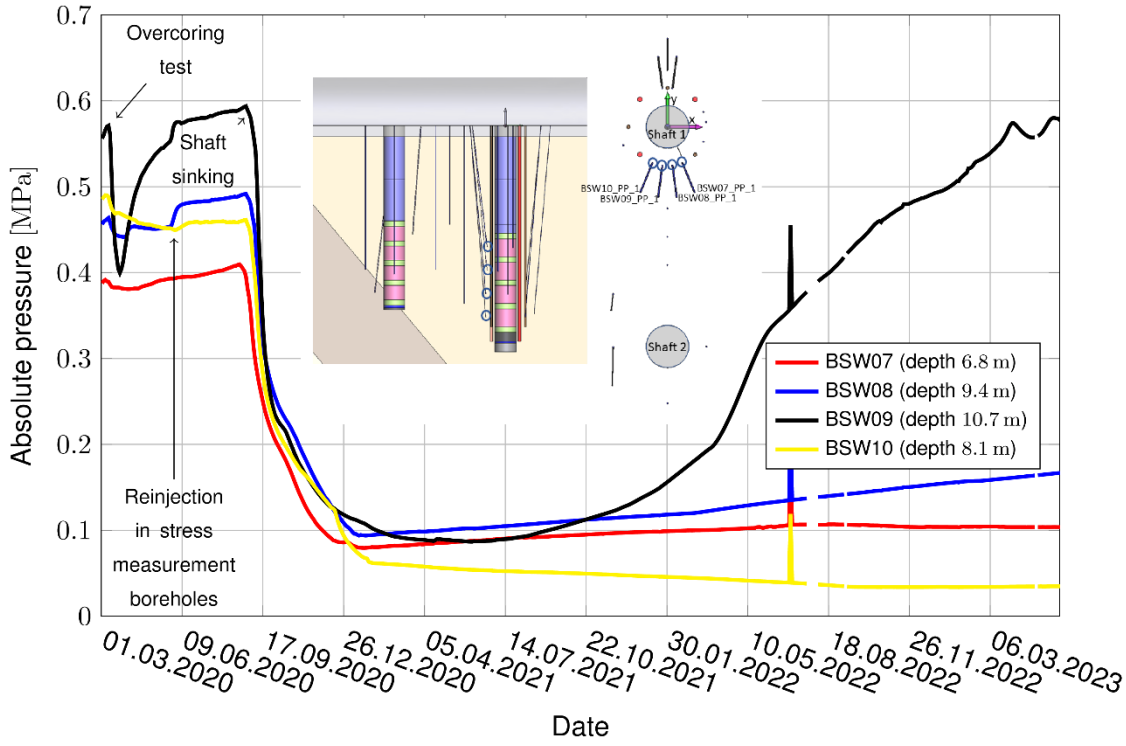

Fig. 4.3 Pore pressure data of the mini-piezometers north of, but close to, Shaft 1 (towards the niche entrance)

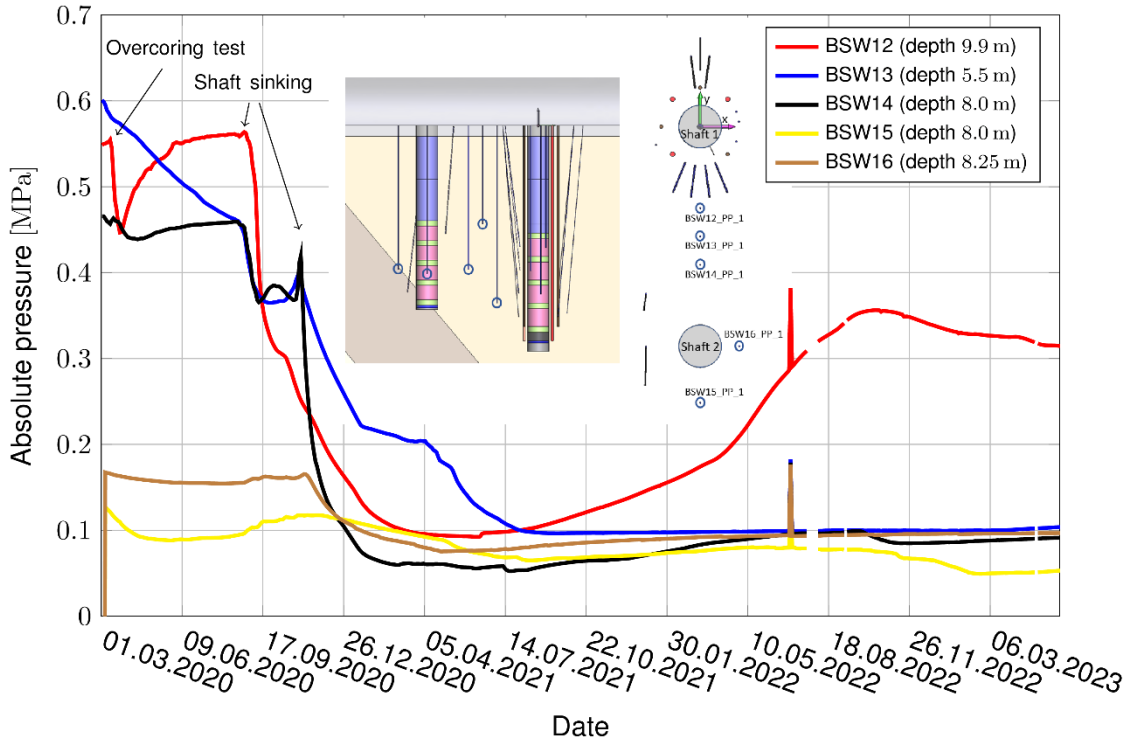

Fig. 4.4 Pore pressure data of the mini-piezometers between the shafts and close to Shaft 2

4.1.2 Radial stress

The measured stresses since installation of the stress cells in the boreholes and baseline measurements are depicted in Fig. 4.5 to Fig. 4.10. The results until May 2021 are the response to installation of the stress cells, the sinking of Shaft 1 and the installation of the sealing system. The measured stress developments from May 2021 until May 2023, especially in Fig. 4.8 to Fig. 4.10, represent the response of the rock mass to the hydration and swelling processes in the Sandwich sealing system. Negative stress changes in the figures are not realistic, because they are calculated in relation to different reference time points (installation of stress cells Fig. 4.5 to Fig. 4.7 and start of hydration Fig. 4.8 to Fig. 4.10).

After installation and grouting the boreholes, a slight increase of stresses up to 1 MPa in the first five months has been observed. At the end of May 2020, reinjections in the boreholes with resin with a small overpressure were done to fill remaining pores in the grout and gaps between the stress cells and the grout. Therefore, the measured stress increased at this moment of reinjection and decreased afterwards, converging to different stress levels between 2 MPa and 4 MPa. After sinking of Shaft 1 in September 2020, the stresses decreased in hours and reached 1 MPa to 3 MPa. These remaining stresses after shaft sinking are probably caused by residual stresses in the resin. The emplacement of the sealing system in the shaft from October to December 2020 had no influence on the measured stresses in the rock mass. The little data gaps in December were caused by disconnection of the wires due to the installation of the plug at the top of the shaft.

The stress cells in borehole BSW-A20 measure the stress changes in the rock mass parallel to bedding. After shaft sinking, the sensor BSW20_SR_2 started to oscillate in ranges up to 1 MPa. Increasing and decreasing phases over days and weeks can also be observed until October 2022 (see Fig. 4.5). In October 2022, the stress change increased from an approximately unstressed state up to the level of the other stress changes in BSW-A20. It seems that this stress cell recovered, but oscillation still exists in a small range.

The database relates measurements along the sensor to the actual position within the project in profile and contour plots and 3D-views. Plots can be saved and reloaded. Both plots and table data can be downloaded to your computer.

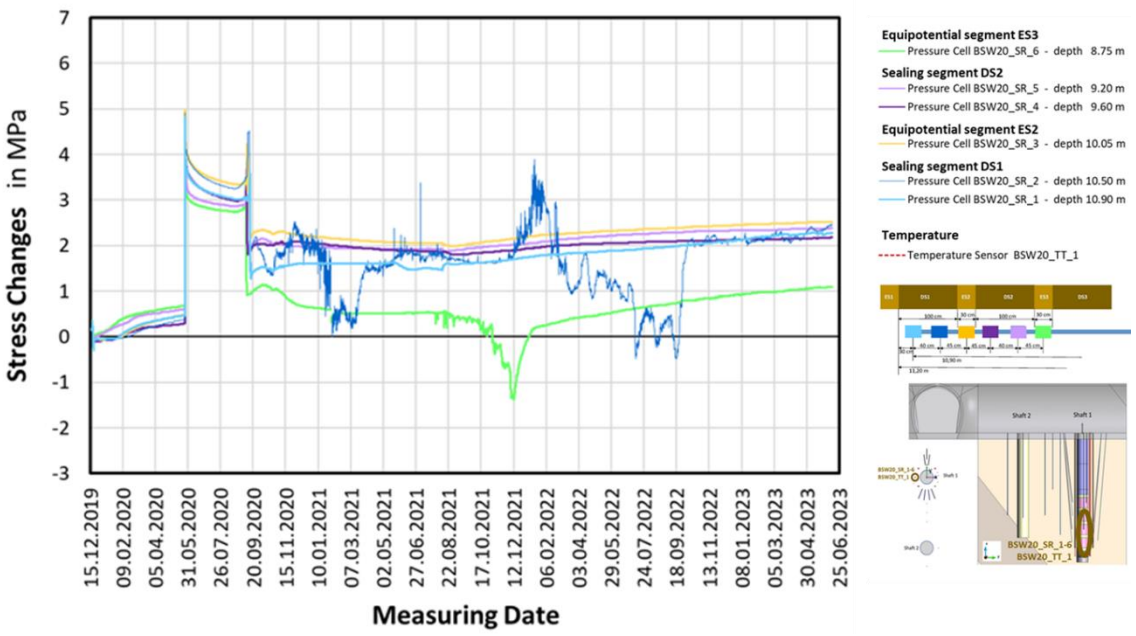

Fig. 4.5 Stress changes development in the borehole BSW-A20 (BSW20_SR_1 – BSW20_SR_6)

The stress change at sensor BSW20_SR_6 reached a lower level than at the other sensors in borehole BSW-A20 (see Fig. 4.5). From August 2021 to December 2021, an oscillation and increase of the stress change occurred at this sensor. After that, the stress change increased again about more than 1 MPa in one month and subsequently more slightly up to 1 MPa in 2023. The other sensors in borehole BSW-A20 show a slight increase of stress changes from the start of hydration until the end of May 2023 (see Fig. 4.5).

Borehole BSW-A21 is located in the dipping direction of the claystone layers. The failure of sensor BSW21_SR_4 has to be stated for borehole BSW-A21 in the depth of 9.6 m (see Fig. 4.6). Therefore, the measured data of BSW21_SR_4 are neglected. With the stress cell BSW21_SR_4 first an increase of stress change in November and December 2021 was recorded. The stress change at this stress cell dropped suddenly to zero in January 2022 and increased again in March 2022 approaching approximately the level of the stress changes at the other stress cell from summer of 2022 until May 2023.

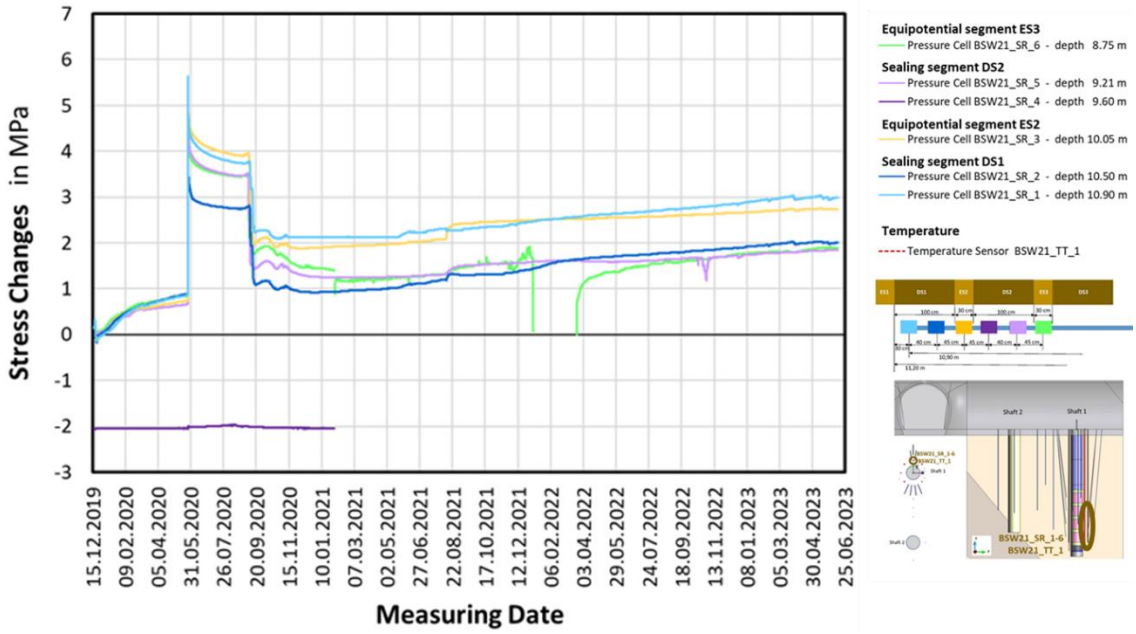

Fig. 4.6 Stress changes development in the borehole BSW-A21 (BSW21_SR_1 – BSW21_SR_6)

The other stress cells in borehole BSW-A21 show a continuous elevation of stress changes about 1 MPa from the start of hydration until the end of May 2023 (see Fig. 4.6). The same can be seen at all sensors in the borehole BSW-A22 in Fig. 4.7 (BSW22_SR_1 to BSW22_SR_6). The stress changes increase slightly about 1 MPa from the start of hydration until May 2023.

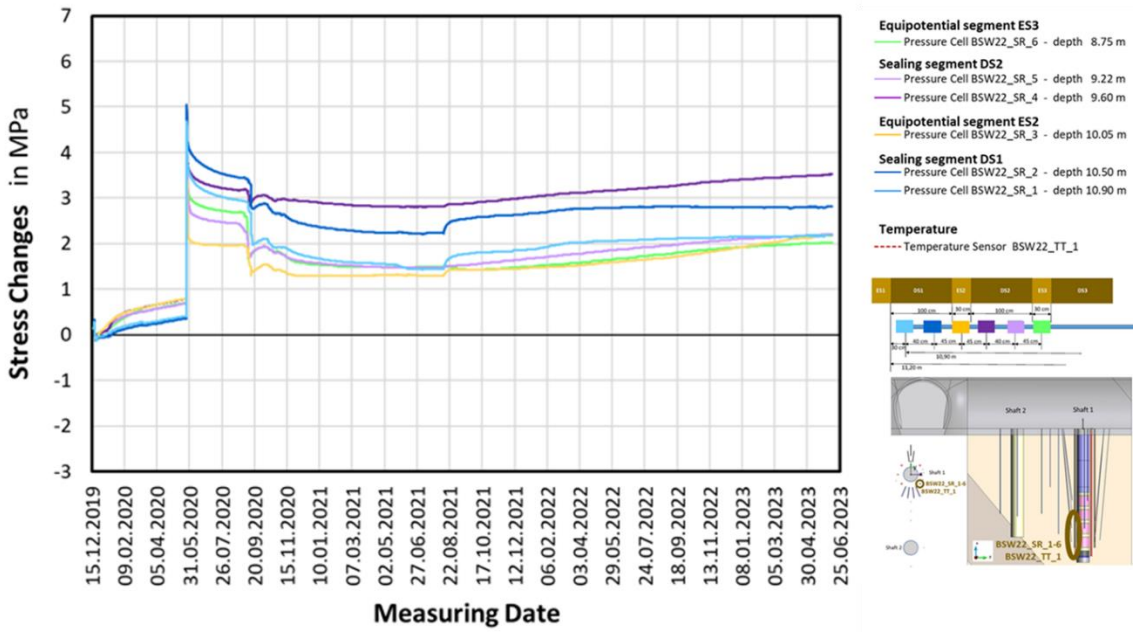

Fig. 4.7 Stress changes development in the borehole BSW-A22 (BSW22_SR_1 – BSW22_SR_6)

A more detailed view to the stress changes caused by hydration of the sealing systems and possible swelling processes of the bentonite are depicted in Fig. 4.8 to Fig. 4.10. With the start of hydration, the measured stresses set to zero. Therefore, only the stress changes during the hydration process are shown.

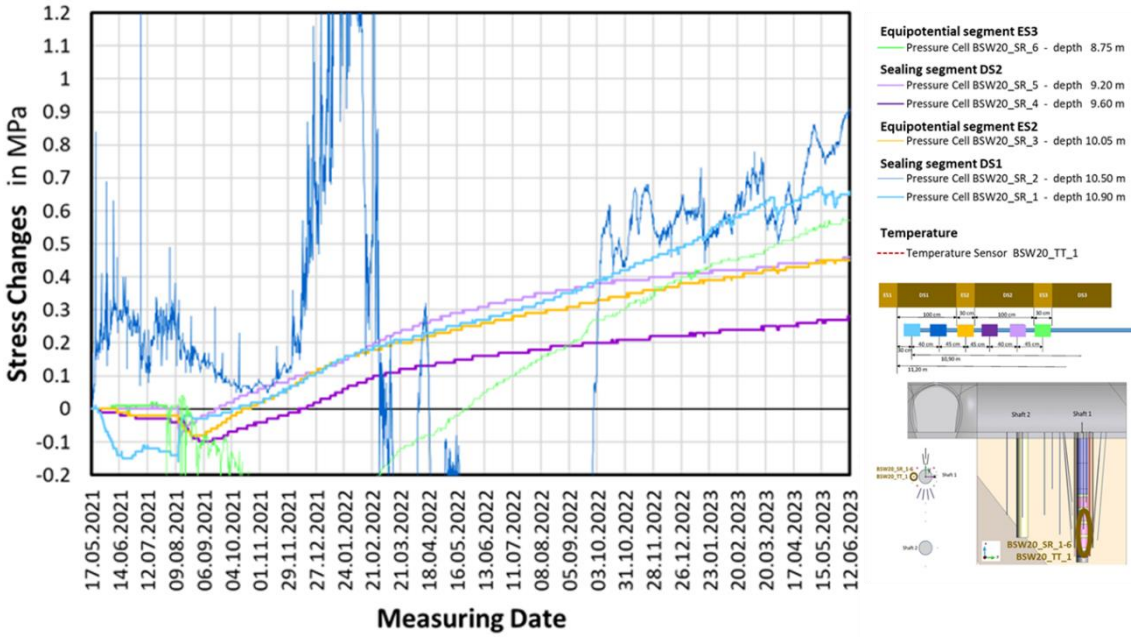

Fig. 4.8 Stress changes development since the start of Shaft 1 hydration in the borehole BSW-A20 (BSW20_SR_1 – BSW20_SR_6)

With the start of hydration, the (calculated) stress changes parallel to the bedding (BSW-A20) first got into the negative range from May to August 2021 (Fig. 4.8). In the following months, the stress changes increased up to 0.2 MPa to 0.65 MPa. The greatest stress changes can be observed at the deepest levels at DS1 (blue curves in Fig. 4.8). The stress changes at BSW20_SR_2 reach almost the same level as the one at stress cell BSW20_SR_1 after the supposed recovery of sensor BSW20_SR_2. In March 2023 and May 2023, there were short sawtooth-like oscillations at the sensors BSW20_SR_1 and BSW20_SR_2 at the depths of DS1. The same phenomenon can be observed with the sensors in the other boreholes BSW-A21 (Fig. 4.9) and BSW-A22 (Fig. 4.10) at the depths of DS1. These oscillations correlate with interruptions in the feeding systems. Accordingly, a very sensitive reaction of the rock mass concerning stresses to the liquid pressure in the sealing system can be stated.

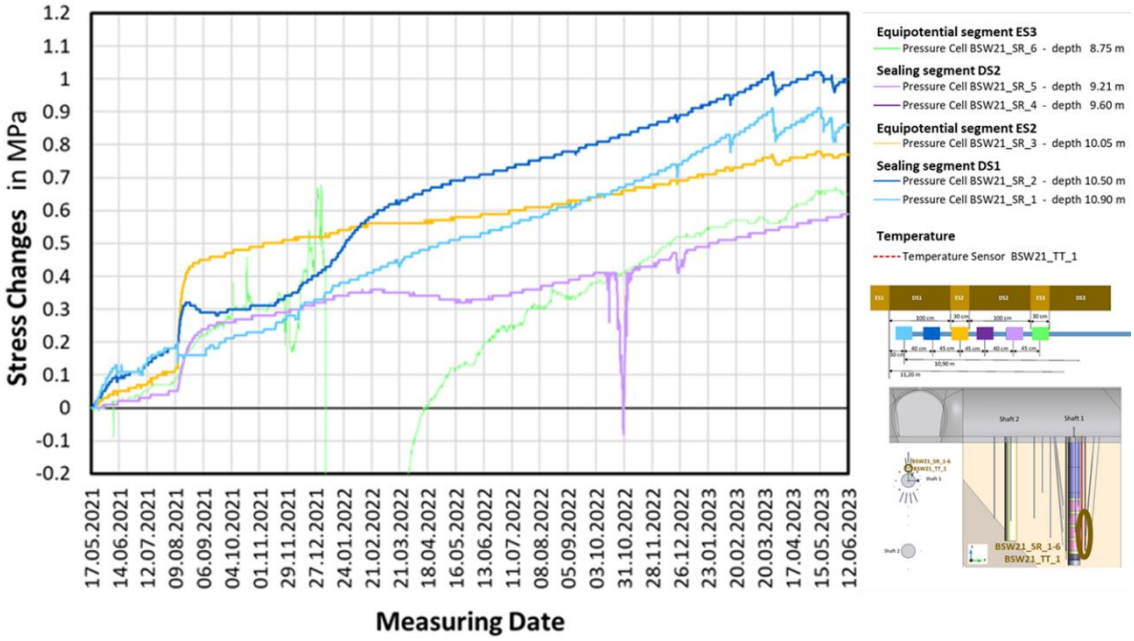

Fig. 4.9 Stress changes development since the start of Shaft 1 hydration in the borehole BSW-A21 (BSW21_SR_1 – BSW21_SR_6)

In dipping direction, no stress decrease occurred after start of hydration like the one parallel to bedding in borehole BSW-A21 (Fig. 4.9). However, a sharp increase of stresses can be seen due to the water ingress in August 2021. After that, the stress at BSW21_SR_2 is reduced first and then increases again after November 2021. At the other sensors in BSW-A21, the increase is more slightly but continuously. The stresses at the end of May 2023 reach values between 0.5 MPa and 1 MPa in BSW-A21.

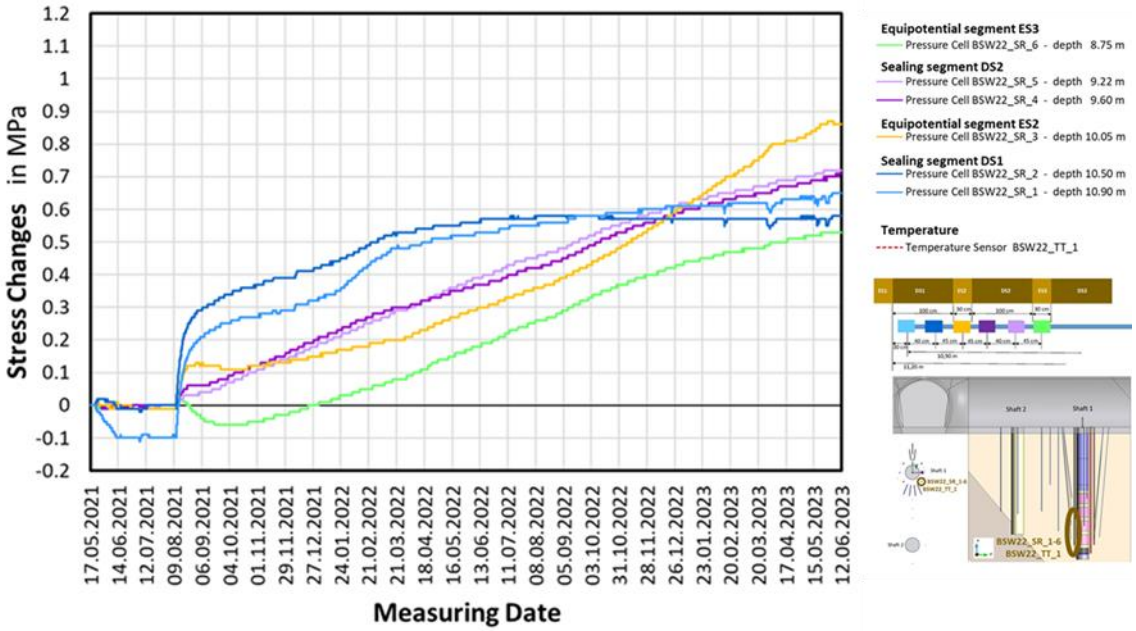

Fig. 4.10 Stress changes development since the start of Shaft 1 hydration in the borehole BSW-A22 (BSW22_SR_1 – BSW22_SR_6)

At the level of DS1 for the stress cell BSW22_SR_1, negative values of the stress change were calculated from May to August 2021 after the start of hydration (Fig. 4.10) like the (calculated) stress changes parallel to the bedding in BSW-A20 (Fig. 4.8). With the water ingress in August 2021, a sudden increase of stress changes at the deepest level at DS1 (BSW20_SR_1 and BSW20_SR_2) was observed. In the following months, the increase of stress changes was continuous but with a decreasing rate. Since September 2022, the stress changes at BSW20_SR_1 increased in a roughly linear course and at BSW0_SR_2 a constant value has been reached. At the depth of DS2 the stress changes increased with an almost constant rate. The stress changes in BSW-A22 reached values between 0.6 MPa and 0.8 MPa since the start of hydration.

Overall, it is assumed that the reaction of the rock mass to swelling pressures due to the hydration of the sealing elements are small so far. However, there is a very sensitive response of the rock mass to the fluid pressure used for hydration of the Sandwich sealing system, especially in the deepest levels of DS1.

4.1.3 Temperature

Each of the three frames with the stress cells in the boreholes BSW-A20, BSW-A21 and BSW-A22 include one temperature sensor in the center of the frames (see Chap. 3.2.2). Sensor BSW22_TT_1 failed during installation, so there are no measurement data available for that sensor. The measured temperature developments in the other two boreholes (see Fig. 4.11) are almost the same. The small differences are negligible.

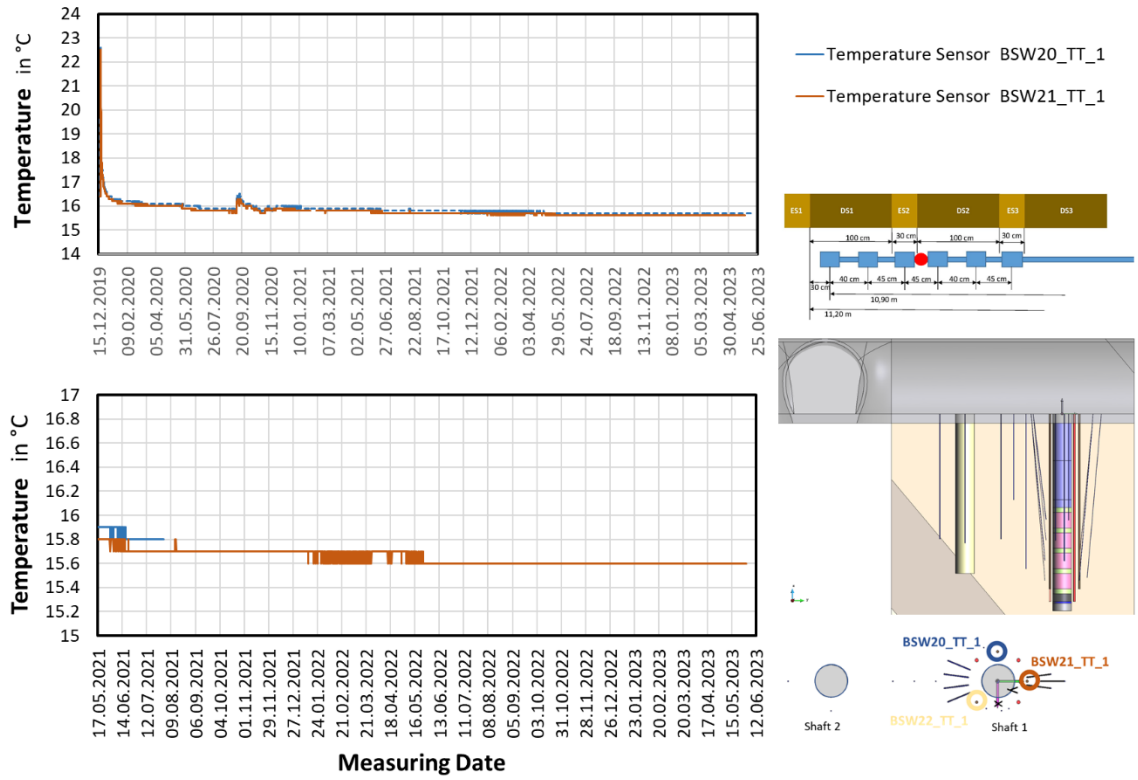

Fig. 4.11 Temperature development in the rock mass 50 cm to the shaft wall (BSW20_TT_1 & BSW21_TT_6)

Because of grout hydration in the observation boreholes the measured temperatures started about 22.5 °C and decreased in a few days to the former value in the rock mass of about 16 °C. Shaft sinking lead to a short and small temperature increase of about 0.5 K. Then, the temperature decreased slightly from 16 °C to 15.6 °C over time. An influence of the installation or the hydration of the sealing system cannot be observed.

4.1.4 Seismics

The seismic datasets obtained are shown in Tab. 4.1. Seismic data still have to be processed. Preliminary results are shown in the following figures. Data processing in both figures is currently based on sensor positions calculated for the borehole axis (although in-situ data were acquired on the borehole wall, in practice resulting in several cm shorter travel distances). Fig. 4.12 gives an impression of raw picked travel times of all channels, expressed as seismic velocities of pressure and shear wave first break (vP0, vS0). Despite a distinct scatter towards higher velocities, the figure shows a high data density and, for BSW-B17, an increase in seismic velocity from roughly 3700 m/s (vp0) and 1500 m/s (vS0) near the borehole mouth (x < 1 m) to roughly 3800 m/s (vp0) and 1900 m/s (vS0) near the end of the borehole. The automatically picked travel times are currently under revision to reduce errors in the velocity profiles.

Tab. 4.1 Recorded IVM and XHM datasets for the vicinity of Shaft 1

Type	Receiver			Source (XHM)			Date [dd.mm.yyyy]	Depth [m]
	Borehole	Orien-tation	Step size [m]	Borehole	Orien-tation	Step size [m]		
IVM	BSW-B17	90 °	0.05				10.09.2020	12.00
IVM	BSW-B19	90 °	0.05				11.09.2020	12.00
IVM	BSW-B18	90 °	0.05				12.09.2020	12.00
XHM	BSW-A1	0 °	0.1	BSW-B17	0 °	0.1	14.10.2020	11.90
XHM	BSW-B17	180 °	0.1	BSW-B19	0 °	0.1	16.09.2020	12.00
XHM	BSW-B17	90 °	0.1	BSW-B18	270 °	0.1	13.09.2020	12.00
XHM	BSW-B17	90 °	0.1	BSW-B18	270 °	0.1	21.01.2020	12.10
XHM	BSW-B17	180 °	0.1	BSW-B19	0 °	0.1	21.01.2020	12.10
XHM	BSW-B17	90 °	0.1	BSW-B18	270 °	0.1	14.10.2020	12.00
XHM	BSW-B17	180 °	0.1	BSW-B19	0 °	0.1	14.10.2020	12.00

Fig. 4.13 shows vP0 inversion results of seismic cross-hole data that were measured on September 13 and October 14, 2020, between BSW-B18 (transmitter) and BSW-B17 (receiver). The inverted velocity models show a general velocity decrease in the repeat survey data of about 600 m/s. The relative velocity distribution of the cross-hole data remains the same, comprising relatively high velocities near 4 m distance from borehole mouth of BSW-B18 and relatively low velocities in the middle between both boreholes at a distance of about 6 m from the borehole mouth.

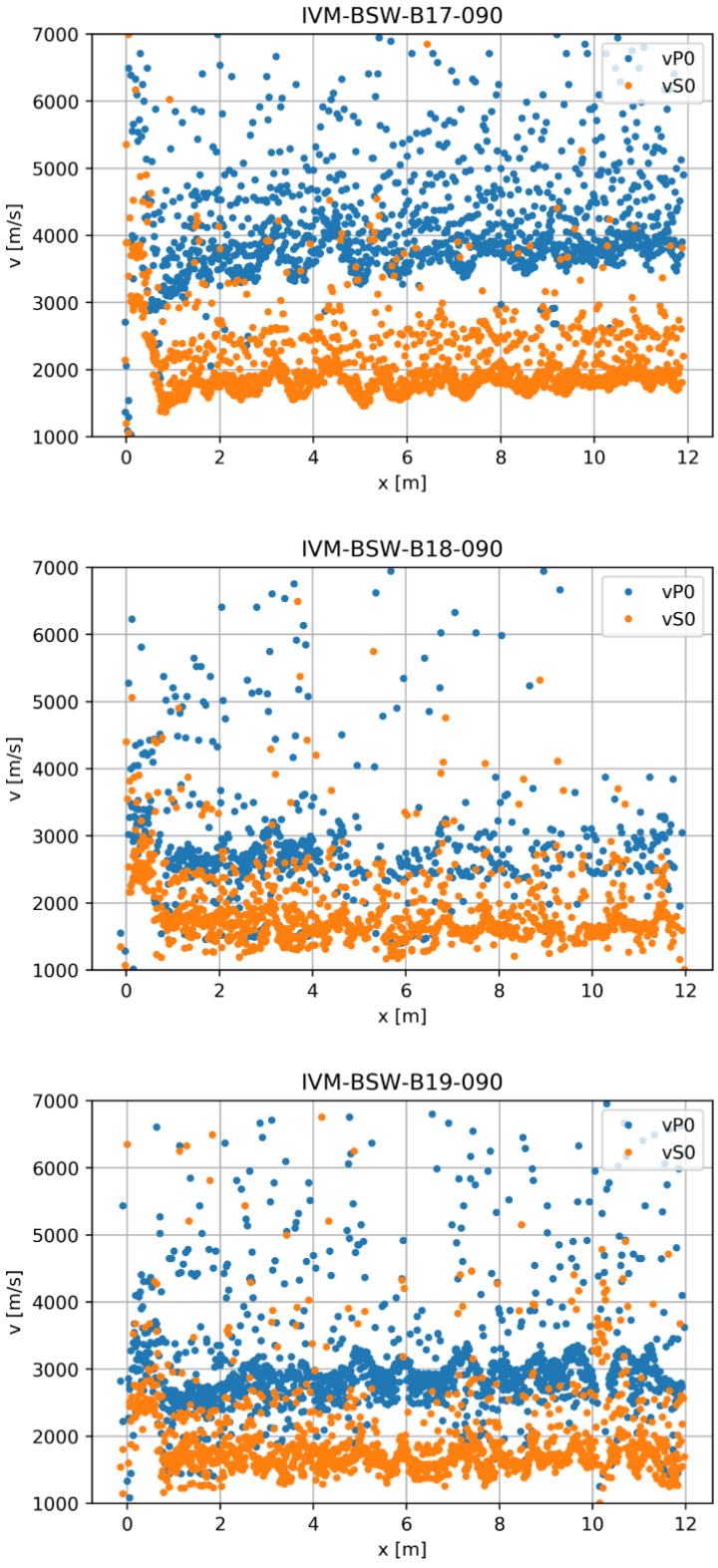

Fig. 4.12 Raw data picks of IVM datasets at BSW-B17, BSW-B18, and BSW-B19

Blue: velocity of pressure wave. Orange: velocity of shear wave. All picks with respect to first break. x: midpoint between transmitter and receiver with respect to borehole mouth.

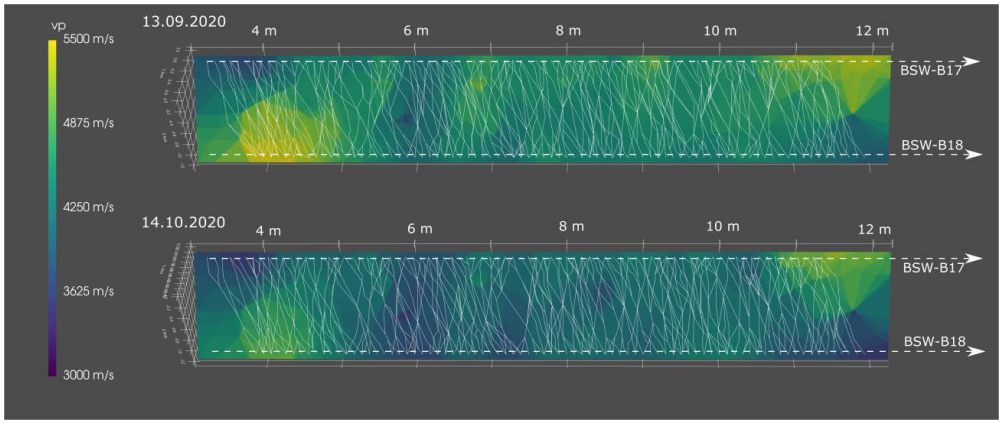

Fig. 4.13 Inverted vp velocity model for seismic cross-hole measurements between BSW-B18 (transmitter) and BSW-B17 (receiver)

Data were acquired on September 13 (top) and October 14 (bottom) 2020

Fig. 4.14 shows vP0 inversion results of seismic cross-hole data that were measured on September 13 and October 14, 2020, between BSW-B19 (transmitter) and BSW-B17 (receiver). The inverted velocity models exhibit generally lower velocities compared to Figure 4 and the velocity decrease between both time steps is less distinct (~ 400 m/s). In the dataset measured first, a velocity increase towards the borehole end is noticeable along BSW-B17. In the inverted velocity model of the second time step, several low velocity areas appear along BSW-B19 (at 6 m, 8 m, and 11 m distance from the borehole mouth).

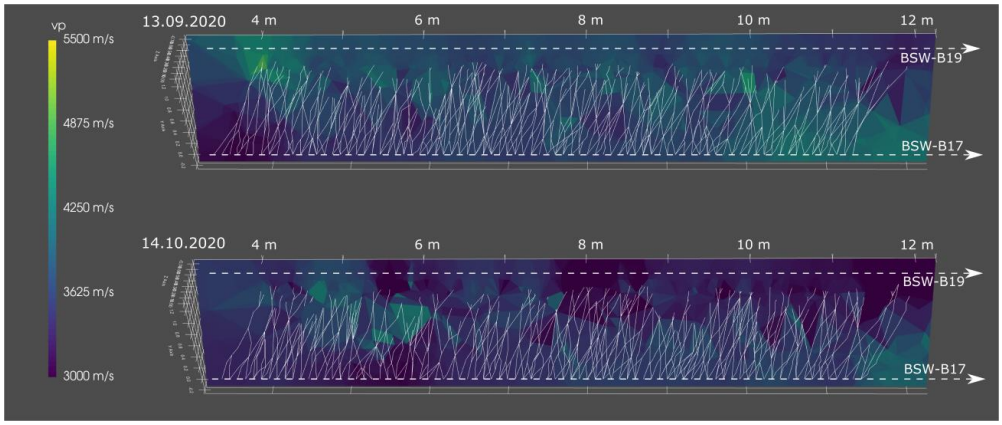

Fig. 4.14 Inverted vp velocity model for seismic cross-hole measurements between BSW-B19 (transmitter) and BSW-B17 (receiver)

Data were collected on September 13 (top) and October 14 (bottom) 2020

A joint inversion of interval velocities measured along single boreholes and cross-hole measurements is in preparation and will lead to mutually constrained results.

4.1.5 ERT

Fig. 4.15 shows the results of the ERT measurements in the three geophysics observation wells prior to installing the casing. The layout of the boreholes is shown again in the upper left part of the illustration.

Variability of the values is clearly visible in all borehole profiles, high-resistance layers are in interchangeable bearing with low-resistance layers. The measured sequence is typical for the lower sandy facies. /KNE 21/ was able to show that the resistivity correlates with the carbonate content of the layers. The measurements show that the environment of the experiment is clearly heterogeneous.

On the other hand, the measurements can be used to confirm the geological model of the area below the niche. Fig. 4.16 shows a corresponding investigation. Since facies transition from the sandy to the carbon-rich sandy facies is not captured by the boreholes, results from the BAD-2 borehole (see /KNE 21/) were used as a reference. The location of the facies transition corresponds to the one expected from the geological model, except for a few centimeters.

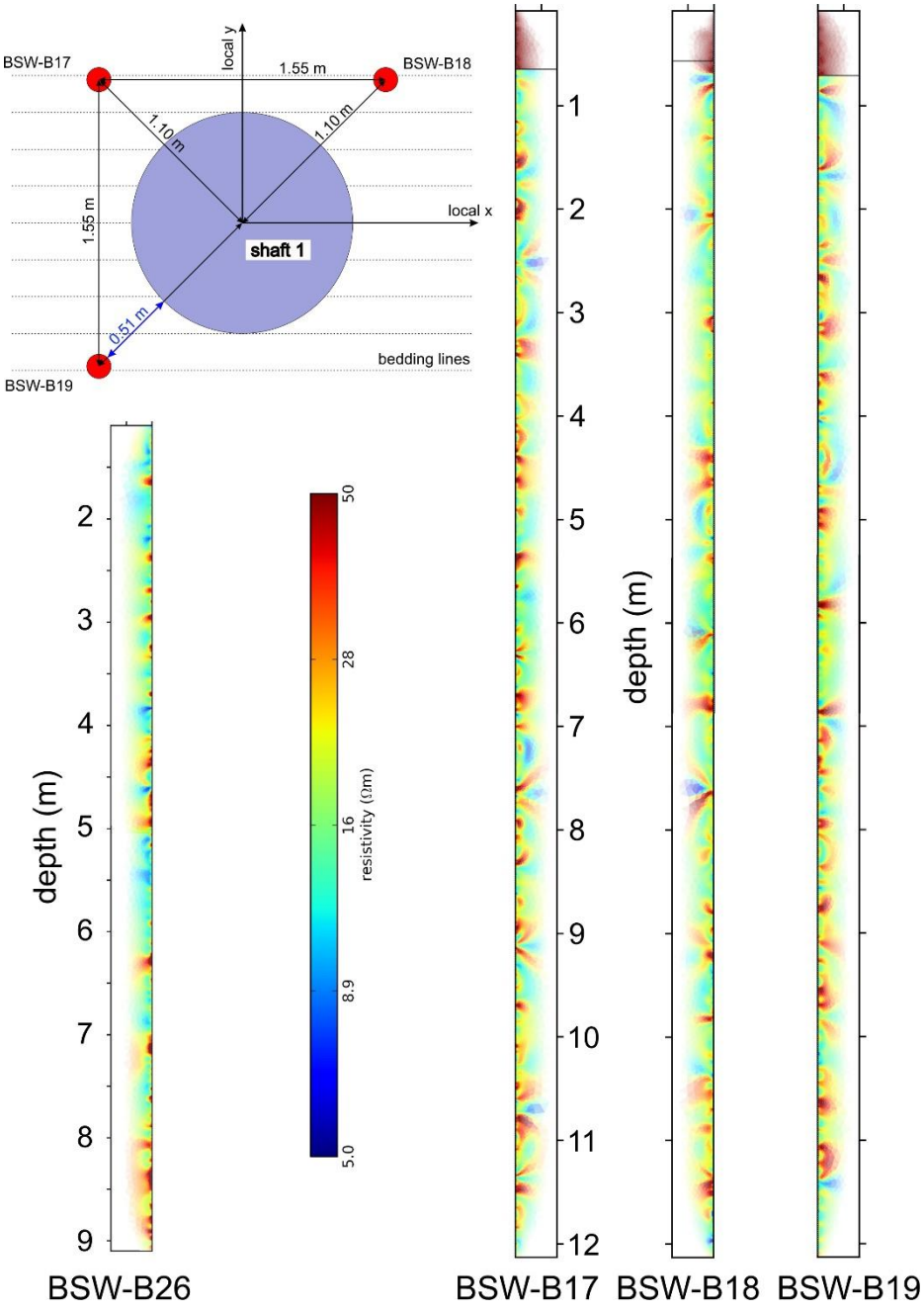

Fig. 4.15 Results of the ERT measurements in the three geophysics boreholes in the vicinity of Shaft 1 and in the pre-borehole of Shaft 2 (BSW-B26)

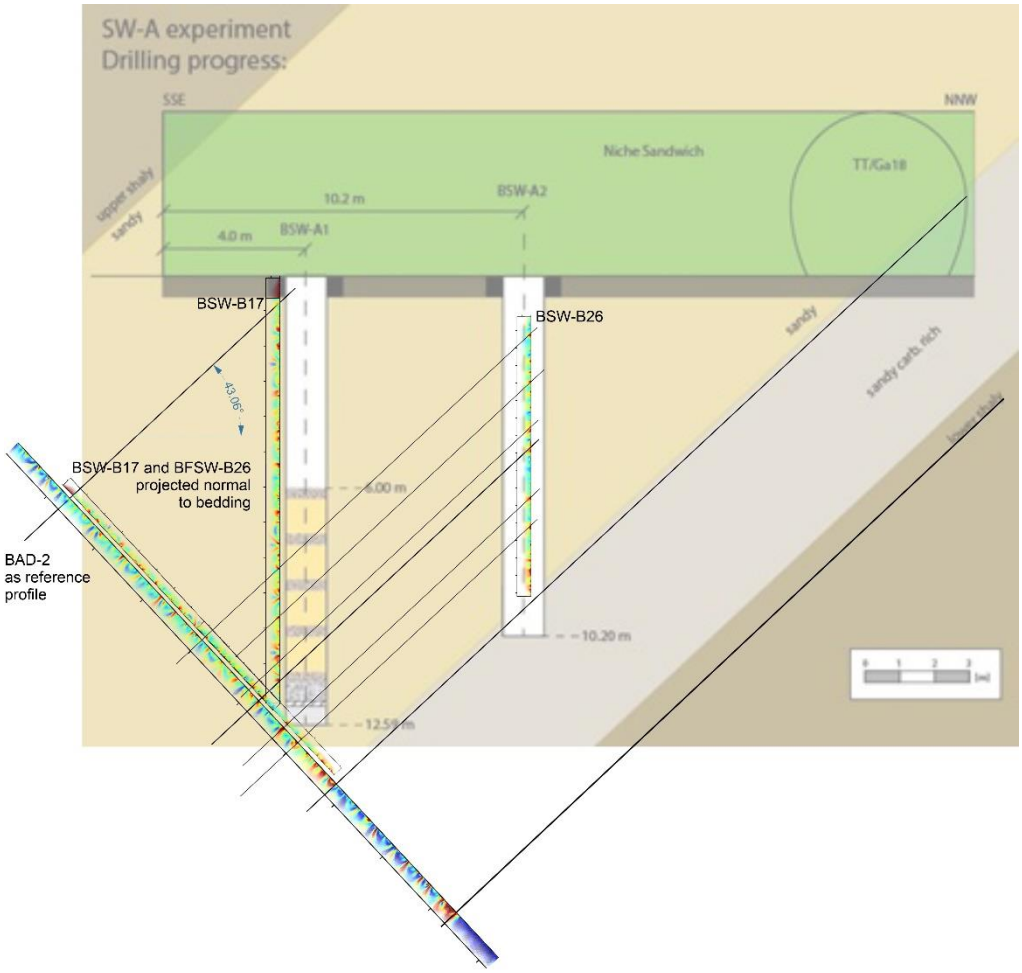

Fig. 4.16 Geological model and ERT results from different boreholes underneath the Sandwich niche

4.2 Shaft 1 hydration regime and measurements

4.2.1 Hydration history

The hydration of the sealing system with Pearson water A3 via the pressure chamber started on 18 May 2021 by using the low-pressure tank. The feeding borehole, pressure chamber, gravel, and ES1 were initially hydrated at hydrostatic pressure for about one week. Subsequently, the fluid pressure was increased in steps of 1 bar until cable leaks of sensors in the pressure chamber occurred at the beginning of June 2021 (Fig. 4.17). When the leakage had been detected, pressurized hydration was stopped and the water level in the pressure chamber was decreased. The leaking cables were sealed with sheaths reaching into ES5 and hydration could be resumed on 12 July 2021.

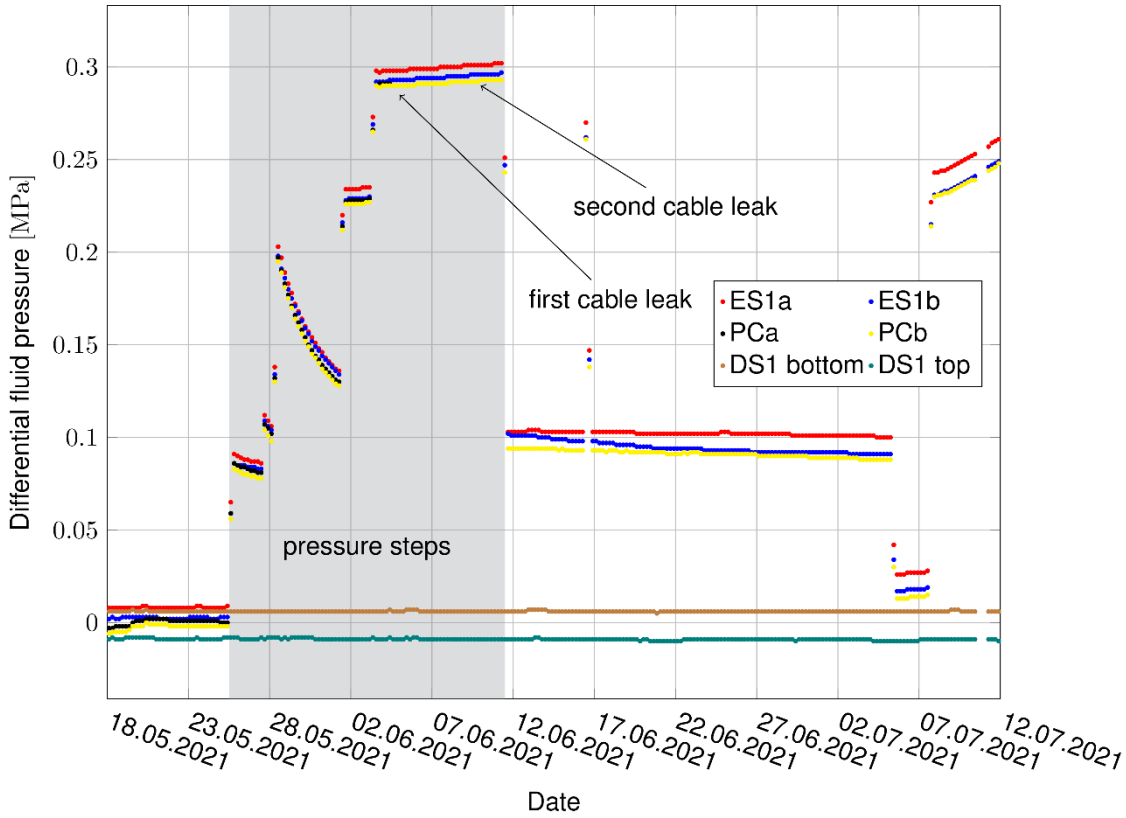

Fig. 4.17 Initial pressure evolution in the pressure chamber and the lower segments of Shaft 1

On 11 August 2021, after an injection pressure increase from 5 bar to 8 bar, the pressure tank emptied completely into the shaft and the pressure was lost. It was found that a short pressure increase in ES2 and DS2 occurred during this event and this could be interpreted as a fluid bypass of DS1. The bypassing fluid (and increased pressure) was captured by ES2 and absorbed by DS2 showing the functionality of the Sandwich sealing system (Fig. 4.18). Moreover, cable leakage occurred during this event due to untight cables of the ERT and PP sensors which lead to an unwanted hydration of ES5 (and DS4 due to suction). All cables were sealed within connection boxes filled with resin and hydration could be resumed in November 2021.

The further pressure increase was realized without additional major problems. In May 2022, the pressurization was switched from LPT to HPT. The continuous pressure increase, visible especially in the HPT pressure curve (Fig. 4.19), was caused by the single-stage pressure regulator controlling the injection pressure which is not working correctly at very low injection rates. The regulator has been replaced by a two-stage model.

The short-term pressure losses in 2023 occurred due to necessary refills of the HPT and a rupture of the hydration line that was fixed directly. The slow re-regulation of the target pressure was also related to the single-stage pressure regulator.

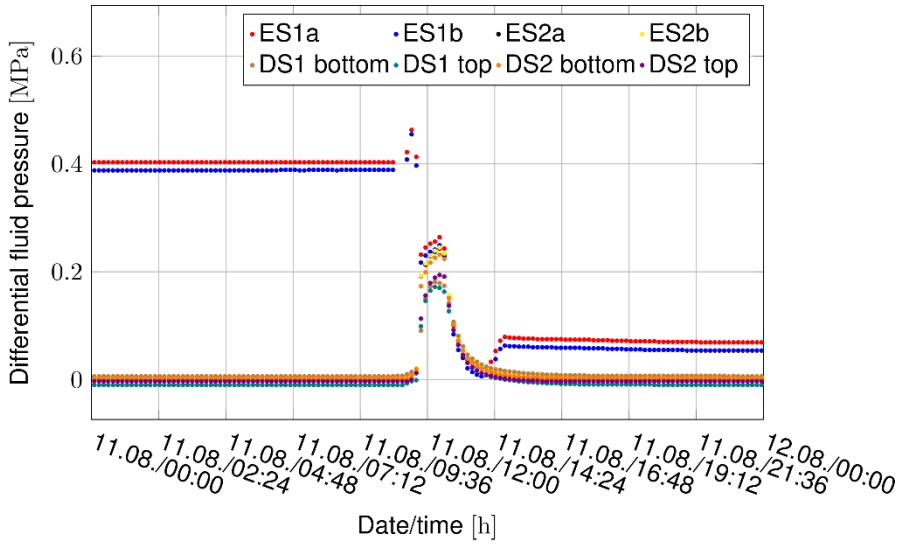

Fig. 4.18 Pressure response in ES1, ES2, DS1, DS2 during fluid bypass of DS1 in August 2021 in Shaft 1

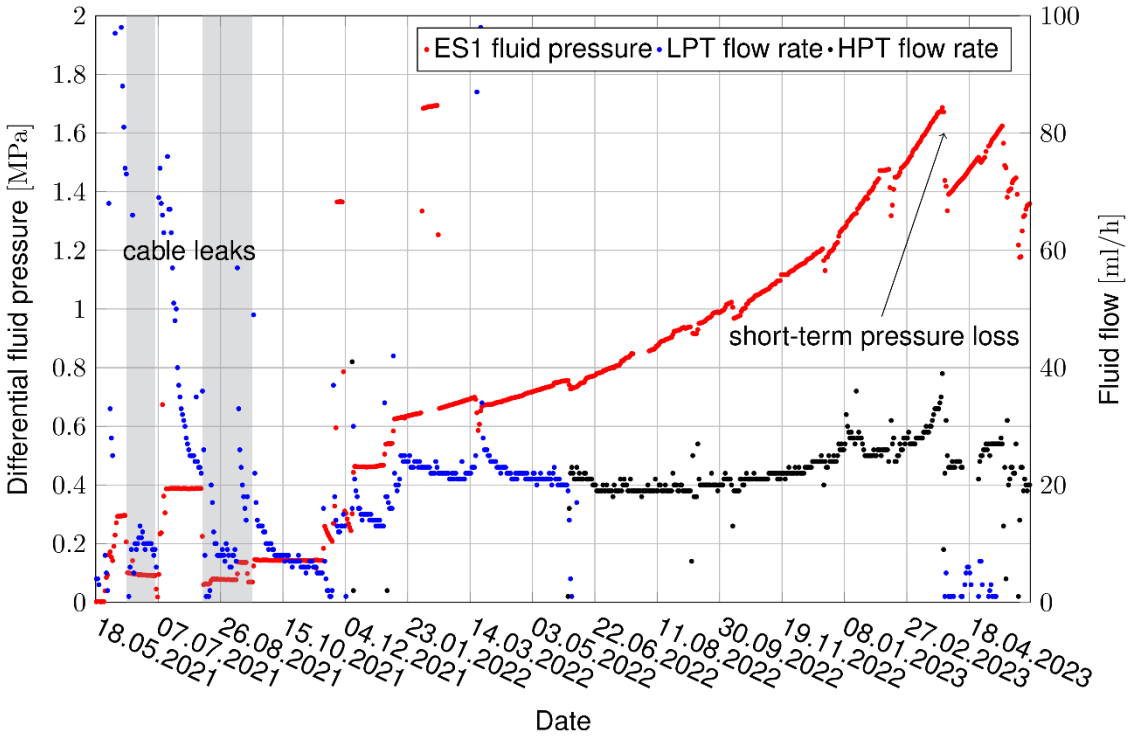

Fig. 4.19 Hydration history of Shaft 1

4.2.2 Shaft 1 interface to rock

Twin rod TDR

At the start of the experiment, the measurements of twin rod TDR sensors PICO 64 (IMKO GmbH) for ARDP, electric conductivity (EC) and temperature worked well. But when hydration started in Shaft 1 in ES1 (day 189), and later in ES2 (day 271), the ARDP increased significantly from around 6 to about 15, which are reasonable results. However, reaching this effect, EC and ARDP started to oscillate, ARDP between about 6 and 15, EC between 0 and 5 mS/cm. The temperature reduced when liquid reached the sensor. In ES5, the inflow of liquid from cable leakage reached the IMKO sensor on day 243, which was not visible in the ARDP results but in a slight increase of EC from 4 mS/cm to 4.5 mS/cm. The temperature dropped in each case by about 0.5 °C. After the signal oscillation had started, no useful results could be obtained from IMKO sensors and thus the measurement has been stopped.

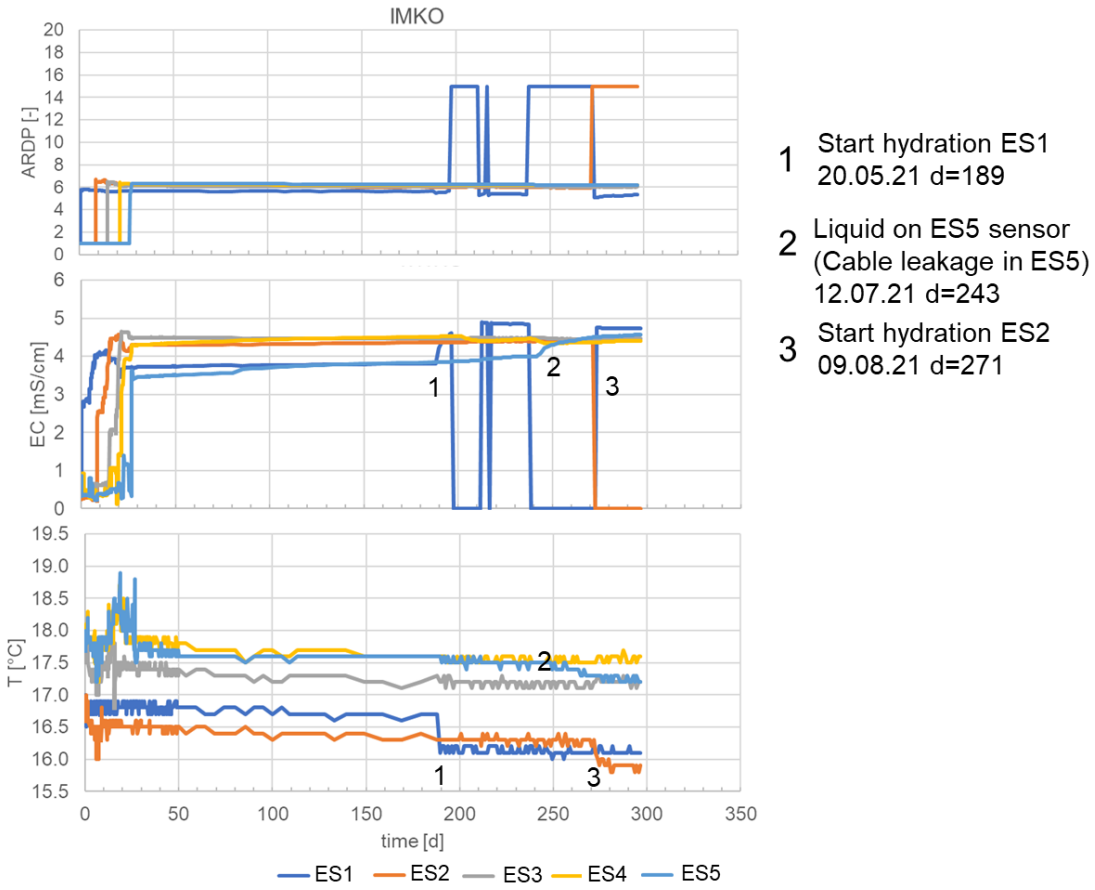

Fig. 4.20 Results of PICO 64 IMKO TDR twin rod sensors in Shaft 1: ARDP (top), electrical conductivity EC (middle), sensor temperature (bottom) and hydration events

ERT

The ERT measuring system provides the three-dimensional distribution of electrical resistivity in the vicinity of the installed electrodes. Fluid entering the backfill changes the local saturation, and the local pore space geometry is changed via the swelling behavior of the clay.

These are quantities that also influence the electrical resistivity. Long-term observation by means of monitoring on a daily basis makes it possible to visualize both temporal and spatial changes, which allows a conclusion to be drawn on the water content change in the backfill.

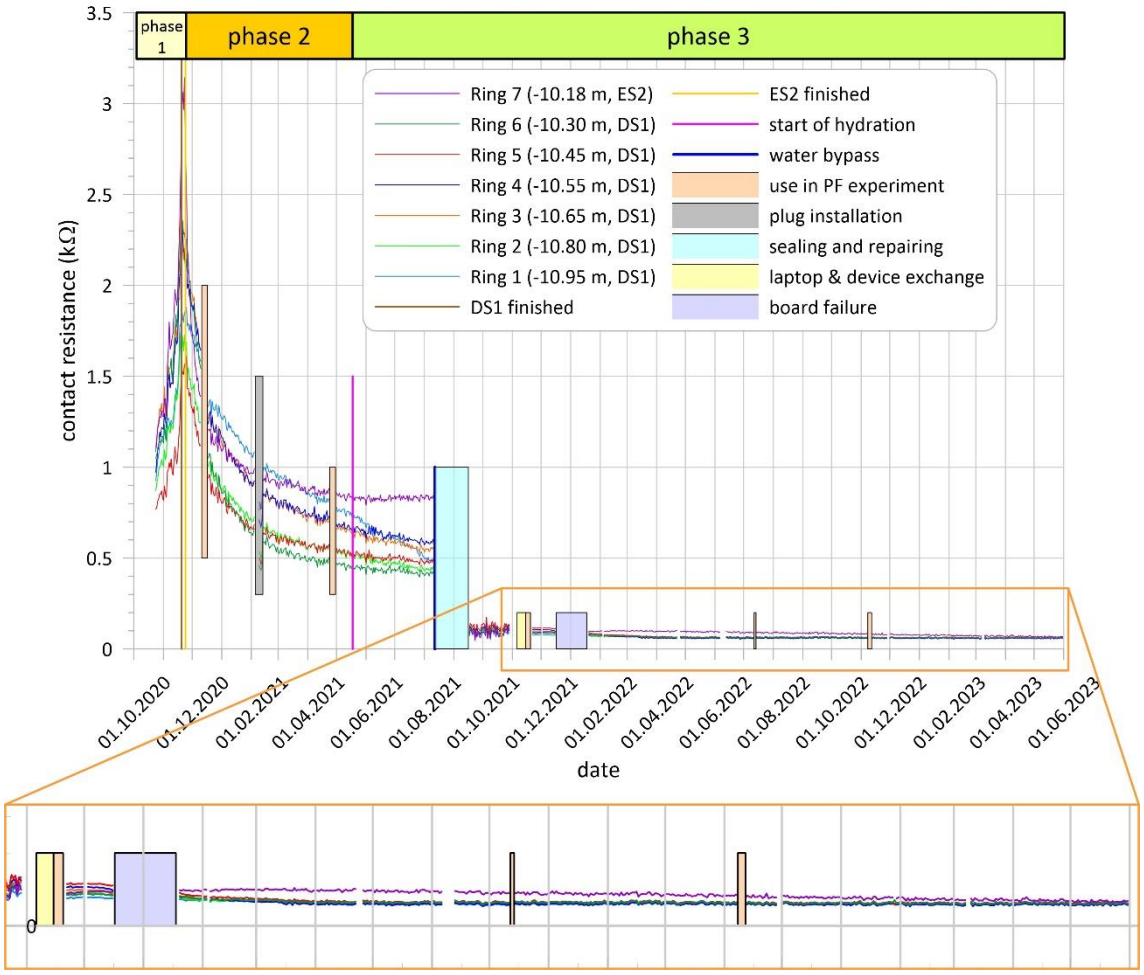

Fig. 4.21 Contact resistances in the 7 ERT rings (each as an average over 36 electrodes) in Shaft 1 plotted over time

First indications of changes can be found by looking at contact resistances over time. This is shown in Fig. 4.21. For each of the 36 electrodes of a ring, the mean value was

determined and plotted as a curve over time. Important milestones of the experiment and some downtimes are also recorded. The contact resistances characterize the area directly at the electrodes and are measured before each data set for quality assurance reasons. In the first phase of the experiment, when the shaft was still open, a marked increase in contact resistances was observed. After the shaft had been filled (phase 2), the contact resistances decreased again. This tendency can also be seen after the beginning of hydration (3rd phase). For the lowest ring, the decrease was even very clear. The water bypass ensured a significant decrease in the contact resistances. It can be assumed that the water has broken through at the shaft wall. After that, the changes become much smaller, whereby one can now distinguish the rings in DS1 from those in ES2 of the level. The value for all rings in DS1 stabilized in April 2022, while the value for the 7th ring decreased continuously until May 2023.

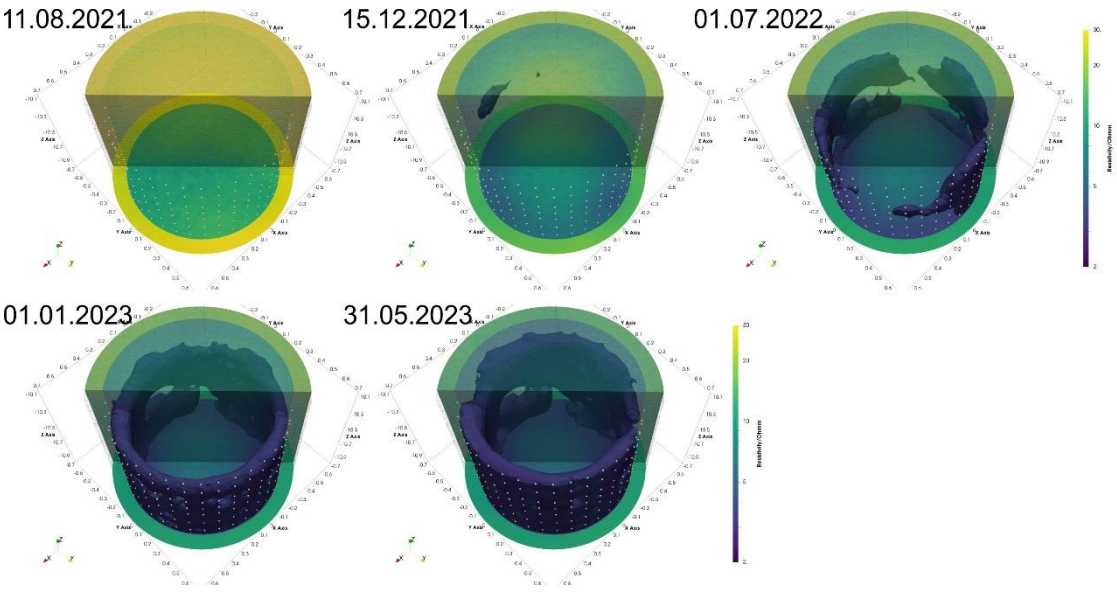

Fig. 4.22 Cut through the 3D resistivity model for Shaft 1 at different time instances

The developing body comprises elements whose resistivity is less than 3.5 Ωm.

The ERT measurement system has worked satisfactorily over the experimental period so far. The biggest failure occurred when during the bypass water penetrated the cables into the multiplexer boxes and destroyed all the boards. In the course of this, the cables were sealed (see /WIE 23b/). Another major period without data was over Christmas 2021, when two of the bords were defective and had to be replaced. Since then, the system has been running extremely reliably. Sensitivity analyses and measurements in the open shaft showed the efficiency of the arrangement (see /WIE 23b/).

Fig. 4.22 shows sections through the 3D models at different times. The date of 11.08.2021 can serve as a reference. Before that, only minor changes were visible. After the water bypass, all resistivities have decreased significantly, especially in the area of the shaft wall. This is illustrated by the display of particularly conductive elements (upper barrier 3.5 Ωm). In December, such elements appeared for the first time, in July 2022 an extensive area of the shaft wall was already covered. It is striking that the area of particularly low resistivities has no connection with the lower surface. In the following steps, the conductive sheath of the shaft wall became increasingly closed, with only small gaps visible at the end of May 2023.

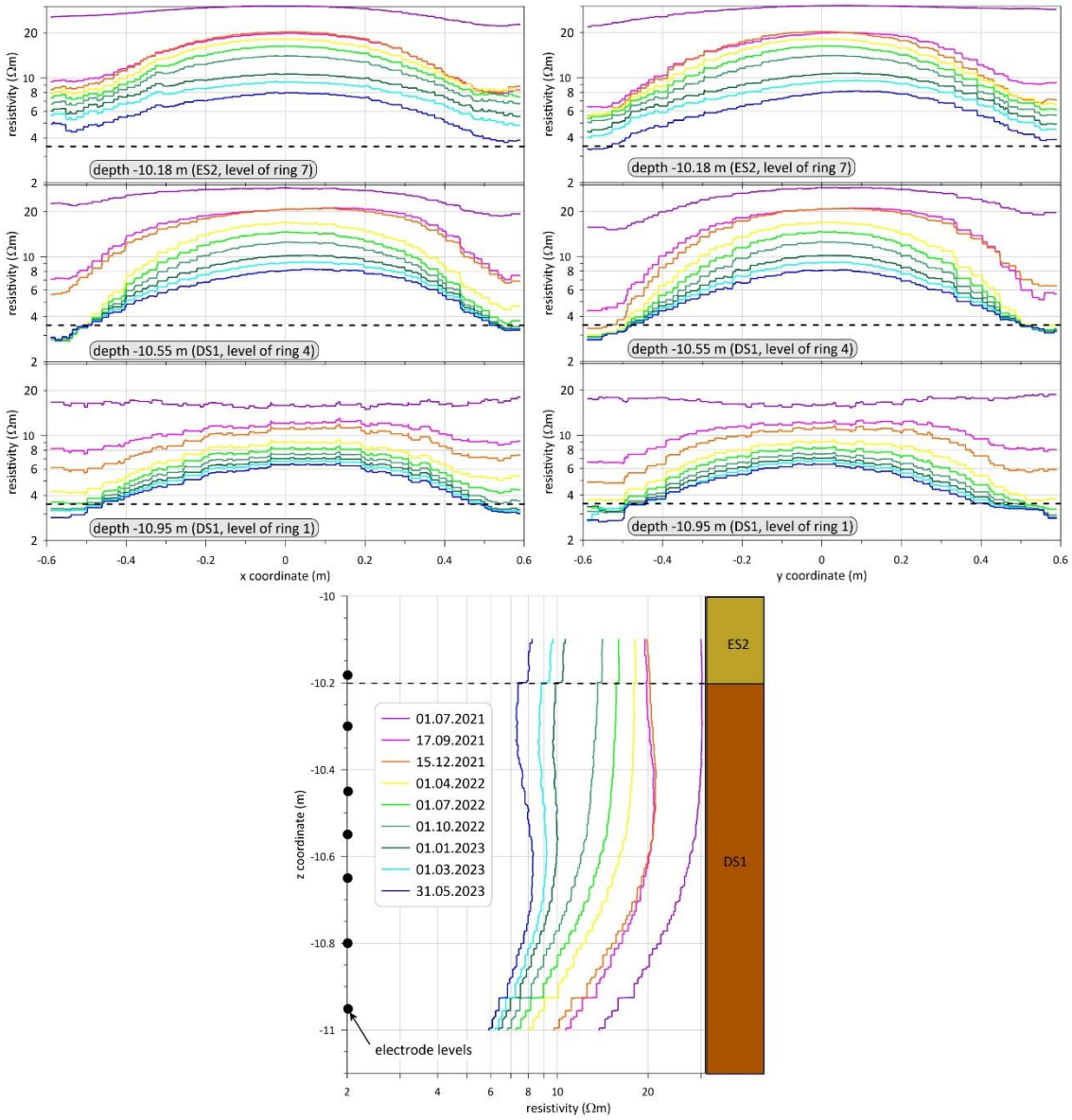

Fig. 4.23 Temporal development of resistivity along the x-axis (3 depths), y-axis (3 depths), and z-axis in the center of Shaft 1

The calculated 3D models can also be used to represent the resistivity along certain lines. This is shown in Fig. 4.23 for different cases:

- Along the x-axis (upper left part picture): For three different depths (corresponding to the depths of rings 1, 4, and 7) and a total of 9 time points the curves are plotted here. The resistivities are continuously getting smaller. The most obvious change can be seen at all depths via the water bypass, especially in the vicinity of the shaft wall. Whereas the curves were almost horizontal before, they now show a clear maximum around the center. Otherwise, with increasing depth the resistivity is smaller. On the wall, the values have stabilized (at 3 to 3.5 Ωm) for the two rings in DS1 since about April 2022, while in the upper ring the resistivity has also decreased further at the edge. The curves are not symmetrical, the values at the two edges are partly clearly different (indication of different conditions in the rock mass).
- Along the y-axis (upper right part of the picture): Same type of projection, and similar observations can be made.
- Along the z-axis (lower partial illustration): Here only the line of the shaft axis is considered. Decreasing resistivities are observed with increasing depth. Since the beginning of 2023, the curves in the upper part of the DS1 show slightly lower values than in the middle, so that the relatively highest resistivities are reached here.

Radial stress

Radial stress measurement data at the shaft wall since May 2021 are shown in Fig. 4.24 (DS1), Fig. 4.25 (DS2), and Fig. 4.26 (DS3 and DS4). Hydration has led to an acceleration of stress uptake at the DS1 sensors already in May 2021 (Fig. 4.24). In August 2021, there was a strong reaction to the water bypass event at the DS1 and DS2 sensors, but the DS3 and DS4 sensors also show a small peak. Afterwards, since water was available at the DS2 face, stress uptake has also accelerated at the DS2 sensors (Fig. 4.25).

The DS1 sensors (Fig. 4.24) also reacted strongly to a short-term loss of injection water pressure at the end of March 2023. There is a direct correlation between these stress sensors and the water pressure in ES1 (see Fig. 4.19).

Radial stress increased more slowly at the levels of DS3 and DS4, where there is no water supply from the pressure chamber (Fig. 4.26). This stress increase can be explained by water uptake from the rock.

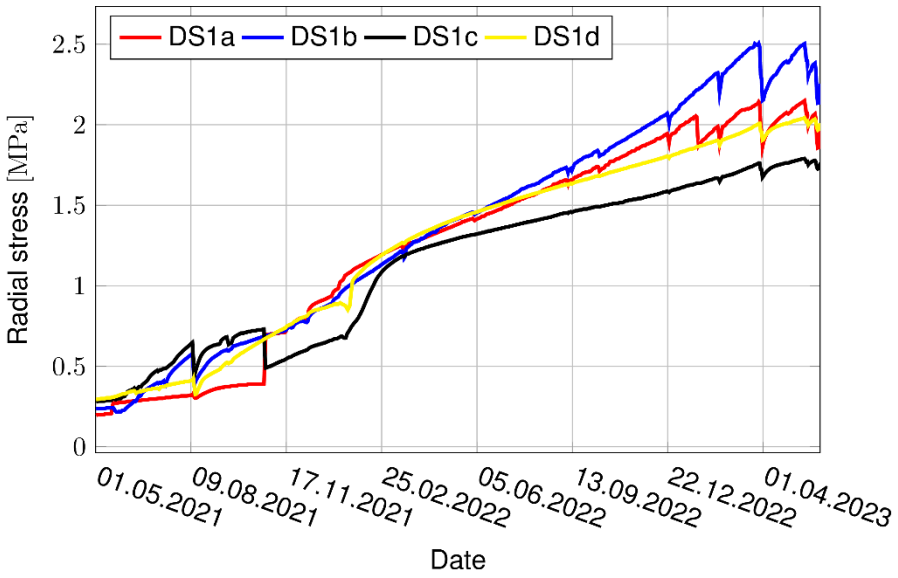

Fig. 4.24 Radial stress evolution at the level of DS1 in Shaft 1

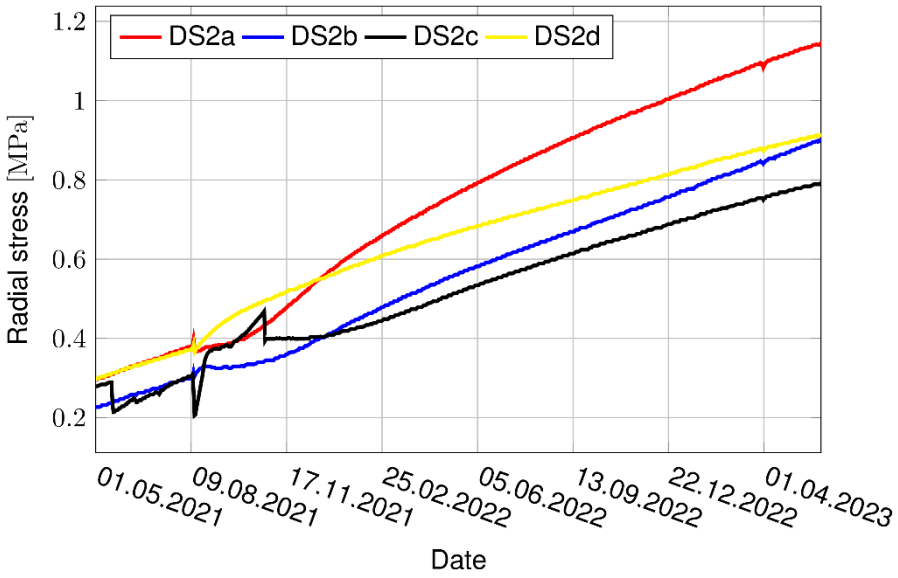

Fig. 4.25 Radial stress evolution at the level of DS2 in Shaft 1

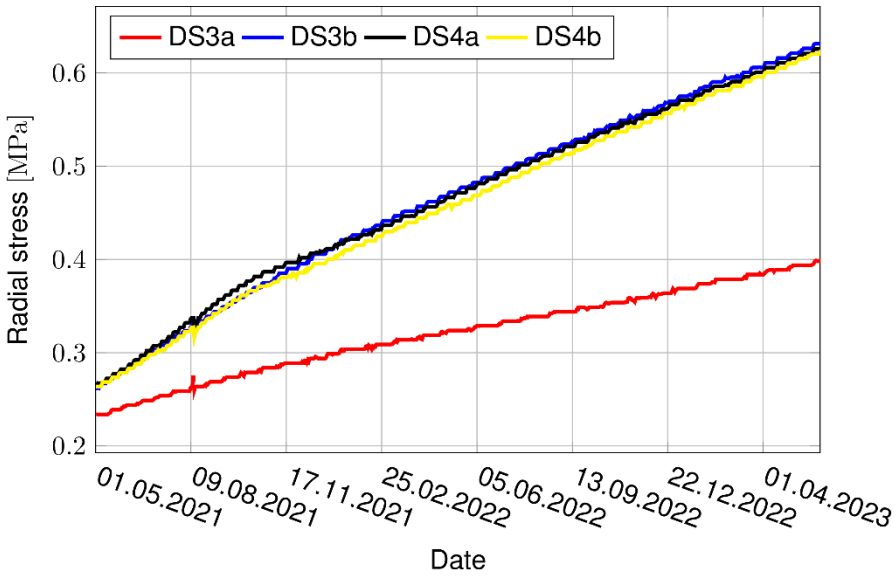

Fig. 4.26 Radial stress evolution at the level of DS3 and DS4 in Shaft 1

4.2.3 Shaft 1 embedded sensors

Taupe TDR

Fluid propagation is monitored using the TDR method /EMM 19/ with five TAUPE TDR sensors installed in two vertical central cross sections running through the complete sealing system and five horizontally installed sensors in the ES. The data acquisition started on January 1st, 2021, after shaft installation and before plug installation (day 33…36).

Liquid (Pearson Water A3) inflow started on 18.05.2021 (day 138) and was immediately visible in ES1 (Fig. 4.27), which was saturated very rapidly. Lower parts of DS1 have been affected only slowly. On day 154, inflow of liquid occurred due to cable isolation faults in ES5, starting at the back side of the sensor S10h. After a second successful try to repair the faults, liquid distributed slowly over the volume of ES5 and into DS4. With the next hydration step on day 223, a breakthrough of liquid happened, again at the backside of the sensor S10h in the area between vertical sensors S2v und S4v, crossing DS1 up to ES2 and into the lower half of DS2. Starting swelling pressure in DS1 reduced the inflow significantly and liquid in ES2 redistributed over ES2 and in direction of DS1 and DS2. ES3 and ES4 remained nearly dry, only a very small increase of ARDP seemed to appear at the start of sensor S9h in ES4, close to vertical sensors S3v and S4v, possibly coming from the rock wall.

Integral results of ARDP for a complete sensor show the same behavior as the locally resolved contour plots.

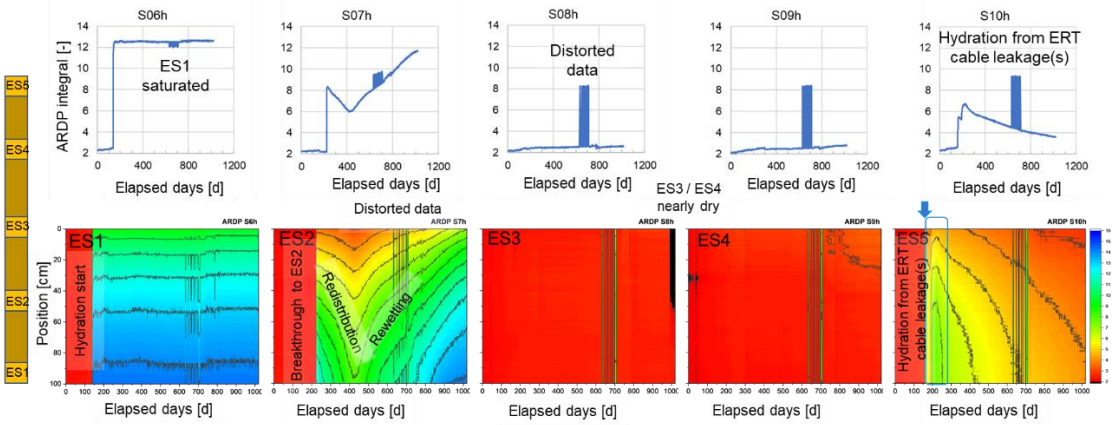

Fig. 4.27 ARDP distribution (bottom) of the horizontally installed TAUPE sensors S6h, S7h, S8h, S9h and S10h in ES1 to ES5. Integral results (top) for all sensors describing the overall process (Start 01.01.2021)

Between day 630 and day 710, several distorted data occurred, where data from the measurement system have been received, but, for all sensors, the form of the raw data was not as expected. The reason is not clear, maybe there were strong electromagnetic distortions coming from machines working somewhere in the URL.

The same findings can be identified in Fig. 4.28 for the vertically installed Taupe TDR sensors. After installation of the plug, a small increase of the ARDP on all vertical sensors was monitored, possibly due to a slight compaction of the materials, especially on the upper half of the shaft. Start of hydration and infiltration of ES1 is not clearly visible, because vertical sensors end at about half height of ES1 and are later affected by the inflowing liquid. However, the second pressure increase is clearly visible by a progress of liquid to ES2 and the lower half of DS2. Redistribution of liquid to the surroundings and, consequently, reduction of ARDP occurred, because swelling pressure started to evolve. After increasing the amount of inflowing liquid, an equilibrium phase was followed by an increase of ARDP, when more liquid entered the materials. After a further pressure step, DS1 was nearly saturated and higher ARDP values could also be monitored in DS2, DS3 and DS4, but, significantly, not strongly expressed along the center (S1v). Possibly, the data were influenced by fluid coming from the rock wall, because ES3 and ES4 did not react visibly. Furthermore, vertical compaction and, hence, increasing ARDP, resulting from increasing swelling pressure possibly affected the DS. Moreover, temporal hydration of ES5 by leakages along ERT cables could be observed.

Effects coming from data distortion are also visible. Especially, sensor S5v suffers from this effect, showing after day 700 a remaining different raw signal structure. Data coming from S5v are no longer reliable. But it seems that ARDP variations due to effects inside the shaft could still be found in these distorted signals. Data processing will be continued for, possibly, identifying a reason for the behavior.

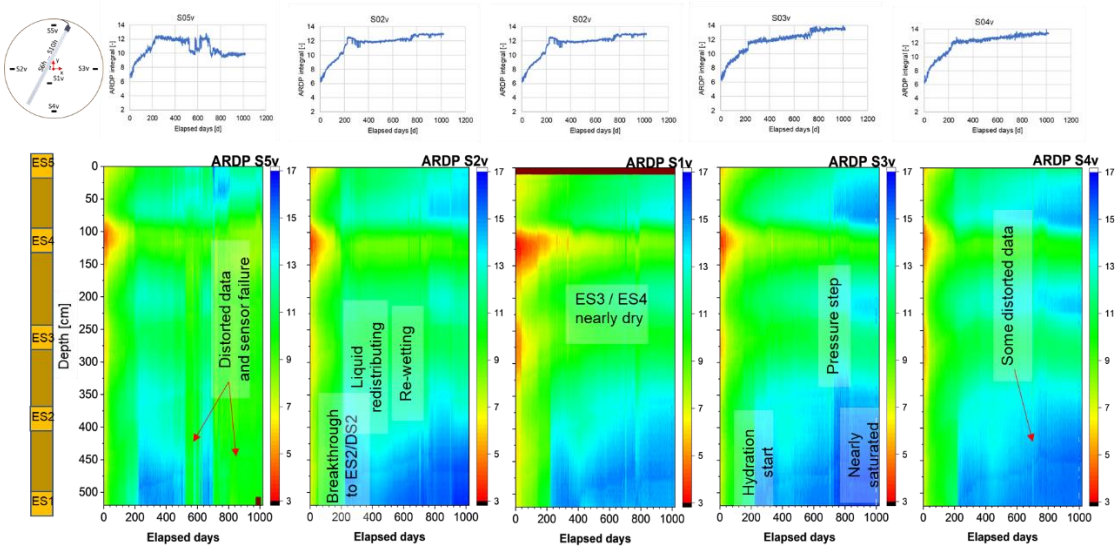

Fig. 4.28 ARDP distribution (bottom) of the vertically installed TAUPE sensors S1v (center), S2v, S3v, S4v and S5v (close to rock wall). Integral results (top) for all sensors describing the overall process (Start 01.01.2021)

Fig. 4.29 shows interpolated perpendicular vertical cross-sections along S5v-S1v-S4v and S2v-S1v-S3v for several dates. On the first date (01.06.2021, day 152), hydration of ES1 has already started and is not really visible below 500 cm on the sensors. But on day 338 (04.12.2021), the strong influence of the second pressure step in DS1 is obvious. This is continued in the graph of day 424 (28.02.2022) with an increasing ARDP up to ES2 and, partly, to DS2, on day 714 (15.12.2022) with higher ARDP in the lower half of DS2, increasing ARDP in ES2, DS3, ES4 and DS4, and finally, on day 911 (30.06.2023) showing nearly saturated DS1 and higher ARDP values reaching DS3. ARDP values in DS3 have also increased, possibly by some interaction with the rock wall. Incorrect S5v data are also found in this graph.

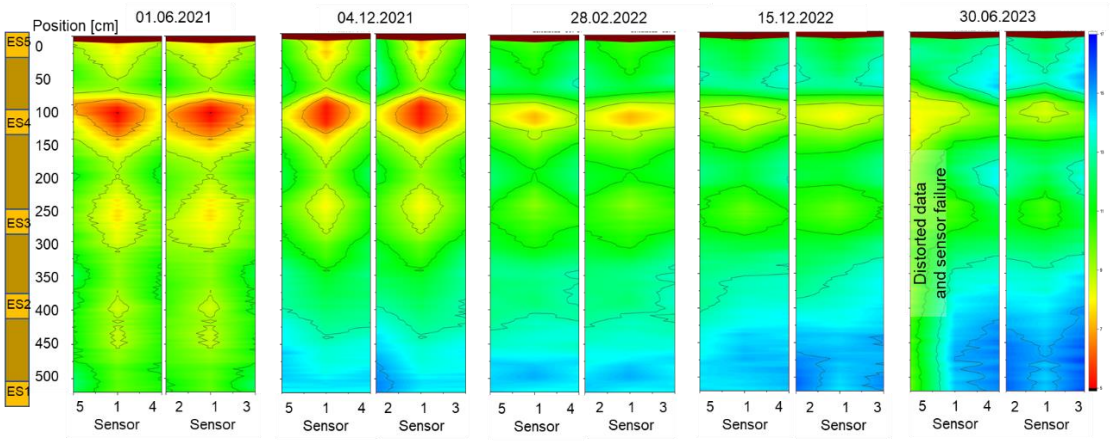

Fig. 4.29 Interpolated ARDP distribution in two vertical cross-sections, S5v-S1v-S4v and S2v-S1v-S3v for four different dates

Liquid inflow after two and a half years is mostly restricted to DS1, building up enough swelling pressure to preserve the function of the sealing system for a longer time, even at higher inflow pressure.

Pore pressure

The following figures show the differential fluid pressure data in the pressure chamber (Fig. 4.30), the ES (Fig. 4.31), and the DS (Fig. 4.32) since May 2021. All sensors showed zero pressure until start-up of hydration, as expected. When the pressure chamber was filled and ES1 was hydrated, the respective sensors reacted directly. With the cable leaks of the pressure chamber sensors occurring in June and July 2021, one of the sensors in the chamber started producing erroneous data (Fig. 4.30). The second pressure sensor in the chamber also failed in November 2021.

One of the pressure sensors in ES1 also failed in November 2021 (Fig. 4.31). Since then, injection pressure inside Shaft 1 is only measured by the second pressure sensor in ES1. The curve of this sensor shows the alternating injection / no injection phases during the early hydration phase (before November 2021) when the cable leaks occurred and sealing measures had to be taken. Since November 2021, the ES1 water pressure has been rising, first in a controlled stepwise manner, later continuously. The continuous pressure rise is due to the fact that the single-stage pressure regulator controlling the injection pressure is not working correctly at the very low injection rates. The regulator has been replaced by a two-stage model in the meantime. At the end of March 2023, there was a

short-term pressure loss due to a rupture of the injection line that was fixed directly. There is no elevated differential fluid pressure in the upper ES (ES2 – ES5, Fig. 4.31).

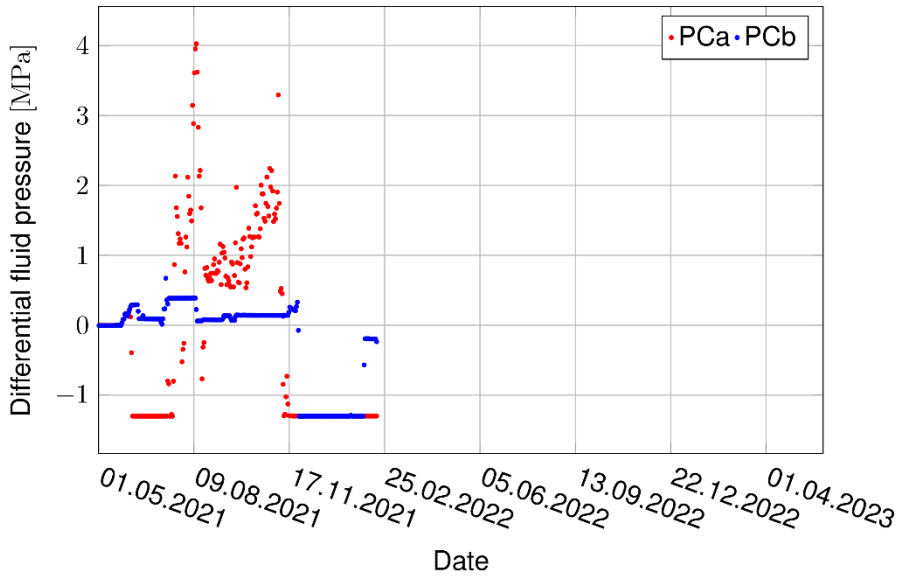

Fig. 4.30 Pressure evolution in the pressure chamber of Shaft 1

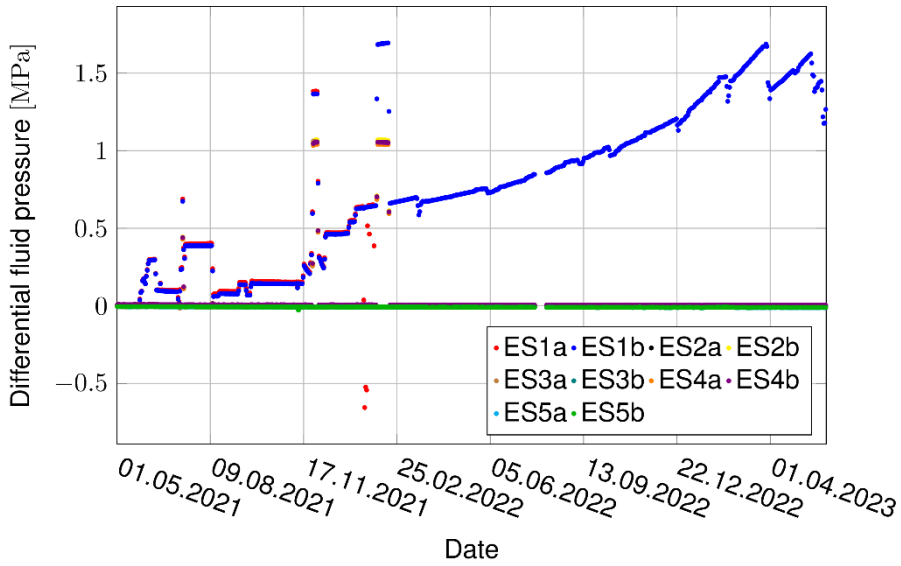

Fig. 4.31 Pressure evolution in the ES of Shaft 1

Inside DS1, pore pressure is steadily increasing since July 2022 which indicates that DS1 must be close to full saturation (Fig. 4.32). Note that the pressure values are still very small. The other DS, being still poorly saturated, show no increase in pore pressure, except for a short-term reaction during the water bypass event of 11 August 2021 (Fig. 4.18). The reason for the short-term pressure increase at DS1 (Fig. 4.32) in May 2022 is not clear as there is no corresponding peak in the ES1 curve.

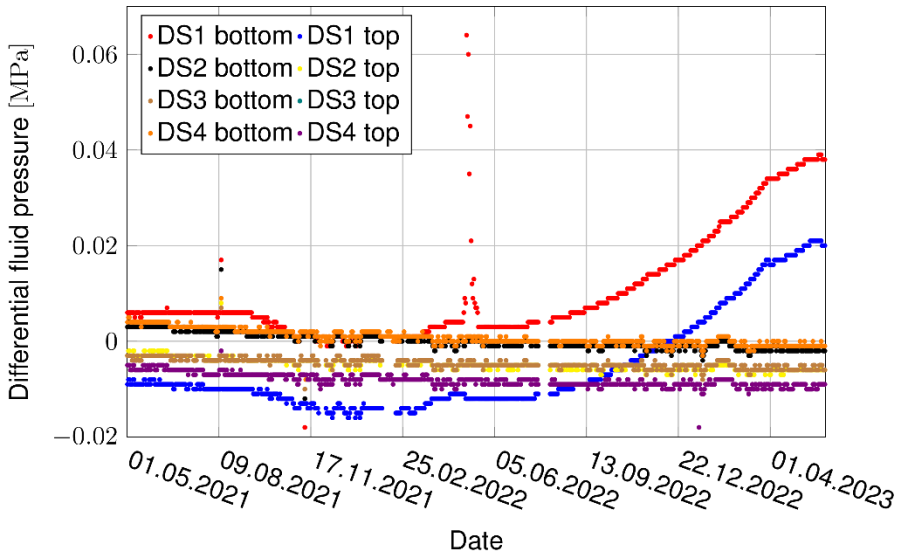

Fig. 4.32 Pressure evolution in the DS of Shaft 1

Relative humidity and temperature

Continuous recording of relative humidity started in May 2021 shortly before hydration start. The evolution of relative humidity in the DS is shown in Fig. 4.33. The lowest sensor S1_DS01_L03_HR_1 shows a slightly higher relative humidity than the others. At all sensors, relative humidity is slowly increasing. Sensor S1_DS03_L03_HR_1 does not provide any data.

The lowest sensor S1_DS01_L03_HR_1 shows a slightly higher relative humidity than the others from the beginning. Sensor S1_DS03_L03_HR_1 does not provide any data from the very beginning. All relative humidity values are increasing steadily, which shows that the sealing segments are saturated from the rock. The one at the bottom is also saturated from the pressure chamber.

With the DS1 bypass event on 11 August 2021, there has been a significant increase in relative humidity at both DS1 sensors and at the lower DS2 sensor. The top sensor of DS4 also shows a higher rate of relative humidity increase since August 2021, which is caused by water entering the system from the top because of the cable leakages in the early phase of the experiment.

DS01_L03, the lower DS1 sensor, has been close to full saturation (97.8 % RH) at the end of May 2023. DS01_L03, the upper DS1 sensor, was lost by 6 November 2022.

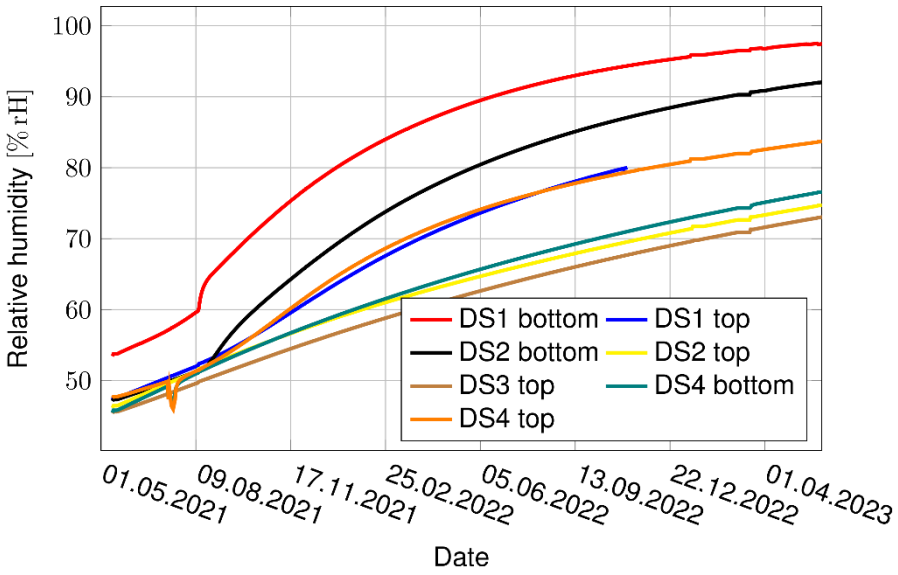

Fig. 4.33 Relative humidity evolution in the DS of Shaft 1

Temperature in the DS is recorded with the relative humidity sensors. Sensor S1_DS03_L03_TT_1 does not provide any data. With the start of hydration, all measured temperature values were close to 16 °C (Fig. 4.34). Temperatures have been decreasing very slowly with an average reduction of around 0.3 °C in the two years period. The same temperature reduction with time is also recorded at the temperature sensors in the rock.

With the DS1 water bypass in August 2021, there has been a significant impact on temperature at both DS1 sensors and at the bottom DS2 sensor, which can be explained by water reaching the vicinity of these sensors, leading to (exothermic) bentonite saturation.

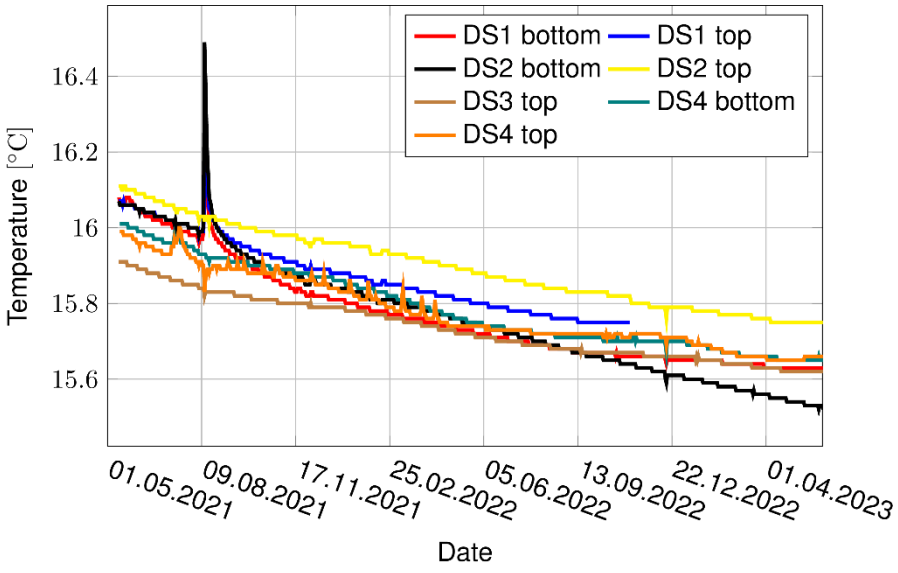

Fig. 4.34 Temperature evolution in the DS of Shaft 1

Temperature in the pressure chamber

The temperature sensors in the pressure chamber were not recorded until end of May 2021 because the Geomonitor DAS was not yet equipped for Pt-100 sensors. Sensor 2 became faulty very soon, by 8 June 2021, and caused a water leakage that required to unplug the cable by July 2021. Sensor 1 remained in operation but showed an extremely noisy signal (amplitude of 2 °C), so it is also considered as failed. The pressure chamber temperature sensors are therefore not shown here.

Axial stress

Data of the axial stress cells installed on top of each DS are shown in Fig. 4.35. With the start of hydration, the readings have slowly increased, with the sensor on top of DS1 more affected than the others, due to hydration from the bottom. The water bypass in August 2021 first lead to an axial stress drop. Afterwards, the stress increased at a much higher rate, comparable to the radial stress measurements at DS1 (see Fig. 4.24). The reaction to the short-term injection pressure loss at the end of March 2023 is also comparable to the behaviour of the radial stress cells. The stress increase of the sensor at DS2 is also accelerated after August 2021, but remains at a much lower level than at DS1.

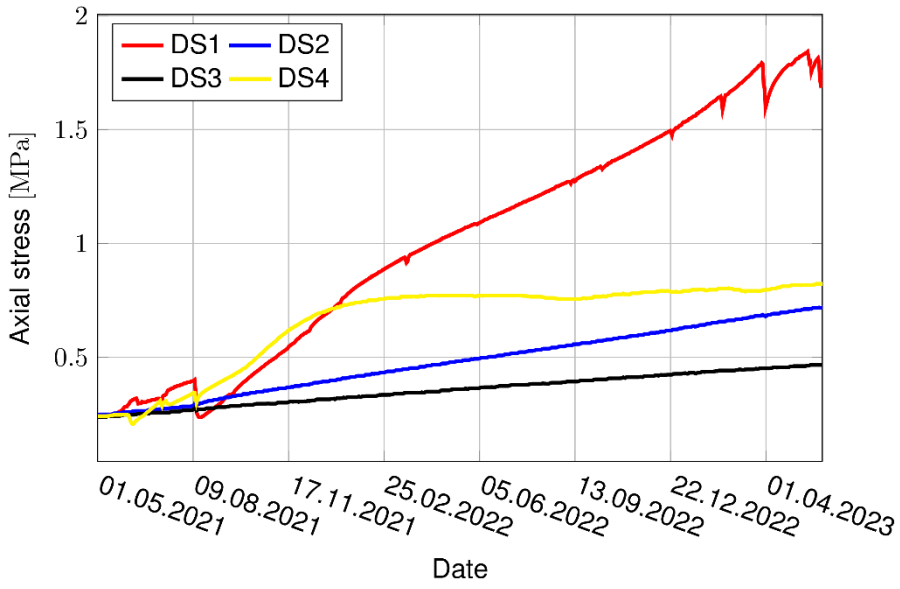

Fig. 4.35 Axial stress evolution on top of the DS of Shaft 1

The sensor on top of DS4 also shows a strong reaction to the event of August 2021. This is, however, not caused by the water bypassing DS1, but by water entering the sealing

system from the top via cable leaks. The water passes ES5 and reaches the top of DS4 where it leads to swelling. Since the water supply is limited (the leaks were sealed), the stress stabilizes after 4-5 months and remains constant afterwards.

Axial displacement

In Fig. 4.36 the readings of the axial extensometers at the level of ES3 are shown. Sensor 1 (S1_ES03_L02_DP_1) had some faulty data in the beginning (not shown in the graph). The sensor cable was damaged during the insertion of the metallic plug. It was repaired but the data seemed to be wrong afterwards.

Since 2022, the other two sensors show stable or slightly decreasing values, indicating only a small uplift of the lower part of the sealing system. Apparently, swelling of DS1 and parts of DS2 is almost completely absorbed by the compression of the unsaturated parts of the lower sealing system.

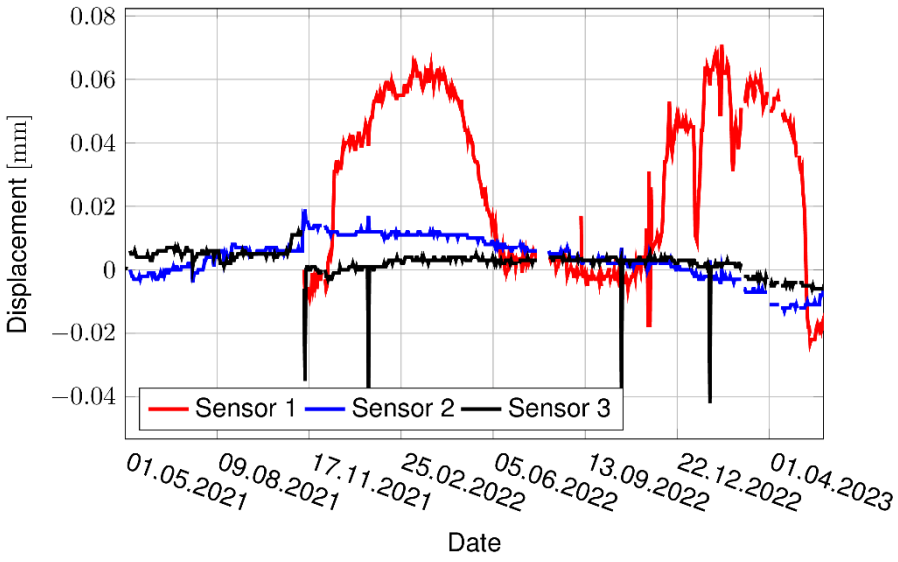

Fig. 4.36 Axial displacement evolution in ES3 of Shaft 1

4.2.4 Assessment and interpretation

The hydration status of Shaft 1 can be summarized as follows:

– Hydration via the pressure chamber: ES1 was saturated immediately after filling the pressure chamber. DS1 hydration from the bottom followed first slowly but was accelerated by the bypass event of August 2021. Since then, saturation has increased from the bottom and the sides of DS1, as shown by the ERT measurements. Most of

DS1 is almost fully saturated now (relative humidity is at 98 % at the lower sensor in DS1, a pore pressure has started to evolve, TDR measurements show high water content, and a strong radial and axial stress has developed). Parts of the center of DS1 may still be slightly desaturated, as the ERT measurements suggest. ES2 was saturated during the bypass event, but at least part of the water has been transferred to DS1 and DS2 since then. TDR measurements still show an increased water content in ES2, but also in the lower half of DS2. Relative humidity in the lower part of DS2 is 92 %, but only 75 % in the upper part. There is no increased pore pressure in ES2 or DS2. In summary, hydration from the bottom pressure chamber has until now affected the sealing system up to the middle of DS2.

- Hydration from the top: This was an unwanted effect due to the leaking cables of the sensors in the pressure chamber and the ERT electrodes in June and August 2021. Water entered the system via ES5 and reached DS4, leading to an increase in water content (TDR measurements and relative humidity in the upper part of DS4) and axial stress. This development stopped some months after sealing of the cables.
- Hydration from the rock: In the DS not affected by water injection (upper part of DS2, DS3, lower part of DS4) there is a slow increase in water content, relative humidity, and radial stress, showing the water is also taken up from the rock due to the high suction of the bentonite.

The radial stress development in the lower DS leads to a response of the rock, leading to an increase in both the stress and the pore pressure at the corresponding depth.

4.3 Shaft 2 hydration regime and measurements

4.3.1 Hydration history

The hydration of the sealing system with Pearson water A3 via the pressure chamber started on 30 May 2023 by using the low-pressure tank. The feeding borehole, pressure chamber, gravel, and ES1 were hydrated at hydrostatic pressure until the end of the reporting period. The absolute fluid pressure in ES1 reached an equilibrium after a few days and the measured pressure value corresponds to the pressure head (Fig. 4.37). The equilibration of the injection flow rate took a little more time as initial leaks in the hydration circuit had to be repaired in advance.

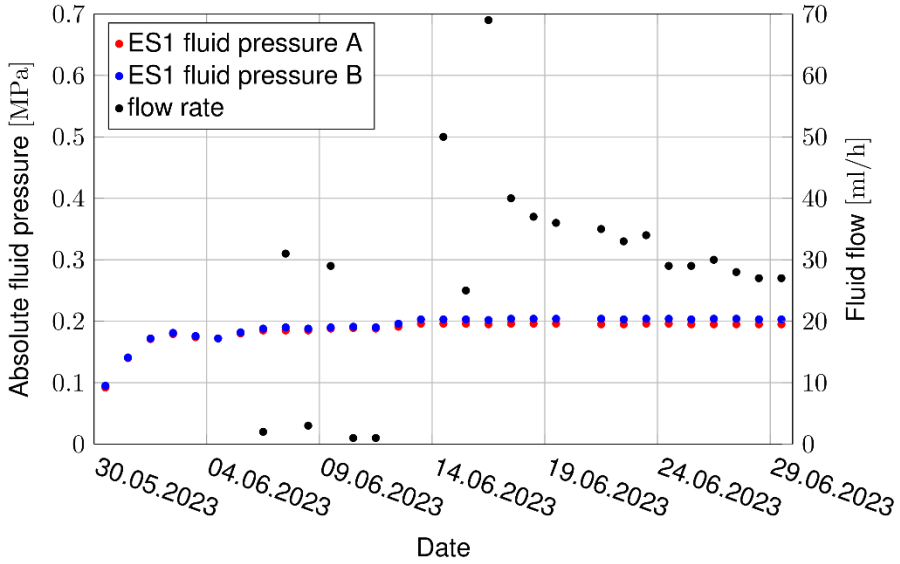

Fig. 4.37 Hydration history of Shaft 2

4.3.2 Shaft 2 interface to rock

ERT

The increased number of electrodes and the significantly increased cover in the z-direction allow additional measurement configurations compared to Shaft 1. These are indicated in Fig. 4.38 by exemplary current or voltage lines.

- Vertical Wenner-α configurations with 20 electrodes each (left part picture), 24 in total
- Horizontal ring arrangements (Wenner-α and Wenner-β, middle partial illustration above), similar to arrangements in Shaft 1, 20 in total
- Bipole-bipole (BB) configurations between two vertical opposite electrode profiles (right partial deflection), three voltage measurements each (dotted lines) to a current bipole. The position of the BB profiles can be seen in the lower middle part-image, a total of 12

In total, this results in a complete dataset of more than 15,000 individual measurements.

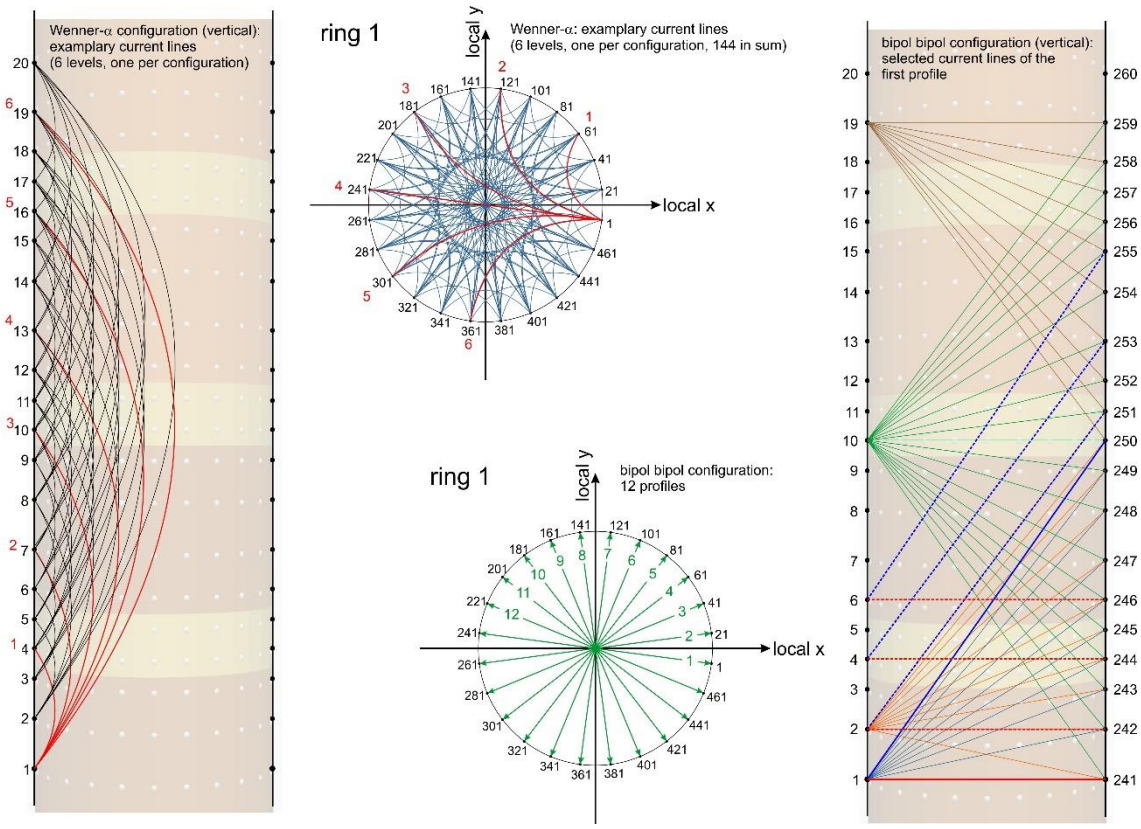

Fig. 4.38 Electrode configurations used in Shaft 2

Vertical Wenner-α configuration (left), horizontal ring configuration (middle) and vertical bi-pole-bipole configurations (right).

Fig. 4.39 shows a cross-section of the grid used for the inversion. Here all segments are considered as separate regions, so the grid consists of 11 regions.

Fig. 4.40 shows the inversion result as a section through the 3D model for the dataset from July 12, 2023.

The outer rock mass is characterized in the picture by rather low resistivities, with some high-resistance layers. This is in line with expectations. The backfill, on the other hand, shows slightly higher resistivities, especially in the upper area (ES4, DS4). There is no clear separation between the sealing and equipotential segments.

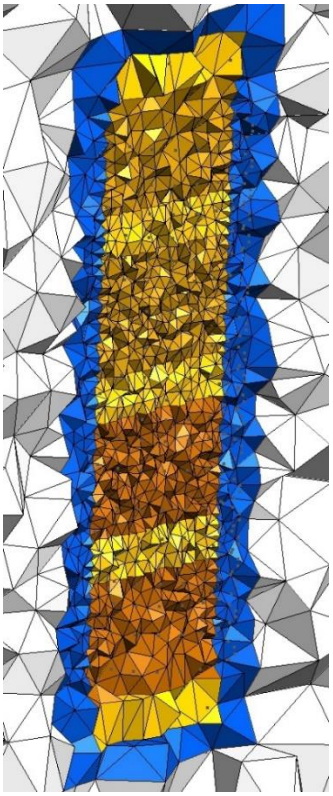

Fig. 4.39 Cut through the three-dimensional grid with the considered regions described by different colors

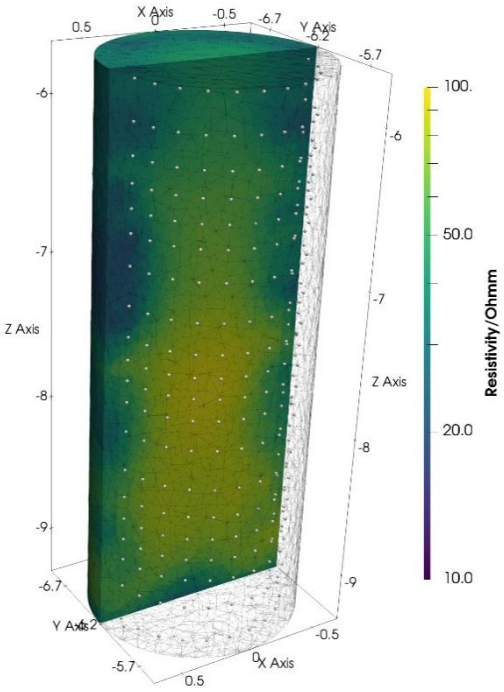

Fig. 4.40 3D model of resistivity based on measurements from July 12, 2023

Taupe TDR

The positioning of Taupe TDR sensors in Shaft 2 is different to Shaft 1. To replace the IMKO twin-rod sensors, additional four Taupe TDR sensors have been installed at the interface between bulk material and shaft wall. The sensors have been placed at the same orientation as the bulk TDR sensors close to the rock wall, which allows to collect more information from the perpendicular vertical cross-sections along the sensors in the bulk material and at the interface. The interface sensors are fixed to the rock wall, but a tight contact over the complete sensor length cannot be assured. During the installation of the materials, some grains of materials could have slipped behind the cable, offering a path to the liquid. To prevent a direct breakthrough from ES1, the far ends of the sensor cables were U-bended about 5 cm above the top of ES1, inside DS1, according to the graph of sensor positions in Fig. 4.41. That means, these TDR sensors cannot detect liquid in ES1 directly after hydration start.

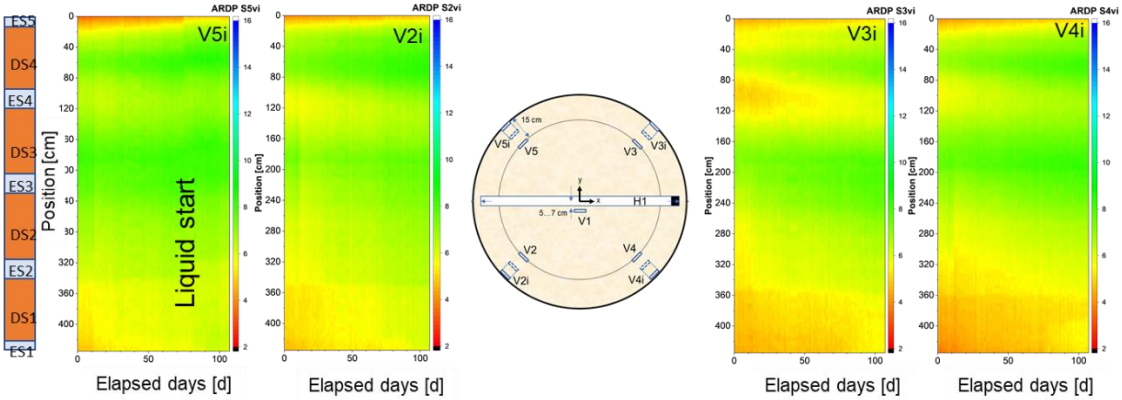

Fig. 4.41 ARDP distribution of vertically installed TAUPE sensors V2i, V3i, V4i and V5i at the interface between rock wall and embedded bulk material (Start March 16, 2023)

The TDR sensors show a different response for the two bentonite materials installed in Shaft 2 (Calcigel in DS3 and DS4 and Securosol MHP1 (70/30) in DS1 and DS2). The ES and DS materials can be well separated in the upper half of the shaft, but not in the lower part. This is due to the lower built-in material density to reach a dry density of about 1.56 g/cm^3. The measurement started on March 16, 2023, and the hydration on day 76 (May 30, 2023). A small increase of ARDP in DS4 could be detected by all sensors from the start, perhaps due to some liquid coming from the rock wall. After hydration start, a possible influence of liquid is visible in the area between V2i and V5i, but not strongly pronounced. The ARDP values of the vertical interface TDR sensors are higher than that

from the embedded sensors, due to the higher ARDP of the rock wall. The sensors have the advantage to be influenced both directions, the rock wall, and the embedding and the ARDP result is about the mean value of both.

Radial stress

A pronounced stress increase in DS1 occurs during the first days of hydration. The much slower but steady stress increase in the upper DS can be explained by water uptake from the rock (Fig. 4.42).

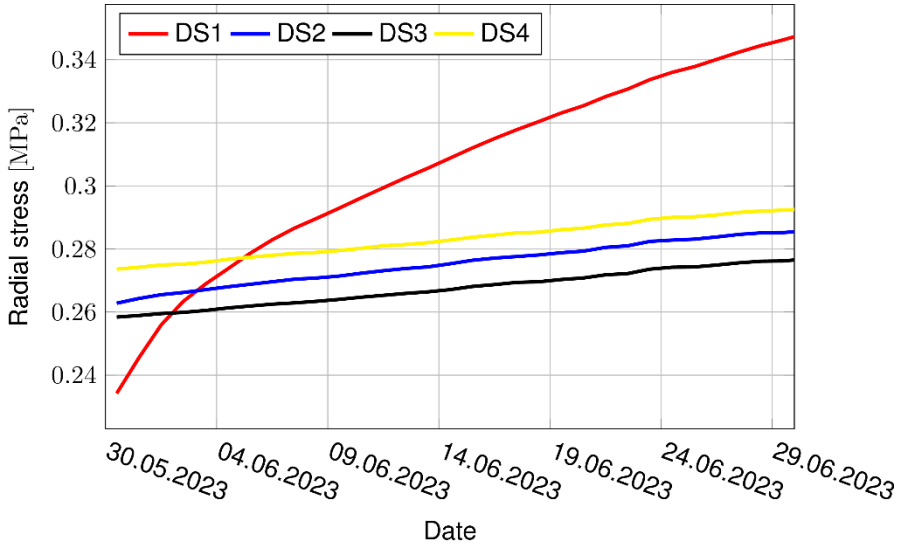

Fig. 4.42 Radial stress evolution in Shaft 2

4.3.3 Shaft 2 embedded sensors

Taupe TDR

The embedded bulk Taupe TDR sensors show the same effect regarding the two bentonite materials as the interface TDR sensors, except the lower ARDP values of the nearly dry embedding materials (Fig. 4.43). The small increase of ARDP in the area of DS4 close to the rock interface (V2, V3, V4, V5) is lower than from the interface sensors. The center sensor V1 does not seem to be affected. Hydration is clearly visible in an increase of ARDP in sensors V2 and V5, but less expressed for sensors V3 and V4, and even much less for sensor V1. For the close-to-wall sensors, the hydration start seems to have an effect along the complete vertical structure, possibly due to fast propagating

liquid along the sensors V2 and V5. But this possible breakthrough was immediately healed by swelling pressure along the sensors.

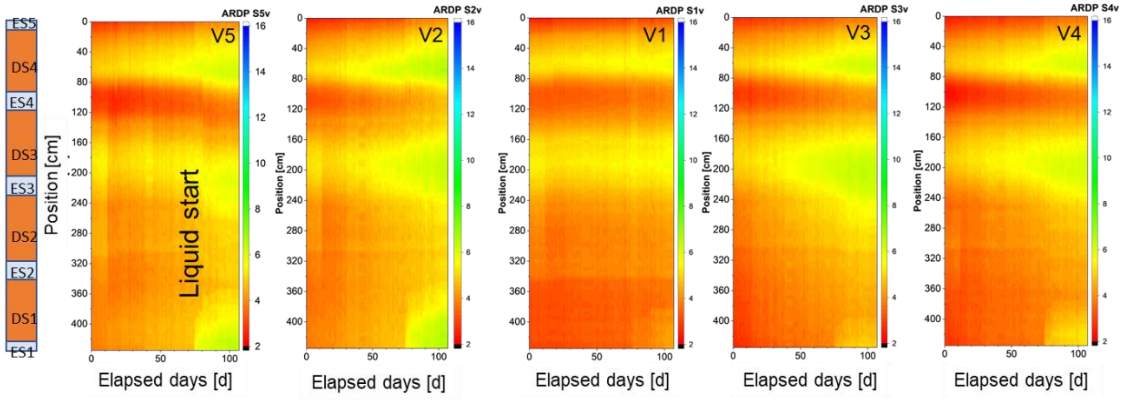

Fig. 4.43 ARDP distribution of vertically installed TAUPE sensors V1 (center), V2, V3, V4 and V5 (close to rock wall).

In Fig. 4.44 it is obvious, that TDR sensors in ES2, ES3, and ES4 are not yet affected by liquid. ES5 seems to have been affected by a very small amount of compaction in the material.

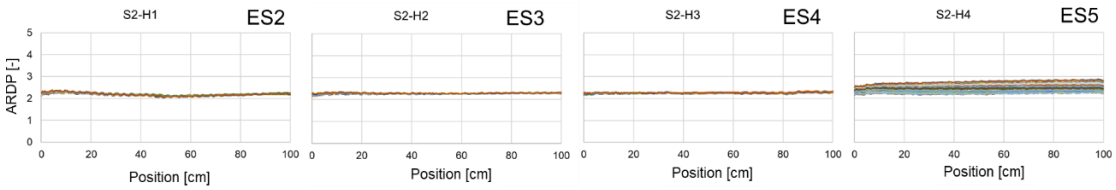

Fig. 4.44 Integral results of horizontally installed TAUPE sensors, H1, H2, H3, and H4 in ES2 to ES5

Pore pressure

No pore pressure build-up in the DS (Fig. 4.45) and ES (except for ES1, see Fig. 4.37) could be assessed during the reporting period.

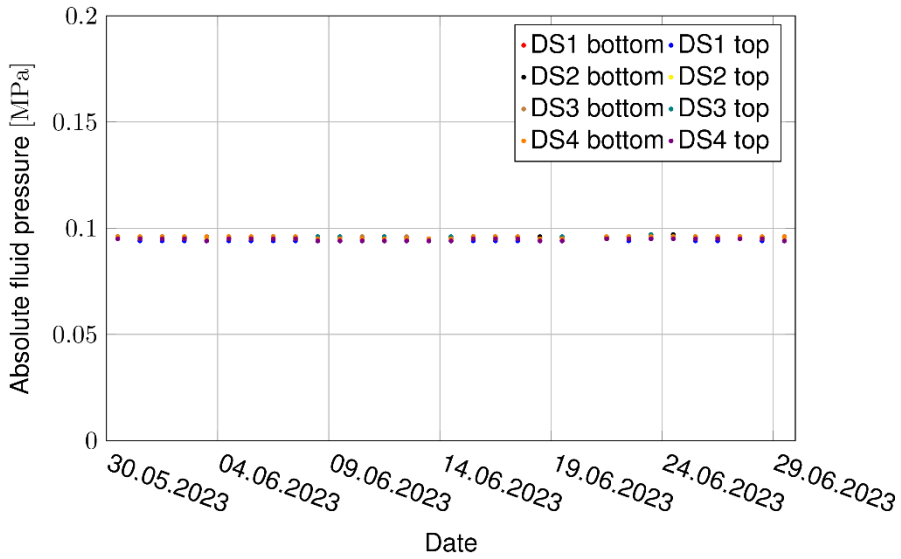

Fig. 4.45 Pore pressure evolution in the DS of Shaft 2

Relative humidity and temperature

The relative humidity has increased slightly in all DS from the beginning of the measurements due to hydration from the rock. In mid-June 2023, the signal of the lowermost RH sensor shows a steeper increase due to hydration from the pressure chamber (Fig. 4.46).

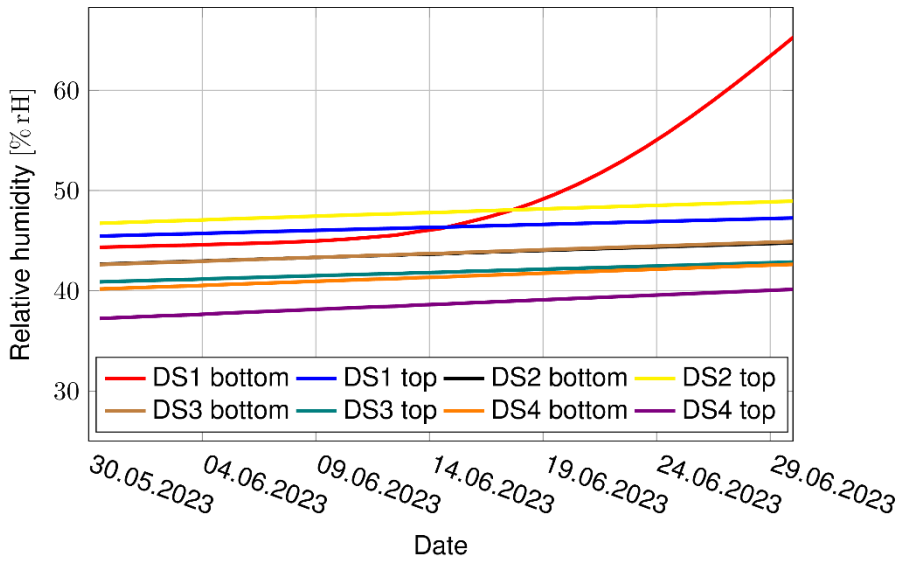

Fig. 4.46 Relative humidity evolution in the DS of Shaft 2

Most of the temperature sensors in the DS show constant values between 15.8 °C and 16.1 °C. Only the lowermost sensor shows a slight temperature decrease (Fig. 4.47).

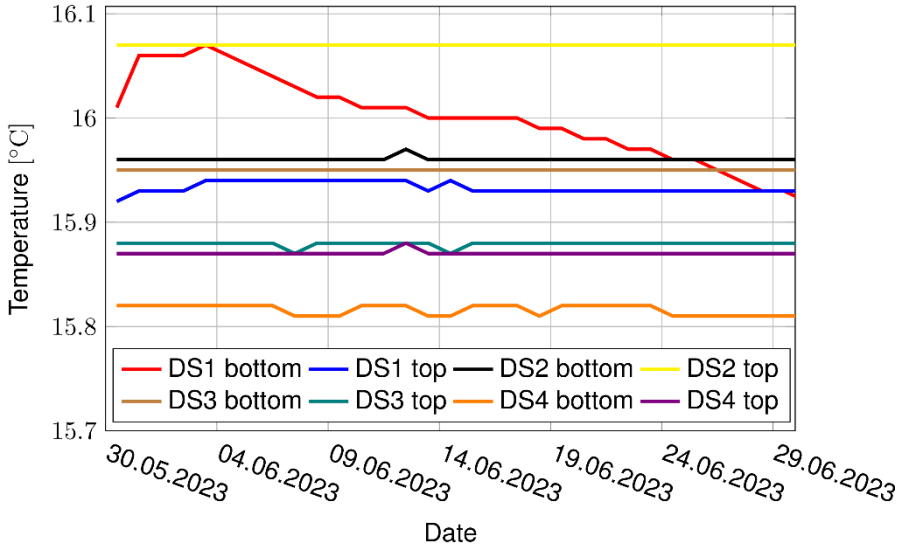

Fig. 4.47 Temperature evolution in the DS of Shaft 2

Axial stress

The axial stress cell on top of DS1 shows an initially steep increase due to hydration of the sealing system from the bottom and swelling of DS1. The axial stress on top of the other DS increases much more slowly due to hydration from the rock (Fig. 4.48).

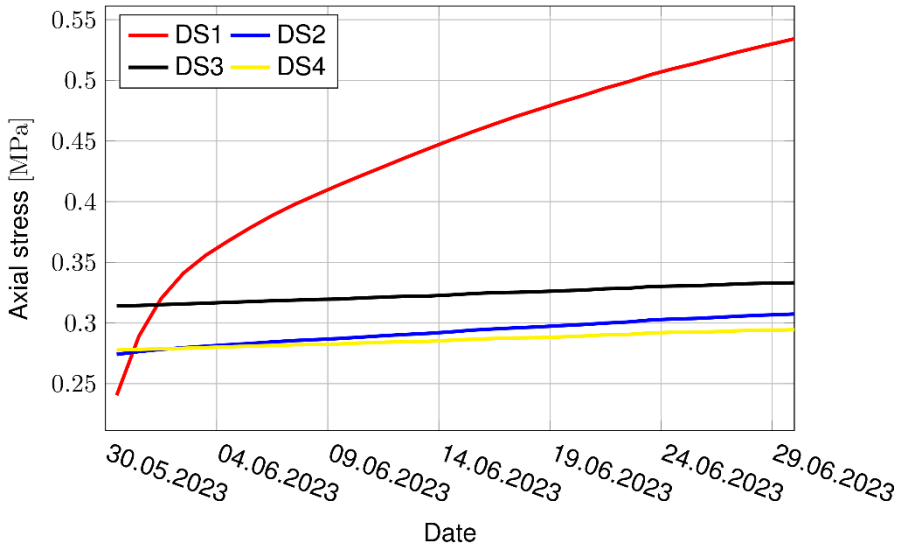

Fig. 4.48 Axial stress evolution in the DS of Shaft 2

Axial displacement

After complete installation of the sealing system, it was observed during testing of the 2D FO sensor that one of the sensing fibers would be damaged. However, it was

assessed in /GAR 23a/ that the sensor works properly (but probably less accurate) with one fiber as long as the temperature in the sealing system remains constant (which is currently the case). The 2D displacement data collected within the reporting period are almost constant. The data interpretation has to be performed later after a longer duration of the experiment. However, the three unidirectional displacement sensors show a clearly decreasing trend indicating a small uplift of the lower part of the sealing system of several micrometers (Fig. 4.49).

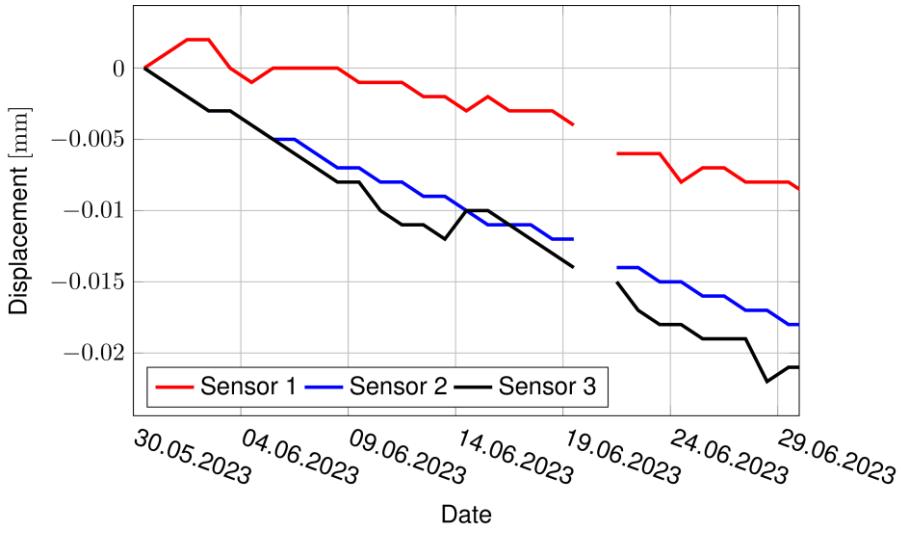

Fig. 4.49 Vertical displacement evolution on top of DS2 in Shaft 2

Wireless transferred data

The wireless data transfer for the sensors connected to the transmitter unit works in principle. Data of all connected sensors are collected. Within the reporting period, there still was an issue in transformation of the wireless data by the Amberg wireless DAS. Accordingly, the sensor values are currently not interpretable, but the issue is about to be solved.

4.3.4 Assessment and interpretation

The effect of gravitational hydration of the sealing system in Shaft 2 from the bottom for about one month is visible in all ES1 and DS1 sensors (particularly TDR, relative humidity, axial and radial stress sensors). DS1 has induced a stress increase due to swelling and a small upward movement of the lower part of the sealing system. An additional hydration from the rock is visible in all DS.

In comparison to Shaft 1, a new sensor setup is used in Shaft 2. The performance of the newly introduced vertical TAUPE TDR sensors at the rock wall is good (and much better than for the IMKO rock TDR sensors in Shaft 1). Some issues regarding the 2D FO displacement measurement system occurred, and it is not clear yet whether the 2D sensor works accurate. The unidirectional displacement sensors (magnetostrictive linear position sensors) currently show a better performance than the extensometers in Shaft 1. The processing of the wireless data collected in Shaft 2 still has to be improved.

5 Material characterization and laboratory-scale testing

5.1 Methods

The mineralogical and geotechnical methods (Tab. 5.1) to characterize the material properties are described in detail in the final report of the Sandwich-VP /EMM 19/. Methods whose execution has been changed or for which different protocols exist in the laboratories of the project partners are described in detail in App. B.

Tab. 5.1 Mineralogical and geotechnical methods

Method	Short description/remarks
Sample preparation	Bentonite pillows and compacted bentonite from laboratory experiments were reduced in size by crushing (App. B.1) and grinding in a mortar mill followed by aliquoting for mineralogical analyses. Raw bentonites were pretreated at the production plant.
X-ray diffraction analysis (XRD)	Oriented preparation (air dry, ethylene glycol saturated and heated) together with Sybilla^{TM} software was used for qualitative analysis of clay minerals. Powdered samples and Rietveld analysis by Profex /DÖB 15/ was used for quantitative analysis.
X-ray fluorescence analysis (XRF)	The major elements of the chemical composition of the mineral materials was determined utilizing discs of fused material with $Li_2B_4O_7$.
Loss on ignition (LOI)	The LOI was either determined in connection with XRF analysis or by /DIN 02/.
C/S Analysis	The total carbon and sulphur content of the raw clay and bentonite samples was determined.
Simultaneous thermal analysis (STA)	The thermal behavior of the mineral materials and the evolved gases during heating were observed by TG/DSC-MS to verify phase analyses.
Cation exchange capacity (CEC) measurement and analysis of exchangeable cations	CEC was measured by Cu-Trien method. Exchangeable cations were measured in the supernatant by ICP-OES.

Tab. 5.1 (continued) Mineralogical and geotechnical methods

Method	Short description/remarks
Conductivity measurement and analysis of dissolved ions	The conductivity of dispersions is measured to determine the salt content and soluble ions of DS and ES materials in initial state and after hydration with different fluids in experiments. Cations were determined by ICP-OES and anions were determined by IC.
pH	The pH of Pearson water batches was measured.
Ion content of fluids	The composition of Pearson water batches, breakthrough fluids from experiments and supernatant from conductivity measurements was determined by ICP-OES (cations) and IC (anions).
Water content (w) and moisture (w_m)	The mass loss during isothermal heating of DS and ES materials at 105 (110) °C and 200 (240) °C was measured to calculate gravimetric water content and moisture based on /DIN 06/.
On-site water content measurement during pillow production	During pillow production the moisture was determined by an infrared heating scale (App. B.9).
Bulk, dry, specific density (ρ_b,ρ_d, ρ_s), effective montmorillonite dry density (EMDD)	Bulk density is determined from mass and volume of a sample. The volume of a sample was either determined from geometry or by immersion weighing method. The dry density is calculated from bulk density and water content. The specific (grain density) is either measured with a gas or water pycnometer or calculated from phase content of DS and ES materials. EMDD is calculated based on the smectite content of DS materials.
Bulk and dry density of binary mixtures	The bulk density of binary mixtures of bentonite pillows and BGM is determined from the mass of the DS material and the filled volume. The corresponding dry density is calculated based on the water content and mixing ratio of both components.
Proctor density	The Proctor density of the ES material was determined according to /DIN 12/ and /DIN 22/.
Particle size distribution (PSD)	The particle size distribution of DS materials was determined in suspension by: sedimentation: d < 63µm (mass%) and laser granulometry: d < 500 µm (volume%)
Particle size distribution of BGM	The particle size distribution of BGM was determined by dry sieving.

Tab. 5.1 (continued) Mineralogical and geotechnical methods

Method	Short description/remarks
Mass gain of air-dry bentonite at elevated relative humidity	The mass gain test was performed at 85 % RH and 20 °C.
Suction measurements	The relative humidity and temperature of the compacted samples were measured with psychrometers or capacitive sensors depending on the water content.
Swelling pressure (p_s)	The swelling pressure (axial stress) is measured by devices with different sample geometry d = 50 mm, h ≤ 50 mm (set 1, IBeWa) d = 38 or 50 mm, h = 12 mm (set 2, CIEMAT) d = 100 mm, h ≤ 20 mm (set 3, IfG) d = 50 mm, h ≤ 20 mm (set 4, RUB)
Gas permeability	Gas permeability was determined with nitrogen at different pressures prior to swelling pressure tests of set 1 and prior to MiniSandwich tests.
Liquid permeability	Permeability of DS material was determined after swelling pressure measurement in device 1 by the method of two-chamber experiment. Permeability of ES material was determined according to /DIN 21/. Permeability was although determined in MiniSandwich experiments.
Gas entry pressure	The gas entry pressure was determined in device 1 after determination of liquid permeability.
Time-domain reflectometry (TDR)	TAUPE TDR cable sensors were used to measure apparent relative dielectric permittivity (ARDP) as a measure for the volumetric water content and fluid distribution in HTV experiments.

5.2 Materials

5.2.1 Opalinus clay (sandy facies)

Drill cores were obtained from the drilling project carried out at the Mont Terri Underground Rock Laboratory (URL) between 5 August 2019 and 27 March 2020. Four core samples of approximately 10 cm length from each of three boreholes BSW-B20, BSW-B21 and BSW-B22 (Fig. D. 1, Fig. D. 2, Fig. D. 3) were vacuum-sealed in aluminum sample bags stored until mineralogical analysis was performed. The sandy facies of the Opalinus clay (OPA) at Mont Terri has been rarely studied, therefore this analysis provides a unique characterization of the OPA specifically in the Sandwich niche and

allows comparison with other OPA sandy facies. Mineralogical analysis was carried out on < 1 mm particles obtained after splitting, crushing and milling of the samples (Fig. 5.1). STA, XRF, and XRD were performed in order to characterize the mineralogy of the samples, and analysis of cation exchange capacity, conductivity, and exchangeable and soluble ions was used to define sample chemistry.

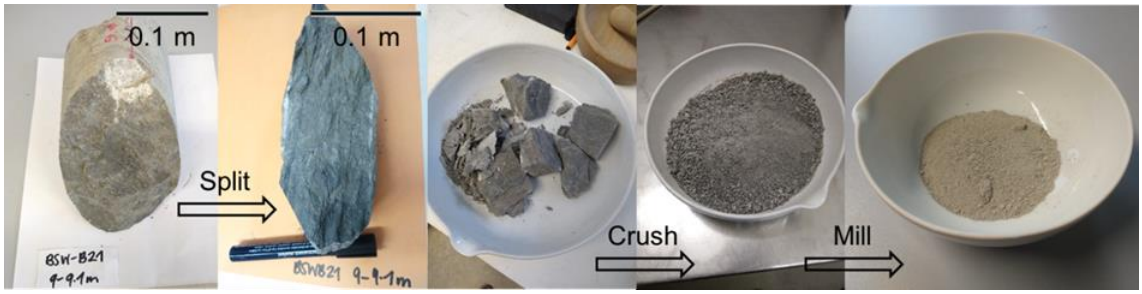

Fig. 5.1 Core piece BSW-B21_9 and sample preparation

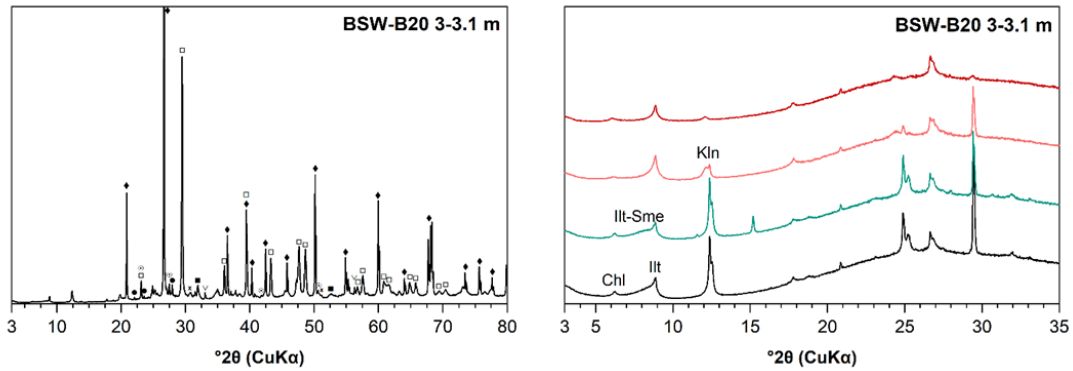

Fig. 5.2 Representative pXRD (left) and oXRD (right) data of sample at 3 to 3.1 m from core of BSW-B20

Solid black diamonds indicate quartz, solid black and hollow black circles plagioclase and K-feldspar, hollow squares calcite, exes dolomite/ankerite, solid black squares siderite, and hollow down-pointing triangles pyrite. Anatase, gypsum and rutile reflections are not indicated. oXRD include AD (black), EG solvated (blue), and heat treated and 375 (orange) and 550 °C (red). Chl, Ilt, Kln and Ilt-Sme indicate the position of reflections used to identify chlorite, illite, kaolinite and interstratified illite-smectite respectively.

Powder XRD (pXRD) traces showed similar phases present in all samples. Main non-clay phases identified were quartz, calcite, dolomite/ankerite, pyrite and both plagioclase and K-feldspars. pXRD data also indicated the presence of the clay minerals chlorite, mica/illite, and kaolinite. The position of the d060 reflection (d = 1.49-1.50 Å) is consistent with dioctahedral clay minerals. Oriented slide preparations (oXRD) of < 2 µm fractions were used to confirm the presence of clay phases identified from pXRD. A very small reflection indicating gypsum was identified in only several of the core samples and could

arise from pyrite oxidation during the drilling process or sample preparation. Changes in the position and shape of intensity between 10-14 Å between air-dry (AD) and ethylene glycol (EG) solvated samples in oriented slide preparations also indicate the presence of a mixed-layer phase, likely interstratified illite-smectite (Fig. 5.2), consistent with other analyses of OPA samples and with the diagenetic history of the OPA formation.

Results of simultaneous thermal analysis (STA) also support the phase identification from XRD data, with evolved gas analysis providing extra information on the nature of carbonate phases and the presence of pyrite. STA also confirmed the main nature of the clay minerals as dioctahedral, and also suggests they are primarily trans-vacant in nature (Fig. 5.3).

Rietveld refinement of the pXRD data indicates a total clay content between 23-52 %, with mean values of 19 % interstratified dioctahedral Ilt-Sme, 13 % muscovite/illite, 11 % kaolinite and 2 % chlorite. Quantification of non-clay minerals gives 26-46 % quartz, 3-6 % feldspars, 8-34 % calcite, 1-8 % dolomite/ankerite, and pyrite, rutile and anatase all < 1 % (Tab. 5.2). These results are consistent with previous analyses of Opalinus Clay, see /MAZ 98/, /GAU 03/. There is a strong correlation between both STA carbonate content (calculated from mass loss between 700-900 °C) and CaO content from XRF with carbonate content from Rietveld analysis (R^2 = 0.99 and R^2 = 0.98 for STA and XRF respectively). This strongly supports the quantification results.

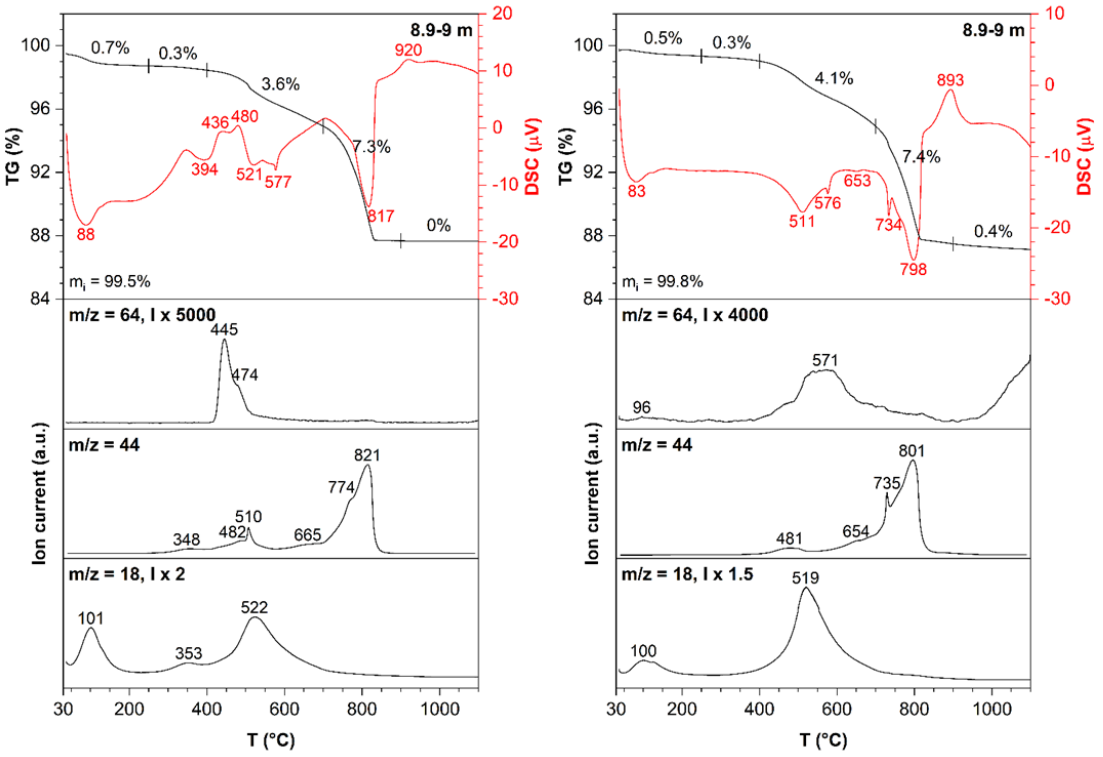

Fig. 5.3 TG/DSC and evolved gas analysis curves for a representative OPA core (BSW-B22 8.9-9 m) under synthetic air/N_2 (left) and N_2/N_2 (right)

Analysis of AD and EG < 2 µm preparations using the Sybilla™ software provided more information on the nature of the interstratified Ilt-Sm contribution /APL 06/. Sybilla results identify pure illite, an interstratified Ilt-Sm phase with ~ 90 % illite layers, and an additional Ilt-Sm interstratified phase with ~ 70 % illite layers. Phase composition was consistent between both AD and EG states. Results also suggest layers with an interlayer distance close to 14 Å, with a vermiculitic nature. Illitization of smectite during burial diagenesis involves an increase in tetrahedral charge, loss of divalent interlayer cations, and enrichment of interlayer potassium with a concurrent decrease in d001 spacing. This could result in a transitory vermiculitic intermediate detected in XRD modelling as 14 Å layers.

The CEC of all the core fragments studied indicates a low proportion of swelling clay minerals, supported by quantitative XRD results, where there is a correlation between Ilt-Sme content and CEC (R^2 = 0.39). While smectite is expected to be the main phase contributing to CEC and therefore a stronger correlation between Ilt-Sme content and CEC expected, there is some variation in the exact composition of the Ilt-Sme phase which is not considered with the correlation.

Tab. 5.2 Mineralogical composition of OPA core samples from Rietveld analysis

Sample	Phase content [wt.%]						
	Mica (di)	Kaolinite	Chlorite (di-di)	Ilt-Sme	Calcite	Dolomite/ Ankerite	Siderite
B20-3	8.3	6.8	1.3	10.3	23.9	1.5	1.1
B20-6	10.4	8.4	1.3	26.5	9.6	1.5	1.1
B20-9	9.2	7.5	1.5	20.0	9.6	3.1	1.1
B20-11	8.7	6.2	1.3	16.7	9.1	8.4	1.0
B21-3	9.7	8.7	1.5	20.7	8.7	1.8	1.4
B21-6	12.8	10.7	1.9	36.9	8.0	1.8	1.6
B21-9	7.0	4.9	1.6	8.7	33.9	0.9	1.4
B21-11	8.3	4.9	1.1	13.9	14.7	6.1	0.9
B22-3	8.9	7.3	1.5	18.2	13.7	2.7	0.7
B22-6	9.4	7.0	1.5	13.3	16.2	1.3	1.4
B22-9	9.3	5.1	1.1	16.2	10.7	6.9	0.8
B22-11	10.1	8.7	1.2	22.8	8.2	2.1	0.9
	Quartz	Plagioclase (albite)	K-feldspar (microcline)	Pyrite	Anatase	Rutile	Gypsum
B20-3	40.1	3.2	2.8	0.4	0.4	-	-
B20-6	34.1	3.2	2.0	0.5	0.5	0.3	0.6
B20-9	40.6	3.2	2.5	0.5	0.4	0.2	0.5
B20-11	41.0	3.2	2.7	0.4	0.5	0.3	0.5
B21-3	40.4	3.1	2.5	0.5	0.6	0.2	-
B21-6	20.8	1.8	1.6	0.7	0.9	0.4	-
B21-9	35.2	2.6	3.1	0.3	0.4	0.0	-
B21-11	42.8	3.3	3.0	0.3	0.4	0.3	-
B22-3	40.8	3.5	2.1	0.4	0.3	0.1	-
B22-6	43.3	3.4	2.4	0.3	0.4	0.1	-
B22-9	42.6	2.6	2.9	0.4	0.4	0.4	0.4
B22-11	39.4	3.0	2.1	0.5	0.5	0.2	0.4

Furthermore, due to the broad, diffuse reflections of the interstratified phase, quantification is associated with a large uncertainty. Low amounts of smectite in the Ilt-Sme phase also mean that edge and surface sites have a more signification portion of the CEC and these factors could explain the variation.

Tab. 5.3 Exchangeable cation content and CEC of OPA samples

Sample	Exchangeable cation content [cmol(+) kg^{-1}]						CEC [cmol(+) kg^{-1}]
	Mg^{2+}	Ca^{2+}	Na^{+}	K^{+}	Fe^{3+}	Sum	
B20-3	2	32	3	1	0	37	3
B20-6	2	27	3	1	0	33	3
B20-9	2	27	3	1	0	33	4
B20-11	2	26	3	1	0	32	2
B21-3	2	27	3	1	0	34	4
B21-6	2	25	4	1	0	32	6
B21-9	2	32	2	1	0	36	3
B21-11	2	29	2	1	0	34	3
B22-3	2	23	3	1	0	29	4
B22-6	2	30	3	1	0	36	3
B22-9	3	29	3	1	0	36	2
B22-11	3	28	3	1	0	35	5

Analysis of exchangeable cations reveals an anomalously high total cation content (Tab. 5.3). This is an experimental artefact owing to the solubilization of carbonate phases in the presence of Cu-trien used for CEC measurement, which increase soluble Ca^{2+} and Mg^{2+} /BOH 19/. The increase in Ca^{2+} is much higher as calcite is the more dominant carbonate phase and has a higher solubility. When compared with soluble ion content (Tab. 5.4), results indicate that the interlayer cation composition of the OPA samples consists of Mg^{2+}, Na^{+} and Ca^{2+}. Porewater composition at Mont Terri has a relatively high amount of Na^{+} compared to Ca^{2+} and Mg^{2+}, which could explain the persistence of Na^{+} as an interlayer cation. Higher soluble sulphate content correlates with presence of gypsum in a sample, with the exception of B21-11 sample. This could indicate that B21-11 contains some gypsum at a level under the detection limit in XRD.

Tab. 5.4 Soluble ion content of OPA samples

Sample	Soluble ion content						
	[cmol(+) kg^{-1}]					[cmol(-) kg^{-1}]	
	Mg^{2+}	Ca^{2+}	Na^{+}	K^{+}	Fe^{3+}	Cl^{-}	SO_4^{2-}
B20-3	0	1	2	0	0	0	1
B20-6	0	1	3	1	0	1	2
B20-9	0	1	3	1	0	1	2
B20-11	0	1	3	1	0	0	2
B21-3	0	0	3	1	0	1	1
B21-6	0	1	2	0	0	0	1
B21-9	0	0	3	1	0	1	1
B21-11	1	1	2	1	0	1	2
B22-3	0	0	3	0	0	0	1
B22-6	0	1	2	1	0	0	1
B22-9	0	1	2	1	0	0	2
B22-11	1	1	3	1	0	1	3

5.2.2 Fluids

Pearson water A3 (Tab. 5.5) that resamples the pore fluid of the sandy facies of Opalinus clay at Mont Terri URL /PEA 98, 03/ /VAN 03/ was used for swelling pressure tests, MiniSandwich experiments, HTV-6 to HTV-9 and hydration of Shaft 1 and Shaft 2. While Pearson water A3 for the laboratory tests was prepared by the involved partners (Tab. F. 2 and Tab. F. 3), the 2000 L of Pearson water A3 for hydration of Shaft1 and Shaft2 were obtained from Louis Tempia SA, Carouge (GE), CH.

Tab. 5.5 Pearson water A3

	[g/mol]	[mmol/L]	[mg/L]	[-]	[g/cm³]	[mS/cm]
Na^+	23	128	2951			
K^+	39.1	0.81	31			
Mg^{2+}	24.3	4.94	120			
Ca^{2+}	40.1	6.94	278			
Sr^{2+}	87.6	0.32	28			
Cl^-	35.45	130	4607			
SO_4^{2-}	96.1	11.47	1102			
HCO_3^-	61	0.60	36			
pH				7.9		
Density					1.007	
Conductivity						19.3

For experiments at laboratory scale solutions of sodium and potassium salts, $CaCl_2$/$SrCl_2$ and $MgCl_2$ (Tab. 5.6) were prepared separately in suitable volumes of deionized water to prevent precipitation. Afterwards the three solutions were combined and deionized water was added to obtain the final volume.

Tab. 5.6 Salts for Pearson water preparation (1 L)

Salt	**M**	**γ**	**c**
	[g/mol]	[g/L]	[mmol/L]
NaCl	58.5	6.13	104.8
Na_2SO_4 *10 H_2O	322 (142 + 180)	3.70	11.5
$NaHCO_3$	84	0.05	0.6
KCl	74.6	0.06	0.8
$CaCl_2$ * 2 H_2O	147 (111+36)	1.02	6.9
$SrCl_2$ * 6 H_2O	266.6 (158.6 + 108)	0.08	0.3
$MgCl_2$ * 6 H_2O	203.3 (95.3 + 108)	1.00	4.9

5.2.3 Gravel and materials for equipotential segments (ES)

Basalt gravel 22/32 mm and 32/63 mm /EMM 19/ was used in the lower and upper abutment of the semi-technical scale experiments (HTV) (chapter 5.5).

Fine sand N45 (Nivelsteiner Sandwerke und Sandsteinbrüche GmbH) with a specific density of 2.65 to 2.66 g/cm³ that consists of 99 % quartz and contains traces of muscovite, kaolinite, plagioclase and rutile /EMM 19/ was used for the ES and as pore

filling in the upper abutment of the HTV to protect the sensor cables. The main particle sizes are 63-90 µm (28 %) and 90-125 µm (62 %) /KÖN 08/. The rising height of this fine sand is about 60 to 70 cm and the water retention curve with a steep slope was determined during the Sandwich-VP /EMM 19/. The proctor density was 1.53 g/cm³ at 13.95 % water content (Fig. 5.4). The permeability at two different dry densities varied between 6.76 and 8.22 *10^{-12} m² (Tab. 5.7) and hydraulic conductivity at 10 °C was about half of the estimated value based on the particle size distribution /EMM19/.

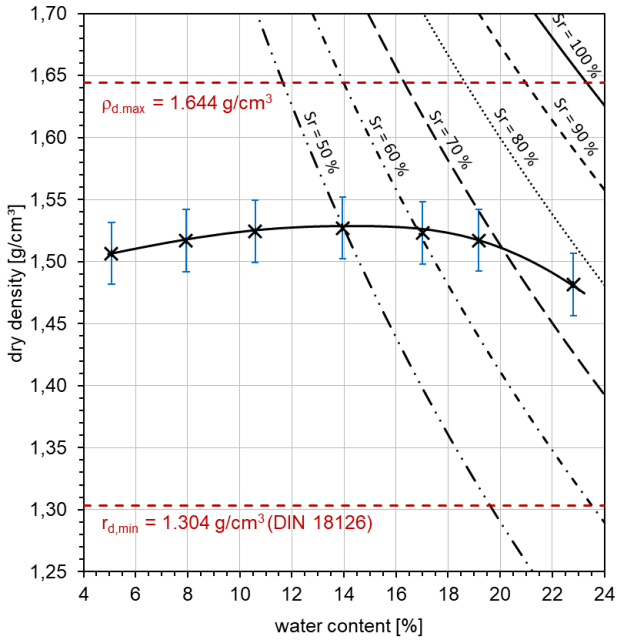

Fig. 5.4 Proctor curve of fine sand N45

Tab. 5.7 Hydraulic conductivity of fine sand N45 installed at water content 11.6 % (105 °C)

ρ_D [g/cm³]	i [-]	T [°C]	k_T [m/s]	k_{10} [m/s]
1.465	3-5	19.5	8.22E-05	6.42E-05
1.599	4-6	17.9	6.76E-05	5.28E-05

5.2.4 Materials for sealing segments (DS)

Raw materials

Tab. 5.8 Bentonite batches of the project

Bentonite	Batch	Weight	Compacted	Pillows	BGM	Experiment
		[t]	[t]	[t]	[t]	
Calcigel	2017	12	10	4	4	HTV-5, HTV-7
Calcigel	2020[#]	24	22	8.5	5.1	Shaft1 installation tests
						HTV-9, Shaft 2
Secursol UHP (G1580, Ruppach)	2018	8	8	2	2	HTV-6
Secursol MHP1 (70/30)*	2021	8	8	2	2	HTV-8
Secursol MHP1 (70/30)*	2022	16.5	16.0	6.1	2.3	HTV-9, Shaft 2

[#] two compaction campaigns (Shaft 1: 2020 and Shaft 2 and HTV-9: 2022) *prepared of the same batch of Secursol UHP (70 %) 2021 but different batches of G1621 (30 %) 2021 and 2022

Calcigel

Calcigel is a powdered product of Bavarian bentonite of Clariant AG. A first batch of about 12 t has been already ordered for the Sandwich-VP /EMM 19/. This batch was used for both HTV-5 and HTV-7 (current project). A new batch of 24 t was ordered for the production of the pillows and the BGM installed in DS of Shaft 1 and 2 as well as in HTV-9 (Tab. 5.8).

Originally, Calcigel was dried by the producer to a moisture of about 10 % (110 °C; water content: 11.1 %) and ground by a hammer mill to a grain size < 500 µm (100 %; 93 % < 125 µm) (Fig. 5.5).

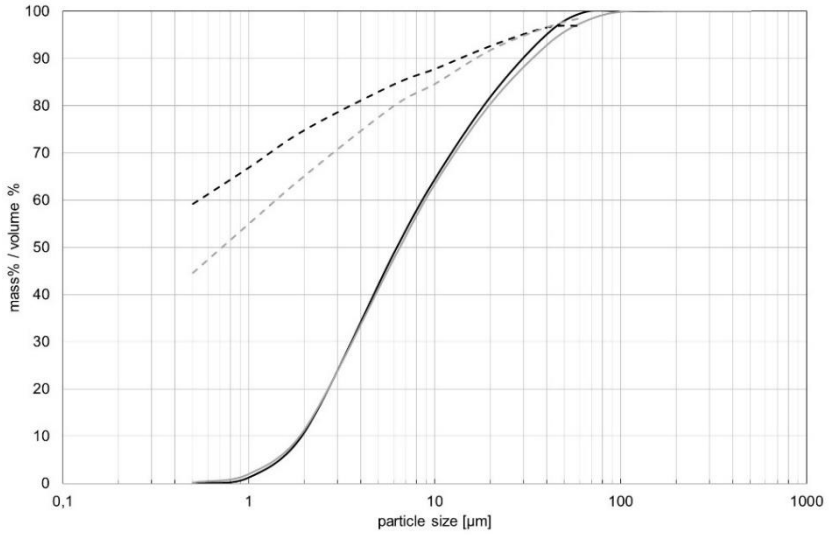

Fig. 5.5 Particle size distribution of Calcigel, dotted lines: Sedigraph (mass%), solid lines: Laser diffraction analysis (volume%), black: batch 2017, grey: batch 2020

The chemical composition of the Calcigel batches corresponded to the phase content of the bentonite (Tab. 5.9, Tab. 5.10).

Tab. 5.9 Chemical composition (normalized to ignited weight), LOI (of air dry sample) and CEC of Calcigel

	2017[a]	**2020[a]**	**2020[b]**	**HTV-7[b]**	**Shaft 1[b]**	**Shaft 2[b]**
	[mass%]					
SiO_2	62.16	62.66	63.24	62.61	63.30	63.29
TiO_2	0.53	0.57	0.56	0.56	0.61	0.58
Al_2O_3	21.40	20.41	20.23	21.25	20.23	20.30
Fe_2O_3	7.51	6.47	6.33	7.34	6.40	6.24
CaO	2.21	3.52	3.50	2.15	3.37	3.34
MgO	3.45	3.71	3.79	3.54	3.70	3.70
K_2O	2.21	2.12	2.06	2.16	2.08	2.10
Na_2O	0.53	0.54	0.30	0.39	0.30	0.44
LOI	8.97	9.57	18.07	13.58	18.54	16.05
	[cmol(+)/kg]					
CEC	73	67	61	68	62	62

a) receiving inspection, b) repeat measurement

The iron and aluminum content decreased slightly from batch 2017 to 2020 while the calcium and magnesium content and thus the carbonate content increased slightly. The increased SiO_2 content resulted from a slightly increased quartz content.

Tab. 5.10 Phase content of Calcigel

	2017		**2020**		**HTV-7**		**Shaft 1**		**Shaft 2**	
	1	2	1	2	1	2	1	2	1	2
	[wt.%]									
Dioctahedral smectite (montmorillonite)	**64**	**61**	**56**	**50**	**65**	**62**	**56**	**50**	**62**	**56**
Dioct. mica/illite	17	19	16	18	17	18	16	18	13	14
Quartz	10	11	14	16	10	11	15	17	14	16
Chlorite	2	2	3	3	2	2	1	2	2	2
Kaolinite	2	2	3	3	3	3	5	5	3	3
Feldspars (Plagioclase)	1	1	2	2	1	1	2	2	2	2
Calcite	1	1	2	2	1	1	2	2	2	2
Dolomite	2	2	3	3	1	1	2	2	2	2
Rutile	1	1	1	1	1	1	1	1	1	1

1) air dry, 2) anhydrous

The specific density was 2.68 g/cm³ after drying at 105 °C and 2.76 g/cm³ after drying at 200 °C determined from BGM of Shaft 1 used in swelling pressure tests (set 1). A measured specific density of 2.66 g/cm³ and a calculated specific density of 2.76 g/cm³ was also reported in /EMM 19/ for the batch 2017.

Securisol UHP and Securisol MHP1 (70/30)

During the Sandwich-VP Securisol UHP, a Ca-bentonite from the Westerwald, was considered an alternative DS material with high content of dioctahedral smectite /EMM 19/. The high smectite content caused swelling pressures too high for application in the MTRL as the lowest main stress at the site of the in-situ experiment is about 3 MPa. Thus, a blended material Securisol MHP1 (70/30) with reduced smectite content was developed (App. C.2). The final blend contains 70 % of Securisol UHP and 30 % of a plastic, non-swellable clay G1621/F1623 (Tab. 5.11).

The main selection criteria for those swelling-pressure-reducing clays are:

- Availability: raw materials were selected whose geological reserves amount to at least several tens of thousands of tons and are available in the long term. The valid general operating plan for the Meudt mine, from which the clays were selected, allows mining activities until 2037. The reserve areas that are to be mined after 2037 are already owned by Stephan Schmidt Gruppe and designated as raw material reserve areas in the state development plan and may not be overplanned, e.g. by commercial, new construction or nature conservation areas.
- Mineralogy: in order to reduce the swelling pressure, raw materials with low proportions of swellable minerals but with sufficiently good plasticity should be selected for shaping. Compared to the CEC of > 80 cmol(+)/kg of Securisol UHP, the selected raw material G1621 had a CEC of max. 20 cmol(+)/kg.
- Sulphur-content (S-content): the content of sulphur-containing minerals, especially sulphides, should be as low as possible. The selected raw materials have S contents of < 40 ppm and are therefore not critical.
- Carbonate content: a low carbonate content is expected from all raw materials used for the DS. This requirement is guaranteed due to the genesis of the Westerwald clays and the geological framework conditions.
- Processability: the raw materials should have a sufficiently high clay content and thus a plasticity that ensures both compaction with Securisol UHP and stability of the pillow. Therefore, sandy clays, so-called lean clays, were to be excluded.

The moisture of the mined Securisol UHP, that overlies the kaolinitic-illitic clays, varies between 25 and 30 % (110 °C; water content: 33 to 43 %). The plastic clay G1621 from the Meudt/Westerwald mine exhibit, due to the position in the mine, a relative low moisture (110 °C: 11.4 and 13.4 mass-%, respectively; water content: 12.9-15.5 mass-%).

The grain size of the plastic clay G1621 is <100 µm and by sedimentation a <2 µm content of about 70 % was found (Fig. 5.6).

Securisol UHP contains tuff relicts after processing prior to compaction that are too large for measurement of particle size distribution by Sedigraph or laser diffraction analysis.

Aggregates of these tuff relicts could be destroyed during dispersion by ultrasonic treatment but does not result in reproduceable results.

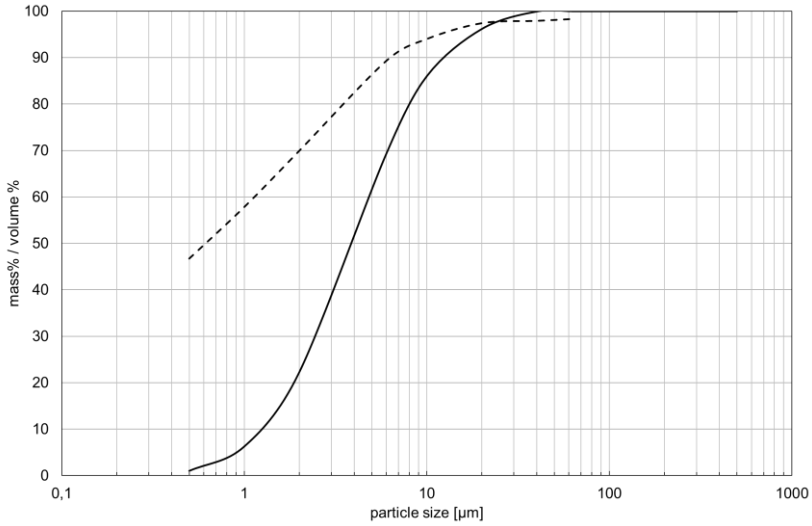

Fig. 5.6 Particle size distribution of plastic clay G1621, dotted lines: Sedigraph (mass%), solid lines: Laser diffraction analysis (volume%)

The specific density of Securso UHP was 2.66 g/cm³ after drying at 105 °C and 2.77 g/cm³ after drying at 200 °C and 2.77 g/cm³ calculated from phase content /EMM 19/.

The specific density of Securso MHP1 (70/30) was 2.70 g/cm³ after drying at 105 °C and 2.79 g/cm³ after drying at 200 °C determined from BGM of HTV-8 used in swelling pressure tests (set 1).

The chemical composition of Securso UHP corresponds to a bentonite containing a high content of dioctahedral smectite (Tab. 5.11, Tab. 5.12). Thereby the iron content is about twice as high as in Calcigel (Tab. 5.9). Reevaluation of the phase content resulted in a slightly lower smectite and slightly higher quartz content compared to /EMM 19/. The main components of the non-swellable clay used for blending Securso UHP mainly consists of kaolinite, illite/mica (di) and quartz (Tab. 5.12). In the second batch of this clay of 2022 the SiO_2 content increased while the Al_2O_3 content decreased.

Tab. 5.11 Chemical composition (normalized to ignited weight), LOI (of air dry material) and CEC of Securso UHP, plastic clay G1623 and Securso MHP1 (70/30) during production and prior to installation (a)

	Securso UHP	**Securso UHP[a]**	**Securso UHP**	**G1621 / F1623**	**G1621 / F1623[a]**	**Securso MHP1 (70/30)**	**Securso MHP1 (70/30)[a]**	**Securso UHP**	**G1621 / F1623**	**Securso MHP1 (70/30)**	**Securso MHP1 (70/30)[a]**
	HTV-6	HTV-6	HTV-8	HTV-8	HTV-8	HTV-8	HTV-8	Shaft 2 / HTV-9	Shaft 2 / HTV-9	Shaft 2 / HTV-9	Shaft 2 / HTV-9
	[Mass%]										
SiO_2	59.98	60.12	60.57	67.23	67.63	63.05	64.00	59.97	73.10	63.31	62.84
TiO_2	2.94	2.95	3.07	1.49	1.49	2.54	2.38	3.04	1.33	2.52	2.52
Al_2O_3	17.37	17.22	16.34	25.37	25.27	19.11	18.05	16.98	19.32	17.73	18.99
Fe_2O_3	12.12	12.28	12.46	1.96	1.87	9.01	9.76	12.50	3.09	9.86	9.05
CaO	2.62	2.63	2.79	0.23	0.16	1.94	1.73	2.60	0.23	1.89	1.99
MgO	3.91	3.92	3.86	0.49	0.50	2.73	2.62	3.78	0.37	2.76	2.94
K_2O	0.85	0.85	0.73	2.95	2.93	1.39	1.35	0.88	2.11	1.28	1.49
Na_2O	0.21	0.01	0.18	0.28	0.16	0.23	0.11	0.25	0.24	0.24	0.18
LOI	10.01	20.69	9.34	6.23	7.67	7.14	17.21	8.20	5.29	7.52	15.04
C	n.d.	n.d.	0.012	< 0.005	n.d.	< 0.005	n.d.	n.d.	0.06	0.08	n.d.
S	n.d.	n.d.	0.076	0.01	n.d.	< 0.005	n.d.	n.d.	< 0.005	< 0.005	n.d.
	[cmol(+)/kg]										
CEC	89	96	100	9	5	73	61	99	n.d.	65	60/67[b]

b) For pillows and bentonite granular material respectively.

Tab. 5.12 Phase content of Securosol UHP, non-plastic clay G1621 and Secursol MHP1 (70/30)

	Secursol UHP		**G1621**	**Secursol MHP1 (70/30)**			
	(HTV-6)			(HTV-8)		(HTV-9, Shaft2)	
	1	2	1	1	2	1	2
	[wt.%]	[wt.%]	[wt.%]	[wt.%]	[wt.%]	[wt.%]	[wt.%]
Smectite (di)	79	75	-	63	58	63	59
Quartz	10	12	28	22	25	19	21
Kaolinite	2	2	48	4	4	5	6
Illite/Mica (di)	3	4	22	5	5	7	8
Feldspars (Plagioclase)	1	2	-	1	1	2	2
Anatase	3	4	-	3	3	3	3
Rutile	-	-	1	-		1	1
Apatite	<1	<1	-	<1	<1	<1	<1
Hematite	<1	<1	<1	1	1	<1	<1
Maghemite	1	1	-	<1	<1	<1	<1

1) air dry (2W)
2) anhydrous (0W)

Processing

Mining

Secursol UHP and the plastic clay G1621/F1623 are extracted by excavator and stored on a pile (Fig. 5.7). The quantities required for the individual project tasks (HTV-8/HTV-9/Shaft 2) were taken from the stockpile and stored in a covered box until further processing (compaction). This procedure had the advantage that no further soaking by rain took place and an initial air drying began.

Fig. 5.7 Open pit Lower Saxony North, Ruppach-Goldhausen

Left: From top to bottom: basalts (grey); alterated tuffs (brown, Securisol UHP), overlying illitic-kaolinitic clays (white).
Right: 30,000 t of mined Securisol UHP

Fig. 5.8 Excavation and transport of plastic clay F1623 in the Meudt mine

Preparation of raw materials for compaction

Calcigel

Calcigel was fed into the briquetting process as delivered without further mechanical pretreatment.

Securisol UHP

As a result of an altered tuff Securisol UHP exhibits relics up to 10 mm in size, that have to be crushed during further processing /EMM 19/. The bentonite, which was extracted at 25 to 30 % moisture (110 °C; water content: 33 43 %), had to undergo two drying processes before compaction. The first drying step to approx. 15 % moisture (110 °C; water content: 17.6 %) is necessary in order to be able to carry out the comminution on the roller mill (< 3.5 mm). After crushing, further drying takes place to the target moisture of approx. 10 % (110 °C; water content: 11.1 %) required for the compaction. This drying process was carried out at a temperature below 100 °C on a drum dryer, which is installed upstream of a vertical roller mill. After drying the Securisol UHP, the raw material is discharged in front of this mill.

Securosol MHP 1 (70/30)

Securosol MHP1 (70/30) was produced of 70 mass% Securosol UHP (G1580) and 30 mass% of the plastic, non-swellable clay (G1621/F1623).

Due to the high initial moisture of approx. 30 %, the bentonite first had to be dried to a moisture of approx. 15 %. Subsequently, the agglomerates were crushed and the dried bentonite was sieved (Fig. 5.8). Due to the high initial fineness of the plastic clay (maximum grain size 100 µm), only a crushing of the coarse clay lumps from the pit after excavating was necessary. After the so-called shredding, the agglomerate size of the plastic clay is below 35 mm (moisture approx. 16 %).

After equalizing the moisture of the bentonite and the plastic clay, both raw materials were mixed in the mass ratio of 70/30 (bentonite/clay). The mixing ratio refers to the dry weights of the raw materials. Thereafter the mixture is dried again to lower the moisture to about 10 % prior to grinding in a rolling mill to < 3 mm.

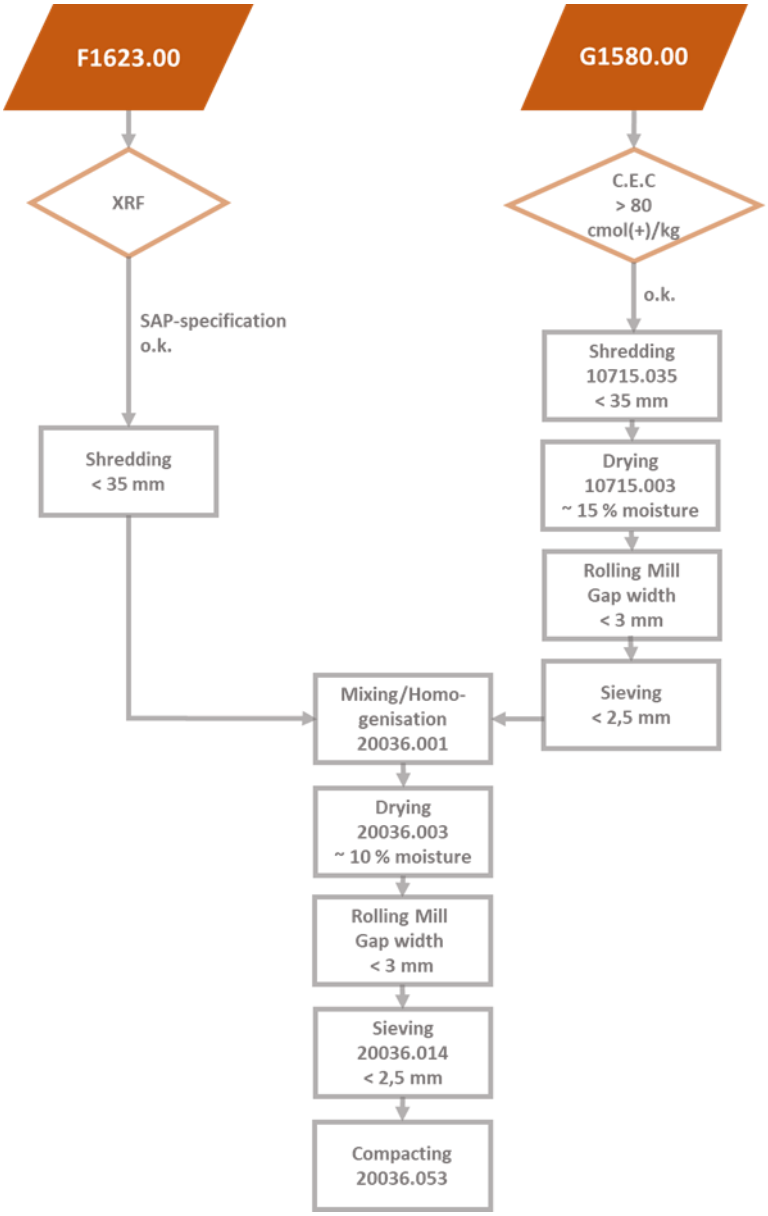

Fig. 5.9 Preparation scheme for the product Securisol MHP 1 (70/30)

XRF: SAP specification for Al_2O_3: 19.5 – 23.5 mass-%. The first five SAP digit numbers describe the type of raw material and blend, the last three SAP digits describe the process steps. 001: homogenized; 003: dried; 014: sieved; 035: sieved; 053: compacted

It turned out that the process settings listed in Fig. 5.9 for the production of the Securisol MHP1 (70/30) still show too large a variation range. While the Securisol MHP1 (70/30) for HTV-8 showed a sufficiently good homogeneity and low coarse grain content, this was not the case for material produced for HTV-9/Shaft 2.

To improve homogeneity and batch size distribution, the pit-moist plastic and sticky clay has to be dried after shredding to a moisture of < 16 % and crushed and screened on a roller mill in the same way as bentonite preparation.

Compaction of pillows

Because the compacting facility at the Hosokawa Technical center (Augsburg), that has been used for producing the pillows for HTV 5 doesn't allow a production on a ton scale, it was decided to compact Calcigel as well as Securisol UHP during the Sandwich-VP and later in the current project at KeiBeton GmbH (Geldern) (Tab. 5.13). The machine setting for compacting took place under the following aspects:

- compactability of the prepared raw material (moisture, grain size distribution)
- availability of the different roller presses
- dimension of pockets (large scale plant or Köppern roller press (Fig. 5.10))
- roller speed, corresponding with pressure time
- pressure

Tab. 5.13 Equipment for compaction of bentonite pillows

Experiment	**Material**	**Machine**	**Dimension of pillows L x W x H [mm]**
HTV 5	Calcigel	Hosokawa CS 25	35 x 35 x 10
HTV 6	Securisol UHP	Large-scale plant, self-built (Köppern principle)	30 x 15 x 10
HTV 7	Calcigel	Large-scale plant, self-built (Köppern principle)	30 x 15 x 10
Shaft 1	Calcigel	Large-scale plant, self-built (Köppern principle)	30 x 15 x 10
HTV 8	Securisol MHP 1 (70/30)	Köppern roller press	25 x 20 x 10
HTV 9/Shaft 2	Securisol MHP 1 (70/30)	Köppern roller press	25 x 20 x 10
HTV 9/Shaft 2	Calcigel	Köppern roller press	25 x 20 x 10

Compaction Secursol UHP

Best results for the compaction of Secursol UHP (HTV-6) were achieved with moisture between 9.5 and 10.5 % (110 °C; water content: 10.5 – 11.7 %), a roller velocity of 0.12 m s^{-1} and a preload pressure of 18 MPa.

Compaction Secursol MHP1 (70/30)

For compaction of Secursol MHP1 (70/30) the Köppern roller press was used.

Fig. 5.10 Large-scale plant (left) and Köppern roller press (right) (KeiBeton/Geldern)

Compaction Calcigel

A first attempt to compact the powdered Calcigel for HTV 7 was in the “as delivered” state (moisture 10.7 %; 110 °C, water content: 12 %). For this purpose, compacted pillows and broken pillows were first circulated for one hour. The idea behind this was to granulate the material similar to a process with a tamping screw at Hosokawa (HTV 5).

It was not possible to form pillows of the Calcigel in the required quantity under the facility conditions at KeiBeton (large scale plant). Pillows could only be produced this way after four passes over the roller press and only with a very low output (approx. 50 kg/h). Therefore, it was decided to carry out the compacting with wetting of the raw material. Therefore, local tap water (Tab. F. 1) was added to improve the compaction process. Pretests were performed by adding the tap water in steps of 4, 6 and 8 % (in the relation to the material “as delivered”). Finally, Calcigel was processed (HTV-7 and Shaft 1) with a moisture (110 °C) between 16.3 and 18.2 % (water content 19.5 and 22.2 %) and the pillows were dried afterwards to a moisture (110 °C) of about 9 % (water content 10 %). Thereby pillows produced for HTV-7 were dried at the drying facility of KeiBeton (Geldern, Germany). It was found, that the direct gas firing was too insensitive, the dryer length was too short and the belt speed couldn’t be reduced any further. Also, capillary cracking could not be avoided, so that the core of the pillows was not dried. The moisture decreased from BB1 to BB3, according to the settings made for temperature and belt speeds at the dryer (App. E.1). The moisture of the pillows remained constant on the way from the production site of SSG (shredding) to Freiberg but decreased on the way to Toledo (Amberg). The moisture of BGM increased, but different between Freiberg (TUBAF) and Toledo (Amberg) (App. E.1).

For the Calcigel pillows produced for Shaft1 air drying was discussed but dismissed because there were insufficient covered areas available for the spreading of approx. 12 t of pillows. Moreover, to avoid destruction, 12 t of pillows would have had to be transferred manually into BigBags. Finally, it was decided to dry the pillows on a gas-fired dryer of SSG at the Ruppach plant at moderate temperatures below 100 °C. The dryer has a longer drying distance than the dryer at KeiBeton and also allows greater flexibility in terms of belt speed. After preliminary tests in the laboratory (App. E.3) and with a test big bag the optimal dryer constellation with a moisture reduction of 6.5 percentage points was found to be at a belt speed of setting 17 % and a dryer temperature of 80 °C.

For the production of Calcigel pillows for HTV-9 and Shaft 2 the large-scale plant was not available and the small Köppern roller press had to be used. With this device it was not possible to add water. Therefore, compacted pillows and broken pillows had to be circulated several times. As a result, pillows with a very high density were obtained, which were comparable to the first tests on the Hosokawa plant (HTV 5). Furthermore, since these pillows were not moistened, they did not have to be dried back (App. E.4).

However, this way of compaction of the Calcigel was by no means economical. The production rate was less than 1 t/d.

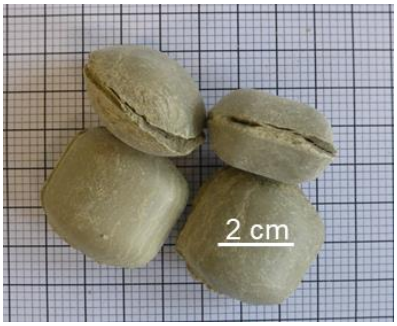

Calcigel, HTV-5
$\rho_{d,105\,°C}$ = 1.98g/cm³

Calcigel, HTV-7
$\rho_{d,105\,°C}$ = 1.91 g/cm³

Calcigel, Shaft 1
$\rho_{d,105\,°C}$ = 1.70* g/cm³

Calcigel, Shaft 2 and HTV-9
$\rho_{d,105\,°C}$ = 2.05 g/cm³

Secursol UHP, HTV-6
$\rho_{d,105\,°C}$ = 1.91g/cm³

Secursol MHP1 (70/30), HTV-8
$\rho_{d,105\,°C}$ = 1.93 g/cm³

Secursol MHP1 (70/30), Shaft 2, HTV-9
$\rho_{d,105\,°C}$ = 1.87g/cm³

Fig. 5.11 Geometry and dry density of bentonite pillows as produced

For dry densities at 200 °C see App. E; dry density of Calcigel BGM for Shaft 1 = 1.93 g/cm³.

Production of bentonite granular material (BGM)

In order for the BGM to ideally fill the pore spaces between the pillows, it is necessary for the pillows to have only a small proportion of fragments. But, during processing and handling of pillows (compacting, transport, drying), fragments are generated and unavoidable. To reduce this proportion of fragments in the pillows, the pillows were initially sieved on a 10 mm sieve after drying. In order to sieve off even more fragments, the sieving for HTV 9/Shaft 2 was carried out using a 15 mm sieve.

These fragments were used to produce the BGM. The main part of the BGM consists of the fragments of the pillows. If the quantity of fragments was not sufficient for the total BGM quantity required, intact pillows, which had always been produced in sufficient quantity, were crushed for the difference. This ensured that pre-compacted material was available as BGM.

Fragments and pillows were crushed by a rolling mill type 865 (Händle) to < 2 mm to test the pourability. To ensure a high packing density of pillows together with BGM as pore fillers (binary mixture) different sub-fractions of the fraction < 2 mm have been tested on a laboratory scale. The best result was achieved with the fraction 0 – 1.4 and 0 – 0.12 mm depending on the pillow geometry. Finally, the pre-crushed fraction 0 – 2 mm was sieved with a Mogensensizer on a production scale to the target fraction range (0). The particle size distribution of the BGM was adjusted to about a Fuller distribution with an exponent between 0.5 and 0.8 (Fig. 5.12).

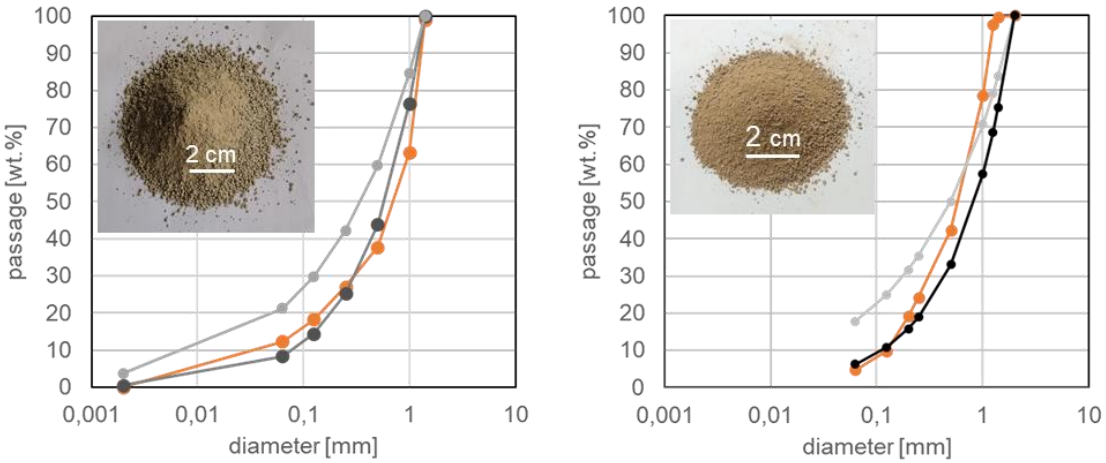

Fig. 5.12 Particle size distribution (sieved, orange curve) of BGM (left: Calcigel, Shaft1; right: Securosol MHP1(70/30), HTV-8) with Fuller curves (grey: exponent 0.5 and black: exponent 0.8)

Packing, storage and delivery

Bentonite moisture/water content equilibrates corresponding to the surrounding relative humidity and temperature. For the Ca-bentonite Calcigel, the equilibrium moisture under standard conditions (20 °C, 50-60 % RH) is about 10 % /EMM 19/. At Mont Terri rock laboratory temperature is about 14.5-15.0 °C and the relative humidity is about 80 to 90 % between May and November and 65-80 % between December and April each year. Without protection, the equilibrium moisture of the dried Calcigel products, which is too high for the experimental set-up, would develop very quickly (Fig. 5.13).

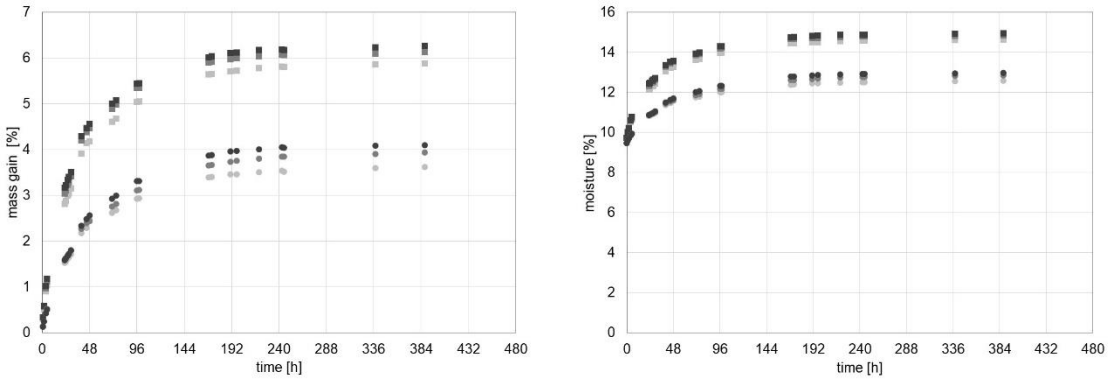

Fig. 5.13 Mass gain (left) and moisture (right) of Calcigel pillows (squares) and Calcigel BGM (circles) with starting moisture of 9.73 % and 9.49 %, respectively, during storage at 85 % RH and 20 °C) (App. B.14)

On this basis, measures were taken in production, for storage and for transport in order to check the development of moisture and to guarantee the target moisture along the process chain. Therefore, each big bag was sampled at the place of compaction to obtain the moisture distribution (App. B.9). The moisture determined on-site during compaction did not deviate significantly from moisture determined in the laboratory subsequently after arrival (App. D).

The Calcigel pillows and BGM were stored in the processing plant of SSG. Regularly taken samples showed that the moisture was constant between 10.3 and 10.8 % (110 °C).

All BigBags (pillows and BGM) were specially packed. A cardboard covered by a plastic film was placed at the pallet below the big bags as a diffusion barrier. These packages were then covered with a plastic shrink bonnet.

5.3 Water retention and Swelling pressure tests

5.3.1 Water retention behavior

BGM of Securosol UHP and of Securosol MHP1 (70/30) as used in HTV-8. The bentonites have a high water retention capacity due to the smectite content. The shape of the WRC reflected the existence of adsorption processes typical of clays, with water contents being relatively high even for high suction pressures /EMM 2019/. The WRCs in terms of degree of saturation were fitted to the van Genuchten expression /VAN 80/ with parameters given in Tab. 5.14. The nominal dry density of 1.55 g/cm³ could be achieved by ± 0.02 g/cm³ (E.6). As well, depending on the sensor used to measure suction, psychrometer or capacitive sensor, the accuracy of the measurement was different. The degree of saturation was computed from the actual water content, dry density and a specific density of 2.86 and 2.84 g/cm³, respectively. With these specific densities a slight overestimation of the saturation was observed. As expected, the Securosol UHP bentonite had higher water retention capacity in the whole suction range than the Securosol MHP 70/30, which contains 30 % of a non-swelling clay. Calcigel had a slightly lower water retention capacity for the suctions higher than 10 MPa and higher for the lower suctions than Securosol UHP.

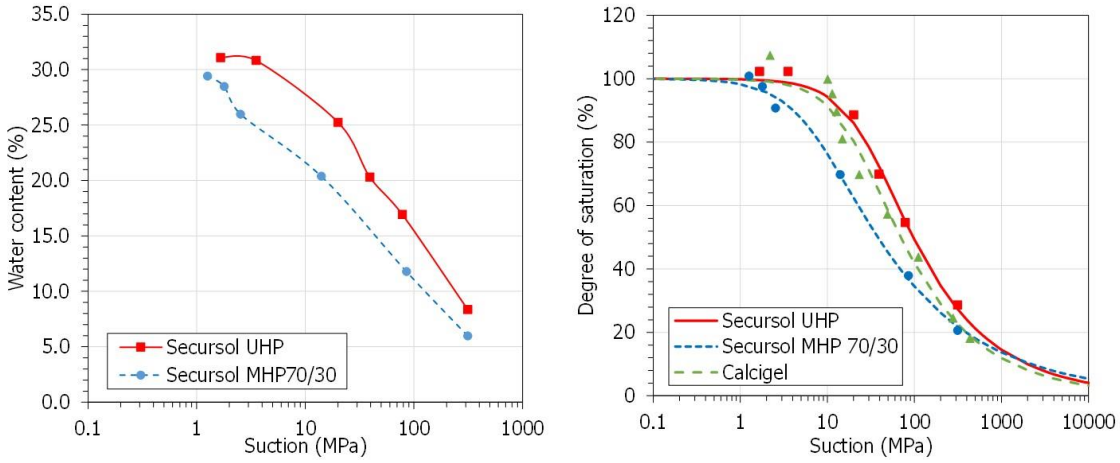

Fig. 5.14 Water retention curves (left) and fitting of the water retention curves to the van Genuchten expression (right) (Calcigel values taken from /GUT 18/ in /EMM19/); water content determined at 110 °C

Tab. 5.14 Fitting parameters of the water retention curves (Calcigel values taken from /GUT 18/ in /EMM19/)

Reference	Securisol UHP	Securisol MHP1 (70/30)	Calcigel
P (MPa)	30.4	7.3	22.4
λ	0.355	0.287	0.359

5.3.2 Calcigel

Porosity, initial saturation and gas permeability

A first set of swelling pressure test was performed with Calcigel at 11.7 % water content (105 °C) installed with dry densities between 1.40 and 1.75 g/cm³ (105 °C) and hydration by Pearson water A3. The resulting porosity ranged from 0.35 to 0.48 (105 °C) and the initial saturation was 0.34 to 0.58 (105 °C) (Fig. 5.15).

In addition, swelling pressure tests were carried out with the same material at an increased water content of 16.9 % (105 °C) to study the influence of an increased water content due to equilibration during transport and storage prior to in-situ installation. The tests were carried out for installation densities of 1.45 to 1.60 g/cm³ on only one sample each. Thereby, the porosity ranged from 0.46 to 0.40 and the initial saturation varied between 0.534 and 0.675.

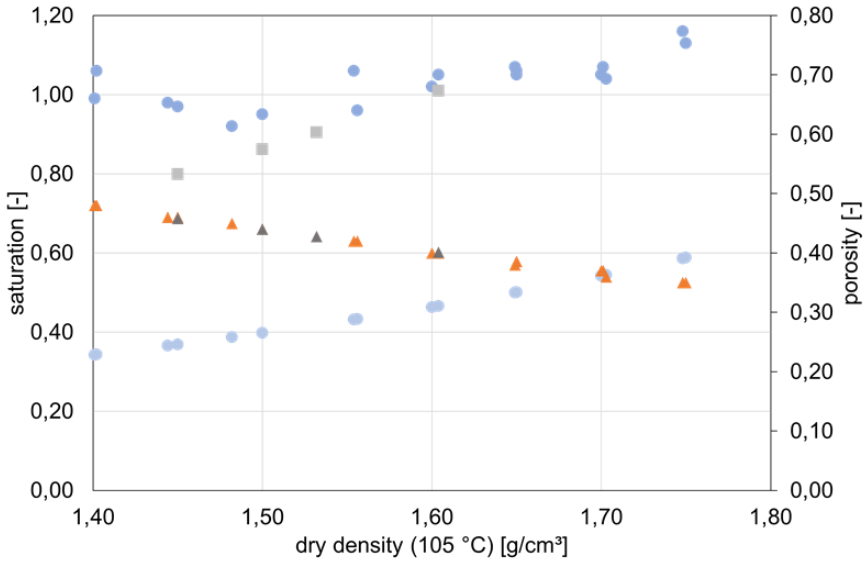

Fig. 5.15 Saturation (light blue circles: initial, dark blue circles: final) and total porosity (orange triangle) of Calcigel installed at 11.7 % water content and 16.9 % water content (105 °C) (grey symbols)

The effective gas permeability of the Calcigel samples installed with different dry densities for swelling pressure measurements was in the range of 1.7E-14 m² to 7.2E-12 m² (Fig. 5.16).

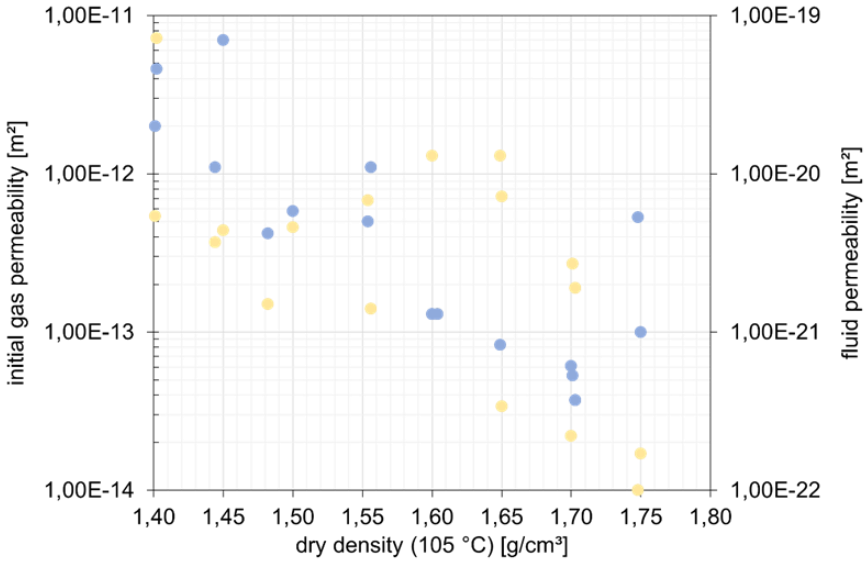

Fig. 5.16 Initial effective gas permeability (yellow) and fluid permeability (blue) after saturation with Pearson water A3 of Calcigel installed at 11.7 % water content depending on the installation dry density

A second set of swelling pressure tests of Calcigel was performed with deionized water and Pearson water A3, too.

Calcigel was installed with a water content of 12.06 and 12.16 % (105 °C), respectively. The dry densities during installation varied between 1.35 and 1.75 g/cm³. The corresponding porosity was 0.51 to 0.37 with an initial saturation between 0.32 and 0.58 (Fig. 5.17).

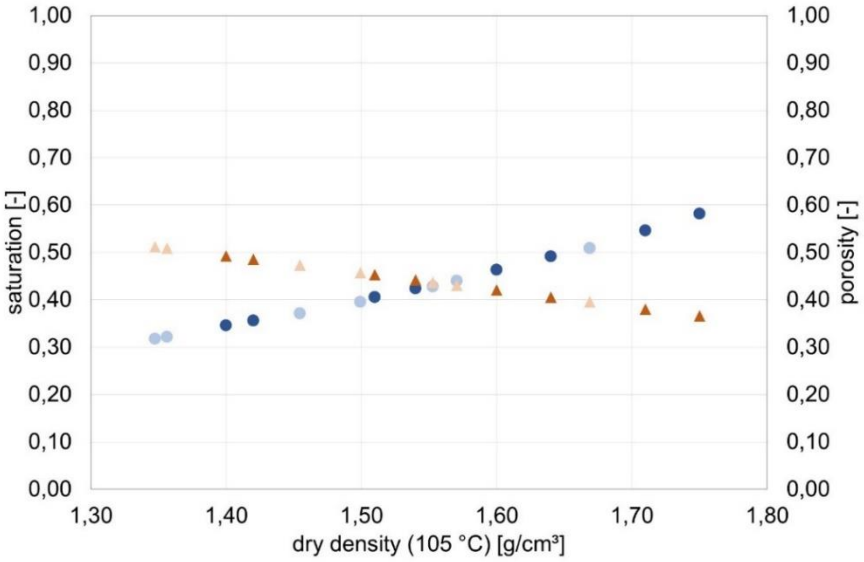

Fig. 5.17 Initial saturation (blue circles: initial) and porosity (orange triangle) of Calcigel installed at 12.06 (light symbols) and 12.16 % water content (105 °C) (dark symbols)

Swelling pressure, fluid uptake, liquid permeability and gas entry pressure

The swelling pressure of Calcigel increased with increasing dry density varied between 0.38 and 5.07 MPa (Fig. 5.18) for the material installed at 11.7 % water content. In the dry density range of 1.45 to 1.60 g/cm³ the swelling pressure of Calcigel installed with 11.7 % varied between 0.87 and 2.62 MPa and installed with a water content of 16.9 % (105 °C) it varied between 0.89 and 2.11 MPa (Fig. 5.19). As Calcigel was at the 2 W hydration state for both water contents the decrease of the final swelling pressure in the samples installed with the increased water content was marginal.

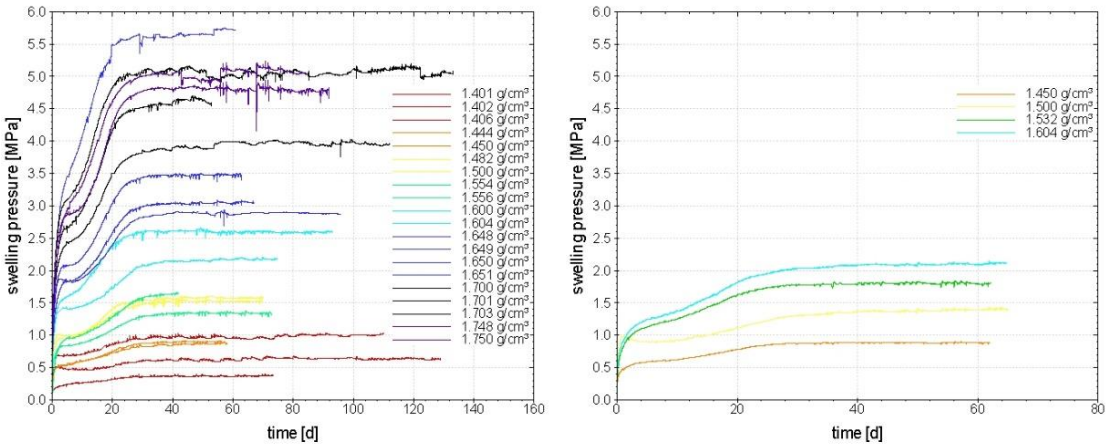

Fig. 5.18 Swelling pressure development of Calcigel installed at water content (105 °C) of 11.7 % (left) and 16.9 % (right)

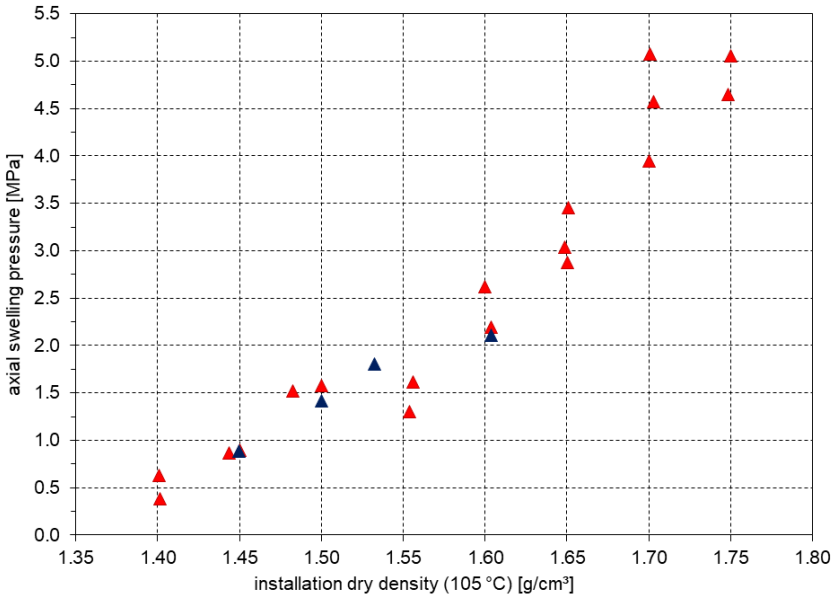

Fig. 5.19 Swelling pressure of Calcigel installed in 2W hydration state at water contents of 11.6 % (red triangle) and 16.9 % (blue triangle) and saturated with Pearson water A3

For all samples an almost constant mass was reached at the end of the experiment (Fig. 5.20). This indicates a maximum liquid saturation in the pore space and the formation of the final swelling pressure is assumed. For the lower installation densities an extended period of time seems to be required until a constant mass was achieved. This result is somewhat unexpected due to the higher initial permeability of the samples at lower installation dry density. It is assumed that this effect is due to lower capillary pressures,

higher residual gas saturation and reduced effective liquid permeability in the initial phase. At the same time, the samples with the lower installation densities show the largest increase in mass. This is due to the high porosities and has an influence on the time required to reach the maximum liquid mass.

The sometimes unsteady curves of the mass-uptake for individual samples are due to experimental boundary conditions. The mass increase until the end of the swelling pressure test characterizes the maximum liquid uptake of the sample over the duration of the test. The estimated saturation > 0.9 shows a high degree of saturation of the pore space for all samples. A maximum saturation >1 was determined for some samples with an installation density >1.55 g/cm³ (105 °C) (Fig. 5.20). Possible reasons for determining a saturation >1 are the uncertainties from the weighing of the pressure cells and the small mass differences due to the fluid uptake. Small deviations in the installation dry density lead to the determination of excessive saturation. In addition, it cannot be prevented that an uncertainty of weighing and mass differences caused by liquid content in connected pipe ends. These cannot be reliably assessed according to the filled volume or mass.

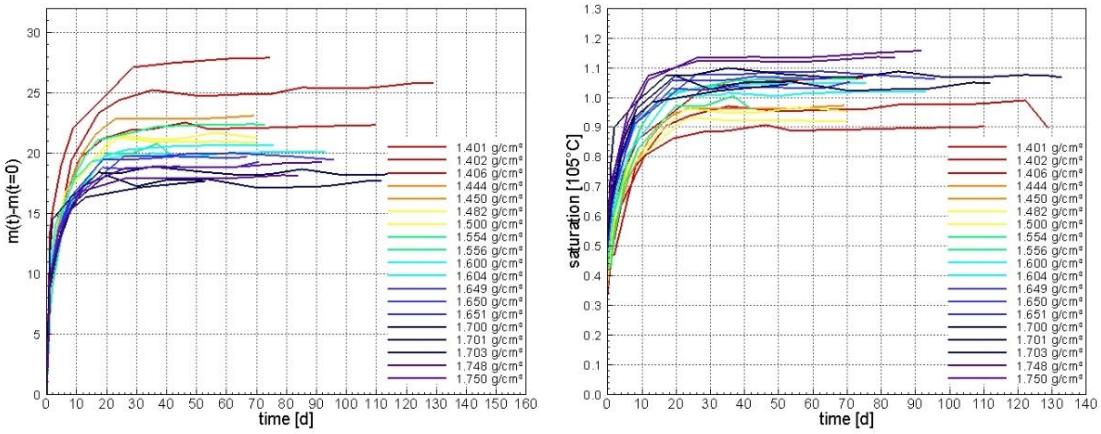

Fig. 5.20 Fluid uptake by mass change (left) and saturation (right) of Calcigel installed with water content 11.7 % (105 °C) and saturated with Pearson water A3

The same liquid used for the swelling pressure tests was used for the permeability test. When measuring liquid permeability, the solution pressure for each test is chosen with a constant pressure differential to the swelling pressure of the sample. The difference between the swelling pressure achieved and the liquid pressure should be at least 0.5 MPa. Flow around the sample can thereby be avoided.

The calculated liquid permeability of Calcigel varied between 3.7 E-22 m² and 7.0 E-20 m², depending on the dry installation density (105 °C). As expected, permeability decreases with increasing built-in dry density (Fig. 5.16).

If there are reproducible pressure curves, the gas entry pressure was determined at the same sample. The gas entry pressures ranged from 0.005 MPa to 0.066 MPa (Fig. 5.21). A dependency on the swelling pressure or the determined liquid permeability cannot be derived from the tests carried out.

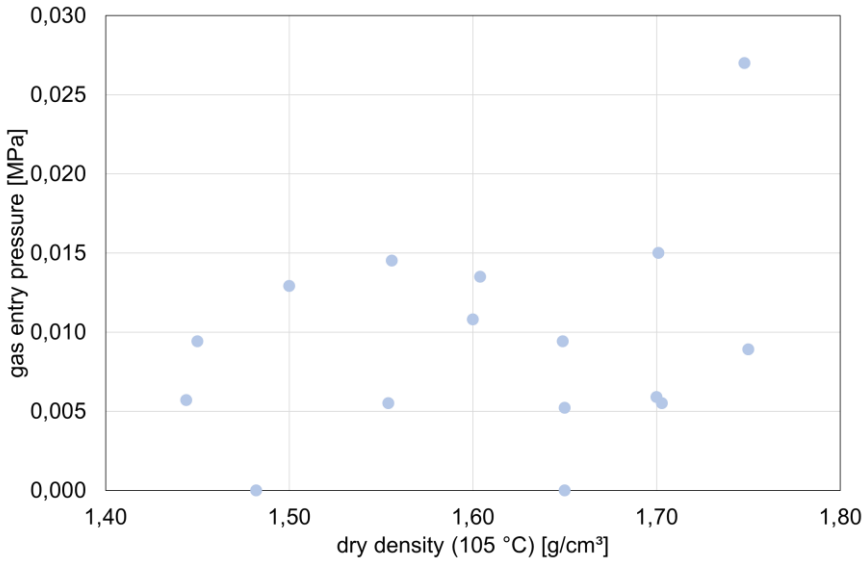

Fig. 5.21 Gas entry pressure after swelling pressure tests of Calcigel installed with water content 11.7 % (105 °C) and saturated with Pearson water A3

A second set of swelling pressure tests with Calcigel and Pearson water A3 at dry densities of 1.51 and 1.64 g/cm³ (105 °C) and 1.49 and 1.63 g/cm³ (200 °C), respectively, corresponding EMDD of 1.16 and 1.29 g/cm³ (200 °C) resulted in swelling pressures between 1.04 and 3.60 MPa (Fig. 5.23). These swelling pressures were slightly higher than swelling pressures measured under the inflow of deionized water.

During the third set of swelling pressure measurements a nearly constant swelling pressure was obtained after about 16 to 20 d with deionized water at 0.7 to 3.4 MPa (Fig. 5.22 left) and with Pearson water A3 after 15 d at 0.8 to 6.8 MPa (Fig. 5.22 right).

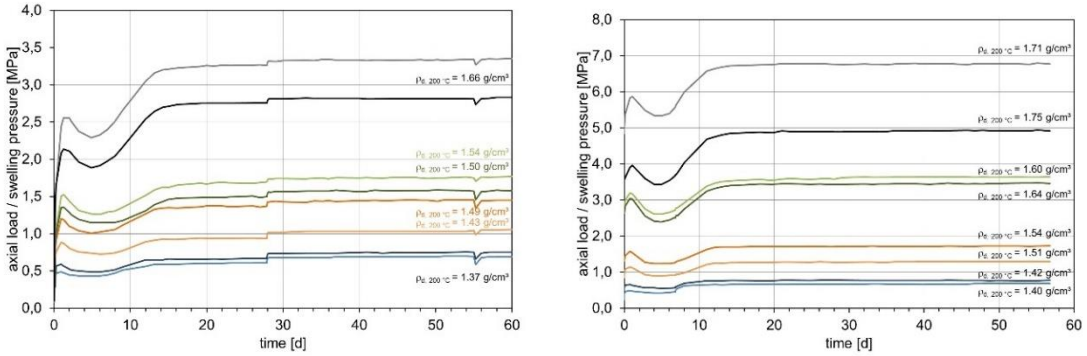

Fig. 5.22 Swelling pressure development of Calcigel installed at 12.06 % (200 °C) water content (left) hydrated with deionized water and 12.16 % (200 °C) water content (right) and hydrated with Pearson water A3

An increased swelling pressure was obtained at installation dry densities larger than 1.50-1.55 g/cm³ (200 °C) with Pearson water A3 compared to deionized water (Fig. 5.23).

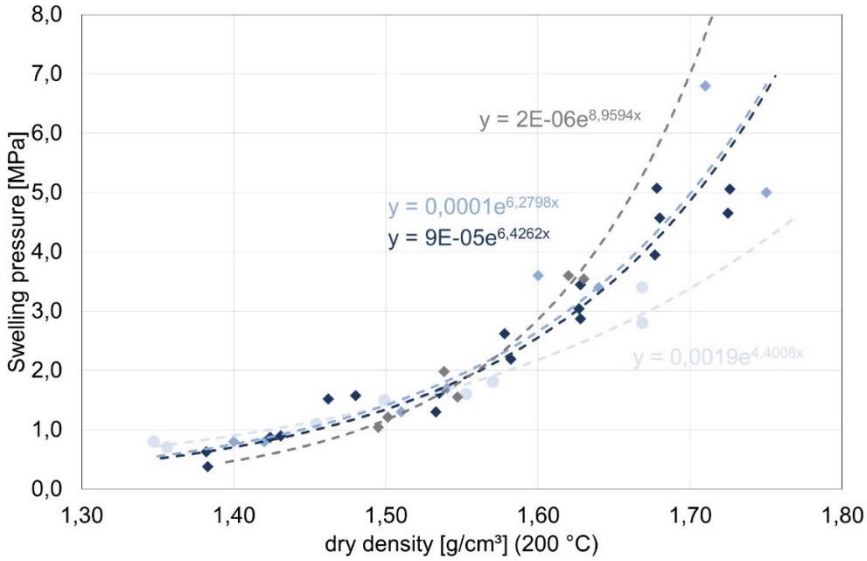

Fig. 5.23 Swelling pressure of Calcigel installed in 2W state (air-dry, water content 12.06 to 13.19 %, 200 °C) light blue circles (set3): saturated with deionized water, diamonds: saturated with Pearson water A3 (dark blue, set1; grey, set2; light blue, set3)

5.3.3 Securosol MHP1 (70/30)

Porosity, initial saturation and gas permeability

Swelling pressure tests were performed with Securosol MHP1 (70/30) at 11.1 % water content (105 °C) installed with dry densities between 1.40 and 1.65 g/cm³ (105 °C) and hydration by Pearson water A3. The resulting porosity ranged from 0.39 to 0.47 with decreasing installation dry density (105 °C) and the initial saturation was 0.345 to 0.474 (105 °C) (Fig. 5.24).

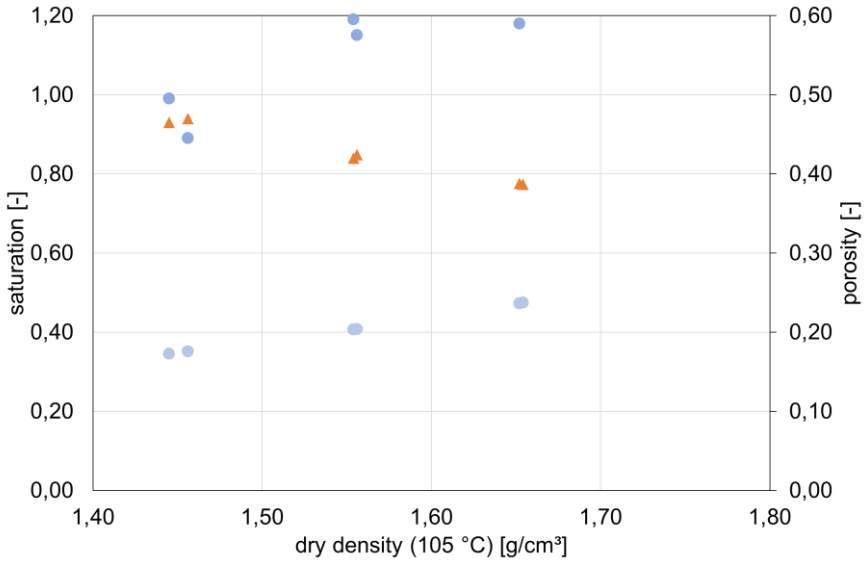

Fig. 5.24 Saturation (light blue circles: initial, dark blue circles: final) and total porosity (orange triangle) of Securosol MHP 1 (70/30) installed at 11.1 % water content (105 °C)

The effective gas permeability of the Securosol MHP1 (70/30) samples installed with different dry densities for swelling pressure measurements was in the range of 1.39E-14 m² to 1.8E-12 m² (Fig. 5.25).

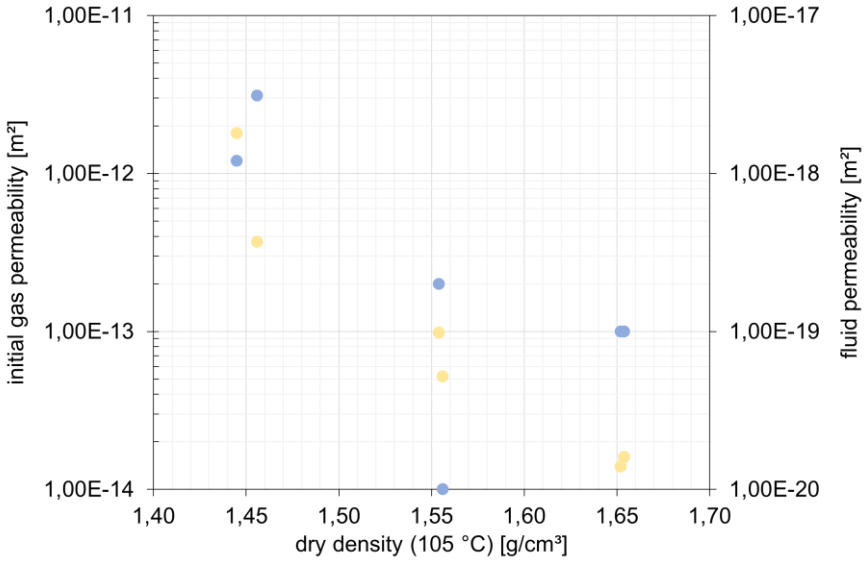

Fig. 5.25 Initial effective gas permeability and fluid permeability after saturation with Pearson water A3 of Sursol MHP1 (70/30) installed at 11.1 % water content depending on the installation dry density

Swelling pressure, fluid uptake, liquid permeability and gas entry pressure

The swelling pressure varied between 0.60 and 3.79 MPa (Fig. 5.26). For almost all samples there is a mass constancy was reached at the end of the experiment (Fig. 5.27). This indicates a maximum liquid saturation in the pore space. It is assumed that the swelling pressure has reached the final maximum level. At the lower installation densities, a shorter time span is required before a constant mass is reached (Fig. 5.27).

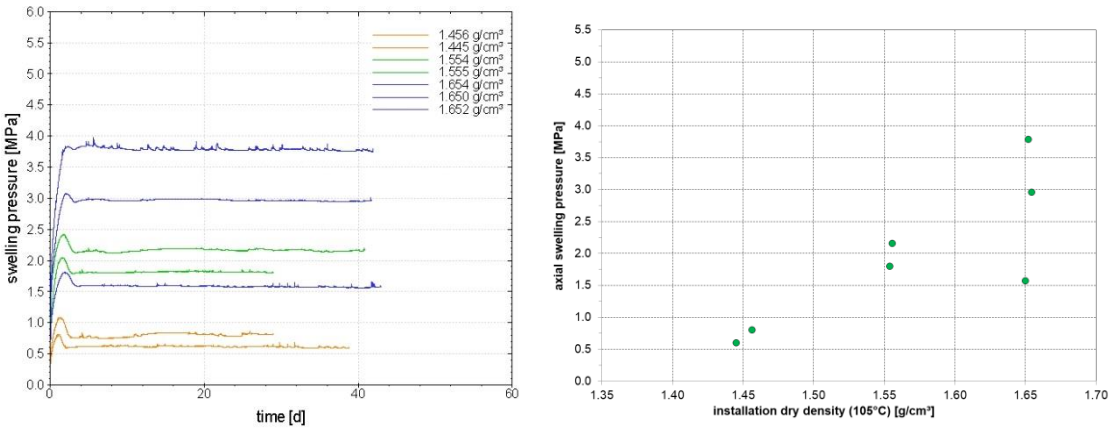

Fig. 5.26 Swelling pressure development and final swelling pressure of Sursol MHP 1 (70/30) installed at 11.1 % water content (105 °C) and hydrated with Pearson water A3

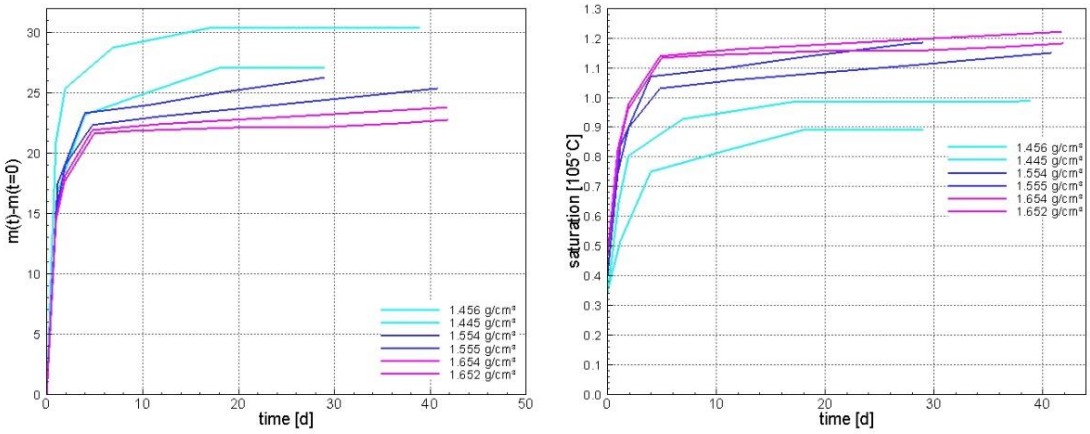

Fig. 5.27 Fluid uptake by mass change (left) and saturation (right) of Securisol MHP1 (70/30) installed with water content 11.7 % (105 °C) and saturated with Pearson water A3

This result is plausible due to the higher initial permeability of the samples at lower installation dry density. At the same time, the samples with the lower installation densities show the greatest increase in mass. This could already be seen in the Calcigel test. The curves of the mass uptake of individual samples, some of which are still slightly rising, are due to experimental boundary conditions. The experiments were nevertheless ended because the swelling pressure reached a constant value. The increase in mass up to the end of the swelling pressure test characterizes the maximum liquid absorption of the sample over the duration of the test. The estimated saturation > 0.9 indicates a high degree of saturation of the pore space for all samples. A maximum saturation > 1 was determined for some samples (Fig. 5.24). Possible reasons for determining a saturation > 1 are the uncertainties mentioned above.

Liquid permeability was determined with Pearson water A3 and a solution pressure about 0.5 MPa lower than the detected swelling pressure of the saturated sample. The calculated liquid permeability of Securisol MHP1 (70/30) varied between 1.0E-20 m² and 3.1E-18 m², depending on the dry installation density (105 °C) and decreased as the installation dry density increased (Fig. 5.25).

If there are reproducible pressure curves, the gas entry pressure was determined at the same sample. The gas entry pressures ranged from 0.006 MPa to 0.028 MPa (Fig. 5.28). A dependency on the swelling pressure or the determined liquid permeability cannot be derived from the tests carried out.

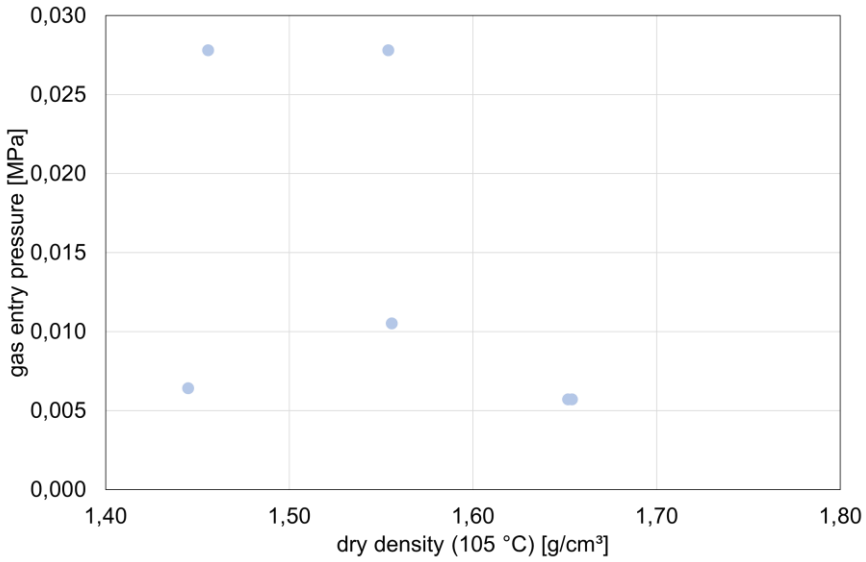

Fig. 5.28 Gas entry pressure after swelling pressure tests of Securisol MHP1 (70/30) installed with water content 11.1 % (105 °C) and saturated with Pearson water A3

5.3.4 Securisol UHP

Porosity, initial saturation and gas permeability

Compaction of Securisol UHP installed at a water content of 11.7 % (105 °C) and 15.1 % (200 °C), respectively, to dry densities between 1.31 and 1.84 g/cm³ (105 °C) or between1.27 and 1.78 g/cm³ resulted in porosities of 0.51 to 0.31 (105 °C) or 0.54 to 0.36 (200 °C) and initial saturations between 0.31 and 0.71 (105 °C) or 0.35 and 0.75 (200 °C) /EMM19/.

An effective gas permeability of $1.4*10^{-15}$ m² to $3.7*10^{-12}$ m² for the different installation densities was observed /EMM19/.

Swelling pressure and liquid permeability

The swelling pressure of Securisol UHP installed at water content (105 °C) of about 11.7 % increased from 1.47 to 17.52 MPa for tap water (Freiberg/Saxony) with increasing dry density from 1.31 to 1.84 g/cm³ (105 °C) and from 1.92 to 11.02 MPa for Pearson water with increasing dry density from 1.31 to 1.67 g/cm³ (105 °C) /EMM19/.

The liquid permeability of Securisol UHP for tap water varied between $3.3*10^{-19}$ and $2.5*10^{-17}$ m² (N = 3) and the permeability for Pearson water varied between $1.9*10^{-19}$ and $2.5*10^{-16}$ m² (N = 5) as a function of dry density at the installation water content (105 °C) of about 11.7 % /EMM19/.

5.4 MiniSandwich Experiments

Numerical evaluation of the HTV experiments and of the large-scale in-situ tests requires a sufficient understanding of the underlying material processes, e.g. swelling and the corresponding permeability decrease associated with geochemical changes, as well as validated material parameters. For this purpose, the MiniSandwich experiments were realized.

5.4.1 Experimental protocol

Modified oedometer cells with a sample diameter of 90 mm and a sample volume of about 800 cm³ (see /EMM 19/) are installed in hydraulic load frames where the axial strain during swelling of the specific bentonite material is measured by three gauges (displaced by 120°). During the test the axial strain is regularly reset to zero by increasing the axial load ensuring quasi-constant volume conditions.

Prior to hydration gas accessible porosity and gas permeability were determined. For the gas accessible porosity, a porosimeter was used according to the principle of the Boyle-Mariotte-law with $p_1*v_1 = p_2*v_2$. For that a defined gas volume (storage) is pressurized transferred into the MiniSandwich and with the pressure change the gas accessible porosity could be measured. For the determination of the gas permeability the inflow pressure, the fluid volume and the geometry of the sample were estimated and after the law of Darcy the gas permeability was calculated.

During saturation the gas outflow and the fluid volume balance (in- and outflow, i.e., the fluid uptake capacity) is monitored and the stationary fluid permeability could be calculated. For the measurement of gas outflow a Hoffman's apparatus for electrolysis is used. One of the columns was filled with water and the escaping gas displaced the water and was measured. Cation and anion concentration are measured in the fluid at the outflow if sufficient volume could be collected. Duration of the MiniSandwich experiments was several months up to few years (Tab. 5.15). Some experiments have

been started during the Sandwich-VP and terminated during the current reported project phase. Other experiments started during the current project phase and will be running for another few months.

Tab. 5.15 Overview of MiniSandwich experiments

	Series 3	**Series 5**	**Series 6**	**Series 7**
Tests	5 & 6	9 & 10	11 & 12	13 & 14
DS material	Calcigel	Tempered Securisol UHP	Calcigel	Calcigel
ES material	N45	N45	N45	N45
Fluid	4 M NaCl	Pearson water	Pearson water	Pearson water
Fluid pressure	0.1/0.3 MPa#	0.3 MPa	0.3 MPa	0.3 MPa
Δ h	-	-	5 %	-
Duration	1786 d	685 d	882 d	>900 d *
Break through	489 d /230 d	14 d/ 14 d	no	348 d/ 469 d

*) still running
#) Applied for 606 d and 1175 d, respectively.

The specimens are prepared of three equipotential segments (ES) of sand (N45, 15 mm per layer) and two sandwiched sealing segments (DS) of bentonite (height of a single DS about 40 mm). The bentonite was pre-conditioned to obtain a different hydration state prior to hydration. The bentonite was either installed in air dry state (stored at ambient conditions) or after drying over concentrated H_2SO_4 (95.0 %, rh = 3.2 % at 23 °C) for several months (Tab. 5.16). After installation of the MiniSandwich the gas accessible porosity and the initial gas permeability were determined. Thereafter saturation with artificial pore fluids was started and the development of the swelling pressure and the hydraulic permeability were observed. After stationary flow conditions are obtained the material was dismantled and analyzed regarding its chemical/mineralogical changes.

Tab. 5.16 Setup and main HM parameters of MiniSandwich experiments

Test		5	6	9	10	11	12	13	14
DS material									
Hydration state		1W	2W	1W	2W	1W	2W	1W	2W
w (105 °C)	[%]	2.1	8.8	1.4	9.6	1.3	9.6	1.2	10.4
w (200 °C)	[%]	3.7	10.2	3.1	12.9	2.9	11.2	2.6	11.9
ρ_d (200 °C)	[g/cm³]	1.55	1.55	1.31	1.29	1.58	1.56	1.40	1.37
ρ_{EMD} (200 °C)									
ES material		1.56	1.56	1.56	1.56	1.56	1.56	1.56	1.56
w (105 °C)	[%]	<0.1	<0.1	<0.1	<0.1	<0.1	<0.1	<0.1	<0.1
Total porosity	[-]								
Gas accessible porosity	[%]	60.5	39.4	66.8	46.5	39.3	31.7	44.0	36.8
Gas permeability	[10^{-13} m²]	0.67	0.47	86	56	93	76	3.7	1.1
Pore volume	[ml]	310	260	380	315	321	261	350	297
Initial saturation (200 °C)	[-]								
Swelling pressure	[MPa]	1.5	0.7	0.7	0.6	1.0	0.5	1.1	0.6
Fluid uptake at breakthrough	[ml]	277	245	354	309	-	-	327	301
Fluid uptake	[ml]	380	292	154	200	370	350	358	318
Fluid trough flow	[ml]	283	1183	4332	2955	0	0	64*	76*
Final flow rate	[10^{-6} ml/h]	6.06	10.1	34.1	46.0	27.5	2.84	1.92	2.62
Fluid permeability	[10^{-18} m²]	4.4	11	21	28	12	0.97	1.2	1.4

*) still running

5.4.2 Results (HM)

Series 3

The tests ran over five years as long-term tests and fluid at the outflow was collected regularly for analysis. Under the inflow of a 4M NaCl brine (p_{inflow} = 1 bar) a constant swelling pressure for the Calcigel installed in 1W state of 1.5 MPa (test 5) and for Calcigel installed in 2 W state of 0.7 MPa (test 6) was observed within a short period of time after 100 d. The breakthrough in test 5 was significantly delayed and occurred after 607 d

while the breakthrough in test 6 occurred after 180 d. After the breakthrough a permeability of 4.4 * 10^{-18} m² (test 5) and 1.1 * 10^{-17} m² (test 6) was observed (Tab. 5.16, Fig. 5.29).

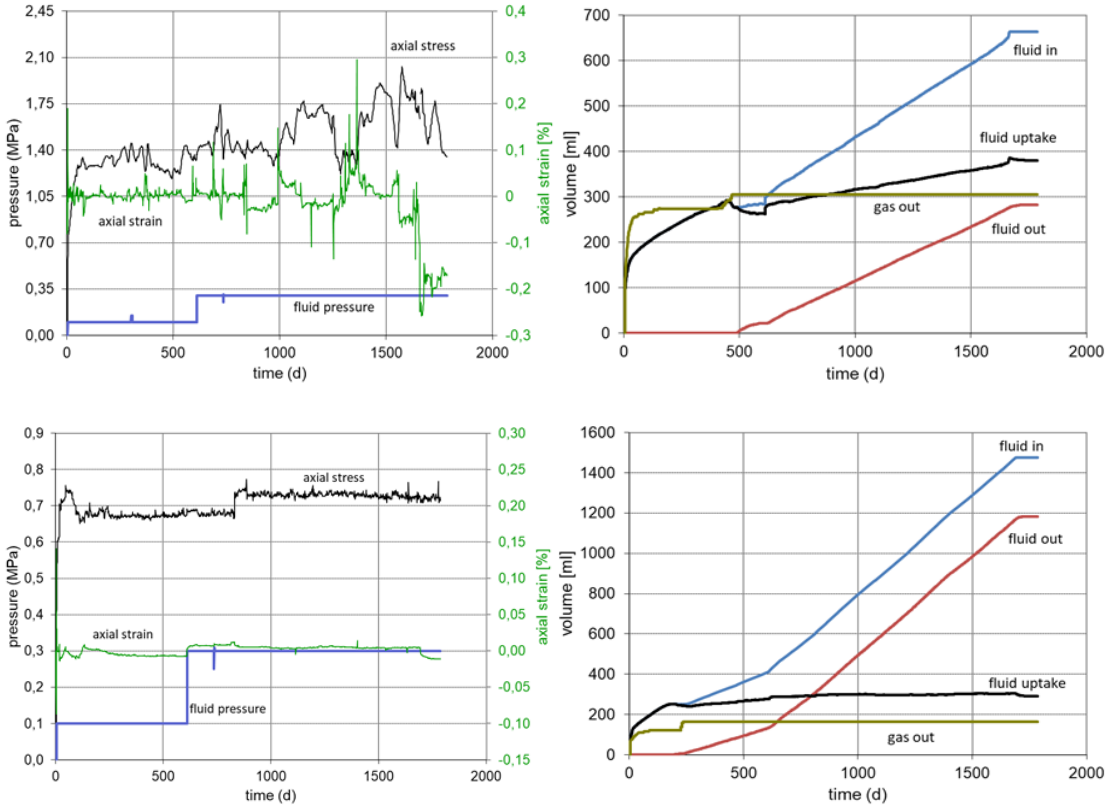

Fig. 5.29 HM behavior of MiniSandwich series 3 (top: test 5, bottom: test 6)

Shortly before the breakthrough a phase of brine inflow stagnation occurred, until a more or less simultaneous fluid and gas outflow happened. This may indicate air buffer effects inside the partially saturated Calcigel. After the breakthrough in test 5 the fluid pressure was increased for both test 5 & 6 from 0.1 to 0.3 MPa. This resulted in a significant flow rate increase. Both tests are finished after nearly 1800 d (around 5 y) and the material was dismantled for mineralogical analysis. The water content after dismantling was close to saturation in ES1 and both DS but lower in ES3 and very low in ES2 of both experiments (Fig. 5.30).

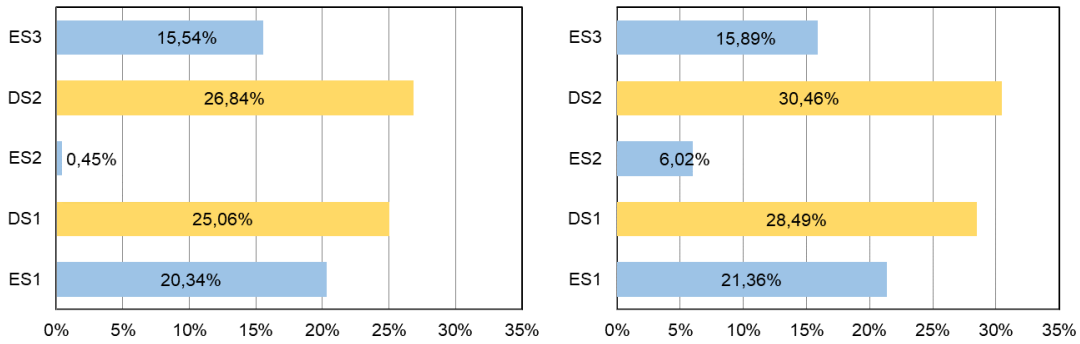

Fig. 5.30 Water content (105 °C) after dismantling of MiniSandwich series 3 (right: test 5, left: test 6)

Series 5

The test conditions of series 5 are qualitatively equal to the test series 4 (Sandwich-VP, /EMM 19/). The Securisol UHP was tempered with N45 to lower the smectite content. Under the inflow of Pearson water at 3 bar the breakthrough occurred after 14 d and the average flow rate in both tests was about 50 ml/week (7.143 ml/d). A constant swelling pressure of 0.7 MPa (test 9, DS in 1W) and of 0.6 MPa (test 10, DS in 2W) was observed. For both tests the stationary fluid permeability at the end of the experiments was in the order of $2.1 * 10^{-17}$ to $2.8 * 10^{-17}$ m² (Tab. 5.16, Fig. 5.31). More detailed information about series 5 are provided in /EMM 21/. The water content was close to saturation in all ES and both DS of both tests (Fig. 5.32).

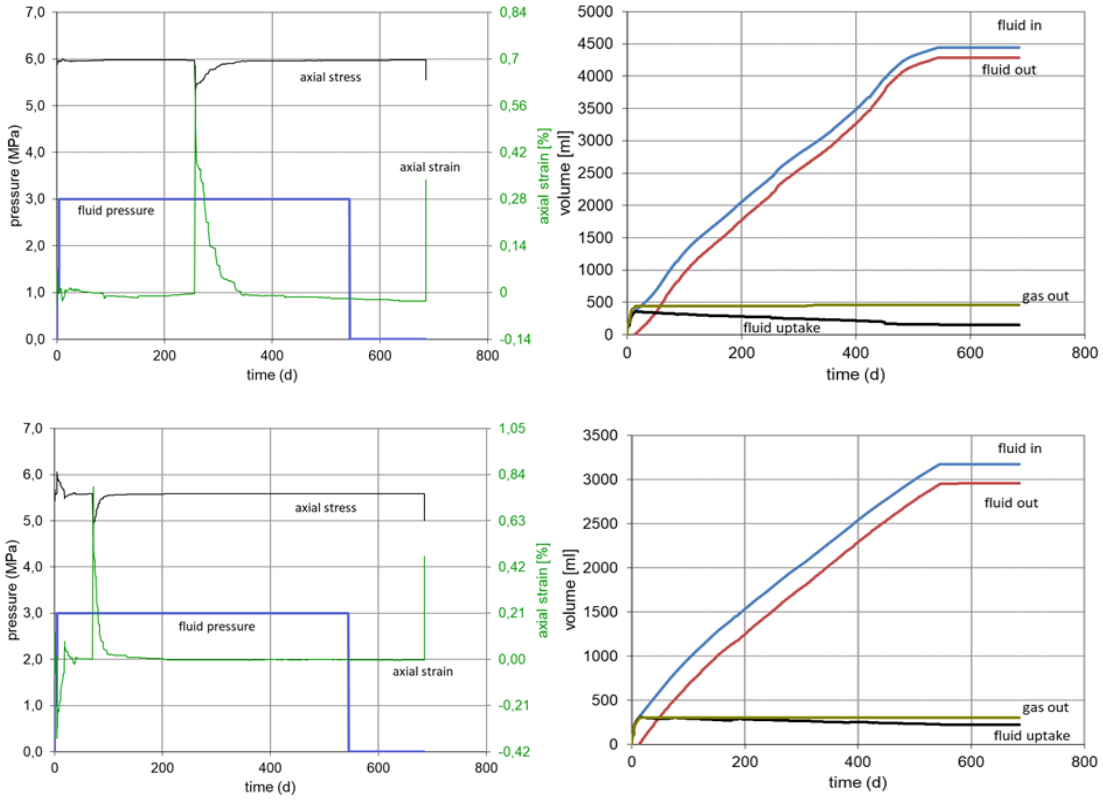

Fig. 5.31 HM behavior of MiniSandwich series 5 (top: test 9, bottom: test 10)

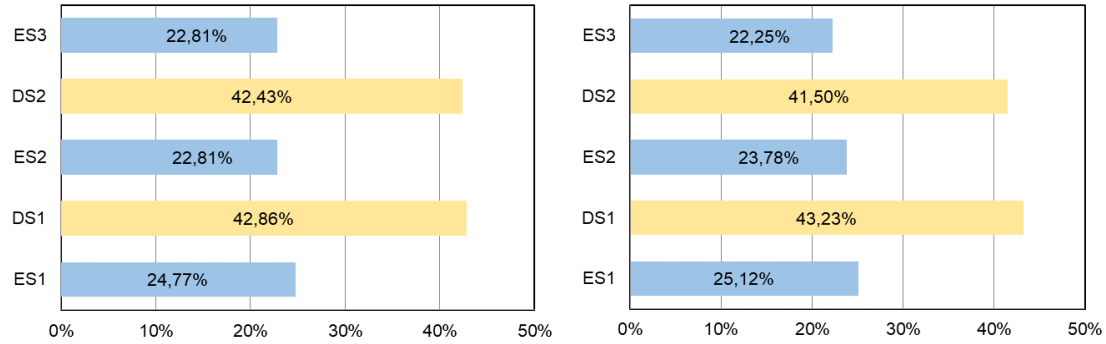

Fig. 5.32 Water content (105 °C) after dismantling of MiniSandwich series 5 (right: test 9, left: test 10)

Series 6

The target of series 6 was the investigation of the influence of a volume increase of DS due to swelling. Within in these MiniSandwich tests it was allowed to swell up to 5 %. For that the pistons of the oedometer cell were exchanged for larger pistons. After a short phase of volume constant conditions, the MiniSandwich could swell free and all parameters was measured (axial load, displacement, in- and outflow, fluid pressure). In

test 11 a leakage on the inflow side occurred after 700 d and both tests were stopped after 880 d. These tests will be repeated during the next project phase.

No fluid breakthrough was observed in both tests until they had to be terminated. Anyway, in both MiniSandwich nearly full saturation could be obtained. Therefore, only an inflow permeability could calculate (Tab. 5.16). The developed swelling pressure at the end of the tests was between 1 MPa (test 11, Calcigel installed in 1 W) and 0.5 MPa (test 12, Calcigel installed in 2W).

The swelling of both tests was different. In test 11 the swelling was nearly constant with a decrease of the axial load. After stopping the fluid inflow after leakage, the swelling also stopped, and the pressure staid nearly constant. Test 12 started similar until day 557. Thereafter, the axial load dropped abruptly und stayed constant. The sample height increased very fast after day 557 by swelling and stopped at day 690. Afterwards the material swelled only slowly (Fig. 5.33).

After dismantling the water content in the DS of both tests was close to saturation while the water content in ES2 of test 11 was lower than in ES1 and ES3 and in test 12 the water content in the ES decreased from ES1 to ES 3 (Fig. 5.32).

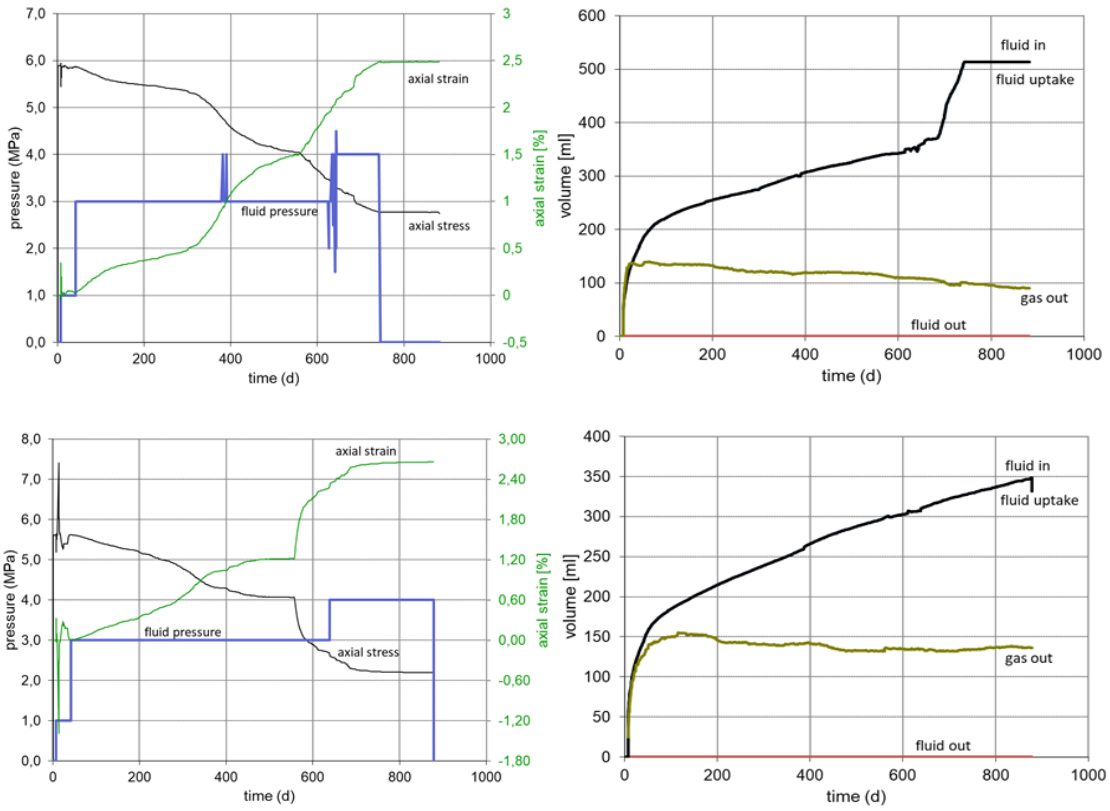

Fig. 5.33 HM behavior of MiniSandwich series 6 (top: test 11, bottom: test 12)

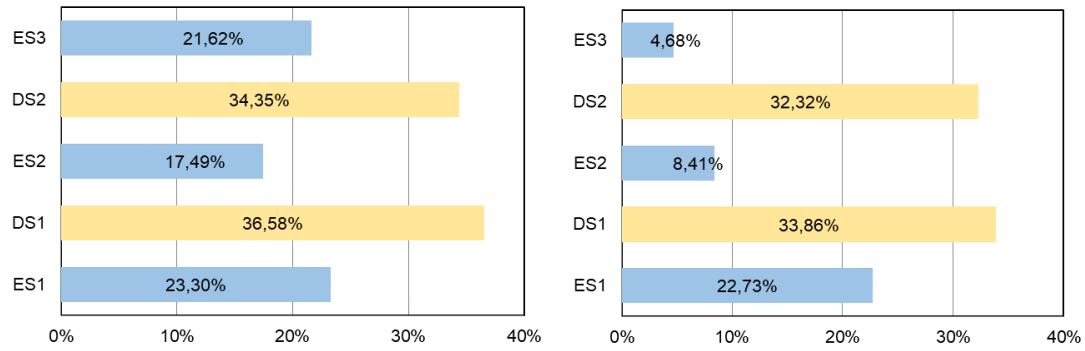

Fig. 5.34 Water content (105 °C) after dismantling of MiniSandwich series 6 (right: test 11, left: test 12)

Series 7

The bulk density (after installation) and material of series 7 is the same as for Shaft 1 in the in-situ experiment. The dry density is the same as the dry density of series 2 in the ELSA project. A constant swelling pressure of 1.1 MPa (test 13) and 0.6 MPa (test 14) was obtained after about 50 d in both tests. The breakthrough in test 13 occurred at day 348 and in test at day 469. The measured permeability is in the order of 10^{-18} m² (Tab. 5.16) as an average for in- and outflow of both tests. The outflow fluid is collected for the chemical analysis. The test duration is planned for ca. three years.

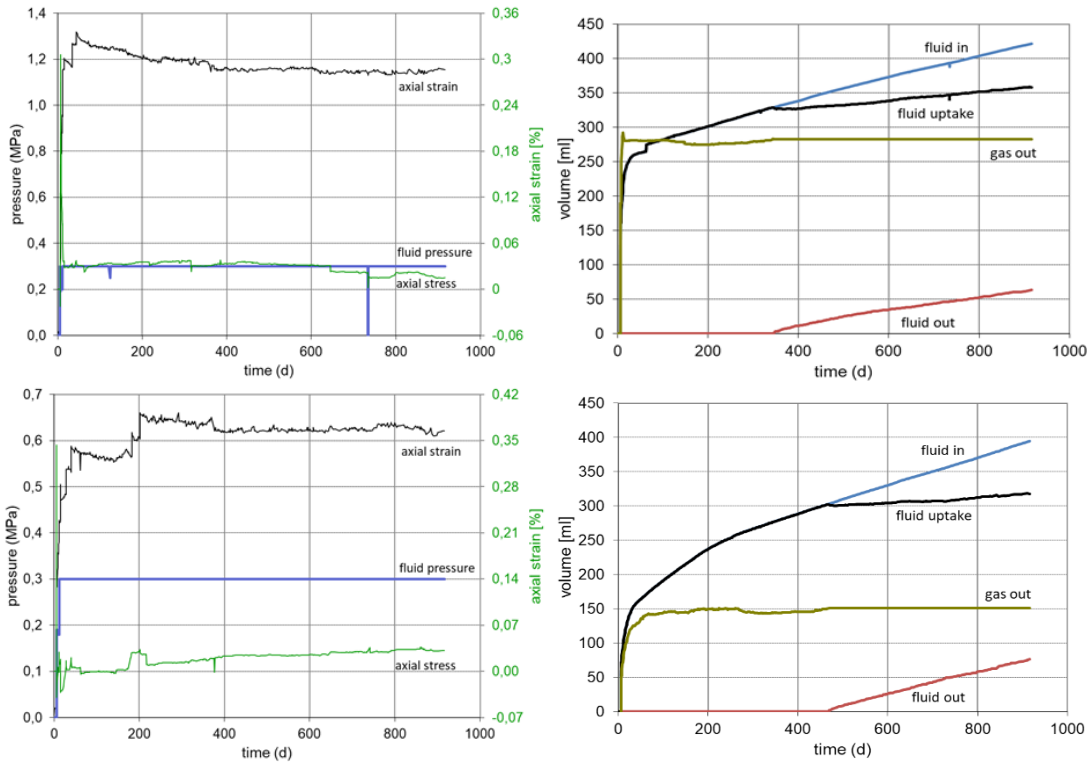

Fig. 5.35 HM behavior of MiniSandwich series 7 (top: test 13, bottom: test 14)

Summary/Discussion

The developed experimental setup enables the simultaneous investigation of the swelling and hydraulic flow behavior of a bentonite-based Sandwich sealing system in reasonable time periods in a laboratory scale. After characterizing the initial pore space conditions (gas permeability and gas accessible porosity), the Sandwich aggregates are flooded with NaCl-brine or Pearson water, respectively. In the progress of the saturation process the swelling pressure (volume-constant system) and the fluid flow balance (in- and outflow) is measured enabling determinations of the effective fluid permeability.

The continuously measured swelling and hydraulic parameters, which are changing with time according to the saturation process, deliver a high-quality data base for numerical back-analysis of the tests.

In summary, the MiniSandwich-experiments have been proven to be a useful and necessary complement of the HTV-experiments. They are also important for the material parametrization and the calibration of the different models.

In all tests the fluid permeability decreases over time from 10^{-14} m² (initial state) to the order of 10^{-17} to 10^{-18} m². In comparison the gas permeability for the initial state is in the order of 10^{-12} up to 10^{-13} m².

The fluid uptake at breakthrough is a little below the calculated pore volume. Over time the fluid uptake increases a bit in the range of 3 to 2 % over the calculated pore volume with exception of series 5, where the fluid uptake at the end of the test is quite lower due to the calculated pore volume. The reason for the increased value in fluid uptake has not yet been fully clarified. One point could be the swelling of the DS during the experiments.

The measurements of the gas leakage during the experiments are very challenging due to the expansion of the gas. So far it is not possible to confirm the calculated pore volume.

5.5 Semi-technical scale experiments

HTV-6 was already performed within the Sandwich-VP (see /EMM 19/) but its mineralogical and chemical analyses were part of the current project. Furthermore, realization of HTV-7 to HTV-9 were part of the current project. HTV-7 and HTV-8 were

dismantled and mineralogical and chemical analyses were performed. HTV-9 is still running and will be dismantled during the next project phase.

The overall objective of the semitechnical scale experiments was to simulate vertical Sandwich sealing systems under the inflow of pore water characteristic of clay host rocks and to test different German bentonites for the DS with specific objectives for each HTV (Tab. 5.17).

Tab. 5.17 Overview HTV experiments

HTV	Project	DS material	Objective
5	ELSA /EMM 19/, /KUD 21/	Calcigel	Hydration with Pearson water
6	Sandwich-VP /EMM 19/	Secursol UHP	Alternative bentonite to Calcigel, new pillow geometry
7	Sandwich-HP	Calcigel	Pre-hydration of ES, Mock-up test of Shaft 1
8	Sandwich-HP	Secursol MHP1 (70/30)	Test of tempered Secursol UHP
9	Sandwich-HP	Calcigel and Secursol MHP1 (70/30)	Mock-up test of Shaft 2

5.5.1 Experimental design and setup

HTV-7 to HTV-9 were performed in a cylindrical steel column with internal dimensions of 0.80 m diameter and 1.89 m length and follow the same basic set up (Fig. 5.36). In each case, four sealing segments (DS) with a thickness of about 25 cm are arranged one above the other, intercepted by equipotential segments (ES) of about 15 cm thickness (Tab. 5.18). Below the lowest DS and above the uppermost DS, gravel elements are arranged by which the load is transferred to the cell bottom and the cell lid. The gravel elements are composed of basalt with a grain size range between 32 and 56 mm. On top of the lower abutment, large unevennesses were levelled with small gravel pieces. To avoid material mixing, geotextile layers (each 1 mm thick, specific weight of 200 g/m²) were installed between the lower basalt gravel element and DS1 as well as between DS1 and ES1. Two layers were placed on the lower gravel abutment and one layer on DS1. In the two lower DS, an approximately 10 cm high sand lens (SL) was purposefully installed in the middle segment height to simulate preferential flow paths. In HTV-7 and HTV-8, an approximately 3 cm thick connecting zone of sand was also placed in DS2, which connected the lower two equipotential segments ES1 and ES2 along the cell wall

over a width of approximately 20 cm and simulated an excavation disturbed zone (EDZ) with higher hydraulic conductivity providing the pathway for a hydraulic short circuit.

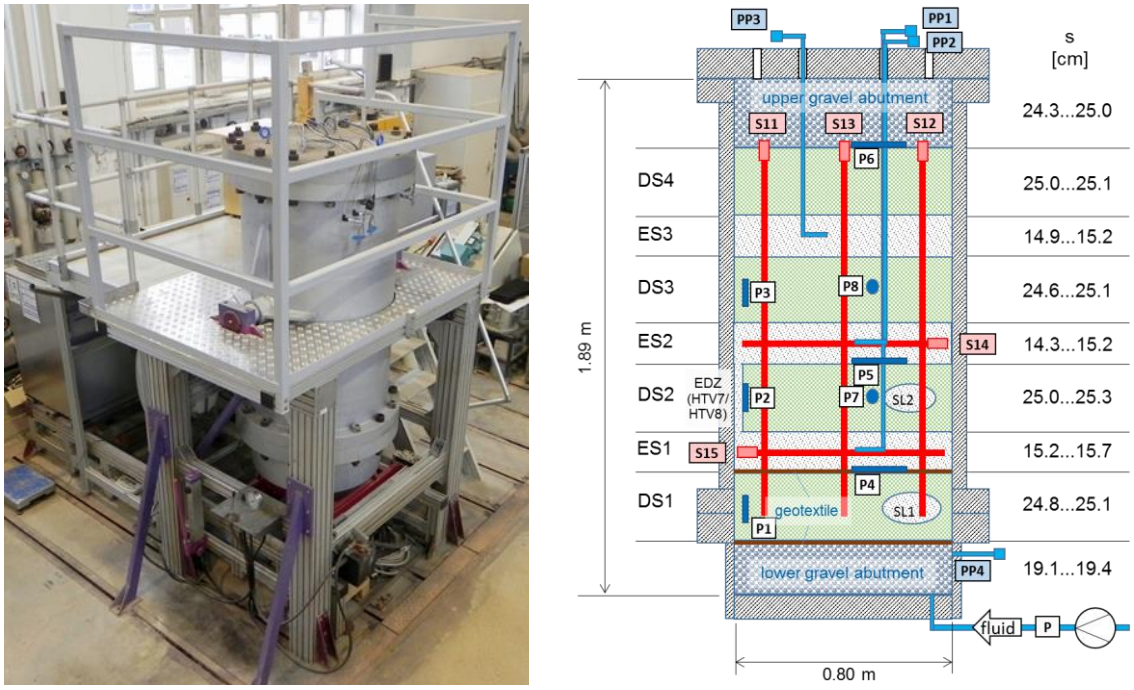

Fig. 5.36 Pressure cell of the HTV (left) and experimental setup in longitudinal section through the cell (right)

Fig. 5.37 DS2 with EDZ and vertical TAUPE TDR sensors in HTV-8 (left) and DS2 with sand lens SL2 and vertical TAUPE TDR in HTV-7 (right)

Tab. 5.18 Thicknesses of the segments in the installed condition in HTV-7, -8 and -9

	installation - thickness [cm]		
	HTV-7	**HTV-8**	**HTV-9**
upper abutment	24.9	24.3	25.0
DS4	25.0	25.1	25.1
ES3	14.9	15.0	15.2
DS3	24.6	25.0	25.1
ES2	15.2	14.3	14.5
DS2	25.0	25.3	25.0
ES1	15.2	15.7	15.3
DS1	24.8	25.1	24.9
lower abutment	19.3	19.4	19.1

The liquid is supplied and pressurized from below the assembly via a connection at the bottom of the cell. The pore volume in the lower gravel element is flooded with liquid and the liquid is present over the entire surface of the bottom of DS1. The calculated pore volume in the lower gravel abutment (including the geotextile) for the installed condition was 39.1 dm³ for HTV-7, 39.4 dm³ for HTV-8 and 38.5 dm³ for HTV-9. In the evaluation of the tests, only the amount of liquid injected into the sealing system was considered without the pore volume in the lower gravel abutment.

The pressurization was carried out by means of a piston metering pump (pump system with control unit from GIESA, pump from ALLDOS/ GRUNDFOS, type: 281-9.6 and 281-4.2, max. metering capacity 9.6 dm³/h/ 8.2 dm³/h). In addition, it was possible to flood individual ES separately via installed pipelines. In HTV-7, the three ES were flooded before pressurization. The piping was routed to the outside through openings in the cell lid. Openings in the cell lid also allow the air contained in the segments to escape to the outside when the liquid displaces the air from the pores.

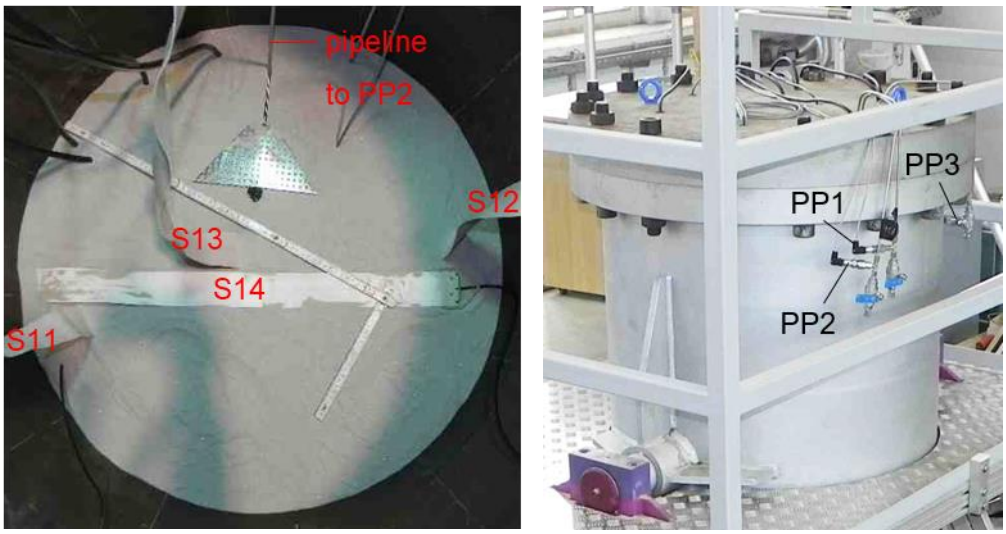

Fig. 5.38 ES2 with horizontal TAUPE TDR S14 and pipe to pore pressure sensor PP2 in HTV-8 (left) and Pore pressure sensors PP1, PP2, PP3 on the pipes into the ES (right)

To track the spreading of the liquid during the experiment, three TAUPE TDR sensors (S11-S13) and two in horizontal alignment (S14, S15) were installed (Fig. 5.38 left). The sensors in the vertical direction go through all segments and the horizontal sensors are installed in ES1 and ES2, respectively, at the mid-segment height.

The radial stress/pressure in the DS was recorded via the surface pressure transducers P1 to P3 (GLÖTZL, type E Ø12 AU 200) (Fig. 5.39 left). The pressure acting in the axial direction was measured via the surface pressure transducers P4 to P6 (GLÖTZL, P4 and P5: type E 10/20 AU 200, P6: EEKE 10/20 KM200 Z4 VA2) (Fig. 5.39 right) at the interfaces DS1/ES1, DS2/ES2, as well as between DS4 and the upper gravel abutment. Pressure transducers P7 and P8 (from KELLER, type: PA 7LC/ 200 bar/ design: in elastomeric casting) were installed in DS2 and DS3 in the segments' vertical center, by which the total pressure could be measured independently of direction (Fig. 5.39 left).

Fig. 5.39 Surface pressure transducers (left) from GLÖTZL for measurement in axial direction (top), in radial direction (bottom), pressure transducer from KELLER for non-directional measurement (middle) and axial surface pressure transducer P6 on top of the DS4 in HTV-8 (right)

Using pressure transducers on the pipelines of ES, pore pressures in the ES could be recorded (PP1...PP3) (Fig. 5.38 right). In addition, the fluid pressure in the pipe between pump and pressure cell (P) and in the lower gravel abutment (PP4) was recorded (Fig. 5.36 right).

The bentonite of a DS is installed as a binary mixture of pillows and bentonite granular material (BGM). The BGM is placed on top of a level of pillows and worked into the pore space of the pillows by poking and tamping the surface. The individual levels of the DS were compacted with a squared timber (4.5 kg, impact surface: 9.5 x 9.7 cm, HTV-7: 6.3 kg, 9 x 10 cm) (Fig. 5.40 right). If appropriate, compaction was also carried out with a 30 kg vibratory plate (RAVI Baugeräte GmbH) (Fig. 5.40 left). Each DS was built up from three individual levels and measured. In some cases, however, thinner levels of pillows were filled with BGM to achieve complete filling of the pores. In the case of HTV-9, a significantly higher dry density was achieved in DS3 and DS4 without compaction using a vibratory plate than in the lower two DS. The reason for this was a particularly high pillow dry density of the Calcigel batch with a value exceeding 2.0 g/cm³.

Fig. 5.40 Compaction of the DS using a vibratory plate in HTV-7 (left) and compaction of the DS using a square timber (right)

The material used for the ES in all tests was dried quartz sand N45 (Chapter 5.2.3). In the upper gravel abutment, the pore space between the gravel was filled with the same sand of the ES to protect sensor cables that were routed through the abutment.

The fine sand N45 was installed with a water content (105 °C) < 0.1 % while the bentonite in DS was installed with a water content (105 °C) of 9.4 to 12.6 % (10.6 to 14.3 % determined at 200 °C) (Tab. 5.19) corresponding to a 2W state of the smectite in the bentonite and its equilibrium water content at ambient conditions. The Calcigel pillows produced for HTV-7 were not fully in equilibrium with ambient conditions and part of them had to be pre-dried in an oven at 60 °C prior to installation. The average water content (105 °C) of the pillows in the upper part of the big bag was 15.9 % (moisture: 13.7 %) while in the lower part of the big bag, the average water content (105 °C) was only 8.3 % (moisture: 7.6 %). During installation an average water content of 10 % were obtained by mixing pillows of different water contents.

Tab. 5.19 Water content and moisture of the segments in the installed condition in HTV-7, -8 and -9

segment	water content [%] / moisture [%]					
	after 105 °C - drying			after 200 °C - drying		
	HTV-7	HTV-8	HTV-9	HTV-7	HTV-8	HTV-9
DS4	10.1 / 9.1	11.9 / 10.6	9.4 / 8.6	11.4 / 10.3	13.7 / 12.1	10.6 / 9.6
ES3	0.0 / 0.0	0.0 / 0.0	0.1 / 0.1	-	-	-
DS3	10.2 / 9.3	12.3 / 10.9	9.6 / 8.8	11.6 / 10.4	14.0 / 12.3	10.8 / 9.8
ES2	0.1 / 0.1	0.1 / 0.1	0.1 / 0.1	-	-	-
DS2	10.0 / 9.1	12.5 / 11.1	9.4 / 8.6	11.4 / 10.2	14.2 / 12.5	11.0 / 9.9
ES1	0.1 / 0.1	0.1 / 0.1	0.1 / 0.1	-	-	-
DS1	10.0 / 9.1	12.6 / 11.2	9.5 / 8.7	11.4 / 10.3	14.3 / 12.5	11.1 / 10.0

The dry densities and the pore volume and the degree of saturation were determined on the basis of the water contents after 105 °C drying (Tab. 5.20) and 200 °C (Tab. 5.21). For the calculation of DS1 and DS2, density values were assumed for the integrated sand zones (SL1, SL2, EDZ) based on the ES densities. The pore volume was calculated based on a specific density value of 2.66 g/cm³ (105 °C) and 2.76 g/cm³ (200 °C) for Calcigel and 2.65 g/cm³ for N45 /EMM 19/. From the results presented in the Sandwich-VP report, it appears that Calcigel and Secursol UHP have almost the same specific density after 200 °C drying /EMM 19/. Therefore, the value for the specific density of Secursol UHP was also used for the pore calculation of the DS made of Secursol MHP1 (70/30). To calculate the unsaturated pore volume a liquid density of 1.0 g/cm³ was used.

Tab. 5.20 Dry densities, pore volume and saturation (105 °C) of DS and ES in HTV-7 to HTV-9

segment	dry density			pore volume, unsaturated			saturation		
	[g/cm³]			[dm³]			[-]		
	HTV-7	HTV-8	HTV-9	HTV-7	HTV-8	HTV-9	HTV-7	HTV-8	HTV-9
DS4	1.46	1.64	1.70	38.0	23.6	25.1	0.33	0.51	0.44
ES3	1.60	1.60	1.54	29.5	29.8	31.8	0.00	0.00	0.00
DS3	1.50	1.63	1.70	35.1	23.3	24.9	0.35	0.52	0.45
ES2	1.59	1.62	1.62	30.2	27.8	28.1	0.00	0.00	0.00
DS2 SL2, EDZ	1.50 value ES2	1.62 mean ES1,2	1.54 value ES1	35.4 0.9	23.5 0.9	34.0 0.6	0.34 0.00	0.52 0.00	0.35 0.00
ES1	1.59	1.54	1.56	30.6	33.2	31.6	0.00	0.00	0.00
DS1 SL1	1.50 value ES1	1.60 mean ES1,2	1.55 value ES1	35.2 0.8	24.2 0.5	33.6 0.4	0.34 0.00	0.51 0.00	0.35 0.00
lower gravel abutment				39.1	39.4	38.5			

Tab. 5.21 Dry densities and pore volume (200 °C) of DS and ES in HTV-7 to HTV-9

segment	dry density			pore volume, unsaturated			saturation		
	[g/cm³]			[dm³]			[-]		
	HTV-7	HTV-8	HTV-9	HTV-7	HTV-8	HTV-9	HTV-7	HTV-8	HTV-9
DS4	1.45	1.61	1.69	39.0	24.4	26.5	0.35	0.53	0.46
ES3	1.60	1.60	1.54	29.5	29.8	31.8	0.00	0.00	0.00
DS3	1.48	1.61	1.68	36.1	24.1	26.3	0.37	0.54	0.47
ES2	1.59	1.62	1.62	30.2	27.8	28.1	0.00	0.00	0.00
DS2 SL2, EDZ	1.48 value ES2	1.60 mean ES1,2	1.52 value ES1	36.4 0.9	24.2 0.9	34.9 0.6	0.36 0.00	0.54 0.00	0.37 0.00
ES1	1.59	1.54	1.56	30.6	33.2	31.6	0.00	0.00	0.00
DS1 SL1	1.48 value ES1	1.58 mean ES1,2	1.53 value ES1	36.1 0.8	25.0 0.5	34.5 0.4	0.37 0.00	0.53 0.00	0.38 0.00
lower gravel abutment				39.1	39.4	38.5			

The indicated densities result from distance measurements between the segment tops. If the next segment is placed and compacted on a finished measured segment, it cannot be ruled out that the already measured segment will be slightly post-compacted. This also affects the lower gravel abutment with the geotextile above it. The geotextile is pressed against the gravel stones by the installation of the bentonite. It is possible that the pore volume in the gravel abutment is approx. 1 dm³ less than calculated for the installation condition. The post-compaction could potentially be detected in future HTV via position sensors.

Dismantling

All HTV are dismantled after termination. After opening the column, the segments were removed within two weeks, if possible. Samples were taken from different levels and all level and segment boundaries were measured.

All DS were dismantled in three levels: one level close beneath the top of the segment, a second at medium depth, and a third just above the bottom of the segment, resulting in overall 12 sampled levels (DS1: E16 – E18, DS2: E11 – E13, DS3: E6 – E8, DS4: E1 – E3). ES were dismantled in two levels, one near the top and one just above the bottom of the segment, resulting in overall 6 sampled levels (ES1: E14 - E15, ES2: E9 – E10, ES3: E4 – E5). 19 samples were taken at each level (Fig. 5.41 left). In addition, the artificial EDZ and, if required, the sand in the upper gravel abutment were sampled. The water content of the samples was determined immediately after dismantling. For some samples (DS only), the density was determined by the immersion weighing method (App. B.12). The samples for density determination were taken next to sites P1, P2, P4, P7, P10, P12, P13, P16, P17 and P18.

The layer boundary positions were measured in the same grid. The measurements were made with a laser distance meter (type: Leica DISTO^{TM} X310) from a steel gauge (Fig. 5.41 top right). The steel gauge was placed on the flange of the hollow cylinder. The display accuracy of the device was ±1 mm.

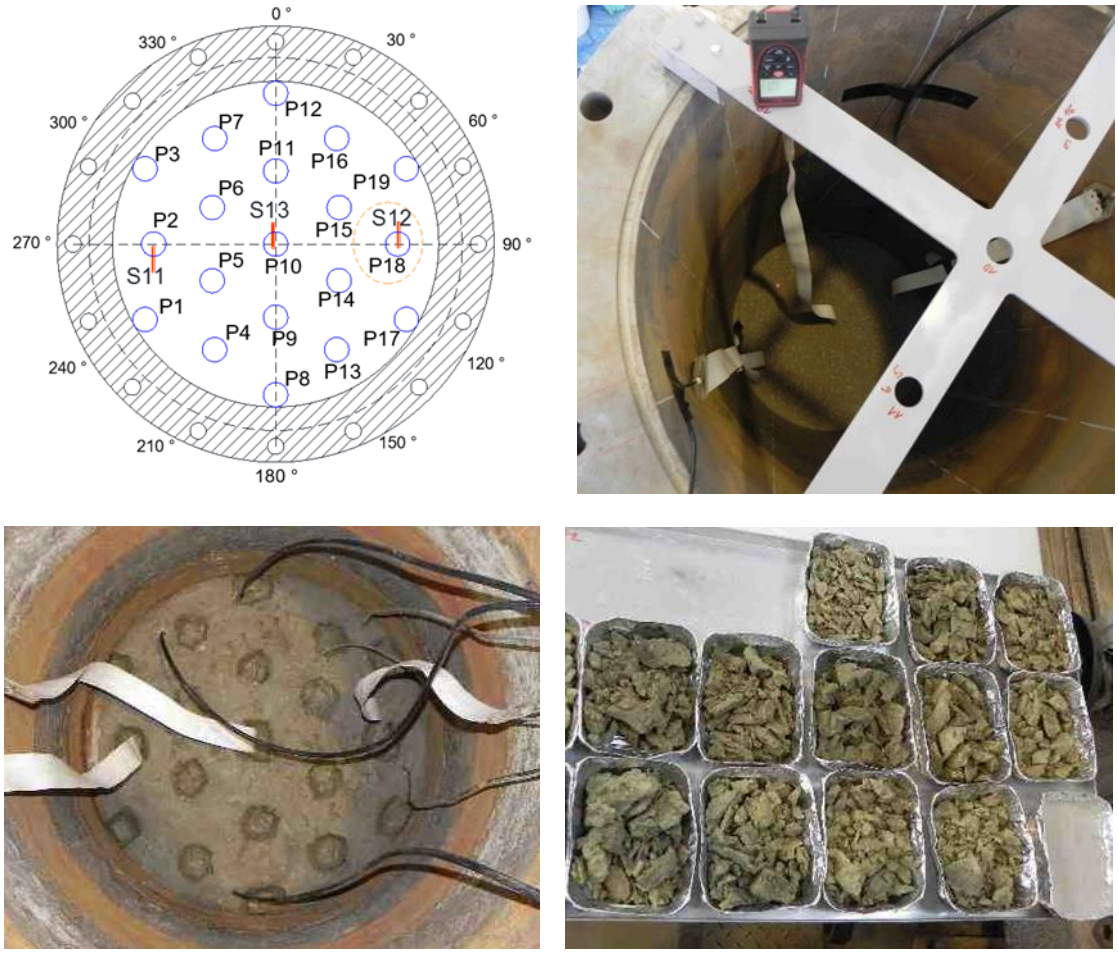

Fig. 5.41 Sampling during dismantling of HTV experiments

Top left: Grid scheme for distance measurements and sampling.
Top right: Distance measurement by means of steel gauge and laser tracking. (Image from installation HTV-6)
Bottom left: Upper level of DS2 in HTV-7 after taking samples for water content determination.
Bottom right: Samples for water content determination from the middle level of DS2 in HTV-7.

When excavation was interrupted for a longer period (overnight or over the weekend), the exposed surface was carefully covered with foil to prevent drying of material by the ambient air. In addition, during interruptions, layer heave caused by slow relaxation of the segments and post-swelling of bentonite was recorded. Such displacements on the exposed surface affect the integrally calculated density and saturation of a segment. To infer the actual condition before the segments were removed, the measured displacements can be used. Nevertheless, such back-calculations represent only an approximation to the original state before opening the cell. By installing position sensors, which is intended for future HTV experiments, the actual position of a layer boundary will probably be able to be determined at any time during the test and during removal,

facilitating a more accurate quantification of each layer's state and its evolution during the different experimental phases.

5.5.2 HTV-6

HTV-6 was performed and dismantled during the Sandwich-VP project. Fluid transport was limited to the lower part of DS2. Strong swelling of DS1 reduced its dry density to 1.27 g/cm³ while DS2 was compacted to 1.67 g/cm³. DS3 and DS4 were also compacted to 1.63 and 1.58 g/cm³, respectively /EMM 19/.

As fluid did not penetrate DS3 into ES3 and DS4, these segments were not fully analyzed following dismantling. A small number of samples from DS4 were analyzed for use as reference samples.

The following values refer to mean values calculated over the 19 samples in a sampling level unless a specific sample is specified. Samples from the sandy lenses in E17 and E12 are excluded from the mean calculation due to the large differences between sand and bentonite materials obscuring trends. Water content (200 °C) in DS sampling levels from E6-E8 (DS3) and E11 (upper level of DS2) was 15.0 % (Fig. 5.42). In E12 the water content was slightly increased to 15.7 % and there was a linear increase in water content as a function of column height in DS sampling levels to reach 59.0 % in E18 ($H_2O\ content\ (\%) = 0.835\ \times height(cm) - 80.28, R^2 = 0.996$, note that increasing height indicates lower sampling levels as height is measured from the top of the column). Water content in ES1 (E14 and E15) was 1.1 %, and that of ES2 was 0.0 %. The mean water content in E15 was slightly higher than that of E14 but the difference was not significant.

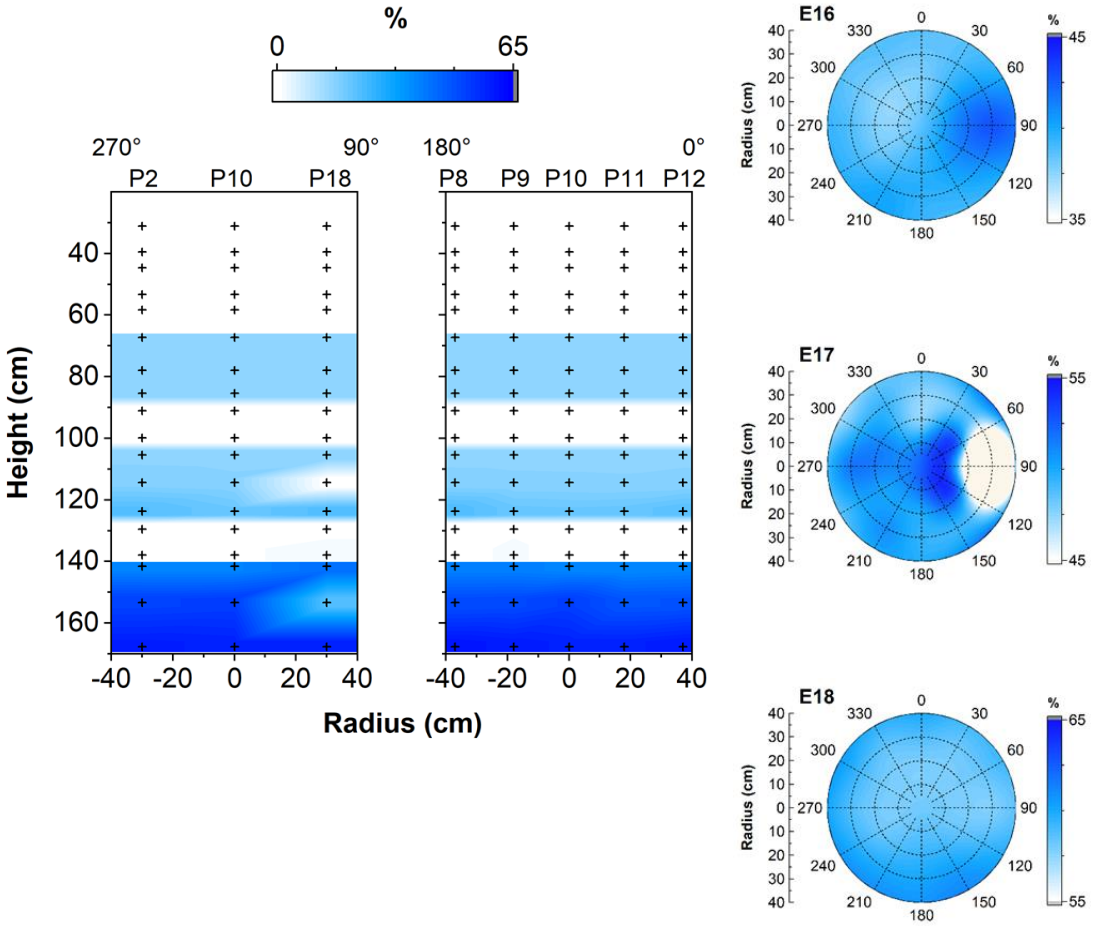

Fig. 5.42 Water content of HTV-6

Top: perpendicular cross sections (sampling points indicated with black crosses)
Bottom: horizontal cross sections of DS1 (adjusted color scales to highlight details less evident in the larger figure). The large white patch in E16 indicates the position of the sandy lens. Note that the large difference between water contents of the sandy lens and surrounding bentonite material exaggerated the size of the shortcut in this representation.

Ion transport (conductivity, salt content, soluble ions) and cation exchange (CEC, exchangeable cations)

Conductivity measurements were transformed into NaCl content (wt.%, referred to as LF-salt). The highest LF-salt content (mean 0.52 wt.%) was recorded in E18, and lower values of 0.43 and 0.35 wt.% were found E17 and E16 respectively (Fig. 5.43). LF-salt was <0.1 wt.% in E15 (ES) and in DS sampling levels E12 to E6. In ES level E14 and DS level E13 the LF-salt content was 0.1 wt.%. However, in E10 and E9 the LF-salt content was close to 0 wt.%. LF-salt content correlated well with mean water content

measurements for the same sampling level. There was little variation within a sampling level, with standard deviations < 0.02 wt.% with the exception of E14 and E13 where the standard deviation was 0.05 and 0.08 wt.% respectively. In the sampling levels E12 to E6, variation was lower than the remainder of the column at < 0.003 wt.%.

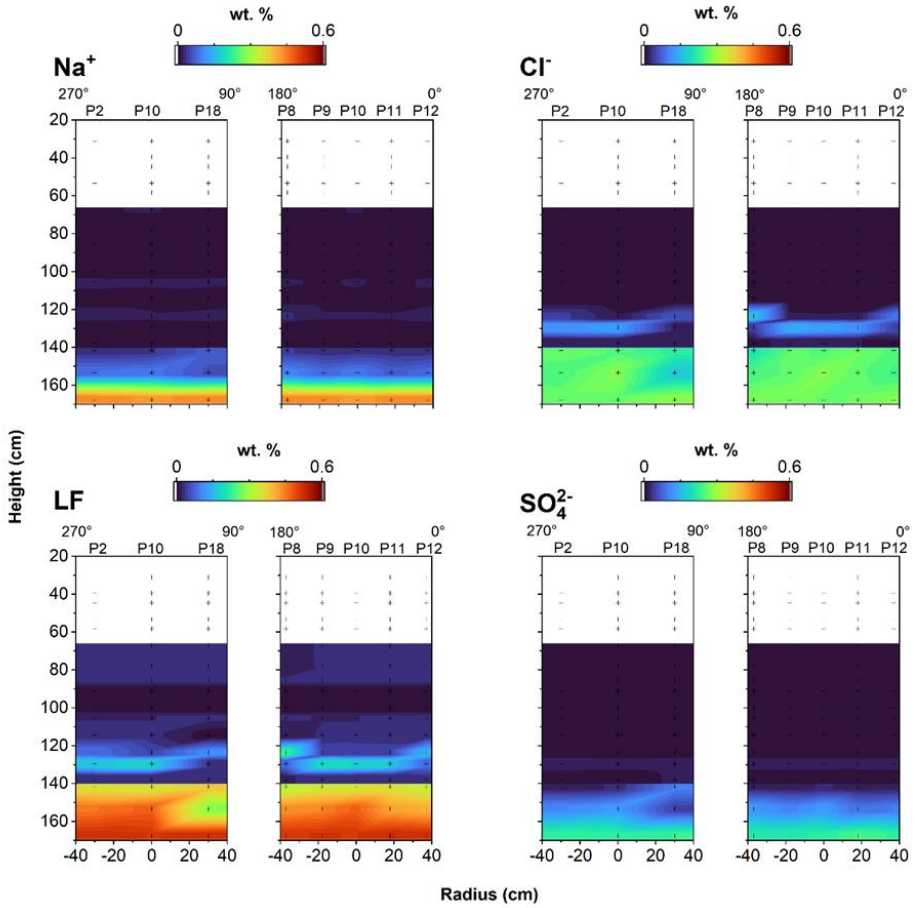

Fig. 5.43 Vertical cross sections of HTV-6

Bottom: salt content from conductivity and SO_4^{2-} content

Top: Salt content from Na^+ and Cl^- content. Sampling points are marked by black crosses. Note the different scales.

Salt content (NaCl and Na_2SO_4) was also calculated from soluble Na^+, Cl^- and SO_4^{2-} ($Na^+{}_{sol}$, $Cl^-{}_{sol}$, and $SO_4^{2-}{}_{sol}$) concentrations (abbreviated as Na-salt, Cl-salt and SO_4-salt) (Fig. 5.43). The values of Na-salt, Cl-salt and SO_4-salt did not consistently match the LF-salt content. In the case of Cl-salt, there is a good overall match of salt distribution within the column but maximum value of Cl-salt is consistently lower than that of LF-salt. In the case of Na-salt and SO_4-salt, neither of them matched the distribution of LF-salt content, although the value of Na-salt in E18 of came close to the value of LF-salt (Fig. 5.43).

Looking at the concentrations of all soluble ions provides further insight into the different distributions of salt content. The highest LF-salt content in E18 matched to the maximum concentrations of $Na^{+}{}_{sol}$, $Cl^{-}{}_{sol}$, and $SO_4^{2-}{}_{sol}$ in the column. In comparison the maximum mean concentrations of soluble Ca^{2+}, Mg^{2+}, and K^{+} ($Ca^{2+}{}_{sol}$, $Mg^{2+}{}_{sol}$, and $K^{+}{}_{sol}$) were found in E17 or E16, and the concentrations of these ions in E18 was lower.

The concentration of $Na^{+}{}_{sol}$ was not constant across DS1 but dropped off steeply from 7.5 cmol(+) kg^{-1} in E18 to 1.4 and 0.6 cmol(+) kg^{-1} in E17 and E16 respectively. In the remainder of the column $Na^{+}{}_{sol}$ was ~0 in ES and <0.3 cmol(+) kg^{-1} in DS sampling levels.

The concentration of soluble $SO_4^{2-}{}_{sol}$ had a similar distribution to that of $Na^{+}{}_{sol}$, but at lower concentration. The concentrations in E18, E17 and E16 were 3.2, 1.4, and 0.3 cmol(-) kg^{-1} respectively, and 0.3 cmol(-) kg^{-1} in E14. In remaining ES sampling levels the concentrations of $SO_4^{2-}{}_{sol}$ were ~ 0 cmol(-) kg^{-1} and < 0.1 cmol(-) kg^{-1} in DS (Fig. 5.47).

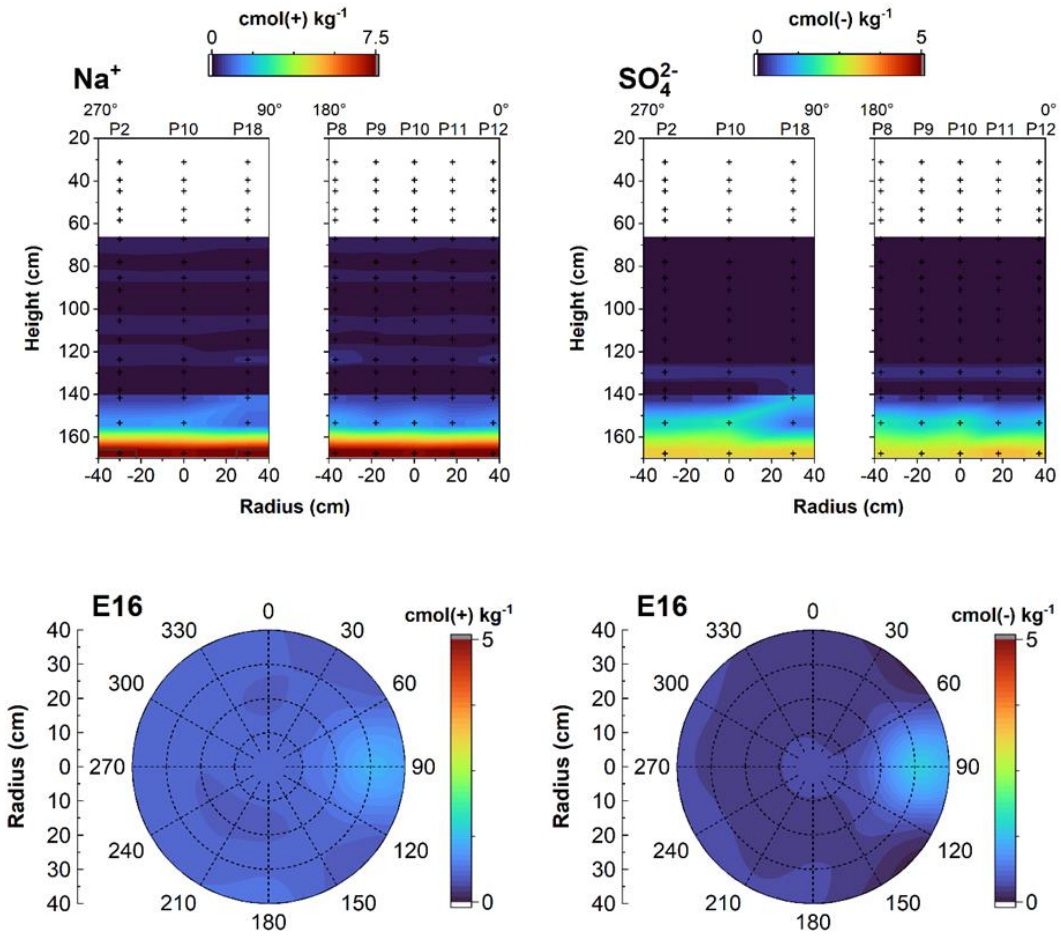

Fig. 5.44 Cross sections through HTV-6; $Na^{+}{}_{sol}$ (left) and $SO_4^{2-}{}_{sol}$ (right)

The mean concentration of $Ca^{2+}{}_{sol}$ was 0.7 cmol(+) kg^{-1} in E18, 3.4 cmol(+) kg^{-1} in E17 and 3.2 cmol(+) kg^{-1} E16. In ES1, there was a large difference between the concentration in E15, 0.3 cmol(+) kg^{-1}, and that of E14, 1.2 cmol(+) kg^{-1}. In comparison, in ES2 the values in E10 and E9 were ~0 cmol(+) kg^{-1}. $Ca^{2+}{}_{sol}$ concentrations decreased through DS2 from 1.0 cmol(+) kg^{-1} in E13 to 0.5 cmol(+) kg^{-1} in E12 and the remainder of DS sampling levels with the exception of E8 which had a concentration of 0.6 cmol(+) kg^{-1} (Fig. 5.45, Fig. 5.47).

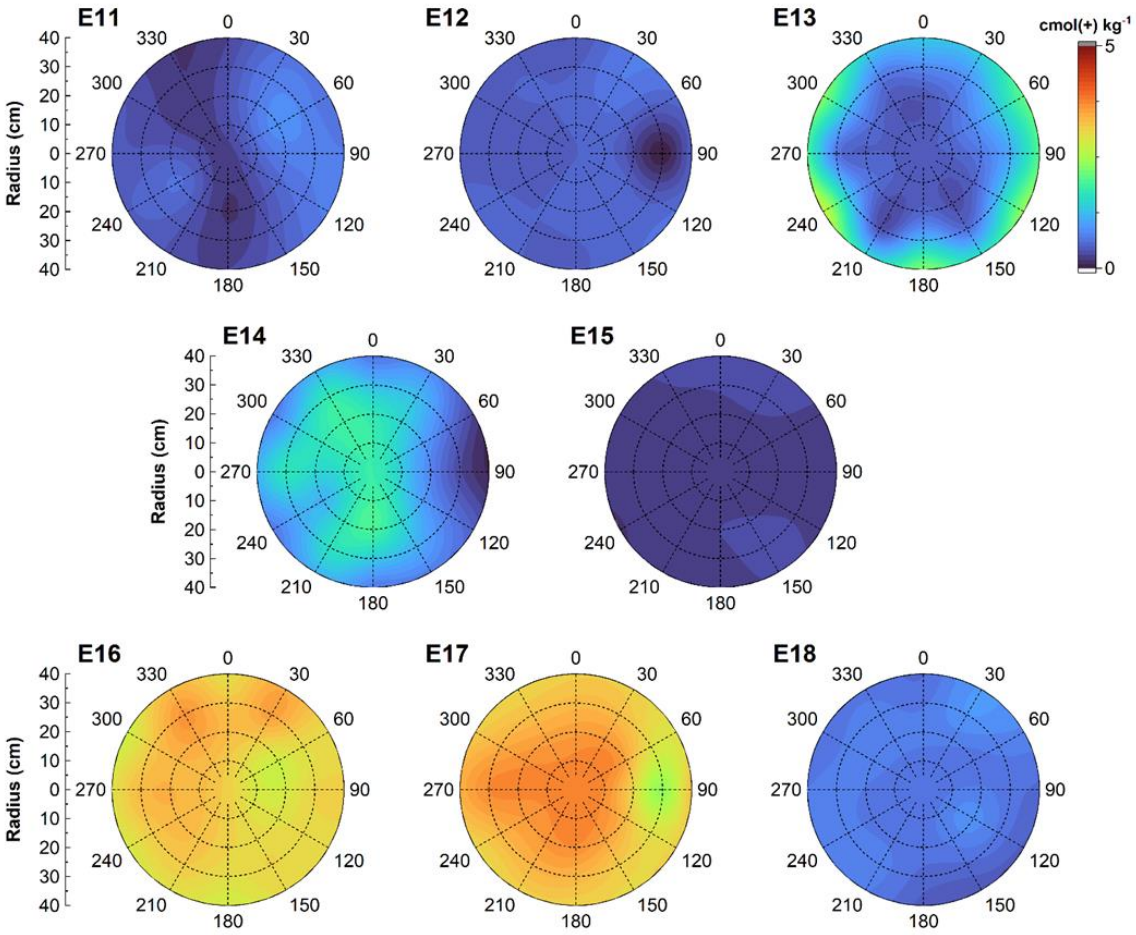

Fig. 5.45 Soluble Ca^{2+} content for sampling levels from E11 (top left) to E18 (bottom right)

The concentration of ${Mg^{2+}}_{sol}$ had a similar distribution to ${Ca^{2+}}_{sol}$. A lower concentration of 0.3 cmol(+) kg^{-1} in E18 increased to a column maximum of 1.2 cmol(+) kg^{-1} in E17 then decreased slightly to 1.1 cmol(+) kg^{-1} in E16. The concentration across ES1 increased from 0.1 cmol(+) kg^{-1} in E15 to 0.4 cmol(+) kg^{-1} in E14. In E13 the concentration of ${Mg^{2+}}_{sol}$ was 0.5 cmol(+) kg^{-1}, 0.7 cmol(+) kg^{-1} in E12 and 0.2 cmol(+) kg^{-1} in E11. In ES2 the concentration of ${Mg^{2+}}_{sol}$ was ~ 0 and 0.1 cmol(+) kg^{-1} in E10 and E9 respectively. In the remaining DS levels E8 – E6 ${Mg^{2+}}_{sol}$ concentration was close to 0.6 cmol(+) kg^{-1}.

Mean concentrations of ${K^{+}}_{sol}$ were very low through the whole column and while they were slightly higher in DS samples the difference between ES and DS was not large (< 0.3 cmol(+) kg^{-1}).

The mean concentration of Cl^-_{sol} was 4.6 cmol(-) kg^{-1} in E18, and decreased slightly to 4.3 and 4.2 cmol(-) kg^{-1} in E17 and E16 respectively. There was a large decrease in concentration to 0.2 cmol(-) kg^{-1} in E15, followed by an increase to 1.3 cmol(-) kg^{-1} in E14. Concentration then decreased slightly to 1.1 cmol(-) kg^{-1} in E13. Cl^-_{sol} concentration was ~0 cmol(-) kg^{-1} in the remainder of the column (E12- E6) (Fig. 5.46).

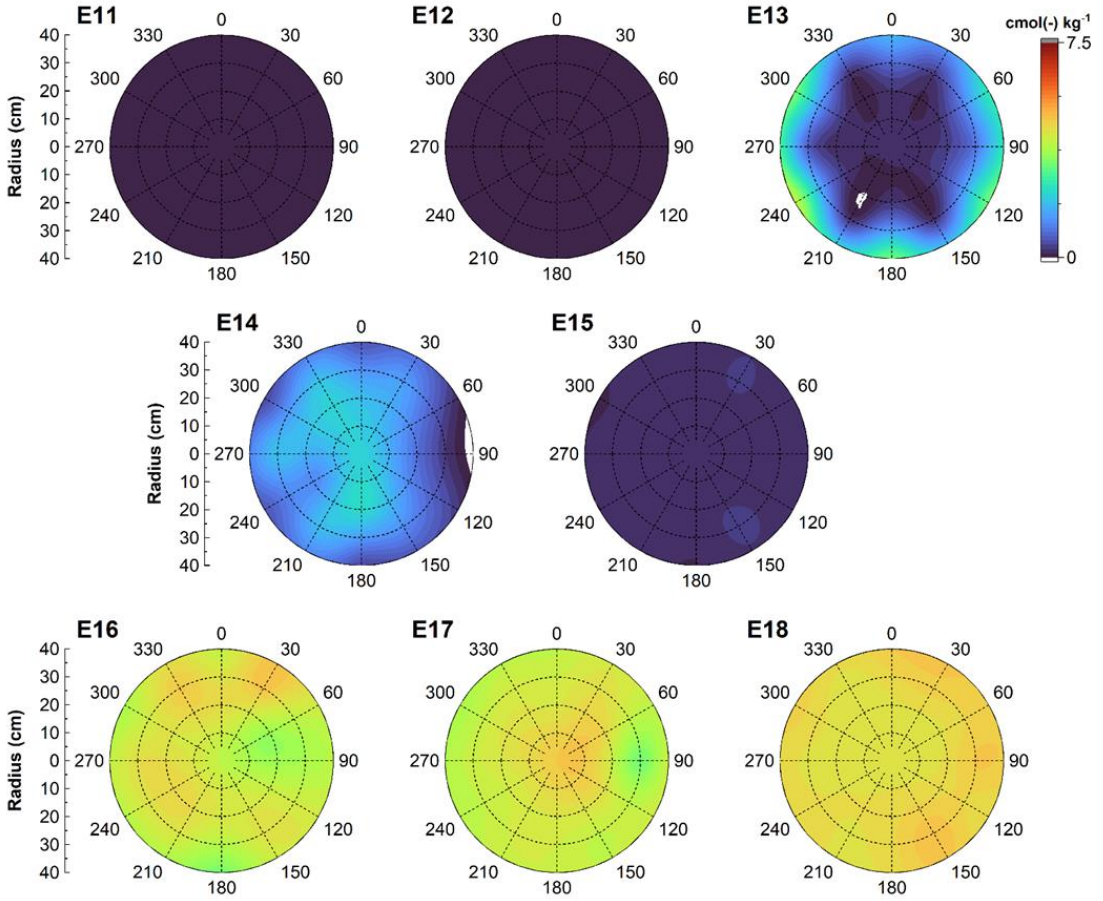

Fig. 5.46 Horizontal cross sections through HTV-6 showing the concentrations of $\boldsymbol{Cl^-_{sol}}$ in sampling levels E11 (top left) to E18 (bottom right)

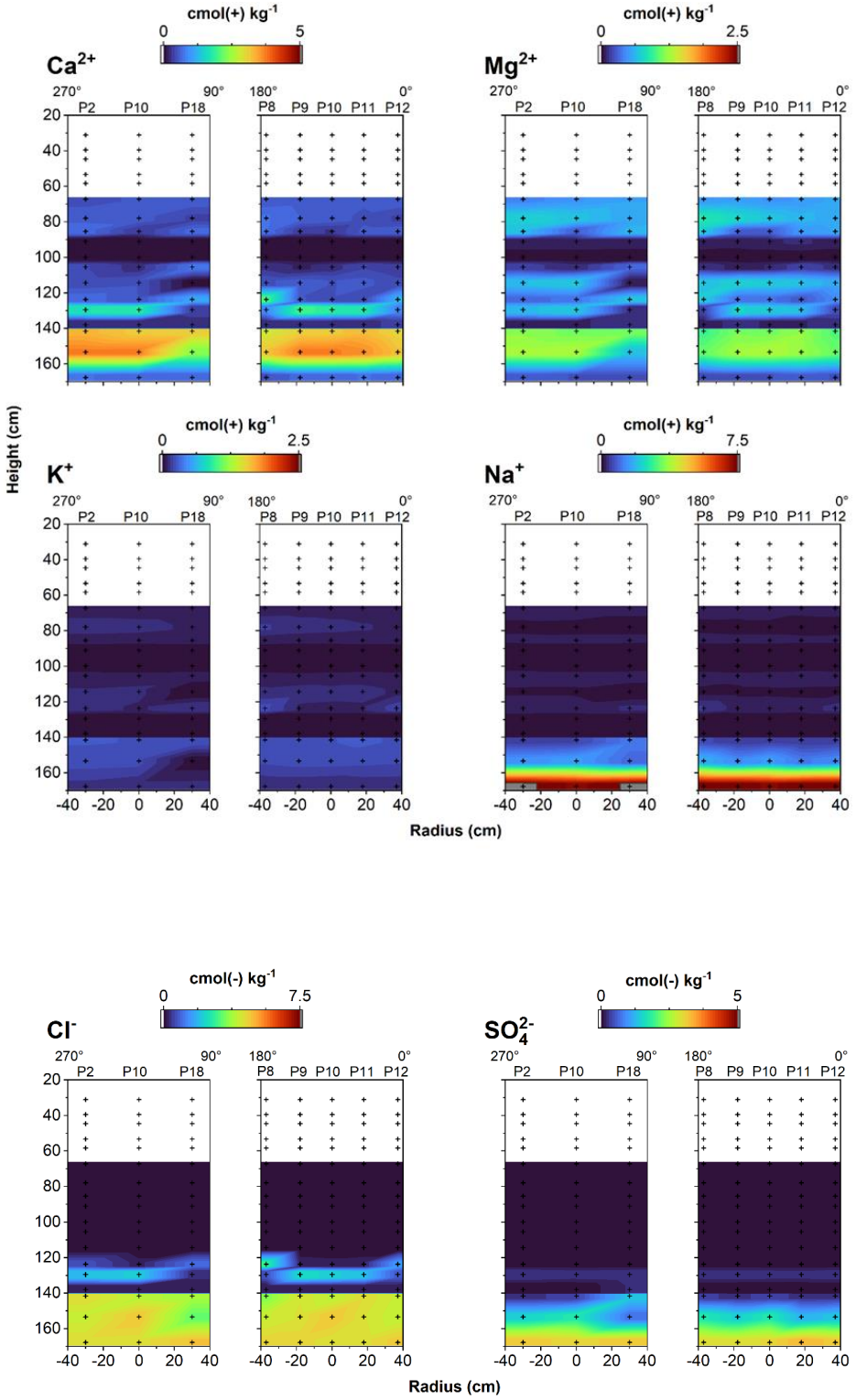

Fig. 5.47 Cross sections through HTV-6 showing the concentrations of soluble ions. Sampling points are marked with black crosses

Apart from sampling levels impacted by the sand lens, soluble ion levels within a sampling level were fairly uniform. For $Na^{+}{}_{sol}$ and $SO_4^{2-}{}_{sol}$ the largest standard

deviations were in DS1, where the standard deviation for $Na^{+}{}_{sol}$ was 0.2 cmol(+) kg^{-1}, and 0.2-0.3 cmol(+) kg^{-1} for $SO_4^{2-}{}_{sol}$. The impact of the sand lens was evident in E17 and E16 (Fig. 5.44). In the rest of the column variation of $Na^{+}{}_{sol}$ was low, with standard deviations close to zero in E15 – E6 except for E13 which had a standard deviation of 0.1 cmol(+) kg^{-1}. In E15 and E14, standard deviation of $SO_4^{2-}{}_{sol}$ was 0.1 cmol(+) kg^{-1} and ~0 cmol(+) kg^{-1} for E13 – E6. For $Ca^{2+}{}_{sol}$, $Mg^{2+}{}_{sol}$, $K^{+}{}_{sol}$ and $Cl^{-}{}_{sol}$, the largest standard deviations were found in E13 (bentonite), closely followed by E14 (sand). This was caused by differences between samples nearer the center of the column and samples towards to the edge. E14 had higher concentration in samples at the center and lower edge concentrations, while the opposite was true in E13. Standard deviation of $Ca^{2+}{}_{sol}$ was 0.7 cmol(+) kg^{-1} and 0.5 cmol(+) kg^{-1} in E13 and E14 respectively, compared to 0.2 and 0.3 cmol(+) kg^{-1} in E16 and E17.

The average CEC of DS in HTV-6 was found to be between 76.8 and 85.3 cmol(+) kg^{-1}, which was within the range of the predicted decrease from the raw Securesol UHP. A minimum value of 71.4 cmol(+) kg^{-1} was measured for E16-P8 and a maximum value of 89.2 cmol(+) kg^{-1} for E17-P17, The standard deviation of all CEC measurements taken in the column (228 samples) was ±3.7 cmol(+) kg^{-1}, approximately double the variation expected from the Cu-trien CEC method used (variation of ± 1-1.5 cmol(+) kg^{-1}).

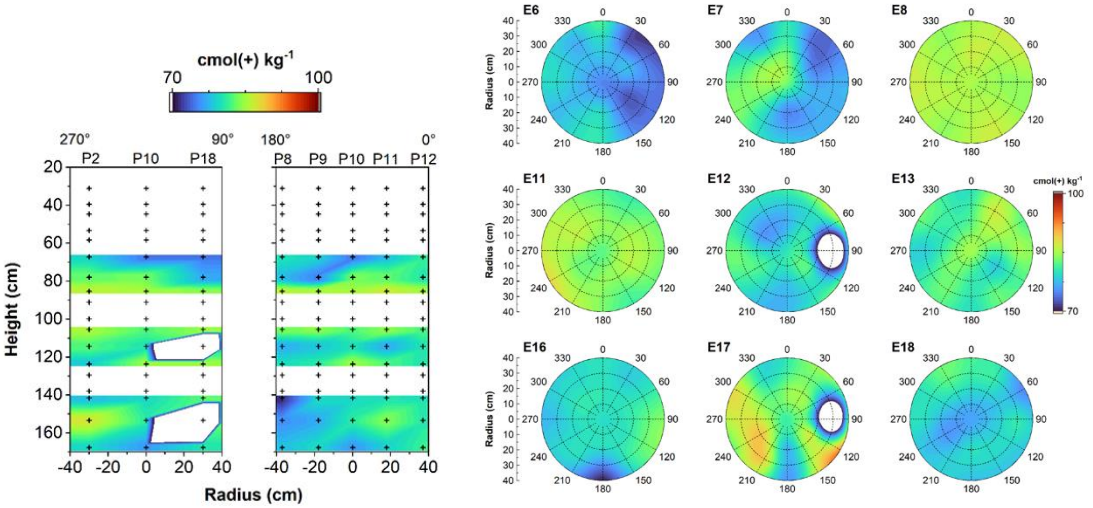

Fig. 5.48 Cross sections through HTV-6 showing CEC for DS sampling levels

Left: Sampling points are marked with black crosses.
Right: CEC distribution at sampling levels.

The variation in DS1 (E16 – E18) was slightly higher than that of the other two DS, ± 5.5 cmol(+) kg^{-1} vs ± 3.6 cmol(+) kg^{-1}. Individual levels show a fairly high variation in

CEC, with standard deviations between 0.8 and 4.0 cmol(+) kg^{-1}. In DS1, CEC was 78.8 cmol(+) kg^{-1}, increased to 83.5 cmol(+) kg^{-1} in E17, then decreased again to 79.5 cmol(+) kg^{-1} in E16 (Fig. 5.48). CEC values in DS2 showed the reverse trend: CEC in E13 was 82.0 cmol(+) kg^{-1}, *decreased* to 79.5 cmol(+) kg^{-1} in E12 and *increased* to 84.1 cmol(+) kg^{-1} in E11. DS3 showed yet another trend, where the CEC of E8 was 85.3 cmol(+) kg^{-1}, E7 was 78.9 cmol(+) kg^{-1} and E6 was 76.8 cmol(+) kg^{-1}. There was no correlation with salt content, water content or ion contents.

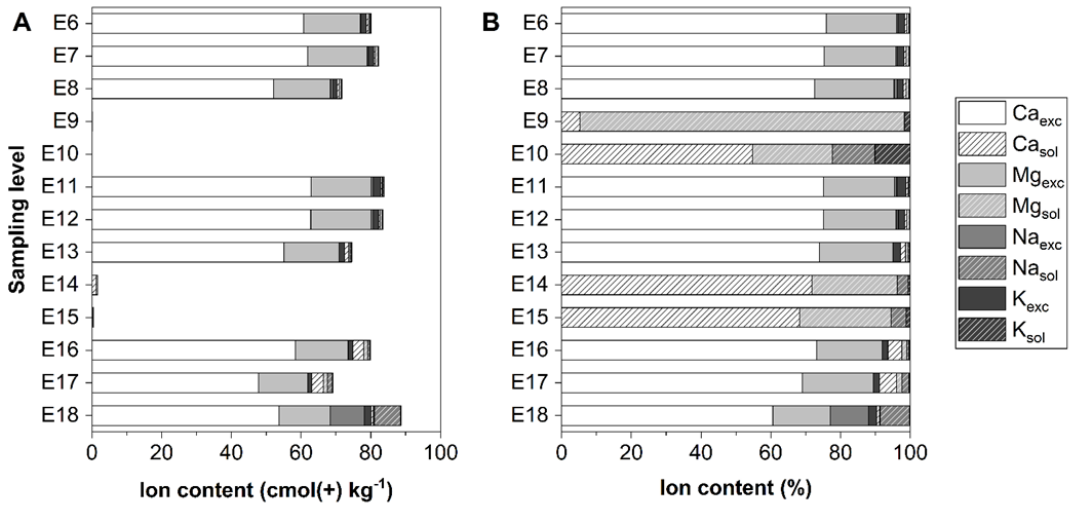

Fig. 5.49 Comparison of absolute ion contents in cmol(+) kg^{-1} (left) and ion content normalized to 100 % (right) in HTV-6

In addition to the wide range in variability of the CEC, there was similar variability in the EC content within a sampling level and between sampling levels (Fig. 5.49). This variability did not correlate with the measured CEC. For example, the mean $Ca^{2+}{}_{exch}$ concentration in E18 was 54.3 cmol(+) kg^{-1} with a standard deviation of 2.4 cmol(+) kg^{-1}. In E17 these values were 51.1 and 3.0 cmol(+) kg^{-1} respectively and in E16 the mean was 61.2 cmol(+) kg^{-1} and 3.0 cmol(+) kg^{-1}. Meanwhile, the mean CEC of these sampling levels was 78.8 (E18), 83.5 (E17), and 79.5 (E16) cmol(+) kg^{-1}. Sampling levels higher in the column (E11 – E6) tended to have lower variation. As a result of the variation, a clearer impression of the extent of cation exchange and transport was obtained by looking at exchangeable and soluble ion concentrations normalized to 100 %. This showed the impact of cation exchange in E18, where $Na^{+}{}_{sol}$ had replaced a portion of interlayer $Ca^{2+}{}_{exch}$ and $Mg^{2+}{}_{exch}$ in the smectite (Fig. 5.49, Fig. 5.50). There was no clear indication of interlayer cation exchange elsewhere in the column. A higher percentage of soluble $Na^{+}{}_{sol}$ was also observed in E18 than any other sampling levels in the column.

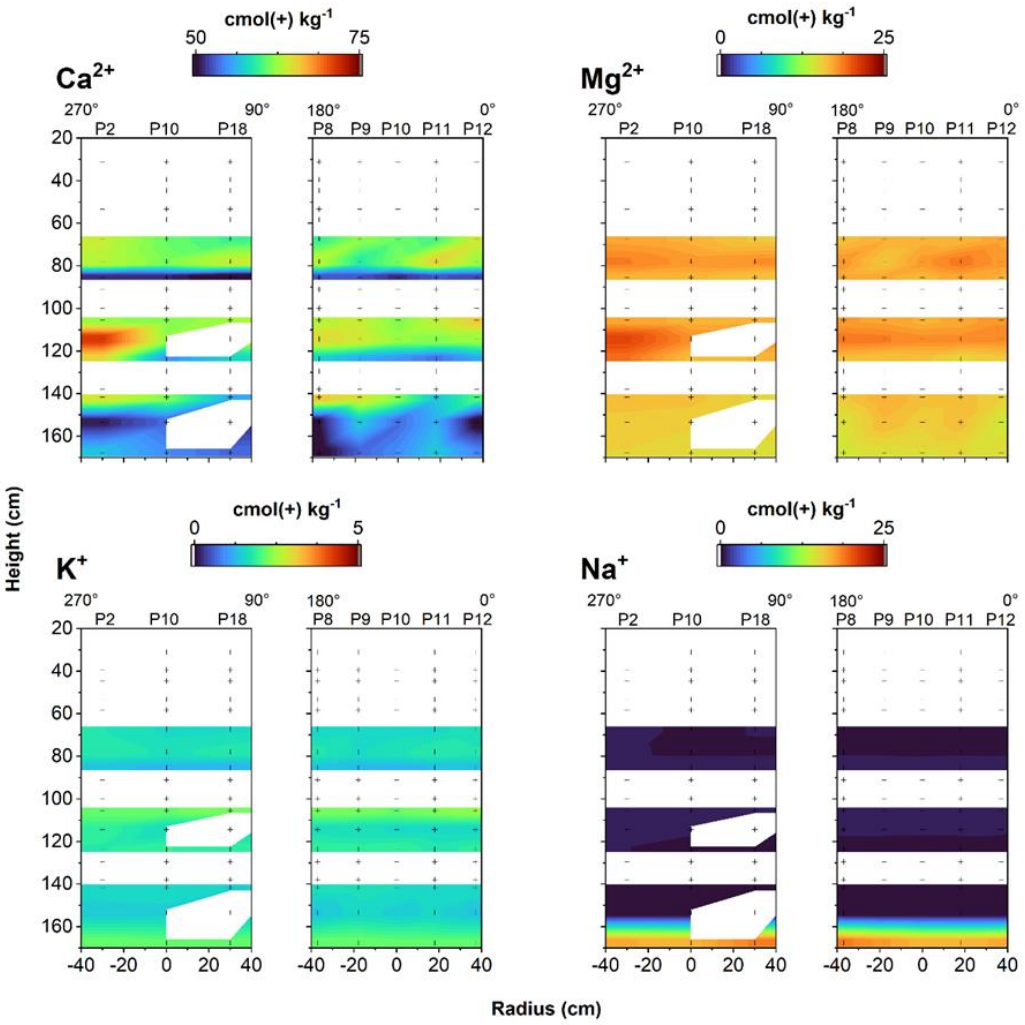

Fig. 5.50 Cross sections through HTV-6 showing exchangeable cation content in DS sampling levels. Sampling points are marked with black crosses

TDR measurements during the HTV-6 experiment indicated that fluid infiltration was limited by high swelling pressure of the Securisol UHP bentonite. The results of analysis of conductivity, soluble ion content and exchangeable ion content are consistent with this limited hydration, as there ion transport and exchange was observed only within E12-E18. Exchange of interlayer cations was limited to E18. This is likely related to ion selectivity of smectite interlayers and a minimum concentration of $Na^{+}{}_{sol}$ being required in the pore fluid for exchange to take place. The main controls on ion concentrations in HTV-6 were expected to be the composition of smectite interlayers (primarily Ca^{2+}/Mg^{2+} in raw Securisol UHP) and the composition of the infiltration fluid (Pearson water A3, 120 mmol L^{-1} Na^{+}). In contrast to previous HTV experiments there is no soluble mineral content to impact the pore fluid composition. Large variations in CEC suggest a non-uniform impact of heating on bentonite sampling levels. Mixing of sand and bentonite at

the edge of DS could contribute further to sample heterogeneity but this is not the primary factor as E17, which is not sand-adjacent, has the highest variation of all the sampling levels. Overall, distribution of results suggests that external factors, such as experimental error, are impacting the CEC measurement.

The higher variation of soluble ion contents in E16 and E17 is due to the effects of the sand lens. The shortcut allowed the infiltrating fluid to permeate directly through E17 resulting in the higher water and soluble ion contents ($Na^{+}{}_{sol}$ and $SO_4^{2-}{}_{sol}$) in the bentonite directly above the sandy lens (E16-P18). Increased water and soluble ion contents were also seen in the bentonite directly adjacent to the sandy lens (E17-P10). However, the sandy lens effect was not observed as clearly for $Ca^{2+}{}_{sol}$, $Mg^{2+}{}_{sol}$, $K^{+}{}_{sol}$ and $Cl^{-}{}_{sol}$. This is not related to concentration in the infiltrating solution, as the initial concentration of $SO_4^{2-}{}_{sol}$ is much lower than that of $Cl^{-}{}_{sol}$ (~12 vs. 130 mmol L^{-1}). Variation within the sampling levels E13 and E14 consisted of differences between the center and edges of the column, but the opposite trend was observed between the two levels. This difference could be due to the different materials, as E13 is a DS sampling level while E14 is an ES sampling level. Another possibility is the interface between the steel column and the Sandwich may not be perfect, and increased porosity at the intersection with the steel column allows for greater uptake in bentonite at edge positions in E13. Large differences between E9 and E10 (ES2) could result from the hydraulic bypass between ES1 and ES2, however there is no difference in mean water content between these sampling levels to indicate that the infiltrating fluid advanced into E10. Rather, the values of soluble ions measured in ES are also very low, so a small absolute difference correlates to a large percent difference.

5.5.3 HTV-7

HTV-7 was installed within 14 d in late 2019 and hydration started subsequently. The duration of the experiment was about 2 months (Tab. 5.22).

Tab. 5.22 Key data for the HTV-7

Material of DS	**Calcigel**
Installation	21.11.2019 - 04.12.2019
Hydration	05.12.2019 - 28.04.2020
Duration	145 d
Maximum fluid pressure	3.1 /2.9 MPa*
Final fluid pressure	2.0/1.9 MPa*
Holding time of final pressure	55 d
Pore volume (installation condition) total (105 °C, unsaturated)[#] total (200 °C, unsaturated)[#] DS (105 °C, unsaturated) ES (105 °C, unsaturated) DS (200 °C, unsaturated) ES (200 °C, unsaturated)	 235 dm³ 239 dm³ 145 dm³ (with SL1, SL2 and EDZ) 90 dm³ 149 dm³ (with SL1, SL2 and EDZ) 90 dm³
Input of liquid[##]	235 dm³ (of which approx. 4 dm³ liquid in the upper abutment)
Flow rate during the last 10 d before the end of the experiment	0.35 cm³/h
Pressure relief	30.04.2020 - 05.05.2020
Dismantling	05.05.2020 - 20.05.2020

*) pump/lower gravel abutment
[#]) without gravel abutments, [##]) without lower gravel abutment

The fluid pressure (P) measured directly behind the pump (pump pressure) differs slightly from the fluid pressure (PP4) measured in the lower gravel abutment. The deviation is larger at higher pressures in particular. In the description of the test the pump pressure is usually specified (rounded values).

Pressure

Prior to hydration of the Sandwich sealing system from the bottom, the ES were flooded individually via pipelines that opened into the respective segments from the top of the steel column. In the process, ES1 was flooded first with Pearson water A3, followed by the lower gravel abutment, then ES2 and finally ES3. The pore space in the gravel abutment was almost completely filled with Pearson water A3, whereas the pore space of the ES was only filled to about 50 %. As ES1 and ES2 were connected via an artificial

EDZ, it can be assumed that part of the liquid from ES2 flowed into ES1 and further filled the pore space of ES1. In addition, it can be assumed that part of the amount of liquid introduced into the ES also penetrated into the adjacent DS below immediately. A further flow of Pearson water A3 into adjacent segments is not taken into consideration (Tab. 5.23).

Tab. 5.23 Flooding of the ES and the lower gravel abutment in HTV-7

flooding step	segment	pore volume	Input of liquid	Flow rate	flooded pore space fraction
		[dm³]	[dm³]	[dm³/h]	[%]
1	ES1	30.6	17.1	9.2	56
2	lower abutment	39.0	38.0	249.1	98
3	ES2	30.2	15.3	9.1	51
4	ES3	29.5	15.8	8.9	54

During hydration the fluid pressure was increased in steps of 0.1 to 0.5 MPa within 90 d and hold at 2 MPa for 55 d (Tab. G. 1). A rapid pressure increase, as originally planned following the experimental regime of HTV-6 (see /EMM 19/), was not possible, since several times after pressure increases, pathways with enhanced liquid flow occurred.

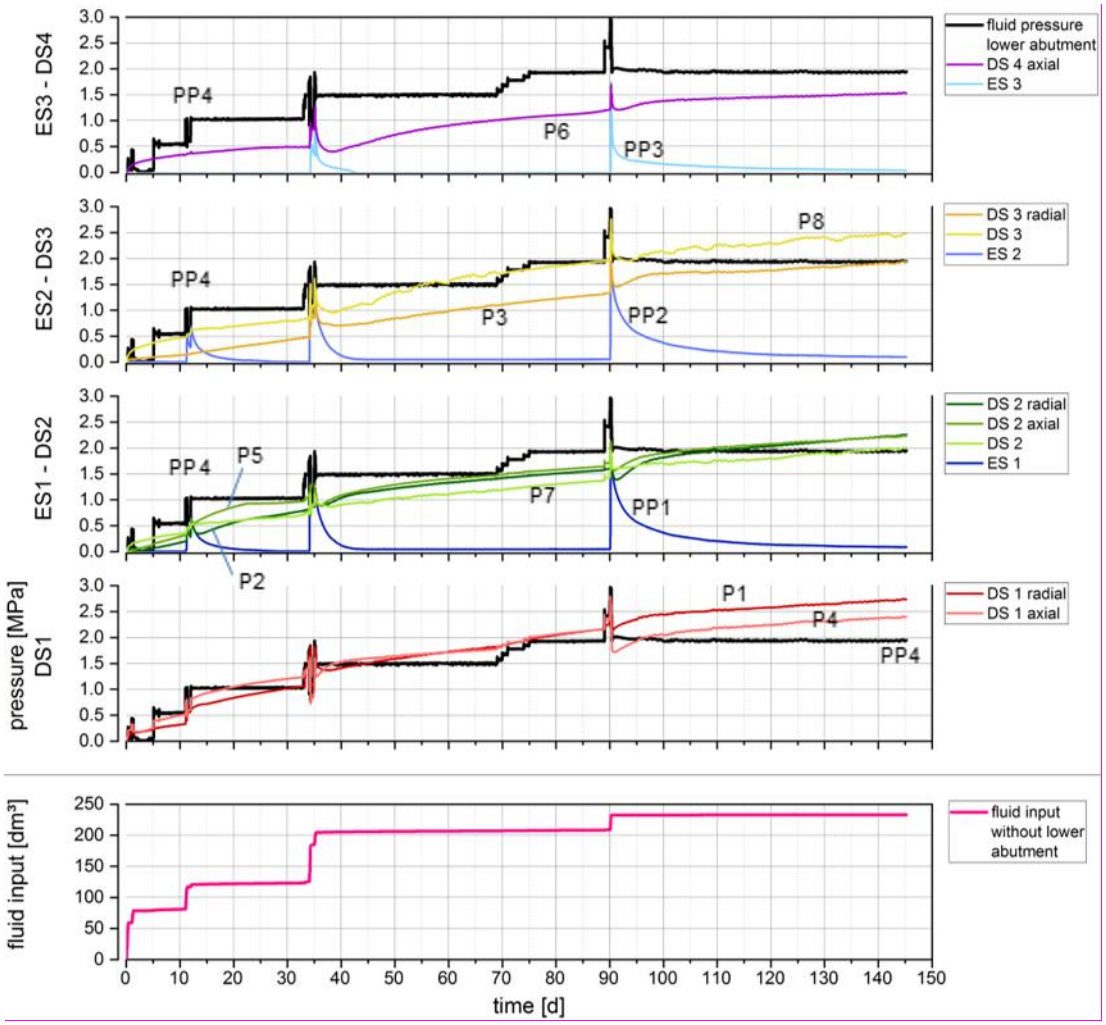

Fig. 5.51 Pressure curves and course of the injected fluid HTV-7

Due to the pre-hydration of all three ES before pressurization, all lower three DS were already hydrated simultaneously from the adjacent ES before the first pressure step. During the first two pressure steps at 0.2 MPa and 0.3 MPa (fluid pressure in the lower abutment), another 32 dm³ of liquid were injected into the segments (Fig. 5.51). The pump was throttled slightly so that the fluid pressure dropped again. After 5 d, the pump pressure was then increased to 0.5 MPa and kept constant for 6 d. When the pressure was further increased to 1.0 MPa after 11 d, a massive penetration of liquid into the lower segments occurred. A sudden increase in pore pressure in ES1 and ES2 to above 0.5 MPa a few hours after the pressure increase indicates that near-complete saturation was reached in the lower two equipotential segments ES1 and ES2 (Fig. 5.51). The pump was switched off for a few hours and then switched on again. After the pump was switched on again, the pore pressure in the two ES rose again. The pump pressure was kept constant at 1.0 MPa for 21 d (Tab. G. 1), sealing the flow paths in DS1, so that the pore pressure in ES1 and ES2 was slowly reduced. The sudden bending of the pressure

curves of the axial and radial pressure transducers in DS2 after a duration of 22 d could indicate a material shift in DS2, in which the material suddenly yielded under the built-up stress. At the same time, there was a sudden slight increase in the pore pressure in ES2, which could indicate a sudden shift in DS.

After 33 d, the pump pressure was increased in individual partial steps to 2.0 MPa. However, pathways in the bentonite again opened up, so that again a lot of liquid penetrated into the segments. Apart from the two lower ES, this time there was also an abrupt increase in the pore pressure in ES3. Subsequently, the pump pressure was reduced to 1.5 MPa and kept constant for 34 d. The pressure was then reduced by small steps. After that, the pressure could finally be increased to the level of 2 MPa with small steps of 0.1 MPa/d within 6 d. After the pressure had been maintained at 2.0 MPa for 14 d, a rapid pressure increase was to be tested again. The first partial stage of 2.5 MPa could still be started and maintained, with the flow rate increasing from 1.8 cm^3/h (mean value over the last 14 h at 2.0 MPa) to 6.6 cm^3/h (at 2.5 MPa). However, the subsequent increase in pressure to 3.0 MPa, one day later, again resulted in the opening of pathways in the bentonite, so that a large amount of liquid was again pumped into the sealing system. The flow rate here was about 6 dm^3/h. Thus, the pump pressure was reduced again to 2 MPa and kept constant for another 55 d until the end of the test. When the fluid pressure in the lower abutment was lowered, the pressures in the segments also fell. The largest pressure drop (approx. 1 MPa) was observed in the axial direction on DS1.

In the last 10 d before the end of the experiment, the flow rate of the liquid into the pressure cell was 0.35 cm^3/h on average (Fig. 5.52). The flow rate was calculated as the first derivative of the fluid volume curve and is shown logarithmically and smoothed in order to better see the progression. The smoothing curve was calculated using the "Savitzky-Golay" method over 150 points using a polynomial order of two. However, due to the smoothing process, peaks that occur in the course are represented too low. As the measurements were not always taken at the same interval, smoothing over data sets with different time intervals may be subject to error. However, as the measurements were taken with constant time intervals for most of the time, this error is considered negligible.

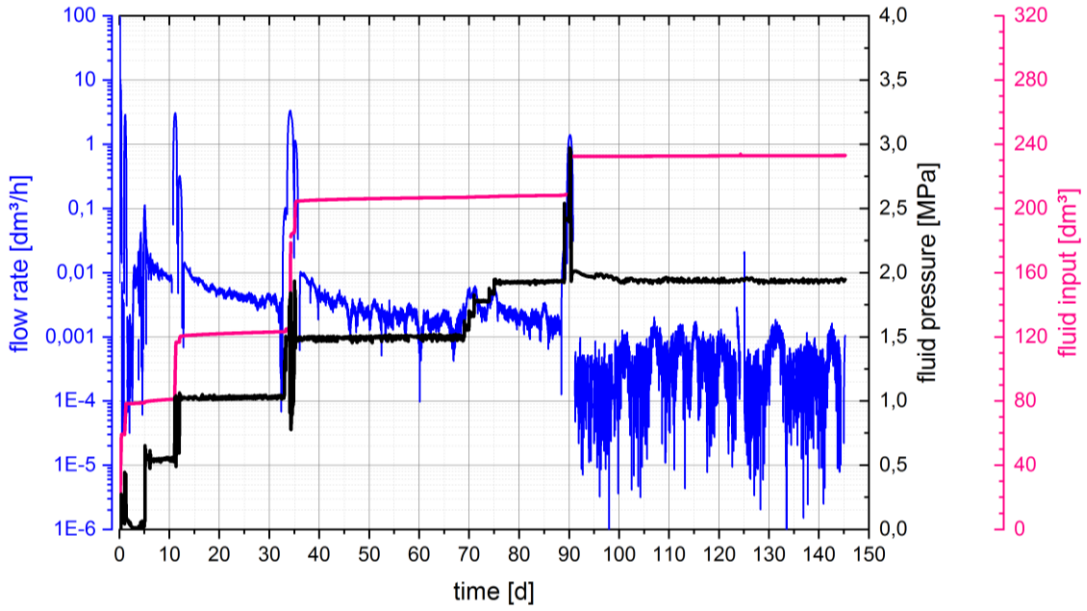

Fig. 5.52 Flow rate, fluid pressure and fluid input into the sealing system in HTV-7

On April 28, 2020, the experiment was stopped after 145 d by disconnecting the liquid supply. By then, a total of 235 dm³ of Pearson water A3 had been pumped into the sealing system (without the lower gravel abutment). After dismantling the test, it was found that the lower gravel abutment (incl. the geotextile) was compressed by 3 mm. This reduced the pore volume in the lower gravel abutment by 1.7 dm³ compared to the installed condition. This volume is taken into account in the final value of the fluid input introduced in the last line in Tab. G. 1. Based on the calculated pore volume in the segments, it could be assumed that all segments in the sealing system were almost completely saturated with Pearson water A3 at the end of the test.

On 30.04.2020, depressurization of the experiment was started by gradually draining fluid from the lower gravel abutment within 7.5 h. The fluid pressure in the lower gravel abutment was brought to near ambient pressure. According to specification, a small residual overpressure of approx. 0.01 MPa was constantly maintained against the underside of the lowest DS (also during the dismantling). In addition, the ES were depressurized by draining liquid through the installed pipelines. Afterwards, the valves were closed again so that an overpressure of 0.9 MPa could build up by 04.05.2020 due to post-swelling of the bentonite (liquid pressure in the lower gravel abutment). One day before the start of dismantling, the overpressure was released by opening the valves again. During depressurization, a total of 2.6 dm³ of liquid were drained from the cell, including 1.2 dm³ directly from the ES.

Fluid propagation

After the start of the hydration at 2 bar (Tab. G. 1), the liquid first arrived in DS1 at S13, followed by S12 and S11, with a nearly immediate reaching of ES1 along the latter two (Fig. 5.53). Distribution back to DS1 and forth to DS2 can be found. At a fluid pressure of 5 bar (day 2) an immediate breakthrough via the EDZ to ES2, top of DS2 and bottom of DS3 occurred. Swelling pressure started in DS1 and reduced liquid inflow.

Liquid pressure was raised stepwise to 15 bar without larger changes in the hydration state until day 18, when next breakthrough occurred on S12, possibly induced by the installed sand lenses. S11 and S13 were not affected, yet. On day 38, S11 followed and, finally S13 reacted the same way on day 41 after increasing pressure to 20 bar. Remaining on this level, a quasi-stable situation established, stopping the liquid progress to DS4 and redistributing liquid between DS1 and DS3. ARDP kept nearly constant in DS1 to DS3, indicating nearly saturation here (Fig. 5.53). Swelling pressure in lower regions reduces inflow of liquid over time and stabilizes the function of the sealing.

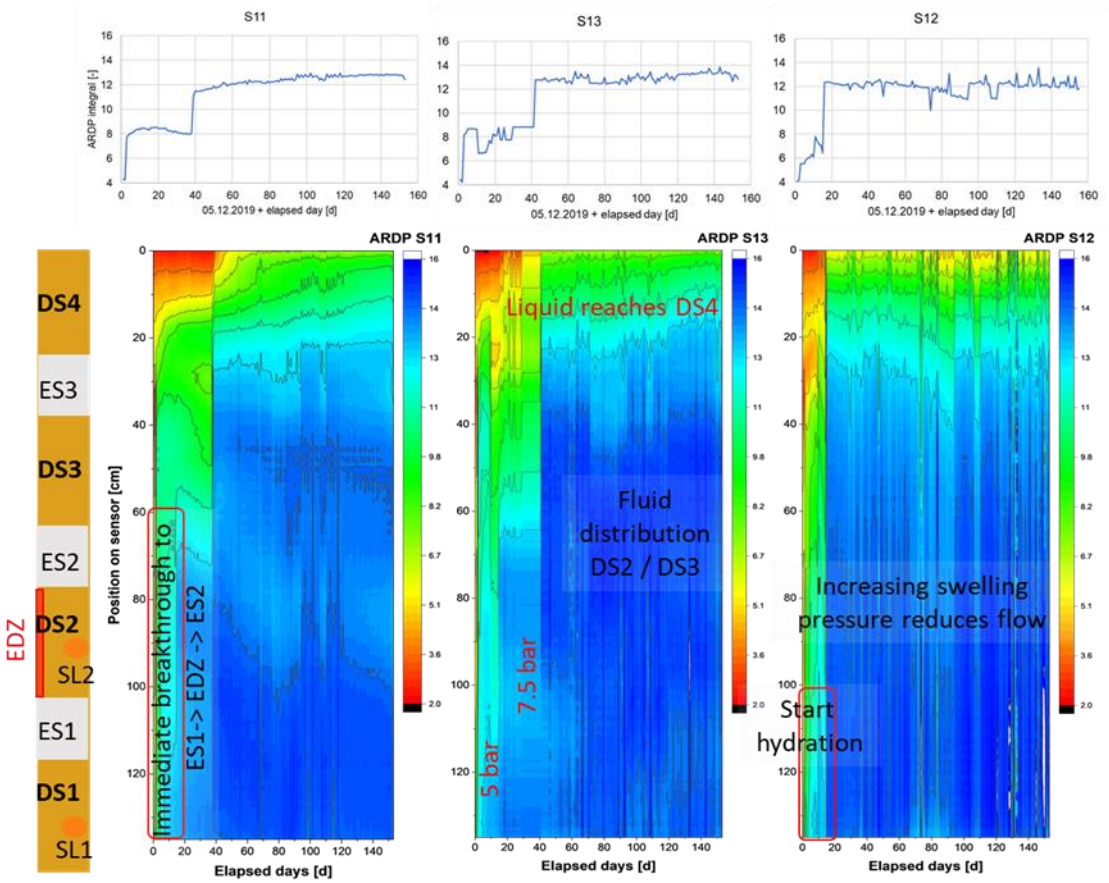

Fig. 5.53 ARDP distribution as indication of liquid progress at three TAUPE sensors, S11, S13 and S12 (bottom). Integral results (top) describe the over-all process

Some difficulties arose from multiplexer contact problems, which caused from time to time some raw signals to be noisy and faulty. Due to the number of measurements taken, this could be compensated for meaningful results. The multiplexer was replaced.

The rapid filling of ES1 and the first breakthrough to ES2 via the artificial EDZ between ES1 and ES2 that led to quick saturation of DS1 after 14 d by increasing the liquid pressure to 7.5 bar was observed by the horizontal TAUPE TDR sensors S14 and S15 (Fig. 5.54). Increasing the pressure to 20 bar induced only a further redistribution of liquid between DS1 and DS3. Building up of swelling pressure reduced the further inflow of liquid. ES2 was not completely saturated, yet.

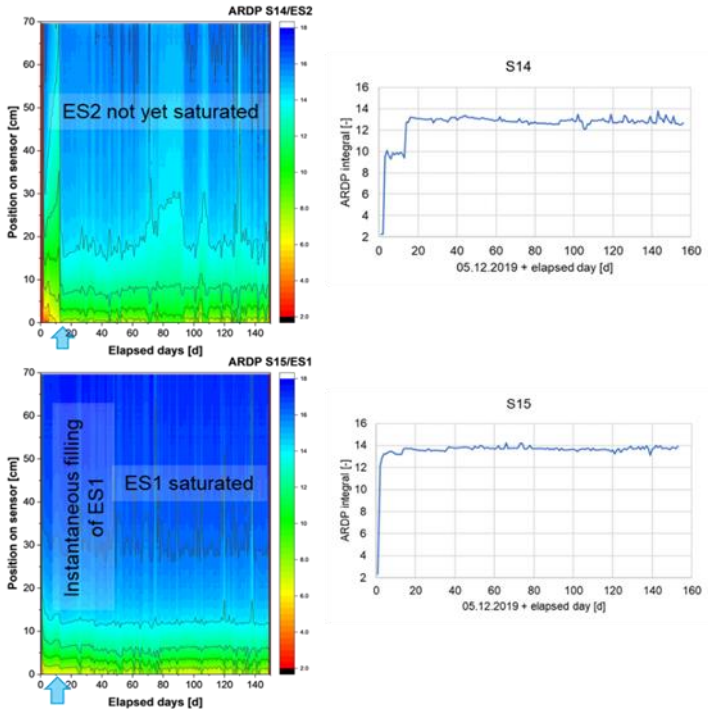

Fig. 5.54 ARDP distribution at horizontal TAUPE TDR sensors (left) and integral ARDP (right) of S15 (in ES1) and S14 (in ES2) describing the overall process in HTV-7

To explain the quick temporal evolution of the liquid transport in HTV-7, vertical cross-sections presenting the interpolation between all three sensors are taken at different dates (Fig. 5.55). Obviously, small differences on the material configuration exists: Close to the wall the dry density seems to be slightly lower than in the center, indicated by lower ARDP values, especially on the S12-side with the sand lenses. After starting the hydration with a liquid pressure of 2 bar, a very rapid inflow of liquid could be found, starting around the center (S13). Liquid has been transported to ES1, then via the artificial EDZ directly to ES2 and through DS3 close to ES3. At day 8 (at 5 bar) building up of swelling pressure has already started and redistribution of liquid in the segments between DS1 and DS3 took place. DS1 has been nearly saturated.

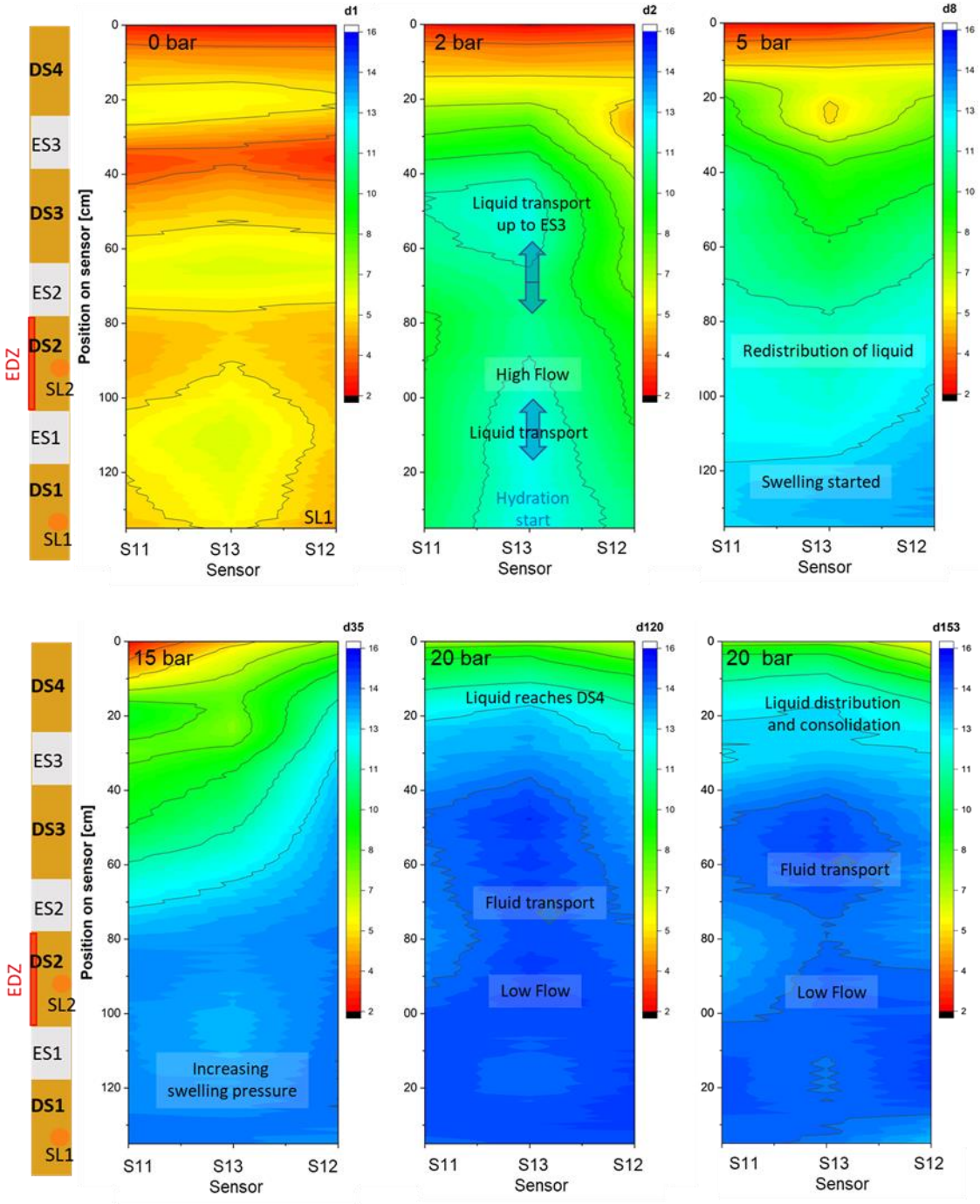

Fig. 5.55 Interpolated ARDP distribution between three vertical TAUPE TDR sensors in HTV-7 (top) taken at day 1, 2 , 8 and (bottom) day 35, 120, 153

This continued by stepwise increase of liquid pressure and at 15 bar, a forced fluid transport in the area of S12, possibly over the two sand lenses in DS1 and DS2, up to ES3 occurred (Fig. 5.55). DS4 has been compressed because of the vertically applied pressure coming from liquid and increasing swelling pressure. DS1 was completely saturated. After 120 days, ES3 and lower parts of DS4 were further affected by the liquid,

DS1 to ES2 was completely saturated, but the inflow of liquid was strongly reduced because of the swelling pressure in the lower DS. After 135 days, the liquid distribution inside the system has been consolidated, even after increasing the pressure to 20 bar. DS4 remained stable and kept the function of sealing perfectly.

Dismantling

After opening the column, the segments were removed within two weeks. All level and segment boundaries were measured. All segment boundaries in the sealing system were shifted upwards during the test due to the fluid pressure and bentonite swelling (Tab. 5.24). The lower three DS expanded due to swelling and compressed the ES in the process. DS1 expanded the most. DS4, on the other hand, has been somewhat compacted. Both gravel abutments were also compressed somewhat by the vertical stress.

The determined position of the segment boundaries is influenced by subsequent heave. The heave was measured and considered in the evaluation of the test in order to approximate the condition of the sealing system before the cell lid was opened. Two variants were calculated to account for the heave. According to variant A, it was assumed that the uplift was only caused by the remaining thickness of the segment that was currently being removed. For variant B, on the other hand, it was assumed that the observed heave was caused by the entire thickness of the bentonite still in place. For both variants, the initial uplift was considered to be the elastic instantaneous strain of all segments.

Tab. 5.24 Displacement and change in segment thickness HTV-7

segment boundary	displacement compared to installation [cm]*			segment	thickness change [%]		
	variant A	variant B	no correction		variant A	variant B	no correction
				upper abutment	-1.5	-1.5	-2.9
DS4 - upper abutment	0.4	0.4	0.7	DS4	-2.9	-1.9	-2.7
ES3 - DS4	1.1	0.8	1.4	ES3	-1.1	-1.1	-0.9
DS3 - ES3	1.3	1.0	1.5	DS3	2.3	2.7	2.5
ES2 - DS3	0.7	0.3	0.9	ES2	-2.2	-2.2	-2.0
DS2 - ES2	1.0	0.7	1.2	DS2	2.3	2.3	2.5
ES1 - DS2	0.5	0.1	0.6	ES1	-3.6	-3.6	-4.7
DS1 - ES1	1.0	0.6	1.3	DS1	5.5	4.0	6.5
lower abutment - DS1	-0.3	-0.3	-0.3	lower abutment	-1.8	-1.8	-1.8

*) positive value: upward shift, negative value: downward shift

Water content and density

After opening the cell on 05.05.2020, it became apparent that the liquid from pressurization had penetrated to the lid. The N45 sand between the gravel stones was somewhat moist. The binary mixture in DS4 had already swollen to a uniform plastic matrix at the top level. The top level in DS4 was already heavily soaked with an average water content (105 °C) of 33 %. A few centimeters below the top, the bentonite was already visibly drier, as indicated by the clearly lighter area after removal of the top centimeters (Fig. 5.56). In all DS, the area at medium depth was drier than the areas near the top and bottom of the segments. In addition, in DS4, DS3, and DS2, the upper area of the segments was slightly wetter than the lower.

Presumably, the liquid was able to penetrate DS4 at local points and spread in the sand of the upper gravel abutment and then moistened DS4 from above. In the case of DS3 and DS2, it can be assumed that a lot of liquid was already able to enter the DS from above during the flooding of the ES and afterwards.

Fig. 5.56 Bentonite in DS4 of HTV-7

Left: Top of upper level prior to sampling, dry area (arrow) below P6.
Right: Towards the middle depth, the bentonite became drier.

In DS4, the bentonite in the front area between 120° and 240° was wetter than in the rest of the segment volume. When DS4 was removed, worm-like sand fingers (Fig. 5.57) were found in this front area in the spaces between the pillows. These sand fingers were also found in deeper levels of the segment. In addition, small holes with a moist looking rim were found in the bentonite. Similar sand areas were also found in DS3 and DS2. It can be assumed that the pore space in the binary mixture was not sufficiently tightly sealed with BGM. Presumably, liquid had penetrated into the DS through small, interconnected pores. Flooding of the ES probably flushed sand from above into the respective DS below, or dry sand had already trickled into the DS during installation. Sand could not penetrate into DS1 because a geotextile was laid on the top side.

Fig. 5.57 Sand areas in DS4 of HTV-7

Left: Front of DS4.
Right: Worm-like sand band in the middle level of DS4 at sampling location 9.

The areas below the P6, P5 and P4 axial surface pressure transducers at DS4, DS2 and DS1 were comparatively drier. They shielded the area in the bentonite from liquid inflow from the overlying ES.

In DS3, the core area was drier over the entire segment thickness and the water content increased outward over the entire circumference. In contrast, in DS2 the area around the center of the cross section had the highest water content. Sand veining was also found in this area. The right side of DS2 (at 30° to 150°) was drier than the rest of the segment volume. The sand lens in DS2 appeared completely dry. However, at one point the adjacent bentonite was somewhat darker (i.e. wetter). Presumably, the liquid inflow to the sand lens was so low that the bentonite was able to completely soak up the amount of liquid. Most likely, the flow paths had occurred mainly along the EDZ and in the area in the center of the cross section. In DS1, the area to the left of the center in the upper level had the highest moisture, whereas the middle level had the lowest water content there. In the lowest level, the area around the center of the cross section had the highest water content. The sand lens had a low water content (105 °C) of 1 %. For DS1 and DS2, the water content of the sand lenses was not included in the respective distribution (level E12 and E17) because of the different material (Fig. 5.58).

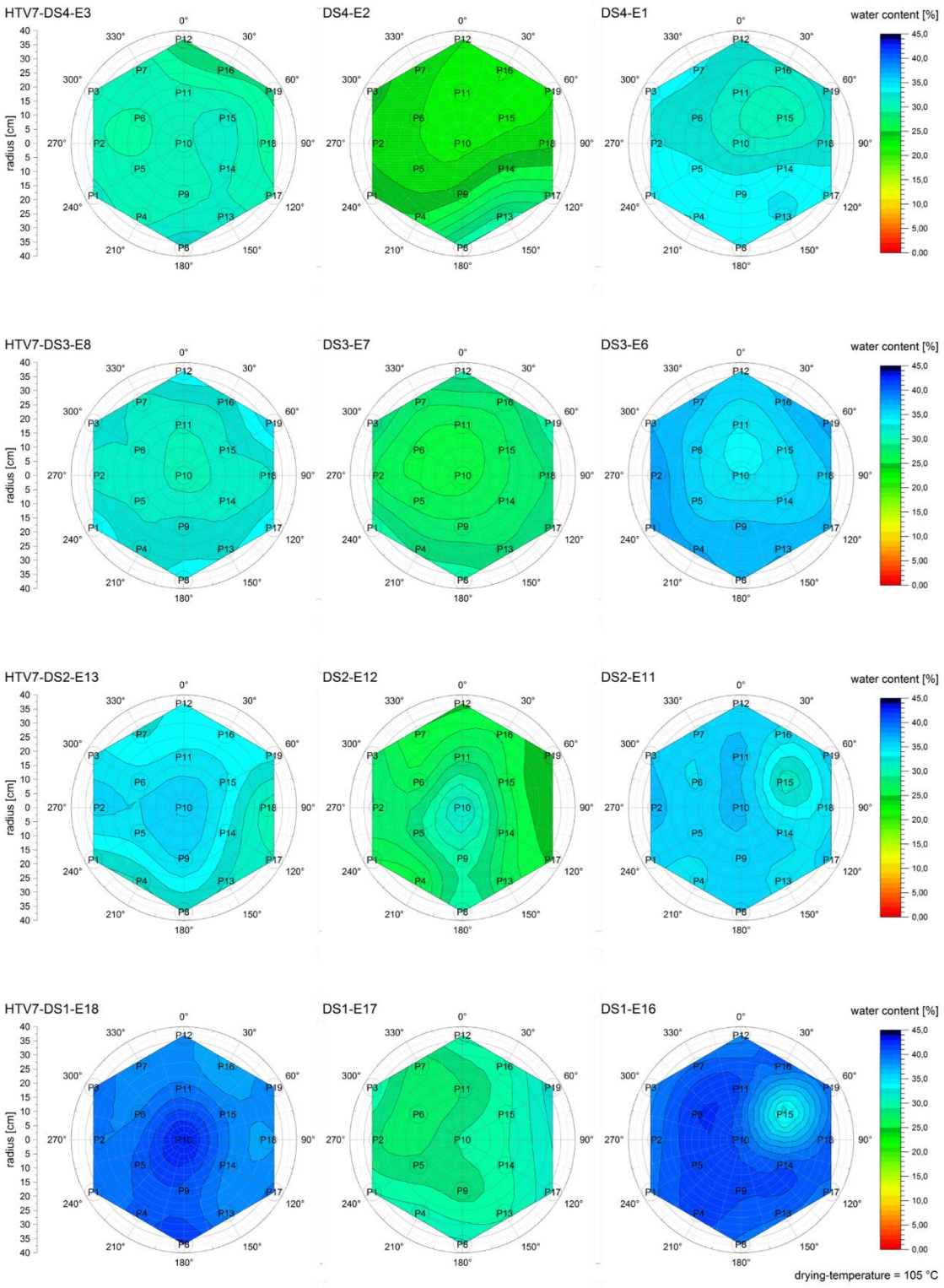

Fig. 5.58 Water content distribution for HTV-7 in the DS, upper, middle and lower levels (from left)

The mean densities from the samples agree relatively well with the integrally determined densities (Tab. 5.25 and Tab. 5.26). The integral values of the segments were calculated

on the basis of the installation mass and the segment boundaries. The measured heave was considered in the integral calculation for dry density and saturation (variant A and variant B).

Tab. 5.25 Water content, dry density and saturation (105 °C) of HTV-7 after dismantling

segment	**level**	**water content [%]**	**sample**				**integral**	
			dry density [g/cm³]		saturation [-]		dry density [g/cm³]	saturation [-]
		/level	/level	mean	/level	mean		
Sand in upper abutment	E01	2.1						
	E02	6.8						
DS4	E1	32.8	1.45	1.50	1.05	0.99	A: 1.51 B: 1.49 no c.: 1.50*	A: 1.02 B: 0.99 no c.: 1.01
	E2	24.4	1.56		0.92			
	E3	30.3	1.48		1.01			
ES3	E4	12.8					A, B: 1.62 no c.: 1.62	A, B: 0.77 no c.: 0.76
	E5	24.0						
DS3	E6	36.1	1.39	1.45	1.05	1.02	A: 1.46 B: 1.46 no c.: 1.46	A: 1.05 B: 1.04 no c.: 1.04
	E7	27.8	1.51		0.98			
	E8	32.4	1.45		1.03			
ES2	E9	13.2					A, B: 1.63 no c.: 1.63	A, B: 0.78 no c.: 0.77
	E10	23.5						
DS2 (bentonite)	E11	35.2	1.41	1.47	1.06	1.04	A: 1.46 B: 1.46 no c.: 1.46	A: 1.04 B: 1.04 no c.: 1.03
	E12	27.0	1.57		1.02			
	E13	33.4	1.44		1.03			
ES1	E14	23.0					A, B: 1.65 no c.: 1.67	A, B: 1.04 no c.: 1.08
	E15	24.8						
DS1 (bentonite)	E16	39.8	1.33	1.39	1.06	1.04	A: 1.42 B: 1.44 no c.: 1.41	A: 1.11 B: 1.14 no c.: 1.08
	E17	29.6	1.49		1.00			
	E18	39.4	1.34		1.06			

*) no c. – without heave correction

Tab. 5.26 Water content, dry density and saturation (200 °C) of HTV-7 after dismantling

segment	level	water content [%]	sample				integral	
			dry density [g/cm³]		saturation [-]		dry density [g/cm³]	saturation [-]
		/level	/level	mean	/level	mean		
Sand in upper abutment	E01	2.1						
	E02	6.8						
DS4	E1	34.5	1.43	1.48	1.03	0.98	A: 1.49 B: 1.47 no c.: 1.49*	A: 1.00 B: 0.97 no c.: 0.99
	E2	25.9	1.54		0.91			
	E3	31.9	1.47		0.99			
ES3	E4	12.8					A, B: 1.62 no c.: 1.62	A, B: 0.77 no c.: 0.76
	E5	24.0						
DS3	E6	37.8	1.37	1.43	1.03	1.00	A: 1.45 B: 1.44 no c.: 1.44	A: 1.03 B: 1.02 no c.: 1.02
	E7	29.5	1.49		0.96			
	E8	34.1	1.43		1.01			
ES2	E9	13.2					A, B: 1.63 no c.: 1.63	A, B: 0.78 no c.: 0.77
	E10	23.5						
DS2 (bentonite)	E11	36.9	1.39	1.46	1.04	1.02	A: 1.45 B: 1.44 no c.: 1.44	A: 1.02 B: 1.02 no c.: 1.01
	E12	28.6	1.55		1.00			
	E13	35.1	1.42		1.02			
ES1	E14	23.0					A, B: 1.65 no c.: 1.67	A, B: 1.04 no c.: 1.08
	E15	24.8						
DS1 (bentonite)	E16	41.6	1.31	1.37	1.04	1.02	A: 1.40 B: 1.42 no c.: 1.39	A: 1.08 B: 1.12 no c.: 1.06
	E17	31.3	1.47		0.98			
	E18	41.3	1.32		1.04			

*) no c. – without heave correction

The bentonite was able to swell and expand more at the top and bottom of the DS than in the central area of the segments. Higher water contents and lower dry densities were found in the area of the segment boundaries in the deconstruction condition than in the installation condition. In contrast, the central area of segments DS2 and DS4 was further compacted during the test. There, the dry densities are higher than in the installed state. The swelling pressure acted as a driving force for the compaction of the central area. However, the fluid pressure applied from below will also have contributed to the compaction of the central area.

The calculation of the saturation shows that the pore space of the lower three DS was completely saturated with liquid and that almost complete saturation was also achieved

in DS4. The fact that saturation values greater than one were determined shows the need to analyze the pore space calculation more closely.

It should be noted that all densities and saturation values determined on samples do not apply directly to the state at the end of pressurization, but to a changed state during dismantling. It cannot be ruled out that the water contents near the boundaries of the DS were lower at the end of the test than at the time of dismantling. By correcting the segment thickness, the saturation values increase when using the undiminished water contents.

All equipotential segments ES3, ES2 and ES1 were almost completely saturated with Pearson water A3 in the lower part. However, in the upper region of ES3 and ES2, the pore space was only about half filled with liquid (Tab. 5.27). It cannot be ruled out that the bentonite continued to absorb liquid from the ES after the liquid pressure reduction and dismantling, so that the upper part of ES3 and ES2 was no longer fully saturated. The upper area in ES1, on the other hand, remained almost saturated, presumably because liquid from ES2 was able to run in via the EDZ.

Tab. 5.27 Saturation of the ES levels

segment	level	saturation (105 °C and 200 °C) [-]	
		variant A, B	no heave correction
ES3	E4	0.53	0.53
	E5	1.00	1.00
ES2	E9	0.56	0.55
	E10	0.99	0.99
ES1	E14	1.01	1.04
	E15	1.08	1.12

Ion transport and cation exchange

The conductivity measurements converted into NaCl content (LF-salt) show a distribution similar to that of water content (Fig. 5.59). LS-salt content in DS decreased slightly through the column, with mean values of 0.41, 0.39, 0.40 and 0.38 wt.% in DS1 to DS4 respectively. Higher values were observed in sampling levels at the edges of DS (“outer” levels, adjacent to ES) than for sampling levels in the middle of DS (“inner” sampling levels, bentonite adjacent). In DS1 the values obtained were 0.41, 0.37 and 0.45 wt.% moving up through the DS from E18 to E16. The difference between inner and outer levels increased slightly moving up the column. In DS4 the values were 0.38, 0.33 and

0.43 wt.% for E3 – E1. In all DS, the difference between the inner and outer sampling levels was greater on the upper side of the DS. In ES, the lower sampling levels (E15, E10 and E5) had higher LF-salt than the upper sampling level in the same ES (E14, E9 and E4 respectively). The difference between ES sampling levels increased moving up the column. For example, in ES1 LF-salt content was 0.28 and 0.25 wt.% for E15 and E14, while in ES2 this was 0.31 and 0.17 wt.% (E10 and E9), and in E3 0.36 and 0.11 wt.% for E5 and E4. Concentrations of selected soluble ions were also converted into NaCl (from $Na^{+}{}_{sol}$ and $Cl^{-}{}_{sol}$, referred to as Na-salt or Cl-salt) or Na_2SO_4 (from $SO_4^{2-}{}_{sol}$, abbreviated SO_4-salt) concentrations. When compared to LF-salt, there are clear differences in the distribution of salt content, although the distribution of Na-salt is relatively similar but at a lower salt content.

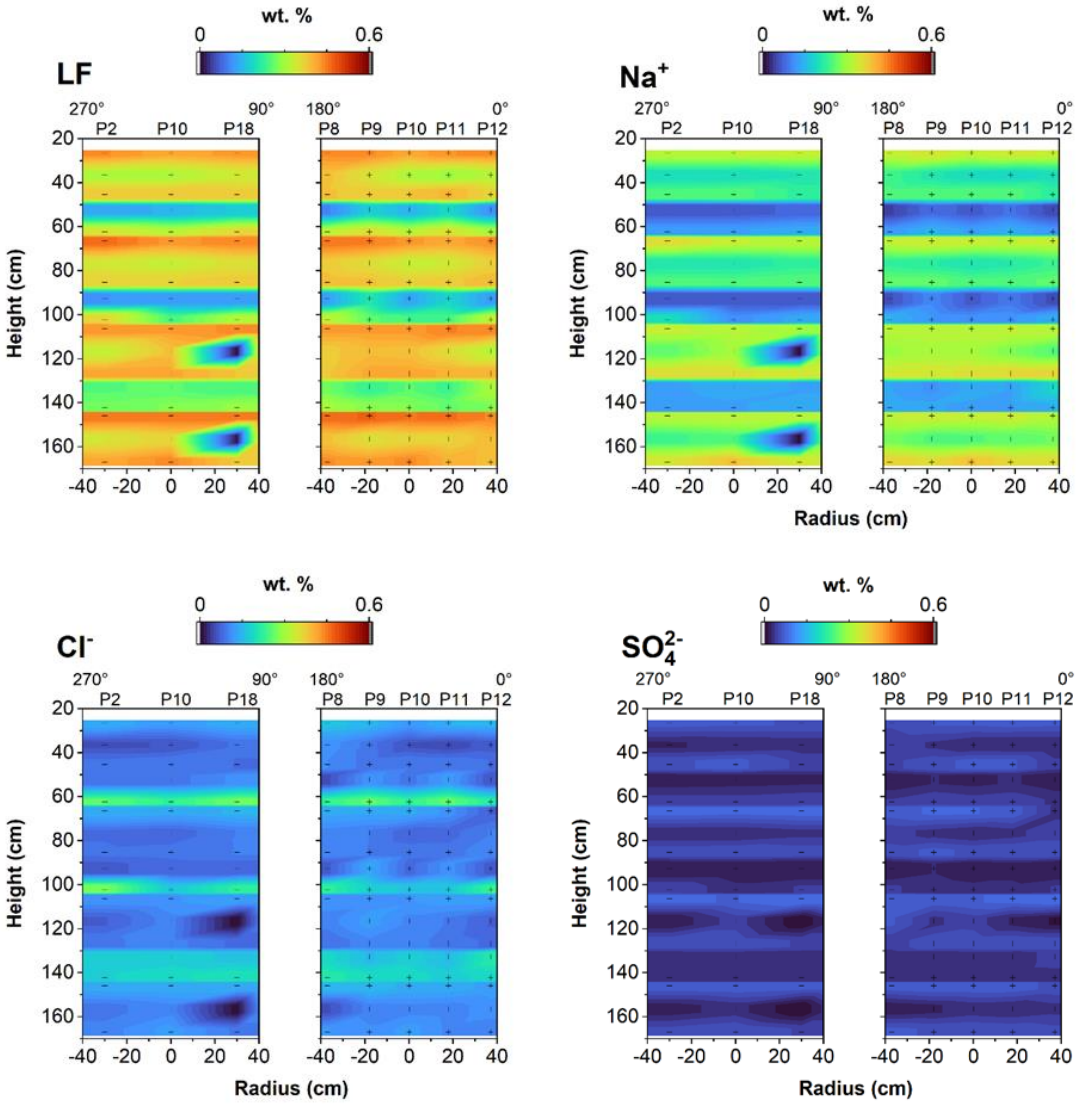

Fig. 5.59 Distribution of LF-salt, Na-salt, Cl-salt and SO4-salt in the HTV-7. Sampling points are indicated by black crosses

Concentration of Na^{+}_{sol} was around twice as high in DS sampling levels than in ES (Fig. 5.60). Outer DS sampling levels had higher mean concentration than inner levels. Average concentration in a DS decreased slightly moving up through the column from 5.4 cmol(+) kg^{-1} in DS1 and DS2 to 4.6 and 4.5 cmol(+) kg^{-1} in DS3 and DS4. A similar decrease was observed in ES from 2.3 cmol(+) kg^{-1} in ES1 to 1.9 and 1.7 cmol(+) kg^{-1} in ES2 and ES3. In ES1 E4 and E5 had almost equal concentrations of 2.3 and 2.4 cmol(+) kg^{-1}, while in ES2 and ES3 there was a difference of close to 1.0 cmol(+) kg^{-1} between the lower and upper sampling levels, e.g. E9 and E10. The highest concentration was in E18 (6.4 cmol(+) kg^{-1}), with the next highest concentrations 6.0 and 5.9 cmol(+) kg^{-1} recorded in E1 and E13 respectively. Lowest DS concentration was 3.5 cmol(+) kg^{-1} in E2.

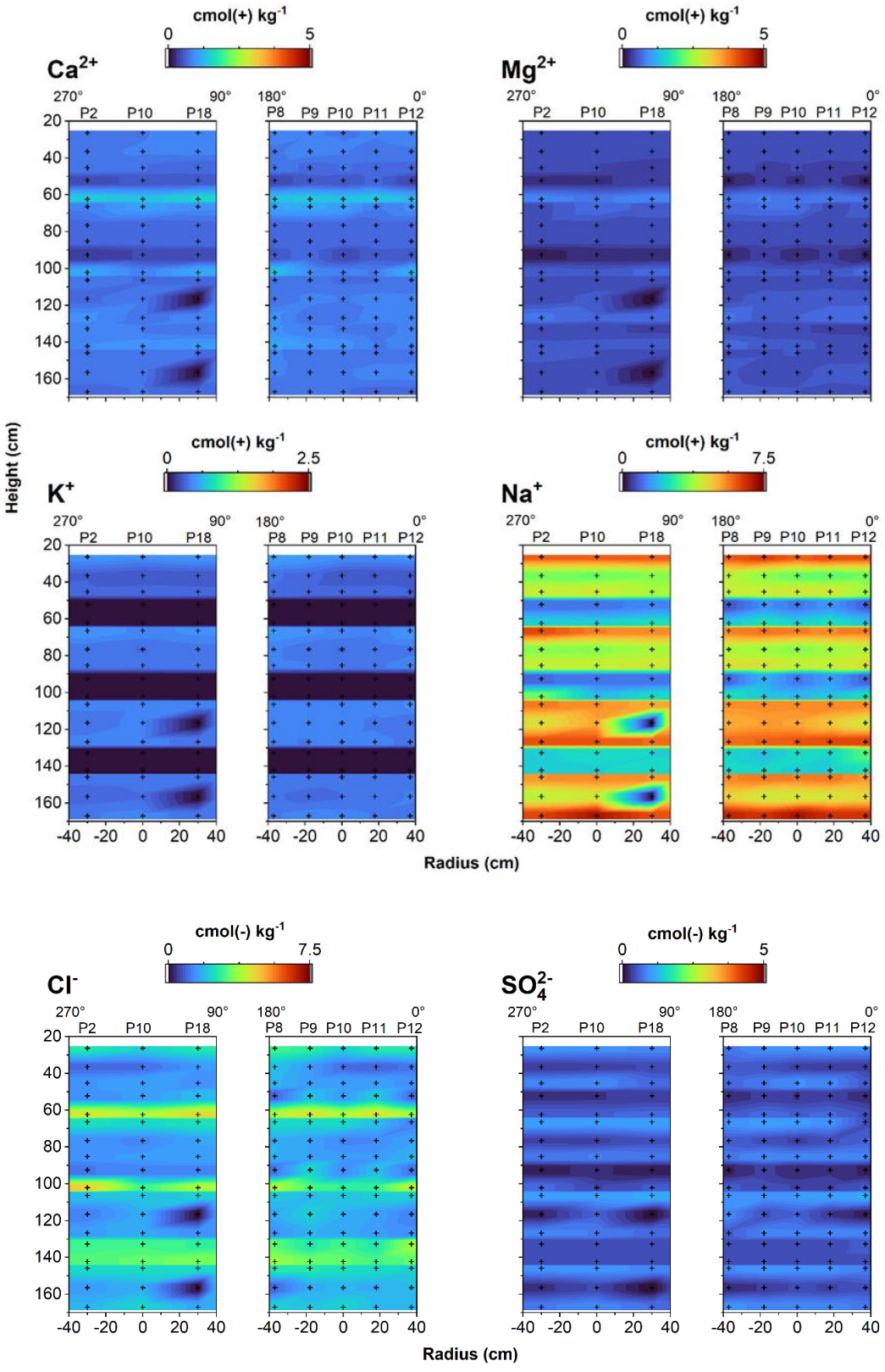

Fig. 5.60 Distribution of soluble ions in the HTV-7. Black crosses indicate sampling points

A similar distribution pattern was found for K^{+}_{sol}, however concentrations in ES << 0.1 cmol(+) kg^{-1}. Mean concentration in DS increased from 0.37-0.42 cmol(+) kg^{-1} between DS1 and DS3 before decreasing to 0.36 cmol(+) kg^{-1} in DS4, but differences are not significant. A very small decrease in concentration of K^{+}_{sol} in ES was observed moving up the column, but again the difference was not significant. K^{+}_{sol} concentrations in DS sampling levels were between 0.29 cmol(+) kg^{-1} (E2) and 0.49 cmol(+) kg^{-1} (E1). DS consistently had higher concentrations in outer sampling levels than inner sampling levels.

The distribution of Ca^{2+}_{sol} and Mg^{2+}_{sol} in the HTV- 7 column was very similar but Ca^{2+}_{sol} consistently had a higher concentration. Concentration maxima can be seen in the lower sampling levels of ES2 and ES3, with values of 1.4 and 1.1 cmol(+) kg^{-1} for Ca^{2+}_{sol} and 0.8 and 0.6 cmol(+) kg^{-1} for Mg^{2+}_{sol}. There is a small peak in Ca^{2+}_{sol} in ES1 but this is not evident for Mg^{2+}_{sol} but rather there is a peak in E13 where the concentration is 0.7 cmol(+) kg^{-1}. Concentrations of both are higher than the DS average in E6, with Ca^{2+}_{sol} 1.0 cmol(+) $^{kg-1}$ and Mg^{2+}_{sol} 0.6 cmol(+) kg^{-1}. There is no clear trend between inner and outer DS sampling levels as observed for Na^{+}_{sol} and K^{+}_{sol}. The concentration of Ca^{2+}_{sol} was similar in all DS at 0.7 – 0.8 cmol(+) kg^{-1} and the variation was not significant. the concentration of Mg^{2+}_{sol} in DS1, DS2, and DS3 was similar at 0.5 – 0.6 cmol(+) kg^{-1} and that of DS4 was lower (0.5 cmol(+) kg^{-1}), but again, differences were not significant.

Maxima of Cl^{-}_{sol} were also located in ES sampling levels and increased going up the column from 3.4 cmol(-) kg^{-1} in E15, to 3.6 cmol(-) kg^{-1} in E10 and 4.1 cmol(-) kg^{-1} in E5. In E14 the concentration was also high at 3.0 cmol(-) kg^{-1}, but the concentration in E9 and E4 was in the range of the majority of DS sampling levels which had concentrations between 1.3-1.9 cmol(-) kg^{-1}. Concentrations in E6, E11 and E16 values higher, between 2.0-2.5 cmol(-) kg^{-1} and ES1 also had a higher concentration at 2.7 cmol(-) kg^{-1}. In contrast to the clear maxima in Cl^{-}_{sol} concentrations, $SO_4^{2-}{}_{sol}$ concentrations appear to fluctuate in a regular fashion around an average value of 0.6 cmol(-) kg^{-1}. Highest concentrations are in outer DS sampling levels (ES adjacent), and vary between 0.9 – 1.0 cmol(+) kg^{-1}. Maximum concentration is in E6 and E11. Values in ES and inner DS sampling levels are similar and vary between 0.3 – 0.6 cmol(-) kg^{-1}, with minimum values in E9, E4 and E12. In the upper ES (ES2 and ES3) the values between the two sampling levels are similar.

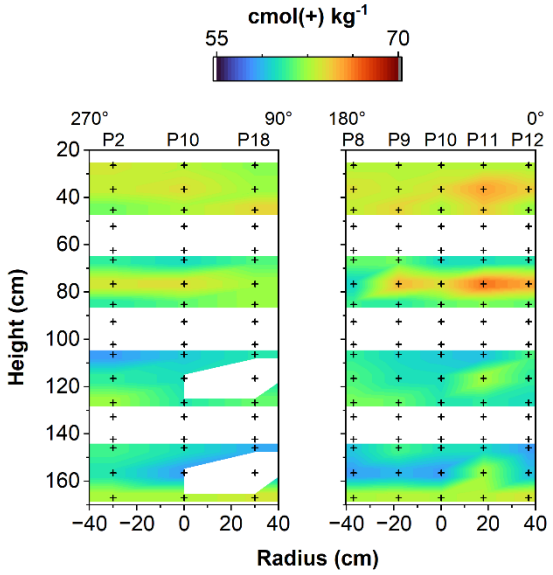

Fig. 5.61 CEC in DS of HTV-7. Black crosses indicate sampling points

Chemical and physical properties of the raw Calcigel bentonite used in the HTV-7 experiment (Tab. 5.9, Tab. 5.10) are used as reference values for the analysis of the samples removed from the experimental column, however due to the reduction in CEC caused by heating of the material for water content measurements the absolute value of exchangeable cation populations is not comparable. Within a sampling level, samples were fairly homogeneous and had a variation of up to 5 cmol kg^{-1} in E7 and E12, which was slightly more than expected for the Cu-trien method. The mean CEC of DS increased through the column from DS1 to DS3+DS4 with values of 63, 62, and 61 cmol(+) kg^{-1} (Fig. 5.61). However, the variation between different sampling levels within a single DS was not similar for all DS. DS1 and DS3 had more consistent values between sampling levels, with variation of 1 – 2 cmol(+) kg^{-1}, while in DS2 and DS4 variation was 3 – 4 cmol(+) kg^{-1} between the sampling levels.

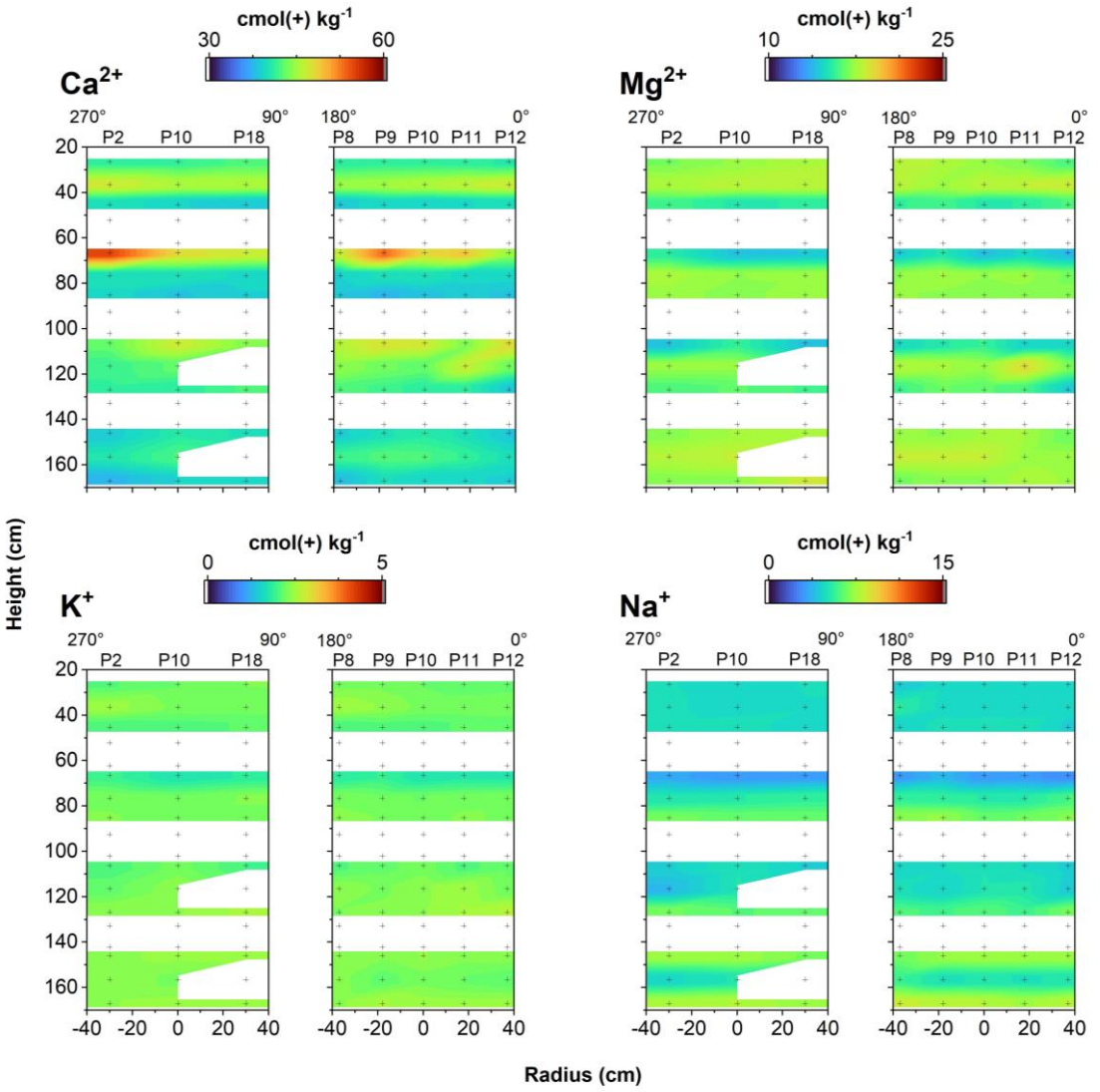

Fig. 5.62 Perpendicular vertical cross-sections of exchangeable cations (total minus soluble ions) in the HTV-7. Black crosses indicate the position of sampling points

The sum of exchangeable ion content varied between 60.4 and 78.9 cmol kg^{-1} for all samples measured. However, the mean values for each DS were 66.3 cmol(+) kg^{-1} in DS1, 66.4 cmol(+) kg^{-1} in DS2, 66.2 cmol(+) kg^{-1} in DS3, and 66.1 cmol kg^{-1} in DS4. Variation was greatest in DS4 with mean values of 65.2, 71.0 and 62.1 cmol(+) kg^{-1} for E1, E2 and E3. In comparison, DS1 had the least variation with mean values of 65.9, 66.5, and 66.6 cmol(+) kg^{-1} in E16, E17 and E18.

The variation in EC content was not consistent with variation in CEC. On average over DS, $Na^{+}{}_{exch}$ concentration decreased moving up through the column from

3.7 cmol(+) kg^{-1} in DS1, to 5.0 and 5.2 cmol(+) kg^{-1} in DS2 and DS3, and finally to 4.8 cmol(+) kg^{-1} in DS4 (Fig. 5.62, Fig. 5.63).

In contrast, $Ca^{2+}{}_{exch}$ concentration was significantly lower (39.8 cmol(+) kg^{-1}) in DS1 compared to the remaining DS (43.2, 42.5 and 42.2 cmol(+) kg^{-1} for DS2, DS3 and DS4 respectively).

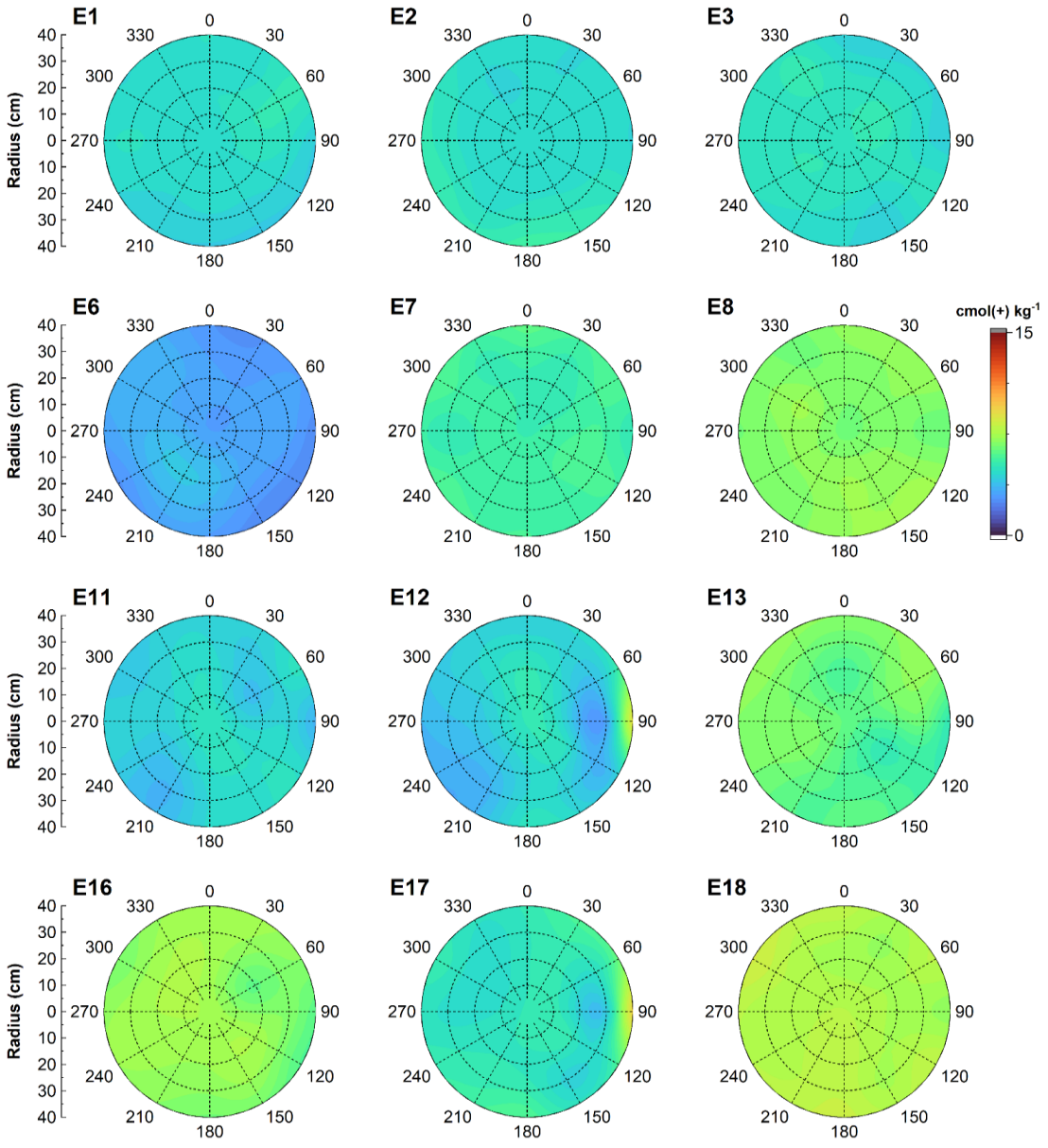

Fig. 5.63 $Na^{+}{}_{exch}$ distribution in DS sampling levels in the HTV-7 experimental column

Variation in $Mg^{2+}{}_{exch}$ concentration did not show a clear trend with values of 17.6, 15.9, 16.3 and 17.0 cmol(+) kg^{-1} from DS1 to DS4.

Average DS K^{+}_{exch} concentration varied only between 2.1 – 2.3 cmol(+) kg^{-1}, with standard deviations of 0.1 – 0.2 cmol(+) kg^{-1}, indicating the variation was not significant. On the scale of individual sampling levels, there was a tendency for concentration of Ca^{2+}_{exch} and Mg^{2+}_{exch} to be lower in outer DS sampling levels, while the concentration of Na^{+}_{exch} increased. The decrease was greatest for Ca^{2+}_{exch}, and was the most pronounced in DS1, where Ca^{2+}_{exch} concentrations were 39.0 cmol(+) kg^{-1} in E18, 39.2 cmol(+) kg^{-1} in E16, and 41.2 cmol(+) kg^{-1} in E17. This was accompanied by Na^{+}_{exch} concentrations of 7.7 and 7.1 cmol(+) kg^{-1} in E18 and E16, and 5.1 cmol(+)kg^{-1} in E17, and Mg^{2+}_{exch} concentrations of 17.4, 18.0, and 17.2 cmol(+) kg^{-1} for E18, E17 and E16 respectively. In E11 and E6 the behavior of Ca^{2+}_{exch} and Na^{+}_{exch} was reversed, so while there was a decrease in Mg^{2+}_{exch} (14.6 cmol(+) kg^{-1} in E11 and 14.4 cmol(+) kg^{-1} in E6), Na^{+}_{exch} also *decreased* (4.4 and 3.2 cmol(+) kg^{-1} in E11 and E6) while Ca^{2+}_{exch} *increased* (45.3 cmol(+) kg^{-1} in E11 and 49.0 cmol(+) kg^{-1} in E6). The concentrations of K^{+}_{exch} did not show any consistent trend between inner and outer DS sampling levels. In DS1 concentrations in outer sampling levels were 2.4 (E18) and 2.3 cmol(+) kg^{-1} (E16) and 2.2 cmol(+) kg^{-1} in E17, while in E13 concentration was also higher at 2.4 cmol(+) kg^{-1} than in E12 (2.3 cmol(+) kg^{-1}) and E11 (2.1 cmol(+) kg^{-1}). The lowest concentration was in E6 at 1.8 cmol(+) kg^{-1}.

Variation within a sampling level was highest for Ca^{2+}_{exch} in sampling levels with highest concentrations (E6 and E11, standard deviations 3.9 and 1.8 cmol(+) kg^{-1} respectively). The standard deviations of Ca^{2+}_{exch} concentrations of all remaining sampling levels were 0.6 – 1.0 cmol(+) kg^{-1}. For the remaining ions, there was no clear link between concentration and variation. Highest variation of Mg^{2+}_{exch} was 0.6 cmol(+) kg^{-1} in E1, E6, and E16, while for Na^{+}_{exch} it was 0.5 cmol(+) kg^{-1} in E12 and E13, and for K^{+}_{exch} 0.2 cmol(+) kg^{-1} in E13. There was no indication that the presence of hydraulic shortcuts influenced variation in either E17 or E12 for any of the cations.

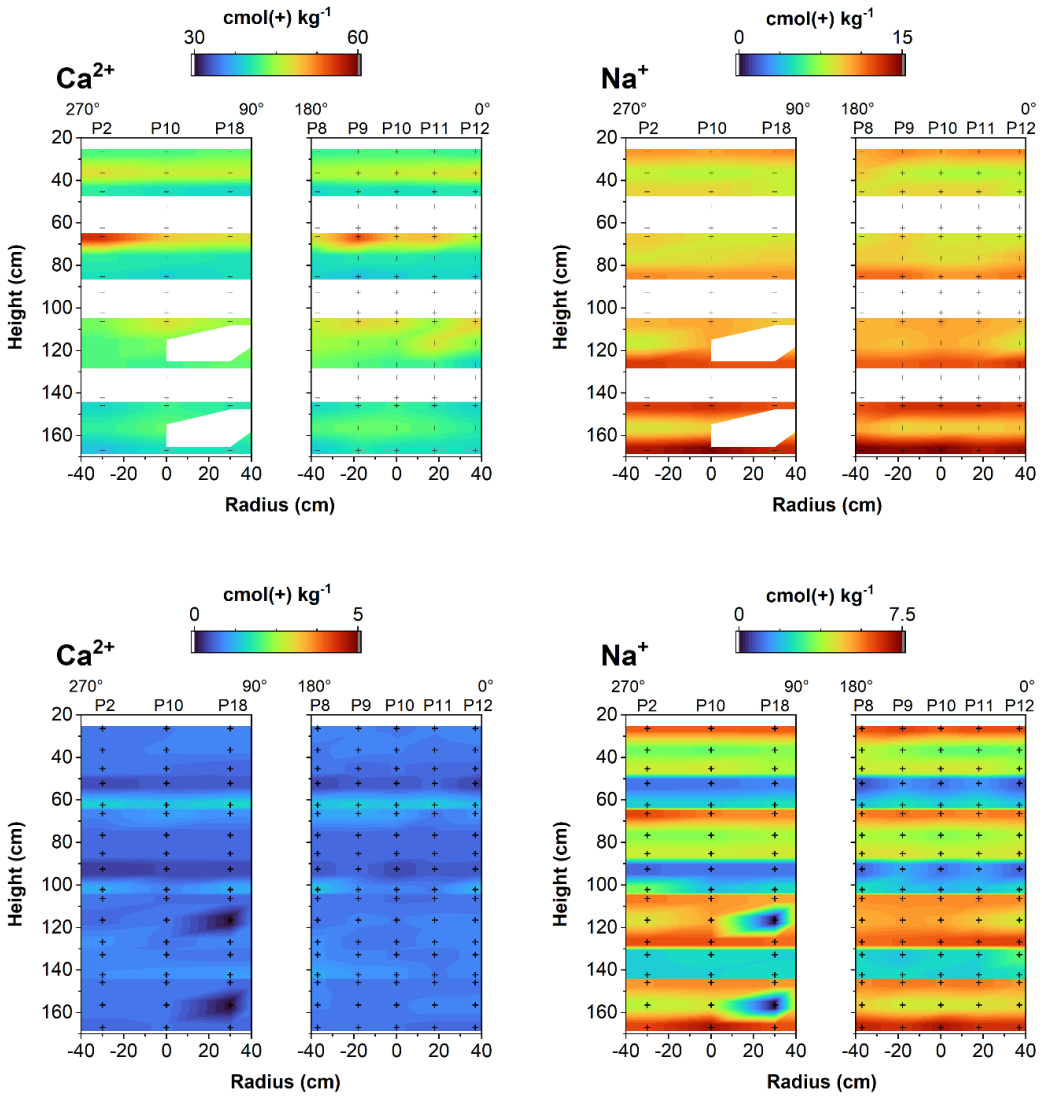

Fig. 5.64 Exchangeable (top) and soluble (bottom) Ca^{2+} and Na^{+} ions. White patches in the exchangeable ion distribution represent sand lenses or ES sampling levels where CEC/EC was not measured. Black crosses represent sampling points

Discussion

There was a strong linear correlation (R^2 = 0.92) between the water content and the salt content calculated from conductivity measurements (LF-salt), suggesting that the infiltrating fluid is the major control on the fluid composition. The sampling levels were divided into groups based on DS/ES nature, with sampling levels from ES having lower water and salt contents compared to DS sampling levels. ES water content was not consistent with height in the column, but rather E5 had a higher hydration and salt content, followed by E10, E15, E14, E9, and E4 in decreasing order. The ES were

prehydrated prior to hydration of HTV-7. In this case, the lower ES would have been next to dry bentonite for longer than upper ES, in which water uptake of adjacent bentonite could be higher lower in the column, e.g. greater in E15 than E5. Hydration from the infiltrating fluid is a gradual process and may not have been sufficient to completely counter this effect, which could contribute to some of the top-to-bottom differences in water content. Within a specific ES, the upper sampling levels E4, E9, and E14, had consistently lower water contents than the lower sampling levels within the same ES, E5, E10, and E15 respectively.

Concentrations of soluble ions in the pore fluid are the result of a complex equilibration involving the smectite interlayer cation composition (starting material Calcigel is a Ca^{2+}-Mg^{2+} bentonite), the composition of the infiltrating fluid (Pearson water A3, 120 mmol L^{-1} Na^{+}, 130 mmol Cl^{-}), and the dissolution of slightly soluble phases such as calcite and dolomite. ${Ca^{2+}}_{sol}/{Na^{+}}_{sol}$ and ${Mg^{2+}}_{sol}/{Na^{+}}_{sol}$, and ${Cl^{-}}_{sol}/{Na^{+}}_{sol}$ are higher in ES sampling levels than in the Pearson water A3 preparation used as the infiltrating fluid. These elevated concentrations indicate that the composition of the infiltrating fluid is not the main control on ES soluble ion composition, but this is more likely to be controlled by material nature (sand vs bentonite). Maxima of ${Cl^{-}}_{sol}$ in ES are suggestive of anion exclusion, however in HTV the pore fluid is not sampled, and concentrations of ${SO_4^{2-}}_{sol}$ and (likely) ${CO_3^{2-}}_{sol}$ are higher in DS. Pairing of ${Ca^{2+}}_{sol}$, ${Mg^{2+}}_{sol}$, and ${Cl^{-}}_{sol}$ in ES could be due to charge cloud of these ion, which are harder and denser than those of ${Na^{+}}_{sol}$, ${K^{+}}_{sol}$, and ${SO_4^{2-}}_{sol}$ and could cause preferential association of these ions.

There was positive result of the difference between total soluble cations and anions (soluble cations minus soluble anions) in DS, indicating a deficiency of negative charge in DS. At least a portion of this deficiency would be compensated by soluble carbonate anions (${CO_3^{2-}}_{sol}$) which are present in the infiltrating fluid, albeit at low concentrations (0.5 mmol L^{-1}), and could also result from the dissolution of carbonate phases. ${CO_3^{2-}}_{sol}$ is clearly excluded from the ES as the difference in total soluble cation and anion concentrations is zero. This would indicate the distribution of ${CO_3^{2-}}_{sol}$ is similar to that of ${SO_4^{2-}}_{sol}$, which would also be consistent with the hard/soft charge clouds previously mentioned. Negatively charged clay surfaces could also contribute to the charge balance in DS sampling levels.

$Na^{+}{}_{sol}$ content within a DS varied between inner sampling levels DS (E2, E7, E12, and E17), which had higher concentrations compared to outer sampling levels adjacent to ES (E18, E16, E13, E11, E8, E6, E3, and E1). This is evidence of functionality of the Sandwich sealing system theory of hydration of DS from multiple fronts due to high hydraulic conductivity in ES. These differences are pronounced through the total height of the column regardless of the length of time of exposure to the infiltrating fluid, as prehydration of ES contributed to hydration of outer DS in the upper column.

The reduction in CEC due to dilution by salt and by heating for water content measurements was between 4 to 8 cmol(+) kg^{-1}. This is slightly higher than the reduction predicted by the heated CEC tests, where a decrease of 2 – 5 cmol kg^{-1} was measured. The average CEC of a sampling level was between 60 and 64 cmol kg^{-1}. Further tests are required to determine if this a bentonite batch-specific behavior or if it is linked to the hydration and cation exchange which takes place in the column, as heated samples in pre-tests were not exposed to Pearson water fluid. Results may indicate that exposure to the infiltrating fluid and exchange of interlayer Ca-Mg for Na impacts the extent of CEC change due to heating. The higher concentration of $Ca^{2+}{}_{exch}$ in E11 and E6 suggests that there is migration of Ca^{2+} through DS via the interlayers of smectite in bentonite. The increasing concentration of $Ca^{2+}{}_{sol}$ and $Mg^{2+}{}_{sol}$ in ES as height increases could represent a front of soluble ions from both interlayer exchange with $Na^{+}{}_{sol}$, but also from dissolution of relatively soluble carbonate phases such as calcite and dolomite. Soluble ions resulting from dissolution are then transported through the column with the hydration front.

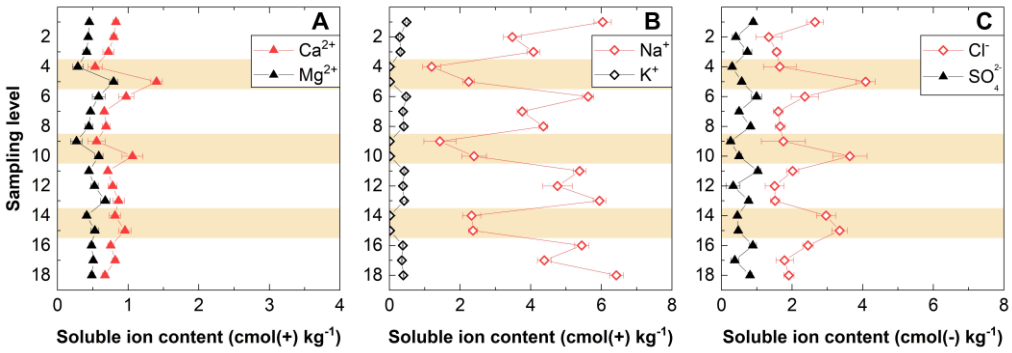

Fig. 5.65 Distribution of mean soluble ion content in the HTV-7. Yellow background blocks represent the position of ES

Both soluble and exchangeable ion concentrations were fairly homogeneous within sampling levels. No impact of artificial hydraulic shortcuts was evident, indicating that the

Sandwich sealing system works effectively to homogenize hydration and ion content across sampling levels. The largest variation of soluble ion concentrations was seen in sampling levels E9 and E10 for most ions measured, with the exception of $K^{+}{}_{sol}$ and $SO_4^{2-}{}_{sol}$. Remaining ES sampling levels also tended to have a higher variation than levels in DS. Variation in exchangeable ion concentration was really only significant for $Ca^{2+}{}_{sol}$ in E6 and E11 and is related to the adjacent peaks of $Ca^{2+}{}_{sol}$ in E5 and E10. Differences between top and bottom ES sampling levels were smaller lower in the column, and the difference between ES and adjacent DS sampling levels reduced. This implies that the difference between ES and DS is minimized with longer exposure to the pore fluid. A measurable difference between the top and the bottom is observed over the relatively short time frame of the HTV-7 experiment. In-situ use of the Sandwich sealing system would involve longer time-frames and slower fluid infiltration, which could allow for greater equilibration and minimization of these differences.

5.5.4 HTV-8

HTV-8 was installed within 10 d in spring 2021 and hydration started 14 d after installation. The duration of the experiment was about 11 months (Tab. 5.28).

Tab. 5.28 Key data for the HTV-8

Material of DS	**Securosol MHP1 (70/30)**
Installation	12.04.2021 - 21.04.2021
Hydration	04.05.2021 - 14.03.2022
Duration	314 d
Maximum fluid pressure	9.3/8.9 MPa*
Final fluid pressure	8.2/7.8 MPa*
Holding time of maximum fluid pressure	55 d
Pore volume (installation condition) total (105 °C, unsaturated)# total (200 °C, unsaturated)# DS (105 °C, unsaturated) ES (105 °C, unsaturated) DS (200 °C, unsaturated) ES (200 °C, unsaturated)	 187 dm³ 190 dm³ 96 dm³ (with SL1, SL2 and EDZ) 91 dm³ 99 dm³ (with SL1, SL2 and EDZ) 91 dm³
Input of liquid#	ca. 162 dm³ (without leakages)
Flow rate during the last 7 d at 9.3/8.9 MPa*	2.9 cm³/h (Leakage rate is not included)
Pressure relief	14.03.2022 - 04.04.2022
Dismantling	04.04.2022 - 19.04.2022

*) pump/lower gravel abutment
#) without gravel abutments

The fluid pressure (P) measured directly behind the pump (pump pressure) differs slightly from the fluid pressure (PP4) measured in the lower gravel abutment. The deviation is larger at higher pressures in particular. In the description of the test the pump pressure is usually specified (rounded values).

Pressure

In HTV-8, the ES were not flooded separately. After the lower gravel abutment was flooded with Pearson water A3 (approx. 39 dm³), the pump pressure was raised in small steps to 0.5 MPa. In the process, another 16 dm³ of liquid entered at the beginning of pressurization. After the pump was throttled back somewhat, the fluid pressure in the lower abutment stabilized.

After a little more than 24 h, a stronger penetration of liquid into the test occurred again. The sensor for the pore pressure in ES1 already showed a minimal deflection. The pump was again slightly throttled, so that a pressure of 0.4 MPa could be maintained in the further course. The pump pressure was further increased without any significant change

in the flow rate. It was only when the pressure was increased from 0.8 MPa to 1.0 MPa that fluid breakthrough occurred in DS1, as a result of which over 40 dm³ of liquid penetrated the sealing system within 2 d, although the pump pressure was reduced back to the previous level half an hour after the start of the pressure increase (Tab. G. 2). There was a significant increase in the pore pressure in ES1 and ES2 connected via the EDZ to 0.6 MPa. In order for pore pressure to build up in the ES, the bentonite at the bottom of DS3 must have already come into contact with liquid and started to swell.

During holding at 0.8 MPa, the radially measuring pressure transducer in DS1 showed a stronger pressure increase than the axially measuring pressure transducer. Due to the swelling process in the bentonite, flow paths for the Pearson water A3 were closed and the flow rate into the cell dropped from 12.7 dm³/h (measured maximum flow rate during breakthrough in DS1) to 0.010 dm³/h. The fluid pressure in the two lower ES was also slowly reduced. This also slowly relieved the pore pressure in the two lower ES, while the liquid slowly infiltrated the adjacent bentonite.

After 8 d, the pump pressure was again increased to 1.0 MPa, this time without liquid breakthrough. The pump pressure was increased in steps of 0.5 MPa up to 4 MPa. A pressure of 1.0 MPa was held for 6 d, and 1.5 MPa for 7 d. 2 MPa were significantly longer held at 20 d. The further pressure steps (2.5 MPa, 3 MPa, 3.5 MPa and 4 MPa) were held for about two weeks. Each pressure increase was performed in two individual steps of about half the pressure difference of the entire step so as not to risk breaking the DS. The pressure steps above 6 MPa, on the other hand, were carried out without an intermediate step, except for the increase from 7 MPa to 7.5 MPa (Tab. G. 2). At the highest pressure level of 9.3 MPa, the difference between the pump pressure and the pore pressure in the lower gravel abutment was 0.4 MPa.

By the end of the 4 MPa step, the radial pressure in DS1 was above the fluid pressure from the gravel abutment and above the axial pressure at the top of DS1, indicating good radial clamping of the segment in the steel column wall. In addition, the pressure increase was greater in the radial direction than in the axial direction. However, as the pressure increased, the increase in radial pressure became smaller, so that the differential pressure between the radial and axial directions also decreased until the pressures converged at 5 MPa. The behaviour of the pressures in DS2 was similar. With increasing penetration of fluid into DS2, the pressure in the radial direction also increased significantly more than in the axial direction, later this difference flattened out and at 7.5 MPa both pressures reached the same level (Fig. 5.66).

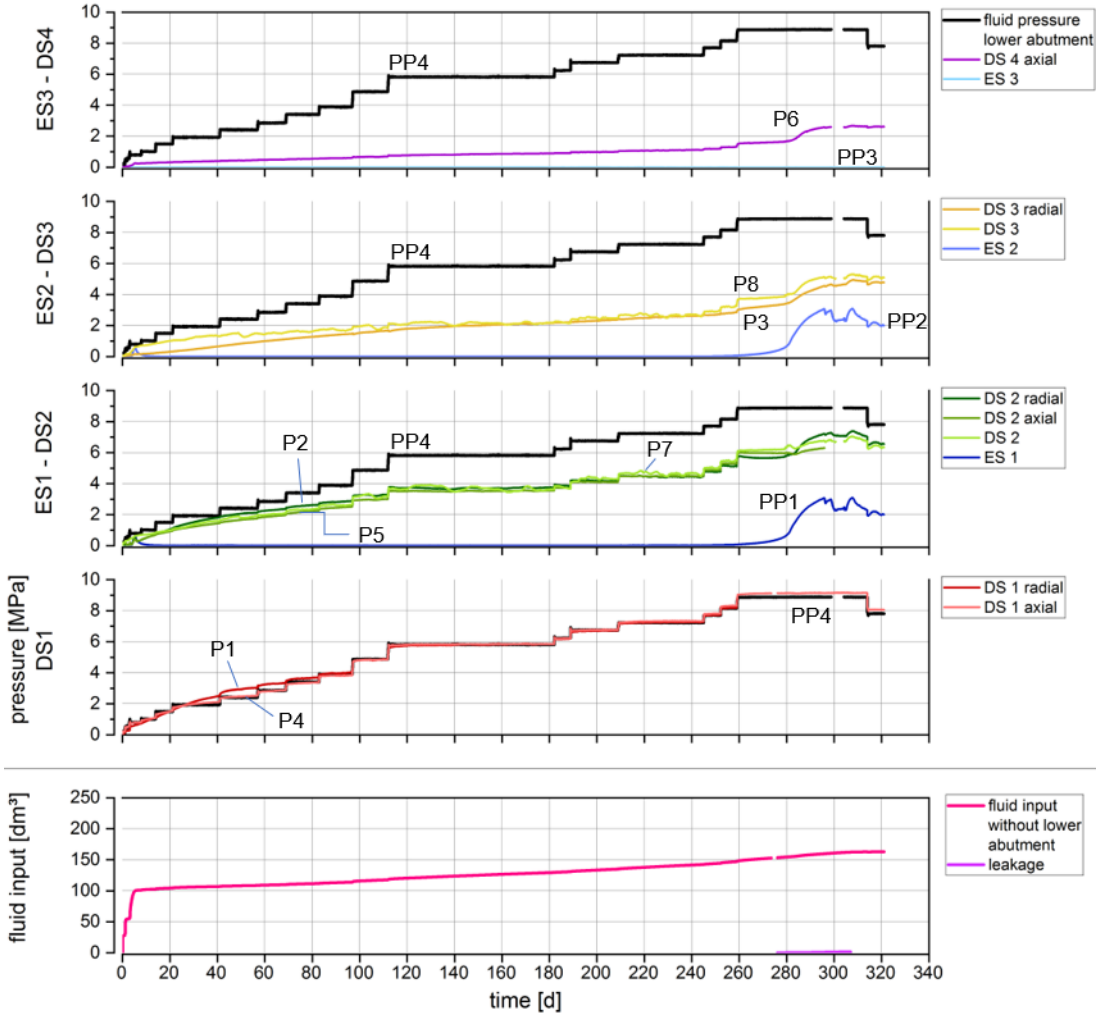

Fig. 5.66 Pressure curves and course of the injected fluid in HTV-8

The smoothed curve of the flow rate (Fig. 5.67) into the pressure cell over the duration of the experiment was calculated using the same method as for the HTV-7. The flow rate was lowest during holding at 2 MPa and at 2.5 MPa and averaged 3.2 cm³/h for both fluid pressures. At 3 MPa, the flow rate increased on average to 3.6 cm³/h, at 3.5 MPa to 4.0 cm³/h and during holding at 4 MPa further to 4.8 cm³/h. In the further course of the test, the fluid pressure in the gravel abutment was increased more than in the previous steps. The double increase in pressure from 4 MPa to 5 MPa resulted in a flow rate of 6.4 cm³/h. Furthermore, in DS1 the radial pressure had equalised to the axial pressure. In order not to increase the flow rate even further, the pressure was kept constant at 6 MPa for 2 months, but the flow rate decreased only slightly (Fig. 5.67).

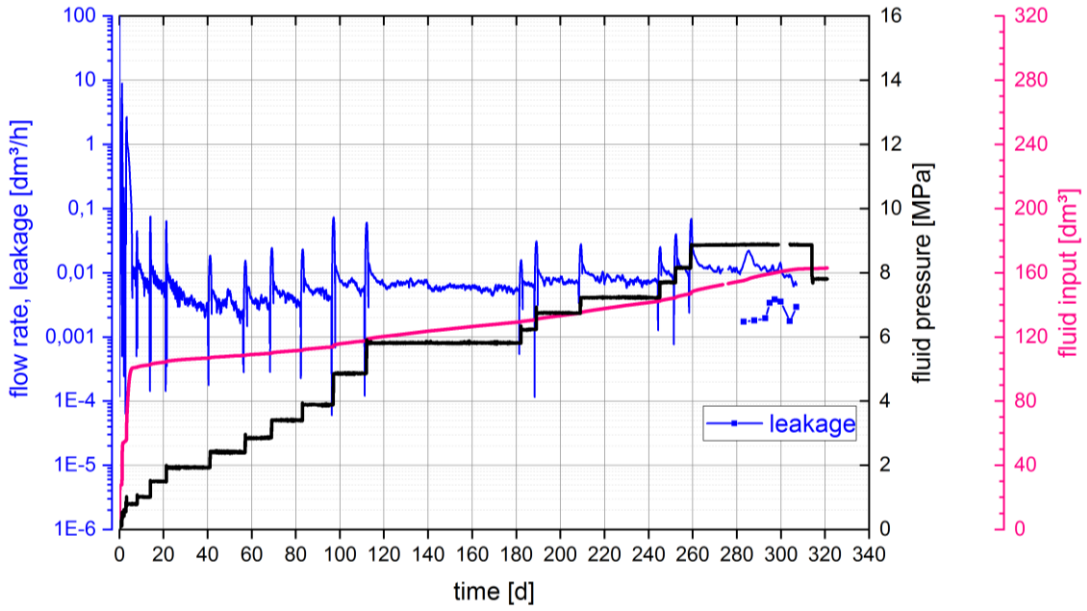

Fig. 5.67 Flow rate, fluid pressure and fluid input into the sealing system in HTV-8

Afterwards, the fluid pressure was raised again in 0.5 MPa steps and the flow rate continued to increase with rising fluid pressure. With the pressure increase from 7.5 MPa to 8 MPa, the pore pressure in ES1 and ES2 increased again. The pore pressure built up slowly at the beginning, suggesting that DS1 is highly swollen and allows fluid to pass upwards at only a slightly greater rate than can penetrate DS2 and DS3. Even during the pressure steps of 8.5 MPa and 9.3 MPa, the pore pressure increased in the ES1 and ES2 was only moderate. Only after a holding time of 21 d at the highest pressure level of 9.3 MPa did the pore pressure begin to increase strongly. After a holding time of 14 d, the flow rate averaged 11.7 cm³/h (more than 3.5 times the flow rate at 2.5 MPa). The pore pressure in the two lower ES reached values of over 3 MPa. During the high pore pressure increase in the lower ES, there was another strong increase in radial pressure in DS2. For the first time, the pressures in DS3 and between DS4 and the upper gravel abutment also increased more strongly over a longer period of time. In DS3, there was never a pore pressure increase during the entire duration. In total, the highest pressure level was maintained for 55 d (Fig. 5.66).

Shortly after the pressure was increased to 9.3 MPa, leakages occurred along the cables of sensors P1 and P5 and the measuring signal of P1 was disturbed. After liquid later leaked from the end of the cable, the transducer was disconnected from the measuring system and the leaking liquid was collected. After 296 d, the P5 sensor failed. Probably liquid from ES2 had suddenly entered the cable, which led to an abrupt drop in the pore pressure in ES1 and ES2. The relaxation of the pressure in these ES also caused an

abrupt drop in pressure at the other sensors, except on the axial transducer P4 in DS1, which remained unaffected. The axial clamping between DS1 and ES1 remained high. After 307 d, the fluid volume was recorded as the difference between the inflowing volume and the leakage volume and no longer the leakage volume separately. Between 304 d and 307 d, the amount of leakage as a proportion of the flow rate into the cell was already 39 %. The flow rate reduced by the leakage rate (flow rate into the sealing system) was 2.6 cm³/h (mean value over 24 h) at the end of the 9.3 MPa step after 314 d.

On 14.03.2022, the pressure in the cell was gradually reduced. The pressure was relieved in 5 steps until 04.04.2022. In the first step, the fluid pressure in the gravel abutment was reduced by 1.1 MPa to 8.2 MPa by briefly draining 0.2 dm³ of fluid from the lateral valve on the column bottom. Afterwards, the pump had to remain switched on, as otherwise the pressure would have fallen further, presumably due to the flow paths through the cables. 8.2 MPa were maintained for 7 d, with the flow rate reduced by the leakage rate remaining unchanged from the flow rate at the end of the 9.3 MPa step. At 8.2 MPa, another 0.4 dm³ of liquid was pumped into the Sandwich sealing system, so that at the end of the pressurization on 21.03.2022, 162 dm³ of Pearson water A3 had been introduced into the DS and ES. After dismantling the test, it was found that the lower gravel abutment (incl. the geotextile) was compressed by 4 mm. This reduces the pore volume in the lower gravel abutment by 2.0 dm³ compared to the installed condition. This volume is considered in the final value of the fluid input (Tab. G. 2).

In the further course of pressure relief, no more liquid was pumped into the cell. After briefly opening the valve at the bottom of the column to reduce the pressure to the desired level, the valve was then closed again. Afterwards, the fluid pressure in the gravel abutment increased again due to the expansion caused in the Sandwich sealing system until, after a few days, the valve was opened again to further reduce the pore pressure in the gravel abutment. When the pressure was reduced from 1 MPa to 0.01 MPa, the valve was left open in order to exclude a subsequent pressure increase in the pore space of the lower gravel abutment. During the pressure relief after the 8 MPa, a total of 4.6 dm³ of fluid had escaped from the cell by 04.04.2022 (drained amount from the lower gravel abutment and leakage through cables). After opening the cell, a further 3.5 dm³ of liquid was released from ES1 and ES2 via the pipelines. No liquid had escaped from ES3 via the pipe.

Fluid propagation

Liquid proceeded nearly immediately after starting the hydration (Tab. G. 2) at a liquid pressure of 2.5 bar on S12 via sand lens to ES1, followed in a reduced manner at S13 and even slower at S11 (Fig. 5.68). Further increase of pressure induced a breakthrough along Sensor 11 to ES1, and, via EDZ to DS2/ES2/DS3. But this was cured by an immediate sealing due to the forming of swelling pressure around the sensor cable. Liquid transport to DS2/ES2 at S13 was slower, and even more reduced around S12. Increasing pressure, liquid transport raised, less through the center and more along the S12 side with the sand lenses. Higher swelling pressure reduced strongly the inflow, so that further propagation was stopped in the range of ES2 and lower DS3. This situation remained stable until end of experiment. Only redistribution of liquid was monitored and following homogenization of ARDP below DS3.

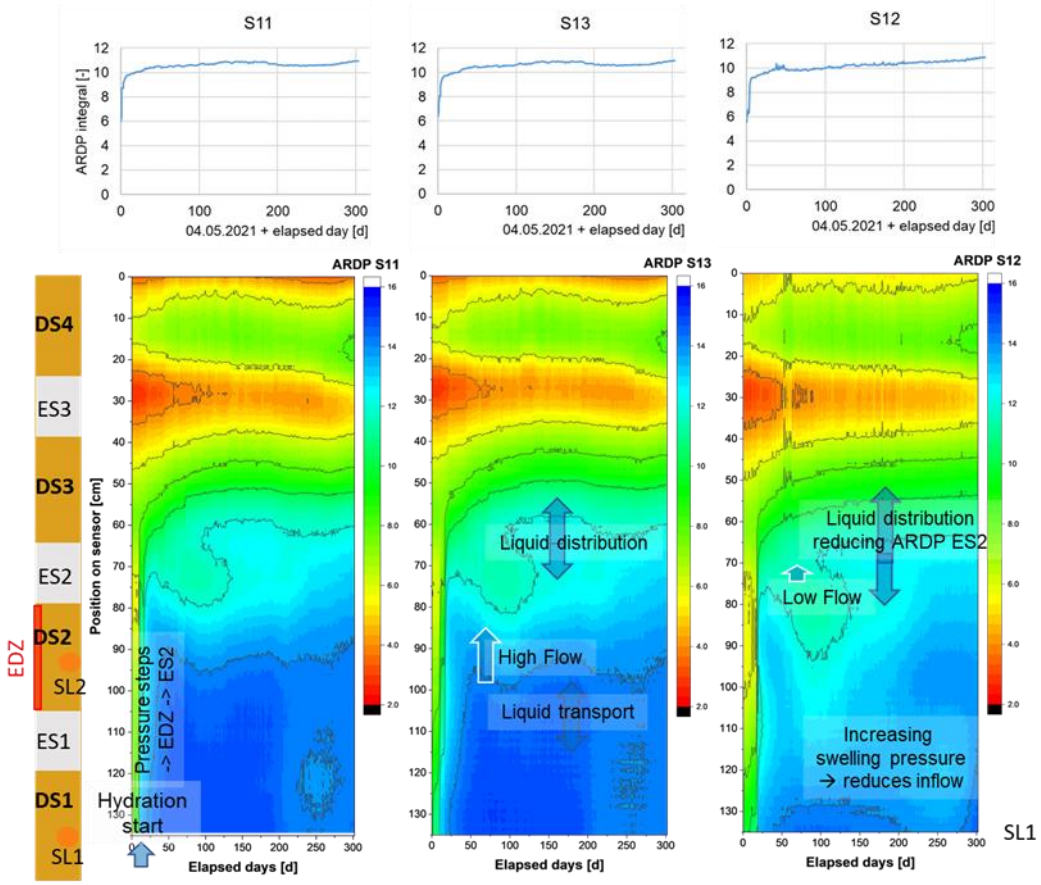

Fig. 5.68 ARDP distribution as indication of liquid progress at three TAUPE TDR sensors, S11, S13 and S12 (bottom), integral ARDP (top)

The same events could be observed for the horizontal sensors in ES1 (S15) and ES2 (S14) (Fig. 5.69). Fast reaction of ES1 at the back-side of S15 and nearly saturation in a

bit more than one day. During a low inflow phase, redistribution to DS1 and DS2 occurred, but no transfer via EDZ to ES2, until liquid pressure was further increased. Around day 10, inflow started to ES2, also on the backside of the sensor S14. As a special configuration, Sensor S14 is installed in opposite direction to S15. This means, inflow to ES2 started directly at the EDZ. Here, increasing swelling pressure in DS1 reduced ARDP during low inflow phase significantly, while redistribution to DS2 and DS3 was active and exceeded inflow. Finally, by increasing the liquid pressure significantly, the amount of liquid was sufficiently to fill ES2 again, but slowly and redistributing the available liquid to DS, ending on a nearly saturated state (Fig. 5.69).

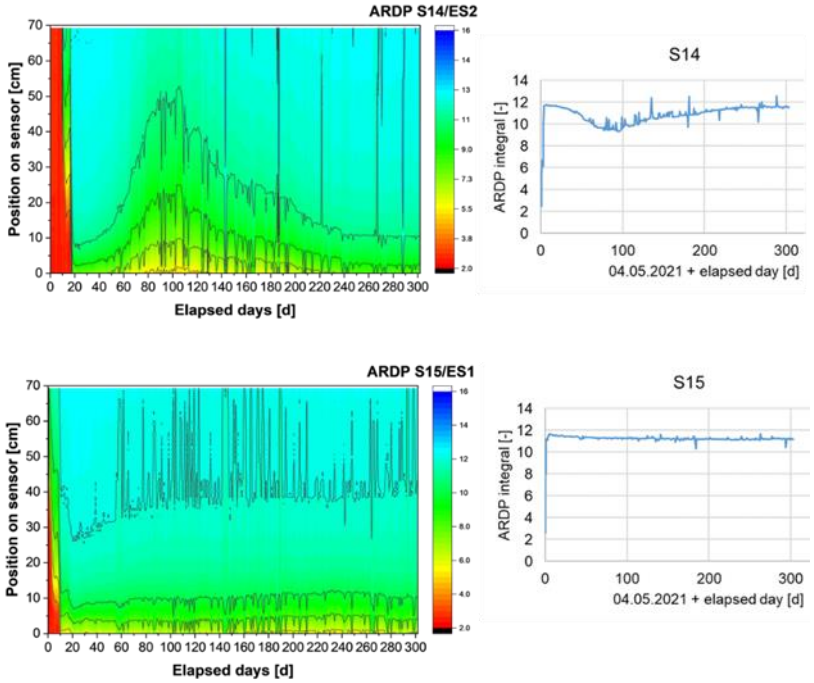

Fig. 5.69 ARDP distribution at horizontal TAUPE TDR sensors (left) and integral ARDP (right) for S15 (in ES1) and S14 (in ES2)

If we look at the interpolation of the data received from all three sensors in vertical cross-sections at different points in time, particularly in the initial phase, the observation made above can be repeated in Fig. 5.70. After installation, the S12-side revealed lower ARDP due to the sand lenses inside DS1 and DS2. On day 2, liquid has entered mostly via S12 to ES1 and, on day 3, as pressure was increased to 5 bar, the direct breakthrough along S11, via EDZ from ES1 to ES2 is visible and already distribution of liquid along ES2 was observed. A small shift on the S11-side of DS3 and ES3 seemed to appear, due to starting swelling pressure in DS1. DS3 was not affected by the liquid, yet.

This changed rapidly during increasing the liquid pressure up to 20 bar (Fig. 5.70, day 30). Liquid propagated fast on the S11-side (EDZ) and, not that strong on the S12-side (sand lenses) to ES2, while the S13-area was less affected. ARDP at the top of DS3 raised slightly. On day 160, at a pressure of 58 bar, DS1 was nearly saturated and the increased swelling pressure hindered the inflow of liquid. Redistribution to DS2 and DS3 used the content of ES1 and ES2 to spread over adjacent DS. Even the raise of liquid pressure to 88 bar did not change the situation significantly. Higher ARDP appeared up to the center of DS3 and ES3/DS4 have been shifted a bit more to the top and have increased material density but are rarely affected by liquid.

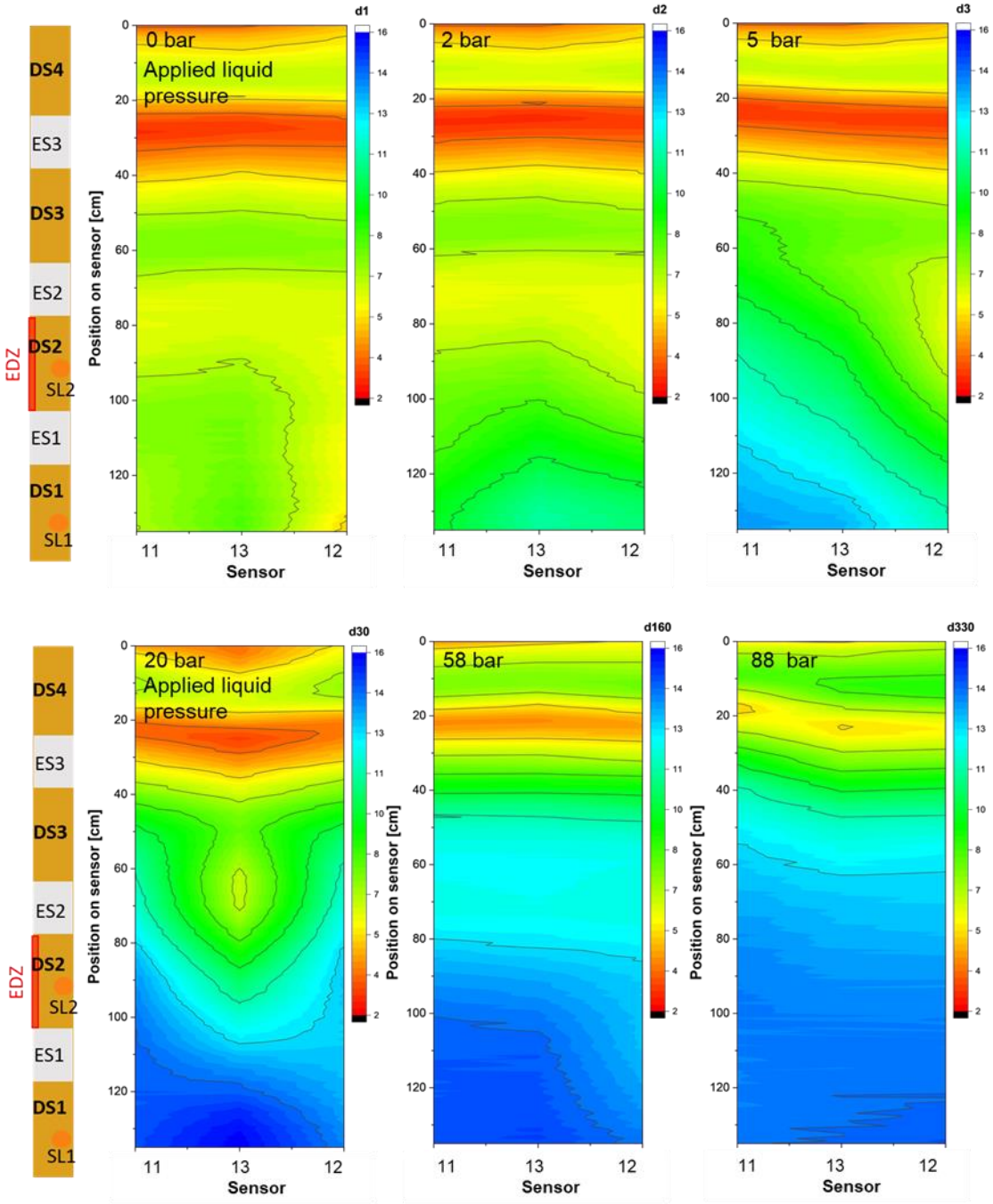

Fig. 5.70 Interpolated ARDP distribution between three vertical TAUPE TDR sensors in HTV-8 taken at (top) day 1, 2 and 3; (bottom) taken at day 30, 160 and 330

Dismantling

After opening the cell on 04.04.2022, it became apparent that the upper abutment of sand and gravel had remained dry and the liquid had not penetrated to the top of the column.

As with the previous HTVs, the distance to the surface was measured in a radial grid at 19 locations (Fig. 5.41 top left) to establish the location of the segment boundaries and the levels for sampling. As with the HTV-7, heaves were detected on the exposed surface during excavation. The segment boundaries were corrected on the basis of these heave values (variant A and B in Tab. 5.29).

Tab. 5.29 Water content, displacement and change of thickness of DS and ES in HTV-8

segment boundary	**displacement compared to installation [cm]***			**segment**	**thickness change [%]**		
	variant A	variant B	no correction		variant A	variant B	no correction
				upper abutment	-1.5	-1.5	-2.6
DS4 - upper abutment	0.4	0.4	0.6	DS4	-5.2	-4.8	-5.1
ES3 - DS4	1.7	1.6	1.9	ES3	-0.9	-0.9	-0.7
DS3 - ES3	1.8	1.7	2.0	DS3	-1.2	-0.8	-1.1
ES2 - DS3	2.1	1.9	2.3	ES2	-1.1	-1.1	-0.9
DS2 - ES2	2.3	2.0	2.4	DS2	2.0	2.2	2.2
ES1 - DS2	1.8	1.5	1.8	ES1	-3.6	-3.6	-3.4
DS1 - ES1	2.4	2.1	2.5	DS1	11.2	10.1	11.4
lower abutment - DS1	-0.4	-0.4	-0.4	lower abutment	-2.0	-2.0	-2.0

*) positive value: upward shift, negative value: downward shift

During the test, the segment boundaries shifted upwards even more the installation condition than with the HTV-7.

Water content and density

Over the entire thickness of DS4, the bentonite was still present as a binary mixture, without a solid bond. Therefore, no samples could be taken from DS4 for density determination.

The water content in the entire segment after removal was only minimally higher than in the installed condition (12.0 %). The water content increased slightly with increasing segment depth. A maximum of 14.0 % was measured in the lower level. Possibly some liquid had already penetrated into ES3, which was then adsorbed by the bentonite at the

bottom of DS4. When removed, the upper level of ES3 was completely dry (as when installed).

Fig. 5.71 Upper level of DS4 in HTV-8 prior (left) and during (right) sampling

At the top of DS4 and DS3, it was found that minor amounts of fine sand had penetrated from the segment above along the pipelines (at DS4) and cables (at DS3 and DS4) (Fig. 5.72 left). The penetration depths reached 2 to 3 cm. Due to the fact that the pipes and also the thicker cables are relatively rigid, movements at the pipes and cables are transmitted downwards during the installation of the ES. Due to the movement, the BGM on the upper side of the underlying DS around the pipe or cable is pushed slightly to the side and fine sand can trickle into the resulting gap from above. However, the fine sand has not penetrated further into the structure of the binary mixture, as was observed in HTV-7.

Fig. 5.72 Sand-filled gap between pipe and bentonite below the top of DS3 in HTV-8 (left). In DS1 of HTV-8, sand oozed out of the sand lens during exposure (right)

The sand in the ES3 segment below DS4 was almost completely dry. Only in the lower part moisture was visible.

In contrast to DS4, a compact bond between pillows and BGM had already formed in DS3, although the structure of the pillows was still clearly visible. The upper and middle levels of DS3 were moderately wet with water contents between 21.5 % and 25.0 % (Tab. 5.30). Thereby, in the upper level the water content was lowest in the center of the cross section and increased towards the outside in the direction of the column wall, as also shown by the water content distributions (Fig. 5.73). This was already observed in the upper level of DS3 in previous HTVs. The distribution with increasing water contents towards the cell wall may be related to the fact that DS3 was slightly curved at the top. At the rim, the segment was lower in the steel column than in the center of the cross section. In order to create a level, perhaps a little more material was removed from the area in the middle than from the rim before sampling, and the uppermost wetter area was removed from the middle.

The lower level in DS3 was somewhat wetter with water contents between 25.4 % and 26.9 %. At 1.62 g/cm³, the dry density in the lower level was significantly lower than in the middle (1.69 g/cm³) and upper levels (1.70 g/cm³). It cannot be ruled out that the bentonite had subsequently absorbed liquid from the underlying ES2, as the bentonite samples were only taken after a weekend's standing time on the moist ES. During this standing time, the bentonite had expanded considerably. 11 mm of heave was measured at the top, whereby it can be estimated that the heave was mainly caused by the still installed lower section of the DS3 and that the underlying segments had only expanded slightly.

As with the HTV-7, the upper level in ES2 was only partially saturated and the lower level was almost completely saturated with Pearson water A3.

DS2 was considerably wetter in the upper level with water contents between 28.5 % and 31.2 % than in the middle and lower levels (Fig. 5.73). The dry density, between 1.52 and 1.56 g/cm³, was clearly below the dry density in the less moist levels. As with the HTV-7, the P5 axial surface pressure transducer had somewhat impeded fluid access to the area below the 10 x 20 cm metal plate in the HTV-8, as the area was found to be drier than the bentonite on the rest of the level. Comparable water contents were found in the middle and lower levels of DS2 as in the same levels in DS3. Over the cross section, the bentonite was very uniformly soaked, in contrast to HTV-7, where -

presumably due to local sand fingers - areas near the EDZ and in the center of the cross section were more soaked (Fig. 5.58).

The sand lens in DS2 was relatively dry with a water content of 3.0 %. This suggests that there was no connection between the sand lens and ES1 and ES2, which were under high pore fluid pressure, during the final pressure steps. The bentonite around the sand lens had probably expanded so well that it had sealed the sand lens very well.

As in HTV-7, ES1 was relatively evenly saturated in both the upper and lower levels. The pore space was almost saturated in the upper level and completely saturated with Pearson water A3 in the lower level.

In contrast to HTV-7, the upper level of DS1 was much drier than the middle level. The Pearson water A3 penetrated the segment of Securisol MHP1 (70/30) from above to a lesser extent than in the HTV-7 segment made of Calcigel. This is probably due to the fact that the ES of HTV-8 were not hydrated beforehand.

In contrast to the HTV-7, the area below the axial surface pressure transducer P4 was similarly moist as the rest of the bentonite on the level. In the HTV-7, the metal plate was embedded in BGM, whereas in the HTV-8 it was embedded in sand. The thin layer of sand under the transmitter allowed the liquid to penetrate evenly into the bentonite below the metal plate.

When the sand lens in DS1 was exposed, the sand oozed out of the disturbance zone (Fig. 5.72, right). The sand lens was therefore still under pore pressure until the time of removal, in contrast to HTV-7, where the sand lens was found to be relatively dry. The water content in the sand lens of HTV-8 was 24.7 %. In the middle level of DS1, the rear area was slightly more soaked than the front area. The lower level was found to be very evenly moistened.

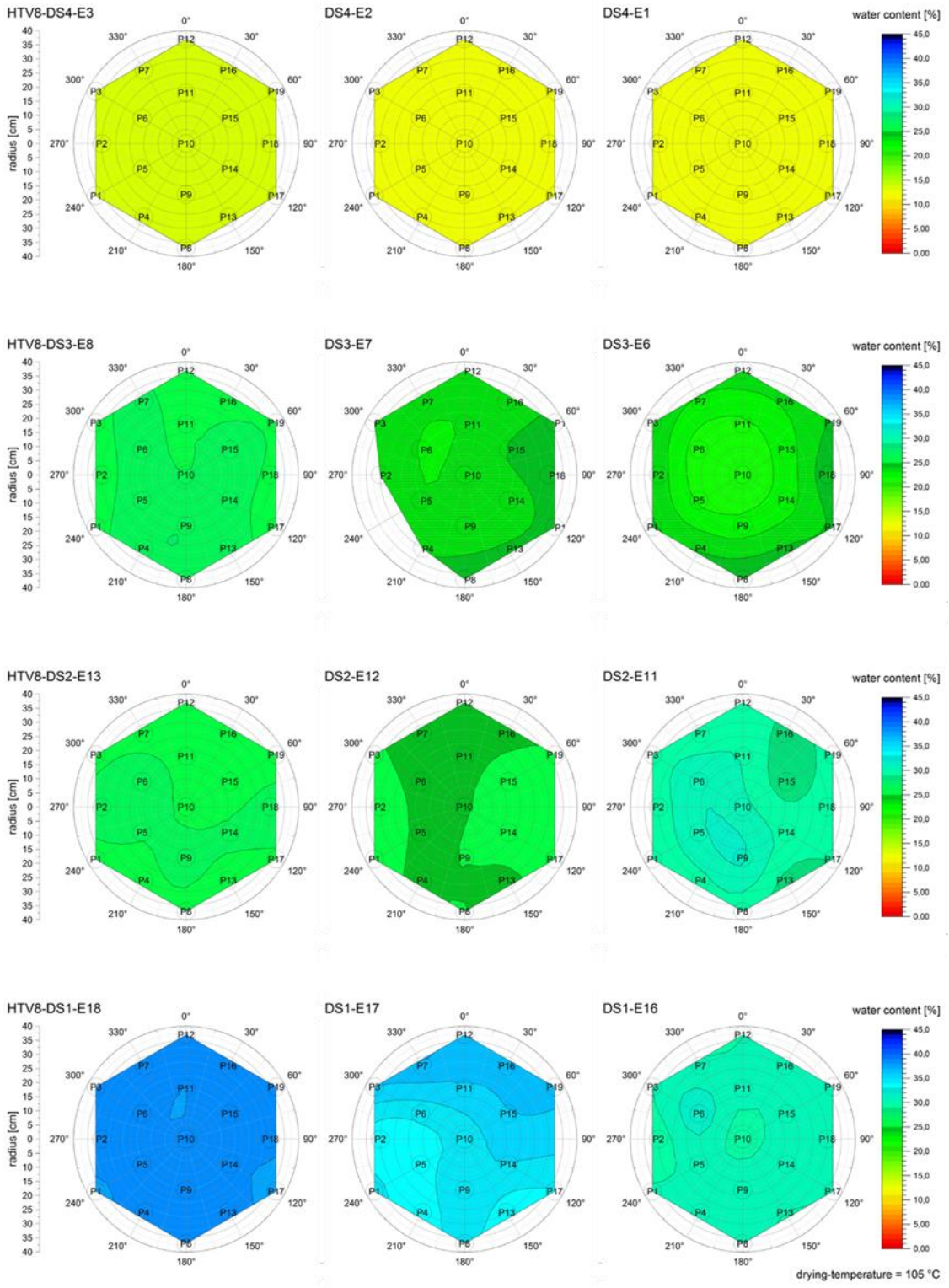

Fig. 5.73 Water content distribution of HTV-8 in the DS, upper, middle and lower levels (from left)

In contrast to the HTV-7, a much more pronounced density gradient of the DS along the sealing system was observed (Tab. 5.30 and Tab. 5.31). DS1 has expanded considerably (change in segment thickness by 11 %!), accompanied by a reduction in density from 1.60 g/cm³ to 1.46 g/cm³, which represents a significantly greater reduction in density than in the HTV-7 (from 1.50 g/cm³ to 1.44 g/cm³). DS2 expanded by 2 % and DS3 was compressed by 1 %. DS4, on the other hand, was compressed by 5 % during the test, which is significantly more than with the HTV-7, although the installation dry density of the DS was already significantly higher with the HTV-8 than with the HTV-7. Compaction caused the saturation value in DS4 to rise to 0.63, although the water content had only increased slightly. A significant driving force for the post-compaction of the segments is the fluid pressure applied to the sealing system from below, which at 9 MPa was significantly higher than the maximum pressure of the HTV-7 (3 MPa). Another driving force is the swelling pressure. Since, in contrast to HTV-7, the DS could not swell simultaneously, the segments that had not yet been moistened were further compacted by the swelling pressure built up from below. DS1 was able to expand more because the DS above it, which had not yet been moistened, could not build up any back pressure through swelling. The calculated saturation values indicate complete saturation of DS1, DS2 and DS3. As with HTV-7, correction calculations were carried out according to two variants (Chap. 5.5.3) in order to take the heave into account.

Tab. 5.30 Water content, dry density and saturation (105 °C) of HTV-8 after dismantling

segment	level	water content [%]	sample				integral	
			dry density [g/cm³]		saturation [-]		dry density [g/cm³]	saturation [-]
		/level	/level	mean	/level	mean		
Sand in upper abutment	E01	0.0						
	E02	0.0						
DS4	E1	12.3					A: 1.73 B: 1.72 no c.: 1.73*	A: 0.64 B: 0.63 no c.: 0.64
	E2	12.8						
	E3	13.6						
ES3	E4	0.1					A, B: 1.61 no c.: 1.61	A, B: 0.01 no c.: 0.01
	E5	0.4						
DS3	E6	23.2	1.70	1.67	1.12	1.10	A: 1.65 B: 1.64 no c.: 1.65	A: 1.06 B: 1.05 no c.: 1.06
	E7	23.7	1.69		1.11			
	E8	26.1	1.62		1.07			
ES2	E9	14.7					A, B: 1.64 no c.: 1.63	A, B: 0.80 no c.: 0.79
	E10	22.4						
DS2 (bentonite)	E11	29.6	1.55	1.62	1.09	1.10	A: 1.59 B: 1.58 no c.: 1.58	A: 1.06 B: 1.05 no c.: 1.05
	E12	25.0	1.66		1.10			
	E13	25.8	1.64		1.09			
ES1	E14	22.6					A, B: 1.61 no c.: 1.60	A, B: 0.96 no c.: 0.95
	E15	24.5						
DS1 (bentonite)	E16	30.3	1.53	1.44	1.09	1.08	A: 1.44 B: 1.46 no c.: 1.44	A: 1.09 B: 1.11 no c.: 1.08
	E17	34.9	1.44		1.08			
	E18	38.3	1.36		1.06			

*) no c. – without heave correction

Tab. 5.31 Water content, dry density and saturation (200 °C) of HTV-8 after dismantling

segment	level	water content [%]	sample				integral	
			dry density [g/cm³]		saturation [-]		dry density [g/cm³]	saturation [-]
		/level	/level	mean	/level	mean		
Sand in upper abutment	E01	0.0						
	E02	0.0						
DS4	E1	14.2					A: 1.70 B: 1.70 no c.: 1.70*	A: 0.66 B: 0.65 no c.: 0.66
	E2	14.7						
	E3	15.6						
ES3	E4	0.1					A, B: 1.61 no c.: 1.61	A, B: 0.01 no c.: 0.01
	E5	0.4						
DS3	E6	25.3	1.68	1.64	1.10	1.08	A: 1.63 B: 1.62 no c.: 1.62	A: 1.04 B: 1.03 no c.: 1.04
	E7	25.7	1.67		1.08			
	E8	28.1	1.59		1.05			
ES2	E9	14.7					A, B: 1.64 no c.: 1.63	A, B: 0.80 no c.: 0.79
	E10	22.4						
DS2 (bentonite)	E11	31.7	1.53	1.59	1.07	1.08	A: 1.56 B: 1.56 no c.: 1.56	A: 1.04 B: 1.03 no c.: 1.03
	E12	26.9	1.64		1.08			
	E13	27.9	1.61		1.08			
ES1	E14	22.6					A, B: 1.61 no c.: 1.60	A, B: 0.96 no c.: 0.95
	E15	24.5						
DS1 (bentonite)	E16	32.5	1.51	1.42	1.07	1.06	A: 1.42 B: 1.43 no c.: 1.42	A: 1.07 B: 1.09 no c.: 1.07
	E17	37.2	1.42		1.07			
	E18	40.4	1.34		1.05			

*) no c. – without heave correction

Ion transport and cation exchange

The salt content from conductivity measurements (LF-salt) decreased through the column in a relatively linear fashion with increasing distance from the fluid inflow between E18 (0.30 wt.%) to E6 (0.16 wt.%) (Fig. 5.74). Two sampling levels, E11 (DS2) and E10 (ES2) had higher LF-salt contents than suggested by the trend, with salt contents of 0.29 wt.% and 0.25 wt.% respectively. In comparison, the other sampling levels in DS2, E12 and E13 had LF-salt contents of 0.20 and 0.21 wt.% respectively. In ES3 (E5 and E4) the salt content was ~0 wt.%. In the final DS, DS4, the mean LF-salt content was 0.10 wt.%, which was close to the value obtained from the raw bentonite material. When compared to salt content from $Na^+{}_{sol}$, $Cl^-{}_{sol}$, and $SO_4^{2-}{}_{sol}$ measurements (Na-salt, Cl-salt, and SO_4-salt), the peak LF-salt in E10 and E11 was matched by high Cl-salt content

in these sampling levels, but neither high Na-salt nor SO_4-salt. The maximum Na-salt, Cl-salt and SO_4-salt contents were consistently lower than the maximum LF-salt content.

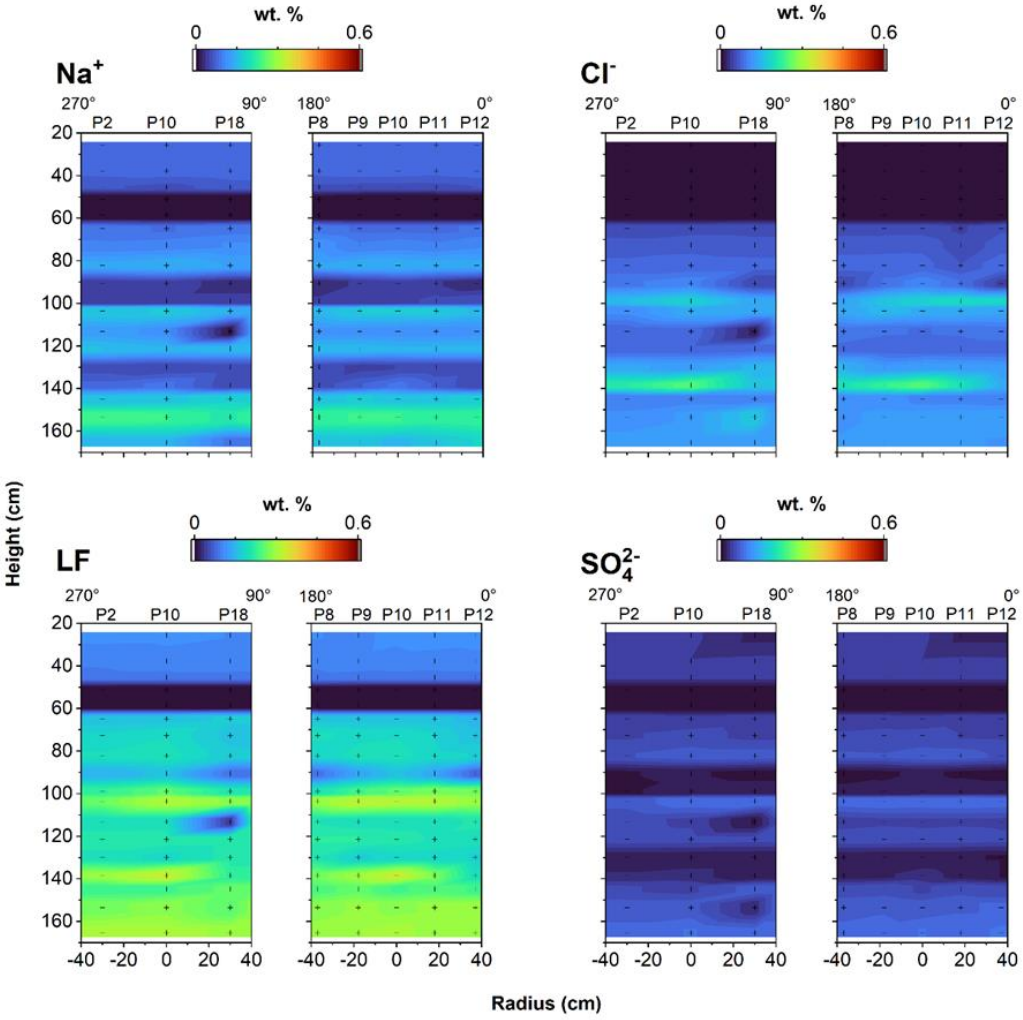

Fig. 5.74 Distribution of LF-salt, Na-salt, Cl-salt and SO4-salt in the HTV-8 experimental column

Each is represented by two perpendicular slices running vertically through the column. Sampling points are indicated by black crosses.

While the total concentration of soluble ions tended to decrease through the column with increasing height, there was heterogeneous distribution of soluble ions between DS and ES (Fig. 5.75). $Na^+{}_{sol}$ had the highest concentrations of all soluble ions, with a maximum of 3.9 cmol(+) kg^{-1} in E17, and 2.7 and 2.8 cmol(+) kg^{-1} in adjacent sampling levels E17 and E16. Concentration of $Na^+{}_{sol}$ in DS2 was lower, at 2.5, 2.0 and 2.7 cmol(+) kg^{-1} in E15, E14, and E13 respectively. $Na^+{}_{sol}$ concentration then decreased across DS3 from 2.4 cmol(+) kg^{-1} in E8, to 1.8 cmol(+) kg^{-1} in E7 and 1.5 cmol(+) kg^{-1} in E6. In DS4 the concentration of $Na^+{}_{sol}$ was 1.1 – 1.3 cmol(+) kg^{-1}. Concentrations in ES were lower, but

decreased with increasing height from 1.0 and 0.8 cmol(+) kg^{-1} in E15 and E14 to 0.8 and 0.6 cmol(+) kg^{-1} in E10 and E9 and further to ~0 cmol(+) kg^{-1} in E4 and E5.

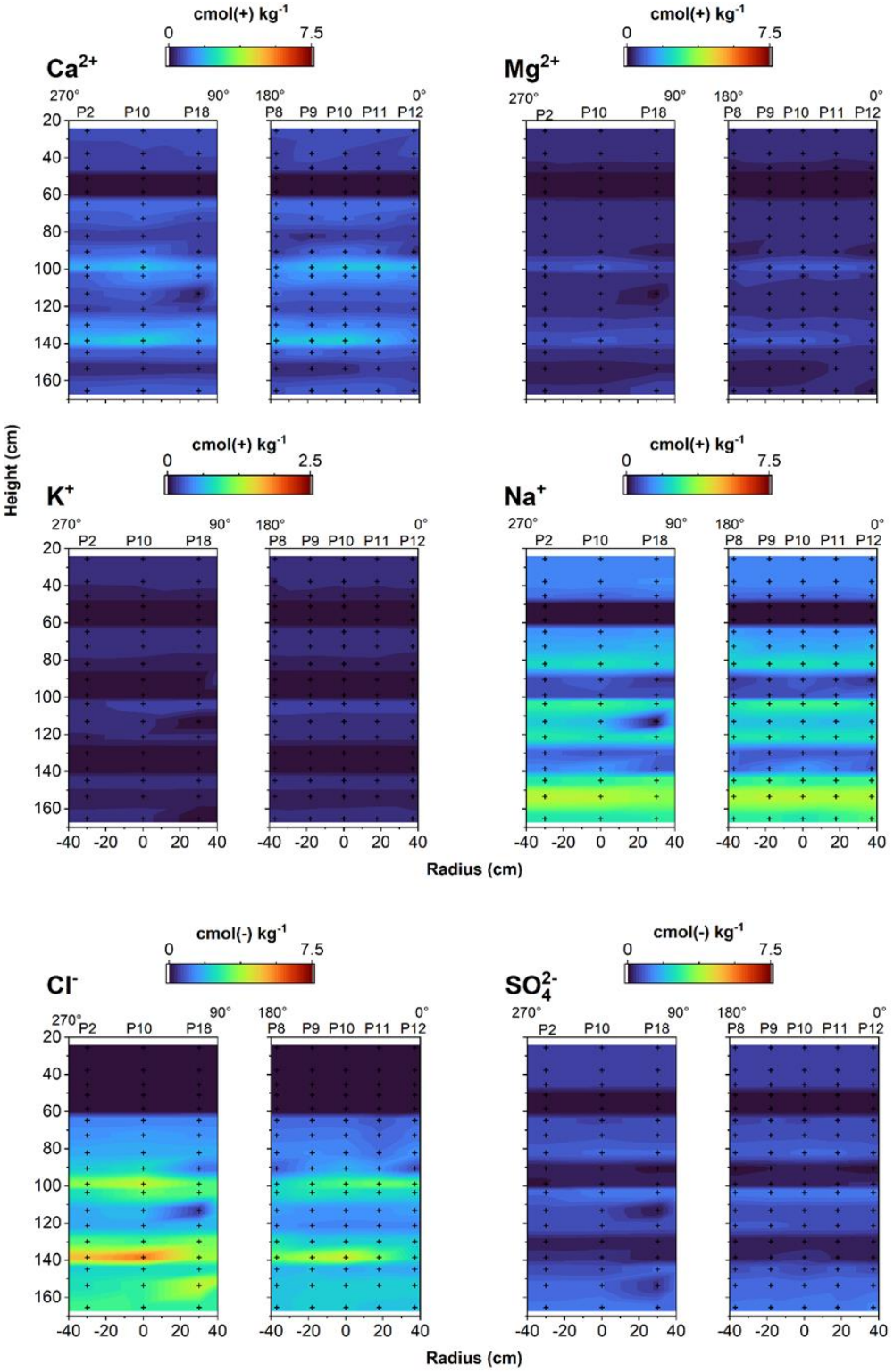

Fig. 5.75 Soluble ions through the HTV-8 in perpendicular cross sections. Sandy lenses shown on the right side of the 90-270 ° slice. Black crosses indicate the position of individual samples

Distribution of K^{+}_{sol} and $SO_4^{2-}{}_{sol}$ was similar to that of Na^{+}_{sol} although their concentration was lower. Values of K^{+}_{sol} were < 0.2 cmol(+) kg^{-1} for all sampling levels in the column. Concentrations in ES were lower than DS with values of ~0 cmol(+) kg^{-1} for ES1, ES2, and ES3. The concentration of K^{+}_{sol} was 0.1 cmol(+) kg^{-1} in all DS sampling levels with the exception of E11 where the concentration was 0.2 cmol(+) kg^{-1}.

The maximum concentration of $SO_4^{2-}{}_{sol}$ was reached in DS1 and DS2 with 1.1 cmol(-) kg^{-1} in E18 and E11. The concentration decreased in DS sampling levels to 1.0 cmol(-) kg^{-1} in E17 and 0.7 cmol(-) kg^{-1} in E16, E13, and E12. There was a slight increase to 0.9 cmol(-) kg^{-1} in E8 before decreasing to 0.7 cmol(-) kg^{-1} in E7 and 0.6 cmol(-) kg^{-1} in E6. In DS4 the concentration of $SO_4^{2-}{}_{sol}$ was 0.5 cmol(-) kg^{-1} for all three sampling levels.

In contrast, the concentration of $Ca^{2+}{}_{sol}$, $Mg^{2+}{}_{sol}$, and $Cl^{-}{}_{sol}$ tended to be higher in ES sampling levels compared to neighbouring DS. There was also a pattern of the lower sampling level in ES having a higher concentration than the upper. For example, the mean concentration of $Ca^{2+}{}_{sol}$ ES1 was 1.7 cmol kg^{-1} in E15 and 1.2 cmol(+) kg^{-1} in E14. E16 (DS1) had a concentration of 0.9 cmol kg^{-1} while E13 (DS2) had a concentration of 0.6 cmol(+) kg^{-1}. Similarly, $Ca^{2+}{}_{sol}$ in E10 (1.8 cmol(+) kg^{-1}) was higher than in E11 (1.2 cmol(+) kg^{-1} and that of E9 (0.8 cmol(+) kg^{-1} higher than E8 (0.5 cmol(+) kg^{-1}). Concentration dropped to 0 – 0.1 cmol(+) kg^{-1} in ES3 while in DS4 the concentration was 0.5 – 0.6 cmol(+) kg^{-1}.

The maximum concentration of $Mg^{2+}{}_{sol}$ was 0.7 cmol kg^{-1} in ES sampling levels E15 and E10. The concentration of $Mg^{2+}{}_{sol}$ in the four DS was similar, varying between 0.3 – 0.4 cmol(+) kg^{-1} across all DS sampling levels. Concentration in E14 was 0.5 cmol(+) kg^{-1}, higher than adjacent DS E13, but that of E9 was the same as the neighboring DS. In ES3 the concentration of $Mg^{2+}{}_{sol}$ was ~ 0 cmol(+) kg^{-1}.

The highest concentrations of $Cl^{-}{}_{sol}$ were 3.1 cmol(-) kg^{-1} in E15 and 2.9 cmol(-) kg^{-1} in E10, while in DS1 (closer to the fluid inflow) the concentration in E18 and E17 was 2.1 cmol(-) kg^{-1} and 1.8 cmol(-) kg^{-1} in E16. In E14 the concentration was 2.2 cmol(-) kg^{-1}, which was higher than the 1.3 cmol(-) kg^{-1} of E13. In the remainder of DS2 the concentrations were 1.5 cmol(-) kg^{-1} in E12 and 2.2 cmol(-) kg^{-1} in E11. The concentration in E9 was 1.3 cmol(-) kg^{-1}, similar to the concentrations of 1.3, 1.1, and 1.0 cmol(-) kg^{-1}

in E8 – E6 in DS3. In the upper portion of the column (E5-E1) concentration was ~ 0 cmol(-) kg^{-1} in ES3 and 0.1 cmol(-) kg^{-1} in DS4 (the same values were recorded for all sampling levels within the segments).

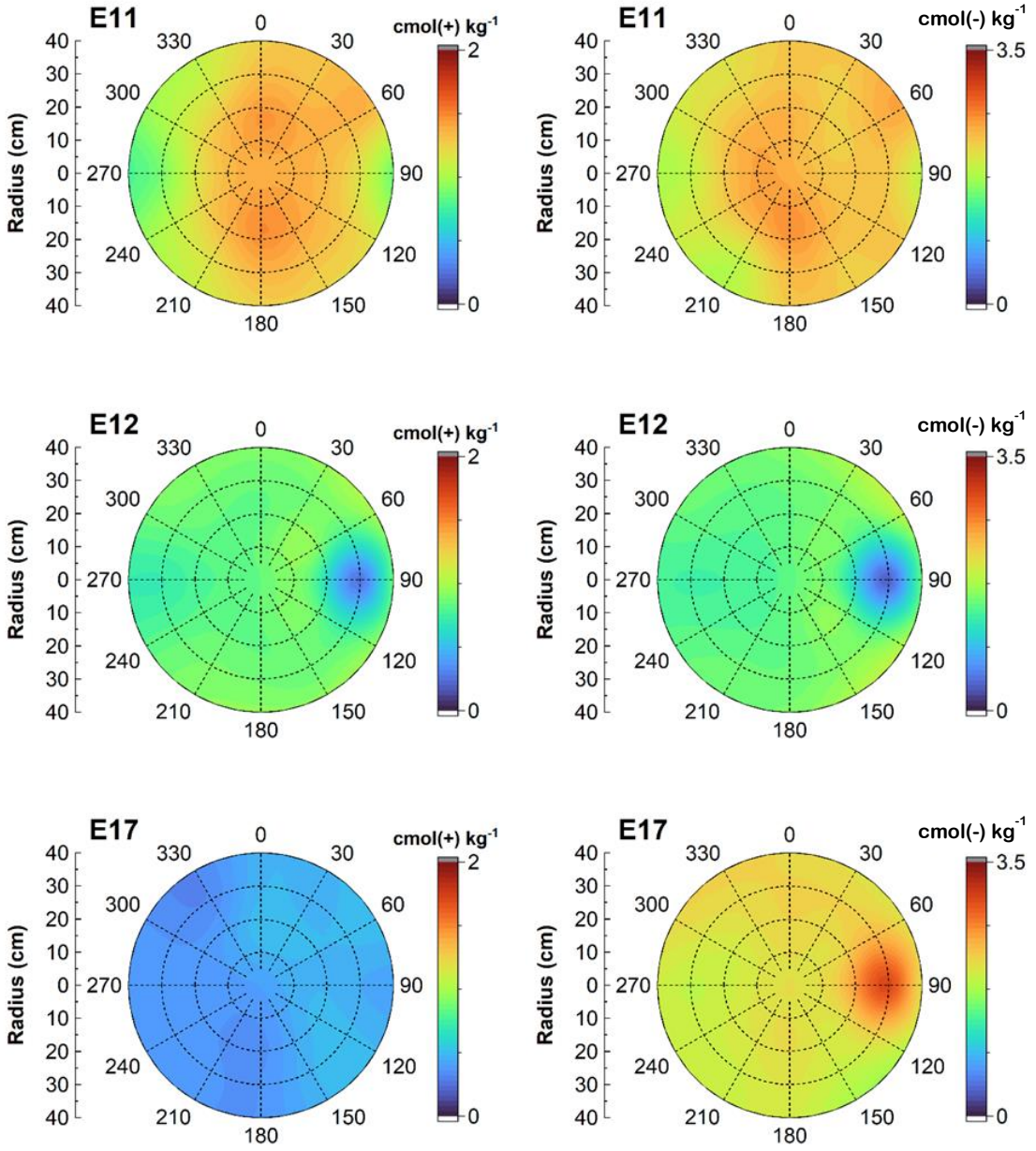

Fig. 5.76 Ca^{2+}_{sol} (left) and Cl^{-}_{sol} (right) in selected sampling levels either above a sand lens (E11) or containing a sand lens (E12 and E17). Note the different scales for the two ions

Variation in the concentration of soluble ion concentrations within sampling levels tended to be higher for levels lower in the column. This was true for all ions measured. The standard deviations of sampling levels E6 to E1 was ≤ 0.1 cmol(+/-) kg^{-1} (for all ions). In

the sampling levels with higher variation, there was no evidence of consistent differences based on the position of samples in the level, with the exception of $Na^{+}{}_{sol}$, $Ca^{2+}{}_{sol}$, $Mg^{2+}{}_{sol}$, and $Cl^{-}{}_{sol}$ concentrations in E9 and E10. These ions tended to have lower concentrations in samples closer to the intersection with the steel column. In DS1 there was no clear impact of the hydraulic bypass on the adjacent bentonite. The shortcut was also not visible within E17, e.g., no concentration difference, for all ions except $Cl^{-}{}_{sol}$, which had a higher concentration in the shortcut than in the bentonite (Fig. 5.76). In E12, there was a clear difference in ion concentrations in the shortcut compared to the adjacent bentonite, with lower concentrations in the shortcut. In addition, there was a slight concentration gradient in E11 between samples closer to the shortcut and samples further away. This gradient was observed for all soluble ions except $Na^{+}{}_{sol}$.

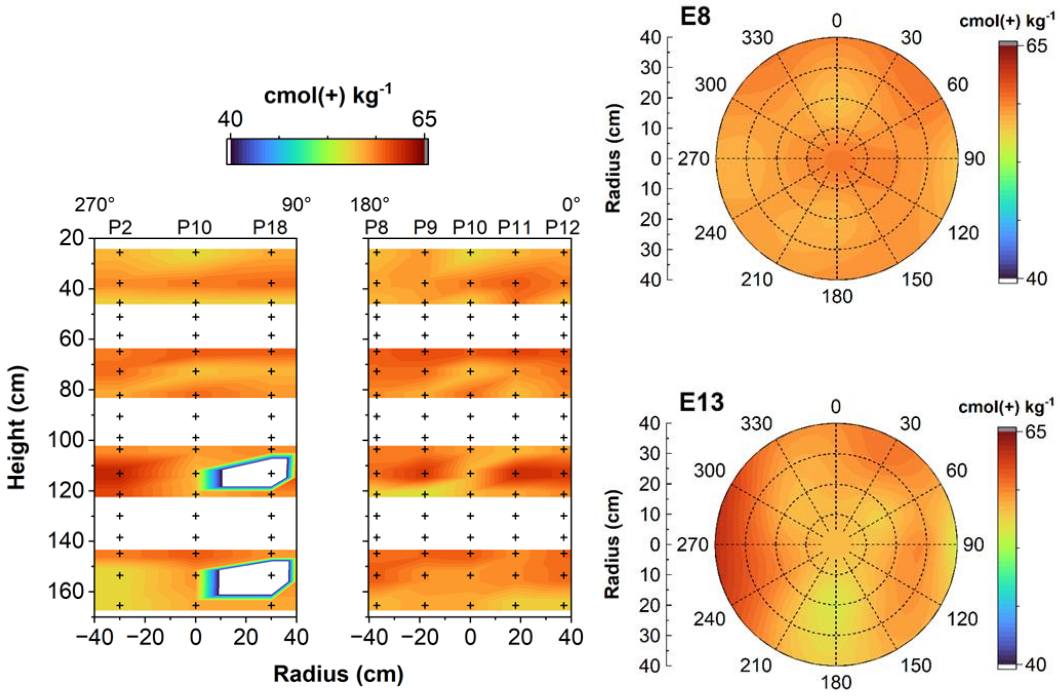

Fig. 5.77 CEC distribution through the HTV-8 (left) in two vertical perpendicular cross sections

Sampling points are indicated by black crosses. Horizontal cross-sections show the difference in CEC variation between the least variation (top right) and most variation (bottom right).

The mean CEC of the DS was 56.1 – 60.5 cmol(+) kg^{-1}. This represented a reduction of 2.5 – 6.9 cmol(+) kg^{-1} from the raw Secursol-MHP1 material which had a CEC of 63.0 cmol(+) kg^{-1}. These values were consistent with the decrease in CEC recorded for the heated material. The highest mean CEC was in E12 and the lowest was in E18.

There was no consistent trend in the variation of CEC between DS sampling levels (Fig. 5.77). The standard deviation of individual sampling levels varied between 0.7 – 1.8 cmol(+) kg^{-1}, which was 2.6 – 6.8 cmol(+) kg^{-1} in absolute values. This is around double what is typically expected from the Cu-*trien* method. However, when looking at individual sampling levels, the majority of the sampling levels had a relatively homogeneous CEC with a variation of < ±2.0 cmol(+) kg^{-1}, which is within the accuracy expected from the method. Levels with a higher variation were E1 and E12 – 17. The position of the samples within a sampling level was not linked to any consistent trend in the variation of CEC.

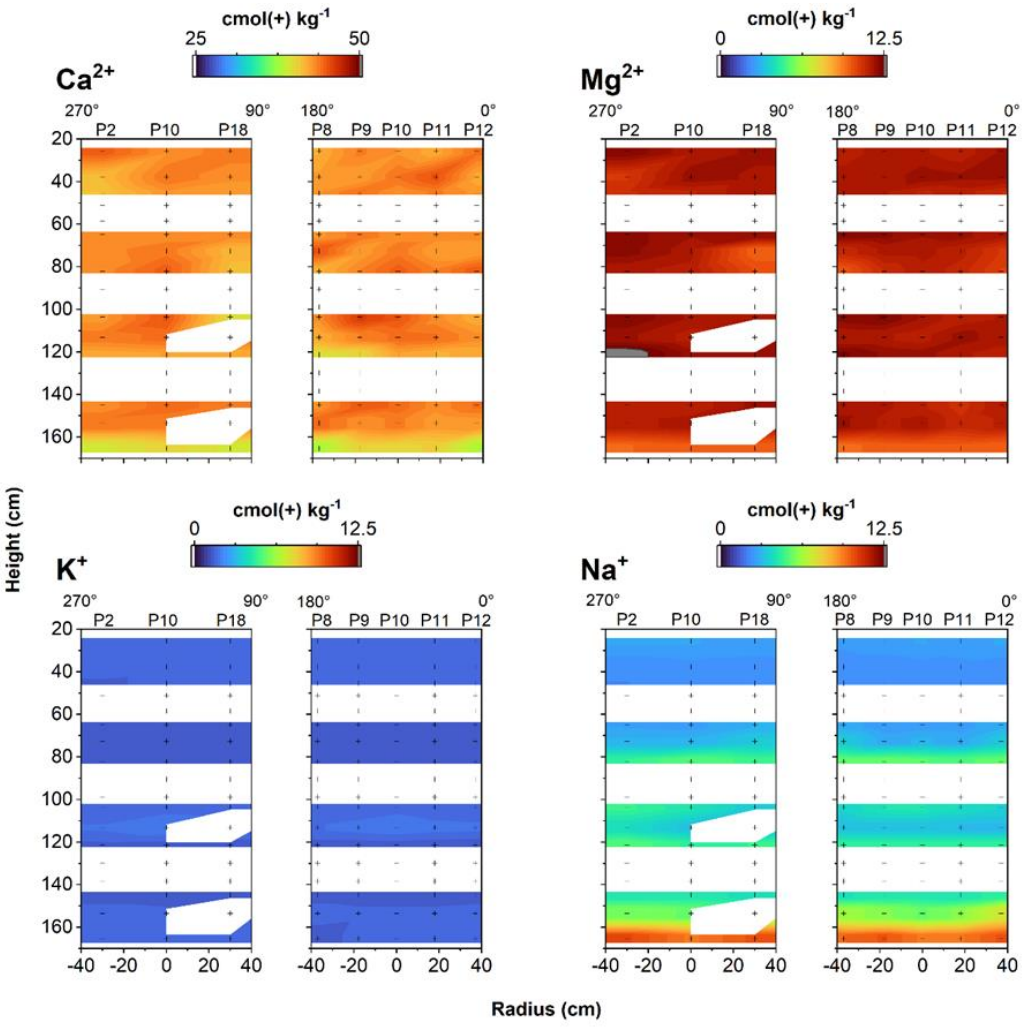

Fig. 5.78 Exchangeable cations of HTV-8 in vertical cross sections perpendicular to one another and black crosses indicate sampling positions

The mean sum of exchangeable cations (total cations minus soluble cations) was between 55.4 in E7 and 57.8 cmol(+) kg^{-1} for E8 (Fig. 5.79 A). The mean for each DS showed very little variation through the column (57.0, 56.4, 56.6, and 56.4 cmol(+) kg^{-1}

for DS1 through DS4, respectively). The amount of $Ca^{2+}{}_{exch}$ varied between sampling levels within the same DS but the mean value for each DS increased through the column with increasing distance from the fluid inflow which was an indication for some exchange of $Na^{+}{}_{sol}$ for $Ca^{2+}{}_{exch}$ (Fig. 5.78). In particular, the mean amount of $Ca^{2+}{}_{exch}$ in E18 was only 38.5 cmol(+) kg^{-1}, in contrast to 42.7 and 42.9 cmol(+) kg^{-1} in E16 and E17. The amount of $Mg^{2+}{}_{exch}$ was fairly consistent in sampling levels E1 through E17 (mean 11.2 cmol(+) kg^{-1}) but also decreased in E18 to 9.5 cmol(+) kg^{-1}. In contrast the amount of $Na^{+}{}_{exch}$ was relatively low through E1 – E17 with a mean of 1.6 cmol(+) kg^{-1}. $Na^{+}{}_{exch}$ content increased dramatically to 7.2 cmol(+) kg^{-1} in E18. In E8 and E13 the amount of $Na^{+}{}_{exch}$ was slightly increased from the baseline but the level of the increase was not significant. The concentration of $Ca^{2+}{}_{exch}$ also increases in E8 which suggests experimental artefact rather than a realistic variation in exchangeable ion content. $K^{+}{}_{exch}$ did not vary through the column. There was no evidence of increased exchange in bentonite adjacent to the hydraulic shortcuts.

Discussion

Combined measurements in DS4 are close to the values of the original bentonite material. This supports the hydration data suggesting that fluid infiltrating in DS4 did not take place. The standard deviation of all measurements was higher in all sampling levels below DS4 (E18 – E6). This indicates that hydration introduces a larger degree of inhomogeneity than the raw material. Despite this increased homogeneity, a gradual hydration and ion exchange transport through the column is observed so it is clear that the duration of exposure to the infiltrating fluid is the main control on the fluid and interlayer composition. The variation in CEC measurement throughout the column, however, cannot be linked to hydration, as there is no clear variation with position. Problems with experimental methodology could be part of the cause, or it may be linked to the heating of samples to measure water content. Further experiments are required to pinpoint the cause.

If the ionic composition of the infiltrating fluid was the was the main factor controlling soluble ion content, then the same relationship between LF-salt and total anion or cation content would be expected in ES and DS. However, instead of a single relationship, two separate relationships are observed, one for ES and one for DS (Fig. 5.79 B). This indicates that the material composition is also playing a role in the distribution of soluble ions. Whilst results are suggestive of anion exclusion-like behaviour, the system is not

fully saturated and therefore diffusion is not to the main driver of ion transport in the experiment. The negative charge on clay surfaces could repel $Cl^{-}{}_{sol}$ resulting in the higher concentrations in ES. In this case, $Cl^{-}{}_{sol}$ would likely be accompanied by $Ca^{2+}{}_{sol}$ and $Mg^{2+}{}_{sol}$ in order to maintain charge balance. The association of these particular ions could be due to their relatively non-diffuse charge (Na^{+} has a comparatively diffuse charge). It is also important to note that $Na^{+}{}_{sol}$ is not completely excluded from ES so this explanation is incomplete. The concentration of $Cl^{-}{}_{sol}$, $Ca^{2+}{}_{sol}$, and $Mg^{2+}{}_{sol}$ in ES decreases moving up the column as a function of distance from the fluid inflow, and therefore to the hydration state of the material. Differences across ES could be due to gravitational effects, as the sampling levels with higher hydration and ion concentrations are lower in the column. However, previous HTV experiments which were performed in horizontal orientation successfully demonstrated that the orientation of the column had no impact on ion distribution across sampling levels, i.e. that there were no gravitational effects. The other cause for the difference across ES could simply be due to their position in the column. Fluid is flowing into the column under pressure, and constant flow from bottom to top is observed. This could cause the $Cl^{-}{}_{sol}$ to be transported from the DS immediately below into the ES level above, and experimental time too short for homogenisation of concentrations within an ES.

Another factor to consider is charge neutrality within the DS. The difference sum between total soluble anions and cations in indicated a deficiency in negative charge. This could be provided by the negative surface charge of clays, or derived from the presence of another anion, such as $CO_3^{2-}{}_{sol}$. $CO_3^{2-}{}_{sol}$ can arise from the infiltrating fluid (0.54 mmol/L in Pearson water A3), or from trace amounts of carbonate minerals in the Secursol MHP-1 (70:30) material although pXRD and DSC-TGA analysis of this material did not reveal any indication of carbonate minerals. While exclusion of $CO_3^{2-}{}_{sol}$ from ES appears unlikely, this exact phenomenon is observed in the HTV-7 experiment where $CO_3^{2-}{}_{sol}$ is present in both the infiltrating fluid and in the form of carbonate minerals. Restriction of $CO_3^{2-}{}_{sol}$ to DS would also mirror the distribution of $SO_4^{2-}{}_{sol}$, which has very low concentrations in ES compared to DS. This could again be related to the charge cloud of the species, as both $SO_4^{2-}{}_{sol}$ and $CO_3^{2-}{}_{sol}$ have larger, more diffuse charge clouds than $Cl^{-}{}_{sol}$ (Fig. 5.79 C, D).

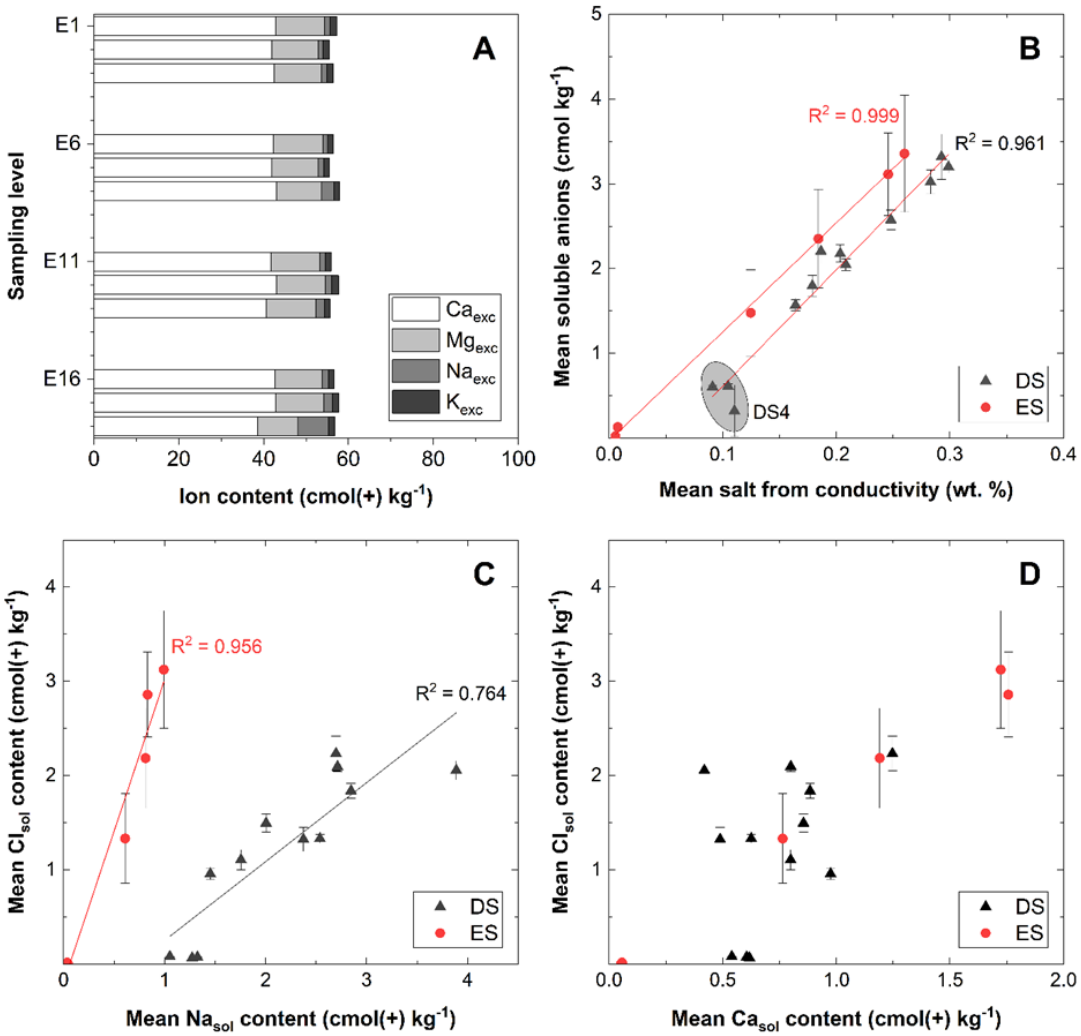

Fig. 5.79 A) comparison of the exchangeable cation content of the DS sampling levels; B) Plot of LF-salt against mean soluble anion concentration; Comparison of C) $\boldsymbol{Na^{+}}_{\boldsymbol{sol}}$ vs $\boldsymbol{Cl^{-}}_{\boldsymbol{sol}}$ and D) $\boldsymbol{Ca^{2+}}_{\boldsymbol{sol}}$ vs $\boldsymbol{Cl^{-}}_{\boldsymbol{sol}}$ concentrations

Future work to clarify the observations of this experiment would include full characterization of the heated material, in addition to the CEC measurement that have already been performed. Obtaining samples from the HTV-9 experiment which have not been heated would also be useful for investigating the impact of the column hydration separate from the impact of heating. Further investigation into the soluble anions in DS would help to determine the source of the difference in total anion vs total cation sums in DS. This could be performed with extended IC analysis including supplemental ions such as ${F^{-}}_{sol}$ or ${PO_4^{2-}}_{sol}$. A method to measure ${CO_3^{2-}}_{sol}$ in DS would be exceptionally helpful.

5.5.5 HTV-9

HTV-9 is a mock-up test of Shaft 2 and was installed within in late 2022/early 2023 and hydration started 7 d after installation (Tab. 5.32). The experiment is still running.

Tab. 5.32 Key data for the HTV-9

Material of DS	**DS1, DS2:** **DS3, DS4:**	**Securso MHP1 (70/30)** **Calcigel**
Installation		30.11.2022 - 02.02.2023
Hydration		since 09.02.2023*
Current fluid pressure as at 31.08.2023		1.0/1.0 MPa*
Holding time as at 31.08.2023		203 d
Pore volume total (105 °C, unsaturated)[#]		210 dm³ (installation condition)
Pore volume total (200 °C, unsaturated)[#]		214 dm³ (installation condition)
Pore volume DS/ES (105 °C, unsaturated) (installation condition)	DS total DS1/DS2 DS3/DS4 ES	119 dm³ (with SL1, SL2 and EDZ) 69 dm³ (with SL1, SL2 and EDZ) 50 dm³ 91 dm³
Pore volume DS/ES (200 °C, unsaturated, installation condition)	DS total DS1/DS2 DS3/DS4 ES	123 dm³ (with SL1, SL2 and EDZ) 70 dm³ (with SL1, SL2 and EDZ) 53 dm³ 91 dm³
Input of liquid[#] as at 31.08.2023		122 dm³
Flow rate into the cell as at 31.08.2023		9 cm³/h
Pressure relief		-
Dismantling		-

*) pump/lower gravel abutment
[#]) without gravel abutments

Pressure

In HTV-9, the fluid pressure was to be increased only very slowly, as the test regime was to be based on the test in Shaft 2. After the lower gravel abutment was flooded with Pearson water A3, a very low fluid pressure of <0.1 MPa was set in the gravel abutment,

which was maintained for 5 d to give the Securisol MHP1 (70/30) time to swell (Tab. G. 3). The amount of liquid supplied was correspondingly low at 12 dm³ until the end of the pressure step compared to the other HTVs. During the holding time, the axial pressures in DS1 and DS2 slowly increased, whereby the increase in DS1 was significantly larger than at the top of DS2, which is further away from the hydration side.

After the fluid pressure in the lower abutment was increased to 0.3 MPa, there was a sharp increase in radial pressure in DS1. The swelling pressure causes the segments to be clamped against the abutments and against the wall. At the same time, displacements occur, further compressing the upper segments. Therefore, the pressures in the non-wetted areas also increased. After about 10 d, the pressure in the radial direction exceeded the pressure in the axial direction. The pressure was clearly above the fluid pressure in the lower gravel abutment. In the further course, however, the curve flattened and had the same increase as the axial pressure in DS1 after about 15 d. The fluid pressure was then increased to 0.4 MPa and then to 0.5 MPa, the level was kept at 0.5 MPa for three weeks.

Afterwards, the fluid pressure in the gravel abutment was increased to 1 MPa. The pressure curve of the axial pressure in DS1 was striking. After an initial surge of the axial pressure parallel to the fluid pressure in the gravel abutment, the curve flattened out and only rose again more sharply after a delay. About 20 d after the fluid pressure increased to 1 MPa, the radial pressure in DS2 also began to increase. From this it can be concluded that the swelling process had also started in the middle height of DS2. However, the pressure increase in the radial direction was lower in DS2 than the swelling process began in DS1.

During the swelling of the bentonite in DS2, the pressures in DS2 increased significantly stronger than in DS1 at the same time. Presumably, the swelling potential in DS1 was almost exhausted, as the pressure increase in DS1 was similarly low as in the middle segment height of DS3 and between DS4 and the upper abutment, where probably no liquid had reached until the end of August. Until this time, the radial pressure in DS1 remained 0.2 MPa above the axial pressure at the top of DS1.

The pore pressures in the ES were all at zero level until the end of May. Since beginning of June, pore pressure has slowly built up in the lower ES (Fig. 5.80). This shows that the swelling process in DS2 reduces the liquid penetration upwards.

From day 149 to 150 (08. / 09.07.2023), there was a brief pressure drop to 7.5 MPa in the applied fluid pressure. Presumably, during the work on the fluid reservoir, an air bubble had entered the line, which temporarily blocked the fluid at the pump from moving towards the cell.

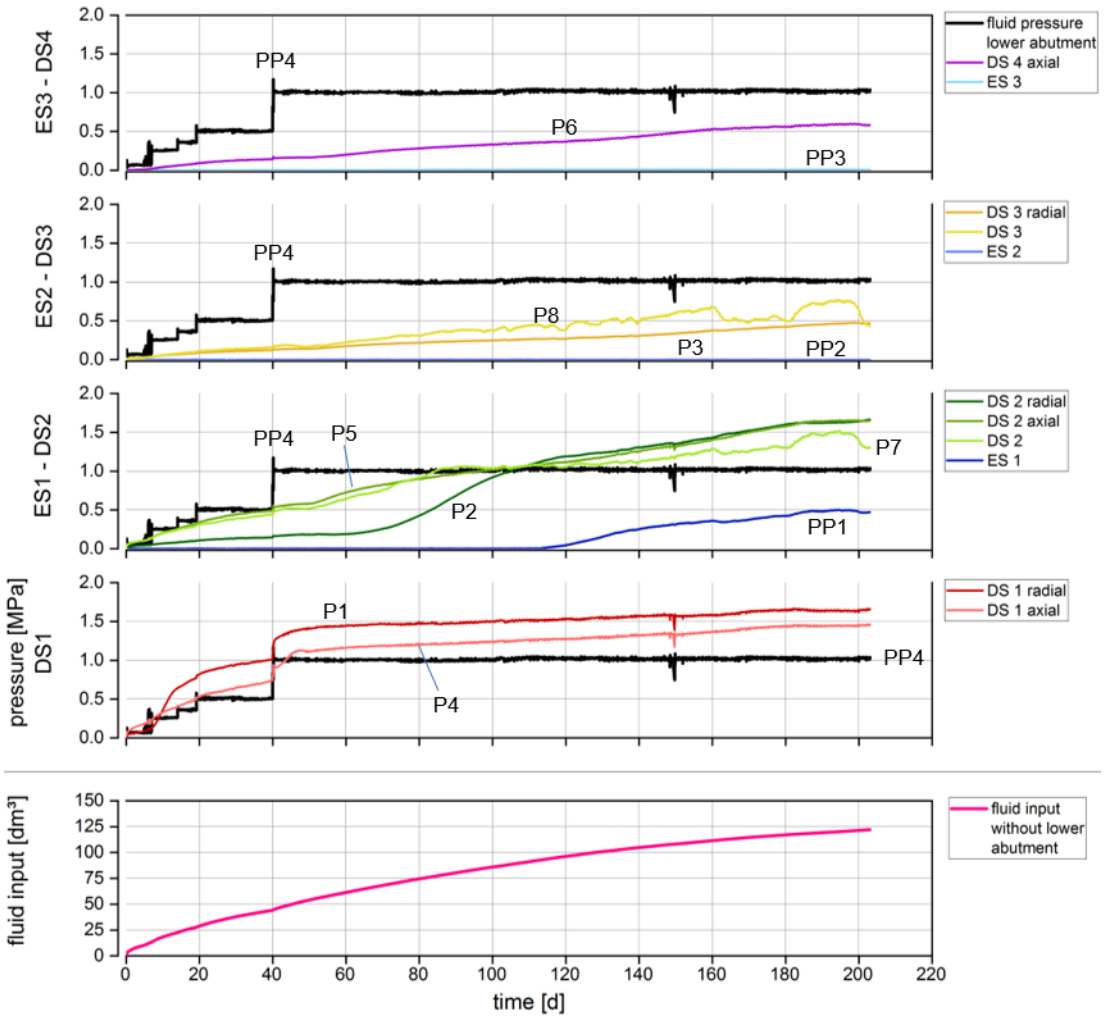

Fig. 5.80 Pressure curves and course of injected fluid in HTV-9

The flow rate of Pearson water A3 into the column decreased only slowly during the 1.0 MPa pressure step. 20 d after pressurization with 1.0 MPa, the flow rate was 0.03 dm³/h, after 80 d holding time the value had dropped to 0.02 dm³/h and after 163 d (on 31.08.23) holding time it was 0.01 dm³/h (Fig. 5.81). The smoothing curve was calculated using the same method as for the HTV-7 and HTV-8.

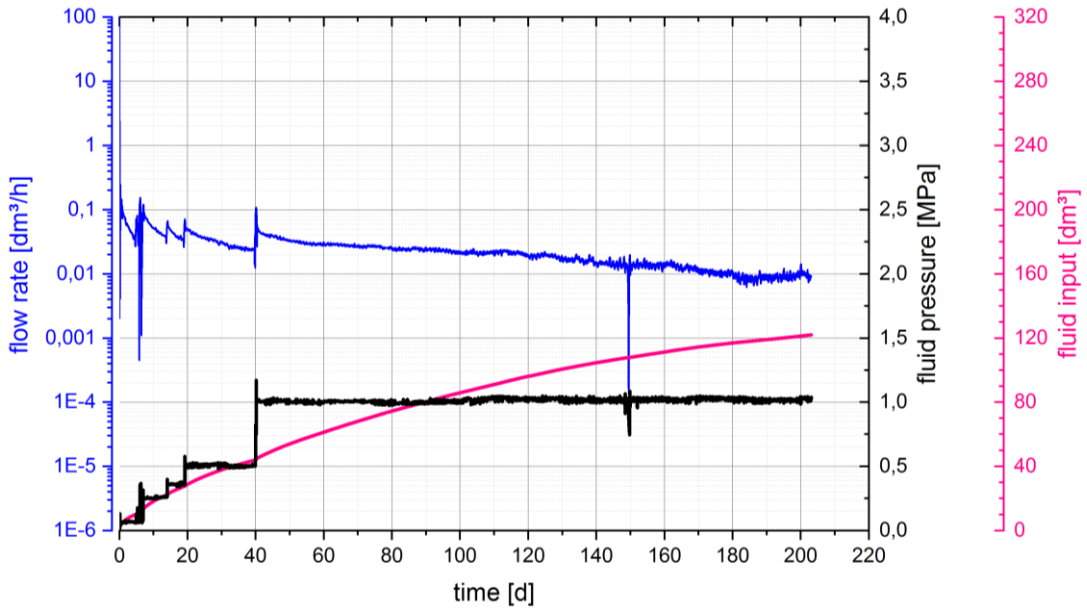

Fig. 5.81 Flow rate, fluid pressure and fluid input into the sealing system in HTV-9

Fluid propagation

During the first 72 days increasing faulty signals appeared due to contact problems on the multiplexer of the measurement system. It was replaced and measurements continued without disruption.

Hydration started with Pearson Water A3 of 1 bar (Tab. G. 3). First raise of ARDP appeared at TDR sensor low ends after increasing the pressure stepwise to 3 bar on day 8 to 5 bar on day 20 (Fig. 5.82). Then, liquid propagated slowly and nearly homogenously, but at a low rate, on all vertical sensors through DS1. After the next pressure step to 10 bar at day 40, fluid reached ES1 and further on over DS2 up to ES2. But still on a low ARDP level. Nevertheless, swelling pressure has built up and shifted DS2, ES2 and DS3 slightly upwards. Around day 150, increase of ARDP diminished or even stopped and restarted for the three sensors on day 175, with stronger increase of ARDP. Liquid has reached ES2 and has possibly propagated already up to the top of DS3. Materials above DS3 seem not to be affected by liquid yet, only a small compaction can be found. ARDP integral results confirm the findings.

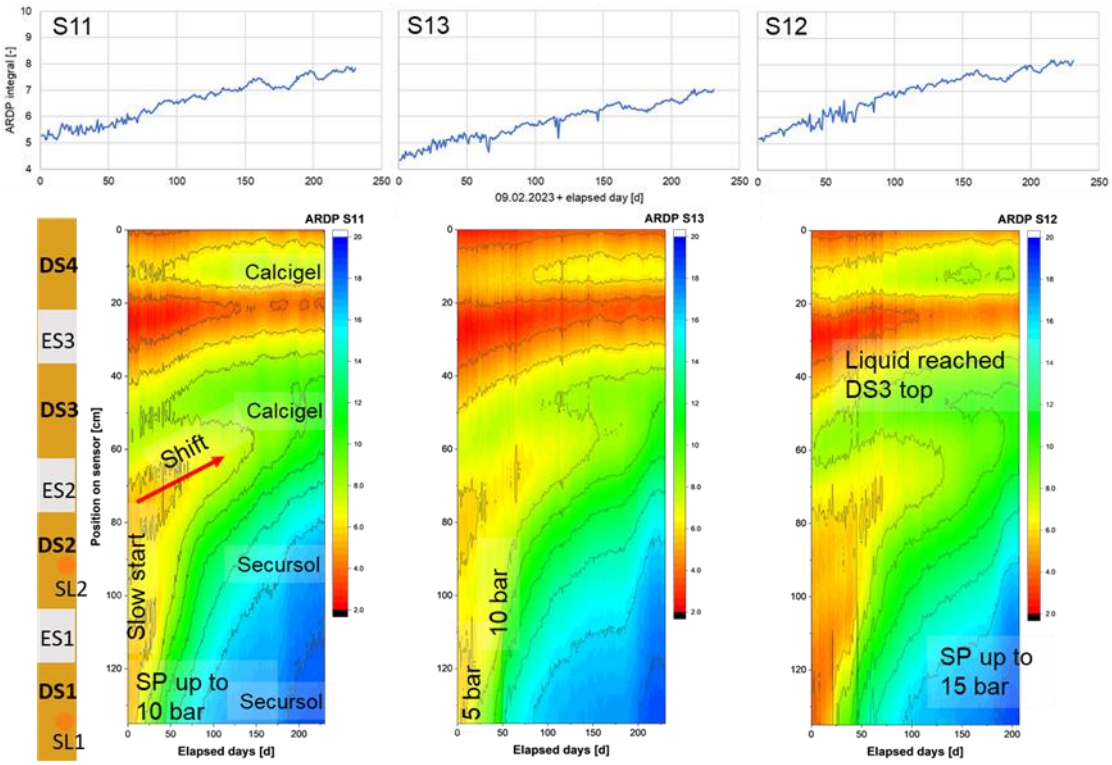

Fig. 5.82 ARDP distribution as indication of liquid progress at three TAUPE TDR sensors, S11, S13 and S12 (bottom), integral ARDP (top) HTV-9

The slow reaction of the system up to the liquid pressure rise of 10 bar on day 40 can also be observed by the horizontal sensors (Fig. 5.83). ES1 started fast, filling from the far end side of the sensor and remained nearly stable on a saturated level after day 120. ES2 responded over time only with compaction and firstly around day 180 with a nearly homogeneous increase of ARDP, when liquid touched ES2.

Temporal resolved graphs of vertical cross-sections along the sensors S11 – S13 – S12 show again the slow start of the experiment (Fig. 5.84). Corresponding to the results of HTV-7 and HTV-8 the influence of the sand lenses in DS1 and DS2 is visible. On day 20 liquid has started to hydrate the lower part of DS1, what has already produced swelling pressure and shifted the S11-side slightly upwards. After the pressure step to 10 bar, liquid has risen up nearly homogenously to ES1 and started to hydrate the lower part of DS2. Swelling has increased and the shift in DS2 has been equilibrated over the complete area.

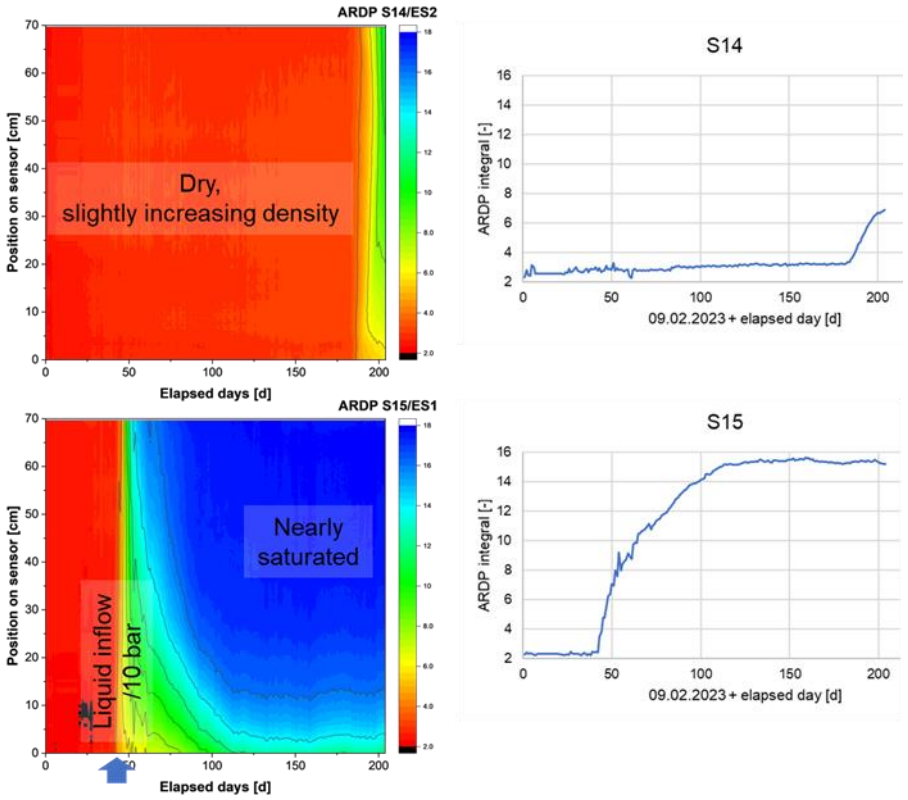

Fig. 5.83 ARDP distribution at horizontal TAUPE TDR sensors (left) and integral ARDP (right) for S15 (in ES1) and S14 (in ES2) in HTV-9

On day 81, day 143 and day 204, this progress in liquid propagation and further building up of swelling pressure at the same liquid pressure continues (Fig. 5.84). On day 81, the liquid level, in low level, has entered the lower part of DS2, producing compaction on the structure above. On day 143, this process has further progressed, a bit stronger on the S11-side, but had still not reached ES2 (what happened around day 180). After 204 days from start, DS1 and ES1 are nearly saturated and inflow of liquid is reduced. ARDP of ES2 had reached mid-level, and was able to distribute liquid further to the lower part of DS3, but has not reached the top of DS3. ES3 has been not yet affected, except of the compaction due to swelling processes in lower segments.

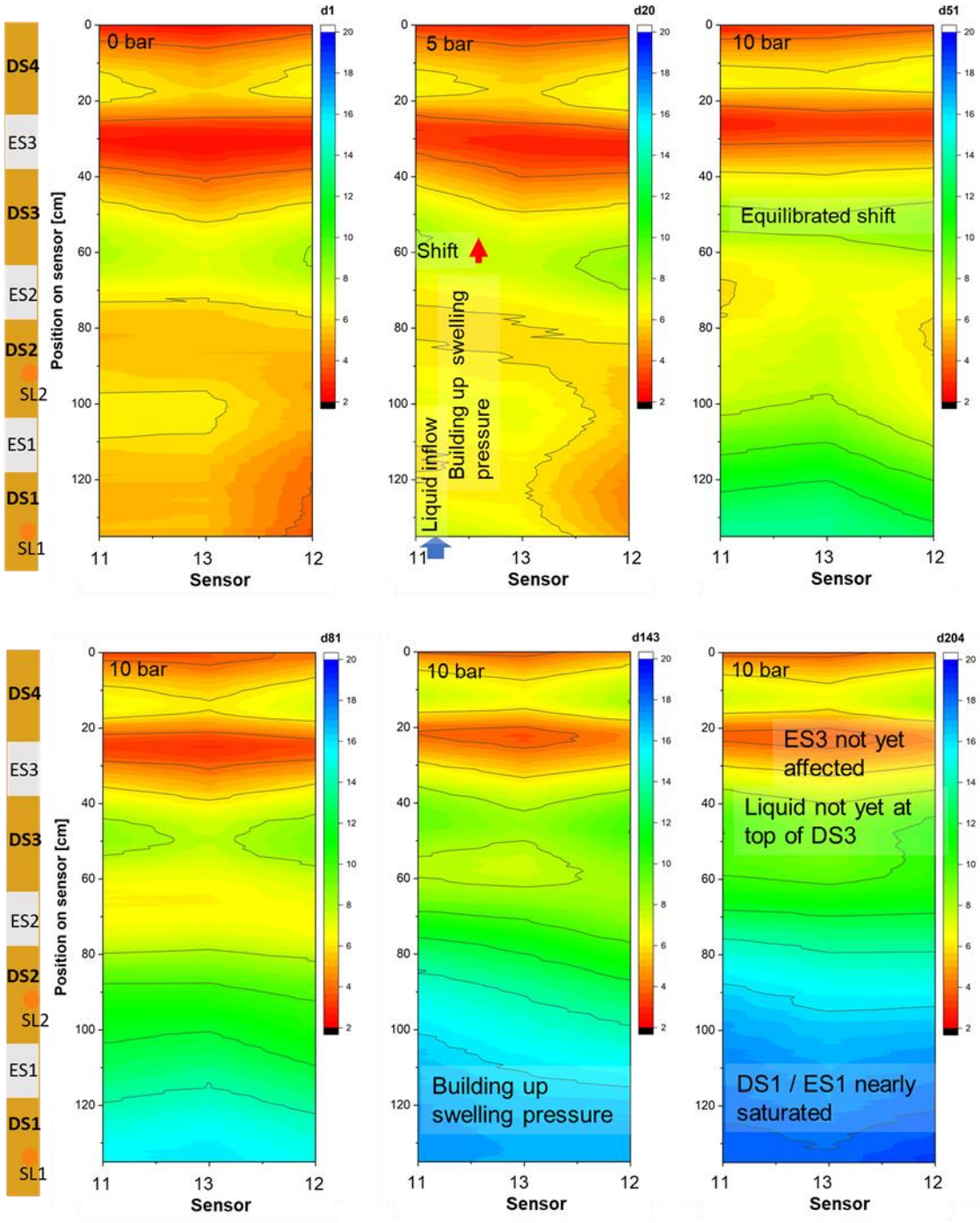

Fig. 5.84 Interpolated ARDP distribution between three vertical TAUPE TDR sensors in HTV-9 taken at (top) day 1, 20 and 51; (bottom) taken at day 81, 143 and 204

6 Model simulation

Numerical simulations were performed in both the Sandwich-VP and the Sandwich-HP. The focus in the Sandwich-VP was on scoping calculations for the layout of the in-situ experiment. Sandwich-HP simulations concentrated on the calibration of the bentonite material models by simulation of lab tests and on interpretative simulation of the in-situ experiment, especially the evolution of Shaft 1.

Hydro-mechanically coupled (HM) simulations were performed by three groups: GRS uses the finite element code Code_Bright /OLI 20/, BGR uses OGS /KOL 12/, and ENSI uses COMSOL Multiphysics® 5.6 /COM 21/. GRS performed additional hydraulic large-scale simulations of load scenarios for a shaft sealing system following the current German concept for argillaceous host rock (concept SOUTH) using TOUGH2 /PRU 99/.

6.1 Summary of Sandwich-VP results

The main objectives of the scoping calculations /EMM 19/ performed in the frame of Sandwich-VP was to give aid in the design of the in-situ experiment, especially regarding the necessary distance between the two experimental shafts, and to try to predict the time required for hydration of the sealing system.

GRS developed a 3D model of the experimental site including a realistic history of excavation of galleries, niches, and shafts. Coupled HM simulations with Code_Bright confirmed that, with the given shaft dimensions, a distance of 5 m between the shaft walls would be sufficient to keep up a positive pore pressure between the shafts at the depth of the sealing systems, so that an undesirable interaction between the shafts would be improbable. Hydration of the sealing system via the pressure chamber was governed by the suction of bentonite rather than by injection pressure, at least in the early phase of the experiment when very high suction pressures exist. At higher bentonite saturation, however, the simulation using the single-porosity elasto-plastic (TEP) model /ALO 90/, /OLI 20/ failed.

Single shaft simulation by BGR using OGS /KOL 12/ predicted decades to reach full saturation and, for the first three years of hydration, significant saturation only at the fringes of the DS. The parameters for this simulation were derived from the MiniSandwich

Test 8 (compare Chap. 6.2.1 and Chap. 6.2.2). This result confirmed the need to include a back-up hydration system (Chap. 3.4.1) in the experiment configuration.

6.2 Bentonite model calibration

Simulation of the Sandwich in-situ and laboratory experiments needs calibrated material models. The critical material with the most complicated behavior is the bentonite. For the first step of calibrating the bentonite model, the MiniSandwich Test 8 (see Chap. 5.4) was chosen, because it involved the same bentonite type, dry density, and initial saturation as the in-situ experiment performed in Shaft 1. Afterwards, swelling tests for Calcigel (see Chap. 5.3) were included in further calibration.

6.2.1 First steps - MiniSandwich Test 8

Code_Bright model used by GRS

First test simulations of Test 8 proved that the single-porosity elasto-plastic bentonite model /ALO 90/ used for the scoping calculations was not able to reproduce the water uptake and the axial stress evolution measured in the experiment in a satisfying way. Therefore, the dual porosity (or double structure) BExM model /ALO 99/ was employed. The BExM model was developed and is used by the Polytechnic University of Catalonia (UPC) for strongly swelling clay materials like bentonite. In the following paragraphs, the model in the version available at project start is shortly described. This version had been successfully used for the modelling of the Mont Terri EB experiment hydration /VAS 14/.

The double structure model distinguishes between micro- and macro-structure with different material behavior. The total porosity is the sum of micro- and macro-porosity. Definition of these model porosities is not necessarily straight forward. In a granular material, three types of porosity may be defined, as shown on the example of an aggregate of minerals in Fig. 6.1: The inner-aggregate space between clay particles, the inner-particle space, and the inter-layer space within a clay particle. In the BExM model, macro-porosity is normally defined as the inner-aggregate or inter-particle space, while the other two add up to the micro-porosity. This is, however, not mandatory /OLI 20/.

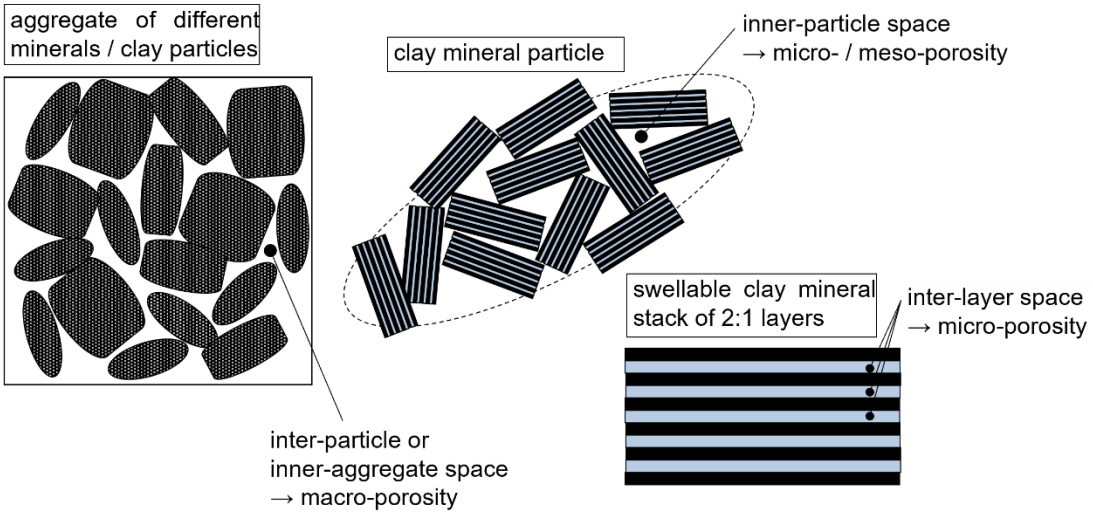

Fig. 6.1 Porosity concept for granular bentonite material, modified after K.-P. Kröhn in /BER 22/

The macro-structure is characterized by an elasto-plastic behavior which is based on the original single-porosity model of /ALO 90/. Fig. 6.2 shows the principal behavior in the space characterized by the axes compressive stress (p) – deviatory stress (q) – suction (s). It can describe swelling/shrinking or collapse of the macro-structure depending on the stress and suction state.

The micro-structure is modelled as an elastic material.

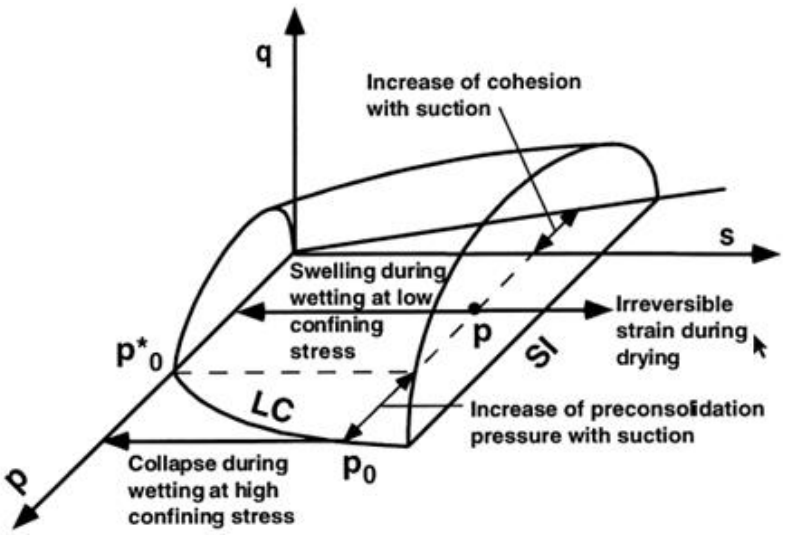

Fig. 6.2 Macro-structural behavior of the BExM model /ALO 99/

The interaction between micro- and macro-structure is controlled by two interaction functions f_D and f_I, depending on whether suction is decreasing or increasing (Fig. 6.3). Depending on the ratio p/p_0 (with compressive stress p and preconsolidation pressure p_0), wetting leads to macro-porosity development and expansion or to micro-pores invading the macro-porosity.

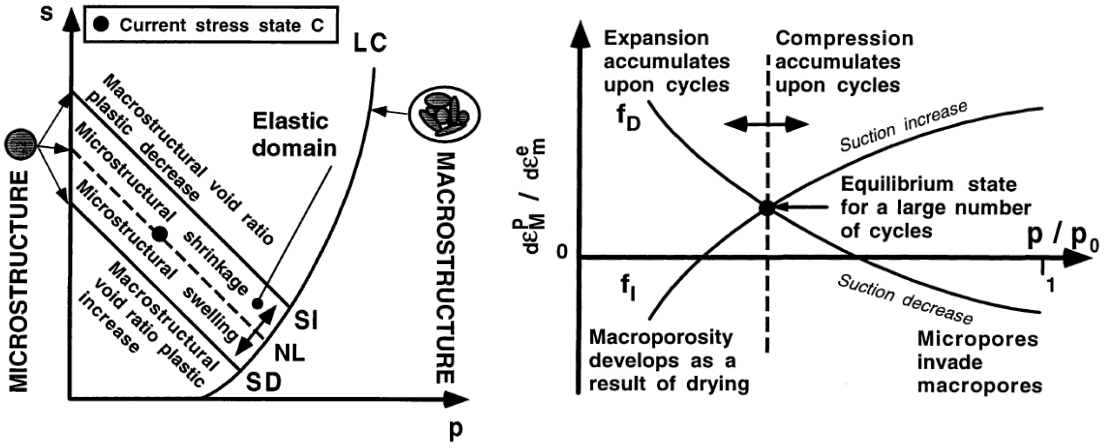

Fig. 6.3 BExM micro-/macro-structure interaction

Left: Yield loci in the p-s plane.
Right: Interaction functions and structural changes due to the mechanical coupling between the two structures /ALO 99/.

A comprehensive description of the behavior including the mathematical formulation is given in /ALO 99/.

The hydraulic behavior of this version of the model is characterized by an overall retention function and a porosity-permeability function that relates permeability to the macro-porosity (it is assumed that the micro-porosity is not relevant for advective flow).

Normally, the distinction between micro- and macro-structure requires separate retention functions and a way to control water transfer between the structures. This feature is implemented in a new version of the BExM that was not available until recently. In the version used here, it is assumed that the micro-structure is mostly saturated and always in equilibrium with the macro-structure. This means that highly desaturated materials cannot be modelled.

For first calibration tests of the BExM model the MiniSandwich Test 8 (see Chap. 5.4) was chosen, because it involved the same bentonite type, dry density, and initial

saturation as the in-situ experiment performed in Shaft 1. Note that Test 7 which was performed with the same material, but with very low initial saturation, could not be used due to the above restriction.

Calibration started with the parameters that had been used in the Mont Terri EB experiment simulation /VAS 14/ except for the initial porosities. The EB experiment /MAY 07/, /MAY 14/ featured a granular buffer of FEBEX bentonite which is a Ca-bentonite like Calcigel.

The initial bentonite porosity in the MiniSandwich Test 8 is 0.44. The initial micro-porosity was set to 0.27 and the macro-porosity to 0.17, which represents the open space between the bentonite aggregates as calculated from the dry densities of a single pellet and the granular material. Thus, micro-porosity in the model represents the sum of micro- and meso-porosity in Fig. 6.1.

The final mechanical parameters used for the bentonite are shown in Tab. 6.1 (explanation of the parameters in /ALO 99/ or /OLI 20/). The only differences to the EB parameters are, beside the porosities, the values for the minimum bulk modulus K (the Sandwich-HP material is somewhat stiffer than the EB material) and the initial preconsolidation pressure p_0* which is the fitting parameter for the swelling pressure.

The ES material (fine sand) of the MiniSandwich was modelled as an elastic material with Young's modulus of 1000 MPa, Poisson's ratio of 0.245 and porosity of 0.41.

Retention curves for the granular Calcigel (DS) material and the N45 fine-grained sand (ES) were determined by CIEMAT (Chap. 5.3.1). The measured data were approximated by van Genuchten curves (Fig. 6.4) with the parameters given in Tab. 6.2. Note that

$$S_e = \left[1 + \left(\frac{P_g - P_l}{P}\right)^{1/(1-\mu)}\right]^{-\mu} \quad \text{with} \quad P_g - P_l \geq 0 \quad \text{and} \quad P = P_0 * \frac{\sigma}{\sigma_0}$$

with the effective saturation S_e, gas and liquid pressures P_g and P_l, water surface tension σ and $\sigma_0 = 0.072$ N/m. The residual liquid and gas saturations are set to 0 and 1, respectively. The initial porosities are 0.44 for the Calcigel and 0.41 for the sand.

Tab. 6.1 Parameters of the BExM model for MiniSandwich Test 8 sealing segments

BExM model parameter		Value	Unit
Elastic Parameters	k(Macro)	0.02	
	k(micro)	0.02	
	k(s)	0.03	
	n(M)	0.2	
	$K(min)_{Macro}$	4.5	MPa
	$K(min)_{micro}$	4.5	MPa
Coupling Params	f(sd0)	-0.1	
	f(sd1)	1.3	
	n(sd)	5	
	f(si0)	-1	
	f(si1)	2	
	n(si)	0.1	
Yield Surface	M	1.3	
	r	0.65	
	b	0.01	MPa^{-1}
	pc	0.075	MPa
	ks	0	
	pt0	0.1	MPa
Plastic Potential	omega	1	
Hardening	l(0)	0.2	
	eta	0	MPa s
History variables	P_0*	0.6	MPa
	Φ_{0micro}	0.27	

Tab. 6.2 Parameters of the retention curves for DS and ES materials in MiniSandwich Test 8

Parameter	DS (Calcigel)	ES (Sand)	Unit
P_0	22.4	0.3	MPa
$б_0$	0.072	0.072	Nm^{-1}
μ	0.359	0.4	
S_{rl}	0	0	
S_{ls}	1	1	
Φ_0	0.44	0.41	

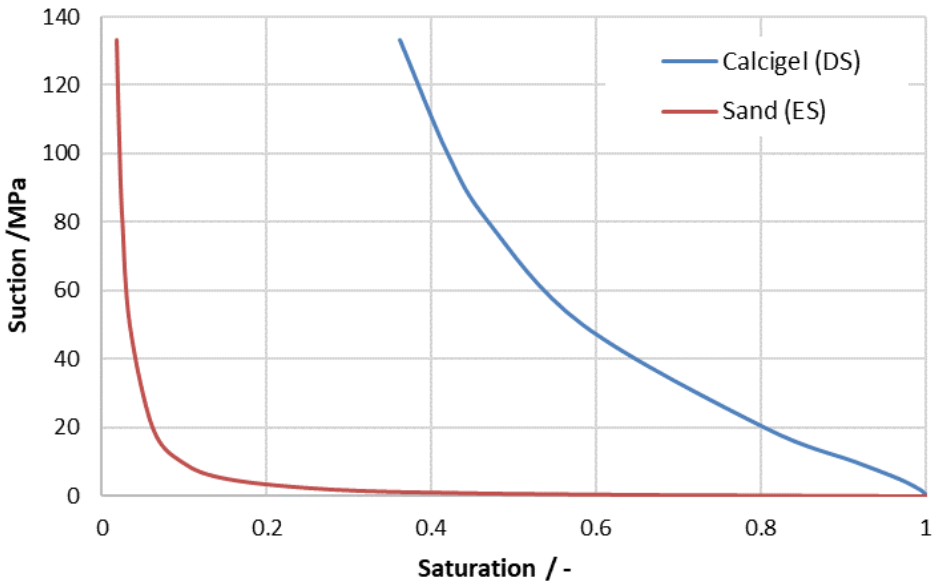

Fig. 6.4 Retention curves employed for DS and ES materials in MiniSandwich Test 8

The permeability of the DS was (beside p_0*) the second optimization parameter of the calibration. The permeability k was described by an exponential function of the macro-porosity Φ_M as

$$\mathbf{k} = k_0 \exp[b(\phi_M - \phi_{M0})]\mathbf{I}$$

With $k_0 = 10^{-20}$ m², b = 60 and $\Phi_{M0} = 0.44$. The permeability of the ES was set to 10^{-11} m². Relative permeabilities are calculated by the effective saturation to a power of 6.

The MiniSandwich Test 8 was simulated with these parameters and an initial suction of 133 MPa in both materials, corresponding to an initial saturation of the bentonite of 36 % and of the sand of 1.7 %. The test setup and the axisymmetric mesh used are shown in Fig. 6.5.

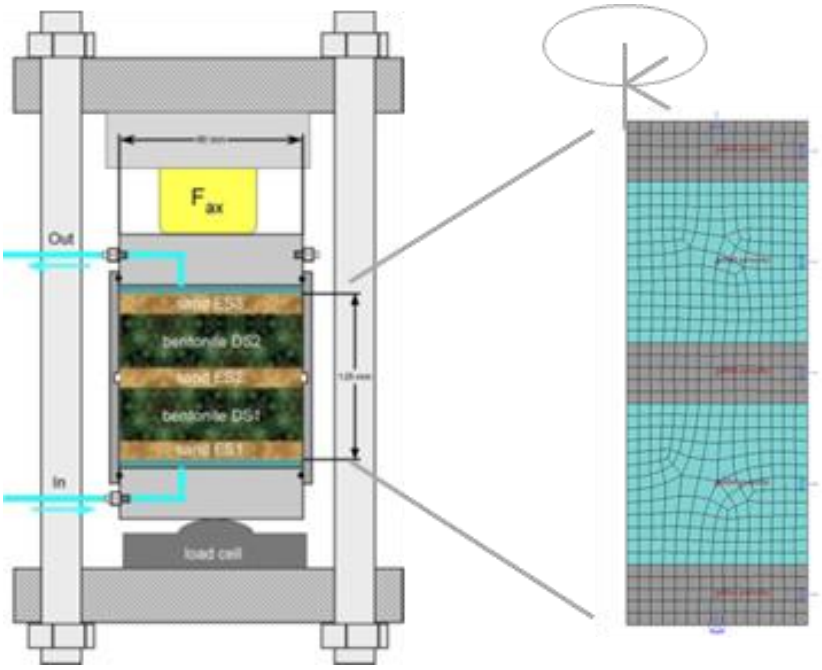

Fig. 6.5 Test setup of MiniSandwich Test 8 and axisymmetric mesh for the Code_Bright simulation

All model boundaries are fixed in either x or y direction. At the lower boundary, hydraulic pressure is raised from -133 MPa to atmospheric within one day, afterwards atmospheric pressure is held. The other boundaries are no-flow.

Fig. 6.6 and Fig. 6.7 show the calculated data for cumulative inflow and axial stress in comparison to the measurement data. It can be stated that, with this calibration, a satisfactory match is reached.

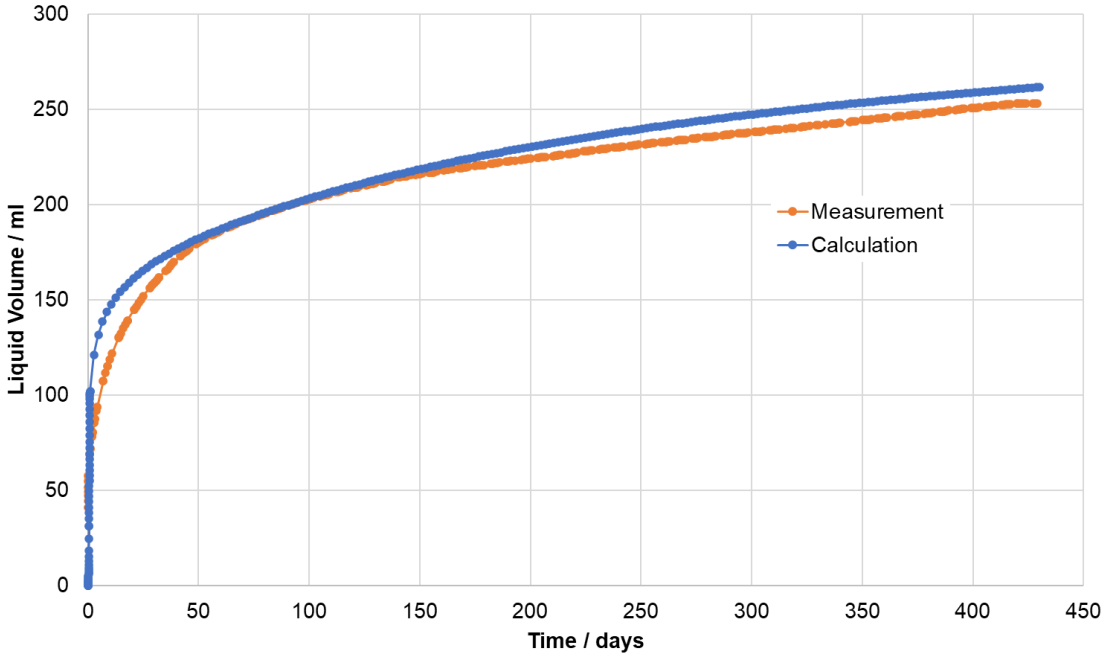

Fig. 6.6 Measured and calculated cumulative inflow of MiniSandwich Test 8

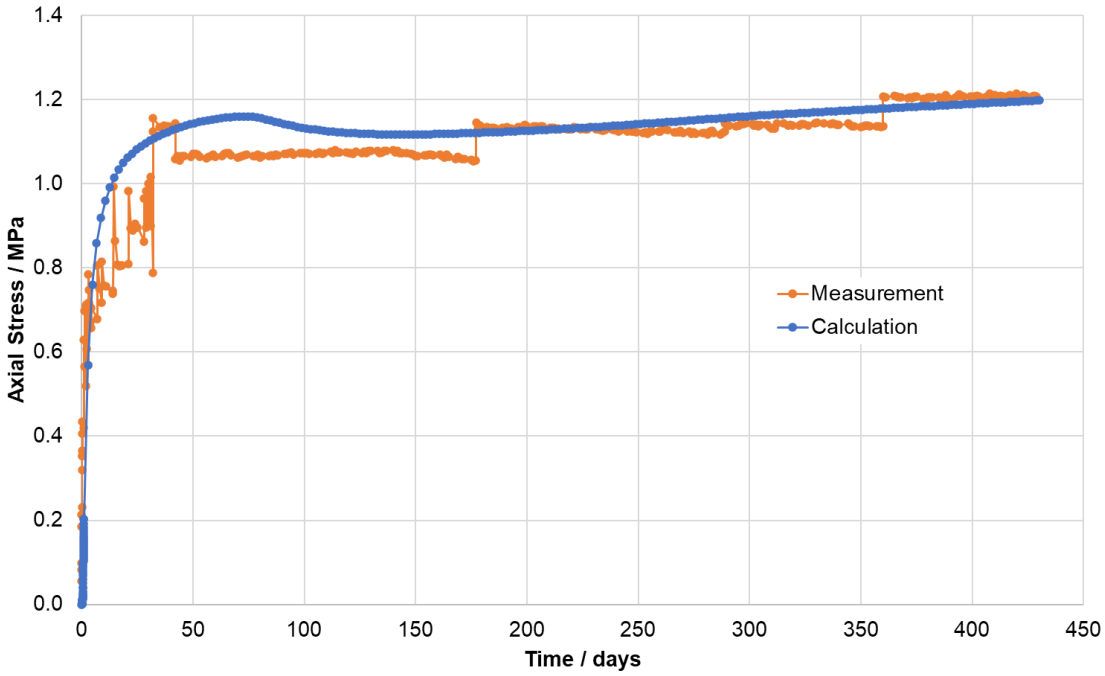

Fig. 6.7 Measured and calculated axial stress of MiniSandwich Test 8

The modelled status of the sample after 430 days of hydration, at the end of the experiment, in terms of axial displacements, total porosity, micro-porosity, permeability, liquid pressure and saturation is shown in Fig. 6.8 and Fig. 6.9, respectively.

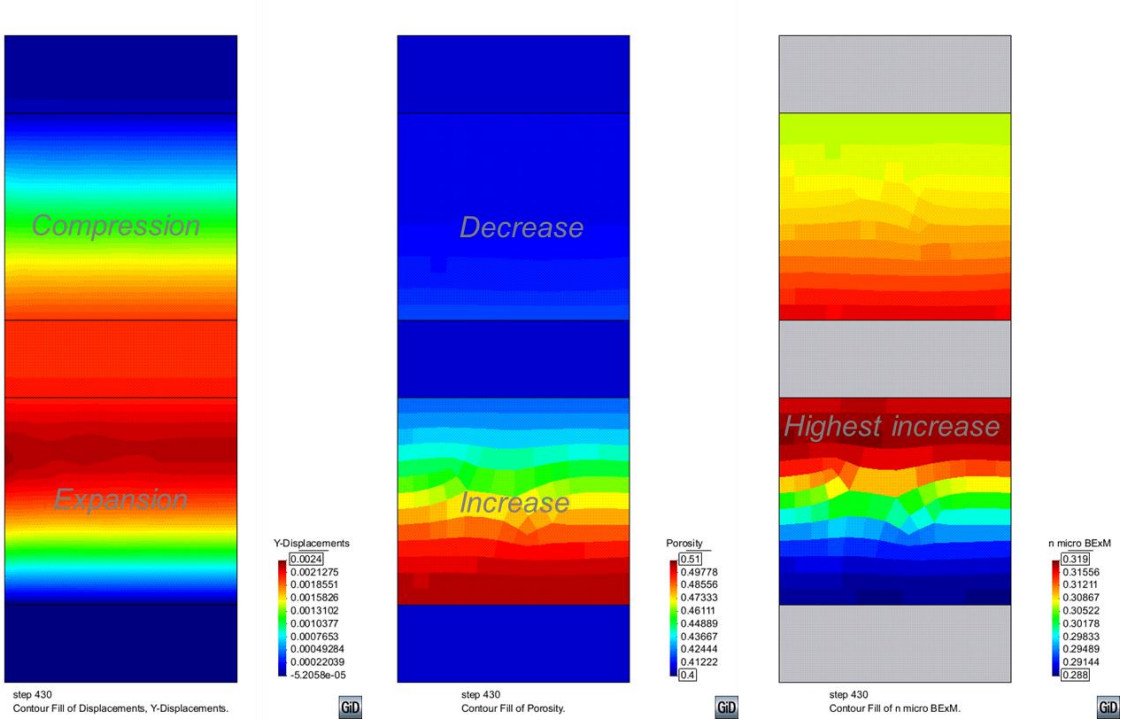

Fig. 6.8 Axial displacements (left), total porosity (center) and micro-porosity (right) in the MiniSandwich Test 8 simulation after 430 days

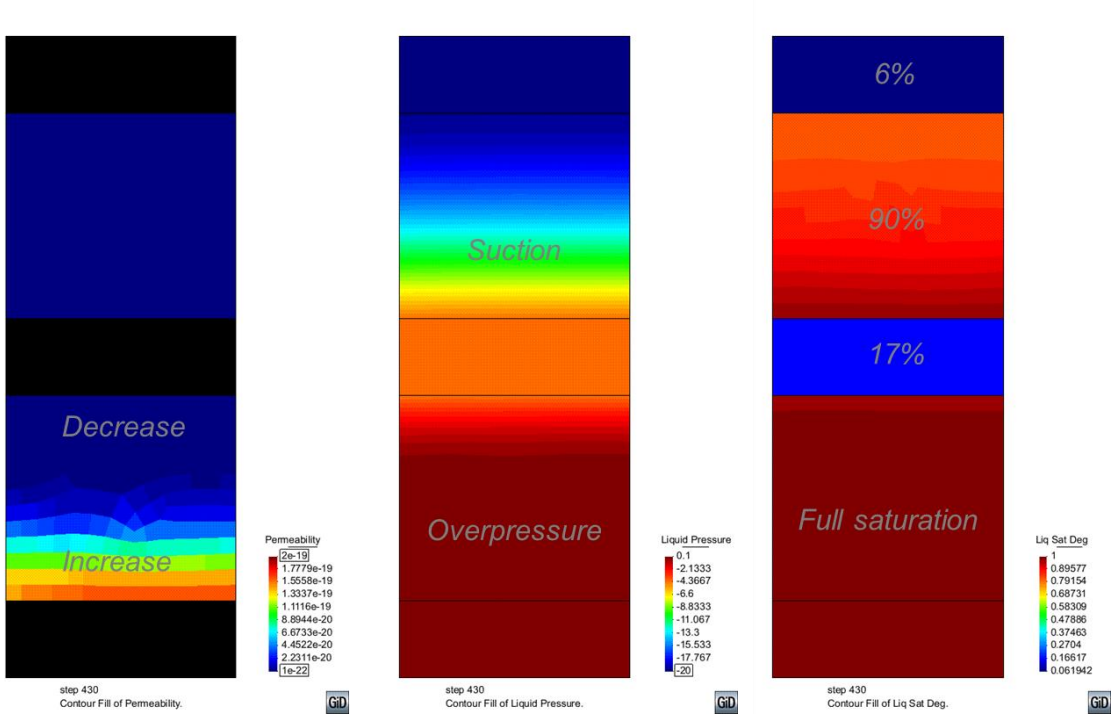

Fig. 6.9 Permeability (left), liquid pressure (center) and saturation (right) in the Mini-Sandwich Test 8 simulation after 430 days

The following observations can be made in the figures:

- On the hydration side (bottom of the model), the bentonite swells, leading to a compression of the upper part of the model. Consequently, total porosity increases in the lower DS and decreases in the upper DS (Fig. 6.8).
- In the beginning, there is no compressive stress, therefore hydration leads to macro-porosity increase near the hydration front. Later, when stress has built up, micro-porosity increases on the cost of macro-porosity (Fig. 6.8).
- Permeability increases where macro-porosity increases and decreases where macro-porosity decreases (Fig. 6.9).
- At the end of the experiment, the lower ES and DS are fully saturated, while the upper DS is still under suction, but with a high saturation of around 90 %. The center and upper ES are still quite dry (17 % and 6 % saturation), which is due to the difference in retention curves of the two materials.

Especially the last observation was confirmed by the post-mortem investigation of Test 8 (see Chap. 5.4).

It must be noted that, while this calibration led to satisfying results, it is not unique. There will be other combinations of parameters that also produce satisfactory matches with the measurements. Many parameters of the BExM model are not readily accessible to direct measurement, and their determination is rather subjective /VAS 21/. The solution could be to derive a consistent set of parameters or a rule to set parameters that is capable of simulating different experiments running under different conditions.

The influence of the choice of micro-/macro-porosity ratio was directly investigated by using a different split: Micro-porosity was set to 0.15 and macro-porosity to 0.29. Thus, micro-porosity would be the actually saturated part of the porosity. A comparison of the results of this simulation to the one presented here shows that, while there are minor differences, the overall behavior of both runs is very close. This seems to show that the choice of micro-/macro-porosity ratio in the model is not critical for a reasonable range.

OGS model of BGR

In the pre-phase of the project, a concept was developed to simulate the hydromechanical interaction between DS and ES /SHA 23/. On this basis, a linear swelling model and an empirical permeability-swelling strain function for DS are introduced in the coupled hydromechanical model with Richards' flow and elasticity. For ES, an empirical permeability-compaction strain function is used.

COMSOL model of ENSI

To compute saturation, swelling and strain for the MiniSandwich Test 8, a system of two coupled equations has been solved, namely Richards' equation for the hydraulic part and the linear elastic equation for the mechanical part. The equations and coupling terms are described in this section. Fluid flow in unsaturated conditions can be solved by Richards' equation by assuming a spatially constant gas pressure. Consequently, the hydraulic part of the system of equations solves for water pressure p as follows:

$$\rho(Se\epsilon\chi C_m)\frac{\partial p}{\partial t} - \nabla\cdot\left(\rho\frac{\kappa_s\,\kappa_{vg,rel}\kappa_{sw,rel}}{\mu}\nabla p\right) = -\rho Se\frac{\partial \varepsilon_{vol}}{\partial t}$$

with the effective saturation been defined by the van Genuchten retention model:

$$Se = \begin{cases} \dfrac{1}{\left(1+\left|\frac{p}{p_e}\right|^n\right)^{1-\frac{1}{n}}}, & p<0 \\ 1, & p\geq 0 \end{cases}$$

and the van Genuchten relative permeability model as:

$$\kappa_{vg,rel} = Se^l\left(1-\left(1-Se^{\frac{1}{m}}\right)^m\right)^2$$

with the storage term as:

$$C_m = \epsilon\frac{\partial Se}{\partial p} = \frac{m}{p_e(1-m)}\epsilon Se^{\frac{1}{m}}\left(1-Se^{\frac{1}{m}}\right)^m$$

An additional term is introduced to account for permeability changes due to swelling. Here a linear relation is chosen as follows:

$$k_{sw,rel} = \begin{cases} \max(0.012, 1 - 980\ \varepsilon_{vol}), & in\ DS \\ \max(0.1, 1 + 900\ \varepsilon_{vol}), & in\ ES \end{cases}$$

With the material parameters, entry pressure p_e, intrinsic permeability κ_s, porosity ϵ, fluid compressibility χ, dynamic fluid viscosity μ, fluid density ρ, and van Genuchten Parameters m, l. The coupling of the mechanical processes to Richards' equation is achieved by introducing the volumetric strain with $\varepsilon_{vol} = \varepsilon_{xx} + \varepsilon_{yy} + \varepsilon_{zz}$.

For the mechanical part of the coupled system of equations, based on a linear elastic assumption, the following equation is solved by:

$$\nabla \cdot \left(\boldsymbol{C} : \varepsilon - Se^{\mathrm{X}} \alpha_B (p + p_{ref}) \boldsymbol{I} - \sigma_{sw,max}\, Se \right) = 0,\ \boldsymbol{C} = \boldsymbol{C}(E, \nu);\ \varepsilon = \frac{1}{2}[(\nabla \boldsymbol{u})^T + \nabla \boldsymbol{u}]$$

With the elasticity tensor $\boldsymbol{C}$, maximum swelling pressure $\sigma_{sw,max}$, Bishop's exponent X, Biot-Willis coefficient α_B, identity matrix $\boldsymbol{I}$, reference pressure $p_{ref} = 1\ atm$, Young's Modulus E, Poisson ratio ν, and displacement vector $\boldsymbol{u}$. The coupling of Richards equation to the mechanical equation is achieved by introducing the effective saturation Se and the pore pressure p.

The initial and boundary conditions for the simulation of the MiniSandwich Test 8 are set according to the description above for the Code_Bright model.

For the mesh a pseudo 1D discretization has been chosen as there are no lateral changes of the primary variables. The discretization of the mesh as shown in Fig. 6.10 is refined at the material interfaces to resolve steep gradients in the system.

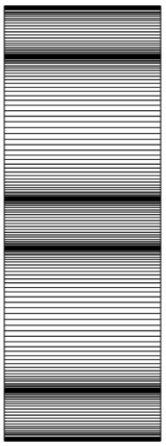

Fig. 6.10 Mesh used for the COMSOL model of MiniSandwich Test 8

Elements are discretized only in axial direction with a refined discretization at the material interfaces.

Tab. 6.3 shows the parameter values used in the COMSOL model.

Tab. 6.3 Parameters of the COMSOL model of MiniSandwich Test 8. The values are based on /EMM 19/, p.152 (Tab. 6.4, Tab. 6.5) and internal project communication.

Parameter	**DS**	**ES**
Intrinsic permeability [m^2]	$6.44x10^{-18}$	$5.00x10^{-14}$
Porosity [-]	0.44	0.4
Entry pressure [MPa]	9	0.1
van Genuchten Parameter l [-]	0.5	
van Genuchten Parameter n [-]	2	
Residual saturation [-]	0	
Maximum saturation [-]	1	
Initial saturation [-]	0.46	0.11
Density, water [kg/m^3]	1000	
Dynamic viscosity, water [Ns/m^2]	0.001	
Compressibility, water [m^2/N]	$4.0x10^{-10}$	
E- Modulus [MPa]	150	300
Poisson ratio [-]	0.42	0.35
Biot-Willis coefficient [-]	0.6	0.6
Bishops exponent [-]	1.4	1.4
Maximum swelling pressure [MPa]	1.6	0
Rock dry density [kg/m^3]	1600	1500

Fig. 6.11 shows the effective saturation in axial direction over the simulation time of 400 days. As expected, the middle ES remains partially saturated for a long time after the two DS have reached full saturation. Thus, the Sandwich principle can be demonstrated

for this mockup test. At the end of the simulation the uppermost ES remains partially saturated while all other segments are saturated.

Generally, the re-saturation strongly depends on the definition of the strain-dependent permeability reduction. To this end a linear relation has been defined, which could be refined in future studies. Furthermore, the re-saturation depends on the initial saturation which introduced small relative permeabilities at initial times.

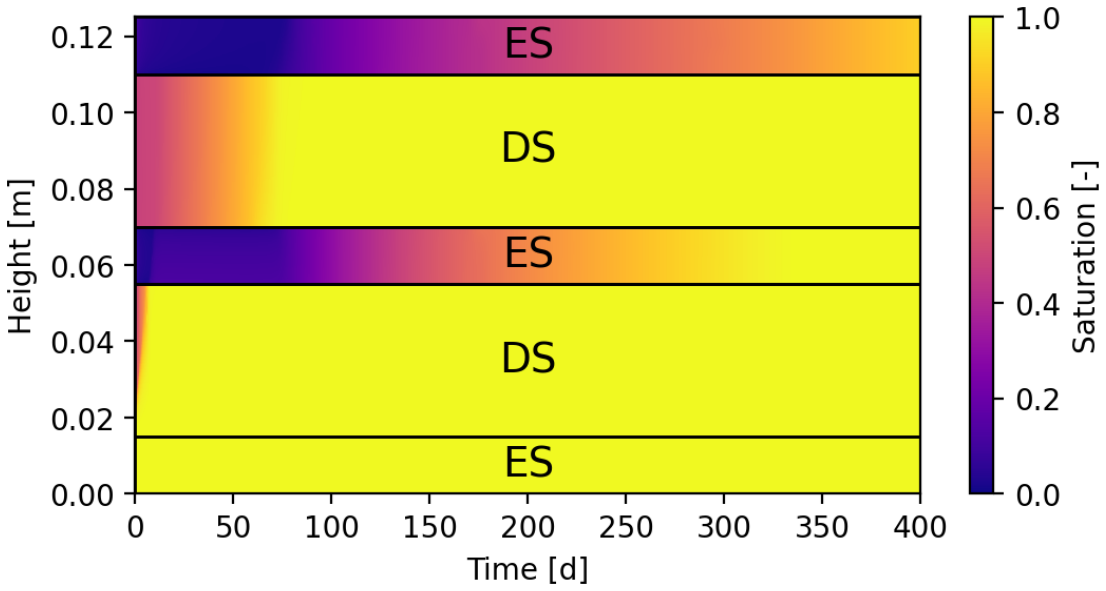

Fig. 6.11 Simulated effective saturation in axial direction of the specimen (y-axis) in MiniSandwich Test 8 over the simulation time of 400 days (x-axis)

6.2.2 MiniSandwich benchmark

The three MiniSandwich Test 8 simulations of GRS, BGR and ENSI were compared in a benchmark presented at the 8th International Clay Conference in Nancy /WIE 22b/. The cumulative water inflow and the axial stress of all three simulations together with the measured data are shown in Fig. 6.12. The evolution of axial stress and water inflow are well represented by all models, so it seems that the main physical phenomena during hydration are captured. The calculated saturation status at the end of the experiment (Fig. 6.13) is largely in line with the post-mortem analyses in /EMM 19/, although saturation of the center and upper ES in the OGS simulation is somewhat high. Despite the good representation of the axial stress and the inflow volume, the COMSOL results show a general overestimation of the saturation.

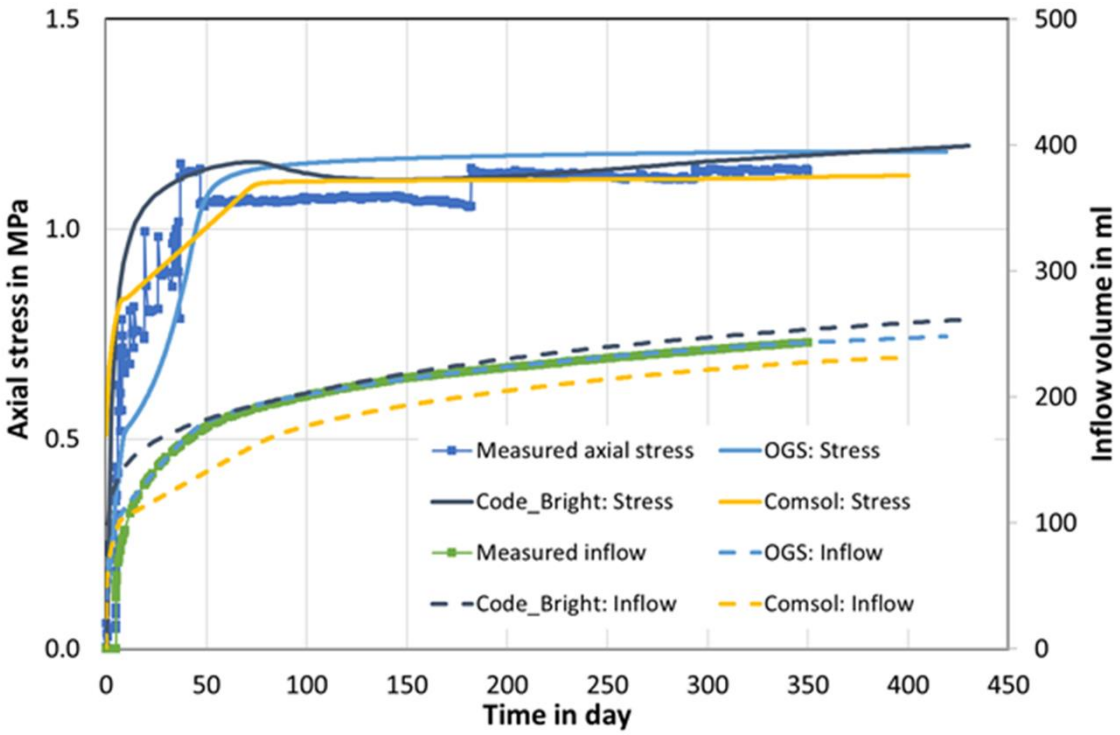

Fig. 6.12 Cumulative water inflow and axial stress of all three simulations together with the measured data of MiniSandwich Test 8

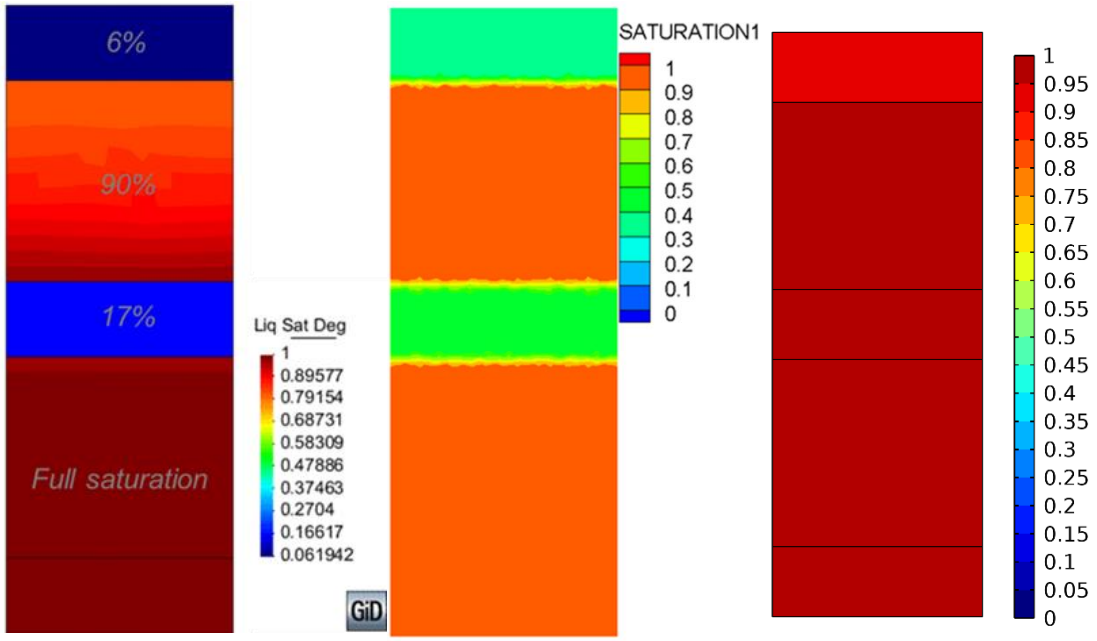

Fig. 6.13 Calculated saturation distribution for MiniSandwich Test 8 at the end of the experiment using Code_Bright (left), OGS (center) and COMSOL (right)

The critical parameters in the simulation were the maximum swelling pressure (for the linear swelling models of OGS and COMSOL) and the initial preconsolidation pressure (for the BExM model of Code_Bright), respectively.

Another critical parameter is the porosity/permeability relation which had not been confirmed at the time of the benchmark. To derive a reliable respective function, more experiments with different porosities and included permeability measurement were required. Therefore, model calibration was continued by simulating IBeWa's swelling tests (see Chap. 5.3).

6.2.3 Swelling test simulation

Swelling pressure tests were performed with samples having dry densities between 1.4 g/cm³ and 1.7 g/cm³. Permeability was measured at the end of each test after reaching full saturation (Chap. 5.3). Fig. 6.14 shows the measured swelling pressure (axial stress) and permeability at full saturation of these tests as functions of dry density. While the swelling pressure largely follows an exponential function of dry density (as expected), permeability values are somewhat erratic, which may be caused by inaccuracy of the dry density determination (some experiments ended at saturations considerably above 100 %). Moreover, the employed non-steady state measurement technique tends to overestimate permeability.

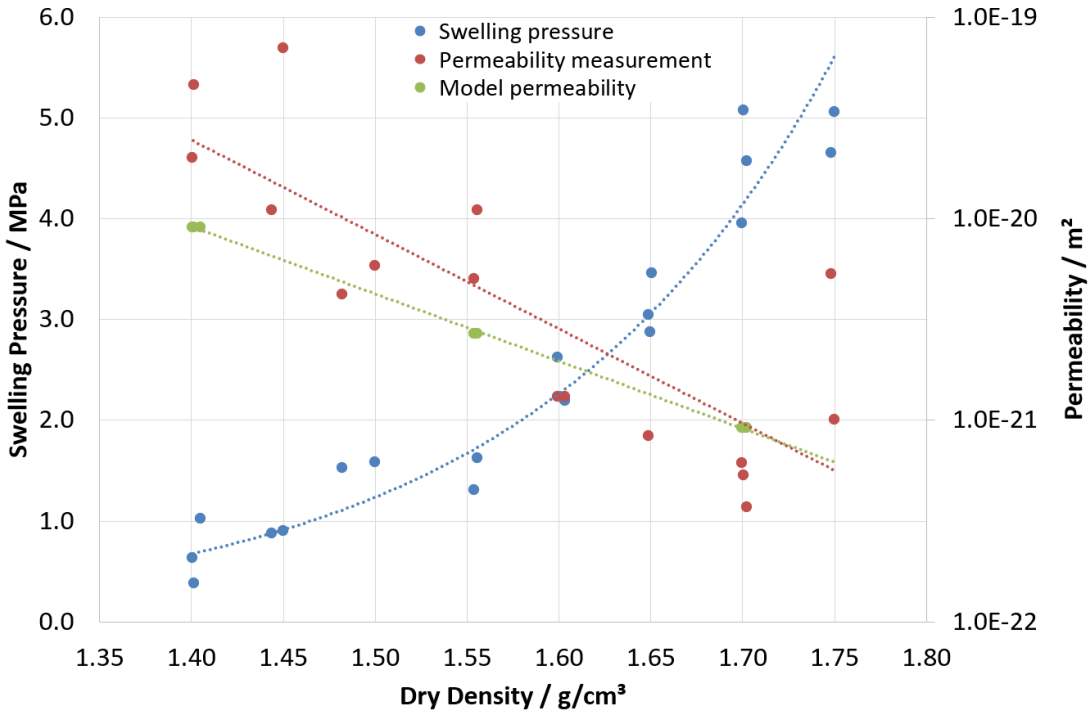

Fig. 6.14 Measured swelling pressure and permeability at full saturation as functions of dry density

Code_Bright model used by GRS

The idea of modelling the different swelling pressure tests was to take a step in deriving a consistent set of parameters for tests at different conditions. For the BExM calibration the approach was to

- Use one (macro-)porosity / permeability relation for all tests,
- Use one dry density / initial preconsolidation pressure relation for all tests,
- Have all other parameters identical.

In the case of the retention function, however, RUB's investigations showed that suction seems more a function of water content than of saturation. Therefore, simulations were performed with identical retention curves and also with modified curves reflecting this dependence. Simulations with dry densities of 1.4 g/cm³, 1.54 g/cm³, and 1.7 g/cm³ were performed. The corresponding retention curves are shown in Fig. 6.15. The center curve for 1.54 g/cm³ dry density is the original one also used for the MiniSandwich and in-situ experiment simulations.

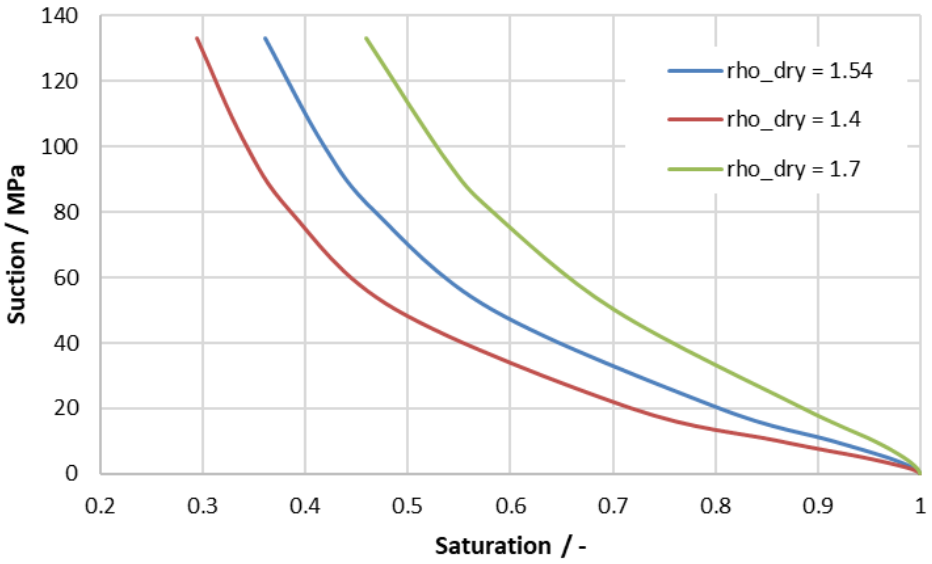

Fig. 6.15 Retention curves for different dry densities of Calcigel hydrated with Pearson water A3

The porosity / permeability relation developed for the simulation of the different tests is again of the form

$$\mathbf{k} = k_0 \exp[b(\phi_M - \phi_{M0})]\mathbf{I}$$

but with $k_0 = 4 \cdot 10^{-20}$ m², b = 27 and $\Phi_{M0} = 0.22$. The resulting permeabilities in relation to dry density (with a micro-porosity of 0.27) are shown in Fig. 6.14 (green curve). Calculation of relative permeabilities remained unchanged.

Initial preconsolidation pressure was optimized in each simulation. In fact, the optimal values show an exponential dependence of the dry density (Fig. 6.16), analogue to the measured swelling pressure of Fig. 6.14. To reach stable calculations, the minimum bulk modulus had to be raised from 4.5 MPa (Tab. 6.1) to 10 MPa.

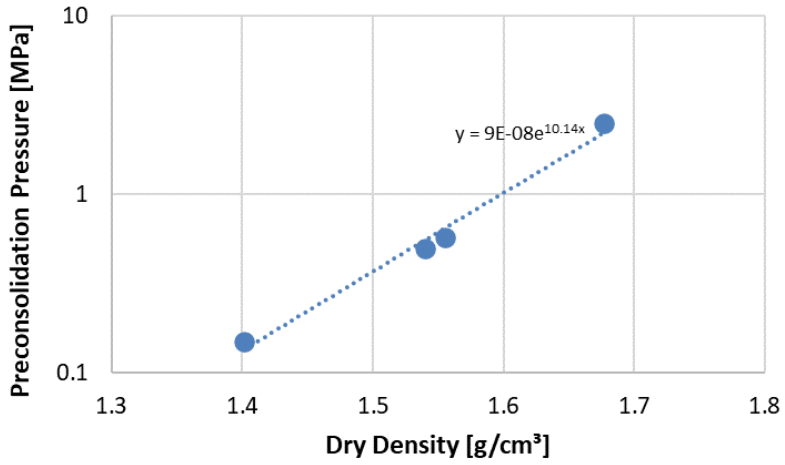

Fig. 6.16 Initial preconsolidation pressure as a function of dry density for the Calcigel model

The following figures show the results of the swelling test simulations with these parameters in terms of mean saturation and axial stress development together with corresponding measurement results.

The curves for a dry density of 1.54 g/cm³ are shown in Fig. 6.17. There is a convincing fit of the measurements, although saturations above 1.0 can naturally not be obtained.

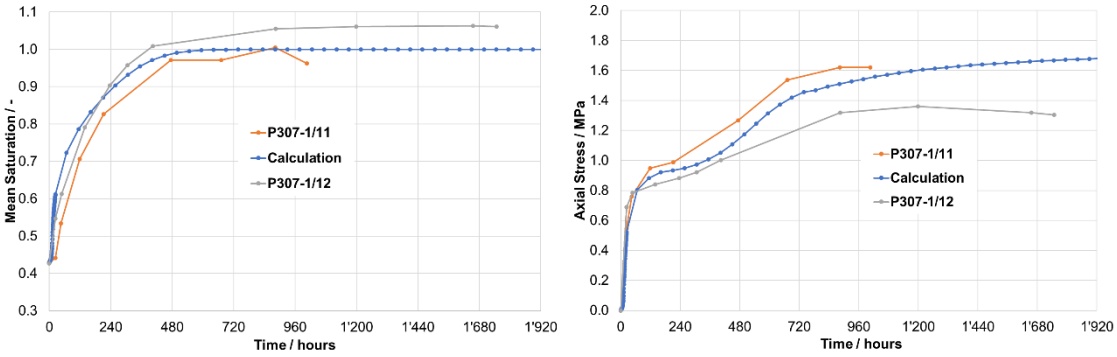

Fig. 6.17 Calculated mean saturation and axial stress development (blue curve) for Calcigel at a dry density of 1.54 g/cm³, with corresponding measurement curves (orange and grey curves)

Results for dry densities of 1.4 g/cm³ and 1.7 g/cm³ are shown in Fig. 6.18 and Fig. 6.19, respectively. Here, the match is less convincing, although the general trends of the measurements are reproduced. It must be noted, however, that the measurement results are not too convincing either, given the saturations above 1.0 and the strong differences in swelling pressure of similar experiments.

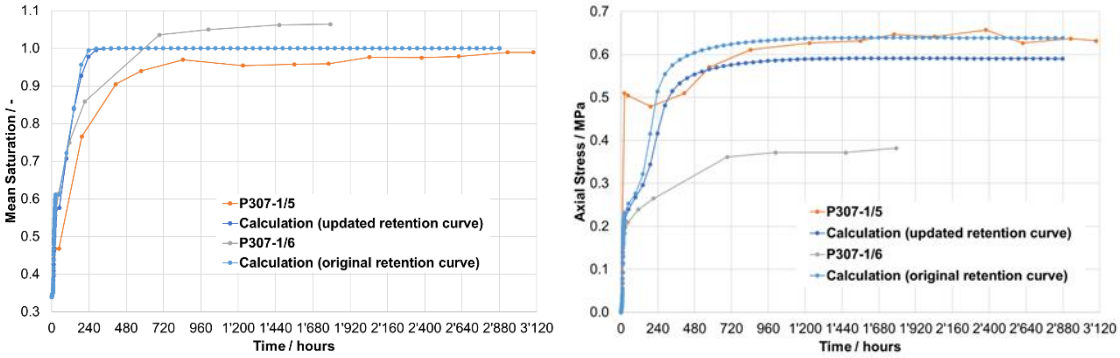

Fig. 6.18 Calculated mean saturation and axial stress development (blue curves) for Calcigel at a dry density of 1.4 g/cm³, with corresponding measurement curves (orange and grey curves)

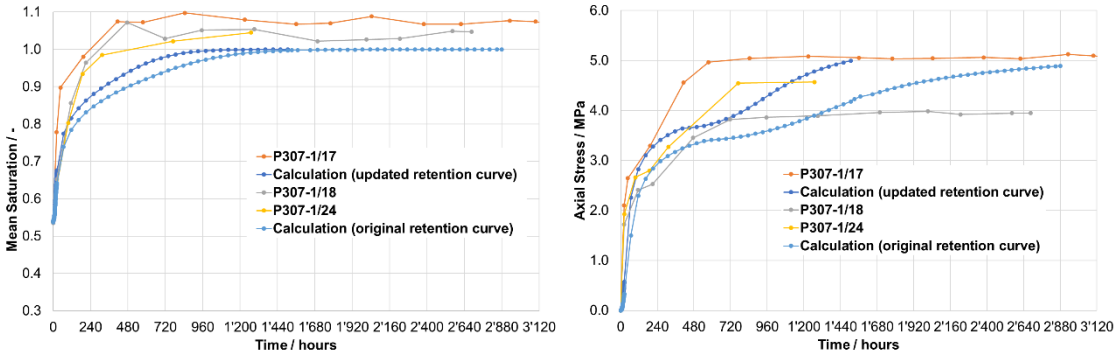

Fig. 6.19 Calculated mean saturation and axial stress development (blue curves) for Calcige at a dry density of 1.7 g/cm³, with corresponding measurement curves (orange, grey and yellow curves)

The new parameter set was also used to recalculate MiniSandwich Test 8. The resulting curves for inflow and axial stress development are shown in Fig. 6.20. A reasonable match of the measured data is obtained, so that the new parameter set seems in fact suitable for simulating different types of experiments. Therefore, it was also used to simulate the in-situ experiment (see next section).

However, the calibration process must not be considered completed. None of the lab tests used for calibration have been performed at elevated injection pressure, the HTV tests (Chap. 5.5) can close this gap. In addition, more tests with reliable permeability measurements are needed to confirm the porosity / permeability relation.

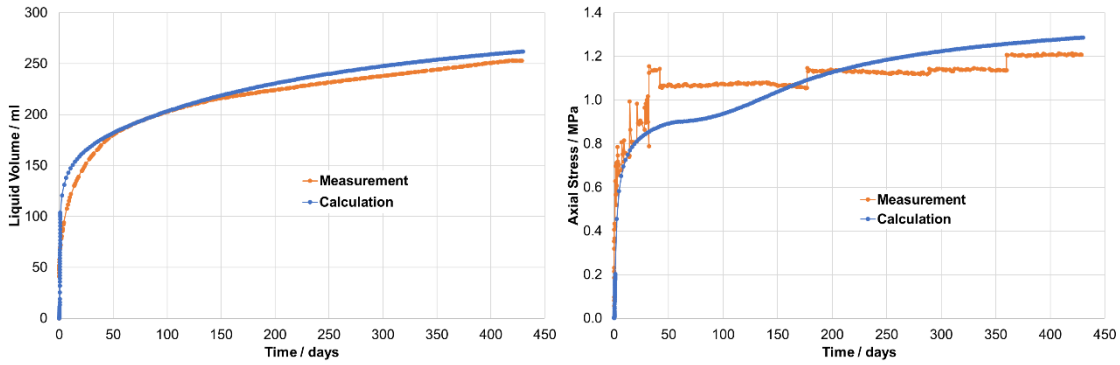

Fig. 6.20 Calculated cumulative inflow and axial stress development for MiniSandwich Test 8 using the new parameter set

OGS model used by BGR

As the model for the DS simulation in the MiniSandwich test, a coupled hydraulic flow model (Richards' equation based) and elastic model was used for the swelling pressure test of Calcigel with Pearson water Type A3 taking into account the linear swelling model and an empirical permeability-swelling strain function. The same retention curve was used for all tests with different dry densities. Four tests with different dry densities 1.4, 1.5, 1.56, and 1.7 g/cm³, for testsP307-1/5, -1/9, -1/11, and -1/18 respectively (Tab. 6.4), using the measurement parameter were extensively studied. Especially the cases P307-1/9 and P307-1/11 represent the design dry density for the experiment in situ.

An axisymmetric model (Fig. 6.21) was used to simulate the swelling pressure test. The permeability relevant to the dry density is a key parameter for the hydration process. The Biot's effective stress coefficient, which represents the coupling effect between hydraulic and mechanical processes, was also varied, particularly at high dry density (Tab. 6.4).

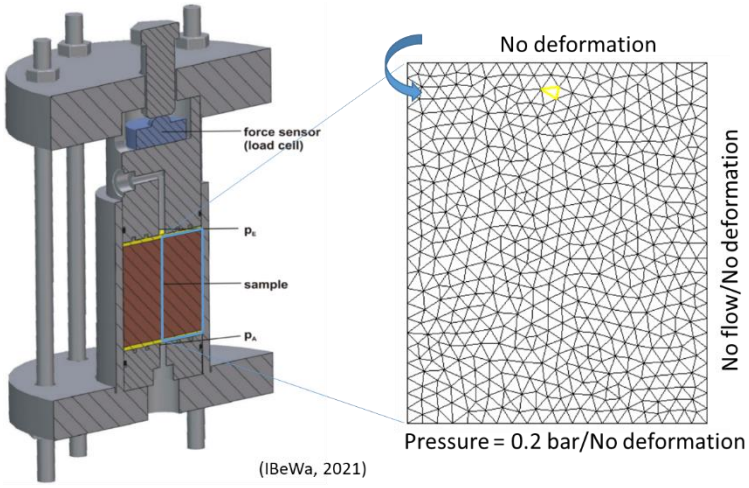

Fig. 6.21 Swelling pressure test (left) and OGS mesh (right)

The simulated results are satisfactory (Fig. 6.22), not only for the swelling stress evolutions but also for the saturation dependent swelling stress in all four cases. It is particularly important to emphasize that both the measured and modelled results show the typical development of the axial swelling stress: increase rapidly over the early period, stabilization for a certain time, and increase again to approach a constant value. The simulated saturation dependent swelling stresses agree well with the measured data. However, according to the measurement data, a linear swelling model used is only valid in the higher saturation range.

Tab. 6.4 Hydromechanical parameters used in the numerical model

Sample	Dry density	Porosity	Swelling pressure	Permeability	Biot coef.
	[g/cm³]	[-]	[MPa] (max/fin./model)	[m²] (gas-/water/model)	(-)
P307-1/5	1.4	0.48	0.68/0.63/0.65	5.4E-13/2.0E-20/2.5E-19	0.1
P307-1/9	1.5	0.44	1.6/1.58/1.58	4.6E-13/5.8E-21/1.0E-19	0.1
P307-1/11	1.56	0.42	1.66/1.62/1.66	1.4E-13/1.1E-20/1.8E-19	0.2
P307-1/18	1.7	0.37	4.02/3.95/4	2.2E-14/6.1E-22/1.0E-20	0.6

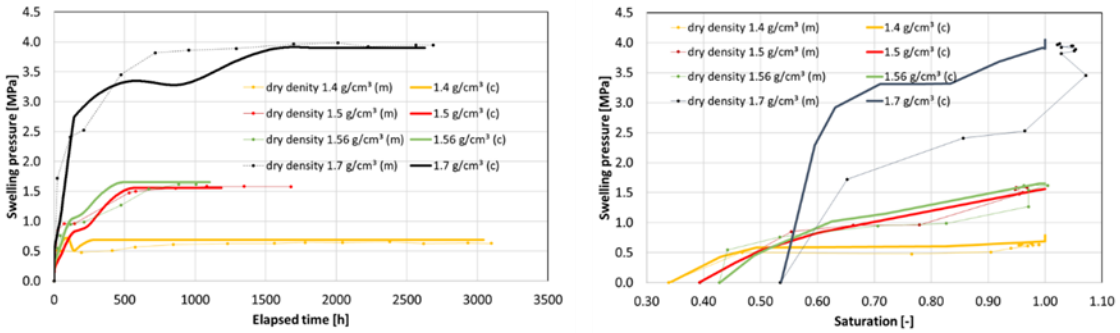

Fig. 6.22 Comparison between simulated and measured swelling stress results for four different dry densities of Calcigel hydrated with Pearson water A3

6.3 Shaft 1 axisymmetric simulation

6.3.1 Code_Bright simulation by GRS

First axisymmetric HM simulations of Shaft 1 were performed with the parameter set obtained in the first BExM calibration using only the MiniSandwich Test 8. The very soft bentonite behavior, together with the low permeability, led to problems: the bentonite in contact with the hydration front underwent an unreastically excessive swelling of the macro-structure, compressing the rest of the bentonite so strongly that further hydration became impossible. In the end, the simulation failed due to stability problems.

With the new parameter set described in the last section, these problems no longer occurred. The details of the new Shaft 1 simulation are described in this section.

Geometry and boundary conditions

The geometrical model, finite element mesh, and boundary conditions are shown in Fig. 6.23. Initially, there is only Opalinus Clay and the concrete of the mine floor. The initial stress is set to 7 MPa (vertical) and 3 MPa (horizontal), respectively. The actually triaxial stress state can obviously not be modelled in an axisymmetric model.

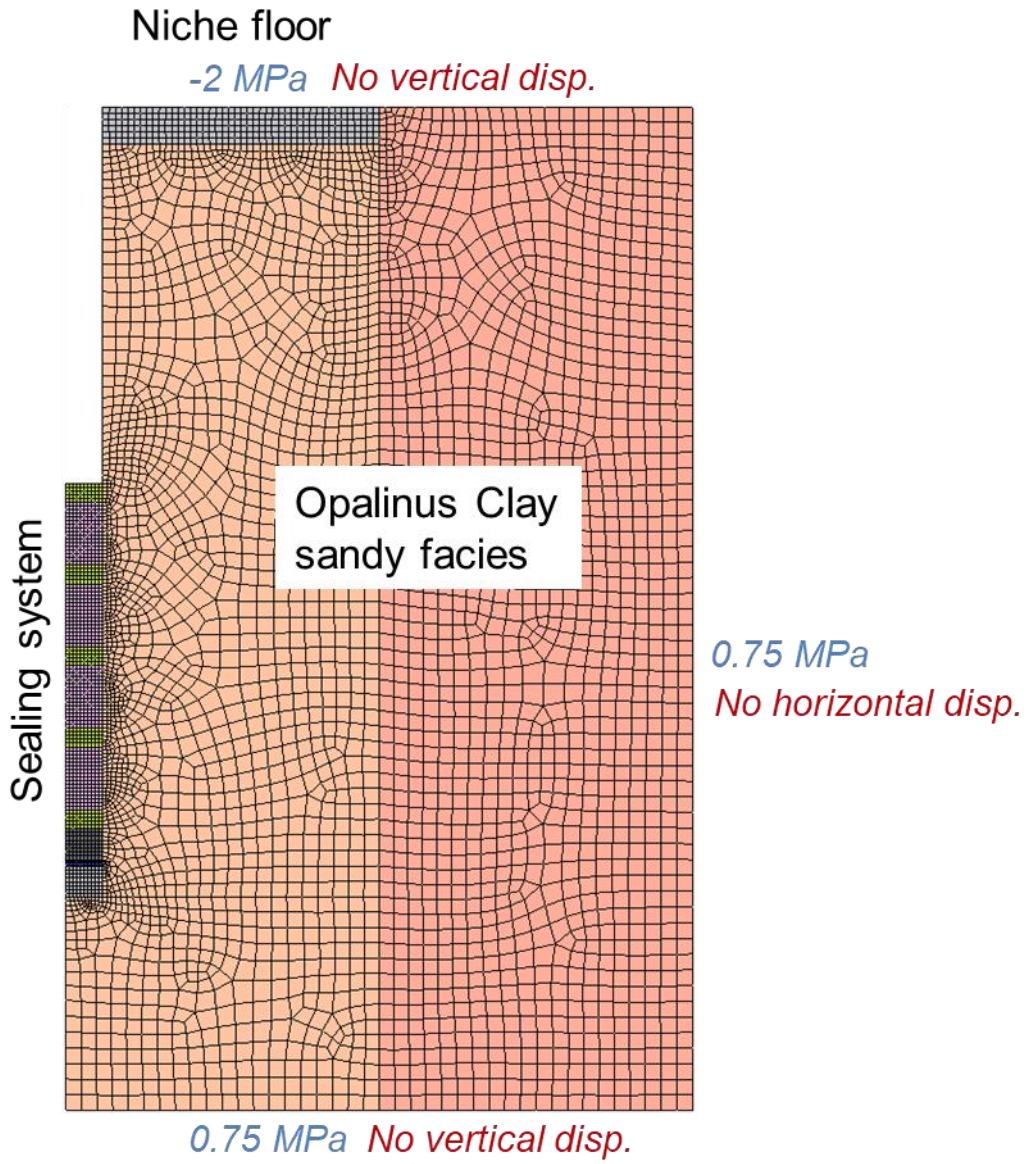

Fig. 6.23 Geometry, mesh, and boundary conditions of the axisymmetric Shaft 1 model (symmetry axis at left side of the figure)

Initial pore water pressure of the Opalinus Clay is 0.75 MPa, based on the measurements in the rock (see Chap. 4.1.1). Shaft sinking and sealing system installation occur

during the simulation. The sealing system (DS and ES) is installed with an initial suction of 133 MPa. Mechanical and hydraulic boundary conditions are as shown in Fig. 6.23. The 2 MPa suction condition at the niche floor represents the ventilation of the niche, the other conditions are straight forward.

Material parameters

The material properties of the DS and ES have been presented and discussed in the previous sections. Material parameters of the other materials present in the model are compiled in Tab. 6.5. All materials except for the DS are linear elastic, all are homogeneous and isotropic. Modelling the Opalinus Clay anisotropy would require a 3D model. Note that the pressure chamber has been modelled as a porous medium, with the porosity (60 %) calculated as the ratio of void volume to the total volume of the chamber (void + steel).

Tab. 6.5 Parameters of the additional materials present in the Shaft 1 model

		OPA Sandy Facies	Concrete	Gravel	Pressure Chamber	Unit
Linear Elasticity	E	4500	27000	3000	210000	MPa
	ν	0.2	0.35	0.245	0.245	
	Φ_0	0.095	0.15	0.41	0.6	
Retention Curve	P_0	8	15	0.3	0.3	MPa
	$б_0$	0.072	0.072	0.072	0.072	Nm^{-1}
	λ	0.35	0.31	0.4	0.4	
	S_{rl}	0.01	0.01	0	0	
	S_{ls}	1	1	1	1	
	Φ_0	0.095	0.15	0.41	0.6	
Intrinsic Permeability	$(k_{11})_0$	2.00E-20	1.00E-20	1.00E-11	1.00E-11	m^2
	$(k_{22})_0$	2.00E-20	1.00E-20	1.00E-11	1.00E-11	m^2
	$(k_{33})_0$	2.00E-20	1.00E-20	1.00E-11	1.00E-11	m^2
	Φ_0	0.095	0.15	0.41	0.6	
Solid Phase Density	ρ_s	2700	2650	2650	"2650"	kgm^{-3}

Simulation schedule

The simulation schedule is shown in Tab. 6.6. The start time of day 3860 represents the time of finishing Gallery 18 since the excavation of Gallery 08, which represents day 0. This time scale had been introduced for the scoping calculations which included Gallery 18 construction. This is not needed for the axisymmetric shaft simulation, therefore calculation starts at day 3860.

Tab. 6.6 Simulation schedule Shaft 1

Interval	Start (d)	End (d)	Explanation	
1	3860	3861	Equilibration	"Dry" phase of the experiment
2	3861	4710	Wait	
3	4710	4740	Excavation Shaft / Wait	
4	4740	4800	Preparation / Ventilation	
5	4800	4980	Construction Seal / Wait	
6	4980	4981	Resaturation Chamber	Hydration phase
7	4981	4984	Chamber at 0.13 MPa	
8	4984	4987	Chamber Press. Ramp 0.4 MPa	
9	4987	4994	Chamber at 0.4 MPa	
10	4994	4995	Chamber Press. Ramp 0.2 MPa	
11	4995	5020	Chamber at 0.2 MPa	
12	5020	5026	Chamber Press. Ramp 0.49 MPa	
13	5026	5055	Chamber at 0.49 MPa	
14	5055	5055.1	Chamber Press. Ramp 0.35 MPa	
15	5055.1	5055.2	Chamber at 0.35 MPa	
16	5055.2	5055.3	Chamber Press. Ramp 0.1 MPa	
17	5055.3	5082	Chamber at 0.2 MPa	
18	5082	5150	Chamber at 0.25 MPa	
19	5150	5210	Chamber Press. Ramp 0.73 MPa	
20	5210	5390	Chamber Press. Ramp 0.9 MPa	
21	5390	5570	Chamber Press. Ramp 1.35 MPa	
22	5570	5654	Chamber Press. Ramp 1.8 MPa	

The first five time intervals include the equilibration of stress and pore pressure in the model, the shaft sinking, and the seal construction. During the first two steps, there is a no-flow/no-displacement condition on the shaft wall, simulating the non-existing shaft. In interval 3 the no-displacement condition on the shaft wall is removed (open shaft), in interval 4 the ventilation condition (2 MPa suction) is applied on the wall. All the materials inside the shaft are activated at the beginning of interval 5, representing installation (complete installation is performed at once).

The remaining time intervals represent the hydration phase of Shaft 1. The actual hydration history was somewhat simplified, but the representation is close to the real pressure history. Fig. 6.24 shows the model boundary condition in comparison to the actual pressure history.

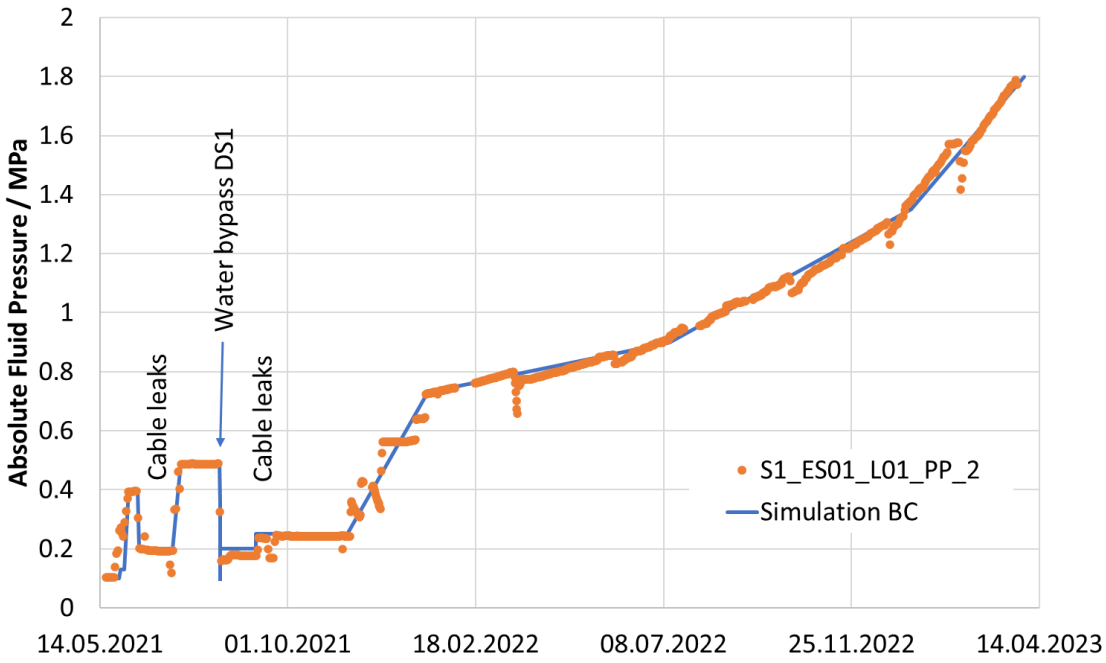

Fig. 6.24 Hydration boundary condition of the model in comparison to the actual pressure history in Shaft 1

The water bypass of DS1 on 11 August 2021 was simulated by a transient pressure boundary condition in ES1, ES2, and on the interface between DS1 and the shaft wall which followed the actual pressure history. Thus, the evolution could be replayed realistically without the need of a transient trial-and-error permeability change.

Simulation results

The situation at seal construction is shown in Fig. 6.25 – Fig. 6.27, in terms of displacements (Fig. 6.25), stress (Fig. 6.26), and liquid pressure and saturation (Fig. 6.27). Displacement values are almost zero low, except for a small convergence of the shaft (negative radial displacement (to the left) at the shaft wall, positive vertical displacement (upward) at the shaft bottom). There is a relaxation of radial stress at the shaft wall; the same applies for vertical stress at the shaft bottom. Liquid pressure shows suction on the niche floor and at the shaft wall because of ventilation. Consequently, there is a small

slightly desaturated zone close to niche floor and shaft. In summary, the situation at seal construction is as expected.

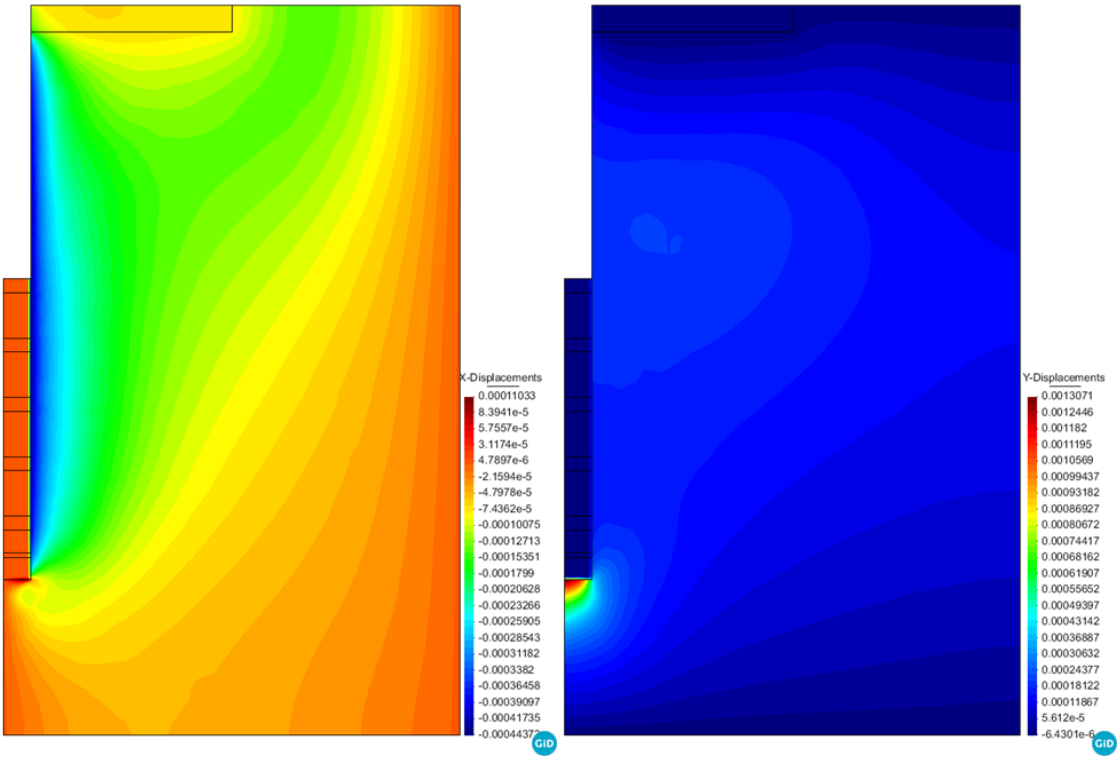

Fig. 6.25 Radial (left) and vertical (right) displacements in and near Shaft 1 at seal construction (day 4800)

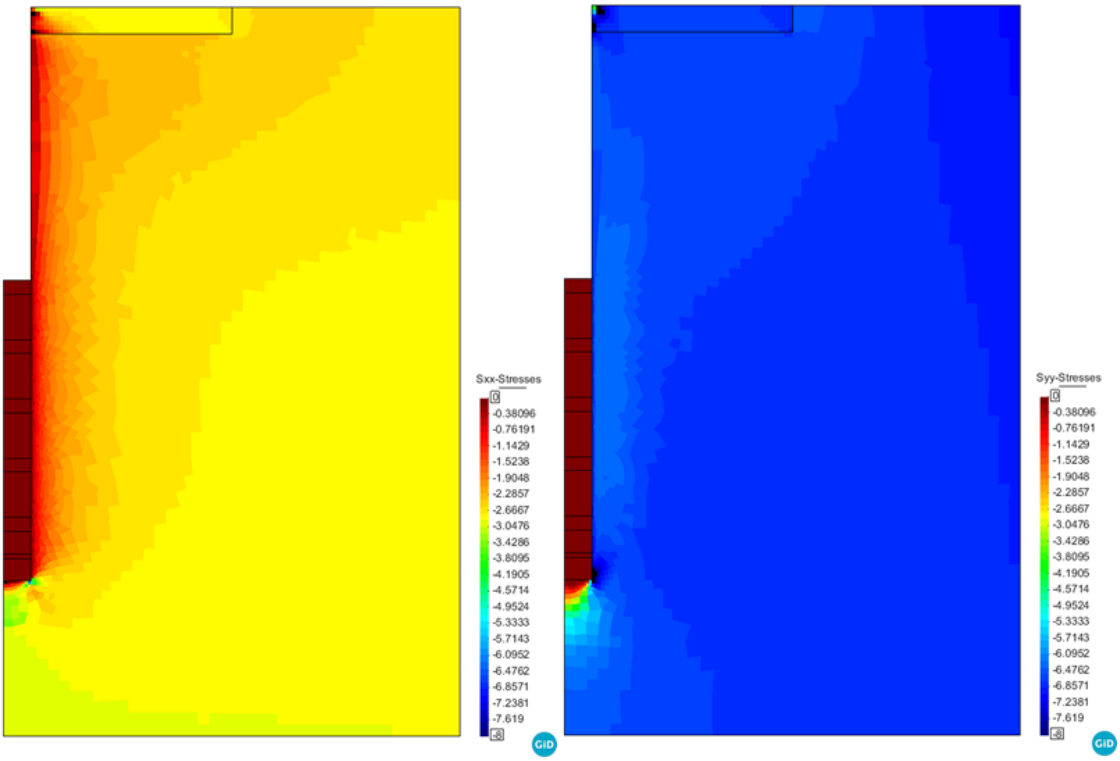

Fig. 6.26 Radial (left) and vertical (right) stresses in and near Shaft 1 at seal construction (day 4800)

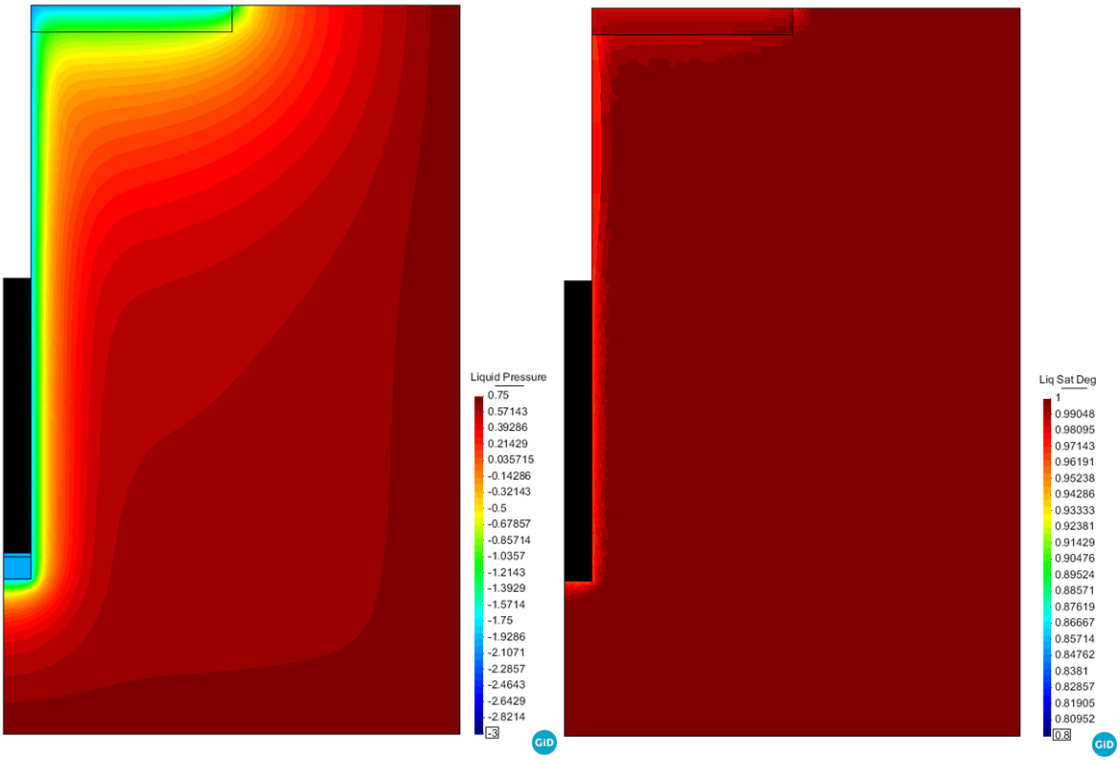

Fig. 6.27 Liquid pressure (left) and saturation (right) in and near Shaft 1 at seal construction (day 4800)

The next figures show the liquid pressure distribution and the saturation close to the shaft for different points in time during hydration. The situation at hydration start is shown in Fig. 6.28. There is already some water uptake of the sealing system from the rock because of the very high initial suction of the ES and DS. This is visible by the suction decrease (increase of the negative liquid pressure) and saturation increase at the boundary of the DS and inside the ES and a corresponding suction increase and saturation decrease in the rock near the shaft wall. The figure illustrates the function of the ES: Due to its high permeability, the complete ES is always in pressure (or suction) equilibrium with the adjacent DS surfaces. Thus, a high suction in the ES is kept up because the water is quickly transferred to the DS. While water keeps entering the ES, it remains rather dry, until the adjacent DS faces approach full saturation. Interestingly, the suction in the uppermost ES5 is lower than in ES3 or ES4. The reason for this is that the water entering ES5 is only transferred to DS4, while the other ES have two adjacent DS faces that take up water.

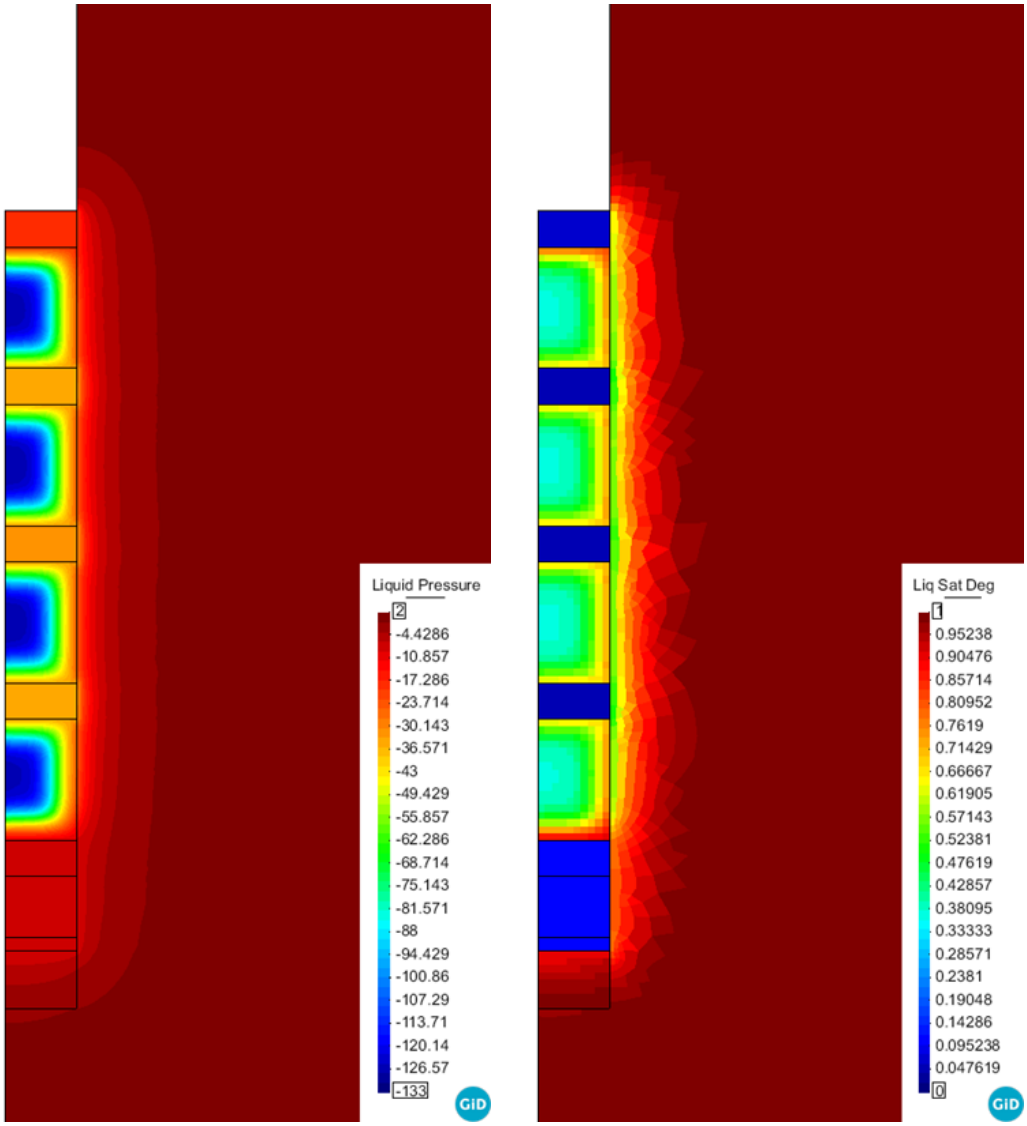

Fig. 6.28 Liquid pressure (left) and saturation (right) in and near Shaft 1 at hydration start (day 4800)

The pressure and saturation distribution immediately prior to the DS1 bypass in August 2021 is shown in Fig. 6.29. The pressure chamber, gravel layer, and ES1 are saturated and show a positive liquid pressure reflecting the water injection via the chamber. Consequently, liquid pressure is increasing in the rock close to this part of the sealing system, and the slightly desaturated zone has disappeared at this level.

Suction in the lower part of DS1 is decreasing as the saturation increases due to hydration. In the upper part of the sealing system, the slow water uptake from the rock has continued.

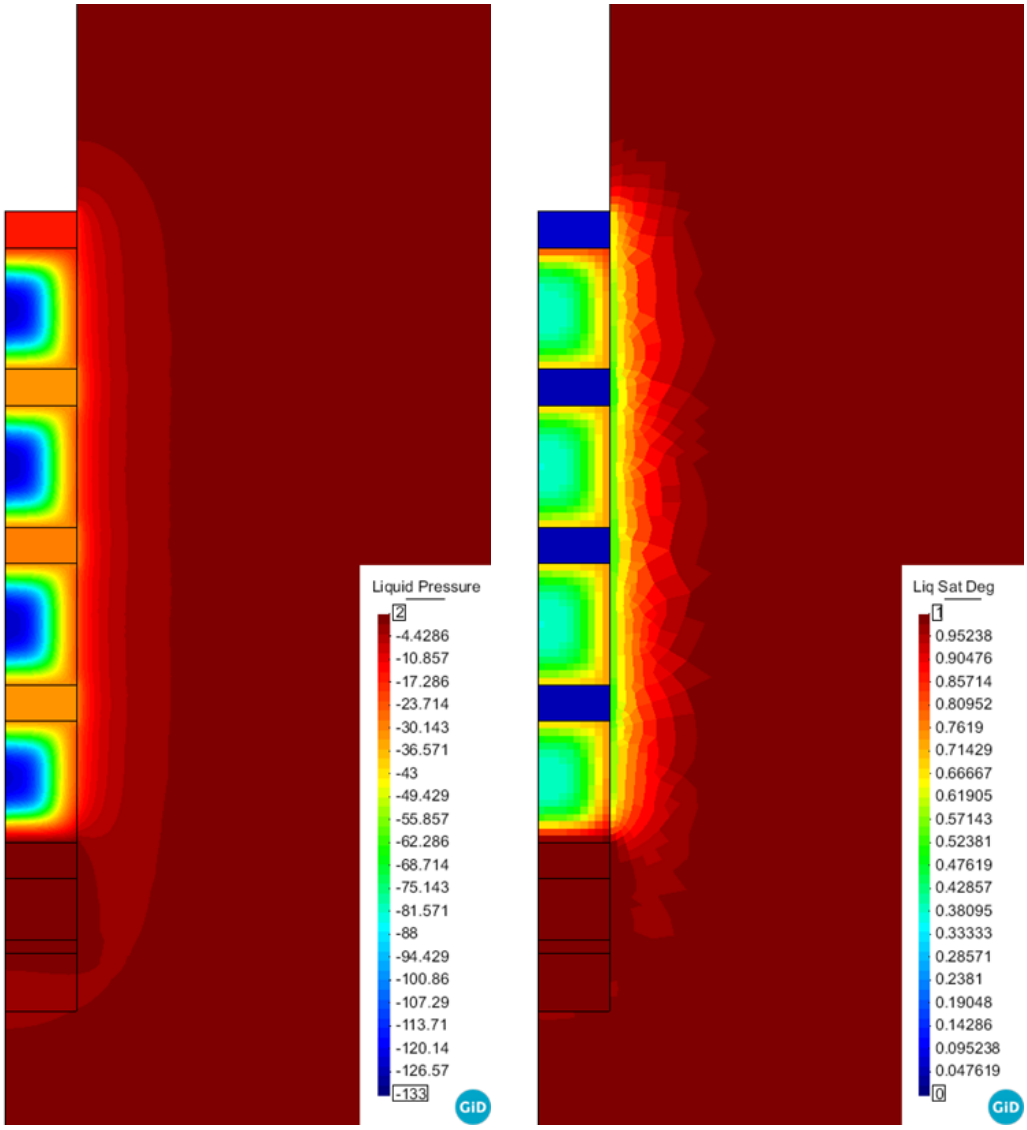

Fig. 6.29 Liquid pressure (left) and saturation (right) in and near Shaft 1 before DS1 bypass (day 5055)

Directly after the DS1 bypass (Fig. 6.30), ES2 is fully saturated and has the same (positive) liquid pressure as ES1, the same applies to the shaft wall at DS1. This brings a suction decrease and saturation increase to the upper face of DS1 and the lower face of DS2.

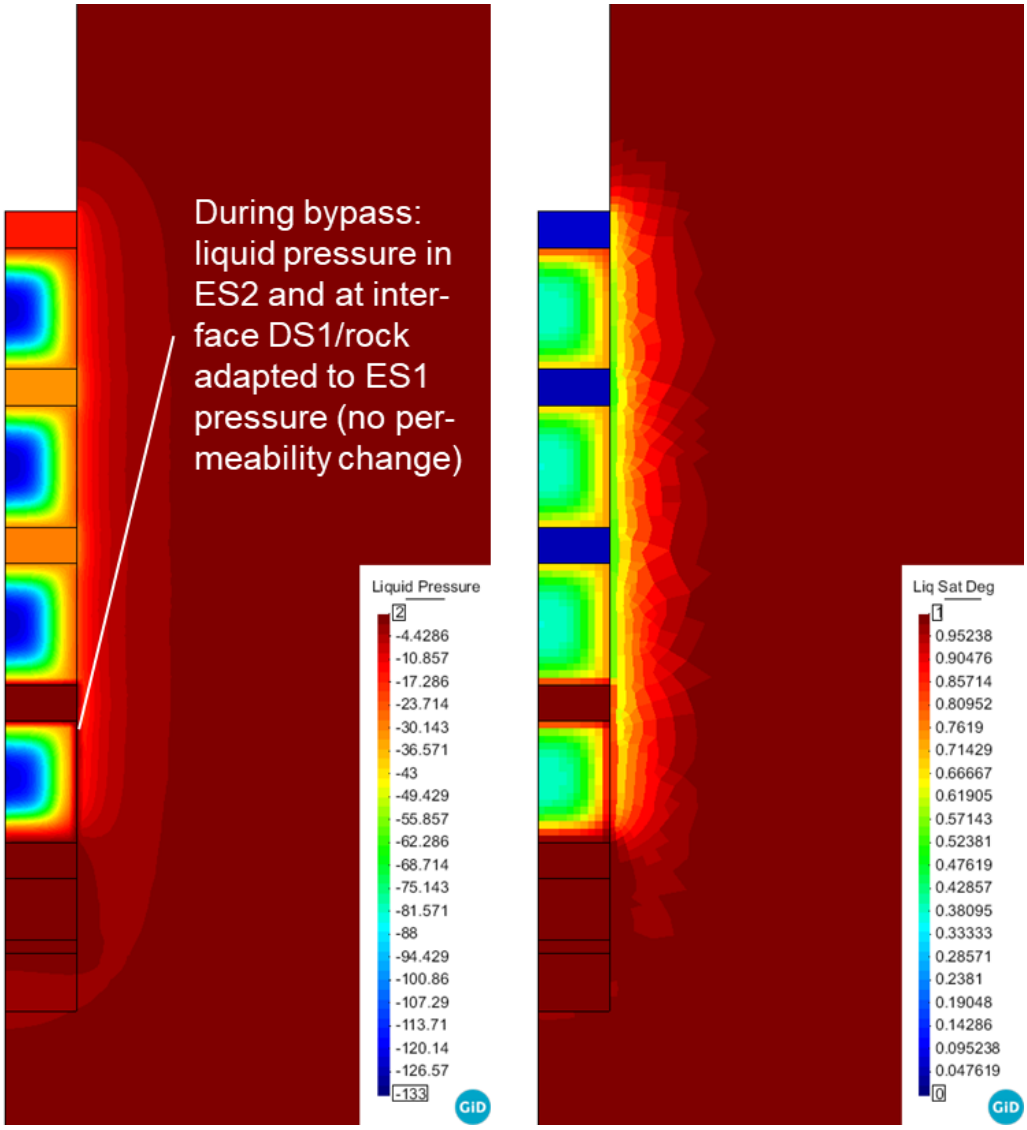

Fig. 6.30 Liquid pressure (left) and saturation (right) in and near Shaft 1 after DS1 bypass (day 5055.3)

The situation at the end of March 2023 (end of the simulation) is shown in Fig. 6.31. Suction has decreased further in all DS and ES, but there is no positive pressure except for ES1, the lower and upper face of DS1, and the lower face of DS2 which are fully saturated. All other parts of the sealing system are still under suction, meaning they are no saturated. The saturation level of DS1 in the simulation is still considerably lower than implied by the measurements.

Water uptake from the rock has continued in the upper segments, and the adjacent unsaturated part of the rock has increased in size.

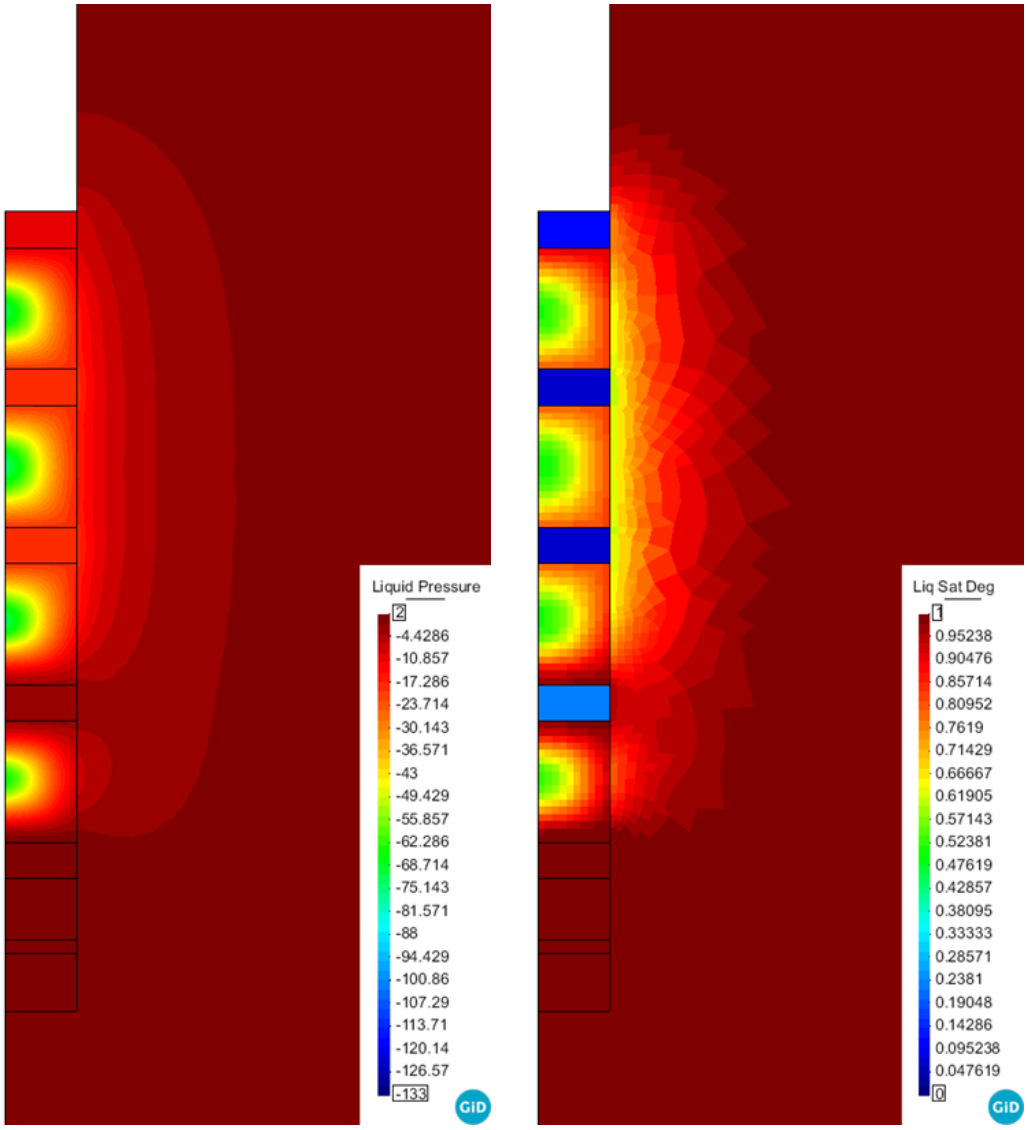

Fig. 6.31 Liquid pressure (left) and saturation (right) in and near Shaft 1 at the end of March 2023 (day 5654)

Finally, vertical displacements and radial stress distribution at the end of the simulation are shown in Fig. 6.32. The vertical displacements (Fig. 6.32 left) show upward movement at the lower sides of the DS and downward movements at the upper sides, caused by the swelling of the DS due to water entering their lower and upper faces via the ES. This is especially visible where water from the pressure chamber has or had access to the DS faces, at DS1 and the lower face of DS2. But the other DS show the same effect because of their (slower) hydration from the rock.

Interestingly, there is practically no vertical displacement at any of the DS/ES interfaces. This means that all swelling deformation is absorbed by compaction inside each DS.

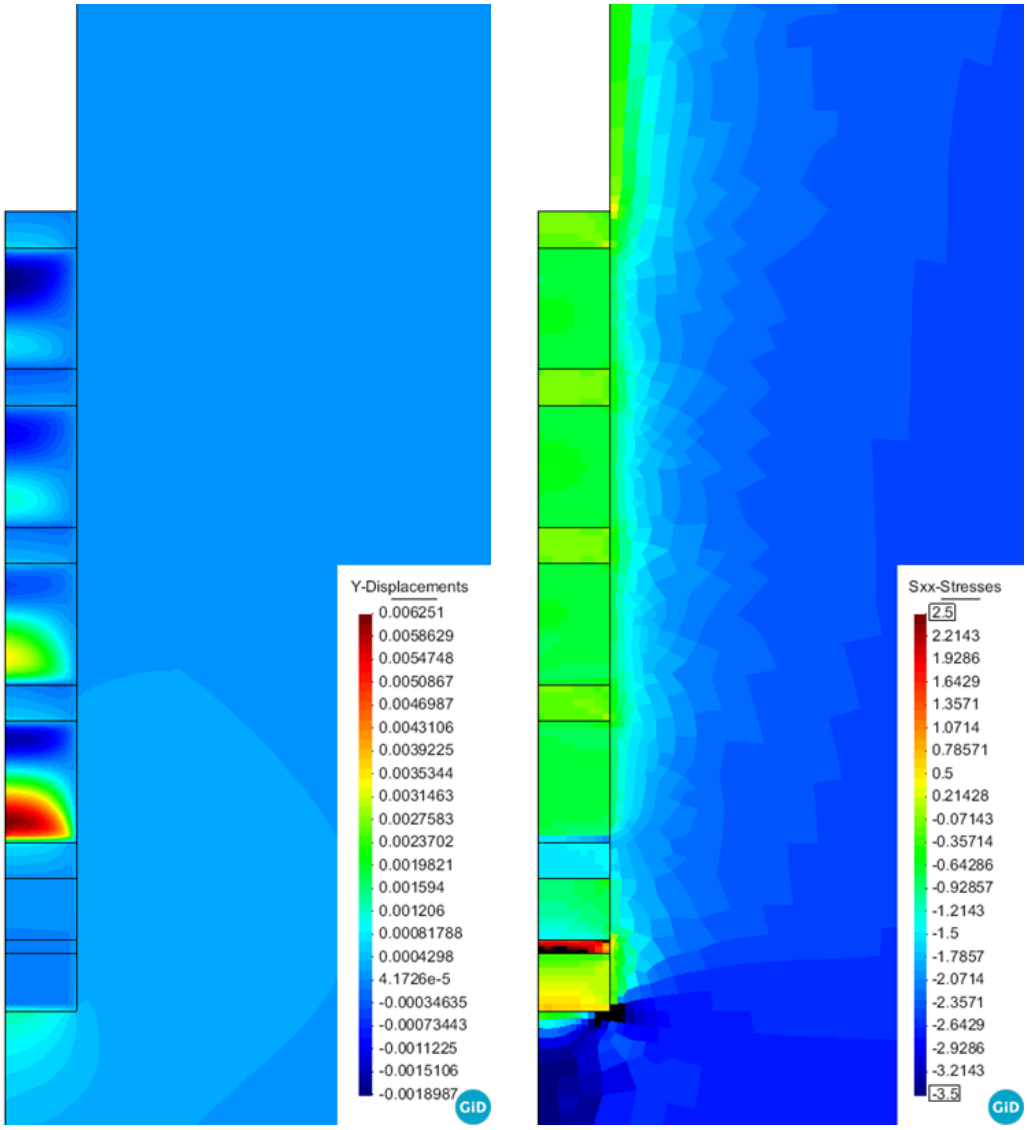

Fig. 6.32 Vertical displacements (left) and radial stress (right) in and near Shaft 1 at the end of March 2023 (day 5654)

At the end of March 2023 some radial stress at the shaft wall has evolved (Fig. 6.32 right), but the range is rather low (below 1 MPa at the level of DS1). This is in line with the low degree of saturation of DS1 at the same time (Fig. 6.31).

Comparison to measurement results

Comparing the simulation results to the in-situ observations, the following statements can be made.

– Deformation: The simulation shows no vertical displacements at the DS/ES interfaces, meaning that all swelling deformation is absorbed by compaction inside each

DS. This is confirmed by the readings of the displacement measurement system in Shaft 1 (Chap. 4.2.3).

- Stress: The radial stress measured at the level of DS1 in the experiment (March 2023: 1.7 MPa – 2.5 MPa, Chap. 4.2.2) is considerably higher than the simulation result (0.8 MPa – 1.0 MPa). This is at least partially due to the low simulated saturation (see next item), but other factors like the geometrical simplification or the rigidity of the DS material may play a role.
- Saturation: Measurements show that saturation of DS1 is very high, and a positive pore pressure has started to evolve (Chap. 4.2.3). This is not reflected by the simulation. Most likely, this discrepancy is caused by the porosity / permeability relation which still needs improvement.

All in all, the model behaves as expected and the measurement trends are correctly reproduced, but there are deviations from the experimentally observed behavior that call for improvements.

Conclusions and outlook

Axisymmetric simulation of Shaft 1 was successful in the sense that stability problems were overcome, and the overall behavior of the system was plausibly modelled. Measurement trends were correctly reproduced, but hydration is too slow, and consequently swelling stress is lower than measured. Thus, calibration still needs to be refined.

Laboratory experiments used for calibration involved different configurations (MiniSandwich, swelling tests) and various dry densities. Lab tests with increased injection pressure as in the in-situ experiment were not available, but are currently under preparation and will be used for further model calibration in the next phase of Sandwich-HP. For simulation of Shaft 2, it will also be necessary to derive a parameter set for Securisol MHP 30/70. Respective lab tests are available (Chap. 5.3 and Chap. 5.4). Switching from the current BExM version to the now available one which does not require a predominantly saturated micro-porosity will widen the range of lab tests suitable for calibration and further increase the trust in the parameter set.

Including the three-dimensional stress state and anisotropy of the Opalinus Clay will require a 3D geometrical model, which can be a one-shaft model again in the first version.

Finally, it is planned to simulate not only the in-situ experiment, but also the semi-technical HTV experiments (Chap. 5.5).

6.3.2 OGS simulation by BGR

A first interpretive/predictive model was used to simulate Shaft 1 of the in-situ experiment. Based on the calibrated parameters for the Sandwich system (DS/ES), the in-situ modelling aims to evaluate the behavior of the total system, including the composite system (DS/ES), shaft EDZ, and Opalinus Clay with a focus on the interface behavior: EDZ development under resaturation and compaction conditions.

An axisymmetric model with 28654 triangle elements (GMSH) (10X10 m) for the FE code OGS has been prepared including seven material groups: OPA, EDZ (1 cm), DS, ES, gravel, injection chamber & concrete (Fig. 6.33). Hydraulic properties of the EDZ were taken from the BGR surface packer tests and all hydraulic and mechanical parameters for OPA and concrete come from the FE project (Tab. 6.7 and Tab. 6.8), see /ALC 19/.

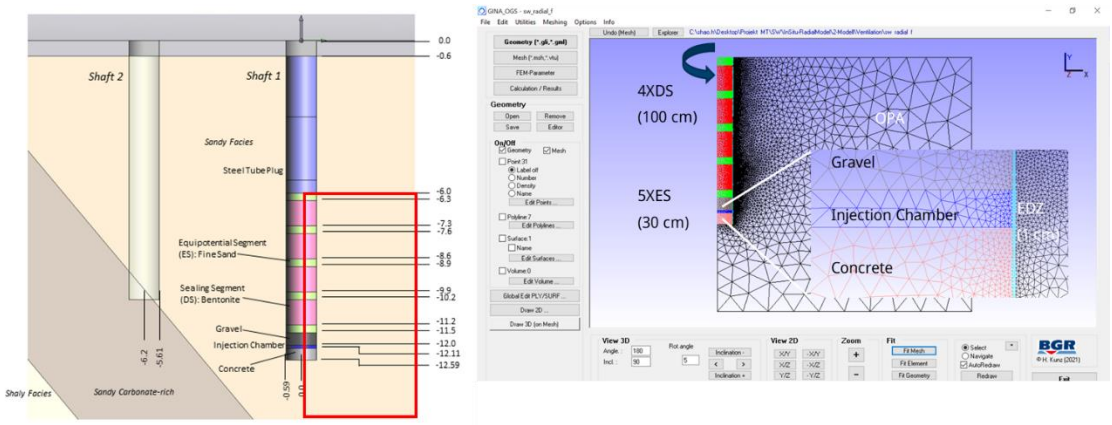

Fig. 6.33 Axisymmetric FE mesh for the simulation of Shaft 1

Tab. 6.7 Hydraulic parameters for the reference case

MG	OPA	EDZ	DS	ES	Chamber	Concrete	Gravel
Permeability [m²]	3.0E-20	1.5E-15	2.5E-18	1.3E-11	1.0E-11	1.0E-19	1.0E-14
Porosity [-]	0.13	0.13	0.5	0.4	0.6	0.25	0.3
Capillary	vG	vG	vG	vG	vG	vG	vG
res. Saturation [-]	0.3	0.3	0	0	0	0.01	0
max. Saturation [-]	1	1	1	1	1	1	1
Entry pressure [MPa]	20	9	22.4	0.1	0.1	1	0.1
vG Lambda	0.4	0.4	0.359	0.5	0.5	0.33	0.5
Storage [/Pa]	Skemp-ton	3.E-10	3.E-10	3.E-10	3.E-10	3.E-10	3.E-10
Tortuosity [-]	0.8	0.8	-	-	-	-	-
Permeability Strain	y	y	y	y	-	-	-

Tab. 6.8 Mechanical parameters for the reference case

MG	OPA	EDZ	DS	ES	Chamber	Concrete	Gravel
Poisson number [-]	0.35	0.35	0.15	0.2	0.2	0.2	0.2
Young's modulus [GPa]	6	6	0.15	0.3	30	20	3
Biot coef.	0.96	0.96	0.6	0.6	0.6	1	0.6
Bishop coef.	0	0	1.4	1.4	-	-	-
Swelling pressure [MPa]	1	1	3.5	-	-	-	-

Two cases were simulated. Prior to the hydration phase, a desaturation phase was simulated to determine the saturation state around the shaft. Based on the suggested permeability, a very limited desaturation zone (0.5 m) may have a saturation lower than 0.99 after 8 months. Therefore, the saturation distribution was not considered in the subsequent hydration phase.

In the hydration phase, the injected flow rate was used as source term from the injection chamber. As expected, all DS strongly suck water and the ES stay relatively dry. The EDZ may form a potential flow path for the hydration process. Without EDZ, the saturation in the upper elements must be much slower (Fig. 6.34), because of the resaturation from the OPA. Radial stress may increase, an increase of 1.5 MPa may be in the immediate near-field (10 cm). The maximum swelling stress of the DS beneath the plug may be lower than 2.5 MPa.

As outlook, sensor data should be analyzed carefully for the interpretative simulation. Moreover, a sounded EDZ model is needed under the compaction and saturation state.

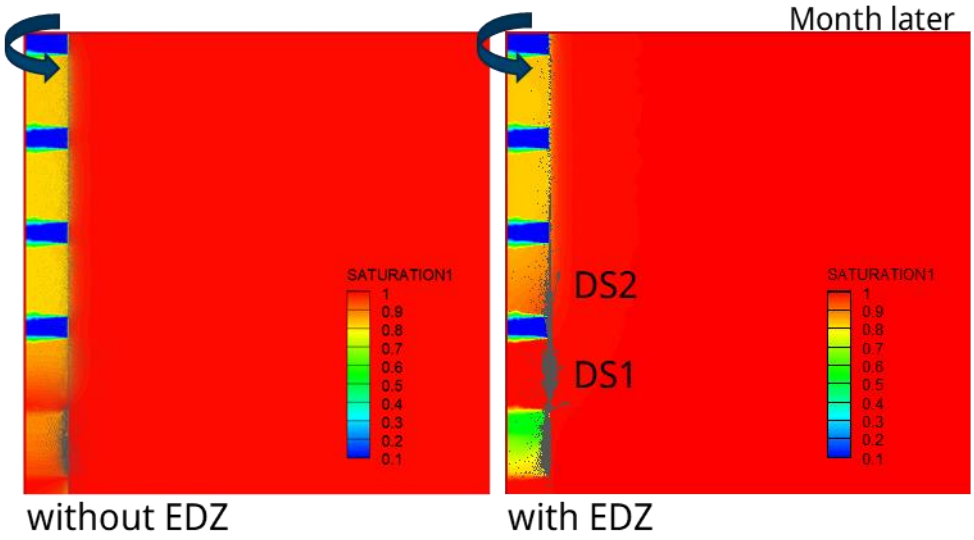

Fig. 6.34 Saturation distribution in and near Shaft 1 after one month of hydration without EDZ (left) and with EDZ (right)

6.4 Load scenarios for a shaft sealing system in argillaceous host rock

6.4.1 Introduction

A shaft sealing system for a deep geological repository consists of diverse sealing components interacting in order to fulfil a complex and time-dependent barrier function: Initially, the sealing system reduces the liquid inflow from the surface and other geologic units to the waste emplacement units and during the later post-closure phase, the release of contaminated fluids from the repository shall be delayed. This hydraulic barrier function must be combined with mechanical stability regarding lithostatic, hydrostatic, gas, and swelling pressure and settlement as well as chemical stability during the functional lifetime of about 50,000 years /LOM 15/. Hydraulic sealing is typically performed by bentonite and bitumen or asphalt components while mechanical support can be given by gravel columns or concrete counter bearings. The chemical stability is particularly critical for bentonite and concrete sections.

In general, the functionality of a given shaft sealing concept (with its interacting components) has to be assessed by experimental and modelling work, which was done for the

case of shaft sealing concepts for German high-level waste repositories within the ELSA project /KUD 13/, /KUD 21/. The associated shaft sealing concepts for a repository in clay formations contain one Sandwich seal as component together with monolithic bentonite, bitumen, and asphalt seals, see Fig. 6.35. As it is one aim of the Sandwich-HP project to assess possible advantages of Sandwich seals over monolithic bentonite seals, a comparison of the performance of entire shaft sealing systems with and without Sandwich seals appears suitable. A comparative hydraulic modelling task in this respect is the overall motivation for the current section.

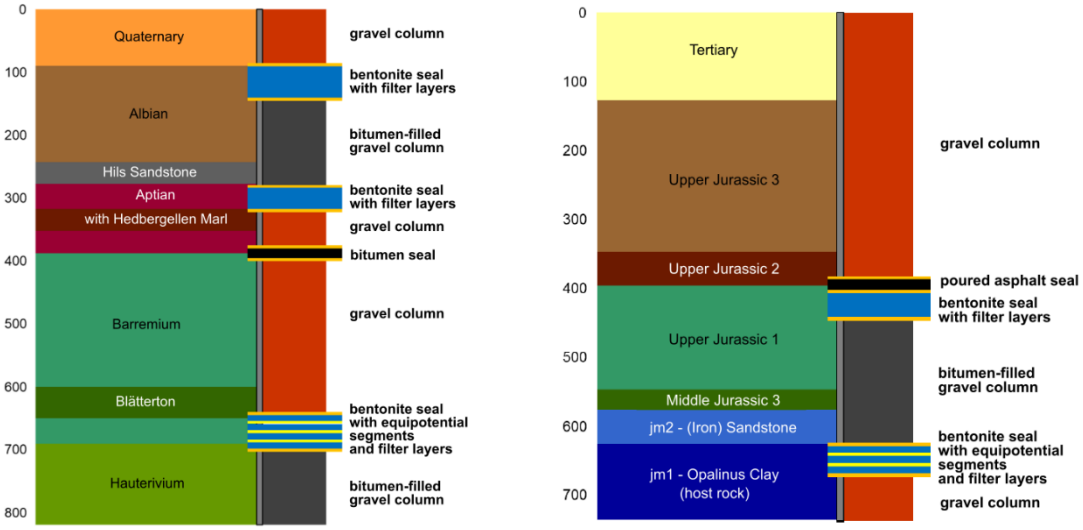

Fig. 6.35 Shaft sealing concepts for the German repository site models in argillaceous host rock NORTH (left) and SOUTH (right) /REI 13/, /REI 16/ including a Sandwich seal as component /KUD 21/

The modelling of different scenarios for shaft sealing systems was widely performed within Work Package 5 in Phase 2 of the ELSA project /HER 20/. The hydraulic modelling in Chaps. 5 and 6 of /HER 20/ is based on different load scenarios for a sealing concept associated to the repository site model NORTH similar to Fig. 6.35 (left). Particularly, a simplified geological model and a sealing system with only one monolithic bentonite seal were assumed. Calculations were run using the numerical simulator TOGHREACT. The considered scenarios and boundary conditions form the basis for the modelling work performed in the current section. In contrast, the detailed site model SOUTH (with Opalinus clay as host rock corresponding to the case in the SW-A experiment) and the associated shaft sealing concept in Fig. 6.35 (right) are considered. The simulator TOUGH2 is used. For the calculations obtained so far, the lower Sandwich seal is substituted by a monolithic bentonite seal. A reasonable comparison to a model including a Sandwich

seal affords some model improvements and was not possible during the current project phase.

The detailed model assumptions and considered hydraulic load scenarios are described in Chap. 6.4.2. Results are shown and discussed in Chap. 6.4.3 and a conclusion together with possible future improvements of the modelling results are given in Chap. 6.4.4.

6.4.2 Modelling assumptions and load scenarios

Mathematical model

The subsequently described modelling efforts assume that the functionality of an entire shaft sealing system in interaction with the surrounding host rock is mainly determined by its hydraulic evolution. Particularly, mechanical, and thermal effects are neglected. This also includes neglecting bentonite swelling and the associated porosity reduction in the current state of the model. The gas and liquid flow in the shaft and its vicinity are evaluated by solving the isothermal two-phase flow / two-component (advective) transport equations for air and water through porous media

$$\frac{\partial}{\partial t}\left[\phi(\rho_\mathrm{l} X_\mathrm{l}^\mathrm{w} S_\mathrm{l} + \rho_\mathrm{g} X_\mathrm{g}^\mathrm{w} S_\mathrm{g}\right] + \mathrm{div}\left(\rho_\mathrm{l} X_\mathrm{l}^\mathrm{w} \boldsymbol{v}_\mathrm{l} + \rho_\mathrm{g} X_\mathrm{g}^\mathrm{w} \boldsymbol{v}_\mathrm{g}\right) = r^\mathrm{w},$$

$$\frac{\partial}{\partial t}\left[\phi(\rho_\mathrm{l} X_\mathrm{l}^\mathrm{a} S_\mathrm{l} + \rho_\mathrm{g} X_\mathrm{g}^\mathrm{a} S_\mathrm{g}\right] + \mathrm{div}\left(\rho_\mathrm{l} X_\mathrm{l}^\mathrm{a} \boldsymbol{v}_\mathrm{l} + \rho_\mathrm{g} X_\mathrm{g}^\mathrm{a} \boldsymbol{v}_\mathrm{g}\right) = r^\mathrm{a}.$$

ϕ	porosity
$\rho_\mathrm{l}, \rho_\mathrm{g}$	mass density of the liquid / gas phase
$X_\mathrm{l}^\mathrm{w}, X_\mathrm{g}^\mathrm{w}$	mass fraction of water / water vapor in the liquid / gas phase
$X_\mathrm{l}^\mathrm{a}, X_\mathrm{g}^\mathrm{a}$	mass fraction of dissolved air / air in the liquid / gas phase
$S_\mathrm{l}, S_\mathrm{g}$	liquid / gas saturation
$r^\mathrm{w}, r^\mathrm{a}$	water / air sink and source terms
$\boldsymbol{v}_\mathrm{l}, \boldsymbol{v}_\mathrm{g}$	Darcy velocity of liquid / gas phase

The advective mass flux terms are assumed to be determined by Darcy's law

$$\boldsymbol{v}_\mathrm{l} = -\frac{k_\mathrm{rl}}{\mu_\mathrm{l}} \boldsymbol{K}(\mathbf{grad}\, p_\mathrm{l} - \rho_\mathrm{l} \boldsymbol{g})$$

$$\boldsymbol{v}_\mathrm{g} = -\frac{k_\mathrm{rg}}{\mu_\mathrm{g}} \boldsymbol{K}\left(\mathbf{grad}\, p_\mathrm{g} - \rho_\mathrm{g} \boldsymbol{g}\right)$$

and the following typical constraints and state equations are considered to hold /HEL 97/:

- Saturations and phase mass fractions add up to one:
  $S_\mathrm{l} + S_\mathrm{g} = 1,\ X_\mathrm{l}^\mathrm{w} + X_\mathrm{l}^\mathrm{a} = X_\mathrm{g}^\mathrm{w} + X_\mathrm{g}^\mathrm{a} = 1$

- The partial pressure of water vapor behaves according to the saturation vapor pressure (depending on temperature only):
  $p_\mathrm{g}^\mathrm{w} = p_{\mathrm{g,sat}}^\mathrm{w}(T),\ p_\mathrm{g} = p_\mathrm{g}^\mathrm{w} + p_\mathrm{g}^\mathrm{a}$

- The mass fraction of dissolved air in the liquid phase is obtained from Henry's law:
  $$X_\mathrm{l}^\mathrm{a} = \frac{M^\mathrm{a}}{M^\mathrm{a} - \left(1 - \left(K_\mathrm{H}\, p_\mathrm{g}^\mathrm{a}\right)^{-1}\right) M^\mathrm{w}}$$

- The mass fraction of gaseous air behaves according to the ideal gas equation
  $$X_\mathrm{g}^\mathrm{a} = \frac{p_\mathrm{g}^\mathrm{a} M^\mathrm{a}}{\rho_\mathrm{g} R T}$$

- Retention curves and relative permeabilities are typically determined by the van Genuchten-Mualem equations:
  $p_\mathrm{c}(S_\mathrm{l}) = p_0 \left(S^{-\frac{1}{\lambda}} - 1\right)^{1-\lambda},\ S(S_\mathrm{l}) = \frac{S_\mathrm{l} - S_\mathrm{rl}}{1 - S_\mathrm{rl}},\ p_\mathrm{c} = p_\mathrm{g} - p_\mathrm{l}$

  $k_\mathrm{rl}(S_\mathrm{l}) = \sqrt{S}\left(1 - \left(1 - S^{\frac{1}{\lambda}}\right)^{\lambda}\right)^2,\ k_\mathrm{rg} = 1 - k_\mathrm{rl}.$

  These equations can (e.g. for computational reasons) be approximated by the linear relations:

$$p_\mathrm{c}(S_\mathrm{l}) = \begin{cases} p_0^*, & S_\mathrm{l} < S_0^* \\ p_0^* \frac{S_\mathrm{p}^* - S_\mathrm{l}}{S_\mathrm{p}^* - S_0^*}, & S_0^* \le S_\mathrm{l} \le S_\mathrm{p}^* \\ 0, & S_\mathrm{p}^* < S_\mathrm{l} \end{cases} \qquad k_\mathrm{rl}(S_\mathrm{l}) = \begin{cases} 0, & S_\mathrm{l} < S_\mathrm{k}^* \\ \frac{S_\mathrm{l} - S_\mathrm{k}^*}{1 - S_\mathrm{k}^*}, & S_\mathrm{k}^* \le S_\mathrm{l} \end{cases}$$

$p_\mathrm{l}, p_\mathrm{g}$	liquid / gas pressure
$p_\mathrm{g}^\mathrm{w}, p_\mathrm{g}^\mathrm{a}$	partial pressure of water vapor / air
$k_\mathrm{rl}, k_\mathrm{rg}$	liquid / gas relative permeability
$\mu_\mathrm{l}, \mu_\mathrm{g}$	dynamic viscosity of liquid / gas
$\boldsymbol{K} = \mathbf{diag}(k_{\|\|}, k_{\|\|}, k_\perp)$	permeability tensor
$\boldsymbol{g}$	gravitational acceleration vector
K_H	Henry coefficient
$M^\mathrm{w}, M^\mathrm{a}$	molar mass of water / air
p_c	capillary pressure
p_0	gas entry pressure
λ	van Genuchten parameter

S_{rl} residual liquid saturation

$p_0^*, S_0^*, S_p^*, S_k^*$ parameters for linear retention and relative permeability curves

Geometry

For the modelling of load scenarios for the shaft sealing concept at the site model SOUTH, the above equations are solved on a two-dimensional axisymmetric model geometry with the help of TOUGH2 (Fig. 6.36). The rectangular model has a height of 700 m and a width of 50 m. The height considers (the central part of) the host rock layer (Opalinus clay) in about 700 m below ground level and all overlaying rock layers. The used model width has been determined in a pre-study, for which a similar model with a width of 1000 m has been investigated and no pressure or saturation change in the rock layers in less than 50 m distance from the shaft center occurred. The shaft radius in the model is considered to be 4 m.

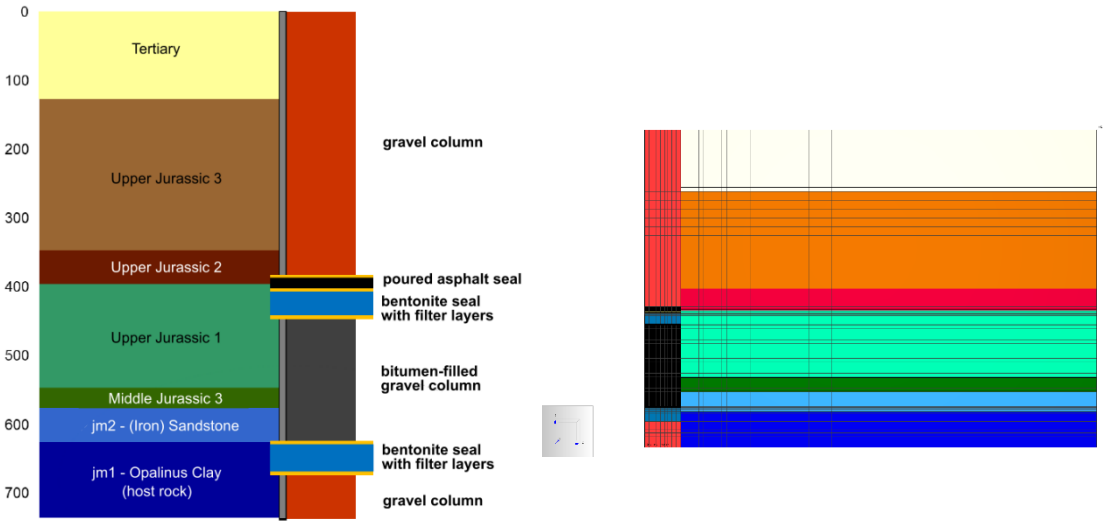

Fig. 6.36 Adapted shaft sealing concept and the associated TOUGH2 model

The location and thickness of the rock layers were adapted from /MAS 16/. The details are given in Tab. 6.9.

Tab. 6.9 Geometric properties of rock layers used in the model adapted from /MAS 16/

quantity	tms	jo3	jo2	jo1	jm3	jm2	jm1
thickness [m]	127	219	50	150	30	46	78
upper boundary [m]	0	-127	-346	-396	-546	-576	-622
lower boundary [m]	-127	-346	-396	-546	-576	-622	-700

As components of the shaft seal, the four different materials gravel, asphalt, sand (N45), and bentonite (Calcigel) are considered according to the sealing concept in /KUD 21/, see Fig. 6.36 and Fig. 6.37. The shaft seal consists in the uppermost and lowermost part of gravel columns for mechanical stability reasons. In the central part of the seal, the diverse sealing segments made of asphalt and bentonite are located, each separated by thin filter layers of sand. The considered location and thickness for the shaft seal components are given in Tab. 6.10.

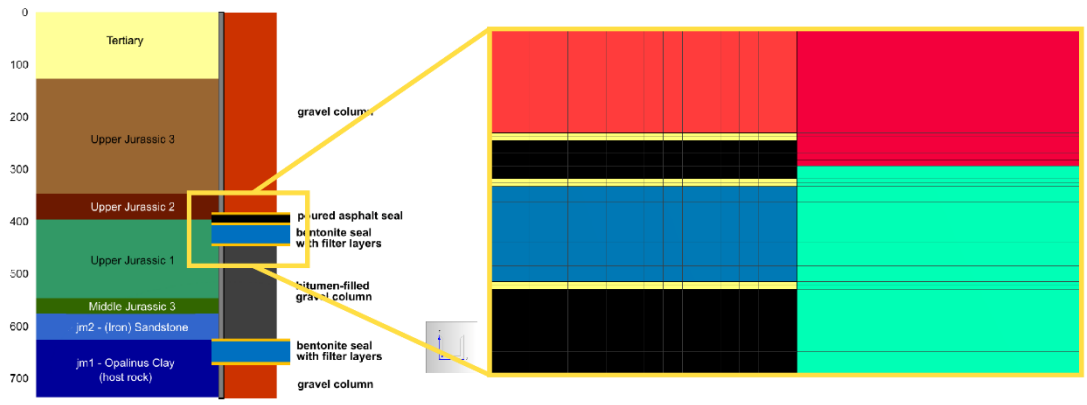

Fig. 6.37 Adapted shaft sealing concept and a segment of the associated TOUGH2 model showing thin filter layers

Tab. 6.10 Geometric properties of shaft seal components used in the model adapted from /KUD 21/

quantity	upper gravel	FL1	upper asphalt	FL2	upper bentonite	FL3	lower asphalt	FL4	lower bentonite	FL5	lower gravel
thickness [m]	389	2	10	2	25	2	180	2	30	2	56
upper boundary [m]	0	-389	-391	-401	-403	-428	-430	-610	-612	-642	-644
lower boundary [m]	-389	-391	-401	-403	-428	-430	-610	-612	-642	-644	-700

Hydraulic properties

The hydraulic properties of water and air for the considered isothermal case ($\vartheta = 25\ ℃$) are predefined within the used equation-of-state module EOS3 in TOUGH2 /PRU 99/. Particularly, the water parameters (density, viscosity, and saturated vapor pressure) are based on the IFC-67 steam table equations, see /SCH 69/. The viscosity of the gas phase is determined from a formulation in /HIR 54/ and a constant Henry coefficient $K_{\mathrm{H}} = 10^{-10}\,\frac{1}{\mathrm{Pa}}$ for air solubility is assumed.

The hydraulic properties of the rock layers are mostly adapted from /MAS 16/ and summarized in Tab. 6.11. Particularly, the rock in the model is assumed fully saturated and no initially desaturated or damaged area with increased permeability near the shaft contour, i.e. no excavation damaged zone (EDZ) is considered. For the materials used in the shaft seal, hydraulic properties are given in Tab. 6.12. The parameters for Calcigel and N45 are adapted from the values used in the other modelling tasks within in the Sandwich-HP project. For gravel and asphalt, the parameters are adapted from /HER 20/. In general, all solid model components are modelled as porous media. This assumption is particularly critical for asphalt, which is considered as an almost impermeable solid although it is a viscous fluid.

Tab. 6.11 Hydraulic properties of rock layers used in the model, see /MAS 16/

quantity	tms	jo3	jo2	jo1	jm3	jm2	jm1
ρ_s [kg/m³]	2750	2750	2750	2700	2760	2800	2720
ϕ [-]	0.1	0.12	0.12	0.12	0.1	0.13	0.07
$S_{l,0}$ [-]	1	1	1	1	1	1	1
$k_{\|\|}$ [m²]	$5 \cdot 10^{-13}$	$5 \cdot 10^{-12}$	$5 \cdot 10^{-10}$	$5 \cdot 10^{-13}$	$5 \cdot 10^{-13}$	10^{-17}	$1.7 \cdot 10^{-20}$
$k_{\perp}$ [m²]	$5 \cdot 10^{-13}$	$5 \cdot 10^{-12}$	$5 \cdot 10^{-10}$	$5 \cdot 10^{-13}$	$5 \cdot 10^{-13}$	10^{-17}	$6.5 \cdot 10^{-21}$

Tab. 6.12 Hydraulic properties of shaft seal components used in the model: Parameters for Calcigel and N45 as in /EMM 19/ and Chap. 5.2; for gravel and asphalt according to /HER 20/

quantity	Calcigel	N45	gravel	asphalt
ρ_s [kg/m³]	2750	2650	2890	1500
ϕ [-]	0.44	0.41	0.377	0.015
w_0 [-]	0.102	0.005	0.01	0
$S_{l,0}$ [-]	0.36	0.02	0.043	0
k [m²]	$4 \cdot 10^{-20}$	10^{-11}	10^{-9}	10^{-23}

ρ_s specific density
w_0 initial water content
$S_{l,0}$ initial saturation

The consideration of two-phase flow phenomena is particularly interesting within the host rock layer (Opalinus clay) as gas generation from canister corrosion in a final repository can possibly lead to high gas pressures such that gas could enter the host rock. Moreover, a two-phase flow in the unsaturated shaft seal components, particularly sand and bentonite, is relevant due to suction. Accordingly, it was the aim to consider realistic water retention curves and relative permeability relations for these materials according to the van Genuchten-Mualem equations, see Tab. 6.13. Due to numerical instabilities, it was necessary to approximate the relations by linear models. The associated parameters are also listed in Tab. 6.13 and a comparison and a comparison between the van Genuchten-Mualem curves and their linear surrogates is shown in Fig. 6.38.

Tab. 6.13 Two-phase flow parameters according to the van Genuchten-Mualem model and the used surrogate linear model

component	λ [-]	p_0 [MPa]	S_{rl} [-]	p_0^* [MPa]	S_0^* [-]	S_p^* [-]	S_k^* [-]
OPA	0.41	20	0	10^3	0.04	0.35	0.8
Calcigel	0.359	22.4	0	10^3	0.1	0.45	0.8
N45	0.861	0.3	0	5	0	1	0.5

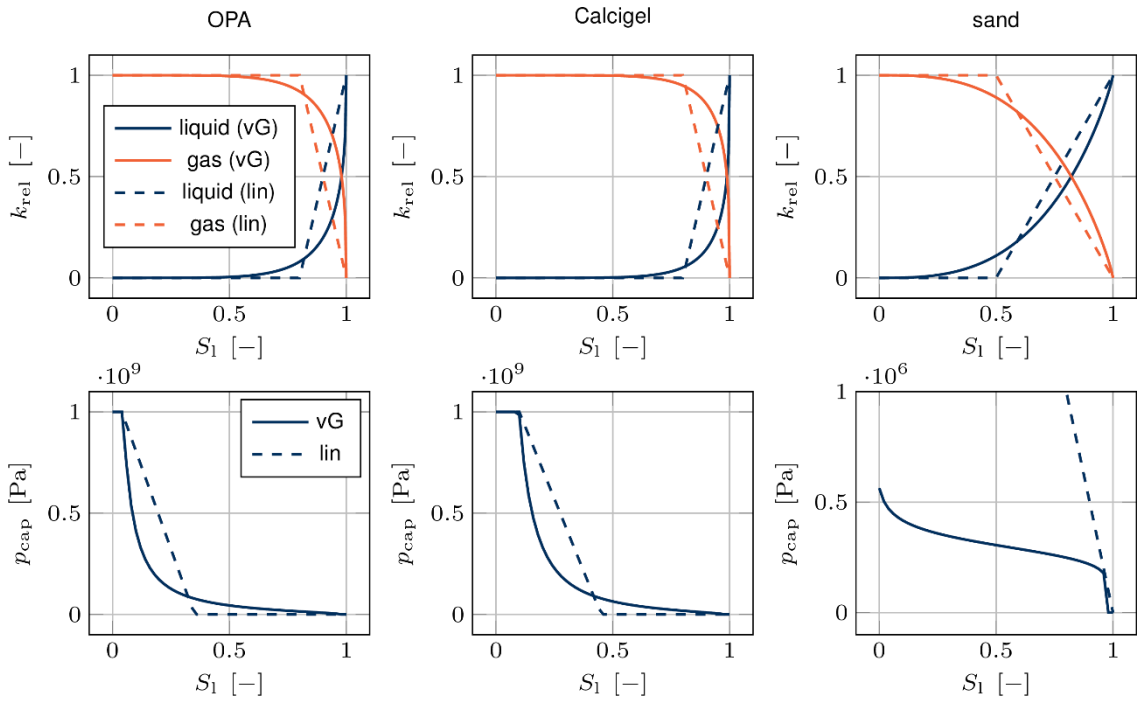

Fig. 6.38 Two-phase flow relations according to the van Genuchten-Mualem model (vG) and the used surrogate linear relations (lin)

Load scenarios

The main scenario considered subsequently assumes an initially partially saturated shaft seal with all components working properly, and initially undisturbed and fully saturated rock layers providing fluid to slowly infiltrate the shaft. The question arises whether the sealing elements can delay the fluid inflow to the shaft region adjacent to the host rock layer. The initial saturations of the seal components are assumed as given in Tab. 6.12 and the gas pressure is at atmospheric level, representing pressure and saturation conditions directly after finishing installation. In the fully saturated rock layers, a hydrostatic pressure gradient is considered which could be obtained by a pre-simulation, in which fluid inflow from the top rock layer through all underlying layers until equilibrium has been

assumed. The pressure initial conditions are visualized in Fig. 6.39 which also shows the mesh used for the simulation. The boundary conditions for the main scenario are given hereafter:

- At the upper boundary, there is a constant atmospheric pressure in the rock zone and no flow at the shaft top.
- At the right boundary, the rock is assumed to be undisturbed and hence, the hydrostatic pressure gradient is maintained.
- There is no flow at the left boundary representing the symmetry axis of the model.
- There is no flow at the model's lower boundary.

As alternative scenario, the gas generation from canister corrosion, possibly leading to a pressure build-up at the shaft bottom is considered. The hydrogen production rate from corrosion of one Pollux-3 or Pollux-9 cask at the site model SOUTH is assumed to be at a constant value of about $30\,\frac{\mathrm{mol}}{a}$ for several thousand years, see /JOB 16/. This leads to a mass production rate for hydrogen of approximately $2 \cdot 10^{-9}\,\frac{\mathrm{kg}}{\mathrm{s}}$. Considering about 8,800 Pollux casks in the repository, see /JOB 15/, a total production rate of $17.6 \cdot 10^{-6}\,\frac{\mathrm{kg}}{\mathrm{s}}$ is obtained. In the alternative scenario, it is assumed that air is injected instantly at the shaft bottom at the constant rate given above. The instant gas release certainly leads to an overestimation of the real gas inflow at the shaft bottom but allows for a first approximation of the shaft evolution under gas pressure increase.

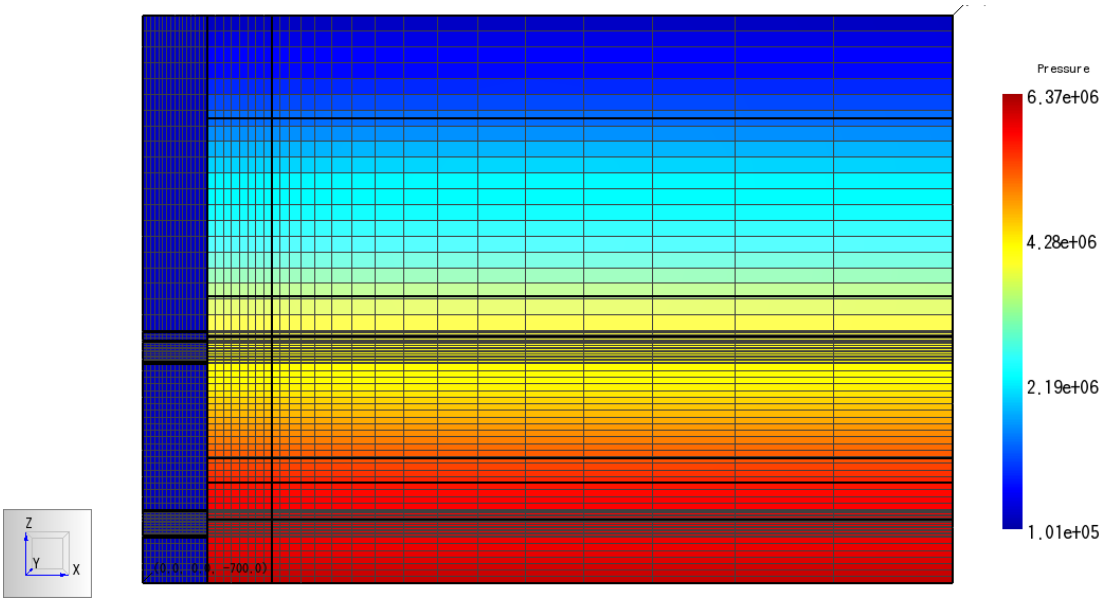

Fig. 6.39 Initial pressure distribution in the full model of the shaft seal and its vicinity

6.4.3 Results and discussion

For the main scenario, a simulation of the first 1000 years of the hydraulic evolution of the shaft was performed. The pressure distribution in the full model after 1000 years is shown in Fig. 6.40 and the pressure evolution in the shaft and the adjacent rock zone is depicted in Fig. 6.41. A hydrostatic pressure gradient in the upper gravel column emerges during the first year of modelling time, as there is a steady inflow from the ground and the adjacent rock zone. The pressure build- up in the bentonite seals is completed after less than 500 years. In the asphalt seals, there is almost no pressure during the full simulation time due to the extremely small permeability. In the lower gravel column at the shaft bottom, there occurs only a very small pressure increase as fluid from the Opalinus clay only very slowly infiltrate the bottom region of the shaft, leading to a pressure decrease in the host rock.

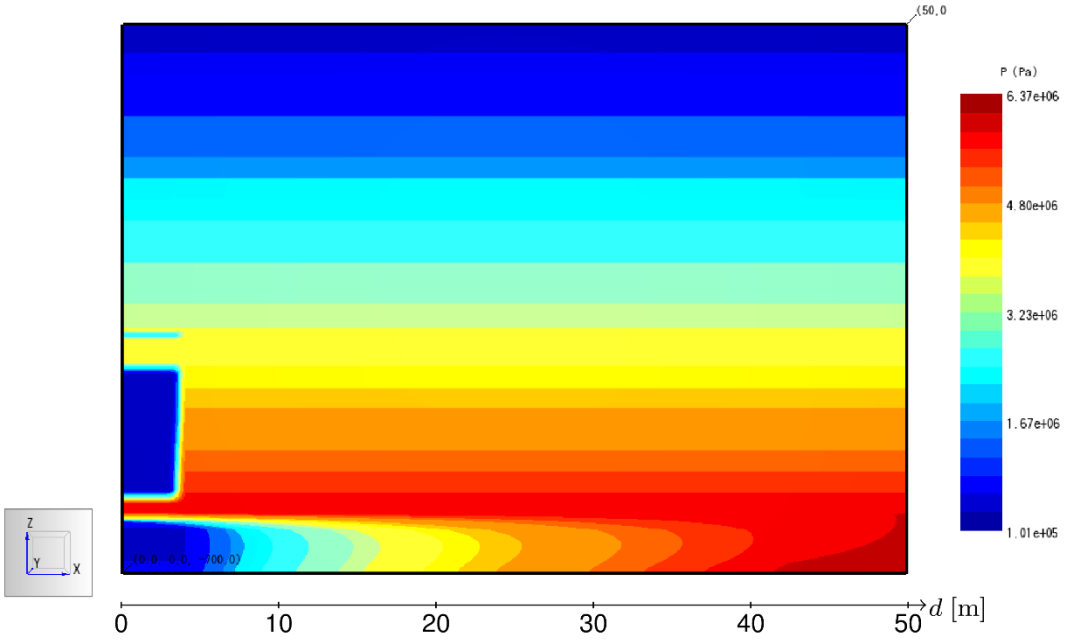

Fig. 6.40 Pressure distribution in and near the shaft seal after 1000 years

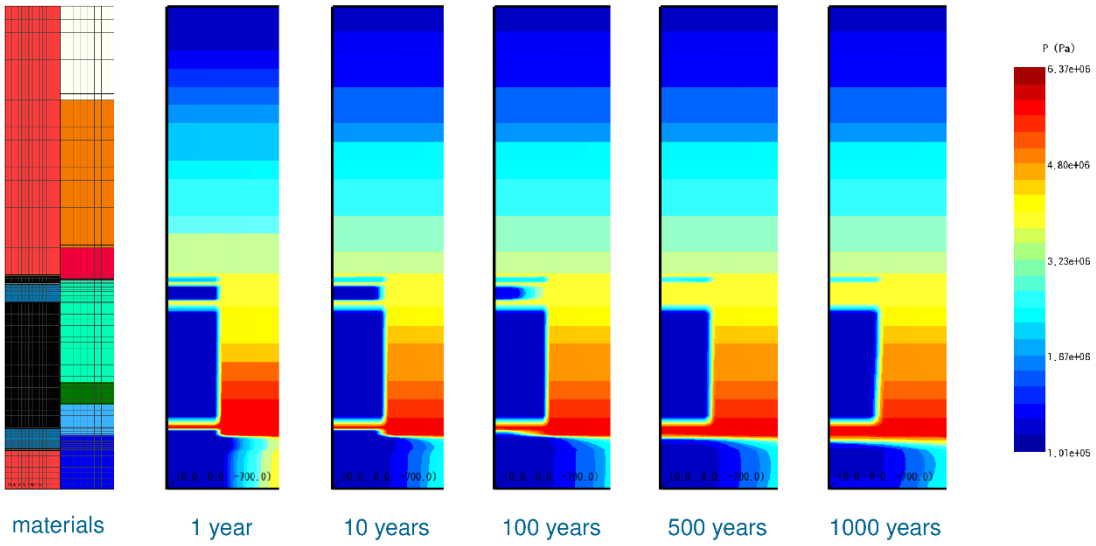

Fig. 6.41 Pressure evolution in the vicinity of the shaft seal

The liquid saturation after 1000 years and its evolution near the shaft are shown in Fig. 6.42 and Fig. 6.43, respectively. There occurs almost no desaturation in the rock zone except for the area near the shaft. The upper gravel column is saturated during the first year of modelling as expected from the pressure evolution. For the bentonite seals the saturation evolves from the adjacent rock zone to the core. Both seals are widely saturated after 500 years. The lower bentonite seal is saturated from the top due to the higher permeability of the adjacent sandstone layer above the Opalinus clay. The asphalt seals remain nearly unsaturated as expected. The saturation of the lower gravel column at the shaft bottom starts after 100 years and only the lower half is saturated after 1000 years.

The simulation results for the main scenario show the efficiency of the sealing concept in principle. A fluid inflow to the shaft from the top is prevented by the sealing elements made of asphalt and bentonite. The bentonite seals absorb intruding fluids from surrounding rock layers with higher permeabilities. Fluid entering the shaft bottom mainly comes from the host rock and the shaft bottom is only slowly saturated.

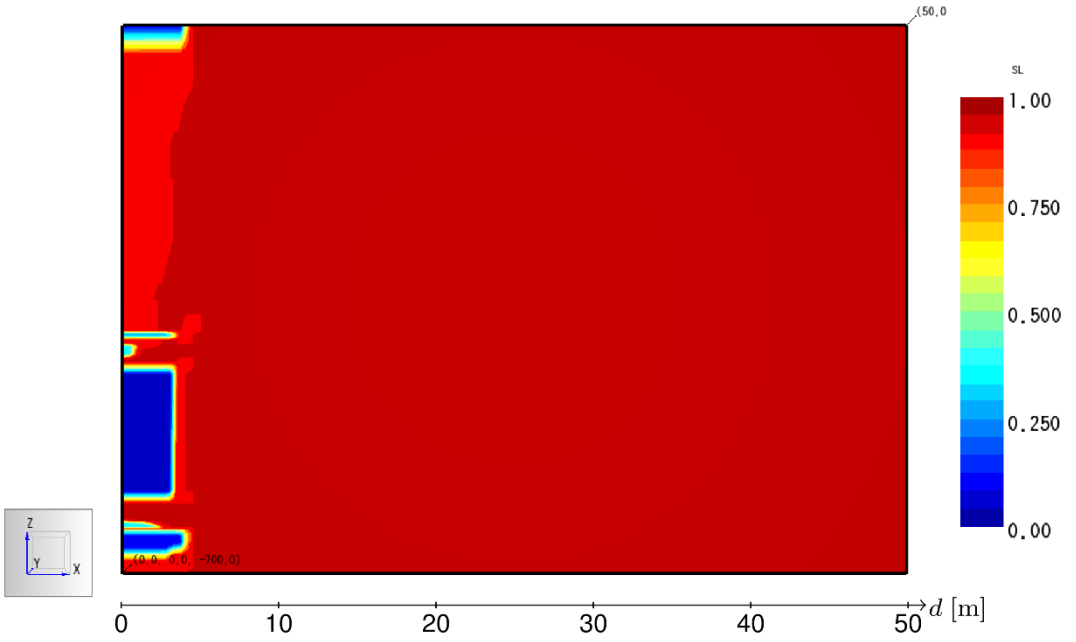

Fig. 6.42 Liquid saturation distribution in and near the shaft seal after 1000 years

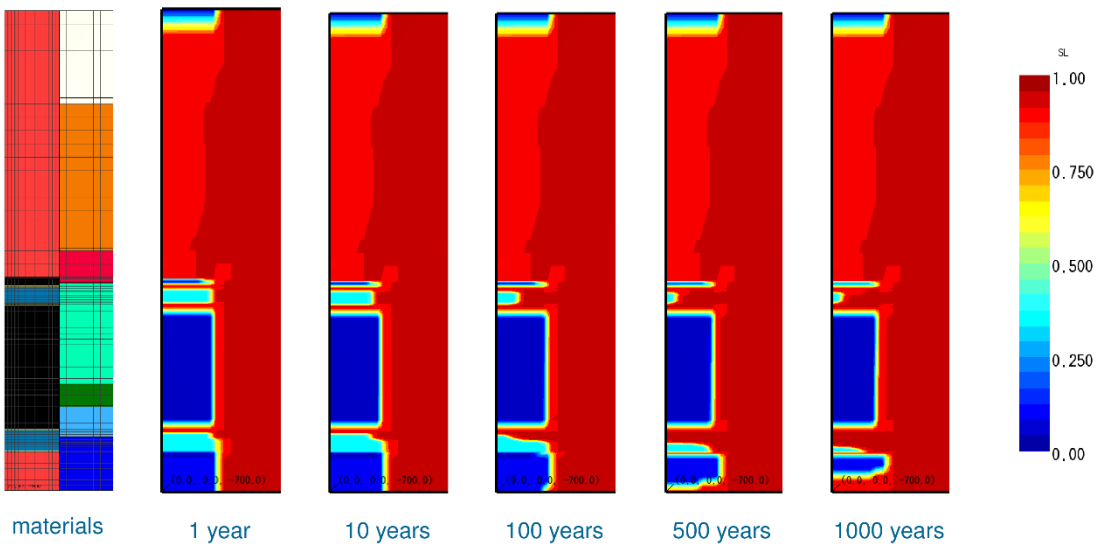

Fig. 6.43 Liquid saturation evolution in the vicinity of the shaft seal

The modelling results for the alternative scenario including gas generation at the shaft bottom are shown in Fig. 6.44 and Fig. 6.45. The simulation was only possible for about 300 years due to numerical issues. The reasons for these problems still must be investigated. The results for the first 300 years show a similar saturation behavior as for the main scenario but a faster pressure increase in the lower gravel column due to the gas pressure build-up. There is however no indication that gas is injected to the rock zone or transported to the upper parts of the sealing system during simulation time.

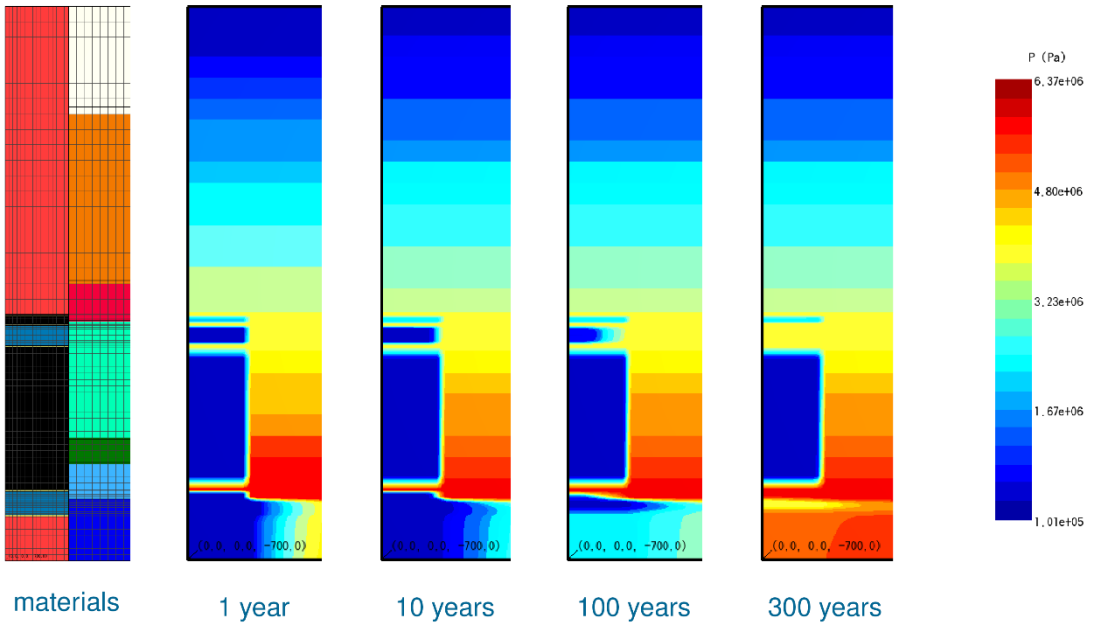

Fig. 6.44 Pressure evolution in the vicinity of the shaft seal for the case of gas injection at the shaft bottom

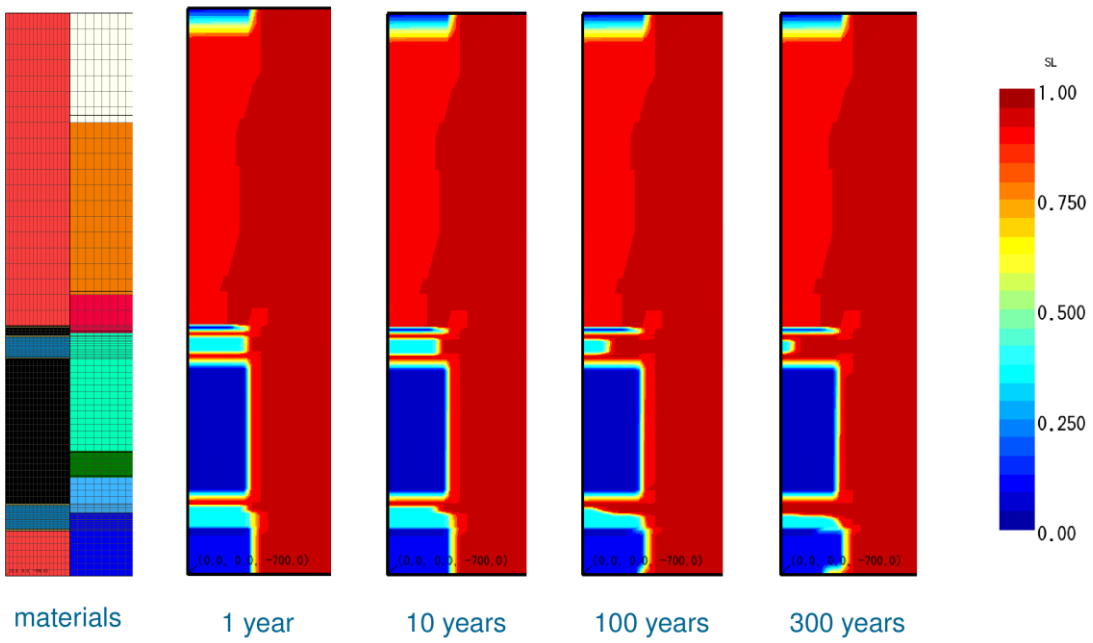

Fig. 6.45 Liquid saturation evolution in the vicinity of the shaft seal for the case of gas injection at the shaft bottom

6.4.4 Conclusion and prospects

The presented modelling and simulation of the hydraulic evolution of a shaft sealing system gives a first impression of the system's functional principle and shows the seal effectiveness. However, the current status is only a starting point for a detailed assessment of the sealing system and, particularly, a comparison of the performance of Sandwich and monolithic bentonite seals in a complete sealing system still has to be performed. For some model configurations, numerical issues lead to early failure of simulation runs, such that simplifications of the two-phase flow properties of the materials (given by linear capillary pressure and relative permeability relations) had to be implemented. The reasons for the numerical issues first have to be assessed before further model variations become reasonable.

Pathways to obtain a more realistic model are already given in /HER 20/. The influence of the EDZ on the sealing behavior could be addressed by an initial desaturation of the shaft contour as well as an increased permeability. Moreover, a permeability decrease in bentonite according to a swelling model could also be implemented. An improved assessment of asphalt seals could be possible by considering bitumen as viscous fluid in the model and investigate the three-phase flow of bitumen, gas and water through the shaft and its vicinity (TOUGH2 provides the EOS9 module to simulate the three-phase flow of oil, water, and air.)

The study of further scenarios for a shaft sealing system would be interesting and necessary for a safety assessment. Such scenarios could include the variation of intruding amounts of gas and liquid or the simulation of failure of sealing components by increasing their permeability.

7 Summary and conclusions

7.1 Summary and lessons learned

In the Sandwich-HP project it was demonstrated that a large-scale Sandwich sealing system of sealing segments (DS) of a binary mixture of bentonite pillows and bentonite granular material (BGM) sandwiched by equipotential segments (ES) of fine material with higher hydraulic conductivity can be installed, hydrated, and monitored within an in-situ experiment. The results obtained so far by the hydration with Pearson water A3, that mimics the pore water of Opalinus clay, indicate the functionality of the Sandwich system interacting with the host rock and provide new experiences in the qualification of monitoring techniques.

The installation and operation of the two experimental shafts was mostly successful during the project period. The rock mass instrumentation and measurements allowed for the confirmation of the bedding dip and facies transition of the Opalinus clay in the vicinity of the experiment by ERT measurements and showed the reaction of rock stress and pore pressure to shaft sinking and pressure increase in the sealing system. It was found that the bottoms of the slim boreholes for pore pressure sensors show a strong deviation from the envisaged location. Shaft sinking could be performed without problems by successful application of a new special drilling technique. The immediate installation of DS and ES and the instrumentation of the sealing system in Shaft 1 demonstrated that a detailed test plan and documentation of working steps would be necessary and that sampling and analyzing installed materials was time-consuming. The installation of the confinement plug in Shaft 1 revealed necessary improvement of cable lead-through and of the sealing capability of the plug for Shaft 2. The hydration system for Shaft 1 was installed with delay due to the Covid pandemic.

The early hydration phase of Shaft 1 revealed some issues. Leaking cables afforded additional sealing measures and some sensors (IMKO TDR and Geosense pressure sensors in the pressure chamber) turned out not to be reliable. From the run-out of the pressure tank during the bypassing event it was learned that emergency cut-off valves in the hydration system would be necessary to avoid the complete emptying of the pressure tank. Thus, the bypass of DS1 also showed the functionality of the Sandwich system and the event could be captured by several sensors. The further hydration of Shaft 1

within the project period proceeded without major interruptions and only very few sensor losses.

The installation of Shaft 2 was performed about two years after the shaft drilling to allow a more pronounced EDZ development. The planning of Shaft 2 incorporated the experience from the installation and operation of Shaft 1. A detailed test plan was prepared prior to installation and the installation work was documented in daily logs. The instrumentation was optimized, and problematic sensors were replaced either by other fabricates or other sensors providing similar information on the hydration progress. The confinement plug and the hydration system were improved. Two different bentonites were installed in DS and a new difficulty occurred during the installation of the DS due to the quality of one type of bentonite pillows which could be resolved after a short delay. The protocol for production of the bentonite pillows has to be adapted to starting bentonite material. Again, sampling and analyzing of DS and ES materials during installation was time consuming and a faster method for on-site water content measurements has to be adapted. The operation phase of Shaft 2 during the reporting period is relatively short. Initial small leaks in the hydration system were sealed and most of the sensors work properly. The wireless data transmission in Shaft 2 works in principal but the data interpretation still must be improved. The assessment of the functionality of the 2D FO sensor is ongoing.

Laboratory work comprised mineralogical and geotechnical characterization of DS and ES materials and chemical analysis of fluids batches, swelling pressure tests, MiniSandwich experiments and semi-technical scale experiments. The variety of experiments on different scales and with different model geometries provides material parameters for modelling work and allows us to recognize and understand different scale-dependent and nonlinear effects on the system behavior. Some experiments were running between about one year up to three years either due to size and experimental conditions or to obtain not only hydro-mechanical equilibrium but also nearly chemical equilibrium. The evaluation of the data is still ongoing and will proceed during the following project phase. A slightly increased swelling pressure of Ca-bentonite hydrated by Pearson water A3 instead of deionized water was confirmed.

The modelling work in the project comprised the calibration of the bentonite model, the MiniSandwich benchmark, the axisymmetric model of Shaft 1 and the simulation of load scenarios for an entire shaft sealing system. It was found that the model calibration

needs a lot of effort and requires data of diverse reliable experiments. The simulation results provide valuable insight into the system behavior.

7.2 Status of the experiment and future steps

At the end of the project period, the two experimental shafts are in different states of hydration. Shaft 1 has been hydrated from the bottom for more than two years and hydration is ongoing at about 2 MPa absolute pressure currently. DS1 is nearly saturated, and a pore pressure has started to evolve. The radial stress in DS1 is in the range of 2 MPa due to swelling. Saturation and stress increase in the upper DS is less pronounced and occurs due to the slow water uptake from the rock prior to and during artificial hydration from the bottom of the Sandwich seal. Hydration of Shaft 2 has just started and all sensors in DS1 show a reasonable reaction.

In the future, it will be interesting two assess possible differences between the evolution of the two shafts resulting from different materials and a different EDZ formation prior to installation. The hydration of both shafts will continue until a stable injection pressure with a maximal value below 3 MPa is reached. Afterwards, hydration via the alternative hydration lines from the top of the sealing system into the ES is possible. Further operation is planned for at least four years. During this time, data from both shafts and the surrounding rock will be recorded, evaluated, and documented in data reports. In parallel, supporting laboratory tests and interpretative simulations will be performed continuously. After this time, a decision will be taken whether the in-situ experiment will be continued or terminated. In the latter case, dismantling and post-mortem investigations will be planned and performed.

References

/ALC 19/ Alcolea, A., Marschall, P., Damians, I. Olivella, S., Gens, A., Madaschi, A., Bosch, J., Laloui, L., Shao, H., Kolditz, O., Nagel, T.: FE-Modelling Task Force /Task 1: Validation of thermally induced THM effects in the rock around the FE-tunnel, NAB 19-40, Nagra, Wettingen, Switzerland, 2019.

/ALO 90/ Alonso, E.E., Gens, A., Josa, A.: A constitutive model for partially saturated soils. Géotechnique, 40 (3), 405-430, 1990.

/ALO 99/ Alonso, E.E., Vaunat, J., Gens, A.: Modelling the mechanical behaviour of expansive clays. Engineering Geology, 54, 173–183, 1999.

/APL 06/ Aplin, A.C., Matenaar, I.F., McCarty, D.K., van der Pluijm, B.A.: Influence of Mechanical Compaction and Clay Mineral Diagenesis on the Microfabric and Pore-Scale Properties of Deep-Water Gulf of Mexico Mudstones. Clays and Clay Minerals, 54, 500–514, 2006.

/BER 22/ Bernachy-Barbe, F., Bosch, J.A., Campos, G., Carbonell, B., Daniels, K.A., Ferrari, A., Graham, C.C., Guillot, W., Gutiérrez-Álvarez, C., Harrington, J.F., Iglesias, R.J., Kataja, M., Kröhn, K.-P., Kröhn, M., Mašín, D., Najser, J., Pingel, J.L., Real, E., Schäfer, T., Svoboda, J., Sun, H., Tanttu, J., Villar, M.V., Wieczorek, K.: Experimental work on bentonite evolution in the frame of BEACON – final report of WP4, Deliverable D4.3., https://igdtp.eu/wp-content/uploads/2022/07/Beacon-D4.3-Experimental-work-on-bentonite-evolution-final-report.pdf, 2022.

/BOH 19/ Bohác, P., Delavernhe, L., Zervas, E., Königer, F., Schuhmann, R., and Emmerich, K.: Cation exchange capacity of bentonite in a saline environment. Applied Geochemistry, 100, 407–413, 2019.

/BMU 20/ Bundesministerium für Umwelt, Naturschutz und nukleare Sicherheit (BMU): Verordnung über Sicherheitsanforderungen an die Endlagerung hochradioaktiver Abfälle (Endlagersicherheitsanforderungsverordnung - EndlSiAnfV), 06.10.2020.

/BUR 22/ Burrus, F., Jaeggi, D., Theurillat, T. & Nussbaum, C.: SW-A Experiment: Security concept for the construction phase of SW-A Experiment. Technical Note TN2020-63rev, Mont Terri Project, August 2022.

/COM 21/ COMSOL Multiphysics® v. 5.6. www.comsol.com. COMSOL AB, Stockholm, Sweden, 2021.

/DIN 02/ Deutsches Institut für Normung e.V. (DIN): Prüfung oxidischer Roh- und Werkstoffe – Bestimmung der Massenänderung beim Glühen. DIN 51081:2002-12, 4 S., Beuth-Verlag, Berlin, 2002.

/DIN 06/ Deutsches Institut für Normung e.V. (DIN): Prüfverfahren für Gesteinskörnungen - Bestimmung der Trockenrohdichte mit dem Messzylinderverfahren und Berechnung des Dichtigkeitsgrades. DIN 52102:2006-02, 9 S., Beuth-Verlag, Berlin, 2006.

/DIN 12/ Deutsches Institut für Normung e.V. (DIN): Baugrund, Untersuchung von Bodenproben - Proctorversuch. DIN 18127:2012-09, 32 S., Beuth-Verlag, Berlin, 2012.

/DIN 21/ Deutsches Institut für Normung e.V. (DIN): Geotechnische Erkundung und Untersuchung - Laborversuche an Bodenproben - Teil 11: Bestimmung der Wasserdurchlässigkeit. DIN EN ISO 17892-11:2021-03, 31 S., Beuth-Verlag, Berlin, 2021.

/DIN 22/ Deutsches Institut für Normung e.V. (DIN): Baugrund, Untersuchung von Bodenproben - Bestimmung der Dichte nicht bindiger Böden bei lockerster und dichtester Lagerung. DIN 18126:2022-10, 27 S., Beuth-Verlag, Berlin, 2022.

/DÖB 15/ Döbelin, N., Kleeberg, R.: Profex: a graphical user interface for the Rietveld refinement program BGMN, Journal of Applied Crystallography 48, 1573-1580, doi:10.1107/S1600576715014685, 2015.

/EMM 18/ Emmerich, K., Giraudo, F., Schuhmann, R., Schnetzer, F., Kaden, H. & Thissen, P.: On the Prediction of Water Contents in Na-Saturated Dioctahedral Smectites. The Journal of Physical Chemistry, 122, 7484-7493, 2018.

/EMM 19/ Emmerich, K., Schuhmann, R., Königer, F., Bohac, P., Delavernhe, L., Wieczorek, K., Czaikowski, O., Hesser, J., Shao, H., Jaeggi, D., Bossart, P., Hansmann, J., Gruner, M., Hofmann, M., Aurich, J., Rölke, C., Popp, T., Diedel, R., Schellhorn, M., Häußer, S., Glaubach, U., Wilsnack, T., Kemper, G., García-Siñeriz, J.L., Villar, M., Gutiérrez-Álvarez, C., Iglesias, R.J.: Joint project: Vertical hydraulic sealing system based on the Sandwich principle – preproject (Sandwich-VP). Final report, Karlsruher Institut für Technologie (KIT) & Gesellschaft für Anlagen- und Reaktorsicherheit (GRS) gGmbH, 2019.

/GAR 22/ García-Siñeriz, J.L., Rey Mazón, M., Tuñón, S.: SW-A Experiment: Shaft 1 as-built report. Technical Note TN2020-19, Mont Terri Project, December 2022.

/GAR 23a/ García-Siñeriz, J.L., Bárcena, I.: SW-A Experiment: As-built of Sandwich FO Extensometer installation. Technical Note TN2022-20, Mont Terri Project, July 2023.

/GAR 23b/ García-Siñeriz, J.L., Bárcena, I., Tuñón, S.: SW-A Experiment: As-built report of the metal plug for Shaft 2. Technical Note TN2022-62 (plug only), Mont Terri Project, May 2023.

/GAR 23c/ García-Siñeriz, J.L., Rey Mazón, M., Tuñón, S.: SW-A Experiment: As-built document of Shaft 2. Technical Note TN2022-62, Mont Terri Project, August 2023.

/GAU 03/ Gaucher, E., Fernández, A., and Waber, H.N.: Rock and Mineral Characterisation of the Opalinus Clay Formation. pp. 281–303 in: Pearson, F.J. et al. (Eds.): Mont Terri Project – Geochemistry of Water in the Opalinus Clay Formation at the Mont Terri Rock Laboratory, Federal Office of Water and Geology (FOWG), Bern, Switzerland, 2003.

/GLÖ 20/ Glötzl Gesellschaft für Baumesstechnik mbH: SW-A Experiment: Installation von Spannungs-Monitor-Stationen (SMS). Technical Note TN2020-06rev1, Mont Terri Project, June 2020.

/GUT 18/ Gutiérrez-Álvarez, C., Iglesias, R.J., Villar, M.V.: Project SANDWICH: Determination of suction and swelling pressure in six samples. Technical Report CIEMAT/DMA/2G218/7/18. Madrid, 15 pp., 2018.

/HEL 97/ Helmig, R.: Multiphase flow and transport processes in the subsurface: A contribution to the modeling of hydrosystems (Vol. 1).; Springer, Berlin, 1997.

/HER 20/ Herold, P., León-Vargas, P., Müller, C., Simo, E., Wilsnack, T., Schieweg, A.: ELSA 2 Teilbericht zum Arbeitspaket 5 Modellierungen. Technical report BGE TEC 2020-21, BGE TECHNOLOGY GmbH, IBeWa, Peine, Freiberg, 2020.

/HIR 54/ Hirschfelder, J.O., Curtiss, C.F., Bird, R.B.: Molecular Theory of Gases and Liquids; John Wiley & Sons, New York, NY, 1954.

/JAE 20/ Jaeggi, D., Galletti, M., Amacher, F., Dunst, R., Nussbaum, C., Raselli, R., Ringeisen, M., Schefer, S., Bossart, P.: Gallery 2018: Excavation and geological documentation. Technical Report TR2018-04, Mont Terri Project, June 2020.

/JAE 22/ Jaeggi, D., Nicaty, C.: SW-A Experiment: Sinking of shafts SW-A1 and SW-A2, incl. geological documentation. Technical Note TN2020-32, Mont Terri Project, August 2022.

/JOB 15/ Jobmann, M., Lommerzheim, A.: Endlagerkonzept sowie Verfüll- und Verschlusskonzept für das Endlagerstandortmodell SÜD. Projekt ANSICHT: Methodik und Anwendungsbezug eines Sicherheits- und Nachweiskonzeptes für ein HAW-Endlager im Tongestein. Technical Report TEC-26-2015-TB, DBE TECHNOLOGY, Peine, 2015.

/JOB 16/ Jobmann, M.; Burlaka, V., Meleshyn, A., Rübel, A.: Spezifische Prozessanalysen. Projekt ANSICHT: Methodik und Anwendungsbezug eines Sicherheits- und Nachweiskonzeptes für ein HAW-Endlager im Tongestein. Technical Report TEC-13-2016-B, DBE TECHNOLOGY, Peine, 2016.

/JOB 17/ Jobmann, M., Bebiolka, A., Burlaka, V., Herold, P., Jahn, S., Lommerzheim, A., Maßmann, J., Meleshyn, A., Mrugalla, S., Reinhold, K., others: Safety assessment methodology for a German high-level waste repository in clay formations. Journal of Rock Mechanics and Geotechnical Engineering, 9(5):856–876, 2017.

/KNE 21/ Kneuker, T., Furche, M.: Capturing the structural and compositional variability of Opalinus Clay: constraints from multidisciplinary investigations of Mont Terri drill cores (Switzerland), Environm. Earth Sci., 80:421-442, June 2021.

/KOL 12/ Kolditz, O., Görke, J., Shao, H., Wang, W. (Eds.): Thermo-Hydro-Mechanical-Chemical Processes in Fractured Porous Media; Springer, Heidelberg, 2012.

/KÖN 08/ Königer, F., Emmerich, K., Kemper, G., Gruner, M., Gaßner, W., Nüesch, R., Schuhmann, R.: Moisture spreading in a multi-layer hydraulic sealing system (HTV-1). Engineering Geology, 98, 41-49, 2008.

/KUD 21/ Kudla, W., Herold, P: Schachtverschlüsse für Endlager für hochradioaktive Abfälle (ELSA - Phase 2): Konzeptentwicklung für Schachtverschlüsse und Test von Funktionselementen von Schachtverschlüssen: zusammenfassender Abschlussbericht für das Verbundvorhaben. Abschlussbericht, 165 S, https://doi.org/10.2314/KXP:1799529851, 2021.

/LOM 15/ Lommerzheim, A., Jobmann, M.: Endlagerkonzept sowie Verfüll- und Verschlusskonzept für das Endlagerstandortmodell NORD. Projekt ANSICHT: Methodik und Anwendungsbezug eines Sicherheits- und Nachweiskonzeptes für ein HAW-Endlager im Tongestein. Technical Report TEC-14-2015-TB, DBE TECHNOLOGY, Peine, 2015.

/MAS 16/ Maßmann, J.: Endlagerstandortmodell SÜD (AnSichT) - Teil III: Auswahl von Gesteins- und Fluideigenschaften für numerische Berechnungen im Rahmen des Langzeitsicherheitsnachweises. Technical Report, BGR, Hannover, 2016.

/MAY 07/ Mayor, J.C., García-Siñeriz, J.L., Alonso, E., Alheid, H.-J., Blümling, P.: Engineered barrier emplacement experiment in Opalinus Clay for the disposal of radioactive waste in underground repositories. In: Bossart, P. and Nussbaum, C. (Eds.): Mont Terri Project – Heater Experiment, Engineered Barriers Emplacement and Ventilation Tests (p. 115-179). – Rep. Swiss Geol. Surv. 1, 2007.

/MAY 14/ Mayor, J.C., Velasco, M.: Long-term Performance of Engineered Barrier Systems (PEBS) – EB dismantling Synthesis report, Deliverable D2.1-8, https://cordis.europa.eu/docs/projects/files/249/249681/eb-dismantling-synthesis-report.pdf, 2014.

/MAY 23/ Mayor, J.C.: WT Experiment: Wireless transmission geotechnical data through clay rock, Technical Note TN2023-24, Mont Terri Project, May 2023.

/MAZ 98/ Mazurek, M.: Mineralogical composition of Opalinus Clay at Mont Terri - a laboratory intercomparison. Technical Report, University of Bern, Bern, Switzerland, 1998.

/NEA 03/ Nuclear Energy Agency (NEA): Engineered Barrier Systems and the Safety of Deep Geological Repositories, State-of-the-art Report (ISBN 92-64-18498-8), 71 p, 2003.

/NOL 02/ Nold, A.L., Zuidema, P., Blümling, P.: NAGRA Technical Report 02-02, Wettingen, Switzerland, 2002.

/NÜE 02/ Nüesch, R., Brandelik, A., Hübner, C., Schuhmann, R.: Verschlussstopfen und Verfahren zum Verschließen von untertätigen Hohlräumen, Deutsches Patent DE 10149972 C1, 2002.

/OLI 20/ Olivella, S., Vaunat, J., Rodriguez-Dono, A.: Code_Bright 2020 User's Guide, Universitat Polytécnica de Catalunya Barcelonatech, https://deca.upc.edu/en/projects/code_bright/downloads/users_guide/view, 2020.

/PEA 98/ Pearson, F.J.: Artificial waters for use in laboratory and field ex-periments with Opalinus clay, June 1998.

/PEA 03/ Pearson, F.J., Arcos, D., Bath, A., Boisson, J.-Y., Fernández, A.M., Gäbler, H.-E., Gaucher, E., Gautschi, A., Griffault, L., Hernán P., Waber, H.N.: Mont Terri Project – Geochemistry of Water in the Opalinus Clay Formation at the Mont Terri Rock Laboratory. Reports of the FOWG, Geology Series No. 5, 321 S., 2003.

/PRU 99/ Pruess, K., Oldenburg, C. M., Moridis, G. J.: TOUGH2 user's guide version 2 (No. LBNL-43134). Lawrence Berkeley National Lab.(LBNL), Berkeley, CA (United States), 1999.

/REI 13/ Reinhold, K., Jahn, S., Kühnlenz, T., Ptock, L., Sönnke, J.: Endlagerstandortmodell NORD-Teil I: Beschreibung des geologischen Endlagerstandortmodells. Technical Report, BGR, Hannover, 2013.

/REI 16/ Reinhold, K., Stark, L., Kühnlenz, T., Ptock, L.: Endlagerstandortmodell SÜD-Teil I: Beschreibung des geologischen Endlagerstandortmodells. Technical Report, BGR, Hannover, 2016.

/RÖS 20/ Rösli, U., Ammon, A., Schwab, L.: SW-A Experiment: Installation of casing in BSW-B24 and BSW-B25. Technical Note TN2020-79, Mont Terri Project, June 2020.

/SCH 69/ Schmidt, E.: Properties of water and steam in SI-units; Springer, Oldenbourg, 1969.

/SCH 09/ Schuhmann, R. et al.: Verschlusssystem mit Äquipotenzialsegmenten für die untertägige Entsorgung (UTD und ELA) gefährlicher Abfälle zur Sicherherstellung der homogenen Befeuchtung der Dichtelemente und zur Verbesserung der Langzeitstabilität: Schlussbericht. http://edok01.tib.uni-hannover.de/edoks/e01fb10/637752392.pdf, 2009.

/SHA 23/ Shao, H., Roelke, C., Emmerich, K., Popp, T., Königer, F., Schumann, R., Wieczorek, K., Hesser, J.: Coupled hydromechanical modelling of a vertical hydraulic sealing system based on the Sandwich principle, Rock Mechanics and Rock Engineering, https://doi.org/10.1007/s00603-023-03404-1, 2023.

/SIG 21/ Sigeom SA: SW-A Experiment: Laserscanning in Shaft 1 and 2. Technical Note TN2020-62, Mont Terri Project, February 2021.

/SIG 22/ Sigeom SA: SW-A Experiment: Convergence monitoring by laser scanning between 2020 and 2022 in shaft SW-A2, Technical Note TN2022-66, Mont Terri Project, August 2022.

/VAN 80/ Van Genuchten, M.T.: A closed-form equation for predicting the hydraulic conductivity of unsaturated soils. Soil Science Society, 44, 892-898, 1980.

/VAN 03/ Van Loon, L.R., Soler, J. M., Bradbury, M.H.: Diffusion of HTO, 36Cl− and 125I− in Opalinus Clay samples from Mont Terri: Effect of con-fining pressure. Journal of Contaminant Hydrology, 73-83, 2003.

/VAS 14/ Vasconcelos, R., Pinyol, N., Alonso, E.E., Gens, A.: Long-term Performance of Engineered Barrier Systems (PEBS) – Modelling and interpretation of the EB experiment hydration, Deliverable D3.1-1/2, https://cordis.europa.eu/docs/projects/files/249/249681/modelling-and-interpretation-of-the-eb-experiment-hydration.pdf, 2014.

/VAS 21/ Vasconcelos, R.: A double-porosity formulation for the THM behaviour of bentonite-based materials. Thesis, Technical University of Catalonia, http://upcommons.upc.edu/tesis, 2021.

/WIE 22a/ Wieczorek, K., Emmerich, K., García-Siñeriz, J.L., Rey Mazón, M., Tuñón, S., Furche, M., Hesser, J., Shao, H., Königer, F., Jaeggi, D., Schefer, S., Ziegler, M.:: SW-A Experiment: Test Plan Shaft 2, Technical Note TN2022-61, Mont Terri Project, December 2022.

/WIE 22b/ Wieczorek, K., Shao, H., Winkler, M., Schädle, P., Rölke, C., Emmerich, K.: Interpretative HM simulation of a MiniSandwich experiment using different numerical codes. 8th Int. Conference: Clays in Natural and Engineered Barriers for Radioactive Waste Confinement, Nancy, 13-16 June 2022.

/WIE 23a/ Wieczorek, K., Emmerich, K., Furche, M., Hesser, J., Jaeggi, D., Königer, F., Rey, M., Tuñón, S.: SW-A Experiment: Sandwich-HP: Vertical Hydraulic Sandwich Sealing System – First Sensor Data Report, Technical Note TN2020-21, Mont Terri Project, March 2023.

/WIE 23b/ Wieczorek, K., Emmerich, K., Furche, M., Hesser, J., Hinze, M., Jaeggi, D., Königer, F., Rey, M., Tuñón, S.: SW-A Experiment: Sandwich-HP: Vertical Hydraulic Sandwich Sealing System – Second Sensor Data Report, Technical Note TN2023-69, Mont Terri Project, August 2023.

List of figures

List of tables

List of abbreviations

ARDP	apparent relative dielectric permittivity
BExM	Barcelona Expansive Model
BGM	bentonite granular material
CEC	cation exchange capacity
DAS	data acquisition system
DS	sealing segment
DSC	differential scanning calorimetry
EBS	engineered barrier system
EDZ	excavation damaged zone
EMDD	effective montmorillonite dry density
ERT	electrical resistivity tomography
ES	equipotential segment
FO	fiber optical
HTV	semi-technical scale experiment
IC	ion chromatography
ICP-OES	inductively coupled plasma optical emission spectroscopy
IVM	interval velocity measurement (seismics)
LF	electric conductivity
LOI	loss on ignition
MHP	medium high performance
MS	mass spectrometry
MTRL	Mont Terri rock laboratory
PP	pore pressure
PVC	polyvinylchloride
RH	relative humidity
RU	receiver unit

STA	simultaneous thermal analysis
TDR	time-domain reflectometry
TG	thermogravimetry
TU	transmitter unit
UHP	ultra high performance
UPS	uninterrupted power supply
WDT	wireless data transmission
WP	work package
XHM	cross-hole velocity measurement (seismics)
XRD	X-ray diffraction analysis
XRF	X-ray fluorescence analysis

The abbreviations related to the sensor nomenclature in the in-situ experiment are given in Tab. A. 5.

A Sensor nomenclature and location

The following tables list the sensors used in the SW-A experiment together with their coordinates expressed in the local coordinate system shown in Fig. 3.1. The nomenclature of the sensors is explained in Tab. A. 1 to Tab. A. 4. The sensors with specifications and location are given in Tab. A. 5 to Tab. A. 12.

Tab. A. 1 Nomenclature for rock sensors: BSWxx_zz_n

BSW	borehole of SW-A experiment
xx	number of borehole (for boreholes up to number 9 it's 0x)
zz	acronym for parameter
n	number of sensor of the same type

Tab. A. 2 Nomenclature for DS and interface DS/rock sensors: S1_DS0x_pyy_zz_n

S1	Shaft 1
DS	sealing segment
0x	number of DS x: 1...4
p	L for installation layer or R for ring (ERT sensors)
yy	number of L (DS were installed in 12/10 layers) or R
zz	acronym for parameter
n	number of sensors of same type

Tab. A. 3 Nomenclature for TAUPE TDR cable sensors: S1_ES0x_L0y_WC_nH / S1_ES01_ES05_WC_nV

S1	Shaft 1
ES	equipotential segment
0x	number of ES x: 1...5
L	installation level
0y	number of L (ES were installed in 2 levels)
n	number of sensors of same type
H	installed horizontally
V	installed vertically intersecting all ES and DS

Tab. A. 4 Nomenclature for ES and interface ES/rock sensors: S1_ES0x_p0y_zz_n

S1	Shaft 1
ES	equipotential segment
0x	number of ES x: 1...5
p	L for installation layer or R for ring (ERT sensors)
0y	number of L (ES were installed in 2 layers) or R
zz	acronym for parameter
n	number of sensors of same type

Tab. A. 5 Parameter acronyms: zz

PP	Pore pressure
SA	Axial stress
SR	Radial stress
TT	Temperature
HR	Relative humidity
WC	Apparent relative dielectric permittivity (ARDP) as measure for water content
CE	Electric conductivity
DP	Displacement
RE	Electrical resistivity
FF	Fluid Flow
PG	Gas Pressure
VL	Volume
WS	Weight
OC	Open-closed

Tab. A. 6 Rock sensors

Sensor name	Parameter	Sensor model	Data acquisition	Organization	x [mm]	y [mm]	z [mm]
BSW01_PP_1	Fluid Pressure, absolute	PAA-23 SX (Keller)	Solexperts	GRS	-144	1091	-9390
BSW02_PP_1					144	1091	-10690
BSW03_PP_1					1016	421	-6790
BSW04_PP_1					1091	144	-9390
BSW05_PP_1					-1247	-517	-10700
BSW06_PP_1					1016	-421	-8090
BSW07_PP_1					421	-1016	-6790
BSW08_PP_1					144	-1091	-9390
BSW09_PP_1					-144	-1091	-10690
BSW10_PP_1					-421	-1016	-8090
BSW11_PP_1					0	1600	-10490
BSW12_PP_1					0	-2300	-9890
BSW13_PP_1					0	-3100	-5490
BSW14_PP_1					0	-3900	-7990
BSW15_PP_1					0	-7800	-7990
BSW16_PP_1					1100	-6200	-8240
BSW20_SR_1	Stress radial	E 10/20 AU 100A (Gloetzl)	Gloetzl	BGR	-1100	0	-10900
BSW20_SR_2					-1100	0	-10500
BSW20_SR_3					-1100	0	-10050
BSW20_SR_4					-1100	0	-9600
BSW20_SR_5					-1100	0	-9200
BSW20_SR_6					-1100	0	-8750
BSW20_TT_1	Temperature	PT100, class A, type SMD (Gloetzl)	Gloetzl	BGR	-1100	0	-8750
BSW21_SR_1	Stress radial	E 10/20 AU 100A (Gloetzl)	Gloetzl	BGR	0	1100	-10900
BSW21_SR_2					0	1100	-10500
BSW21_SR_3					0	1100	-10050
BSW21_SR_4					0	1100	-9600
BSW21_SR_5					0	1100	-9200
BSW21_SR_6					0	1100	-8750
BSW21_TT_1	Temperature	PT100, class A, type SMD (Gloetzl)	Gloetzl	BGR	0	1100	-8750
BSW22_SR_1	Stress radial	E 10/20 AU 100A (Gloetzl)	Gloetzl	BGR	778	-778	-10900
BSW22_SR_2					778	-778	-10500
BSW22_SR_3					778	-778	-10050
BSW22_SR_4					778	-778	-9600
BSW22_SR_5					778	-778	-9200
BSW22_SR_6					778	-778	-8750
BSW22_TT_1	Temperature	PT100, class A, type SMD (Gloetzl)	Gloetzl	BGR	778	-778	-8750
BSW32_PP_1	Fluid Pressure, absolute	PAA-23 SX (Keller)	Solexperts	GRS	-1552	-7293	-9293
BSW33_PP_1					-1585	-5174	-6035

Tab. A. 7 DS and interface DS/rock sensors Shaft 1

Sensor name	Parameter	Sensor model	Data acquisition	Organization	x [mm]	y [mm]	z [mm]
S1_DS01_L03_HR_1	Relative Humidity	HMP7 (Vaisala)	Amberg	Amberg	-310	-60	-10970
S1_DS01_L03_PP_1	Pore Pressure, relative	SGP-3400 (Geosense)	Solexperts	Amberg	-340	80	-10970
S1_DS01_L03_SR_1	Stress radial	E 10/20 AU 100A (Gloetzl)	Gloetzl	ISU	-590	0	-11100
S1_DS01_L03_SR_2	Stress radial	E 10/20 AU 100A (Gloetzl)	Gloetzl	ISU	0	590	-11100
S1_DS01_L03_TT_1	Temperature	PT-100 RTD Class FO.1 (Vaisala)	Amberg	Amberg	-310	-60	-10970
S1_DS01_L09_HR_1	Relative Humidity	HMP7 (Vaisala)	Amberg	Amberg	260	50	-10460
S1_DS01_L09_PP_1	Pore Pressure, relative	SGP-3400 (Geosense)	Solexperts	Amberg	270	60	-10460
S1_DS01_L09_TT_1	Temperature	PT-100 RTD Class FO.1 (Vaisala)	Amberg	Amberg	260	50	-10460
S1_DS01_L11_SR_1	Stress radial	E 10/20 AU 100A (Gloetzl)	Gloetzl	ISU	-590	0	-10340
S1_DS01_L11_SR_2	Stress radial	E 10/20 AU 100A (Gloetzl)	Gloetzl	ISU	0	590	-10340
S1_DS01_L12_SA_1	Stress axial	E 20 AU 100A (Gloetzl)	Gloetzl	ISU	0	0	-10213
S1_DS02_L03_HR_1	Relative Humidity	HMP7 (Vaisala)	Amberg	Amberg	-310	-60	-9810
S1_DS02_L03_PP_1	Pore Pressure, relative	SGP-3400 (Geosense)	Solexperts	Amberg	-380	80	-9810
S1_DS02_L03_TT_1	Temperature	PT-100 RTD Class FO.1 (Vaisala)	Amberg	Amberg	-310	-60	-9810
S1_DS02_L04_SR_1	Stress radial	E 10/20 AU 100A (Gloetzl)	Gloetzl	ISU	-590	50	-9650
S1_DS02_L04_SR_2	Stress radial	E 10/20 AU 100A (Gloetzl)	Gloetzl	ISU	50	590	-9650
S1_DS02_L09_HR_1	Relative Humidity	HMP7 (Vaisala)	Amberg	Amberg	260	50	-9300
S1_DS02_L09_PP_1	Pore Pressure, relative	SGP-3400 (Geosense)	Solexperts	Amberg	270	60	-9300
S1_DS02_L09_SR_1	Stress radial	E 10/20 AU 100A (Gloetzl)	Gloetzl	ISU	-590	-50	-9200
S1_DS02_L09_SR_2	Stress radial	E 10/20 AU 100A (Gloetzl)	Gloetzl	ISU	-50	590	-9200
S1_DS02_L09_TT_1	Temperature	PT-100 RTD Class FO.1 (Vaisala)	Amberg	Amberg	260	50	-9300
S1_DS02_L12_SA_1	Stress axial	E 20 AU 100A (Gloetzl)	Gloetzl	ISU	0	0	-8900
S1_DS03_L03_HR_1	Relative Humidity	HMP7 (Vaisala)	Amberg	Amberg	-310	-60	-8350
S1_DS03_L03_PP_1	Pore Pressure, relative	SGP-3400 (Geosense)	Solexperts	Amberg	-330	80	-8650
S1_DS03_L03_TT_1	Temperature	PT-100 RTD Class FO.1 (Vaisala)	Amberg	Amberg	-310	-60	-8350
S1_DS03_L07_SR_1	Stress radial	E 10/20 AU 100A (Gloetzl)	Gloetzl	ISU	-590	0	-8100
S1_DS03_L07_SR_2	Stress radial	E 10/20 AU 100A (Gloetzl)	Gloetzl	ISU	0	590	-8100
S1_DS03_L09_HR_1	Relative Humidity	HMP7 (Vaisala)	Amberg	Amberg	260	50	-8150
S1_DS03_L09_PP_1	Pore Pressure, relative	SGP-3400 (Geosense)	Solexperts	Amberg	270	60	-8150
S1_DS03_L09_TT_1	Temperature	PT-100 RTD Class FO.1 (Vaisala)	Amberg	Amberg	260	50	-8150
S1_DS03_L12_SA_1	Stress axial	E 20 AU 100A (Gloetzl)	Gloetzl	ISU	0	0	-7600
S1_DS04_L03_HR_1	Relative Humidity	HMP7 (Vaisala)	Amberg	Amberg	-310	-60	-7040
S1_DS04_L03_PP_1	Pore Pressure, relative	SGP-3400 (Geosense)	Solexperts	Amberg	-330	80	-7040
S1_DS04_L03_TT_1	Temperature	PT-100 RTD Class FO.1 (Vaisala)	Amberg	Amberg	-310	-60	-7040
S1_DS04_L07_SR_1	Stress radial	E 10/20 AU 100A (Gloetzl)	Gloetzl	ISU	-590	0	-6800
S1_DS04_L07_SR_2	Stress radial	E 10/20 AU 100A (Gloetzl)	Gloetzl	ISU	0	590	-6800
S1_DS04_L09_HR_1	Relative Humidity	HMP7 (Vaisala)	Amberg	Amberg	260	50	-6540
S1_DS04_L09_PP_1	Pore Pressure, relative	SGP-3400 (Geosense)	Solexperts	Amberg	270	60	-6540
S1_DS04_L09_TT_1	Temperature	PT-100 RTD Class FO.1 (Vaisala)	Amberg	Amberg	260	50	-6540
S1_DS04_L12_SA_1	Stress axial	E 20 AU 100A (Gloetzl)	Gloetzl	ISU	0	0	-6300

Tab. A. 8 ES and interface ES/rock sensors Shaft 1

Sensor name	Parameter	Sensor model	Data acquisition	Organization	x [mm]	y [mm]	z [mm]
S1_ES01_ES05_WC_V1	ARDP Integral	TAUPE cable sensor (KIT/ISU)	TAUPE	ISU	0	-230	-6142
S1_ES01_ES05_WC_V2	ARDP Integral	TAUPE cable sensor (KIT/ISU)	TAUPE	ISU	-450	0	-6142
S1_ES01_ES05_WC_V3	ARDP Integral	TAUPE cable sensor (KIT/ISU)	TAUPE	ISU	450	0	-6142
S1_ES01_ES05_WC_V4	ARDP Integral	TAUPE cable sensor (KIT/ISU)	TAUPE	ISU	0	-450	-6142
S1_ES01_ES05_WC_V5	ARDP Integral	TAUPE cable sensor (KIT/ISU)	TAUPE	ISU	0	450	-6142
S1_ES01_L01_CE_1	Electric conductivity	TRIME-PICO64 (IMKO)	IMKO	ISU	392	-799	-11350
S1_ES01_L01_PP_1	Pore Pressure, relative	SGP-3400 (Geosense)	Solexperts	Amberg	-330	80	-11350
S1_ES01_L01_PP_2	Pore Pressure, relative	SGP-3400 (Geosense)	Solexperts	Amberg	270	60	-11350
S1_ES01_L01_TT_1	Temperature	TRIME-PICO64 (IMKO)	IMKO	ISU	392	-799	-11350
S1_ES01_L01_WC_1	ARDP	TRIME-PICO64 (IMKO)	IMKO	ISU	392	-799	-11350
S1_ES01_L01_WC_H1	ARDP Integral	TAUPE cable sensor (KIT/ISU)	TAUPE	ISU	-171	-469	-11350
S1_ES02_L01_CE_1	Electric conductivity	TRIME-PICO64 (IMKO)	IMKO	ISU	392	-799	-10050
S1_ES02_L01_PP_1	Pore Pressure, relative	SGP-3400 (Geosense)	Solexperts	Amberg	-330	80	-10050
S1_ES02_L01_PP_2	Pore Pressure, relative	SGP-3400 (Geosense)	Solexperts	Amberg	270	60	-10050
S1_ES02_L01_TT_1	Temperature	TRIME-PICO64 (IMKO)	IMKO	ISU	392	-799	-10050
S1_ES02_L01_WC_1	ARDP	TRIME-PICO64 (IMKO)	IMKO	ISU	392	-799	-10050
S1_ES02_L01_WC_H2	ARDP Integral	TAUPE cable sensor (KIT/ISU)	TAUPE	ISU	-171	-469	-10050
S1_ES03_L01_CE_1	Electric conductivity	TRIME-PICO64 (IMKO)	IMKO	ISU	392	-799	-8750
S1_ES03_L01_PP_1	Pore Pressure, relative	SGP-3400 (Geosense)	Solexperts	Amberg	-330	80	-8900
S1_ES03_L01_PP_2	Pore Pressure, relative	SGP-3400 (Geosense)	Solexperts	Amberg	270	60	-8900
S1_ES03_L01_TT_1	Temperature	TRIME-PICO64 (IMKO)	IMKO	ISU	392	-799	-8750
S1_ES03_L01_WC_1	ARDP	TRIME-PICO64 (IMKO)	IMKO	ISU	392	-799	-8750
S1_ES03_L01_WC_H3	ARDP Integral	TAUPE cable sensor (KIT/ISU)	TAUPE	ISU	-171	-469	-8750
S1_ES03_L02_DP_1	Displacement	D5/400AW (RDP)	Solexperts	Amberg	0	590	-8596
S1_ES03_L02_DP_2	Displacement	D5/400AW (RDP)	Solexperts	Amberg	-511	-295	-8596
S1_ES03_L02_DP_3	Displacement	D5/400AW (RDP)	Solexperts	Amberg	-511	-295	-8596
S1_ES04_L01_CE_1	Electric conductivity	TRIME-PICO64 (IMKO)	IMKO	ISU	392	-799	-7450
S1_ES04_L01_PP_1	Pore Pressure, relative	SGP-3400 (Geosense)	Solexperts	Amberg	-330	80	-7470
S1_ES04_L01_PP_2	Pore Pressure, relative	SGP-3400 (Geosense)	Solexperts	Amberg	270	60	-7470
S1_ES04_L01_TT_1	Temperature	TRIME-PICO64 (IMKO)	IMKO	ISU	392	-799	-7450
S1_ES04_L01_WC_1	ARDP	TRIME-PICO64 (IMKO)	IMKO	ISU	392	-799	-7450
S1_ES04_L01_WC_H4	ARDP Integral	TAUPE cable sensor (KIT/ISU)	TAUPE	ISU	-171	-469	-7450
S1_ES05_L01_CE_1	Electric conductivity	TRIME-PICO64 (IMKO)	IMKO	ISU	392	-799	-6150
S1_ES05_L01_PP_1	Pore Pressure, relative	SGP-3400 (Geosense)	Solexperts	Amberg	-330	80	-6150
S1_ES05_L01_PP_2	Pore Pressure, relative	SGP-3400 (Geosense)	Solexperts	Amberg	270	60	-6150
S1_ES05_L01_TT_1	Temperature	TRIME-PICO64 (IMKO)	IMKO	ISU	392	-799	-6150
S1_ES05_L01_WC_1	ARDP	TRIME-PICO64 (IMKO)	IMKO	ISU	392	-799	-6150
S1_ES05_L01_WC_H5	ARDP Integral	TAUPE cable sensor (KIT/ISU)	TAUPE	ISU	-171	-469	-6150

Tab. A. 9 Hydration system sensors Shaft 1

Sensor name	Parameter	Sensor model	Data acquisition	Organization	x [mm]	y [mm]	z [mm]
S1_HS_HPT_FF_1	Fluid Flow	Virtual (OASIS)	OASIS	OASIS	2400	-12000	1000
S1_HS_HPT_PF_1	Fluid Pressure, absolute	Calculated sensor	OASIS	OASIS	2400	-12000	2000
S1_HS_HPT_PF_1_rel	Fluid Pressure, relative	WIKA S-20 (Wika)	Solexperts	Amberg	2400	-12000	1800
S1_HS_HPT_Valve_05	1=Open, 0=Closed	Valve, NC (Not specified)	Solexperts	Amberg	2400	-12000	1200
S1_HS_HPT_VL_1	Volume	Calculated sensor	OASIS	OASIS	2400	-12000	1600
S1_HS_HPT_WS_1	Weight	HY10.32.HRP.H.M2.1 (Radwag)	Amberg	Amberg	2400	-12000	1400
S1_HS_INL_Valve_11	1=Open, 0=Closed	Valve, NC (Not specified)	Solexperts	Amberg	2250	-12000	2200
S1_HS_LPT1_FF_1	Fluid Flow	Virtual (OASIS)	OASIS	OASIS	2100	-12000	200
S1_HS_LPT1_PF_1	Fluid Pressure, absolute	PAA-25 Y (Keller)	Solexperts	Amberg	2100	-12000	1000
S1_HS_LPT1_Valve_03	1=Open, 0=Closed	Valve, NC (Not specified)	Solexperts	Amberg	2100	-12000	400
S1_HS_LPT1_VL_1	Volume	Calculated sensor	OASIS	OASIS	2100	-12000	800
S1_HS_LPT1_WS_1	Weight	Defender 5000, D52XW150RQDX2			2100	-12000	600
S1_PC01_PF_1	Fluid Pressure, relative	SGP-3400 (Geosense)	Solexperts	Amberg	0	0	-12103
S1_PC01_PF_2	Fluid Pressure, relative	SGP-3400 (Geosense)	Solexperts	Amberg	0	0	-12103
S1_PC01_TT_1	Temperature	Pt-100 RTD 4-wires (Termya)	Solexperts	Amberg	0	0	-12103
S1_PC01_TT_2	Temperature	Pt-100 RTD 4-wires (Termya)	Solexperts	Amberg	0	0	-12103

Tab. A. 10 DS and interface DS/rock sensors Shaft 2

Sensor name	Parameter	Sensor model	Data acquisition	Organization	x [mm]	y [mm]	z [mm]
S2_DS01_L02_PP_1	Fluid Pressure, absolute	PAA-23 SX (Keller)	Solexperts	Amberg	-231	-6445	-9409
S2_DS01_L02_RH_1	Relative Humidity	SHT85 V1 (RH) (Amberg)	Amberg	Amberg	-263	-6000	-9409
S2_DS01_L02_TT_1	Temperature	SHT85 V1 (T) (Amberg)	Amberg	Amberg	-263	-6000	-9409
S2_DS01_L05_SR_1	Stress radial	E 10/20 AU 100A (Gloetzl)	Gloetzl	ISU	-584	-6176	-9194
S2_DS01_L08_PP_1	Fluid Pressure, absolute	PAA-23 SX (Keller)	Solexperts	Amberg	255	-5936	-8918
S2_DS01_L08_RH_1	Relative Humidity	SHT85 V1 (RH) (Amberg)	Amberg	Amberg	243	-6508	-8926
S2_DS01_L08_TT_1	Temperature	SHT85 V1 (T) (Amberg)	Amberg	Amberg	243	-6508	-8926
S2_DS01_L10_SA_1	Stress axial	E 20 AU 100A (Gloetzl)	Gloetzl	ISU	-23	-6090	-8762
S2_DS02_L02_PP_1	Fluid Pressure, absolute	PAA-23 SX (Keller)	Solexperts	Amberg	-315	-6447	-8310
S2_DS02_L02_RH_1	Relative Humidity	SHT85 V1 (RH) (Amberg)	Amberg	Amberg	-255	-5922	-8314
S2_DS02_L02_TT_1	Temperature	SHT85 V1 (T) (Amberg)	Amberg	Amberg	-253	-5922	-8313
S2_DS02_L05_SR_1	Stress radial	E 10/20 AU 100A (Gloetzl)	Gloetzl	ISU	-589	-6186	-8058
S2_DS02_L08_PP_1	Fluid Pressure, absolute	PAA-23 SX (Keller)	Solexperts	Amberg	258	-5953	-7824
S2_DS02_L08_RH_1	Relative Humidity	SHT85 V1 (RH) (Amberg)	Amberg	Amberg	251	-6502	-7838
S2_DS02_L08_TT_1	Temperature	SHT85 V1 (T) (Amberg)	Amberg	Amberg	251	-6502	-7838
S2_DS02_L09_DP_2	Displacement	FST400-1100 (Firstrate)	Solexperts	Amberg	533	-6374	-7733
S2_DS02_L09_DP_3	Displacement	FST400-1100 (Firstrate)	Solexperts	Amberg	-310	-6693	-7793
S2_DS02_L09_DP_4	Displacement	FST400-1100 (Firstrate)	Solexperts	Amberg	-146	-5669	-7718
S2_DS02_L09_DP_FO_1	Displacement	2D FO sensor (Amberg)	Amberg	Amberg			
S2_DS02_L10_PP_WL_1	Pore Pressure, absolute	Calculated sensor	Wireless	OASIS	-295	-6467	-7672
S2_DS02_L10_PP_WL_1r	Raw, Pore Press, absolute	PAA-26 Y (Keller)	Wireless	Amberg	-295	-6467	-7672
S2_DS02_L10_RH_WL_1	Relative Humidity	SHT85 V1 (RH) (Amberg)	Wireless	Amberg	246	-6496	-7661
S2_DS02_L10_SA_1	Stress axial	E 20 AU 100A (Gloetzl)	Gloetzl	ISU	-27	-6115	-7658
S2_DS02_L10_SA_WL_1	Stress axial	Calculated sensor	Wireless	OASIS	-36	-6035	-7514
S2_DS02_L10_TT_WL_1	Temperature	PT-100 RTD 4-wires (Termya)	Wireless	Amberg			
S2_DS02_L10_TT_WL_2	Temperature	SHT85 V1 (T) (Amberg)	Wireless	Amberg	246	-6496	-7661
S2_DS03_L02_PP_1	Fluid Pressure, absolute	PAA-23 SX (Keller)	Solexperts	Amberg	-258	-6510	-7216
S2_DS03_L02_RH_1	Relative Humidity	SHT85 V1 (RH) (Amberg)	Amberg	Amberg	-298	-5971	-7225
S2_DS03_L02_TT_1	Temperature	SHT85 V1 (T) (Amberg)	Amberg	Amberg	-298	-5971	-7225
S2_DS03_L05_SR_1	Stress radial	E 10/20 AU 100A (Gloetzl)	Gloetzl	ISU	-598	-6214	-6991
S2_DS03_L08_PP_1	Fluid Pressure, absolute	PAA-23 SX (Keller)	Solexperts	Amberg	238	-5986	-6748
S2_DS03_L08_RH_1	Relative Humidity	SHT85 V1 (RH) (Amberg)	Amberg	Amberg	212	-6446	-6761
S2_DS03_L08_TT_1	Temperature	SHT85 V1 (T) (Amberg)	Amberg	Amberg	212	-6446	-6761
S2_DS03_L10_SA_1	Stress axial	E 20 AU 100A (Gloetzl)	Gloetzl	ISU	-46	-6108	-6565
S2_DS04_L02_PP_1	Fluid Pressure, absolute	PAA-23 SX (Keller)	Solexperts	Amberg	-288	-6466	-6108
S2_DS04_L02_RH_1	Relative Humidity	SHT85 V1 (RH) (Amberg)	Amberg	Amberg	-251	-6004	-6129
S2_DS04_L02_TT_1	Temperature	SHT85 V1 (T) (Amberg)	Amberg	Amberg	-251	-6004	-6129
S2_DS04_L05_SR_1	Stress radial	E 10/20 AU 100A (Gloetzl)	Gloetzl	ISU	-599	-6212	-5873
S2_DS04_L08_PP_1	Fluid Pressure, absolute	PAA-23 SX (Keller)	Solexperts	Amberg	239	-6011	-5658
S2_DS04_L08_RH_1	Relative Humidity	SHT85 V1 (RH) (Amberg)	Amberg	Amberg	246	-6448	-5657
S2_DS04_L08_TT_1	Temperature	SHT85 V1 (T) (Amberg)	Amberg	Amberg	246	-6448	-5657
S2_DS04_L10_SA_1	Stress axial	E 20 AU 100A (Gloetzl)	Gloetzl	ISU	-33	-6108	-5468

Tab. A. 11 ES and interface ES/rock sensors Shaft 2

Sensor name	Parameter	Sensor model	Data acquisition	Organization	x [mm]	y [mm]	z [mm]
S2_ES01_ES05_WC_V1	ARDP Integral	TAUPE cable sensor (KIT/ISU)	TAUPE	ISU	-55	-6287	-5334
S2_ES01_ES05_WC_V2	ARDP Integral	TAUPE cable sensor (KIT/ISU)	TAUPE	ISU	-352	-6508	-5325
S2_ES01_ES05_WC_V2i	ARDP Integral	TAUPE cable sensor (KIT/ISU)	TAUPE	ISU	-447	-6610	-5170
S2_ES01_ES05_WC_V3	ARDP Integral	TAUPE cable sensor (KIT/ISU)	TAUPE	ISU	299	-5905	-5321
S2_ES01_ES05_WC_V3i	ARDP Integral	TAUPE cable sensor (KIT/ISU)	TAUPE	ISU	416	-5846	-5179
S2_ES01_ES05_WC_V4	ARDP Integral	TAUPE cable sensor (KIT/ISU)	TAUPE	ISU	336	-6501	-5322
S2_ES01_ES05_WC_V4i	ARDP Integral	TAUPE cable sensor (KIT/ISU)	TAUPE	ISU	332	-6667	-5187
S2_ES01_ES05_WC_V5	ARDP Integral	TAUPE cable sensor (KIT/ISU)	TAUPE	ISU	-310	-5896	-5328
S2_ES01_ES05_WC_V5i	ARDP Integral	TAUPE cable sensor (KIT/ISU)	TAUPE	ISU	-457	-5864	-5184
S2_ES01_L01_PP_1	Fluid Pressure, absolute	PAA-23 SX (Keller)	Solexperts	Amberg	218	-5975	-9709
S2_ES01_L01_PP_2	Fluid Pressure, absolute	PAA-23 SX (Keller)	Solexperts	Amberg	-212	-6468	-9720
S2_ES02_L01_PP_1	Fluid Pressure, absolute	PAA-23 SX (Keller)	Solexperts	Amberg	-308	-6464	-8620
S2_ES02_L01_PP_2	Fluid Pressure, absolute	PAA-23 SX (Keller)	Solexperts	Amberg	261	-5933	-8622
S2_ES02_L01_WC_H1	ARDP Integral	TAUPE cable sensor (KIT/ISU)	TAUPE	ISU	444	-6202	-8614
S2_ES03_L01_PP_1	Fluid Pressure, absolute	PAA-23 SX (Keller)	Solexperts	Amberg	262	-5968	-7512
S2_ES03_L01_PP_2	Fluid Pressure, absolute	PAA-23 SX (Keller)	Solexperts	Amberg	-276	-6470	-7517
S2_ES03_L01_RH_WL_1	Relative Humidity	SHT85 V1 (RH) (Amberg)	Wireless	Amberg	-275	-5972	-7518
S2_ES03_L01_SA_WL_1r	Raw, Stress axial	CP-02-TO-10-C (Earth Systems)	Wireless	Amberg	-36	-6035	-7514
S2_ES03_L01_TT_WL_1	Temperature	SHT85 V1 (T) (Amberg)	Wireless	Amberg	-275	-5972	-7518
S2_ES03_L01_WC_H2	ARDP Integral	TAUPE cable sensor (KIT/ISU)	TAUPE	ISU	465	-6148	-7512
S2_ES04_L01_PP_1	Fluid Pressure, absolute	PAA-23 SX (Keller)	Solexperts	Amberg	-263	-6477	-6420
S2_ES04_L01_PP_2	Fluid Pressure, absolute	PAA-23 SX (Keller)	Solexperts	Amberg	277	-5962	-6427
S2_ES04_L01_WC_H3	ARDP Integral	TAUPE cable sensor (KIT/ISU)	TAUPE	ISU	505	-6187	-6406
S2_ES05_L01_PP_1	Fluid Pressure, absolute	PAA-23 SX (Keller)	Solexperts	Amberg	-283	-6471	-5329
S2_ES05_L01_PP_2	Fluid Pressure, absolute	PAA-23 SX (Keller)	Solexperts	Amberg	254	-5950	-5341
S2_ES05_L01_WC_H4	ARDP Integral	TAUPE cable sensor (KIT/ISU)	TAUPE	ISU	466	-6199	-5310

Tab. A. 12 Hydration system sensors Shaft 2

Sensor name	Parameter	Sensor model	Data acquisition	Organization	x [mm]	y [mm]	z [mm]
S2_HS_HPT_FF_1	Fluid Flow	Virtual (OASIS)	OASIS	OASIS			
S2_HS_HPT_Fill_OnOff	0=On, 1=Off		Amberg	Amberg			
S2_HS_HPT_PF_1_rel	Fluid Pressure, relative	WIKA S-20 (Wika)	Solexperts	Solexperts			
S2_HS_HPT_Valve_5	0=Open, 1=Closed		Amberg	Amberg			
S2_HS_HPT_VL_1	Volume	Calculated sensor	OASIS	OASIS	2700	-12000	1600
S2_HS_HPT_WS_1	Weight	HY10.32.HRP.H.M2.1 (Radwag)	Amberg	Amberg			
S2_HS_INL_GP_1	Gas Pressure, absolute	Calculated sensor	OASIS	OASIS			
S2_HS_INL_GP_1_rel	Gas Pressure, relative	WIKA S-20 (Wika)	Solexperts	Amberg			
S2_HS_LPT2_FF_1	Fluid Flow	Virtual (OASIS)	OASIS	OASIS			
S2_HS_LPT2_Fill_OnOff	0=On, 1=Off		Amberg	Amberg			
S2_HS_LPT2_PF_1_rel	Fluid Pressure, relative	WIKA S-20 (Wika)	Solexperts	Solexperts			
S2_HS_LPT2_Valve_3	0=Open, 1=Closed		Amberg	Amberg			
S2_HS_LPT2_VL_1	Volume	Calculated sensor	OASIS	OASIS	2600	-12000	1600
S2_HS_LPT2_WS_1	Weight	Defender 5000, D52XW150RQDX2					
S2_HS_LPT3_FF_1	Fluid Flow	Virtual (OASIS)	OASIS	OASIS			
S2_HS_LPT3_Fill_OnOff	0=On, 1=Off		Amberg	Amberg			
S2_HS_LPT3_PF_1_rel	Fluid Pressure, relative	WIKA S-20 (Wika)	Solexperts	Solexperts			
S2_HS_LPT3_Valve_13	0=Open, 1=Closed		Amberg	Amberg			
S2_HS_LPT3_VL_1	Volume	Calculated sensor	OASIS	OASIS	2800	-12000	1600
S2_HS_LPT3_WS_1	Weight	Defender 5000, D52XW150RQDX2					
S2_PC01_TT_1	Temperature	T-Type Thermocou-ple (Termya)	Solexperts	Amberg	-30	-6210	-9943
S2_PC01_TT_2	Temperature	T-Type Thermocou-ple (Termya)	Solexperts	Amberg	30	-6210	-9943

B Methods

B.1 Sample preparation

The jaw crusher (Fig. B. 1) was used at the smallest distance of both jaws to crack the samples of HTV-8 to < 2 mm prior to grinding.

Fig. B. 1 Jaw crusher at AGW, KIT

B.2 X-ray diffraction analysis

B.2.1 Qualitative phase analysis

Due to structural similarity, differentiating between dioctahedral illite and muscovite is difficult, and thus muscovite was used for modelling of pXRD traces which contain > 2 µm particles, as illite is typically considered < 2 µm. Primary reflections from dolomite and ankerite overlap in pXRD due to structural and compositional similarity. Thus, for more samples a single structure file corresponding to ankerite with relatively high iron content was used for modelling dolomite/ankerite reflections, as the main reflection from this structure file corresponding most closely with that of the pXRD. Shifts in peak positions from ideal values may indicate non-stoichiometric composition, and the presence of a separate dolomite phase cannot be ruled out. Furthermore, a donbassite structure file (di-di endmember) was used to model chlorite reflections, however due to low chlorite

abundance it was impossible to distinguish between this and other end-members and the choice was made on the basis of the d_{060} reflection.

B.2.2 Quantitative phase analysis

Rietveld software Profex (Döbelin and Kleeberg, 2015) was used for quantitative analysis.

B.3 X-ray fluorescence analysis (XRF)

XRF analysis was either performed as described in /EMM 19/ or as follows. The major elements were quantified from the raw materials by X-ray fluorescence analysis (XRF) (Bruker S8 Tiger, Karlsruhe, Germany) equipped with a rhodium X-ray tube (1 kW) using powder samples (ground < 750 µm, dried at 110 °C) fused with $Li_2B_4O_7$ (mixing ratio 1:9) in a Fluxana melting unit. The loss on ignition is determined by weighing out the fused sample disc.

B.4 Loss on ignition (LOI)

The LOI was either determined prior to XRF analyses or as follows.
The LOI is determined in accordance with /DIN 02/. 5-10 g of a sample are dried at 110 °C in glazed porcelain crucibles (V = 45 ml, d = 50 mm, h = 40 mm; Haldenwanger Waldkraiburg, VWR Darmstadt, model-nr. 459-0205). After cooling at laboratory conditions to room temperature, the weight before firing is determined to three decimal places using a laboratory balance (Kern PLS, 2100-2). The samples are sintered in the laboratory furnace (N20/H, Nabertherm, Lilienthal, Germany) at 1050 °C and 30 min holding time under air atmosphere. The weight after firing is determined, also to three decimal places, after cooling under laboratory conditions to room temperature.

$$LOI = \frac{(m_d - m_i) * 100}{m_d}$$

LOI [%] Loss on ignition
m_d [g] mass of the sample after drying
m_i [g] mass of the sample after ignition

B.5 C/S Analysis

The Carbon / Sulfur content is determined using the SSKG Test instruction “MPA 8.1.6-02” using the Eltra CS530 Determinator. Duplicate measurements are performed for each sample. After calibrating with a standard sample, 0.2 g of a sample, which were dried previously at 110 °C, are measured by weighing out their mass before and after ignition at 1.350 °C while oxygen is supplied at a pressure of 2 - 4 bar. The signal determination takes place in the IR measuring cells, where the intensity of the IR radiation decreases depending on the concentration of CO_2/SO_2, following the Beer-Lambert law. The integral below the curve is proportional to the concentration of the oxides and thus to the quantity of the respective elements.

B.6 Cation exchange capacity (CEC) measurement and analysis of exchangeable cations

CEC measurement by Cu-Trien method and analysis of exchangeable cations from the supernatant was either performed as described in /EMM 19/ or as follows.

CEC of raw materials for DS was measured according to SSKG test instruction (Prüfanweisung Kationenaustauschkapazität Cu-KAK). The measurement is generally carried out as a double determination on samples which were dried at 110 °C. Depending on the expected CEC, a corresponding sample amount is weighed into a 250 ml PE-bottle:

- 1 g for kaolinitic-illitic clays
- 0.5 g for tuffs, bentonitic tuffs etc.
- 0.2 g for bentonites.

Then, 40 ml of deionized water and 20 ml of a copper-(II)-triethylenetetramine (Cu-trien) stock solution of 0.01 mol/l are added. The dispersions are shaken for 2 h at level 14 in an overhead shaker (Reax 20, Heidolph Instruments GmbH & Co. KG, Schwabach, Germany) and then centrifuged at 5000 rpm for 30 min (Megafuge 16, Thermo Fisher Scientific, Karlsruhe, Germany). Subsequently, the absorbance of the supernatants at a wavelength (λ) of 578 nm is determined by a UV-Vis spectrophotometer (Spectroquant Prove100, Fa. Merck, Germany). The concentrations of Cu-trien in the supernatants are determined from a calibration curve which is measured for each set of measurements and CEC is calculated /EMM 19/.

B.6.1 Influence of drying temperature on the CEC

Samples of HTV were dried at 200 °C to determine the water content. These samples were used for the measurement of the CEC as they were easier to ship and store compared to the samples with high water content after hydration.

CEC measurements were performed on heated and unheated samples to determine the extent of the CEC decrease. Samples were cooled in a desiccator for 12-24 h or at the benchtop. For Calcigel samples, a decrease of 5-7 cmol(+) kg^{-1} was observed, with the higher decrease observed for BGM. The decrease in CEC was higher for Securisol MHP1(70/30) than for Calcigel. CEC decreased by 12 cmol(+) kg^{-1} for pillows and 13 cmol(+) kg^{-1} for granular material. The CEC of Securisol UHP decrease of up to 10-12 cmol(+) kg^{-1}. The decrease of Securisol MHP1(70/30) was different for the batch used in HTV-8 and HTV-9/Shaft 2. While the decrease was low for the first batch it was 12-14 cmol(+) kg^{-1} for the second batch. (Tab. B. 1). Cooling on the benchtop with a bag changes the water content by 1-3 % and there is a small effect on CEC (approx. 1 cmol(+) kg^{-1}).

Tab. B. 1 Impact of heating on CEC of DS material

Batch	**Sample**	**CEC [cmol(+) kg^{-1}]**		
		Unheated	Heated 200 °C*	Heated 200 °C#
HTV-6	Securisol UHP pillow	96	86	87
	Securisol UHP BGM	96	84	84
HTV-7	Calcigel pillow	68	66	66
	Calcigel BGM	69	64	62
HTV-8	Securisol MHP1 (70/30) pillow	64	60	60
	Securisol MHP1 (70/30) BGM	62	60	61
HTV-9	Calcigel pillow	60	55	
	Calcigel BGM	60	53	
	Securisol MHP1 (70/30) pillow	60	48	
	Securisol MHP1 (70/30) BGM	61	47	

*) cooled in a desiccator
#) cooled at the benchtop

B.7 Ion content of fluids

Cation content of fluids was measured by inductively coupled plasma optical emission spectroscopy (ICP-OES) and anion content of fluids was measured by ion chromatography (IC). Pearson water samples were diluted at 1:100 and 4M NaCl samples at 1:500 for both ICP-OES and IC measurements. No dilutions of supernatants from CEC and LF measurements for ICP-OES or IC have been performed.

Acidification for ICP-OES measurements was performed with 0.25 mL 1M HNO3 and 9.75 mL of sample.

Anion content (Cl^-, SO_4^{2-}) was determined by ion chromatography (Dionex Aquion (Thermo Fisher Scientific GmbH, Karlsruhe, Germany), equipped with IonPac™ AG23 RFIC™ and AS23 RFIC™ guard and analytical columns and a Dionex AERS 500 Carbonate 4 mm suppressor using a sodium carbonate/bicarbonate (4.5/0.8 mM) solution as the eluent and using a Dionex AS-DV Autosampler with an injection volume of 25 µL.

B.8 Water content (w) and moisture (w_m)

Water content and moisture are determined at small samples (100 mg to 200 g) either as described in /EMM 19/ or according to DIN 51202 or at large samples as follows. The water content is calculated with respect to dry mass of the sample after heating while moisture is calculated in relation to the initial mass of the sample /EMM 19/.

500-1000 g of a sample (raw material) are heated at 110 °C and at 200 °C for 24 h in metal bowls (diameter 24 cm, height 8 cm, retail trade). Heating to 200 °C is necessary to dehydrate swellable clay minerals /EMM 18/ in bentonites. For heating either a Thermo UT 6760 (Heraeus, Hanau, Germany) or a Heratherm OMH 100 (Thermo Scientific, Karlsruhe, Germany) were used.

B.9 On-site moisture measurement during pillow production

The moisture of the pillows was measured during pillow production. Three pillows were crushed and measured on an infrared balance (VWR MBT 160) after heating at 110 °C.

B.10 Density / Dry density

The bulk density of bentonite pillows is measured using the SSKG test instruction “MPA 8.1.6-13” for formed bodies (pillows), based on the instructions of IBECO for the measurement. First the pycnometer, a 500 ml measuring cylinder (IBECO, Germany) with a glass lid, is calibrated with water. Afterwards, the empty cylinder is filled to about 1/3 with pillows of initial water content and then filled with water (20-25 °C). The weight of the cylinder with pillows and glass lid before and after the filling with water is determined and the mass of filled-in water in the cylinder without pelltes and also the mass of filled-in water in the cylinder containing pillows of initial water content is calculated from these weights. The density and the dry density are calculated using these results and the measured moisture of the samples (see above).

$$\rho_b = \frac{m_{pw}}{m_{H2O,Pyk} - m_{H2O,Pyk+pw}}$$

$$\rho_d = \rho_w * (1 - m_{mpw})$$

ρ_b [g/cm³]: bulk density
ρ_d [g/cm³]: dry density
m_{pw} [g]: mass of the pillows without drying
m_{H2OPyk} [g]: mass of filled-in water in the cylinder without pillows
$m_{H20Pyk+pw}$ [g]: mass of filled-in water in the cylinder containing wet pillows
m_{mpw} [g]: mass of water in wet pillows

B.11 Bulk density of binary mixtures

Pillows in a layer of 5 cm were placed in a three-liter glass beaker. BGM was sprinkled on the layer. Afterwards, the beaker was lightly pushed several times onto the work bench so that the binary mixture was compacted. BGM was then added once more to fill any open pores. Finally, the layer was recompacted with a squared timber, similar to the procedure for HTV. This procedure was repeated until the two-liter mark was reached in the beaker (Fig. B. 2).

Fig. B. 2 Binary mixture of Secursol UHP (symbolic image)

B.12 Density determination by immersion weighing method

The density of compact bentonite samples can be determined using the immersion weighing method. The method is based on weighing the sample in a liquid of known density (Fig. B. 4). For the density determination of bentonite samples, ELBESIL B10 silicone oil was used as the liquid in the measurements.

$$\rho_l = \frac{\rho_R}{\gamma \cdot (T - T_R) + 1}$$

$$\rho = \frac{m}{V} = \frac{m_1}{(m_1 - m_2)/\rho_l}$$

ρ_l [g/cm³]: oil density at T

ρ_r [g/cm³]: Reference density, oil density at 25 °C (0.9323 g/cm³)

γ [K^{-1}]: coefficient of volume expansion of the oil ($1.00822*10^{-3}$)

T [°C or K]: temperature

T_R [°C or K] Reference temperature (25 °C)

m_1 [g]: mass of sample in air

m_2 [g]: mass of sample in oil

m_{mpw} [g]: mass of water in wet pillows

For HTV-8, the density of the silicone oil was newly determined to be 0.9362 g/cm³ at 21.6 °C. Thus, with an unchanged volumetric expansion coefficient, the comparative value for the density of 0.9328 g/cm³ at 25.0 °C is slightly above the value used for HTV-7.

The mass measured in the immersed state (m_2) is the difference mass between the mass of the sample and the mass of the displaced liquid volume. The mass of the sample (m_1) is previously determined by weighing in air (Fig. B. 3). The mass of the displaced liquid is calculated by taking the difference between the weight values m_1 and m_2. The volume of the displaced liquid corresponds to the volume of the sample (without the liquid-accessible pores of the sample).

Fig. B. 3 Weighing M1 of a bentonite sample for density determination in air

Fig. B. 4 Weighing M2 of a bentonite sample for density determination in silicone oil ELBESIL B10

During the immersion weighing, a wire basket was used to hold the sample in the oil (Fig. B. 4), the mass of which was already zeroed in the immersed state before the sample

was placed on it. Depending on how open-pored a bentonite sample was, the value m_2 increased more or less over time due to penetration of oil into pores of the sample. In the measurements with HTV-8, the value m_2 was always read about 30 s after immersion of the sample in the oil.

B.13 Particle size distribution of BGM by sieving

400 g of the BGM were sieved air dry with eight screen decks, starting with 1.4 mm and ending with 0.063 mm (Retsch AS 200 basic.)

B.14 Mass gain of air-dry bentonite at elevated relative humidity

500 g air dry bentonite pillows or BGM were stored in a climate cabinet (Memmert HPP260) at 85 % relative humidity and 20 °C for 16 d. Mass gain was determined relative to the starting mass.

B.15 Swelling pressure

For the swelling pressure tests new cells are developed at IfG (set 2). The bentonite is installed in a metal tube with a diameter of 100 mm with pistons at the end. A load cell is installed (maximal range 100 resp. 200 kN) on the upper part of the piston and the data are recorded via a Delphin® data logging system. The fluid is injected from the lower part of the cell through a sintered plate to the bentonite. The maximum injection pressure goes up to 5 bar.

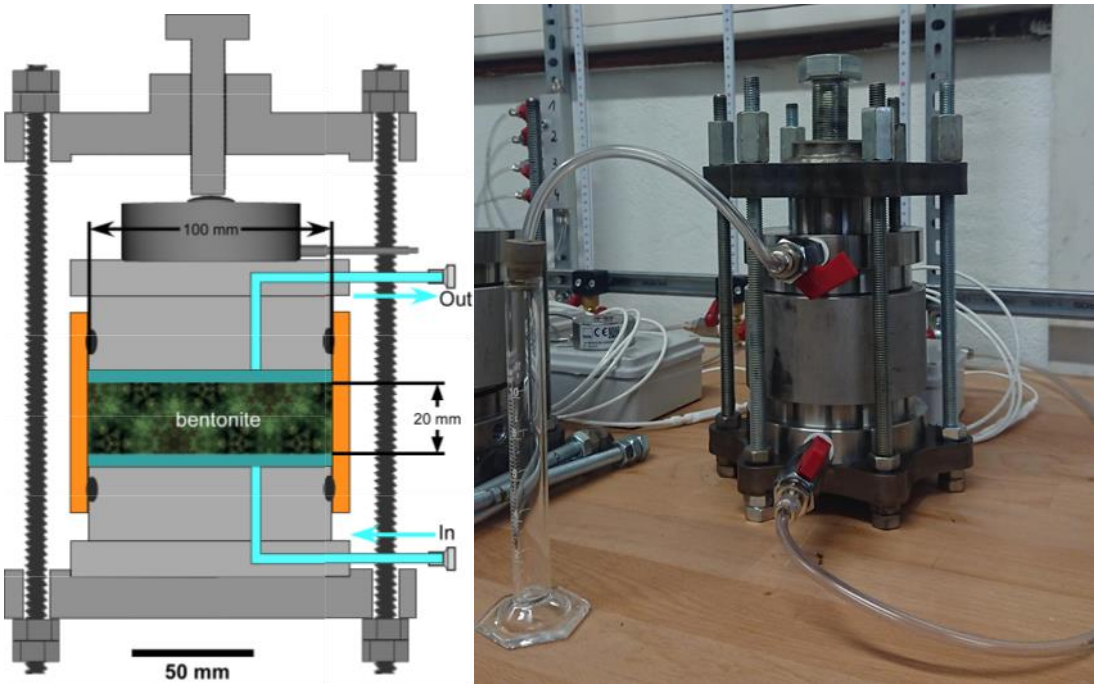

Fig. B. 5 Schematic sketch of the swelling pressure cell (left) and swelling pressure cell with installed fluid injection (bottom) and collection (top) system (right)

Swelling pressure pretests of the blended Securisol UHP have been performed with samples of a diameter of 5 cm and a height of 2 cm (set 4). As a result, the maximum grain size should not be larger than 4 mm. Each of the five materials was sieved through a 4 mm sieve. The oversize grain > 4 mm was crushed to a grain diameter of < 4 mm using a mortar and then mixed again with the first sieve pass in order to retain the original material composition. The sample mass required for the respective target installation dry density was then statically compacted in the sample ring. The sample ring with the sample was then installed in the swelling pressure cell (Fig. B. 6). The components of the swelling pressure cell are fixed in such a way that no swelling expansion of the sample takes place during saturation. During the saturation phase, the fluid (deionized water) is fed from a burette through a hose to the lower filter stone and to the sample resting on it. The pressure head in the burette was approximately 0.1 m water column (WS). The drainage on the upper filter stone was open during this test phase so that the air could escape.

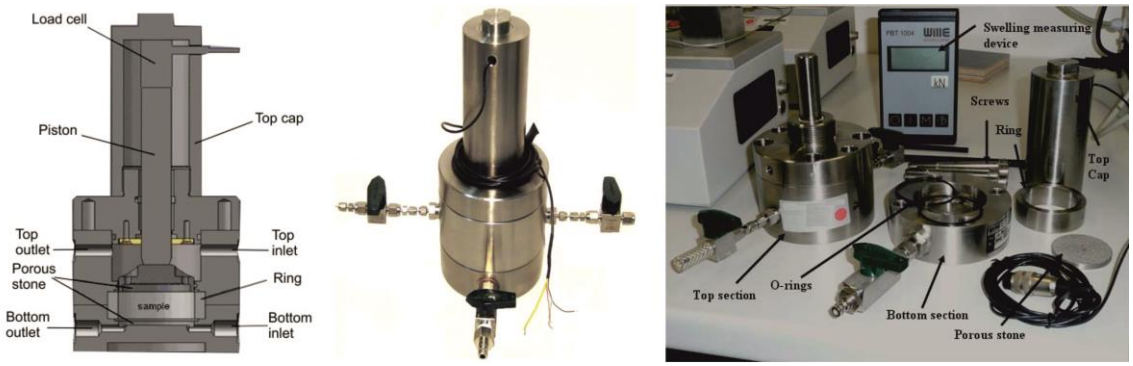

Fig. B. 6 Swelling pressure cell of set 4

B.16 Gas entry pressure

The gas entry pressure was ascertained at a confining pressure after the solution permeability tests. The measurements were carried out with dry compressed air, starting with a low inlet pressure (the target was 0.02 MPa). The test regime provides for a gradual increase in the inlet pressure until a pressure drop is recorded. The pressure was recorded using a differential pressure sensor suitable for up to 500 mbar, with a measurement uncertainty of 0.1 % full scale. This device was installed in a bypass on the upstream side, and according to the measuring range, enabled the detection of even small pressure changes. The pressure difference Δp_F is gradually increased. If no change in the pressure difference or leakage of saline solution on the outlet side is observed, the pressure difference is increased to the next higher pressure level (increment of 0.02 MPa). The length of the observation phase for each pressure level is determined by taking into account the results of the solution permeability measurement.

C Pretests

C.1 Calcigel pillow drying after compaction

Due to the fact that several percent of water had to be added to the Calcigel during production on the large-scale plant and then dried again, it was examined whether the addition of water and the re-drying had an influence on the swelling behavior of the Calcigel pillows. In order to identify possible influences of drying the compacted pillows on the swelling kinetics, additional laboratory tests were carried out. Pillows were either dried at ambient conditions (air drying) or at 110 °C in a laboratory oven.

The dried pillows were placed in one-liter measuring cylinders with holes above the base. These cylinders were placed in a wider beaker, which in turn could be filled with water to achieve hydration of the cylinders from the bottom with the holes. Swelling was monitored up to 24 h (Fig. C. 1). No clear differences were detected in the dissolving speed of the pillows and in the speed and degree of swelling. After 24 h the significant increase of the swollen pillows can be stated.

Experimental setup without water

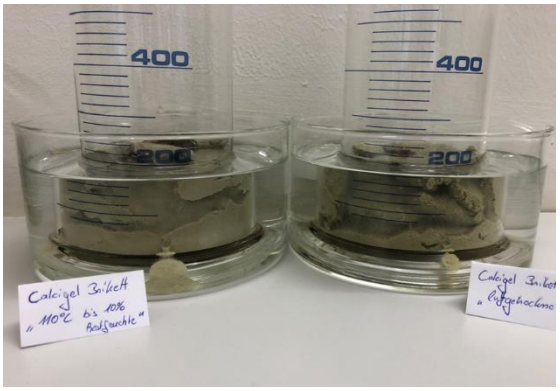

1 min after adding water

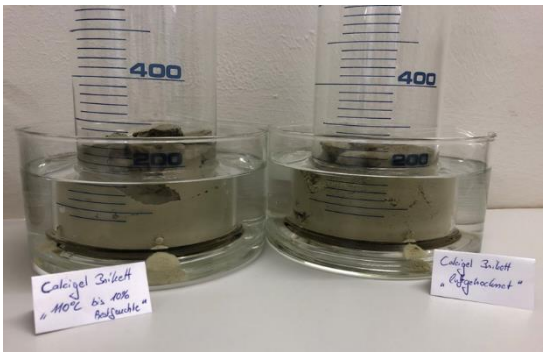

10 min of swelling

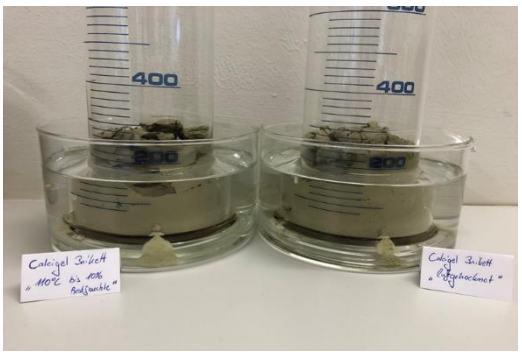

1 h of swelling

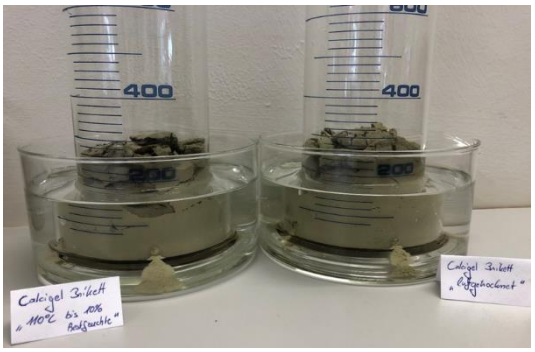

2 h of swelling

24 h of swelling

Fig. C. 1 Swelling of Calcigel pillows after drying at 110 °C to 10 % moisture (left of each picture) and air drying (right of each picture)

C.2 Blending of Securisol UHP

Two plastic clays G1621 and G1625 from the Meudt/Westerwald mine were tested for blending Securisol UHP to reduce the smectite content and thus the swelling pressure

for the use in the in situ experiment at MTRL. The CEC of G1625 was 13 cmol(+)/kg. Both clays in a blend with 70 mass% of Securisol UHP were suitable with respect to swelling pressure (Fig. C. 2). Finally, G1621 was chosen due to the lower iron content (Tab. 5.11; Tab. C. 1).

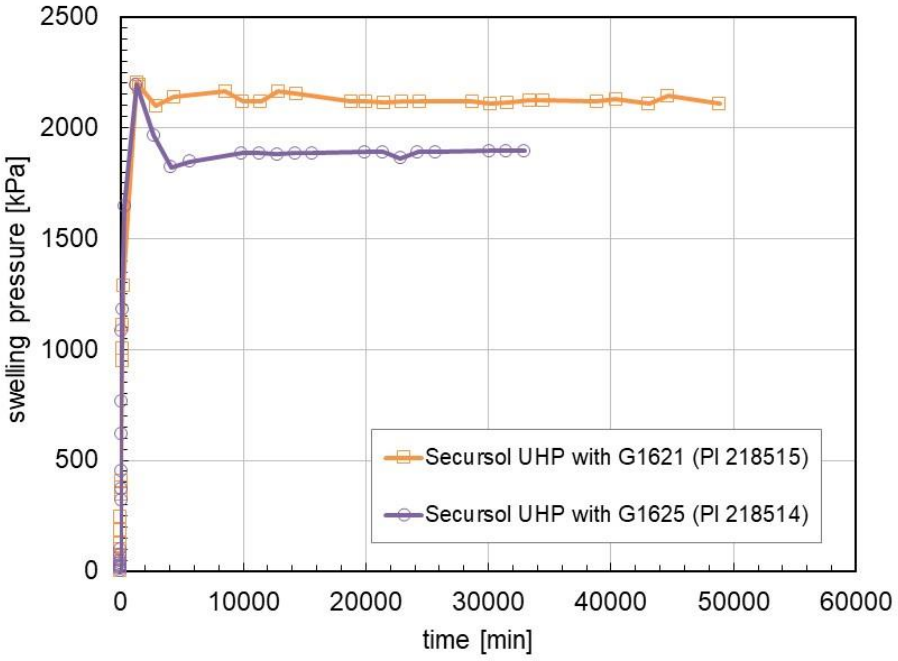

Fig. C. 2 Swelling pressure of blends (installation dry density 1.55 g/cm³, installation water content (105 °C) about 9 %) containing 70 mass% Securisol UHP and 30 mass% plastic clay

Tab. C. 1 Chemical composition of plastic clay G1625

SiO_2	TiO_2	Al_2O_3	Fe_2O_3	CaO	MgO	K_2O	Na_2O	C	S
61.37	1.26	23.81	9.46	0.33	0.65	2.89	0.23	< 0.005	< 0.005

D Opalinus clay

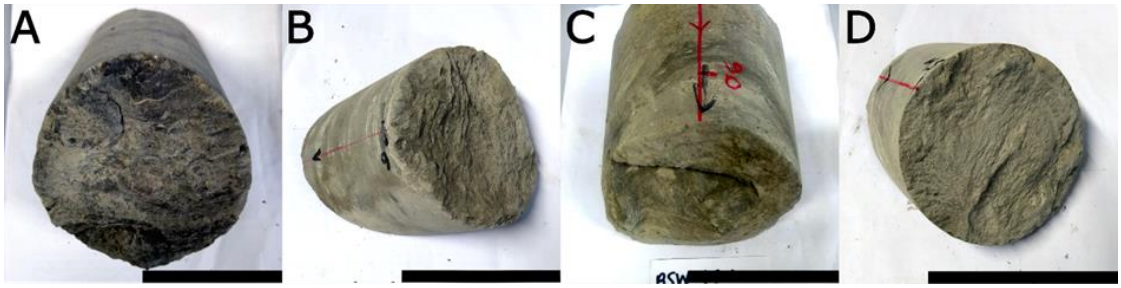

Fig. D. 1 OPA core pieces before characterization BSW-B20 A) 3-3.1 m, B) 6- 6.1 m, C) 8.9-9 m, and D) 11.4-11.5 m

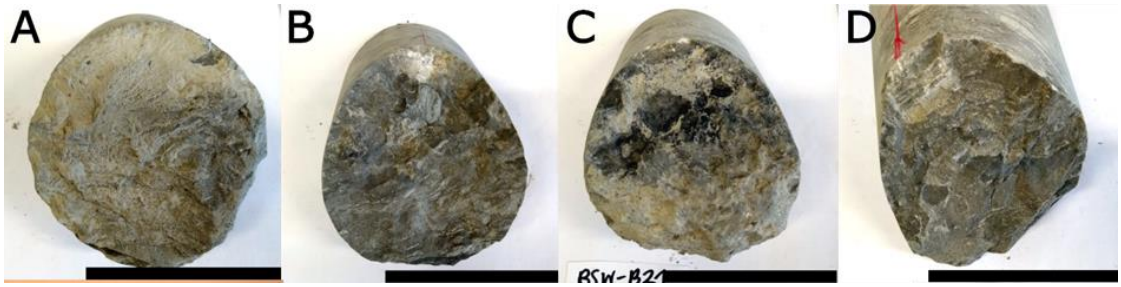

Fig. D. 2 OPA core pieces before characterization BSW-B21 A) 3-3.1 m, B) 5.9-6 m, C) 9-9.1 m, and D) 11.6-11.7 m

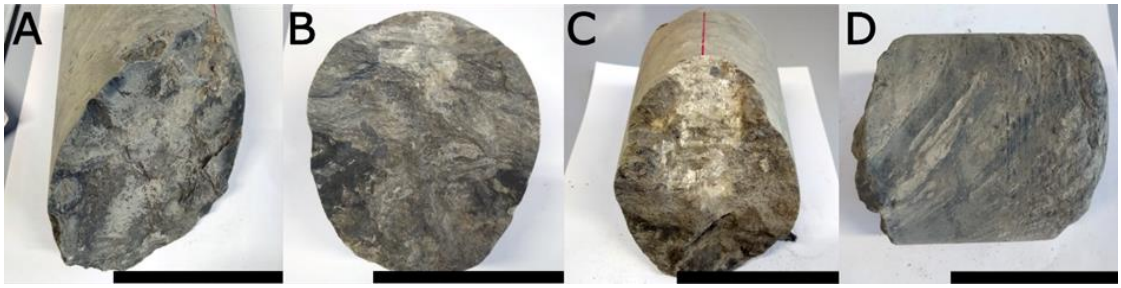

Fig. D. 3 OPA core pieces before characterization BSW-B22 A) 2.9-3 m, B) 5.9-6 m, C) 8.9-9 m, and D) 10.9-11 m

E Bentonite pillows, Granular material and binary mixtures

E.1 Calcigel pillows and BGM produced for HTV-7, dried at SSKG

Tab. E. 1 Moisture, water content and density of Calcigel pillows (HTV-7)

Big Bag	1	2	3	4	5	6	7	8	average	V1.4*
	Moisture w_m [%]									
110 °C	10.66	10.18	10.01	10.18	10.07	9.81	10.03	10.52	10.18	9.12
200 °C	11.79	11.73	11.43	11.63	11.42	11.34	11.51	12.05	11.61	11.09
	Water Content (calculated) w [%]									
110 °C	11.93	11.33	11.12	11.33	11.20	10.88	11.15	11.76	11.34	10.04
200 °C	13.37	13.29	12.91	13.16	12.89	12.79	13.01	13.70	13.14	12.47
	Density, [g/cm³]									
Bulk, measured	2.12	2.1	2.15	2.12	2.15	2.14	2.12	2.13	2.13	2.02
Dry, calc. (110 °C)	1.89	1.89	1.93	1.90	1.93	1.93	1.91	1.91	1.91	1.84
Dry, calc. (200 °C)	1.87	1.85	1.90	1.87	1.90	1.90	1.88	1.87	1.88	1.80

* compacted during pretests with lower mositure

Tab. E. 2 Moisture and water content of Calcigel BGM (HTV-7) produced of Big Bag 7

Big Bag	3	1	2	4	average
	Moisture w_m [%]				
110 °C	9.09	9.5	8.71	9.68	9.25
200 °C	10.47	10.78	10.2	11.09	10.64
	Water Content (calculated) w [%]				
110 °C	10.00	10.50	9.54	10.72	10.18
200 °C	11.69	12.08	11.36	12.47	11.91

Tab. E. 3 Moisture, water content and density of Calcigel binary mixtures (HTV-7)

Big Bag pillows	**2**	**2**	**2**	**2**
Big Bag BGM	3	1	2	4
ratio	50/50	50/50	50/50	50/50
	Moisture w_m [%]			
Calculated (110 °C)	9.64	9.84	9.45	9.93
Calculated (200 °C)	11.10	11.25	10.97	11.41
	Water Content w [%]			
Calculated (110 °C)	10.67	10.91	10.44	11.02
Calculated (200 °C)	12.49	12.25	12.32	12.38
	Density [g/cm³]			
Bulk, measured	1.741	1.736	1.755	1.754
Dry, calc. (110 °C)	1.573	1.565	1.590	1.580
Dry, calc. (200 °C)	1.550	1.541	1.571	1.554

Tab. E. 4 Moisture, water content and densities for Calcigel Pillows and BGM as delivered and received (HTV-7 and compaction test at Amberg/Toledo)

		Moisture w_m [%]		**Water content w [%]**		**density [g/cm³]**		
						Bulk, meas.	Dry, calc.	Dry, calc.
		110 °C	200° C	110 °C	200° C		110 °C	200° C
Calcigel powder (as delivered)		10.7	12.0	12.0	13.6			
BB1, pillows	SSKG	13.7	14.8	15.9	17.4	2.11	1.82	1.80
BB2, pillows	SSKG	12.3	13.8	14.0	16.0	2.10	1.84	1.81
BB3, pillows prior to crushing	SSKG	6.8	9.3	7.3	10.3	2.08	1.94	1.89
BB3 BGM	SSKG	8.0	10.1	8.7	11.2			
		105 °C	200° C	105 °C	200° C			
BB1, pillows	TUBAF	13.7	14.8	15.9	17.4			
BB3, BGM	TUBAF	9.0	10.2	9.9	11.3			
BB2, pillows	Amberg	11.5	13.5	13.0	15.6			
BB3, BGM	Amberg	7.7	10.5	8.3	11.7			

E.2 Securosol MHP1 (70/30) pillows and BGM, HTV-8

Tab. E. 5 Moisture, water content and density of pillows during production

Big Bag	**1**	**2**	**3**	**4**
	Moisture w_m [%]			
110 °C	n.d.	n.d.	11.2	11.2
200 °C	n.d.	n.d.	n.d.	n.d.
	Water Content (calculated) w [%]			
110 °C	n.d.	n.d.	12.61	12.61
200 °C	n.d.	n.d.	n.d.	n.d.
	Density, [g/cm³]			
Bulk, measured	n.d.	n.d.	2.18	2.16
Dry, calc. (110 °C)	n.d.	n.d.	1.94	1.93
Dry, calc. (200 °C)	n.d.	n.d.	n.d.	n.d.

Tab. E. 6 Moisture, water content and density of binary mixtures during pretests 1) trickled in, 2) compacted by vibration

Big Bag pillows	**3**	**3**	**4**	**4**
BigBag BGM	Mixture BB1/BB2 (0 -1.25 mm)			
ratio	70/30[1]	65/35[2]	72/28[1]	66/34[2]
	Moisture w_m [%]			
Calculated (110 °C)	10.56	11.50	10.43	11.30
Calculated (200 °C)	n.d.	n.d.	n.d.	n.d.
	Water Content w [%]			
Calculated (110 °C)	11.81	13.0	11.64	12.74
Calculated (200 °C)	n.d.	n.d.	n.d.	n.d.
	Density [g/cm³]			
Bulk, measured	1.61	1.72	1.63	1.77
Dry, calc. (110 °C)	1.44	1.54	1.46	1.57
Dry, calc. (200 °C)	n.d.	n.d.	n.d.	n.d.

E.3 Calcigel pillows (Shaft 1)

Tab. E. 7 Moisture, water content and density of Calcigel pillows (Shaft 1) after production

Big Bag	Sample	Moisture [%]		Water content [%]		Density [g/cm³]		
		110 °C	200 °C	110 °C	200 °C	bulk	Dry (110 °C)	Dry (200 °C)
1		10.52	11.86	11.76	13.46	2.02	1.81	1.78
	2					2.21	1.98	1.95
2	1	16.97	17.96	20.44	21.89	2.05	1.70	1.68
	2					2.09	1.74	1.71
	3					2.14	1.78	1.76
3	1	17.65	18.65	21.43	22.93	2.06	1.69	1.68
	2					2.05	1.69	1.67
	3					2.04	1.68	1.66
4	1	18.35	19.37	22.47	24.02	2.08	1.70	1.68
	2					2.04	1.67	1.64
	3					2.04	1.66	1.64
5	1	18.78	19.71	23.12	24.55	2.06	1.68	1.65
	2					2.08	1.69	1.67
	3					2.07	1.68	1.66
6	1	16.50	17.76	19.76	21.6	2.10	1.76	1.73
	2					2.07	1.73	1.70
	3					2.13	1.78	1.75
7	1	18.37	19.49	22.5	24.21	1.97	1.61	1.59
	2					2.07	1.69	1.67
	3					2.00	1.63	1.61
8	1	18.01	19.14	21.97	23.67	2.05	1.68	1.66
	2					2.04	1.67	1.65
	3					2.09	1.72	1.69
9	1	17.33	18.6	20.96	22.85	2.07	1.71	1.68
	2					2.06	1.70	1.68
	3					2.05	1.69	1.67
10	1	17.44	18.32	21.12	22.43	2.06	1.70	1.68
	2					1.93	1.60	1.58
	3					1.98	1.64	1.62
11	1	17.52	18.42	21.24	22.58	2.02	1.67	1.65
	2					2.03	1.67	1.66
	3					2.02	1.66	1.65
12	1	17.06	17.93	20.57	21.85	2.00	1.66	1.64
	2					2.03	1.68	1.67
	3					1.99	1.65	1.63
13	1	17.13	18.04	20.67	22.01	2.08	1.72	1.70
	2					2.07	1.72	1.70
	3					2.08	1.72	1.70
Average		17.05	18.10	20.62	22.16	2.05	1.70	1.68

Tab. E. 8 Moisture and water content of the delivered Calcigel Pillows (Batch Shaft1)

	Moisture [%]		**Water content [%]**	
Big Bag	110 °C	200 °C	110 °C	200 °C
2	8.25	9.25	8.99	10.19
3	8.41	9.53	9.18	10.53
4	8.58	9.66	9.38	10.69
5	8.46	9.52	9.24	10.52
6	8.48	9.57	9.27	10.58
7	8.42	9.48	9.19	10.47
8	8.59	9.59	9.40	10.61
9	8.50	9.54	9.34	10.55
10	8.23	9.33	8.97	10.29
11	8.51	9.57	9.30	10.58
12	8.37	9.41	9.13	10.39
13	8.42	9.46	9.19	10.45
average	**8.44**	**9.49**	**9.22**	**10.49**

Tab. E. 9 Moisture, water content and density of Calcigel BGM (Shaft 1) KeiBeton pillow post-dried, crushed, (impact mill) and sieved 0-1.25mm

Big Bag	**1**	**2**	**3**	**4**	**5**	**6**	**average**
	Moisture w_m [%]						
110 °C	9.5	8.71	9.09	9.68	9.95	9.25	9.36
200 °C	10.78	10.2	10.47	11.09	11.27	11.15	10.83
	Water Content (calculated) w [%]						
110 °C	10.50	9.54	10.00	10.72	11.05	10.19	10.33
200 °C	12.08	11.36	11.69	12.47	12.70	12.55	12.14
	Density, [g/cm³]						
Bulk, measured	2.12	2.1	2.15	2.12	2.15	2.14	2.13
Dry, calc. (110 °C)	1.92	1.92	1.95	1.91	1.94	1.94	1.93
Dry, calc. (200 °C)	1.89	1.89	1.92	1.88	1.91	1.89	1.90

Tab. E. 10 Particle size distribution of Calcigel BGM (Shaft 1)

Big Bag	1	2	3	4	5	6	average
mesh size (mm)	Sieve passage (%)						
1.4	99.2	99.5	98.6	98.4	98.6	99.7	99.00
1.25	92.4	95.7	88.1	85.3	98.3	97.2	92.83
1	64.4	77.1	65.3	62.8	90.4	84.1	74.02
0.5	38.3	50.3	39.6	40.4	56.5	61.2	47.72
0.25	27.6	36.4	26.5	26.4	34.6	48.7	33.37
0.2	26.0	33.8	24.2	24.2	26.5	46.1	30.13
0.125	18.4	26.0	17.4	13.5	14.8	38.8	21.48
0.063	12.0	16.2	11.5	8.5	7.6	25.6	13.57

Tab. E. 11 Water content and moisture during installation of Calcigel (Shaft 1)

Segment	Pillows		BGM		Binary Mixture	
	105 °C	200 °C	105 °C	200 °C	105 °C	200 °C
	Water content [%]					
DS 4	11.68	13.42	10.21	12.06	11.12	13.07
DS 3	11.45	13.35	9.42	11.73	10.70	12.91
DS 2	11.58	13.32	10.00	12.19	11.36	13.13
DS 1	11.27	12.96	11.07	12.74	13.40	13.25
	Moisture [%]					
DS 4	10.46	11.83	9.26	10.76	10.01	11.56
DS 3	10.27	11.78	8.61	10.50	9.67	11.43
DS 2	10.38	11.75	9.09	10.87	10.20	11.61
DS 1	10.13	11.47	9.97	11.30	11.82	11.70

E.4 Securosol MHP1 (70/30) pillows and Calcigel pillows, HTV-9* / Shaft 2#

Tab. E. 12 Moisture, water content and density of pillows determined after production

Material	**Securosol MHP1 (70/30)**				**Calcigel**			
Big Bag	1/1#	1/2#	1/3#	1/4*	3/1#	3/2#	3/3#	3/4*
	Moisture w_m [%]							
110 °C	8.3	8.41	8.08	8.37	8.35	8.35	7.41	8.72
200 °C	9.82	9.88	9.56	9.75	9.65	9.62	8.71	10.01
	Water Content (calculated) w [%]							
110 °C	9.05	9.18	8.79	9.13	9.11	9.11	8	9.55
200 °C	10.89	10.96	10.57	10.8	10.68	10.64	9.54	11.12
	Density [g/cm³]							
Bulk, measured	2.02	2.03	2.05	2.04	2.23	2.22	2.24	2.21
Dry, calc. (110 °C)	1.85	1.86	1.88	1.87	2.04	2.03	2.08	2.02
Dry, calc. (200 °C)	1.82	1.82	1.85	1.84	2.02	2.01	2.04	1.99

Tab. E. 13 Moisture and water content of pillows determined after delivery to MTRL for Shaft 2 installation

Material	**Securosol MHP1 (70/30)**						**Calcigel**		
Big Bag	1/1	1/2	1/3	1/4*	1/5*	1/6*	3/1	3/2	3/3
	Moisture [%]								
105 °C	8.37	8.19	8.77	8.68	8.50	8.54	8.42	8.43	8.05
200 °C	10.25	10.02	10.71	10.45	10.35	10.33	10.26	10.36	9.97
	Water content [%]								
105 °C	9.13	8.92	9.61	9.50	9.29	9.34	9.19	9.21	8.76
200 °C	11.42	11.14	11.99	11.67	11.55	11.52	11.43	11.56	11.07

*) additional delivery

Tab. E. 14 Moisture and water content of BGM after production

Material	Securosol MHP1 (70/30)				Calcigel			
Big Bag	2/1#	2/2#	2/3#	2/4*	4/1#	4/2#	4/3#	4/4*
	Moisture w_m [%]							
110 °C	7.78	7.84	8.27	7.81	8.25	8.73		
200 °C	9.15	9.17	9.82	9.35	9.52	9.8		
	Water Content (calculated) w [%]							
110 °C	8.44	8.51	9.02	8.47	8.99	9.57		
200 °C	10.07	10.10	10.89	10.31	10.52	10.86		

Tab. E. 15 Moisture and water content of BGM after delivery at MTRL for Shaft2 installation

Material	Securosol MHP1 (70/30)			Calcigel		
Big Bag	2/1#	2/2#	2/3#	4/1#	4/2#	4/3#
	Moisture w_m [%]					
105 °C	7.83	7.77	8.36	8.93	8.62	8.53
200 °C	9.73	9.76	10.20	10.43	10.24	10.02
	Water Content w [%]					
105 °C	8.49	8.42	9.12	9.80	9.43	9.32
200 °C	10.78	10.82	11.36	11.65	11.41	11.14

Tab. E. 16 Moisture, water content and density of binary mixtures after production

Material	Securosol MHP1 (70/30)	Calcigel
Big Bag pillows	1/1 to 1/4	3/1 to 3/4
Big Bag BGM	2/1 to 2/4	4/1 to 4/4
ratio	66/34	67/33
	Moisture w_m [%]	
Calc. (110 °C)	8.15	8.30
Calc. (200 °C)	9.62	9.55
	Water Content w [%]	
Calc. (110 °C)	8.87	9.05
Calc. (200 °C)	10.65	10.56
	Density [g/cm³]	
Bulk, measured	1.673	1.794
Dry, calc. (110 °C)	1.536	1.646
Dry, calc. (200 °C)	1.495	1.605

E.5 Particle size distribution of BGM

Tab. E. 17 Screening residue of BGM

Experiment	HTV-6	HTV-7	HTV-8	HTV-9/ Shaft2	Shaft1	Shaft1	HTV-9/ Shaft2
Material	Securosol UHP	Calcigel	Securosol MHP1 (70/30)	Securosol MHP1 (70/30)	Calcigel	Calcigel	Calcigel
sample			BB1+BB2	BB 2/1		BB1	BB 4/4
Max (mm)	1.4			1.25			
Min (mm)	0.25			0			
mm	[%]	[%]	[%]	[%]	[%]	[%]	[%]
5.6	0			0			
4	0.06			0			0.03
2.8	0.06			0.25			0.18
2	0.06			11.33			0.21
1.4		0.51	0.29		0.51	1.01	
1.25		2.52	2.21		2.52		
1	18.77	17.13	18.96	38.35	17.13	35.84	27.50
0.5	38.55	36.73	36.21	24.32	36.71	25.33	18.68
0.25		23.90	18.12		23.9	10.73	
0.2		3.73	5.02		3.73		
0.125	40.38	8.82	9.31	20.91	8.82	8.80	16.04
<0.125	2.12			4.85	6.68		37.35
0.063		4.82	5.16			5.95	
<0.063		1.86	4.72			12.35	

Tab. E. 18 Cumulative sieve passage of BGM

Experiment	HTV-6	HTV-7	HTV-8	HTV-9/ Shaft 2	Shaft 1	Shaft 1	HTV-9/ Shaft 2
Material	Securosol UHP	Calcigel	Securosol MHP1 (70/30)	Securosol MHP1 (70/30)	Calcigel	Calcigel	Calcigel
sample			BB1+BB2	BB 2/1		BB1	BB 4/4
Max (mm)	1.4			1.25			
Min (mm)	0.25			0			
mm	[%]	[%]	[%]	[%]	[%]	[%]	[%]
5.6	100						100.00
4	99.94			100.00			99.97
2.8	99.88			99.75			99.79
2	99.82	100.00	100.00	88.42	100	100.00	99.58
1.4		99.50	99.71		99.49	98.99	
1.25		96.98	97.50		96.97		
1	81.05	79.85	78.54	50.07	79.84	63.16	72.07
0.5	42.5	43.12	42.33	25.76	43.13	37.83	53.40
0.25		19.22	24.21		19.23	27.10	
0.2		15.49	19.19		15.5		
0.125	2.12	6.67	9.88	4.85	6.68	18.30	37.35
0.063		1.86	4.72			12.35	

E.6 Suction measurements Securosol UHP and Securosol MHP1 (70/30)

Tab. E. 19 Suction measurements in compacted sample UHP (ρ_d = 1.55±0.02 g/cm^3)

Compaction P	ρ_d	w	S_r	s
[MPa]	[g/cm^3]	[%]	[%]	[MPa]
23.1	1.56	8.4	29	312.6±30.1
14.2	1.52	16.9	55	78.3±4.8
16.9	1.56	20.3	70	39.2±3.6
17.6	1.58	25.2	89	20.1±3.2
48.3	1.54	30.8	102	3.53±0.03
33.1	1.53	31.1	102	1.66±0.03

Tab. E. 20 Suction measurements in compacted sample MHP1 (70/30) (ρ_d = 1.55±0.02 g/cm^3)

Compaction P	ρ_d	w	S_r	s
[MPa]	[g/cm^3]	[%]	[%]	[MPa]
6.1	1.56	6.0	21	313.1±30.4
3.4	1.51	11.8	38	85.5±5.1
4.7	1.55	20.4	70	14.1±3.1
4.1	1.57	26.0	91	2.54±0.03
4.1	1.55	28.5	98	1.79±0.03
13.6	1.55	29.4	101	1.26±0.03

E.7 Binary mixture during installation and fluid pressure HTV experiments

HTV-7
DS1…DS4:
Calcigel
$\rho_{d,\ pillows}$ = 1.89 g/cm³

HTV-8
DS1…DS4:
Securosol MHP1 (70/30)
$\rho_{d,\ pillows}$ = 1.93 g/cm³

HTV-9

DS1, DS2:
Securosol MHP1 (70/30)
$\rho_{d,\ pillows}$ = 1.95 g/cm³

DS3, DS4:
Calcigel
$\rho_{d,\ pillows}$ = 2.05 g/cm³

Fig. E. 1 Bentonite pillows in binary mixture of DS during installation of HTV-7 to HTV-9

F Fluids

Tab. F. 1 Tab water Geldern (water company Hartefeld) May 2022

	[mg/l]	[mmol/l]
Na^+	17.30	0.75
Ca^{2+}	80.80	2.02
Mg^{2+}	15.10	0.62
K^+	4.20	0.11
Cl^-	37.90	1.07
SO_4^{2-}	105.00	1.09
NO_3^-	23.50	0.38

Tab. F. 2 Batches of Pearson water (concentrations)

	V	Na^+	Ca^{2+}	Mg^{2+}	K^+	Sr^{2+}	Fe^{3+}	Cl^-	SO_4^{2-}	HCO_3^-
	[L]	[mg/l]								
NAGRA 12-54 target		**3772**	**477**	**223**	**100**	**-**	**-**	**5672**	**2306**	**33**
HTV-6 (1)		3540	477	214	107	-	-	n.d.	n.d.	-
HTV-6 (2)		3288	437	213	113	-	-	n.d.	n.d.	-
HTV-6 gravel		2460	1130	291	52.0	-	-	6062	2113	-
MiniSandwich (1) (test 7-10)	5	3517	465	211	97.8	-	-			
MiniSandwich (2) (test 7-10)	5	5288	637	120	31.7	-	-			
Typ A3 target		**2951**	**278**	**120**	**31**	**28**	**-**	**4614**	**1102**	
Swelling pressure tests (IBEWA)		2550	223	121	38	22	-	4534	1925	
HTV-7 (1)	200	2737±12	272 ±1	123±1	28±2	-	0	4212±2	1001±1	-
HTV-7 (2)	100	2724±27	274±2	123±1	29±1	-	0	4183±9	956±1	-
HTV-7 gravel	-									
HTV-7 ES2	-	2499±11	830±7	346±2	28±2	-	30±1	5467±3	1017±2	-
HTV-8 (1)	180	2662±81	262±8	117±4	30±4	-	0	4228±3	972±1	-
HTV-8 (2)	75	2659±100	259±8	116±4	32±2	-	0	4181±2	966±6	-
HTV-8 gravel	-	2167±7	754±3	205±1	47±1	-	0	4416±5	873±1	-
HTV-8 ES1+ES2		1187±7	1655±7	407±5	18±2	-	0	5267±14	676±3	-
HTV-9 (1)	180	2746±27	277±3	127±2	30±2	-	0	4244±44	979±7	
HTV-9 (2)	89	2818±33	280±2	129±0	30±2	-	0	4267±16	996±5	
Shaft 1		2872±17	146±1	69±1	54±2	-	0	4022±2	995±1	-
MiniSandwich (test 11-14) & Swelling pressure tests 1-16 (IFG)	20	3357	289	97	38			3687	1441	
Swelling pressure tests (CIEMAT)		2946/ 3033	317/ 297	125/ 126	43/ 48	14/ 53		4890/ 4774	1124/ 1206	38/ 40

The pH varied around 7.6 for Pearson water batches.

Tab. F. 3 Batches of Pearson water (molarities)

	V	Na^+	Ca^{2+}	Mg^{2+}	K^+	Sr^{2+}	Fe^{3+}	Cl^-	SO_4^{2-}	HCO_3^-
	[L]	[mmol/l]								
NAGRA 12-54 target		**164**	**11.9**	**9.17**	**2.55**	**-**	**-**	**160**	**24**	**0.54**
HTV-6 (1)		154	11.9	8.80	2.73			n.d.	n.d.	
HTV-6 (2)		143±9	10.9±1.1	8.76±0.54	2.89±0.40			n.d.	n.d.	
HTV-6 gravel		107±5	28.2±0.1	11.95±0.01	1.33±0.15			171	22	
MiniSandwich (test 7-10) (1)	5	153	11.6	8.7	2.5					
MiniSandwich (test 7-10) (2)	5	230±2	15.9±0.2	11.37±0.04	4.06±0.00					
Typ A3 target		**128**	**6.94**	**4.94**	**0.81**	**0.32**	**-**	**130**	**11.47**	
Swelling pressure tests (IBEWA)		111	5.56	4.98	0.97	0.25	-	128	20.0	-
HTV-7 (1)	200	119±0	6.80±0.03	5.05±0.05	0.71±0.05	-	0	119±0.1	10.5±0.02	-
HTV-7 (2)	100	119±1	6.83±0.05	5.05±0.04	0.74±0.03	-	0	118±0.3	9.95±0.02	-
HTV-7 gravel	-									
HTV-7 ES2		109±0	20.7±0.1	14.2±0.1	0.73±0.05	-	0.53±0.01	154±0.1	10.6±0.02	-
HTV-8 (1)	180	116±3	6.55±0.19	4.81±0.14	0.76±0.08	-	0	119±0.1	10.1±0.01	-
HTV-8 (2)	75	116±4	6.46±0.19	4.76±0.17	0.81±0.04	-	0	118±0.1	10.1±0.06	-
HTV-8 gravel	-	94.3±0.2	18.8±0.1	8.42±0.04	1.21±0.02	-	0	125±0.2	9.09±0.01	-
HTV-8 ES1+ES2		51.6±0.2	41.3±0.1	16.8±0.2	0.42±0.03	-	0	149±0.4	7.04±0.03	-
HTV-9 (1)	180	119±1	6.92±0.06	5.21±0.06	0.77±0.04	-	0	120±1	10.2±0.07	
HTV-9 (2)	89	123±1	6.97±0.05	5.31±0.02	0.77±0.04	-	0	120±0.4	10.4±0.06	
Shaft 1		125±0	3.65±0.01	2.85±0.02	1.39±0.07	-	0	113±0.1	10.4±0.01	-
MiniSandwich (test 11-14) & Swelling pressure tests 1-16 (IFG)	20	146	7.2	4.0	0.97			104	15	
Swelling pressure tests (CIEMAT)		128/ 132	7.9/ 7.4	5.1/ 5.2	1.1/ 1.2	0.2/ 0.6		138/ 135	11.7/ 12.6	0.6/ 0.7

G Hydration regime HTV-7 to HTV-9

G.1 HTV-7

Tab. G. 1 Pressure steps, holding time of pressure steps and fluid input for HTV-7

Date dd/mm/yyyy	Duration	Pump pressure (P)	Fluid pressure in lower abutment (PP4)	Holding time	Fluid input* (end of step)
	[d]	[MPa]	[MPa]	[d]	[dm³]
05/12/2019	0	-	0	Pre-hydration ES and gravel	47
05/12/2019	0.3	0	0.2	0.1	59
06/12/2019	1.0	0.2	0.3	0.3	78
06/12/2019	1.3	0	0.03	4	79
10/12/2019	5	0.5	0.5	6	81
16/12/2019	11	1.0	1.0	0	117
16/12/2019	11	-	0.6	pump off	117
17/12/2019	12	1.0	1.0	21	123
07/01/2020	33	1.2	1.2	0.1	123
07/01/2020	33	1.5	1.5	1	125
08/01/2020	34	1.8	1.7	0.1	126
08/01/2020	34	2.0	1.8	not held, pressure drop	183
08/01/2020	34	0.8	0.8	slow pressure recovery from this value	185
09/01/2020	35	2.0	1.9	not held, pressure drop	203
09/01/2020	35	1.5	1.5	34	207
12/02/2020	69	1.6	1.6	1	207
13/02/2020	70	1.7	1.7	1	207
14/02/2020	71	1.8	1.8	3	207
17/02/2020	74	1.9	1.8	1	208
18/02/2020	75	2.0	1.9	14	208
03/03/2020	89	2.5	2.4	1	209
04/03/2020	90	3.1	2.9	0.3	231
04/03/2020	90	2.5	2.4	0.1	233
04/03/2020	90	2.0	1.9	55	233
28/04/2020	145	end of pressurization, after correction of the pore volume in the lower abutment:			235

*) into the sealing system without lower gravel abutment

G.2 HTV-8

Tab. G. 2 Pressure steps, holding time of pressure steps and fluid input for HTV-8

Date dd/mm/yyyy	Duration	Pump pressure (P)	Fluid pressure in lower abutment (PP4)	Holding time	Fluid input* (end of step)
	[d]	[MPa]	[MPa]	[d]	[dm³]
04/05/2021	0	-	0	flooding gravel	0
04/05/2021	0.03	0.1	0.25	0.1	26
04/05/2021	0.1	0	0.1	1	28
05/05/2021	1.0	0.3	0.3	0.2	31
05/05/2021	1.1	0.5	0.5	0.1	49
05/05/2021	1.2	0.4	0.4	1	54
06/05/2021	2	0.5	0.6	1	55
07/05/2021	3	0.8	0.8	0.2	56
07/05/2021	3	1.0	1.0	0.0	62
07/05/2021	3	0.8	0.8	5	101
12/05/2021	8	1.0	1.0	6	103
18/05/2021	14	1.5	1.5	7	104
25/05/2021	21	2.0	1.9	20	107
14/06/2021	41	2.5	2.4	16	109
30/06/2021	57	2.9	2.9	12	110
12/07/2021	69	3.5	3.4	14	112
26/07/2021	83	4.0	3.9	14	114
09/08/2021	97	5.1	4.9	15	118
24/08/2021	112	6.1	5.8	70	130
02/11/2021	182	6.5	6.2	7	131
09/11/2021	189	7.0	6.8	20	135
29/11/2021	209	7.5	7.2	36	142
04/01/2022	245	8.0	7.7	7	144
11/01/2022	252	8.5	8.2	7	147
18/01/2022	259	9.3	8.9	55	160[#]
14/03/2022	314	8.2	7.8	7	160[#]
21/03/2022	321	end of pressurization, after correction of the pore volume in the lower abutment:			162[#]

*) into the sealing system without lower gravel abutment
[#]) without leakages

G.3 HTV-9

Tab. G. 3 Pressure steps, holding time of pressure steps and fluid input for HTV-9

Date dd/mm/yyyy	Duration	Pump pressure (P)	Fluid Pressure in lower abutment (PP4)	Holding time	Fluid input* (end of stage)
	[d]	[MPa]	[MPa]	[d]	[dm³]
09/02/2023	start	-	0	flooding gravel	0
09/02/2023	0.0	0	0.06	5	10
14/02/2023	4.9	0.1	0.1	1	12
15/02/2023	6.0	0.2	0.2	0.3	13
16/02/2023	6.9	0.2	0.3	7	22
23/02/2023	14.0	0.3	0.4	5	28
28/02/2023	19.1	0.5	0.5	21	44
21/03/2023	39.9	0.7	0.8	0.2	44
21/03/2023	40.1	1.0	1.0	>163[#]	>122[#]

*) into the sealing system without lower gravel abutment
[#]) status 31/08/2023

H Water content, ion transport and cation exchange in HTV

H.1 HTV-6

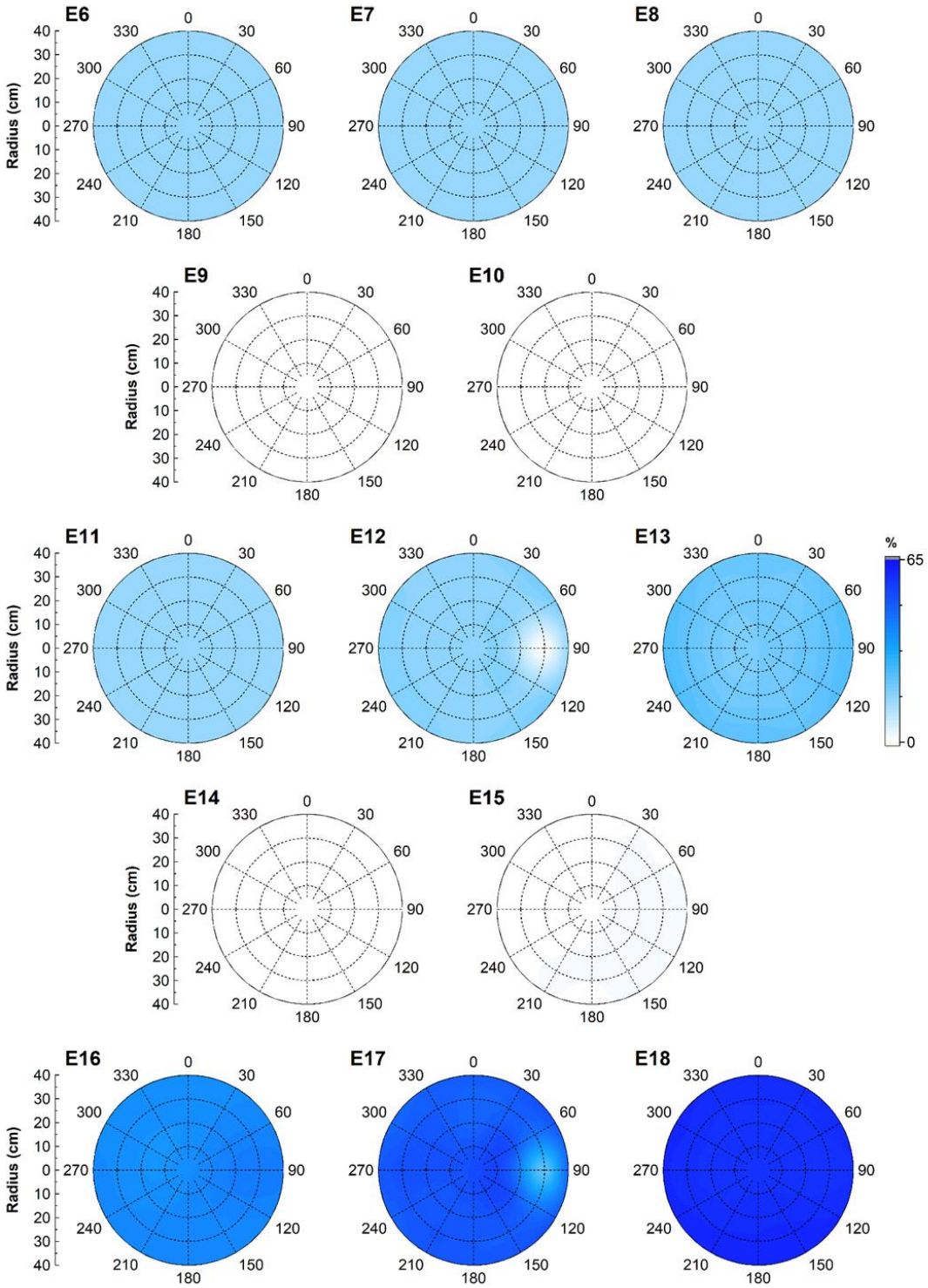

Fig. H. 1 Water content (105 °C) distribution in sampling levels of HTV-6

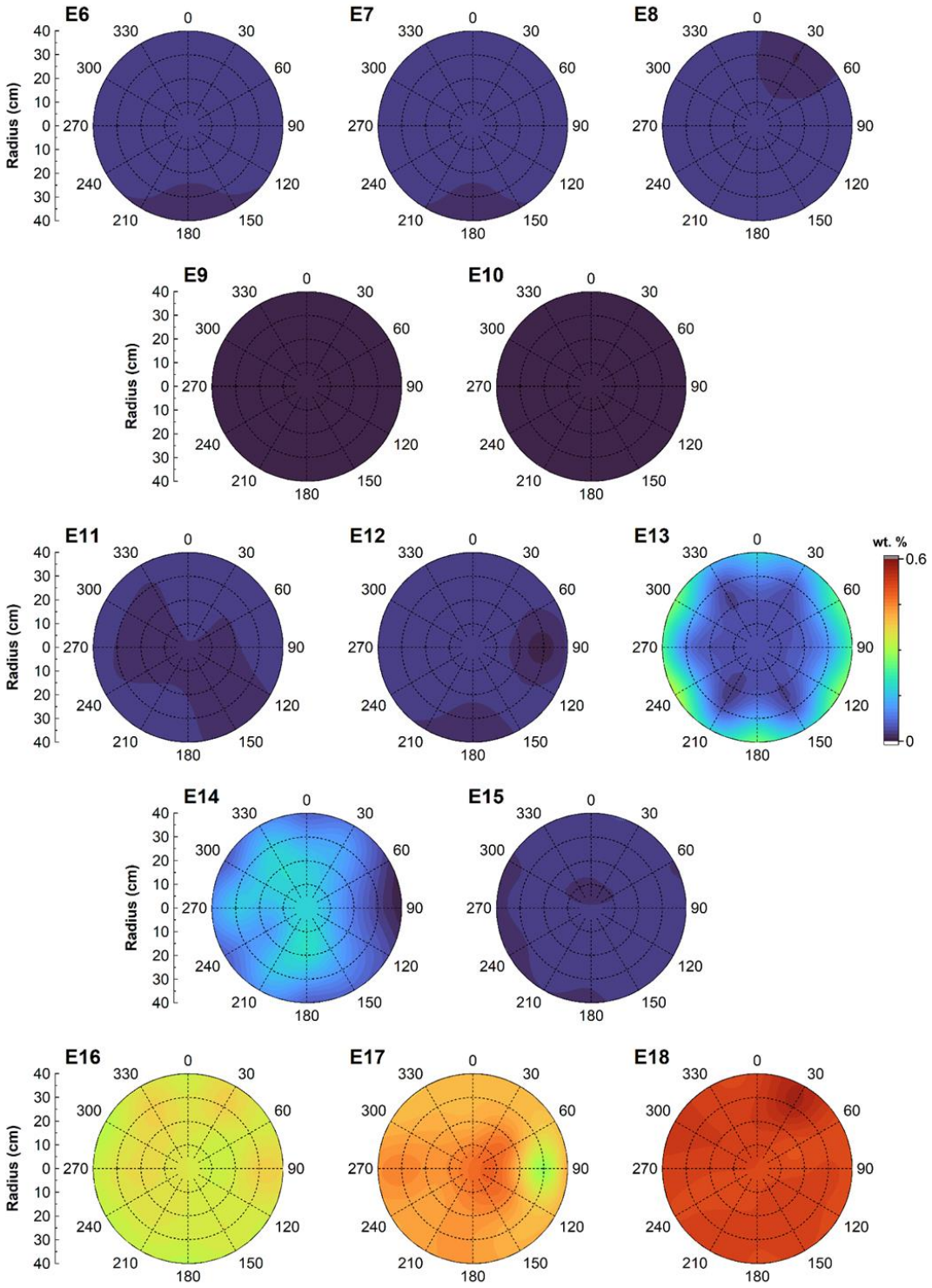

Fig. H. 2 LF salt content distribution in sampling levels of HTV-6

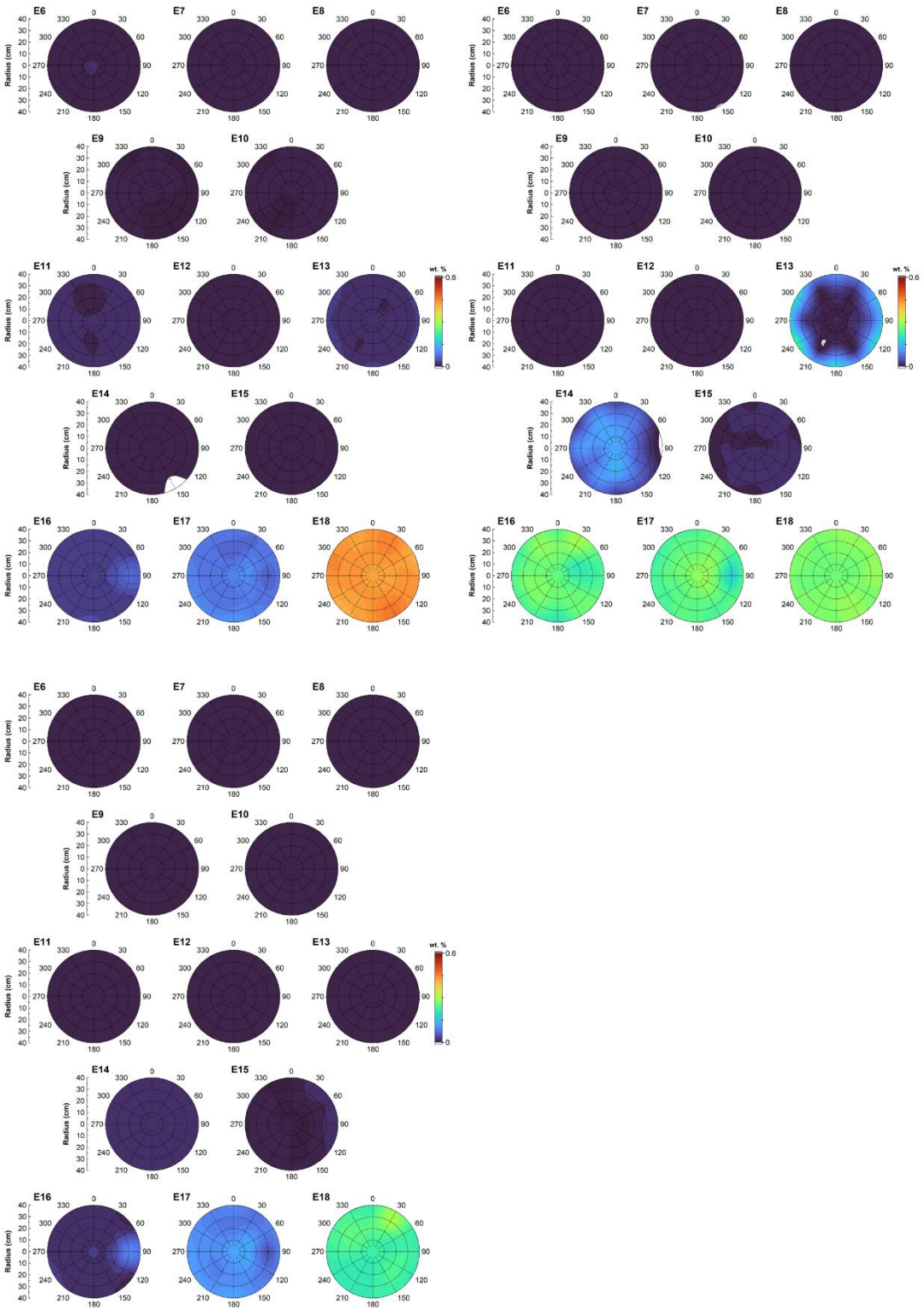

Fig. H. 3 Calculated ion content from LF measurement of HTV-6

Upper left: Na^+, upper right: Cl^-, lower left SO_4^{2-}

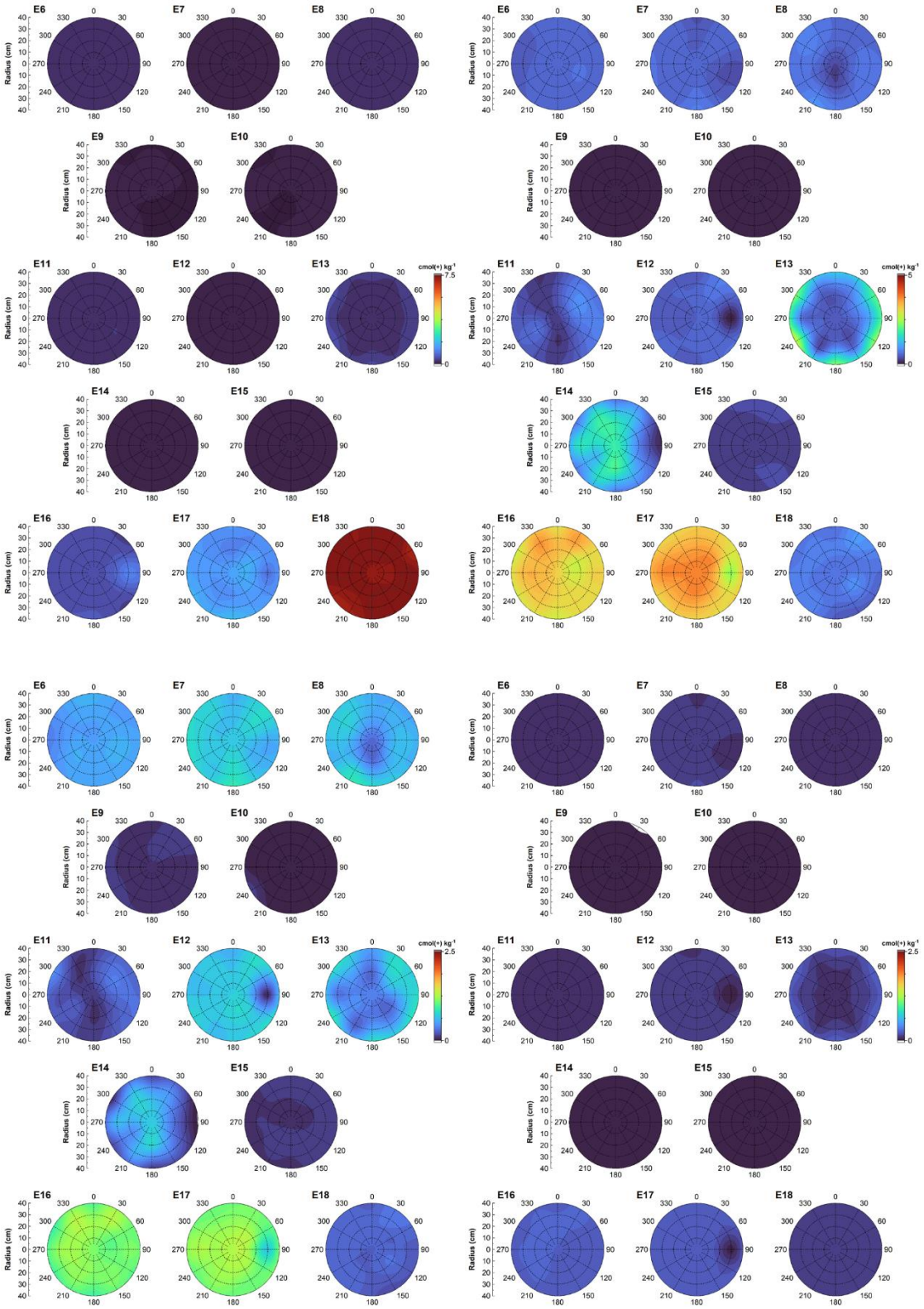

Fig. H. 4 Soluble cation distribution in HTV-6

Upper left: Na^{+}, upper right: Ca^{2+}, lower left: Mg^{2+}, lower right K^{+}

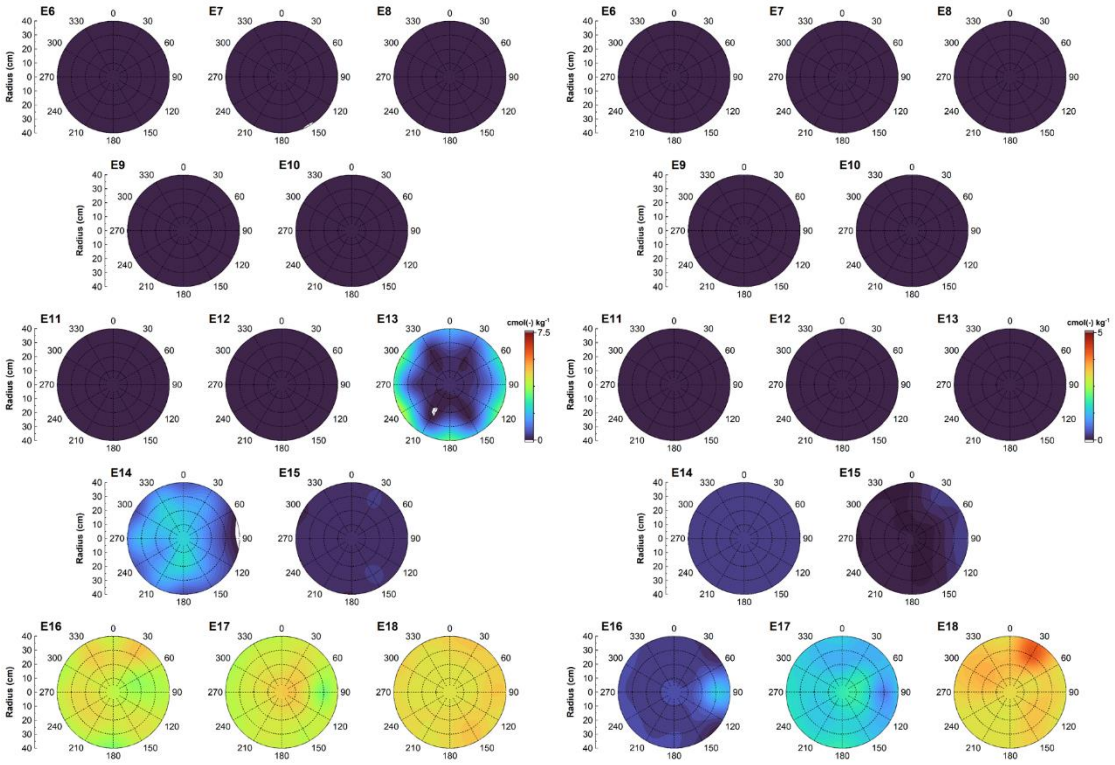

Fig. H. 5 Soluble anion distribution in HTV-6

Left: Cl^-, right: SO_4^{2-}

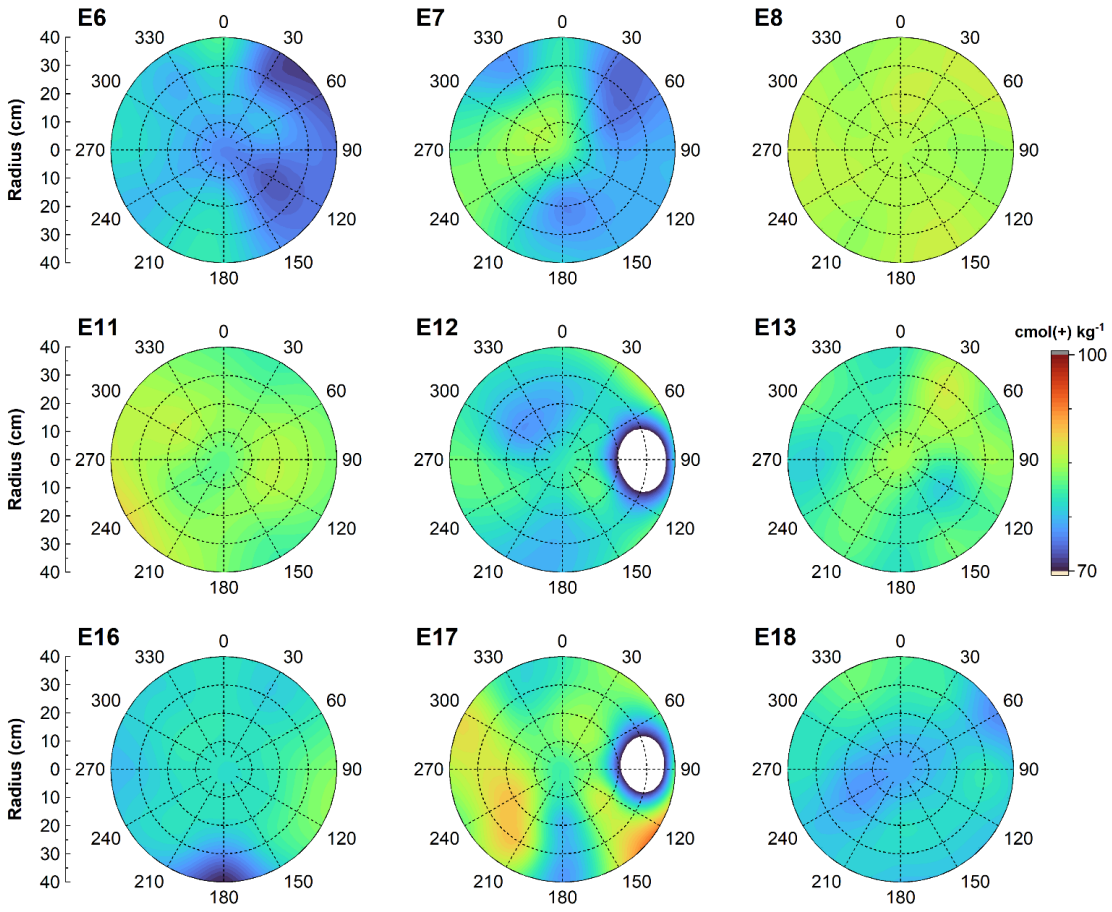

Fig. H. 6 CEC of DS in HTV-6

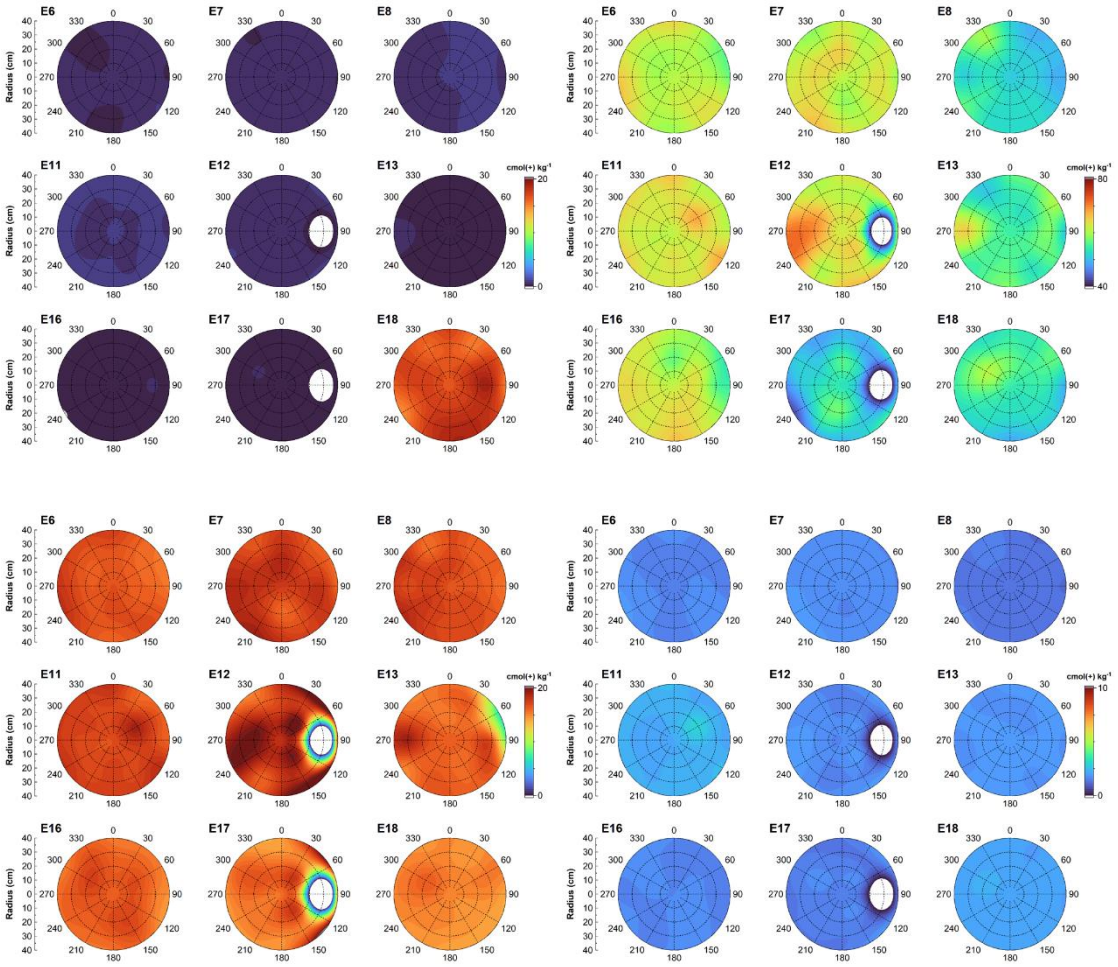

Fig. H. 7 Exchangeable cations in DS of HTV-6

Upper left: Na^{+}, upper right: Ca^{2+}, lower left: Mg^{2+}, lower right K^{+}

H.2 HTV-7

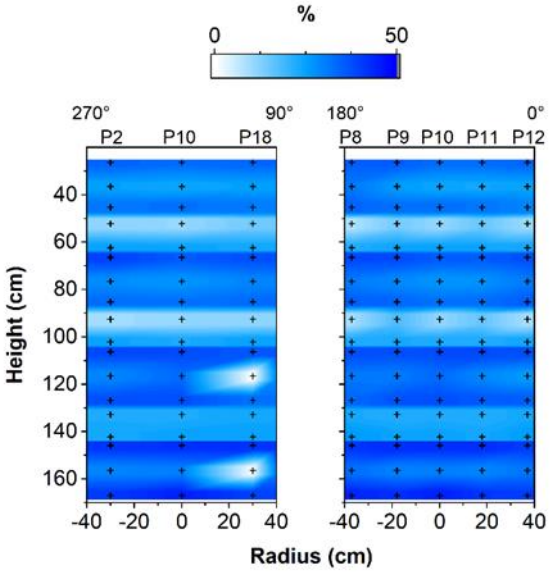

Fig. H. 8 Vertical cross sections (perpendicular to each other) of HTV-7 showing water content distribution

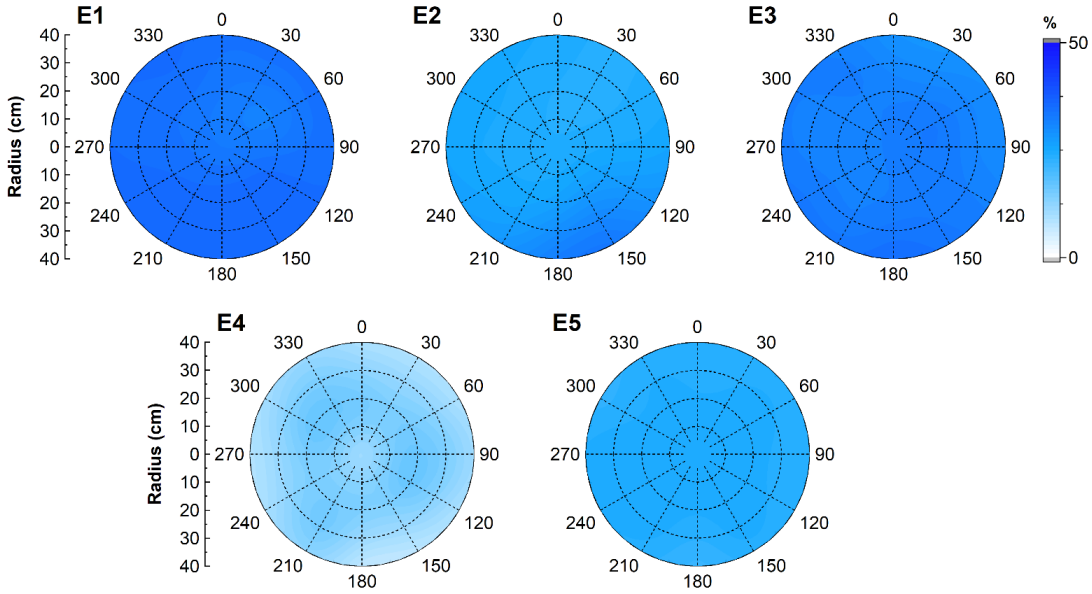

Fig. H. 9 Water content (105 °C) distribution in sampling levels of HTV-7

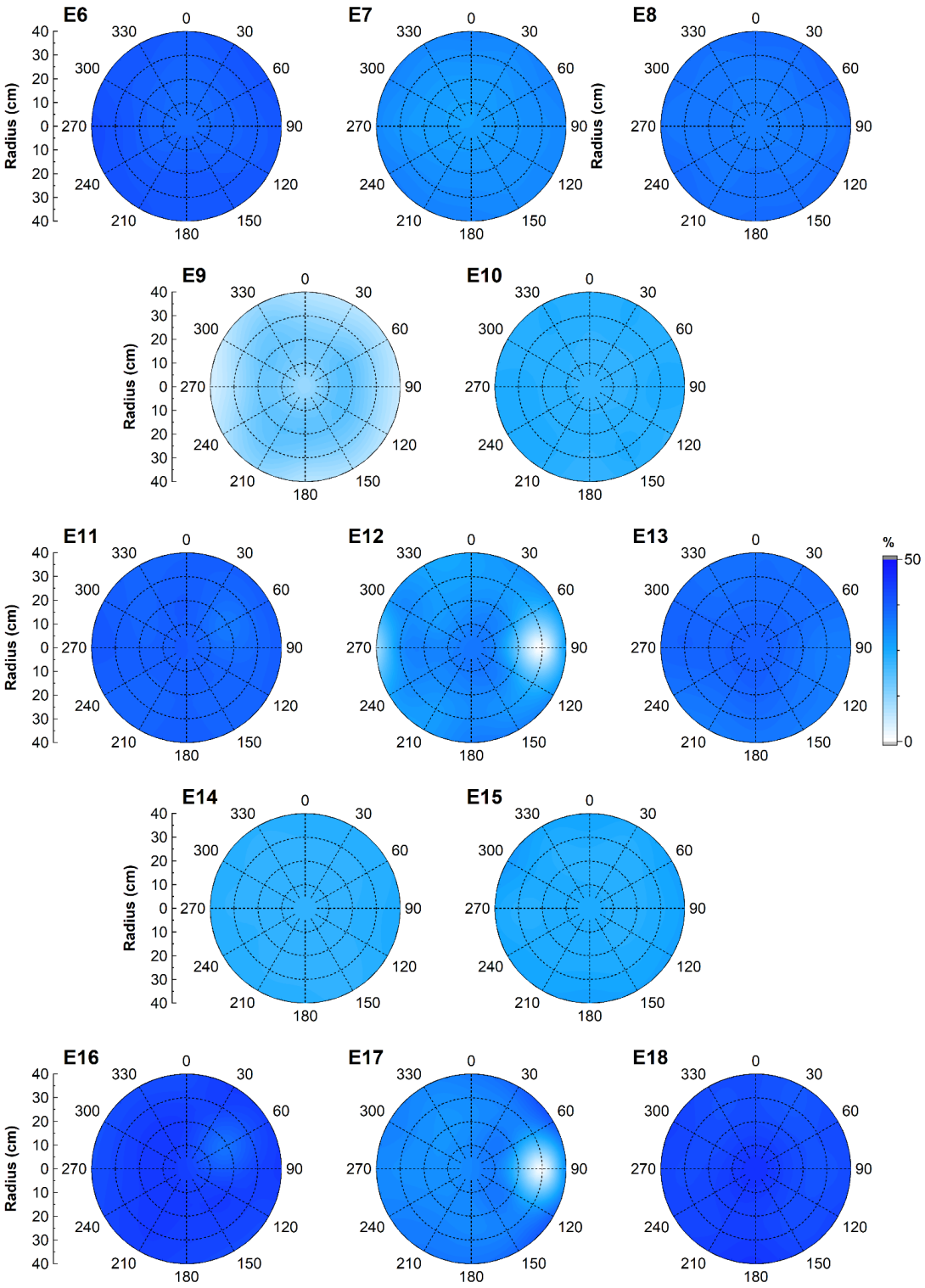

Fig. H. 10 continued: Water content (105 °C) distribution in sampling levels of HTV-7

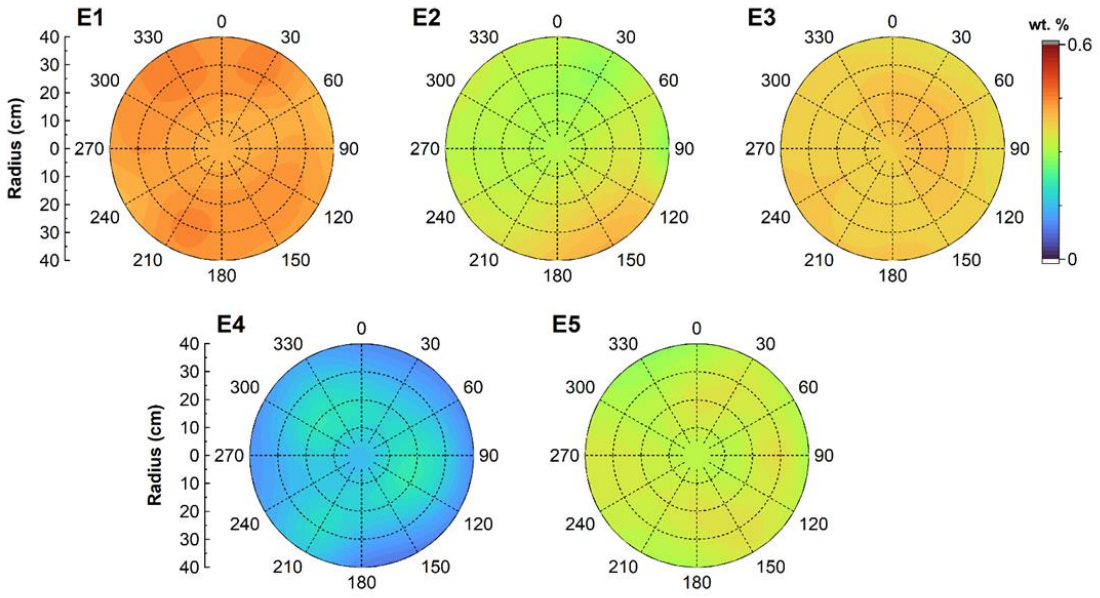

Fig. H. 11 LF salt content distribution in sampling levels of HTV-7

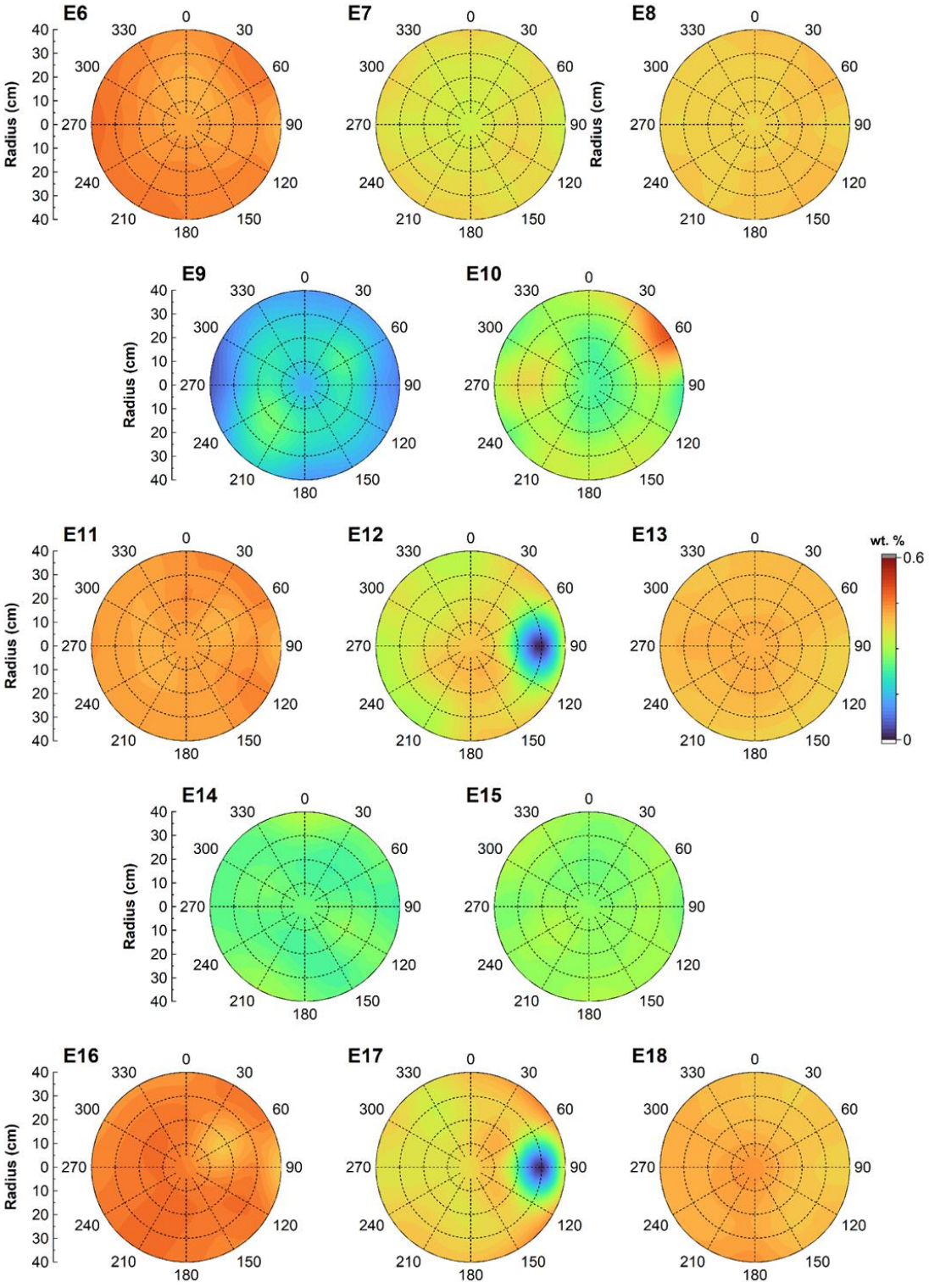

Fig. H. 12 continued: LF salt content distribution in sampling levels of HTV-7

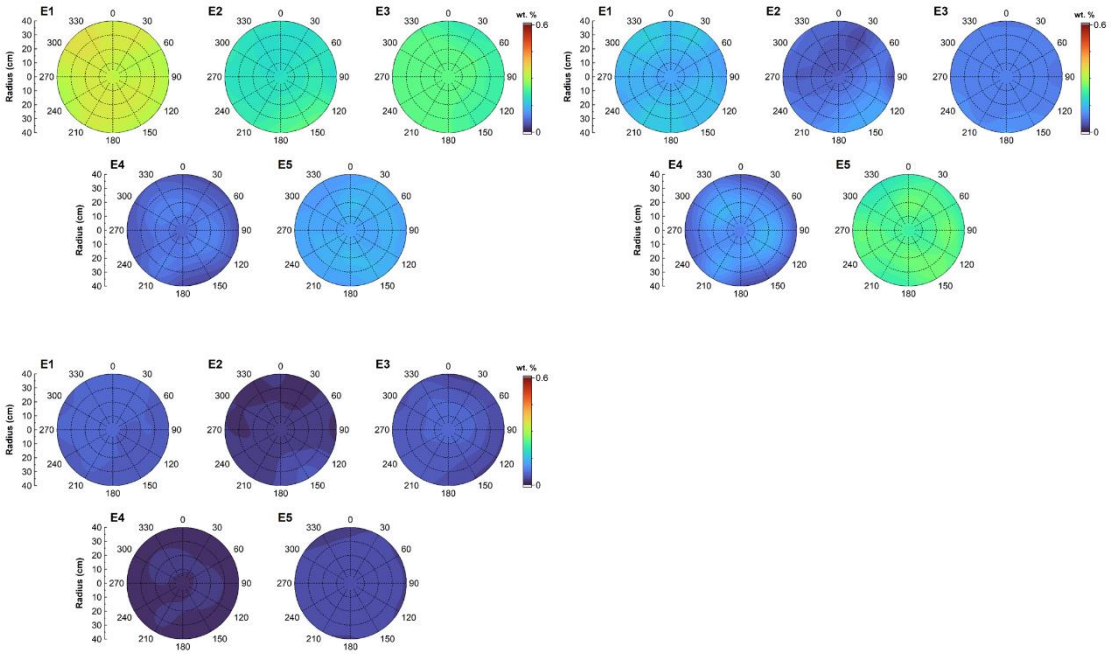

Fig. H. 13 Calculated ion content from LF measurement of HTV-7

Upper left Na^+, upper right Cl^-, lower left SO_4^{2-}

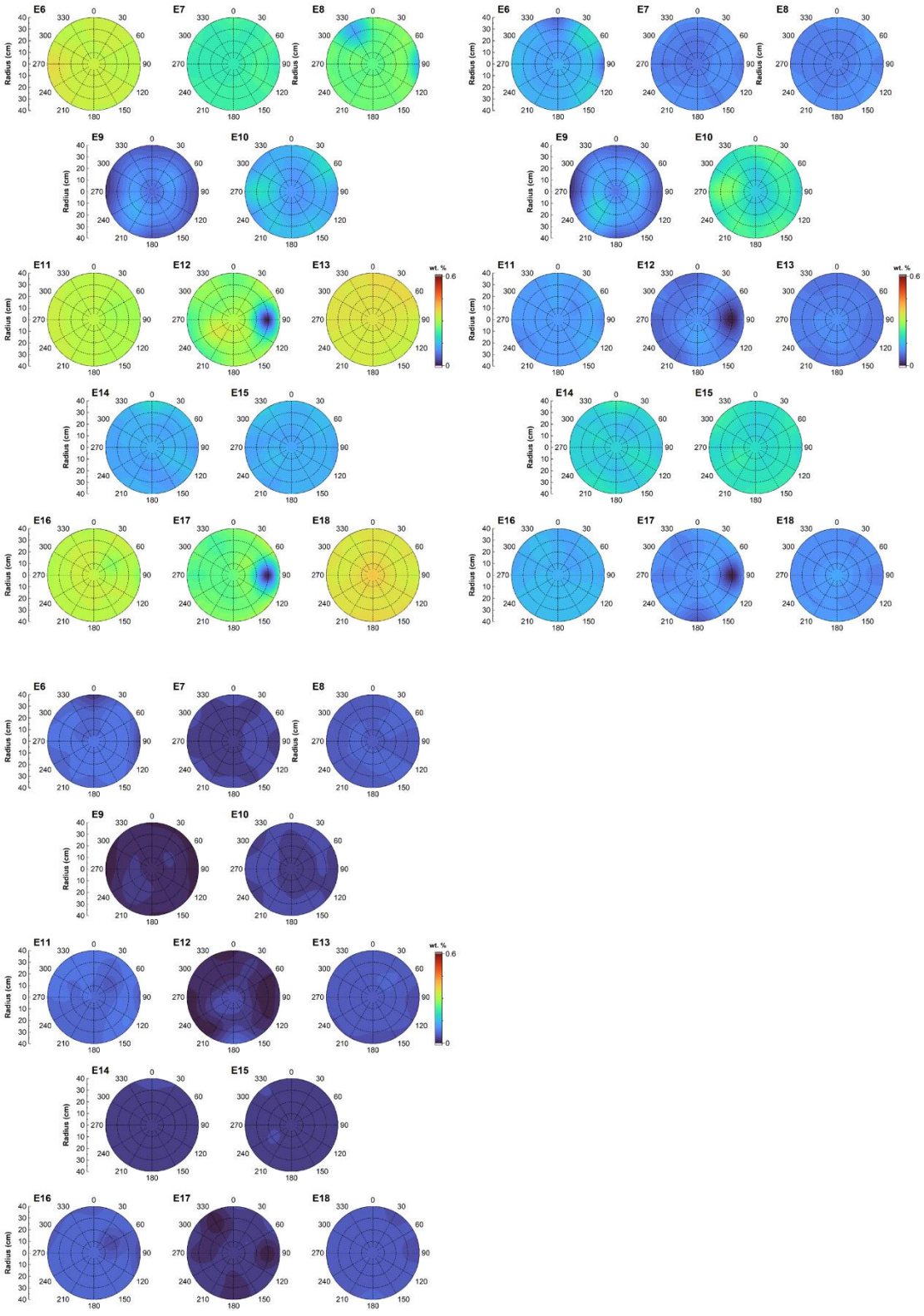

Fig. H. 14 continued: Calculated ion content from LF measurement of HTV-7

Upper left Na^+, upper right Cl^-, lower left SO_4^{2-}

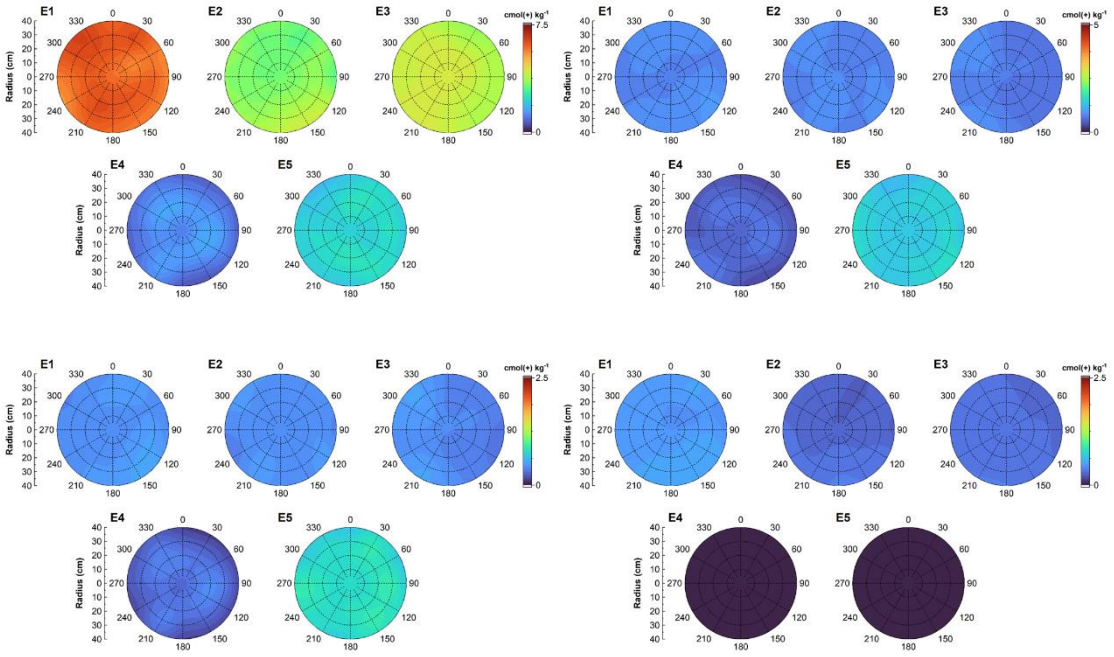

Fig. H. 15 Soluble cation distribution in HTV-7

Upper left: Na^{+}, upper right: Ca^{2+}, lower left: Mg^{2+}, lower right K^{+}

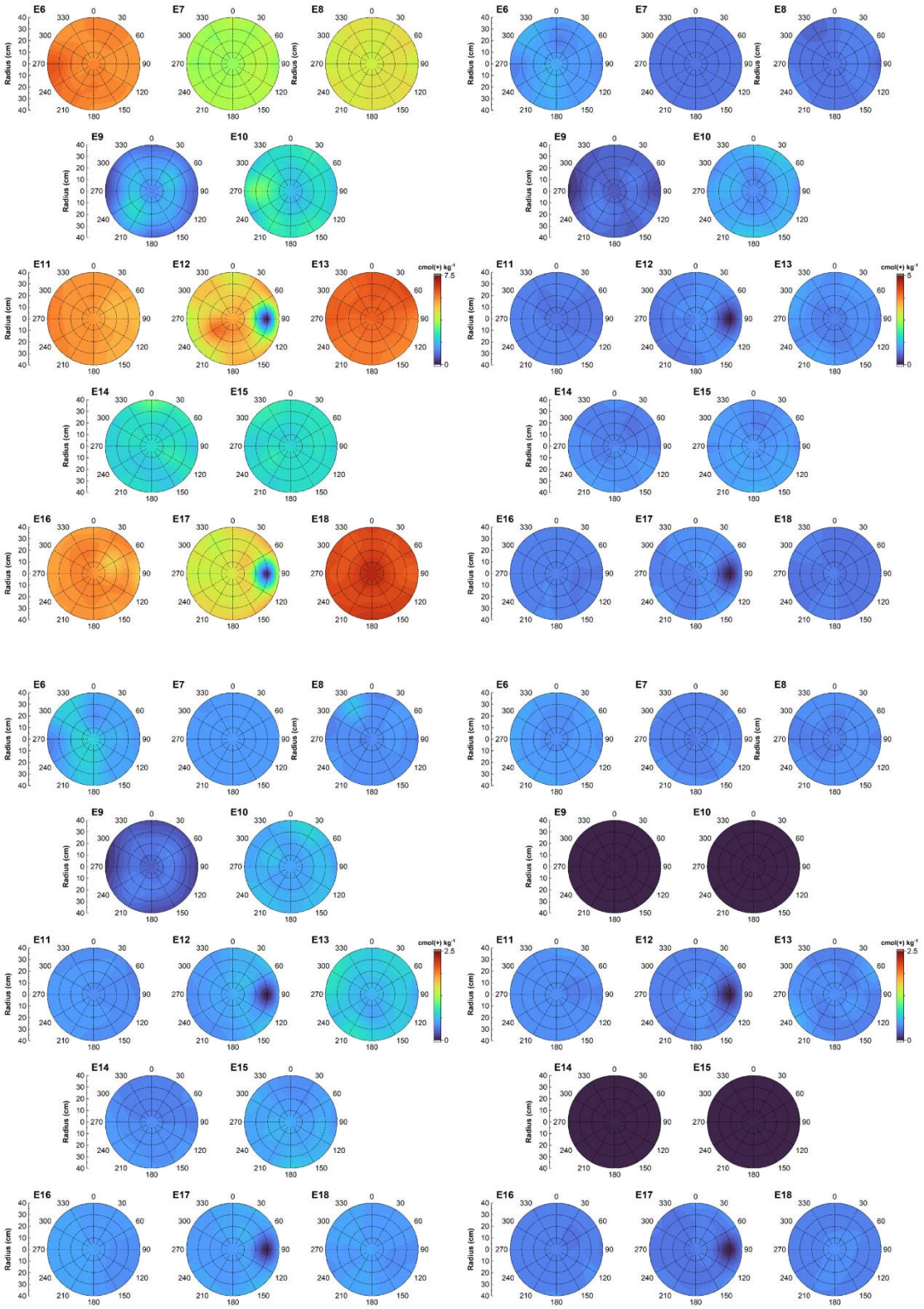

Fig. H. 16 continued: Soluble cation distribution in HTV-7

Upper left: Na^{+}, upper right: Ca^{2+}, lower left: Mg^{2+}, lower right K^{+}

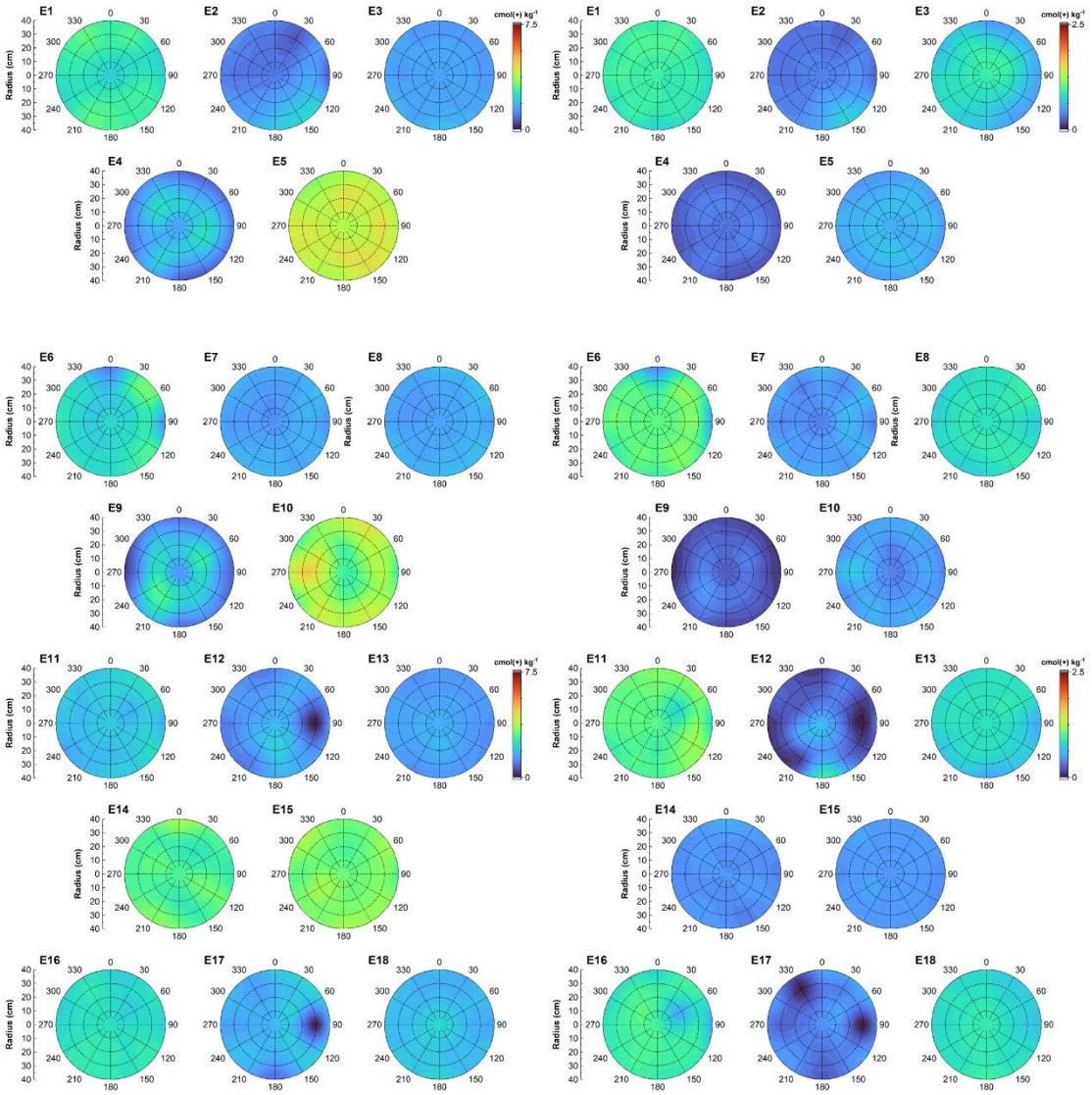

Fig. H. 17 Soluble anion distribution in HTV-7

Left: Cl^-, right: SO_4^{2-}

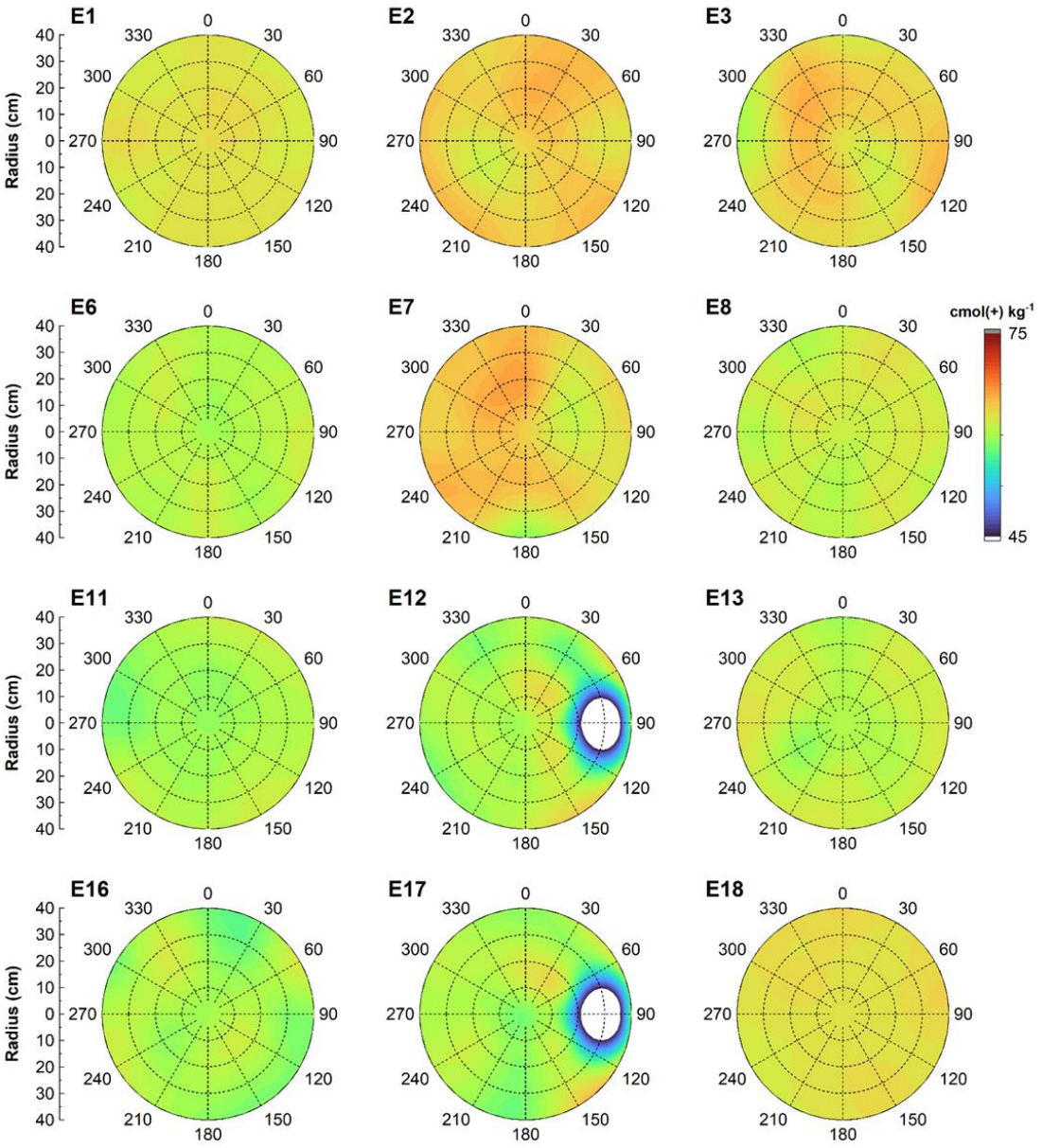

Fig. H. 18 CEC of DS in HTV-7

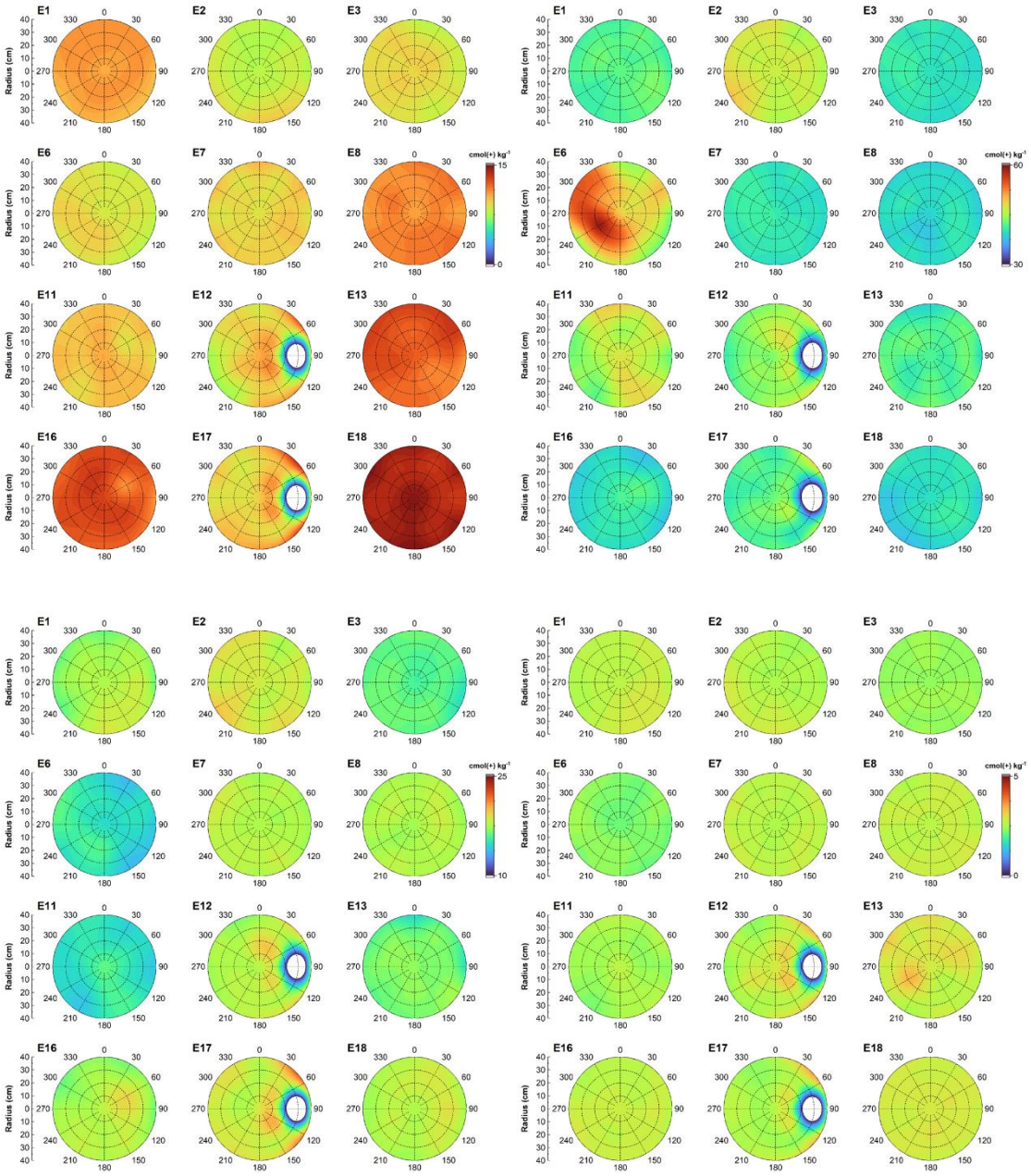

Fig. H. 19 Exchangeable cations in DS of HTV-6

Upper left: Na^{+}, upper right: Ca^{2+}, lower left: Mg^{2+}, lower right K^{+}

H.3 HTV-8

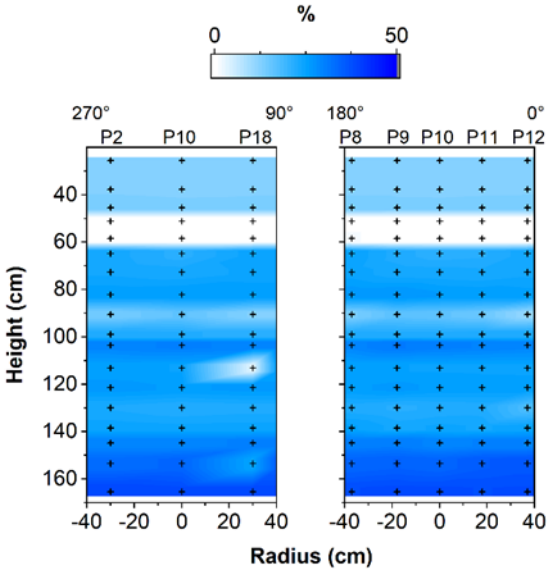

Fig. H. 20 Vertical cross sections (perpendicular to each other) of HTV-8 showing water content distribution

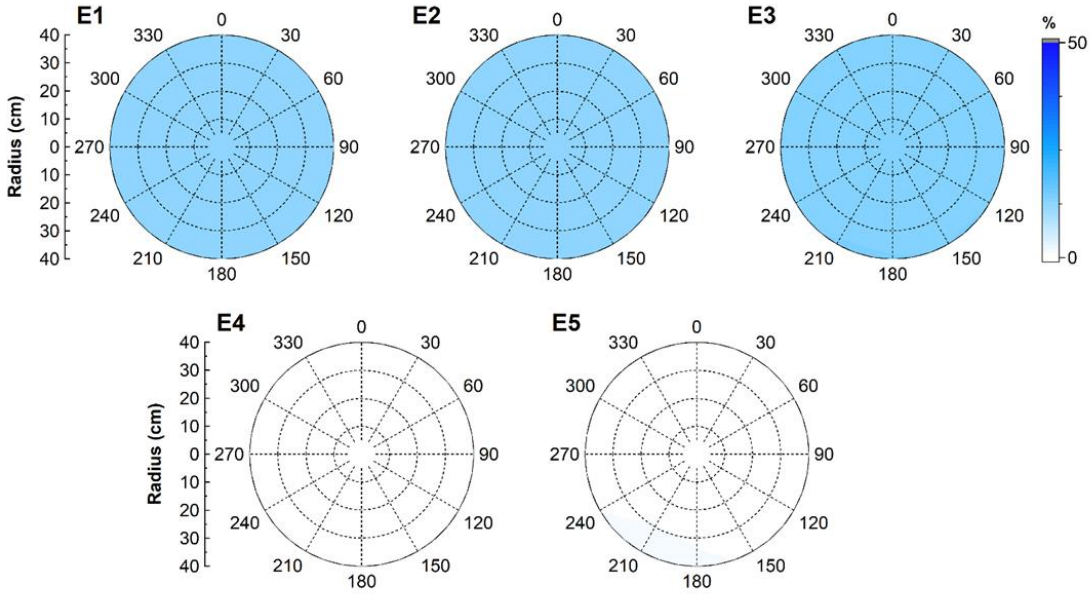

Fig. H. 21 Water content (105 °C) distribution in sampling levels of HTV-8

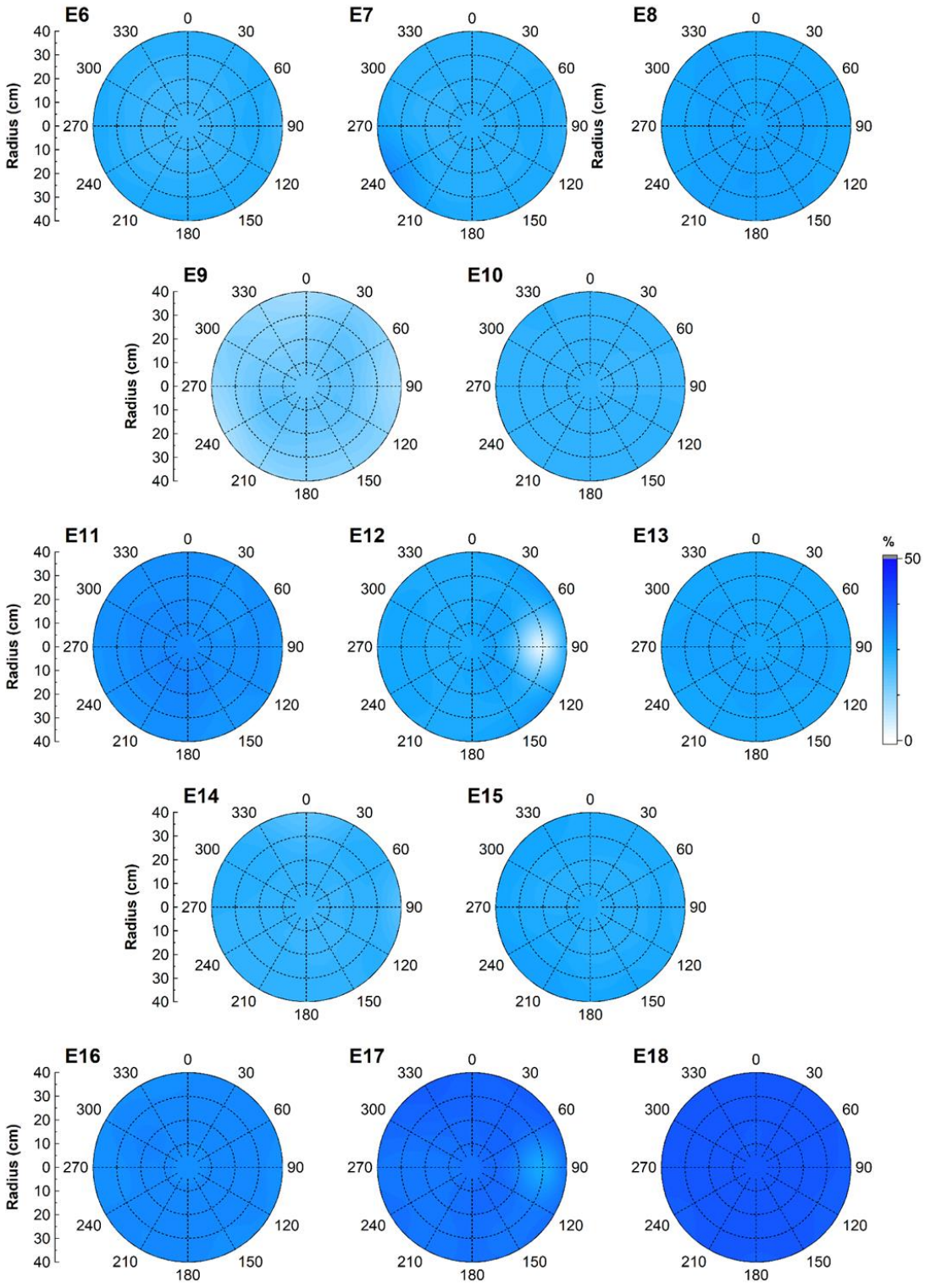

Fig. H. 22 continued: Water content (105 °C) distribution in sampling levels of HTV-8

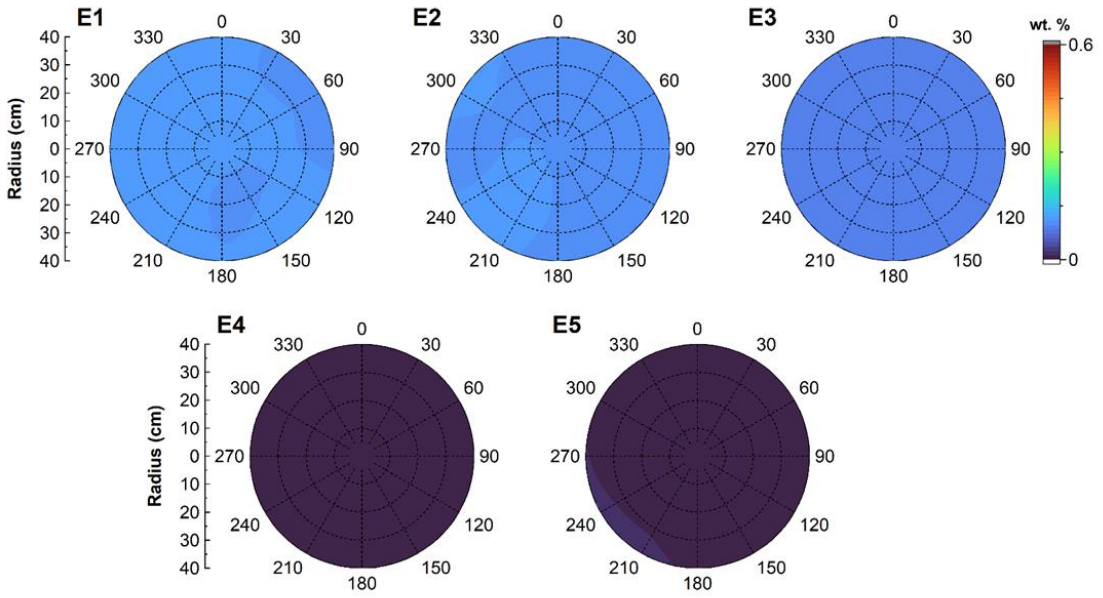

Fig. H. 23 LF salt content distribution in sampling levels of HTV-8

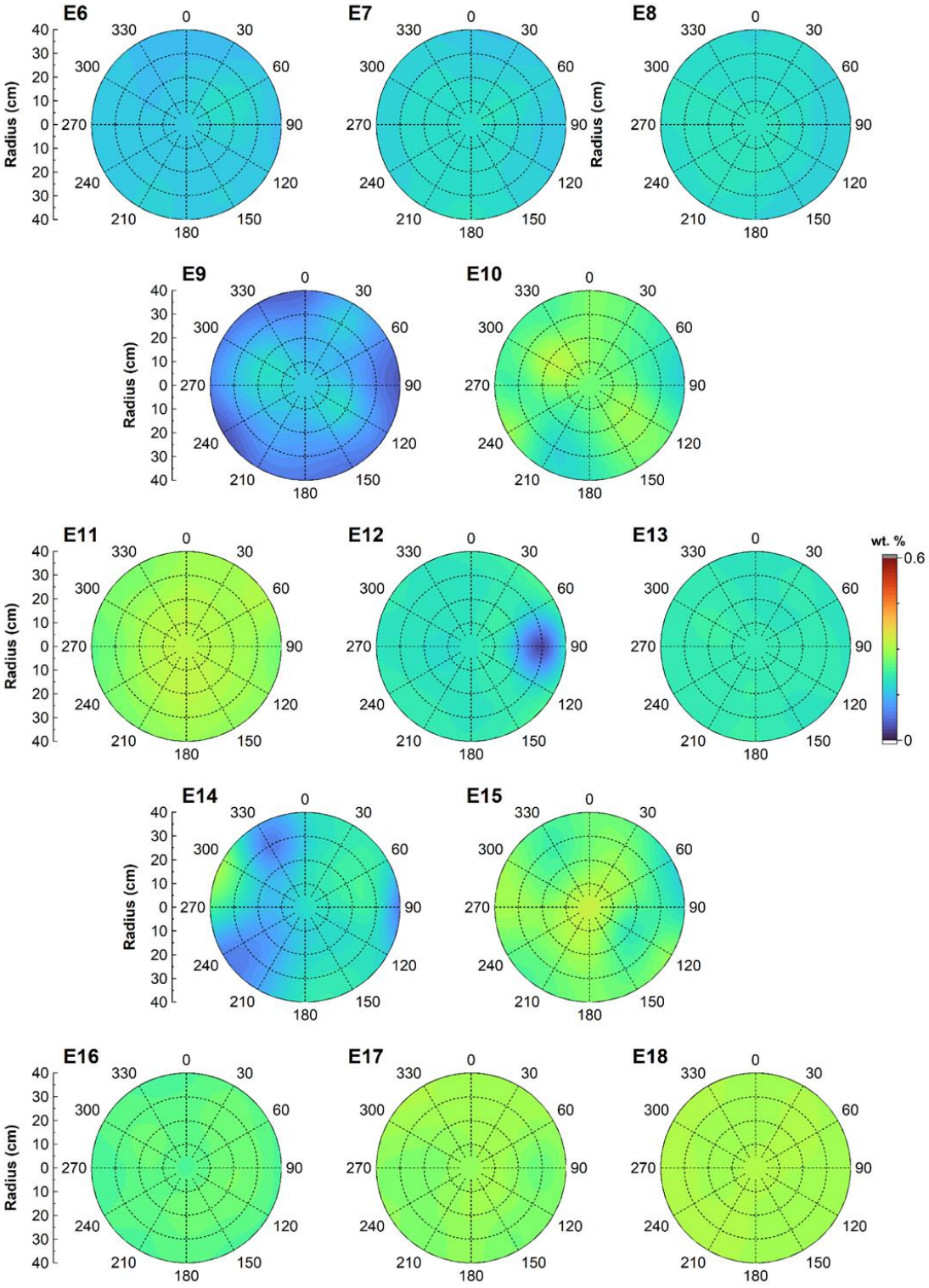

Fig. H. 24 continued: LF salt content distribution in sampling levels of HTV-8

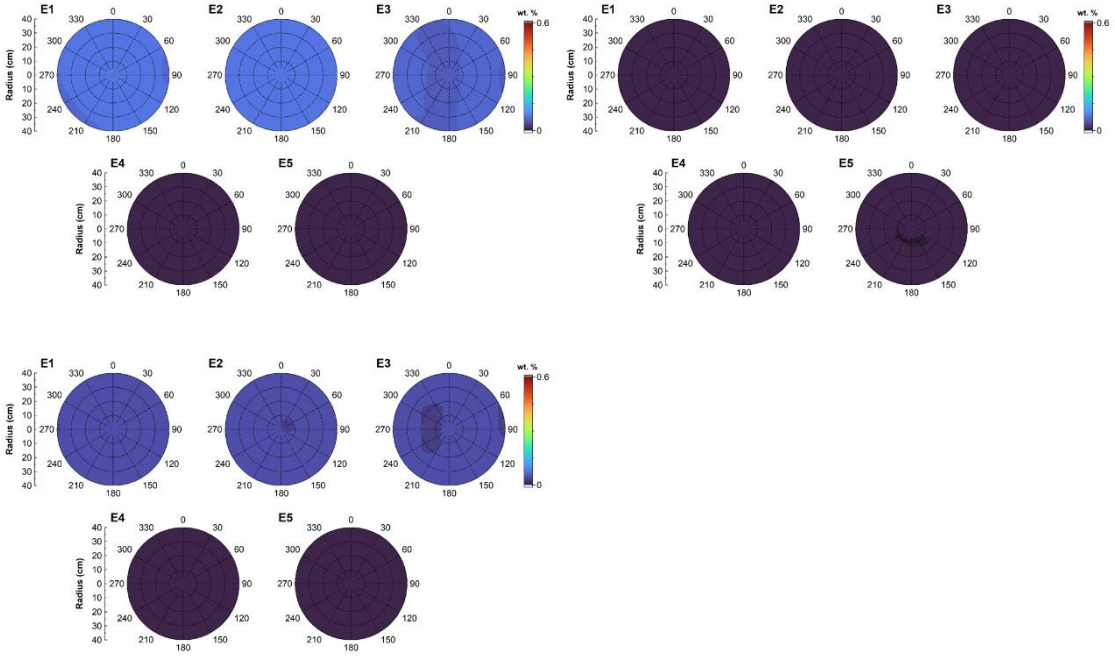

Fig. H. 25 Calculated ion content from LF measurement of HTV-8

Upper left Na^+, upper right Cl^-, lower left SO_4^{2-}

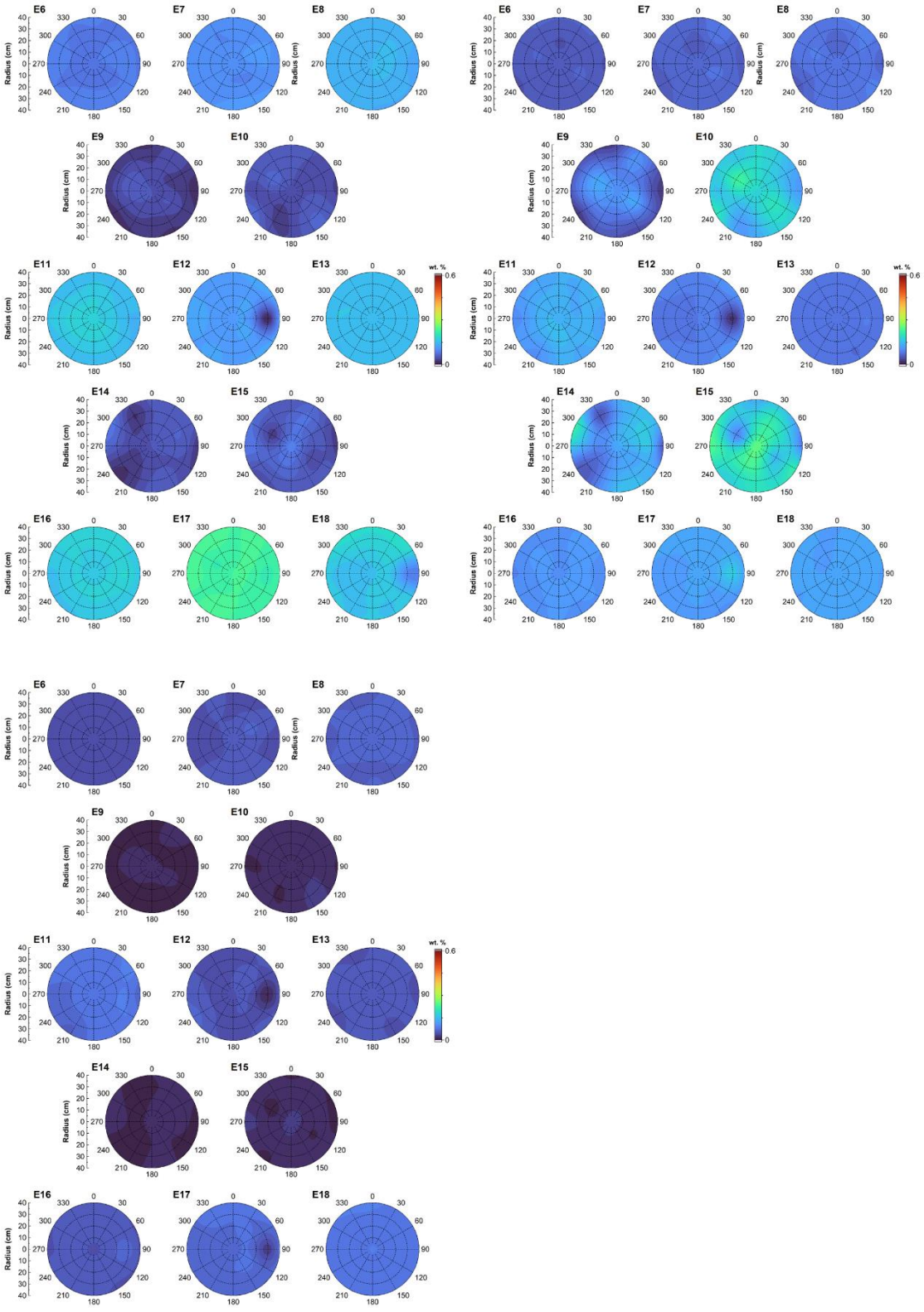

Fig. H. 26 continued: Calculated ion content from LF measurement of HTV-8

Upper left Na^+, upper right Cl^-, lower left SO_4^{2-}

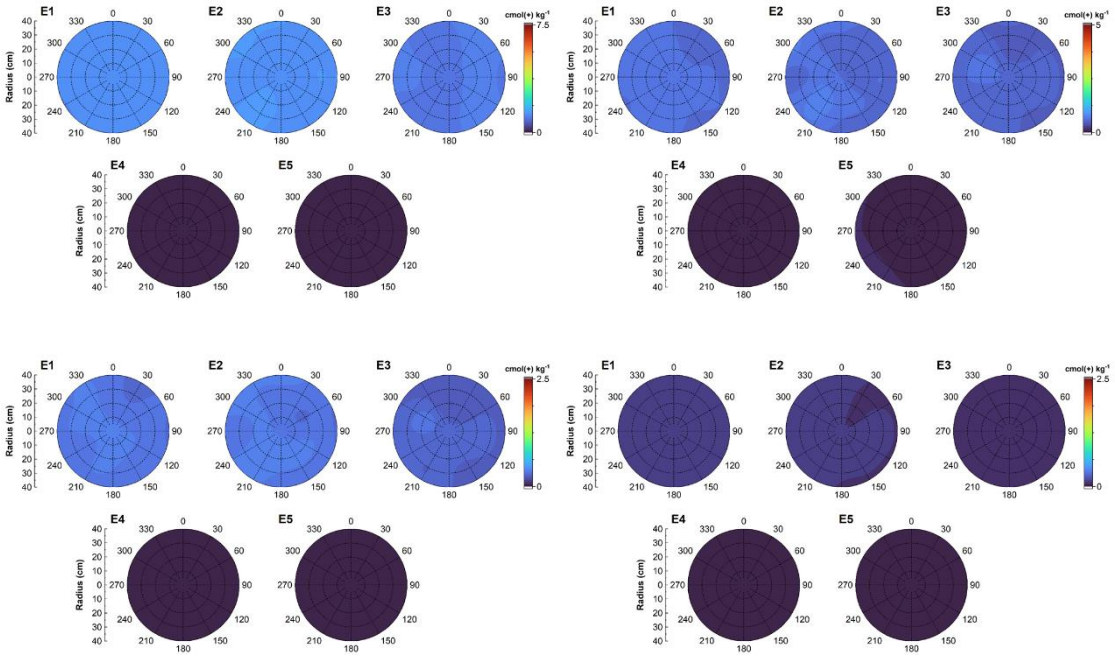

Fig. H. 27 Soluble cation distribution in HTV-8

Upper left: Na^{+}, upper right: Ca^{2+}, lower left: Mg^{2+}, lower right K^{+}

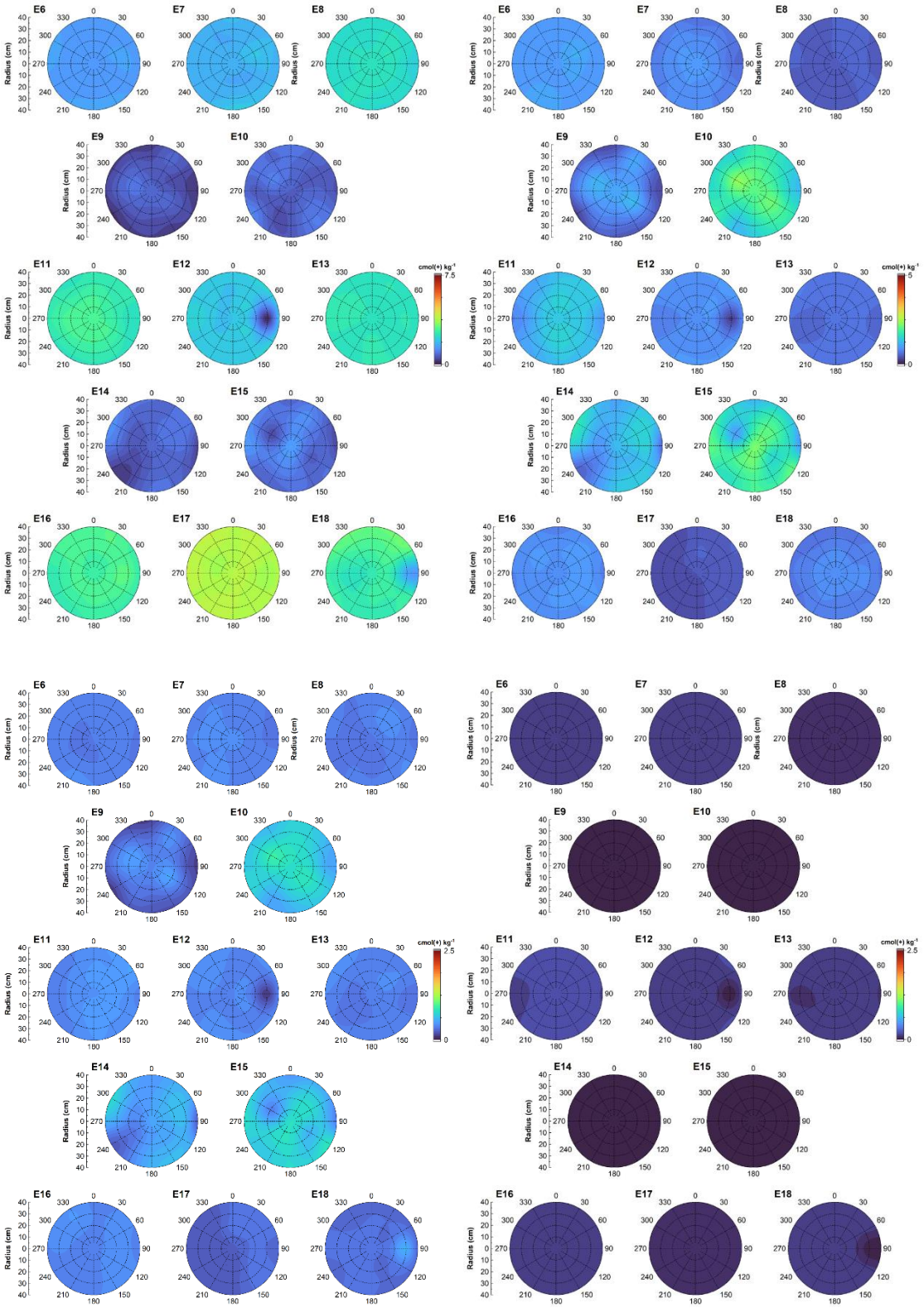

Fig. H. 28 continued: Soluble cation distribution in HTV-8

Upper left: Na^{+}, upper right: Ca^{2+}, lower left: Mg^{2+}, lower right K^{+}

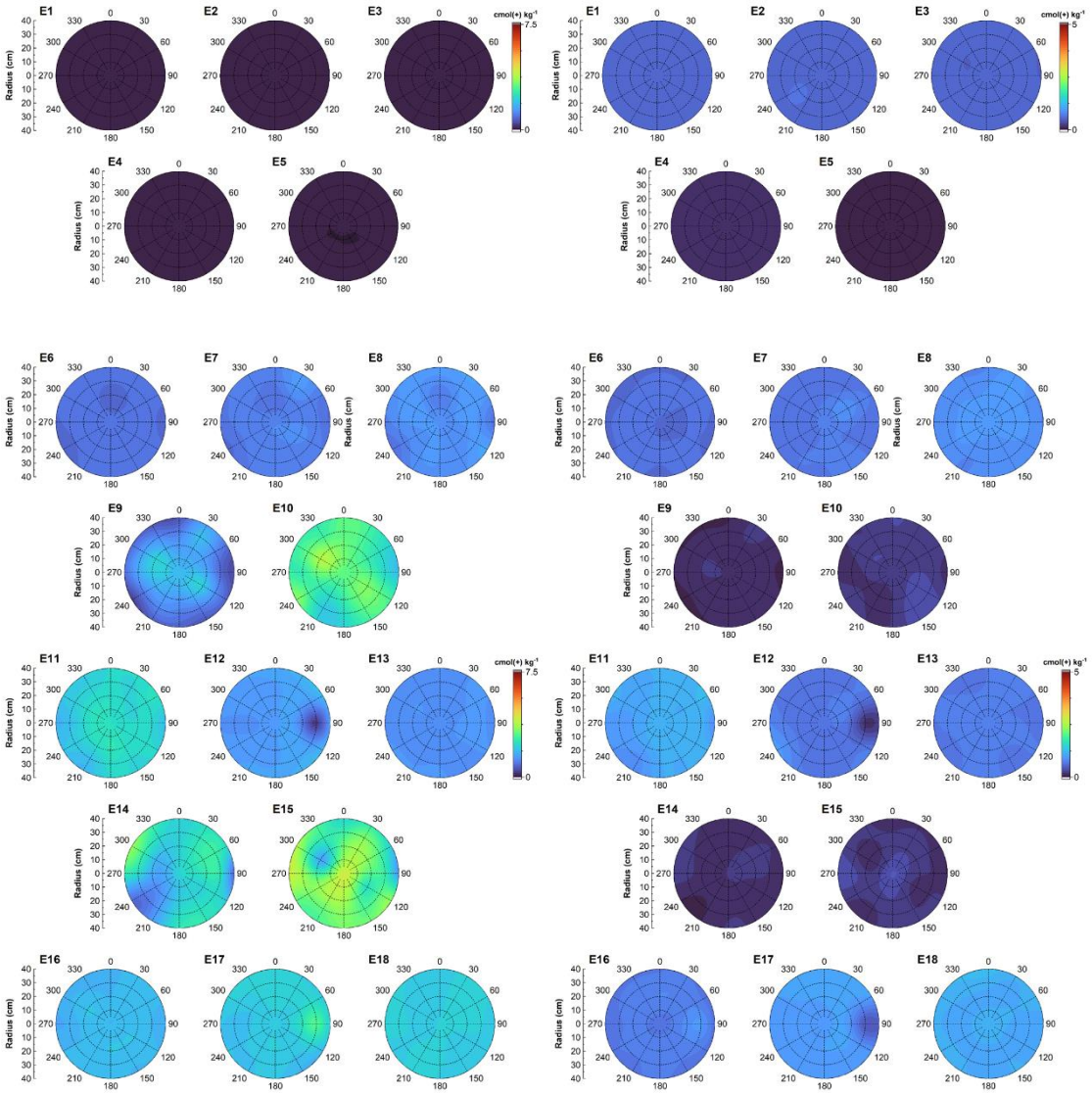

Fig. H. 29 Soluble anion distribution in HTV-8

Left: Cl^-, right: SO_4^{2-}

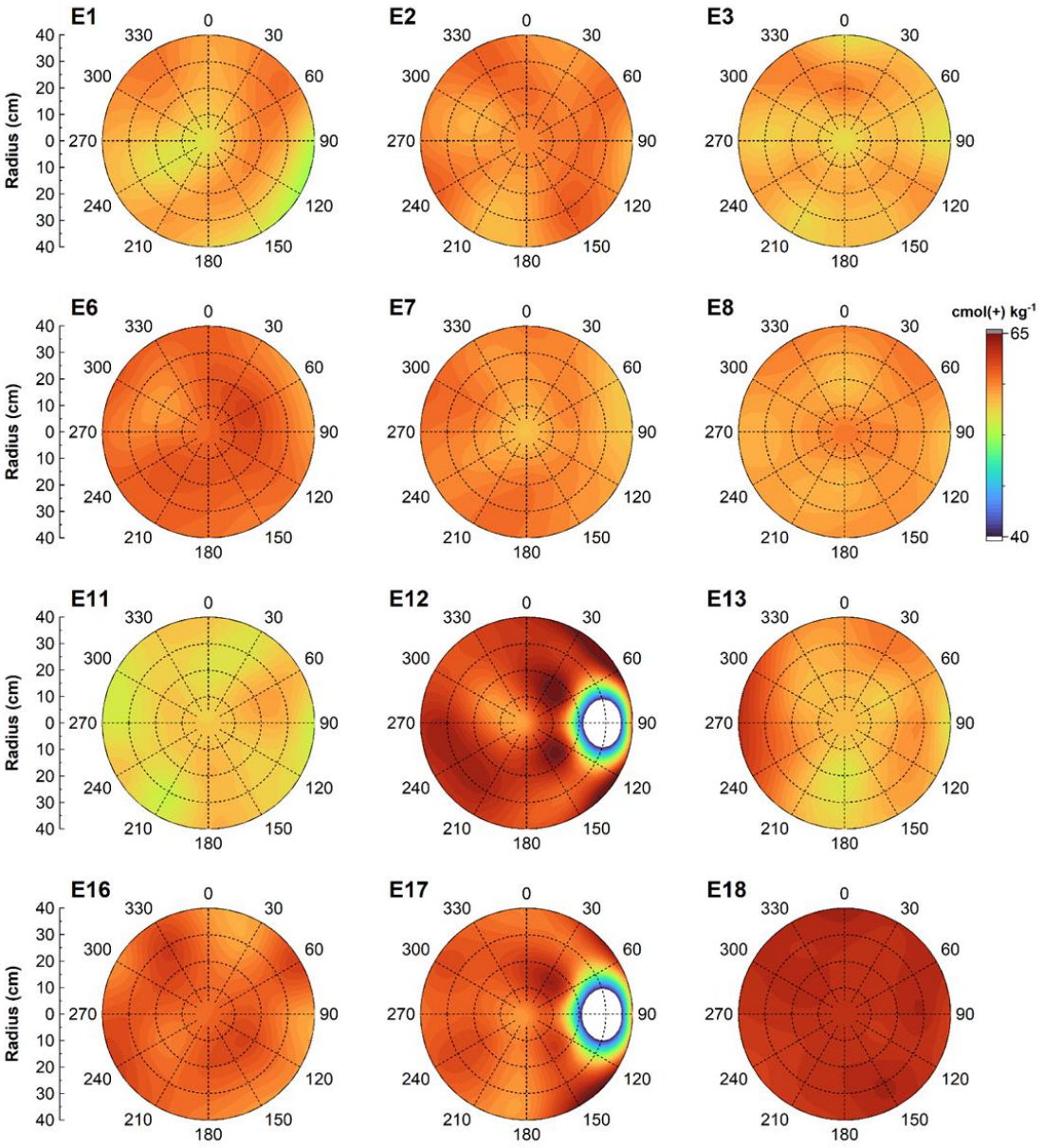

Fig. H. 30 CEC of DS in HTV-8

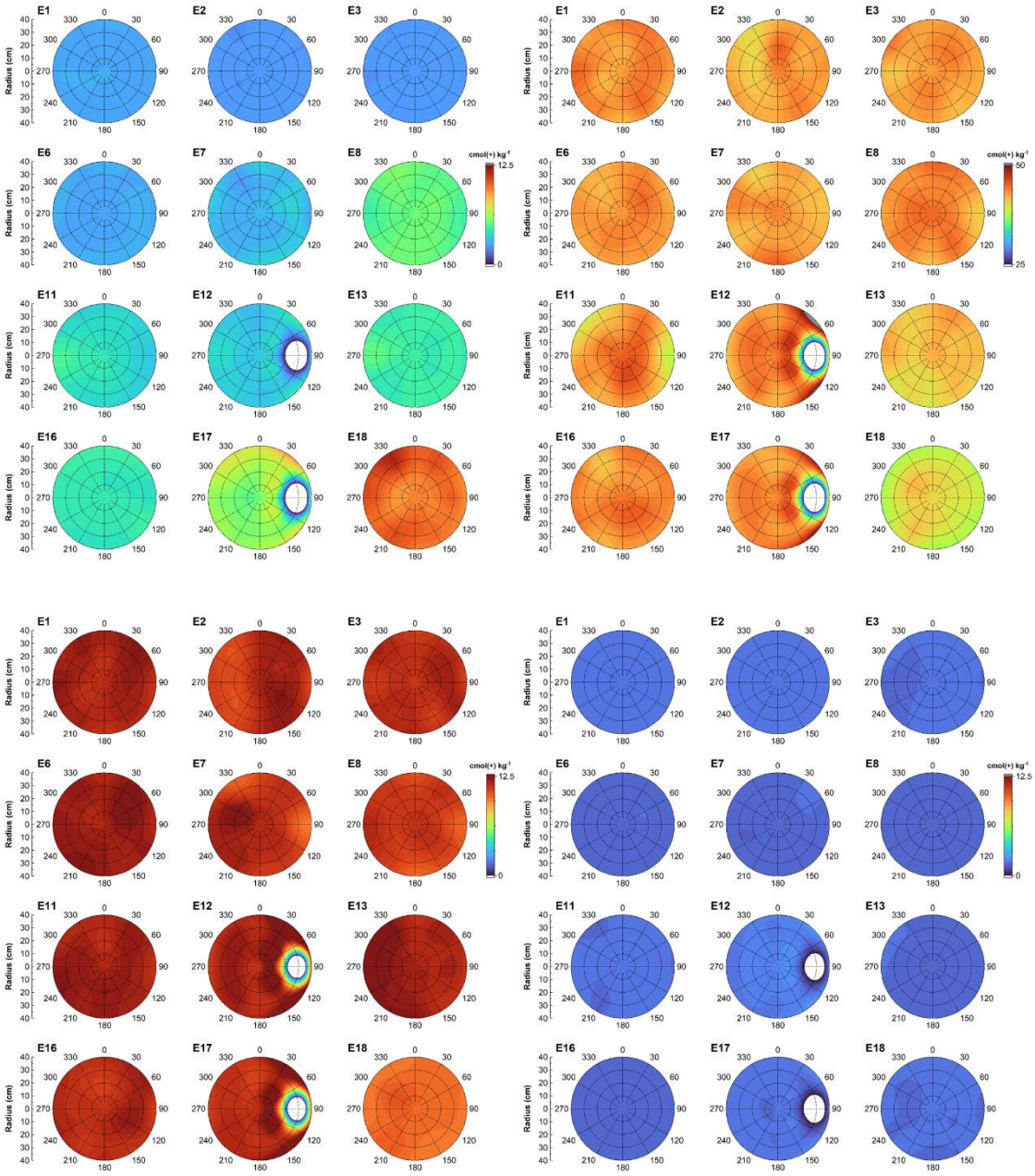

Fig. H. 31 Exchangeable cations in DS of HTV-6

Upper left: Na^{+}, upper right: Ca^{2+}, lower left: Mg^{2+}, lower right K^{+}

Gesellschaft für Anlagen- und Reaktorsicherheit (GRS) gGmbH

Schwertnergasse 1
50667 Köln
Telefon +49 221 2068-0
Telefax +49 221 2068-888

Boltzmannstraße 14
85748 Garching b. München
Telefon +49 89 32004-0
Telefax +49 89 32004-300

Kurfürstendamm 200
10719 Berlin
Telefon +49 30 88589-0
Telefax +49 30 88589-111

Theodor-Heuss-Straße 4
38122 Braunschweig
Telefon +49 531 8012-0
Telefax +49 531 8012-200

www.grs.de

ISBN 978-3-910548-36-7